UNIVERSITÉ DE STRASBOURG

ECOLE DOCTORALE pcp

UNIVERSITÉ DE STRASBOURG

ÉCOLE DOCTORALE DE PHYSIQUE, CHIMIE-PHYSIQUE

Institut de Physique et Chimie des Matériaux de Strasbourg

THÈSE présentée par :

Guillaume FROEHLICHER

soutenue le : **12 décembre 2016**

pour obtenir le grade de : **Docteur de l'université de Strasbourg**

Discipline/ Spécialité : Physique/ Nanophysique

Optical spectroscopy of two-dimensional materials: graphene, transition metal dichalcogenides and van der Waals heterostructures

THÈSE dirigée par:

M. Stéphane BERCIAUD	Professeur, Université de Strasbourg

RAPPORTEURS :

M. Xavier MARIE	Professeur, INSA de Toulouse
M. Francesco MAURI	Professeur, Univerisità di Roma La Sapienza

---

AUTRES MEMBRES DU JURY :

M. Thomas EBBESEN	Professeur, Université de Strasbourg
M. Jean-Jacques GREFFET	Professeur, Institut d'Optique Graduate School
M. Abhay SHUKLA	Professeur, Université Pierre et Marie Curie - Paris VI

À mon père

Contents

Remerciements

Je souhaite tout d'abord remercier chaleureusement les membres de mon jury qui ont accepté d'évaluer mon travail de thèse. J'exprime ma reconnaissance à Jean-Jacques Greffet pour m'avoir fait l'honneur de présider mon jury, à Xavier Marie et Francesco Mauri pour avoir été rapporteurs de cet épais (n'ayons pas peur des mots !) manuscrit, ainsi qu'à Thomas Ebbesen et Abhay Shukla pour avoir été examinateurs, sans oublier le membre invité et collaborateur de l'université du Luxembourg, Ludger Wirtz.

Mes remerciements vont ensuite à Stéphane Berciaud, sans qui ce travail n'aurait pas pu être ce qu'il est. Un énorme MERCI pour m'avoir supervisé (et supporté !) pendant ces quasi quatre années. Je sais, ô combien, que cela n'a pas toujours été facile et que tu as dû user de tous tes talents de docteur (puis de professeur) pour tenter de me guérir de ma « Fröhlichite » chronique. Au final, même si je ne suis peut-être pas encore entièrement guéri, tu m'as « (re)mis sur de bons rails » pour la suite !

Un grand merci à François Federspiel et (Herr Doktor) Dominik Metten qui, à mon arrivée, m'ont tout appris sur la manip. Notre excellente entente, ainsi que l'ambiance de travail dynamique (en musique s'il vous plaît !), ont grandement contribué à la réussite de l'équipe. Je remercie ensuite mes « padawans » : Etienne Lorchat et Olivia Zill. Je leur souhaite bon courage pour cette aventure, avec une mention particulière à Etienne et à sa longue liste de manips. Vous méritez tous les deux la plus grande des réussites. Je tiens également à dire merci à mon fidèle navigateur Florian Godel avec qui j'ai pris plaisir à « naviguer » vers les « îles Graphite », en passant par la Corse bien évidemment. J'en profite pour remercier les premiers postdocs de l'équipe, Kévin Makles et Xin Zhang, avec qui malheureusement je n'ai pas réellement eu la chance de travailler car étant trop occupé à la rédaction de ce manuscrit, ainsi que tous les stagiaires passés dans l'équipe : Rémi Granger, Arthur Baumann, Guillaume Chaumy, François Fernique, Edurne Iriondo, Minghao Li et Jérémie Chrétien. Je leur souhaite à toutes et à tous le meilleur pour le futur.

Je n'oublie pas de remercier chaleureusement les autres membres de l'équipe Nanodispositifs. Tout particulièrement, Fabien Chevrier pour son support technique et Ather Mahmood pour m'avoir initié à la photolithographie d'échantillon de graphène. Merci également à tout le DMONS et à sa secrétaire Véronique Wernher, ainsi qu'à Michelangelo Romeo pour son aide précieuse en LabVIEW, à l'atelier de mécanique, au service informatique et *last*

but not least au personnel de la salle blanche STnano : Sabine Siegwald, Romain Bernard et Hicham Majjad.

Au cours de ces trois années de thèse, j'ai eu la chance de pouvoir enseigner en préparation à l'agrégation de sciences physiques de l'université de Strasbourg. Ce fut une expérience particulièrement enrichissante que j'ai effectué avec un immense plaisir et j'espère que ce plaisir fut partagé ! Merci à Marguerite Barzoukas et Thierry Charitat de m'avoir confié cette mission, et à Anne Flieller et François Stuber pour leur incroyable accueil.

Bien évidemment la réussite de cette thèse doit beaucoup à l'excellent environnement de recherche de l'IPCMS et à tout son personnel permanent et non permanent. Mention spéciale aux vieux briscards Jean-François Dayen, David Halley, Yves Henry, Guillaume Schull et Guillaume Weick avec qui j'ai régulièrement échangé sur des sujets plus ou moins sérieux, et aussi travaillé de temps en temps. Cette formidable ambiance doit également beaucoup à l'ADDEPT et son président emblématique François Roulland, bien épaulé par sa fidèle acolyte Anne Carton, sa trésorière Véronique Pierron-Bohnes, son monsieur communication Marc Lenertz et tous les autres membres du bureau. J'ai pris un réel plaisir à organiser, mais surtout à participer aux différentes activités et événements. Merci et continuez ainsi ! Je voudrais aussi dire merci à mes collègues de bureau, Olga Gladii, Vadym Iurchuk et Julien Bran, que j'ai probablement dérangé plus d'une fois, mais qui ont rendu mes journées agréables. Enfin, je remercie chaudement toutes les personnes de la « place du café » (pour n'oublier personne) avec qui j'ai partagé de nombreux cafés, mais pas que.

Avant de terminer ces remerciements, il me faut encore dire merci aux personnes qui ont pris sur leur temps pour relire une partie de ce manuscrit : Micheal Chong, François Federspiel, Dominik Metten, Henrique Miranda, Guillaume Point et Olivia Zill.

Pour finir, je remercie mes amis de la TS3 & Co, mes amis « chimistes », les Wolfies, mon binôme d'agreg, Pierre, et toute ma famille pour m'avoir encouragé tout au long de ma thèse et pour être venus en nombre à ma soutenance. Un merci tout particulier aux personnes qui ont participé à la préparation du pot de thèse. Je conclus ces remerciements en les adressant à ma mère, Martine, qui n'a jamais cessé de me soutenir tout au long de ma scolarité et bien sûr à ma femme, Steffi, qui m'a supporté au jour le jour même dans les moments difficiles. Mille mercis, sans toi ce travail n'aurait pas été possible.

Chapter 1

Introduction

General introduction

The famous Noble Prize physicist Richard Feynman in his visionary 1959 lecture *There's plenty of room at the bottom* [Feynman60] was asking "What could we do with layered structures with just the right layers?". More than half a century later, we are close to answering this question and echoing his intuition "we will get an enormously greater range of possible properties".

Layered materials are composed of covalent crystalline layers stacked through weaker van der Waals interactions. Because these layers are one or few atoms thick, they are said to be two-dimensional. Such materials are known for a long time and are currently employed in the industry, especially as dry lubricants [Hilton92]. However, in the past twelve years, they have attracted tremendous attention. Indeed, in 2004 and 2005, Geim and Novoselov (Nobel Prize in Physics in 2010) have shown that one or few layers can be isolated using adhesive tape [Novoselov04, Novoselov05b] without damaging the crystallinity owing to the strong in-plane covalent bonds and weak out-of-plane van der Waals forces.[1] Surpringly, two-dimensonal crytals are experimentally stable contrary to theoretical predictions that they should be thermodynamically unstable (e.g., see [Landau80]). Due to their reduced dimensionality, they show very different properties from their three-dimensional bulk counterparts, making them ideal candidates to investigate the effects of dimensionality, and are highly sensitive to their local environment.

Figure 1.1 gives an overview of the broad catalogue of two-dimensional materials which goes from metal and semimetal to semiconductor and insulator. Among them, graphene, and the vast family of transition metal dichalcogenides are currently the most actively investigated layered crystals. Graphene is a one-atom thick single layer of graphite. As a

[1] Interestingly, decades ago Frindt and coworkers have already demonstrated that these materials can be mechanically exfoliated using adhesive tape down to few layers [Frindt66] and even monolayers [Joensen86]. Unfortunately, their work has not been noticed by the scientific community.

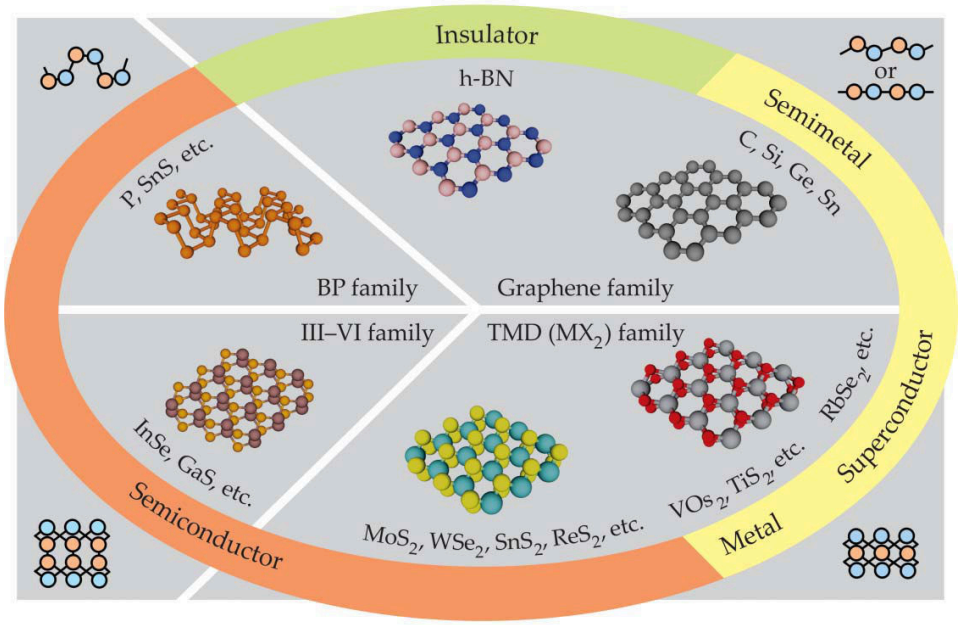

Figure 1.1 *– The world of two-dimensional materials. It is composed of graphene and its analogues, especially hexagonal boron nitride; black phosphorus (BP) and its analogues; the III-VI family of semiconductors; and the transition metal dichalcogenides (TMDs). The properties of these materials are ranging from semimetal and metal to semiconductor and insulator. The cross section of the different materiald are sketched at the four corners. Most are not strictly planar. Figure extracted from Ref. [Ajayan16].*

genuine two-dimensional electron gas, it is endowed with unique electrical [Novoselov04, Zhang05, Novoselov05a], optical [Mak08, Nair08, Mak12b], thermal [Ghosh10] and mechanical [Lee08] properties, widely tunable by doping, strain, external fields and environmental effects. Transition metal dichalcogenides, with chemical formula MX_2 (where M is transition metal and X a chalcogen) [Frindt63, Wilson69, Chhowalla13, Xu13], offer a broad range of physical properties. In particular, the three-atom thick single layer of semiconducting transition metal dichalcogenides displays exceptional optoelectronic properties in the visible and near-infrared that are distinct from their bulk counterpart [Wang12, Xia14, Mak16], together with a valley pseudospin that can be exploited to process information [Xu14].

Furthermore, because the surfaces of two-dimensional materials display no dangling bonds and because layers are coupled by van der Waals interactions, it is possible to artificially stack these layered materials in any chosen sequence to form so-called van der Waals heterostructures [Geim13]. Compared to traditional epitaxial heterostructures, which are widespread in industrial applications [Alferov01], van der Waals heterostructures do not suffer from 'lattice mismatch' problems. Due to the diversity of layered materials, there is a large amount of possibilities that pave the way towards new physical phenomena. Let us mention two remarkable examples. First, the Hofstadter butterfly, predicted by Hofstadter [Hofstadter76], was experimentally observed in the energy spectrum of graphene stacked on hexagonal boron nitride (hBN, which is an insulator see Fig. 1.1) [Dean13, Hunt13, Ponomarenko13]. Second, superfluidity at high temperature of indirect excitons, where electrons are in one layer and holes in another, has been predicted

in transition metal dichalcogenides based heterostructures [Fogler14]. In addition to van der Waals heterostructures, two-dimensional materials can also be combined with nanoobjects, such as quantum dots or plasmonic structures, to form hybrid heterostructures.

From a more technological perspective, two-dimensional materials and their heterostructures are very promising for a broad range of applications ranging from health and environment to (opto)electronics and energy storage and conversion [Ferrari15]. They offer potential advantages over most materials currently employed in today's technologies such as silicon. Among these advantages are semi-transparency, low weight, large area, flexibility, high performance, low power consumption, scalability, and low cost. Graphene and semiconducting transition metal dichalcogenides offer complementary properties that can be harnessed in a variety of novel optoelectronic devices [Koppens14, Xia14, Mak16, Mueller16], such as solar cells, photoconductors, photodiodes or light-emitting diodes, operating in the visible and near-infrared spectrum. However, researches in this emerging field are at their beginning, in particular numerous fundamental questions still have to be addressed and new fabrication techniques suitable for large-scale production have to be developed.

In this general context, this PhD project aims **to build optoelectronic devices based on van der Waals heterostructures, made of graphene and transition metal dichalcogenides, to study and electrically control the interlayer interactions that govern their photophysics.** These systems are investigated using **micro-optical spectroscopy** with submicrometer resolution. Compared to other techniques, optical spectroscopy presents the advantage to be a non-invasive, contactless, local and fast tool to probe physical properties of solids. The common technique employed throughout this thesis is **Raman spectroscopy** [Ferrari13, Zhang15b] which provides various information, such as the crystalline quality or the charge carrier density and which is employed here in an original way to investigate the interlayer couplings. The second technique used in this work is spatially- and time-resolved **photoluminescence spectroscopy** [Kolobov16] which is an accurate tool to probe the charge carrier dynamics, the excitonic manifolds and exciton dynamics that are largely affected by interlayer coupling.

The group was in its early stages when I joined it in March 2013 as a master student. Two PhD students, François Federspiel and Dominik Metten, had just started their PhD projects. The former was studying the energy transfer in hybrid heterostructures made of colloidal quantum dots and graphene [Federspiel15a] and the latter was investigating the optoelectronic properties of ultra-clean suspended graphene membranes [Metten16]. My project was to combine these two works by fabricating optolectronic devices based on hybrid heterostructures in which the energy transfer could be electrically controlled through the fine tuning of graphene's properties. However, rapidly we choose to replace the hybrid heterostructures by van der Waals heterostructures made of graphene and semiconducting transition metal dichalcogenides because they offer interlayer distances of only few Ångströms where unexplored regimes of energy and charge transfer occur, yielding to richer, yet more challenging, studies. To reach the ultimate goal of this project, I have defined the following milestones:

1. Fabricating robust devices to efficiently and finely tune graphene's Fermi energy and developing a method to accurately monitor it.

2. Characterizing semiconducting transition metal dichalcogenides as a function of the number of layers. Among the vast family of transition metal dichalcogenides, we have selected molybdenum ditelluride ($MoTe_2$) since it remained poorly known and, importantly, has an optical bandgap in the near-infrared (around 1 eV) which should make the electrical control of the interlayer interactions easier.

3. Fabricating van der Waals heterostructures and integrating them into the devices developed in the first step.

Almost all these points were successfully achieved and are described in this manuscript. As this work marks the beginning of the study of transition metal dichalcogenides and van der Waals heterostructures in our group, I had to provide detailed introduction of their fundamental properties that are most relevant to this PhD.

Manuscript organization

This manuscript contains nine chapters including this one. Three chapters (Chapters 2 to 4) are dedicated to the presentation and scientific context of two-dimensional materials and their heterostructures, to the theoretical basis of Raman spectroscopy and to the experimental methods. Three chapters describe already published experimental results (Chapters 5 to 7) and one chapter to unpublished work (Chapter 8). The last chapter concludes this work and exposes few perspectives. The full list of publications, six appendices and a general summary (in French) complete the manuscript. Note that at the end of each chapter, the 'take-home messages' are listed, together with the list of related publications and communications.

Chapter 2 provides an overview of the **scientific context** of this thesis. It gives a general presentation of graphene, semiconducting transition metal dichalcogenides and their heterostructures with a focus on optoelectronic application. These are obviously vast topics and we have focused on selected aspects that are particularly relevant to the work described in the following chapters. In addition, relevant optoelectronic devices are introduced to provide an overview of today's state of the art and to show the tremendous possibilities offered by these materials and structures.

Chapter 3 introduces **Raman scattering** from a theoretical standpoint, as it is our common technique used to study the three different types of system investigated in this work. It is probably the most technical chapter. However, the following chapters can be addressed without reading it in detail. In a first part, we briefly summarize the essential principles and notations of group theory needed to understand the analysis performed in the next sections. A more detailed introduction to group theory is presented in Appendix A. In a second part, we apply group theory to graphene and N-layer and bulk semiconducting transition metal dichalcogenides. The results of this part are important, especially for Chapter 6. In a last

part, the classical and quantum theoretical basis of Raman spectroscopy are presented in order to obtain the two fundamental relations of Raman scattering, to define the Raman tensor, to establish the dependance of the Raman intensity and to give the Raman selection rules.

Chapter 4 describes **sample preparation methods and introduces our experimental setup**. The samples were prepared in the STnano cleanroom facility. Three techniques are explained: the mechanical exfoliation with adhesive tape, the all-dry transfer technique and the fabrication of electric-field effect transistors based on graphene. The experimental setup consists in a confocal microscope that can be used for Raman, PL and time correlated single photon counting (TCSPC) measurements on electrically connected samples. Finally, the important effects of optical interferences on the measurements are introduced and their complete treatment is displayed in Appendix C.

Chapter 5 focuses on the comprehensive Raman scattering study of **electrochemically-gated graphene field-effect transistors**. The geometrical capacitance of the electrochemical top-gates is accurately determined from dual-gated Raman measurements, allowing a quantitative analysis of the two prominent Raman features of graphene. This analysis provides a measurement of the electron-phonon coupling for zone-center and zone-edge optical phonons. In addition, correlations between the frequencies and linewidths can be utilized for accurate estimations of the charge carrier density. Finally, we also show that electrochemical reactions, occurring at large gate biases, can be harnessed to efficiently create defects in graphene.

Chapter 6 is dedicated to the Raman spectroscopy of N-layer semiconducting transition metal dichalcogenides and more precisely to how interlayer interactions modify their Raman spectrum. First, a unified description of the **Davydov splitting** of all the zone-center optical phonons in N-layer $MoTe_2$ is outlined both experimentally and theoretically. The complete manifold of these phonons is quantitatively described by a **force constant model** including interactions up to the second nearest neighbor and surface effects. This analysis provides both intra- and interlayer force constants and gives a measurement of bulk silent modes. To show the generality of this study, we also present the results obtained on N-layer molybdenum diselenide ($MoSe_2$). Second, the low-frequency phonon modes are addressed for various transition metal dichalcogenides and described using a simplified force constant model allowing the determination of the interlayer force constants. Third, an alternative description of the phonon modes in N-layer transition metal dichalcogenides deduced from the bulk phonon dispersion relation is presented. Finally, the influence of **resonance effects** on these measurements are discussed.

Chapter 7 is devoted to the photoluminescence spectroscopy of N-layer semiconducting transition metal dichalcogenides. We begin by displaying the monolayer and bilayer photoluminescence spectrum for different transition metal dichalcogenides. We then focus on the room temperature photoluminescence of N-layer $MoTe_2$. We carefully analyze the photoluminescence lineshape of a function of N to unravel the **direct to indirect bandgap crossover**. To finish, we investigate the evolution of the photoluminescence intensity in monolayer $MoTe_2$

as a function of the absorbed photon flux. The observed sub-linear grow is well-captured by an elementary **exciton-exciton annihilation** rate equation model.

Chapter 8 displays an original study of monolayer graphene/monolayer $MoSe_2$ van der Waals heterostructures by means of micro-Raman and micro-photoluminescence measurements. From Raman measurements of the graphene layer, we show that **photoexcited electrons are transferred from $MoSe_2$ to graphene**. Using the results of Chapter 5, we quantitatively measure the amount of transferred charge and find that this charge transfer levels off as the incoming photon flux increases, suggesting that the interlayer charge transfer rate decreases as graphene's Fermi energy rises. On the other hand, a **massive quenching** of $MoSe_2$ photoluminescence is observed and does not depend on graphene's Fermi energy. These observations cannot be explained if one only consider interlayer charge transfer. This indicates that other fast mechanisms are responsible for the strong photoluminescence quenching. We suggest that **fast interlayer energy transfer**, a process that has been largely overlooking in van der Waals heterostructures, may be responsible for these observations. Finally, a **toy model**, which qualitatively reproduced all these results, is introduced.

Chapter 9 concludes this work and outlines a few of its perspectives.

Appendix A presents a pedagogical introduction to **group theory applied to phonons**. The aim of this appendix is to provide the reader the basis of group theory needed to understand and interpret the Raman measurements. The very simple example of the water molecule is used all along as a pedagogical example. See Chapters 3, 5 and 6.
Appendix B describes how the laser spot area is experimentally measured. See Chapters 7 and 8.
Appendix C introduces a simple model to account for the **optical interference effects** in layered structures. First, the equivalent reflection and transmission coefficients are presented. Then, the theoretical expressions of the absorptance of one given layer and of the whole structure are set. Finally, the **enhancement factor** of the Raman and photoluminescence intensity is defined. See Chapters 5, 6, 7 and 8.
Appendix D shows the vector decomposition method used to **optically separated strain from electron and hole doping** in graphene. See Chapters 5 and 8.
Appendix E exhibits the analytical resolution of the normal modes of a **finite linear chain model** of N identical masses. See Chapter 6.
Appendix F displays the **atomic displacements** associated with the phonon modes for $N = 1$ to $N = 6$ layers of $MoTe_2$. See Chapter 6.

Chapter 2

Introduction to graphene, semiconducting transition metal dichalcogenides and their heterostructures for optoelectronics

In this chapter, we present the basic properties of graphene, semiconducting transition metal dichalcogenides and their heterostructures. These are obviously vast topics and we therefore focus on the properties that are the most relevant for this work. In particular, we thoroughly introduce the near-field coupling mechanisms that govern the photophysics in these heterostructures. We then discuss state of art optoelectronic devices and highlight the fundamental questions raised by the study of their performances. Clearly, the scientific literature on this very active research field is vast and we have done our best to showcase the landmark references.

2.1 Graphene

The first section is devoted to the basic electrical, optical and vibrational properties of monolayer graphene. Few examples of optoelectronic devices are depicted at the end of the section.

2.1.1 Crystal structure

Graphene is made of carbon atoms arranged in a a two-dimensional honeycomb lattice as illustrated in Fig. 2.1(a). From a crystallographic point of view, not all the carbon atoms are equivalent. Two types of atoms can be identified. As shown in Fig. 2.1(a), the atoms labeled A (gray filled circle) have their nearest neighbors at 0°, 120° and 240°, which are labeled B (black open circle), whereas the atoms B have their nearest neighbors (atoms A) at 60°, 180° and 300°. Consequently, the graphene lattice can be seen as two triangular (or hexagonal)

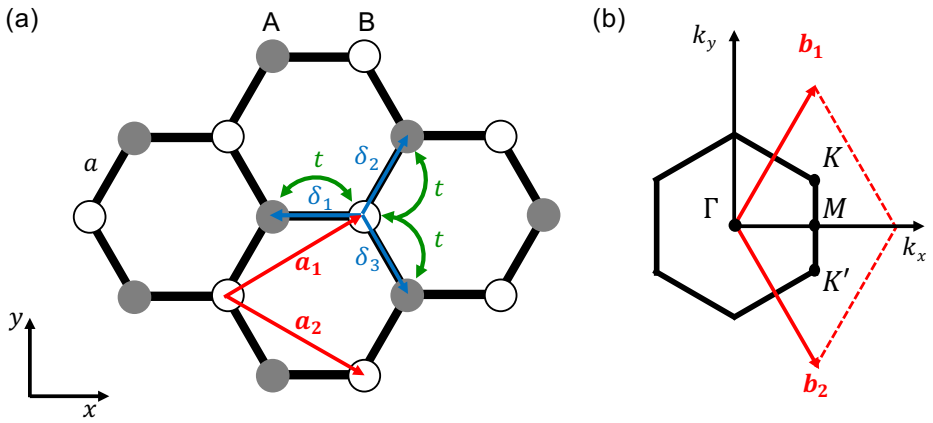

Figure 2.1 *– (a) Honeycomb lattice structure of graphene, composed of a triangular lattice with a basis of two inequivalent carbon atoms, A and B.* $\boldsymbol{a_1}$ *and* $\boldsymbol{a_2}$ *are the primitive unit vectors. the vectors* $\boldsymbol{\delta_1}$, $\boldsymbol{\delta_2}$ *and* $\boldsymbol{\delta_3}$ *connect an atom B to its three nearest neighbors A. In tight-binding picutre, an electron can hop from a carbon atom to one of its three nearest neighbor with hopping parameter t. (b) Corresponding first Brillouin zone.* $\boldsymbol{b_1}$ *and* $\boldsymbol{b_2}$ *are the basis vectors of the reciprocal lattice. High symmetry points are indicated with black dots and labeled.*

sublattices made of atoms A and B, respectively, or as one triangular lattice with a basis of two atoms A and B.

The distance between two neighboring atoms A and B is $a = 1.42\,\text{Å}$, which corresponds roughly to the mean value of the simple ($a = 1.47\,\text{Å}$) and the double ($a = 1.35\,\text{Å}$) carbon-carbon bond length, as it is the case for benzene. The basis vectors of the primitive unit cell are $\boldsymbol{a_1} = \frac{a}{2}(3, \sqrt{3})$ and $\boldsymbol{a_2} = \frac{a}{2}(3, -\sqrt{3})$. The three vectors connecting an atom B to its nearest neighbors A are $\boldsymbol{\delta_1} = \frac{a}{2}(1, \sqrt{3})$, $\boldsymbol{\delta_2} = \frac{a}{2}(1, -\sqrt{3})$ and $\boldsymbol{\delta_3} = -a(1, 0)$ (see Fig. 2.1(a)). The basis vectors of the reciprocal lattice in momentum space are $\boldsymbol{b_1} = \frac{2\pi}{3a}(1, \sqrt{3})$ and $\boldsymbol{b_2} = \frac{2\pi}{3a}(1, -\sqrt{3})$. The first Brillouin zone is hexagonal and characterized by four high symmetry points, indicated by black dots in Fig. 2.1(b) and labeled Γ, M, K and K'. In particular, the two points K and K' are inequivalent, which means that they are not connected by a vector of the reciprocal lattice. These two points play an important role for the physics of graphene, as we will see later. Their positions in momentum space are given by the vectors $\boldsymbol{K} = \left(\frac{2\pi}{3a}, \frac{2\pi}{3a\sqrt{3}}\right)$ and $\boldsymbol{K'} = \left(\frac{2\pi}{3a}, -\frac{2\pi}{3a\sqrt{3}}\right)$. Note that the four others corner of the Brillouin zone can be connected to one of these two points by a vector of the reciprocal lattice.

2.1.2 Electronic properties

Band structure

In its neutral and ground state, each carbon atom possesses six electrons and its electronic configuration is $1s^2 2s^2 2p^2$. Contrary to the four electrons 2s and 2p, the two 1s electron are located in the vicinity of the atomic nucleus and are thus not involved in chemical bonding or reactions. In graphene, the 2s, $2p_x$ et $2p_y$ mix and form three hybrid orbitals labeled sp2, which are separated by an angle of 120° in the xy-plane. The non hybridized orbital $2p_z$ is

perpendicular to this plane. The combination of the sp2 ($2p_z$) orbitals of adjacent carbon atoms give rise to the bonding σ and antibonding σ^* (π and π^*) molecular orbitals. For each pair of adjacent carbon atoms, the energetically more favorable bonding orbitals are therefore filled while the antibonding ones are empty. Going from the picture of individual carbon atoms to the whole graphene lattice, the molecular orbitals merge into bands. Energetically, the π and π^* bands are situated close to the Fermi energy, while the σ and σ^* bands are further away and well separated by an energy of more than 10 eV. As a result, to describe the electronic properties of graphene it is sufficient to consider only electrons in the π and π^* bands [Fuchs08].

The first calculation of the π and π^* bands in graphite was performed by Wallace in 1947 using a **tight-binding model** [Wallace47]. This model was later improved to more accurately describe the properties of graphene and carbon nanotubes [Reich02]. Nevertheless, here we consider only the interaction with the first nearest neighbors. In this model, the electron of a carbon atom can hop to its three nearest neighbors with a hopping parameter $t \approx 3$ eV (see Fig. 2.1(a)). The electronic dispersion of graphene's π (−) and π^* (+) bands writes [Wallace47]:

$$E_{\pm}(\boldsymbol{k}) = \pm t\sqrt{3 + f(\boldsymbol{k})}, \tag{2.1}$$

with

$$f(\boldsymbol{k}) = 2\cos(\sqrt{3}k_y a) + 4\cos\left(\frac{\sqrt{3}}{2}k_y a\right)\cos\left(\frac{3}{2}k_x a\right), \tag{2.2}$$

where $\boldsymbol{k}$ denotes the electron wavevector. This dispersion relation is plotted in Fig. 2.2 and is clearly symmetric with respect to the zero-energy plane. However, by considering the hopping to the second nearest neighbors, the symmetry is broken and the π and π^* bands become asymmetric. In addition, we directly notice that the two bands are degenerate at the six corners of the Brillouin zone (i.e., K and K' points).[1] Since, in neutral graphene, each carbon atom contributes with one π electron and each electron may occupy either a spin-up or a spin-down state, the lower π band is completely filled (valence band) and the upper π^* band is completely empty (conduction band) [Fuchs08]. As a result, the Fermi Energy E_F is situated at the touching points of the two bands, i.e., $E_F = 0$ with the choice of origin made here. Graphene is therefore a **semimetal**. Furthermore, an electron close to the Fermi level can occupy a state either around the K or the K' point since the dispersion relation is identical near these two inequivalent points. Hence, for an electron, in addition to the spin, there is a **valley** degree of freedom.

Around K and K' points

Linear dispersion relation The low energy (compared to t) electronic states are in the vicinity of the K and K' points. Their wavevector $\boldsymbol{k}$ can be rewritten as: $\boldsymbol{k} = \boldsymbol{K}^{(')} + \boldsymbol{\kappa}$, with

[1] Note that there is conceptual difference between the K and K' points and the points where the π and π^* bands are degenerate. The latter points can move away from the K and K' points [Hasegawa06] if the hopping parameter t is anisotropic (e.g., under mechanical strain). However, we will not consider this possibility here.

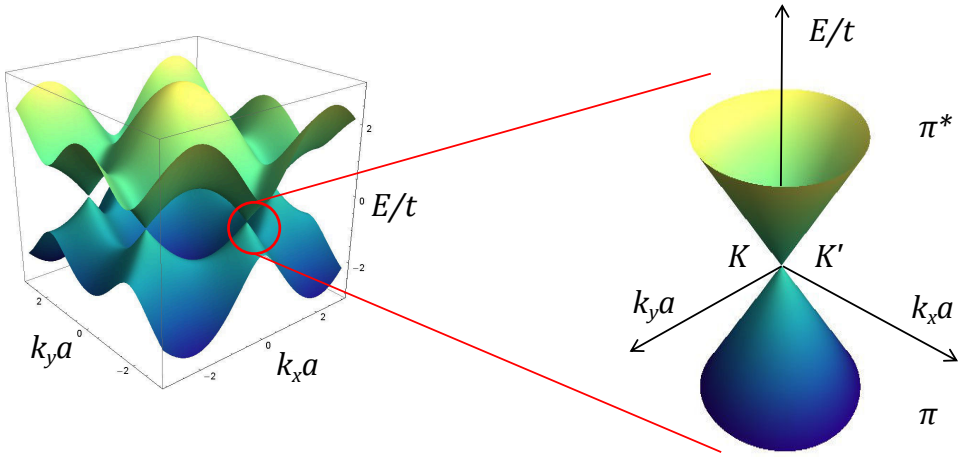

Figure 2.2 *– Electronic dispersion relation of graphene calculated using a first nearest neighbor tight-binding model. A zoom shows more precisely the dispersion relation close to the K and K' points.*

$|\boldsymbol{\kappa}| \ll \left|\boldsymbol{K}^{(\prime)}\right| \sim 1/a$, or more easily $|\boldsymbol{\kappa}|a \ll 1$. In this condition, the Taylor expansion of the dispersion relation of Eq.(2.1) at first order in $|\boldsymbol{\kappa}|a$ yields, regardless of the valley,

$$E_{\pm}(\boldsymbol{\kappa}) = \pm\hbar v_{\mathrm{F}}|\boldsymbol{\kappa}|, \quad \text{with } v_{\mathrm{F}} = \frac{3ta}{2\hbar} \approx 1\times10^{6}\ \mathrm{m\ s^{-1}}. \tag{2.3}$$

v_{F} is called the Fermi velocity. A zoom in Fig. 2.2 shows this dispersion relation, i.e., the famous 'Dirac cones'. Note that because of this name the K and K' points are often called Dirac points. Since the Fermi energy is located around these points and since most of the electronic properties are given in the vicinity of the Fermi energy, this dispersion relation is very important. The expansion up to the second order in $|\boldsymbol{\kappa}|a$ leads to the so-called *trigonal warping* [Castro Neto09], i.e., for higher energy states the cone deforms to adopt a triangular-like shape (in other words the dispersion relation depends on the direction in momentum space). In this thesis such an effect is neglected. Remarkably in supported graphene, many body effects can be neglected, i.e., electrons behave as if there were no electron-electron interactions [Elias11, Hofmann14, Faugeras15]. As a result, the v_{F} can be considered as a constant.

Density of states In the vicinity of the Dirac points, using Eq. (2.3), $g(E)$ is given by

$$g(E) = \frac{2E}{\pi(\hbar v_{\mathrm{F}})^2}, \tag{2.4}$$

where the spin (×2) and the valley (×2) degeneracy are taken into account. Note that due to the electron-hole symmetry, this density of states is valid for both electrons and holes. It has the particularity to scale linearly with the energy E and to vanish at the Dirac points. This situation is different from what is usually happening in a two-dimensional solid, where the density of states is constant (due to the parabolic dispersion relation). Hence, this distinctive feature is a direct consequence of the two-dimensionality and of the linearity of the dispersion relation of Eq. 2.3.

Massless Dirac Fermions One may wonder "what makes Dirac cones so famous?", and the answer is pretty simple "they are cones!". Indeed, rather than being quadratic, as it is usually the case for electrons in solids, the dispersion relation is linear $E \propto p$, where p is the electron momentum measured from the Dirac points. For this reason it strongly reminds the photons dispersion relation, i.e., massless relativistic particles. Equation (2.3) can be written in a relativistic form $E(p) = \pm\sqrt{p^2c^{*2} + m^{*2}c^{*4}} = \pm c^* p$ with an effective mass $m^* = 0$ and an 'effective light velocity' c^* equal to the Fermi velocity v_F. However, electrons in graphene are not strictly speaking relativistic as their velocity is approximately 300 times smaller than the speed of light $c = 299\,792\,458$ m s^{-1}. In addition, the electronic wavefunctions near the K and K' points obey the Dirac equation (and not the Schrödinger one) for massless fermions, and have a well defined chirality (or helicity). In other words, electrons near the K point possess a pseudospin that is parallel (for the π band) or anti-parallel (for the π^* band) to the electron momentum.[2] The pseudospin endows charge carriers in graphene with unique properties, that allow the observation of new phenomena such as the half integer quantum hall effect and the absence of back-scattering (and the subsequent possibility of observing Klein tunneling) [Castro Neto09]. Finally, for all these reasons, electrons and holes in graphene as called **massless Dirac fermions** [Novoselov05a].

2.1.3 Optical properties

Absorption In graphene, light absorption arises mainly from two contributions: **interband** and **intraband** transitions [Mak12b], as drawn in Fig. 2.3(a). Because $g(0) = 0$, intraband transitions make only sense in doped graphene. The relative importance of these two contributions depends on the spectral range. In the far infrared (i.e., photon energies $\lesssim 50$ meV), intraband absorption dominates. In order to fulfill the momentum conservation, an extra scattering by, e.g., phonons or defects is required. The associated optical conductivity is well captured by a Drude model. From the ultraviolet to the mid-infrared, interband absorption dominates. Such processes correspond to vertical transitions (the photon momentum is neglected compared to the electron momentum, see Chapter 3) and lead to the creation of electron-hole pairs. The associated optical conductivity can be calculated from the Fermi golden rule [Dresselhaus99]. The complex dielectric constant of graphene and hence, its complex refractive index can be deduced from these optical conductivities [Dresselhaus99]. In the visible and near-infrared, only the interband conductivity σ_{inter} is not equal to zero and one can show that, in first approximation, the absorptance (i.e., the fraction of absorbed light, see Appendix C Section C.2) of a graphene monolayer is given by [Mak12b]

$$\mathcal{A} \approx \frac{2\omega}{c} \times \frac{\sigma_{\text{inter}}}{2\omega\varepsilon_0} = \frac{e^2}{4\hbar c\varepsilon_0} = \pi\alpha \approx 2.3\ \%, \tag{2.5}$$

[2] Similarly, electrons near the K' point possess a pseudospin that is parallel (for the π^* band) or anti-parallel (for the π band) to the electron momentum.

where ω is the photon frequency and $\alpha = \frac{e^2}{4\pi\hbar c\varepsilon_0} \approx 1/137$ the fine-structure constant. It is remarkable that $\mathcal{A}$ is constant on this spectral range and even more that it does not depend on the properties of the material (such as v_F). An easy way to understand this is to study the ω and v_F dependence of the three main terms in the Fermi golden rule used to calculate σ_{inter} (proportional to $\mathcal{A}$) [Mak12b]: the square of the matrix element scales as v_F^2/ω^2, the density of state (see Eq. (2.4)) as ω/v_F^2 and the incident photon energy as ω. The product of the three terms is independent of ω and v_F. Note that Eq. (2.5) holds only in the linear approximation. This constant absorptance was experimentally confirmed by different groups, see for example Refs. [Mak08, Nair08, Mak12b] (see Figs. 2.3(b)-(c)). Interestingly, for few layers, the absorptance in the visible range is roughly proportional to the number of layers. At last, the magnitude of $\mathcal{A}$ can be regarded as extremely high for an atomically thin material, yet very small for applications of graphene as a transparent electrode.

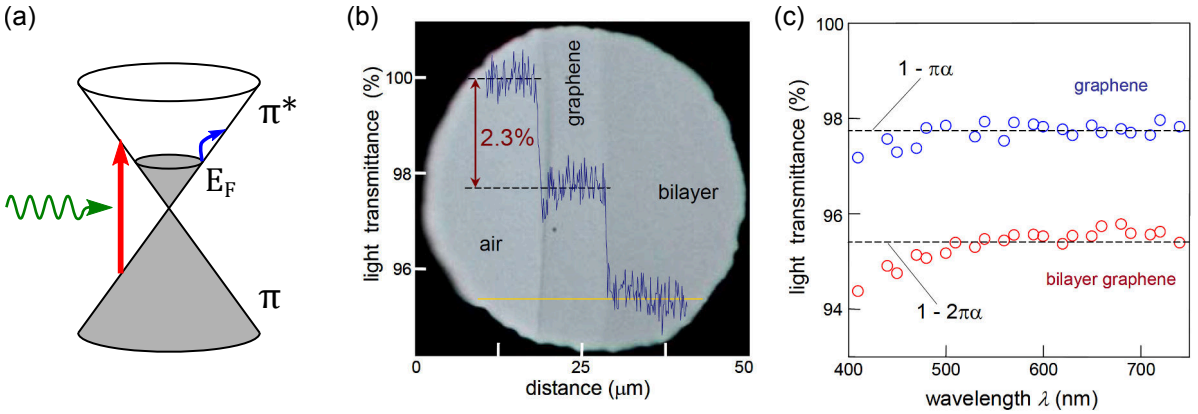

Figure 2.3 *– (a) Scheme of intra- (blue arrow) and interband (red arrow) transitions in graphene, resulting from the absorption of a photon (green wavy arrow). Occupied states are in gray. Note that due to the Pauli principle, a transition occurs from an occupied state below the Fermi level (E_F) to an unoccupied state above it. (b) Optical image of monolayer and bilayer graphene suspended over a hole. The line scan profile shows the intensity of transmitted white light along the yellow line. Increasing the number of graphene layers leads to a drop of 2.3 % of the intensity of the transmitted light. (c) Transmittance of the two graphene regions shown in (b), as a function of the light wavelength. (b) and (c) are adapted from Ref. [Nair08].*

Emission Although light absorption is efficient in graphene, graphene is not an efficiency light emitter because the absence of a bandgap allows very efficient non-radiative charge carrier relaxation on a typical timescale of 100 fs – 1 ps [Kampfrath05, George08, Lui10, Tielrooij13]. However, hot luminescence can be observed [Bonaccorso10, Mak12b] but with weak quantum efficiency $\sim 10^{-9}$ [Lui10], and Black-body-like thermal radiative emission can also be observed [Freitag10, Berciaud10, Lui10, Kim15b] due to graphene's high stability at elevated temperature.

One solution to make graphene emit light with higher efficient would be to open a bandgap. For instance, graphene can be patterned into nanoribbons to confine the electrons, or graphene can be physically or chemically treated to reduce the connectivity of the π-electron network [Bonaccorso10]. However, in that case, graphene is not strictly speaking graphene anymore.

2.1.4 Vibrational properties

Phonons in graphene

Phonon dispersion relation Graphene has two atoms per unit cell. Consequently there are six phonon branches (see Fig. 2.4 and Chapter 3 Section 3.2): three acoustic (A) and three optical (O). Two of them are in-plane longitudinal (iLA and iLO), two are in-plane transverse (iTA and iTO) and two are out-of-plane transverse (oTA and oTO). These six branches can be measured experimentally by inelastic neutron [Nicklow72] or X-ray [Maultzsch04b, Mohr07, Grüneis09] scattering, as well as electron energy loss spectroscopy (EELS) [Oshima88, Siebentritt97, Yanagisawa05] (see symbols in Fig. 2.4). Raman scattering can also be used to measure the phonon modes in graphene. From a theoretical point of view, the phonon dispersion has been determined using empirical force-constant calculations [Nicklow72, Al-Jishi82, Mohr07]. The interaction up to the fifth nearest neighbors was taken into account [Mohr07] to accurately describe the observed dispersion relation. Density functional theory (DFT) was also successfully employed [Dubay03, Wirtz04, Maultzsch04b, Piscanec04, Mounet05, Bonini07, Yan08a] to calculate the phonon dispersion of graphene. A closer look at the agreement between experiment and theory for both approaches reveals that in the vicinity of the K point, the dispersion is not well reproduced. In order to accurately describe the dispersion relation around this point, one has to take into account the long-range character of the electron-electron interaction. For instance, these effects are taken into account by the so-called GW method. It turns out that this method accounts for a notable correction to the standard DFT calculations [Lazzeri08, Grüneis09, Venezuela11]. To date, the reference dispersion relation, calculated using DFT with the GW correction, is displayed in Fig. 2.4.

Kohn anomalies An extremely important feature of this phonon dispersion is that near the Γ and K points the phonon frequency varies abruptly (see Fig. 2.4). Such phenomena are known as **Kohn anomalies**. In 1959, Kohn (Nobel Prize in chemistry in 1998) stated that such anomalies occur in metals for phonon wavevector $\boldsymbol{q}$ such that two electronic states with wavevectors $\boldsymbol{k_1}$ and $\boldsymbol{k_2} = \boldsymbol{k_1} + \boldsymbol{q}$ are both on the Fermi surface [Kohn59]. In the case of neutral graphene, the Fermi surface is composed of six points located at the corners of the Brillouin zone. Thus Kohn anomaly can occur for $\boldsymbol{q} = \boldsymbol{\Gamma}$ or $\boldsymbol{q} = \boldsymbol{K}^{(\prime)}$. More precisely, there are two pronounced Kohn anomalies in graphene: one for the LO phonons at Γ and one the for the TO branch at $K^{(\prime)}$ [Piscanec04]. For these two branches and around these two points, the strength of electron-phonon coupling is particularly important. Physically, this strong coupling can be understood as a manifestation of the conservation of energy and momentum in electron–phonon scattering. Indeed, as the energy of phonons is small compared to the energy of electrons, electron-phonon interaction couples electronic states around the Fermi level (it is Kohn's condition), i.e., phonons are near Γ or $K^{(\prime)}$. Consequently, the Raman features involving near zone-edge and near zone-center optical phonons will dominate the Raman spectrum of graphene layers, as we will see below.

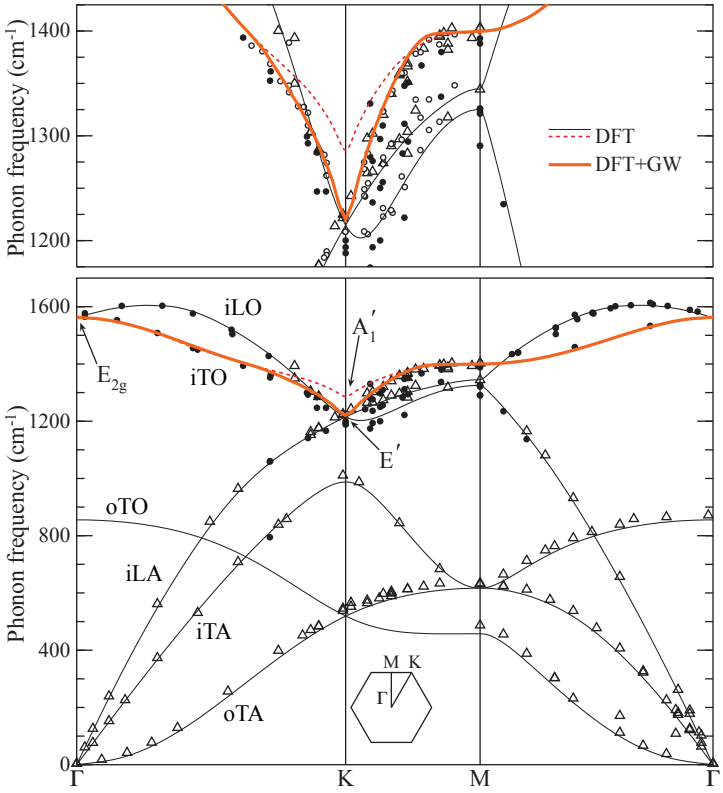

Figure 2.4 *– Phonon dispersion of graphene. The solid lines represent density functional theory calculations with GW corrections from Refs. [Lazzeri08] and [Grüneis09]. The symbols represent inelastic X-ray scattering measurements from Refs. [Maultzsch04b] (full circles) and [Mohr07] (open triangles). The six phonon branches are labeled. This figure is adapted from Ref. [Venezuela11].*

Raman spectrum of graphene

Typcial Raman spectrum As we will see in the other chapters, Raman spectroscopy will be largely employed throughout this manuscript. The first Raman spectrum of graphite was measured in 1970 [Tuinstra70], but the full theoretical understanding of this spectrum was only achieved in the years 2000-2010 [Reich04]. The first Raman spectrum of isolated monolayer graphene was performed in 2006 [Ferrari06]. Figure 2.5 shows the typical Raman spectrum of pristine (i.e., defect free) and defective graphene recorder at a laser energy of 2.33 eV. The two prominent features are:

- the **G-mode** feature at ≈ 1580 cm^{-1}. This mode is associated with the only one-phonon Raman active process in graphene, which involves the Γ-point phonon with E_{2g} symmetry (see Chapter 3). This phonon mode is doubly degenerate and corresponds to the iLO and iTO phonon branches that are degenerate at Γ (see Fig. 2.4). As discussed in Chapter 5, the G mode is a non-resonant process.

- the **2D-mode** feature at ≈ 2675 cm^{-1}. This mode cannot be associated with a one-phonon process since the frequency is too high. Consequently, it is a second order process involving two phonons with opposite momentum $+\boldsymbol{q}$ and $-\boldsymbol{q}$ connecting the two inequivalent valleys K and K'. As $\boldsymbol{K} - \boldsymbol{K'} = \boldsymbol{K}$ and $\boldsymbol{K'} - \boldsymbol{K} = \boldsymbol{K}$ (see Fig. 2.1(b)), the

involved phonon are around K or K', i.e., $|\boldsymbol{q}| \approx |\boldsymbol{K}|$ or $|\boldsymbol{K'}|$. Due to a Kohn anomaly at these two points, only the phonons from the iTO branch are concerned. As we will see in Chapter 5, this mode arises from a resonant mechanism.

The two other important features that are only present in defective graphene are:

- the **D-mode** feature at ≈ 1340 cm^{-1} which involves phonons with $|\boldsymbol{q}| \approx |\boldsymbol{K}|$ or $|\boldsymbol{K'}|$ and an elastic scattering with a defect.
- the **D'-mode** feature at ≈ 1620 cm^{-1} which involves phonons with $|\boldsymbol{q}| \approx 0$ and an elastic scattering with a defect.

Both modes correspond to resonant one-phonon processes which are symmetry forbidden in pristine graphene (see Chapter 3) but are activated by defects. Therefore, the D and D' modes can be used to evaluate the quality of a sample. Note that the D stands for defects. In addition to these four modes, there are other modes in graphene. Especially, overtones of the modes described above (e.g., 2D', 4D) or combinations (e.g., D+D') can be observed.[3] Some of these processes are detailed, for instance, in Ref. [Ferrari13].

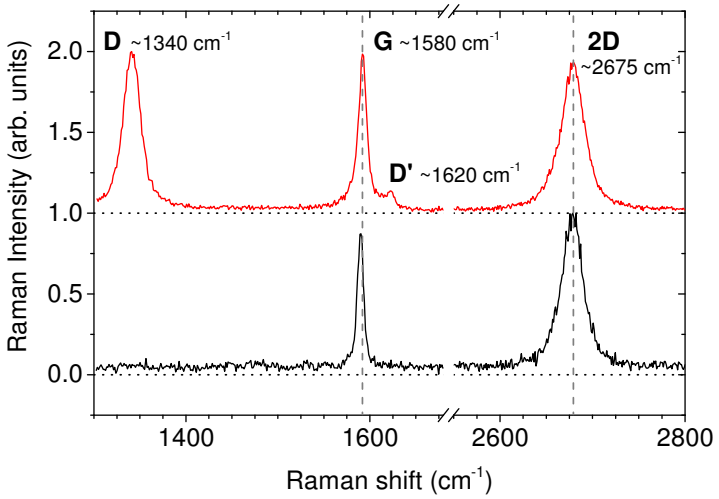

Figure 2.5 *– Typical Raman spectrum of defect-free (black line) and defective (red line) monolayer graphene. The four main features are labeled together with their typical Raman shift. These spectra were recorded using a laser at 2.33 eV. Note that the two spectra were recorded on the same point of the same sample before and after the creation of defects by electrochemical reactions (see Section 5.5).*

Sensitivity to strain and doping The Raman features of graphene are very sensitive to external perturbations, in particular to strain and to the addition of charges (i.e., doping). This sensitivity makes Raman spectroscopy a powerful tool to probe graphene's properties beyond the basic vibrational properties.

[3] The overtone of the G mode is not observed. In fact, as the G mode is a non-resonant process, its overtone has a very tiny intensity compared to resonant two-phonon processes. As the overtone of the G mode is close to the 2D'-mode feature, it is screened by the latter. See Chapter 5 Section 5.1.3 for detail on the 2D' mode.

Influence of strain Applying mechanical strain to graphene results in a change of the lattice parameter which leads to a variation of the phonon frequency. As already mentioned, a sufficiently high uniaxial strain can break the crystal symmetry and thus lift the degeneracy of the G mode (i.e., the degeneracy of the iLO/iTO phonon branches at Γ), which splits into two subfeatures [Huang09, Mohiuddin09, Mohr09]. For sufficiently low strain, only the phonon frequency is modified. Especially, in the case of biaxial strain, the shift of the phonon frequency is proportional to the strain *via* the Grüneisen parameter [Mohiuddin09]. The effects of strain of the vibrational properties of graphene were studied in our group by Dominik Metten and are summarized in detail in his thesis manuscript [Metten16]. Here, we assume that there can be homogenous or inhomogeneous strain in the samples but it is supposed to be constant during the measurements.

Influence of doping The addition of charges in graphene (see Section 2.1.5) has an impact on the phonon modes in graphene. Indeed, as for the strain, doping induces a variation of the bond lengths and thus of phonon frequencies. In addition, the presence of Kohn anomalies at the Γ and $K^{(\prime)}$ points results in strong electron-phonon coupling and hence to phonon renormalizations. As a consequence, this leads to prominent modifications of the Raman features [Yan07, Pisana07]. These modifications will be thoroughly investigated in Chapter 5. In particular, we will show that they can be used to identify the nature of the doping and to accurately quantify it. Then, we will apply these results in Chapter 8.

Raman spectroscopy: an efficient tool to determine the number of layers In this work, we are studying exclusively monolayer graphene. Hence, we need a unambiguous way to identify atomically thin layers. One can use optical contrast (see Section 2.1.3). However, it is not an accurate method. For instance, optical interference effects (see Chapter 4 Section 4.3) can drastically affect the contrast and lead to an incorrect evaluation of the number of layers. On the other hand, Raman spectroscopy is a powerful tool to quantitatively determine the number of layers [Malard09b, Ferrari13]. Indeed, the main features described in this section are also observable in multilayer graphene and graphite samples, with some of them very sensitive to the number of layers. Additional graphene layers change significantly the electronic structure due to the interlayer coupling [Partoens06, Partoens07]. Hence, a more complex electronic structure results in a 2D-mode feature consisting of several sub-features [Graf07, Malard07, Malard09b], since it is a resonant process. The evolution of the 2D-mode feature with increasing number of layers has been studied experimentally [Graf07, Malard07, Malard09b] and the distinctive shapes help to determine the exact number of layers.

Figure 2.6 shows the Raman spectrum of monolayer, bilayer, trilayer and graphite recorded at $E_L = 2.33$ eV. We notice that (i) the G-mode feature is independant of the number of layers which is in agreement with the non-resonant nature of the mode and (ii) the position and shape of the 2D-mode feature clearly evolve with the number of layers. Especially, the 2D-mode feature of monolayer graphene is the lowest in frequency and most importantly the

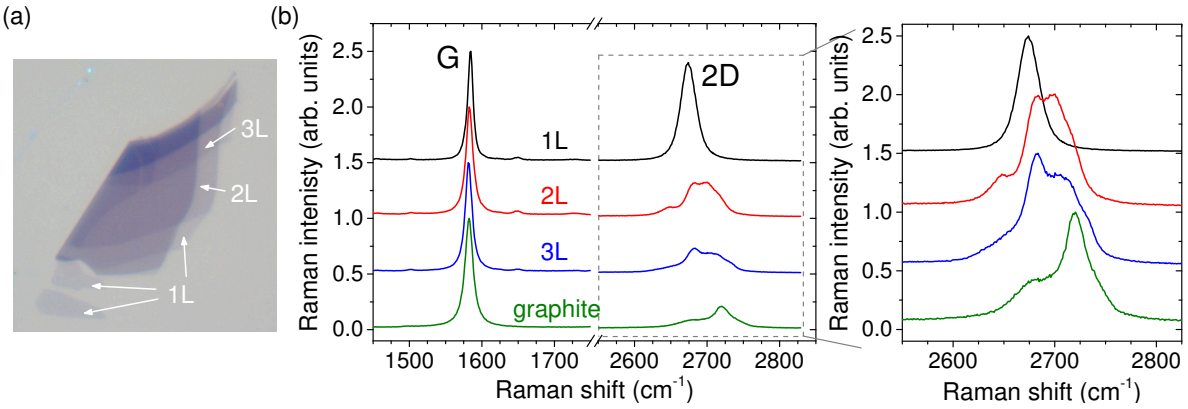

Figure 2.6 *– (a) Optical image of graphene exfoliated onto Si/SiO_2 with monolayer (1L), bilayer (2L) and trilayer (3L) thickness. (b) Raman spectra of pristine monolayer (1L), bilayer (2L), trilayer (3L) and graphite samples recorded at 2.33 eV for different integration times. The spectra are vertically offset for clarity. The G-mode and 2D-mode features are clearly visible. The former is insensitive to the number of layer, while the latter is distinctly affected. The characteristic shapes help to determine the exact number of layers, especially to identify the monolayers which have a quasi-symmetric 2D-mode feature.*

narrower and quasi-symmetric. This criterion can be used to unambigously identify monolayer graphene. Furthermore, the distinctive shapes of the 2D-mode feature for bilayer and trilayer can also be used to identify this number of layers. However, for more than three layers, it becomes complicated to precisely determine the number of layers. One can then use the rigid layer modes [Tan12, Lui14] or combinations of these modes [Lui13, Herziger12] to accurately count the number of layers up to tens of layers. A detailed study of the rigid layer modes is presented in Chapter 6 for transition metal dichalcogenides.

2.1.5 Tuning graphene's optoeletronic properties by the electric field effect

Graphene's physical properties strongly depend on the Fermi energy E_F. In practice, the Fermi energy is tuned by changing the charge carriers density either using chemical (e.g., [Jung09, Zhao10]) or physical (e.g., [Novoselov04, Zhang05]) methods. The latter make use of the **electric field effect**. Typically, graphene is incorporated into a field-effect transistor (FET) which has a geometry similar to a parallel plate capacitor (see Fig. 2.7(a)) where one of the two electrodes is replaced by graphene, the other being the gate electrode. Applying an external electric field through a potential difference V between these two electrodes leads to the injection of charge carriers in the two electrodes (depending on the sign of V electrons or holes are injected). The density of injected charge carriers n is proportional to the gate bias V and to the total capacitance C: $ne = CV$.

The density of charge carriers in graphene is linked to the Fermi energy E_F by [Ashcroft76]

$$n_e = \int_0^{+\infty} f(E)g(E)\mathrm{d}E \quad \textit{and} \quad n_h = \int_0^{+\infty} [1 - f(E)]g(E)\mathrm{d}E, \tag{2.6}$$

where n_e and n_h are the electron and hole density, respectively, $g(E)$ is the density of states

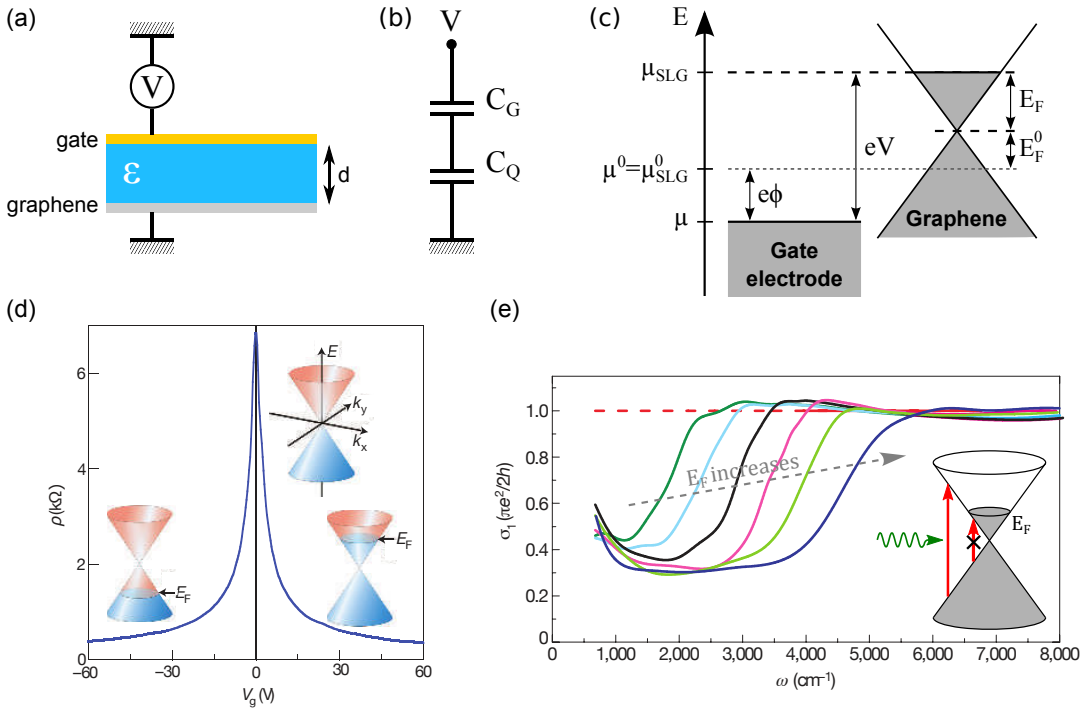

Figure 2.7 *– (a) Schematic cross-section of a parallel plate capacitor composed of a single layer graphene and a metallic electrode separated by a dielectric of thickness d. (b) Equivalent electrical circuit. (c) Schematic energy diagrams of the electronic states of the gate electrode and of graphene. Occupied states are represented in gray. At zero gate voltage ($V = 0$), the electrochemical potentials of the gate electrode μ and the graphene layer μ_{SLG} are equal. The Fermi energy of graphene is E_F^0. Applying a gate voltage V results in an electrostatically-induced shift ($e\phi$) and in a change of the Fermi energy of graphene (E_F). The electrochemical potential difference is equal to eV, leading to Eq. (2.8) with $eV_0 = E_F^0$. (d) Graphene's electrical resistivity ρ as a function of gate voltage V_g in a FET. The insets show the conical low-energy dispersion with changing V_g. Figure adapted from Ref. [Geim07]. (d) Graphene's optical conductivity (which is proportional to $\mathcal{A}$) as a function of the incident photon wavenumber ω for increasing E_F. The insert illustrates that due to Pauli blocking a range of interband transitions are forbidden. Figure adapted from Ref. [Li08].*

from Eq. (2.4) and $f(E) = [1 + \exp(E/k_B T)]^{-1}$ is the Fermi-Dirac distribution at a temperature T. Because of the electron-hole symmetry, it is more convenient to define only one density n counted positively for the electrons and negatively for holes. At $T = 0$,

$$E_F = \mathrm{sgn}(n)\hbar v_F \sqrt{\pi |n|}, \tag{2.7}$$

where sgn is the sign function. In practice, finite temperature effects only induce a very minor correction to this simple scaling [Li11], therefore we will use this expression at any temperature. Note that again, the case of graphene is peculiar since in general the Fermi energy is proportional to n and not to its square root.

In a graphene FET, due to the two-dimensional nature of the electron gas, the capacitance C is not simply equal to the geometrical capacitance C_G of the parallel plate capacitor but to this capacitance in series with the **quantum capacitance** C_Q [Luryi88] (see Fig. 2.7(b)). This capacitance comes from the fact that, as opposed to the metallic gate electrode which can be viewed as a reservoir of electrons, injection in the graphene layer leads to a change of E_F.

Note that C_Q is also observed in Metal-Oxide-Semiconductor FET (MOSFET). To naturally introduce and establish the expression of C_Q let us use the schematic diagram in Fig. 2.7(c). An applied gate bias V creates an electrostatic potential difference ϕ between the graphene monolayer and the gate electrode. Besides, the injection of charge carriers in graphene leads to a shift of its Fermi energy. Note that in this work, a positive (negative) gate voltage corresponds to electron (hole) injection. Consequently, V introduces a difference in the electrochemical potentials of the gate electrode μ and of the graphene layer μ_{SLG}

$$\mu_{SLG} - \mu = eV = E_F + e\phi + eV_0, \tag{2.8}$$

where V_0 is a constant that accounts for the initial doping and implicitly includes the work function difference between the two materials [Giovannetti08]. The electrostatic potential difference ϕ is directly related to C_G by $\phi = ne/C_G$ [Das08, Das09], hence we can rewrite Eq. (2.8)

$$V - V_0 = \frac{E_F}{e} + \frac{ne}{C_G} = ne\left(\frac{1}{C_Q} + \frac{1}{C_G}\right) = \frac{ne}{C}. \tag{2.9}$$

We deduce that the quantum capacitance in graphene is given by

$$C_Q = \mathrm{sgn}(n)\frac{e^2}{\hbar v_F\sqrt{\pi}}\sqrt{|n|} = \frac{e^2}{2}g(E_F), \tag{2.10}$$

where $g(E_F)$ is the density of states at the Fermi level. Noteworthy, in the classical limit $\hbar \to 0$, $C_Q \to 0$ and thus C_Q can be neglected in C. The origin of C_Q is of course quantum! Importantly, the term related to C_Q in Eq. (2.9) scales as E_F (i.e., $\sqrt{n}$), while the term related to C_G scales as E_F^2 (i.e., as n). Consequently, the contribution of C_Q (C_G) dominates at low (high) E_F.

In practice, various structures of FET exist, e.g., solid state FET which make use of a solid dielectric, electrochemical gate that use electrolytes, or layered materials such as hBN in van der Waals heterostructures (see Section 2.3). In any case, tuning the Fermi energy can lead to drastic changes in the optoelectronic properties of graphene. To illustrate this point, we choose two examples depicted in Figs. 2.7(d) and (e). In the first example (Fig. 2.7(d)), graphene's electrical conductivity or resistivity is tuned [Novoselov04, Novoselov05a, Zhang05]. Interestingly, at zero gate voltage the conductivity (resistivity) does not fall to zero (go to infinity). This is an intrinsic property of the Dirac fermions in graphene where the minimum conductivity is $\sigma_{min} = e^2/4\hbar$ [Ando02, Peres06]. In reality, this conductivity is never reached due to residual charge inhomogeneities [Tan07]. Because σ_{min} is nonzero, graphene FET does not show very good on/off ratio (i.e., ratio between the conductive and non conductive states) as compared to the existing MOSFET. The second example (Fig. 2.7(e)) shows that graphene's absorptance can be tuned [Li08, Wang08]. Indeed, due to Pauli blocking, interband transitions with energy lower than $2E_F$ are not allowed. As a result, for photon energies smaller (larger) than $2E_F$, $\mathcal{A}$ is minimal (maximal) as illustrated in Fig. 2.7(e).

2.1.6 Optoelectronic applications

For optoelectronic applications, graphene offers several distinct advantages compared to bulk materials, especially for photodetection [Koppens14]. Despite a low value (2.3%), graphene's absorptance has the benefit to be constant over a wide spectral range going from terahertz to near ultraviolet range. Furthermore, graphene exhibits ultrafast charge carrier dynamics enabling conversion of photon into electrical currents with multi-gigahertz electrical bandwidth [Xia09, Mueller10], and also tunable optoelectronic properties (as shown just below). Accordingly, graphene is suitable for applications in optical communications [Pospischil13, Gan13] and long-wavelength detection [Vicarelli12]. On the other hand due to the peculiar behavior of electrons in graphene, graphene-based photodetectors suffer from high dark currents and thus large power consumption. Most of the studied graphene-based photodetectors consist of lateral p-n junctions created by doping differently two regions of graphene either electrostatically or chemically. An example of such a device with split gates is depicted in Fig. 2.8(a). The built-in electric field at the junction separates the photogenerated electron-hole pair giving rise to a photocurrent (see Fig. 2.8(b)). However, in this device the photo-thermoelectric (Seebeck) effect is believed to be the dominant photocurrent generation mechanism and not the electron-hole pair separation [Xu09, Gabor11]. Note that this mechanism is very fast since the electron thermalization is ultra-fast ($\sim 10-50$ fs) [Tielrooij13].

Thermal radiative emission from graphene was reported by several groups, e.g., [Berciaud10, Freitag10, Engel12, Kim15b]. Recently, Kim *et al.* [Kim15b] have reported bright visible light emission in suspended mono- and multilayer graphene (see Figs. 2.8(c) and (d)). The devices basically consist in graphene transistors that work in the same way as the filament in a light bulb.[4] In contrast to a light bulb's filament (such as tungsten), when temperature increases, graphene conducts less heat resulting in a spatial localization of the hot electrons in a spot at the center of the graphene sheet. Consequently, the efficiency of the thermal radiation is greatly enhanced in this spot. In addition, by playing with optical interference (see Chapter 4 Section 4.3) and with the design of the devices, it is possible to enhance and spectrally filter the light (see also [Engel12]).

[4] Fun fact: they were awarded by the Guinness World Records the record for 'the world's thinnest (0.335 nm) light source'

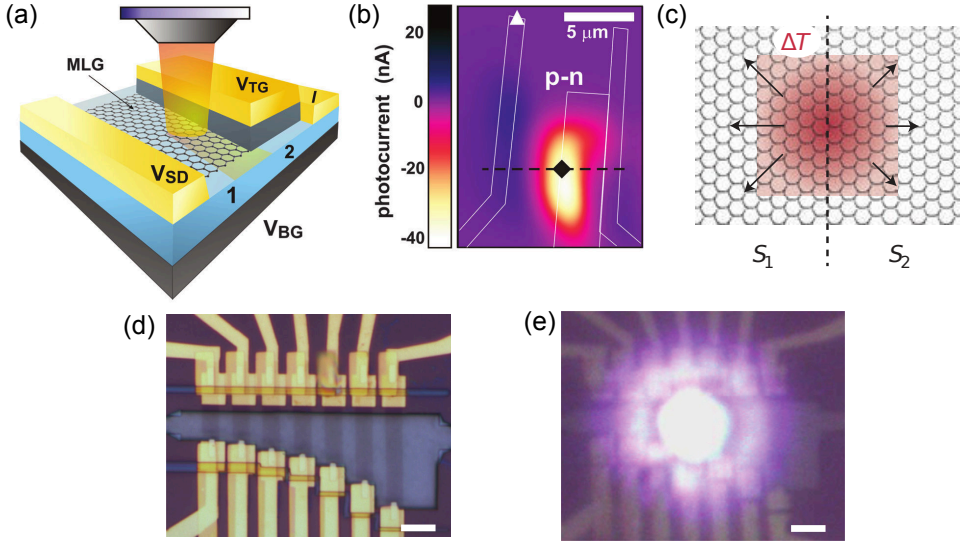

Figure 2.8 – *(a) Three-dimensional schematic view of double-gated (back and top) device used to demonstrate the photo-thermionic effect. By applying appropriate biases to the top (V_{TG}) and back (V_{BG}) gates, two differently doped regions (1 and 2) are created. (b) Photocurrent map of the corresponding device. White lines mark location of gold contact and gate electrodes. A hot spot at the p-n junction is observed. Figures extracted from Ref. [Gabor11]. (c) Schematic representation of the photo-thermoelectric mechanism. The red shaded area indicates elevated electron temperature. S_1 and S_2 are the Seebeck coefficient in graphene areas with different doping. Figure extracted from Ref. [Koppens14]. (d) Optical image of a device with suspended multilayer graphene flakes. Each flake is contacted by source and drain electrodes. No bias is applied. (e) Optical image of the same device but with a source-drain bias $V_{SD} = 7.90$ V. Scale bars, 5 μm. Images extracted from Ref. [Kim15b].*

2.2 Semiconducting transition metal dichalcogenides

This second section is dedicated to the basic properties of semiconducting transition metal dichalcogenides. As for graphene, we give few examples of optoelectronic devices at the end of the section.

2.2.1 Crystal structure

Transition metal dichalcogenides (TMDs) are layered crystals with chemical formula MX_2, where M is a transition metal atom (e.g., Mo, W, Ta, Nb, Zr,...) and X is a chalcogen atom (S, Se, Te) [Wilson69, Chhowalla13, Xu13]. These crystals consist in one layer of transition metal atoms sandwiched between two layers of chalcogen atoms, thus forming a X-M-X structure (see Fig. 2.9). Within each layer, the atoms are held together by strong covalent bonds while adjacent layers are connected by weaker van der Waals interactions. Among all existing TMDs, we focus only on semiconducting transition metal dichalcogenides (SCTMDs). Despite the fact that all TMDs have an hexagonal structure, thery can display different polytypes [Wilson69, Katzke04, Ribeiro-Soares14]. The two most common polytypes of SCTMDs are trigonal prismatic (H) and octahedral (T). These terms refer to the metal atom coordinations in the monolayer (see Fig. 2.9(a) and (b)). For bulk TMDs, these two polytypes are denoted 2H (since two layers are required to form the primitive unit cell) and 1T (as only one layer is required to form the bulk primitive unit cell), respectively. The 2H polytype can exist in two forms with different stacking order: 2Ha with /AbA CbC stacking and 2Hc with /CaC AcA/ stacking, where upper cases represent chalcogen atoms and lower cases metal atoms (see Fig. 2.9(d) and (e)). In the former, a metal atom is always on top of another metal atom of the subsequent layer. In the latter, any metal atom is sitting on top of two chalcogens of the next layer. In this thesis, we focus only on the 2Hc polytype[5] which occurs in many TMDs such as MoS_2, $MoSe_2$, $MoTe_2$, WS_2 and WSe_2. Let us just mention two points. First, many 1T TMDs, such as ReS_2 and $ReSe_2$, adopt a distorted structure (denoted 1T') with lower symmetry in which the metal atom is displaced away from the center of the coordination unit [Ho97, Ho98, Ho04, Tiong99]. Second, phase transition between different polytypes can occur, for instance MoS_2 crystals can be brought in the metastable 1T/1T' phase by lithium intercalation and then brought back to the thermodynamic stable 2H phase by deintercalation due to heat [Guo15b].

Figure 2.10(a) displays the top view of 2Hc TMDs. Like graphene, the Bravais lattice is hexagonal with two basis vectors $(\boldsymbol{a_1}, \boldsymbol{a_2})$. Consequently, the first Brillouin zone is also hexagonal (see Fig. 2.10(b)) with basis vectors $(\boldsymbol{b_1}, \boldsymbol{b_2})$ and there are two inequivalent points K and K' at the corner of the zone. Noteworthy, in the bulk case, the first Brillouin zone is a hexagonal prism with an additional high symmetry point A located on top of the Γ point at half the length of the reciprocal basis vector along k_z (see Fig. 2.10(c)). In addition, the absence of inversion center in the monolayer, and more generally in all odd number of layers

[5] If not mentioned, in the following when we refer to SCTMDs, we implicitly refer to the 2Hc polytype.

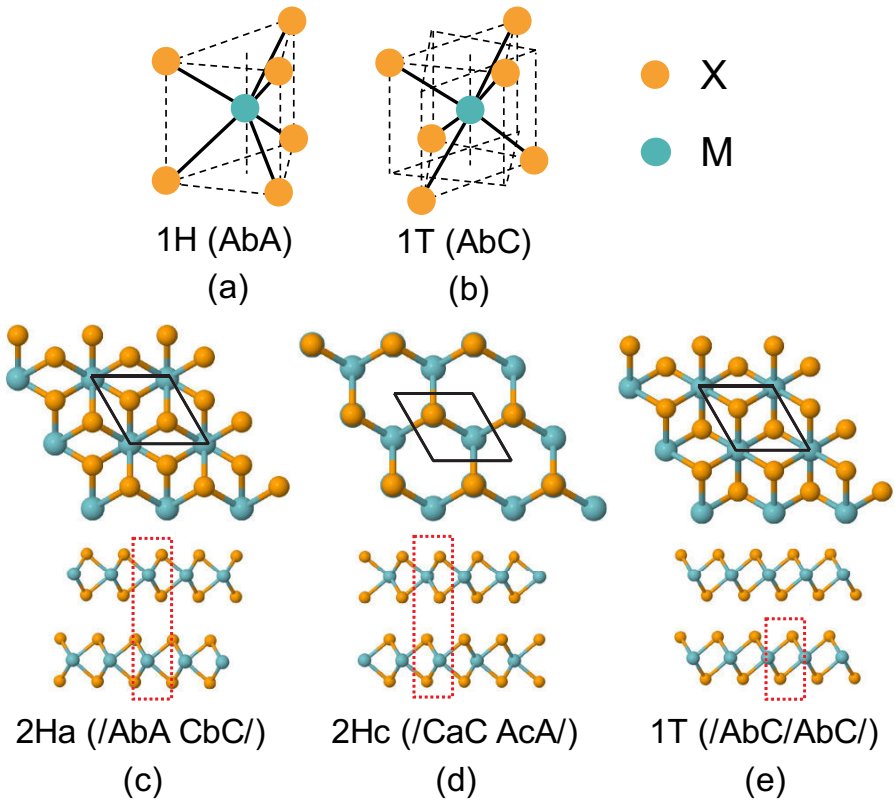

Figure 2.9 *– The two most common semiconducting TMDs polytypes. Transition metal atom coordination for (a) trigonal prismatic H and (b) octahedral T polytypes. The blue spheres represent transition metal atoms and orange ones chalcogen atoms. Top and lateral views of (c) 2Ha, (d) 2HC and (e) 1T bulk polytypes. The primitive unit cells are highlighted with black diamonds in the top views and red dashed squares in the lateral ones. The primitive unit cell of 2H polytypes comprises six atoms, while the one of 1T polytypes has three atoms. The stacking orders are indicated in brackets. Figure adapeted from Ref. [Ribeiro-Soares14].*

(see Chapter 3 Section 3.3), has important consequences on the optoelectronic properties such as valley properties (see below) or second harmonic generation [Kumar13, Li13, Malard13, Zeng13].

2.2.2 Indirect-to-direct bandgap crossover

N-layer molybdenum- and tungsten-based SCTMDs are semiconductors with optical bandgaps in the range 1 – 2 eV making them very attractive for visible and near-infrared applications, but also for fundamental studies. Indeed, they provide a unique platform to investigate the evolution of the physical properties from three-dimensional bulk to quasi two-dimensional (2D[6]) monolayer systems.

The most obvious illustration of the evolution of the physical properties with the N is the transition from an indirect bandgap in the bulk to a direct bandgap in the monolayer. This transition was first observed experimentally by Mak *et al.* [Mak10] and Splendiani *et al.* [Splendiani10] as a drastic enhancement of the photoluminescence (PL) in monolayers.

[6]It should not be confused with graphene's 2D mode.

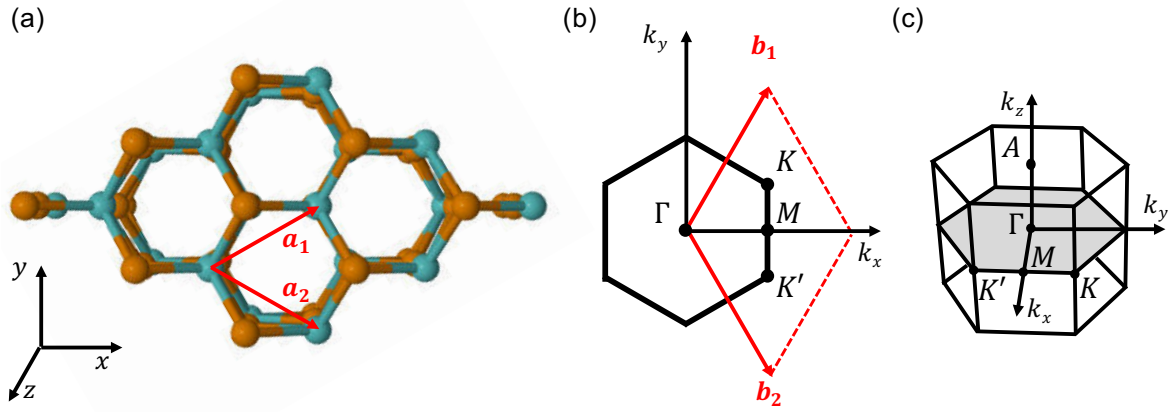

Figure 2.10 *– (a) Top view of 2Hc TMDs. $\boldsymbol{a}_1$ and $\boldsymbol{a}_2$ are the in-plane primitive unit vectors. (b) Corresponding first Brillouin zone. $\boldsymbol{b}_1$ and $\boldsymbol{b}_2$ are the in-plane reciprocal primitive unit vectors. The main four points are labeled: Γ, K, K′ and M. (c) Three-dimensional first Brillouin zone of bulk 2Hc TMDs. In addition to the four points depicted in (b), there is a fifth point labeled A.*

Indeed, a 100-fold enhancement of the quantum yield for monolayers compared with bilayers (see Fig. 2.11(a)) was reported for MoS_2. Compared to bulk, this quantum yield is even four orders of magnitude larger. This observation is confirmed by density-functional theory (DFT) band structure calculations. Figure 2.11(b) shows computed electronic band structure for bulk MoS_2 and various thicknesses. Bulk MoS_2 has an indirect bandgap of approximately 1.3 eV with the valence band maximum at the Γ point and the conduction band minimum halfway along the K–Γ direction in the Brillouin zone. As the thickness decreases the valence band maximum and conduction band minimum shift due to quantum confinement effects. In the monolayer limit, MoS_2 has a direct bandgap of approximately 1.9 eV at K. Interestingly, the direct transition at K remains almost not altered by the thickness variation, while the indirect transition is much more affected. Similar observations were made for others Mo- and W-based TMDs [Gutiérrez12, Tonndorf13, Ruppert14].

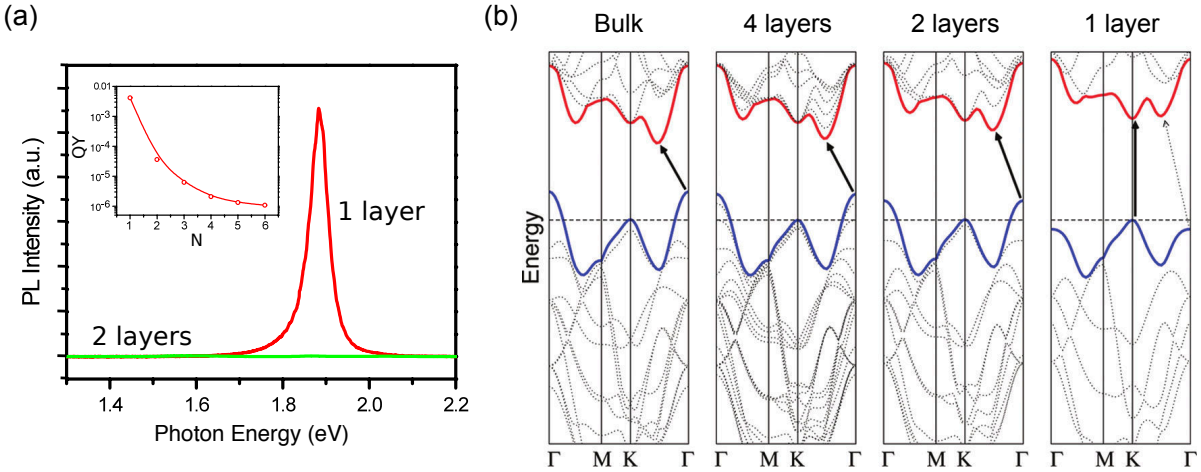

Figure 2.11 *– (a) Photoluminescence spectra of suspended monolayer and bilayer MoS_2 recorded under ambient conditions. The inset shows the quantum yield (QY) for $N = 1$ to $N = 6$ MoS_2 layers. Figure adapted from Ref. [Mak10]. (b) Calculated band structure of bulk, 4 layers, bilayer and monolayer MoS_2. The arrows indicate the lowest energy transitions. Figure extracted from Ref. [Splendiani10].*

Although monolayers SCTMDs are direct semiconductors, they exhibit very poor quantum yield. As an example, the room-temperature quantum yield of monolayer MoS_2 was found to be 4×10^{-3} only [Mak10] (see inset in Fig. 2.11(a)). One order of magnitude better yields were reported for $MoSe_2$ and WSe_2 [Tonndorf13]. Furthermore, very recently, organic superacid treatment has shown to enhance the PL by more than two orders of magnitude resulting in nearly unity quantum yield [Amani15]. All these observations reflect the high sensitivity of monolayers to their environment [Qiu12, Tongay13, Nan14, Lee15a, Gao16] and show that the PL of monolayers SCTMDs is dominated by extrinsic effects rather than intrinsic. The mechanisms associated with these effects are not yet understood and are actively under investigation by many research groups.

2.2.3 Excitonic properties

Excitons The optical properties of SCTMDs are dominated by excitonic effects (see Chapter 7 Section 7.1 for a brief introduction to excitonic effects) especially for monolayers. The values of the bandgaps given below were estimated from the position of the PL feature and thus do not correspond to interband (or band-to-band) transitions. It is essential to distinguish between the **optical bandgap** which is the energy of the emitted or absorbed photons (and therefore takes into account the binding energy of the exciton) and **electrical bandgap** which characterizes single-particle (or quasiparticle) excitations. In the quasi two-dimensional limit of monolayers, such excitonic effects are very strong due to reduced screening of the Coulomb interaction (resulting in strong interactions) and relatively large effective masses [Mak16] (see Fig. 2.12(a)). As expected, the exciton binding energy decreases with thickness due to strong screening. Experimentally, excitonic effects lead to sharp features in the absorption spectrum rather than expected steps for a two-dimensional system, as sketched in Fig. 2.12(b). The inset in Fig. 2.12(c) displays the measured reflectance contrast[7] of WS_2 monolayer allowing to identify the A, B and C excitons.[8] These different excitons arise from distinct excitonic transitions as we will see later. Note that the typical absorptance of monolayers SCTMDs for photon energies higher than the A exciton is on the order of 10 %. The A exciton, which is the band-edge exciton, dominates the PL response of monolayers SCTMDs (e.g., in Fig. 2.11(a) only the A exciton is visible). Consequently, the optical bandgap corresponds to the energy of the A exciton. Let us point out that in general, excitonic effects are particularly strong in low-dimensional system where screening effects are reduced such as SCTMDs or carbon nanotubes [Wang05, Maultzsch05].

Exciton binding energy As the optical response of SCTMDs is dominated by excitonic effects, optical spectroscopy, especially absorption and PL, are primary tools to study excitons (see Chapter 7 Section 7.1 for a brief introduction to PL spectroscopy). Several groups have predicted [Ramasubramaniam12, Cheiwchanchamnangij12, Molina-Sánchez13, Qiu13] and reported [Chernikov14, He14b, Ye14, Ugeda14, Wang15b, Zhu15] tightly bound exci-

[7] The absorption spectrum can be deduced from this quantity, see, e.g., [McIntyre71, Buckley77].
[8] This notation follows the pioneering work of Wilson and Yoffe [Wilson69].

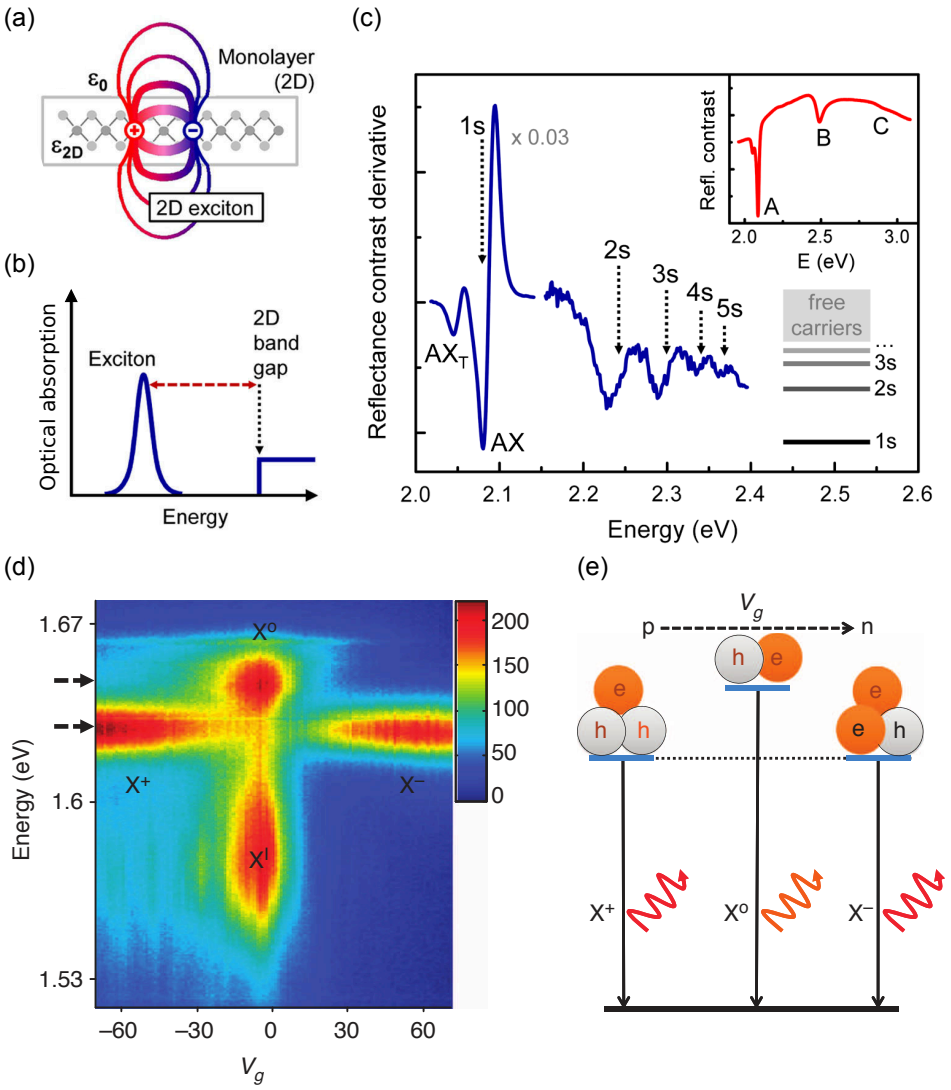

Figure 2.12 *– (a) Cartoon of an exciton in a monolayer TMD. The lines represent the electric field lines of the electron-hole dipole. ε_{2D} is the dielectric constant of the TMD and ε_0 is the vacuum permittivity. (b) Schematic illustration of the absorption spectrum of a monolayer TMD that shows one exciton feature at lower energy than the bandgap. (c) Derivative of the reflectance contrast spectrum. The exciton ground state is labeled 1s and the excited states are denoted 2s, 3s, 4s and 5s (this states are sketched at the bottom right). In addition to these states of the neutral A exciton (AX), the trion is also visible (AX_T). The inset displays the A, B and C exciton transitions. These three figures are adapted from Ref. [Chernikov14]. (d) Color map of the photoluminescence of monolayer $MoSe_2$ as a function of the gate voltage. Near zero doping, the neutral X^0 and impurity-trapped exciton X^I dominate the spectrum, while for electron (hole) doping the negative (positive) trion dominates. (e) Illustration of the gate-dependent trion and exciton quasiparticles and transitions. These two figures are extracted from Ref. [Ross13].*

tons in monolayers SCTMDs. For instance, Fig. 2.12(c) presents the reflectance measurements of monolayer WS_2 reported by Chernikov *et al.* [Chernikov14]. Multiple peaks are resolved (corresponding to optically active states) and can be associated with the *s*-shell excitonic Rydberg series.[9] However, the careful analysis reveals severe deviations from the two-dimensional hydrogen-like model due to the complex screening of the Coulomb interaction. An exciton binding energy of $E_b = 0.32$ eV was extracted. Typical measured val-

[9] Note that the *p*-like states can be probed using two-photon measurements [He14b, Wang15b, Zhu15].

ues of E_b for monolayers SCTMDs lie between 0.3 and 0.6 eV (see Tab. 2.1), which correspond to a Bohr radius of approximately 1 nm. The exciton binding energies exceed by more than one order of magnitude those in the bulk and in conventional two-dimensional systems based GaAs-like semiconductors [Glazov15]. All these results show that the optical properties of monolayers SCTMDs are governed by robust excitons even at room temperature. Furthermore, PL lifetime in the range of one to tens of picoseconds were predicted and reported [Korn11, Lagarde14, Shi13, Wang14, Palummo15, Robert16a] at low and room temperature, showing the high exciton oscillator strength in these 2D materials.

Trions In addition to excitons, higher-order excitonic quasiparticles can also be observed in monolayers SCTMDs due to the strong Coulomb interaction. In particular, trions [Kheng93], which are positively or negatively charged excitons, were reported [Mak13, Ross13]. These observations were accomplished by electrostatic control of the doping level in TMD field effect transistors. Figure 2.12(d) shows the PL measurements by Ross *et al.* [Ross13] for a monolayer $MoSe_2$ under gate bias. When going from hole to electron doping (i.e., from negative to positive gate bias), we observe the evolution from positive trion (X^+) to neutral exciton (X^0) and then to negative trion (X^-). The trion binding energy (i.e., the energy difference between $X^\pm$ and X^0) was found to be around 30 meV for both negative and positive trions, as the effective electron and hole masses are similar. Comparable values were also experimentally measured [Mak13, Jones13, Yang15] or theoretically calculated [Berkelbach13], and far exceed those in conventional quasi two-dimensional semiconductors [Glazov15, Mak16]. The observation of stable trions at room temperature opens very promising perspectives, especially for electrical purpose or quantum coherent states [Mak16]. It is worth mentioning that biexcitons (bound states of two excitons) were reported in monolayer SCTMDs under high optical excitation densities [You15, Plechinger15].

2.2.4 Spin and Valley properties

Let us now focus more precisely on the band structure of monolayers SCTMDs. Various methods, such as DFT, tight-binding models or $\boldsymbol{k}\cdot\boldsymbol{p}$ perturbation theory [Glazov15], can be employed to calculate this band structure. In any case, it exhibits degenerate conduction and valence band-edges around the two inequivalent K and K' points in the Brillouin zone (see Fig. 2.13(a)), which govern most of the electrical and optical properties.

These two inequivalent valleys are coupled by time-reversal symmetry. To distinghuish if a carrier is in one valley or in the other, one can define a **valley pseudospin** [Xu14]. A careful symmetry analysis reveals that interband optical transitions are chiral: the transitions at K (K') valley are only excited by left (right) circularly polarized light σ^+ (σ^-) [Xu14, Glazov15]. Note that such valley-contrasting physical properties are a direct consequence of inversion symmetry breaking in monolayers SCTMDs [Xu14]. Selective valley population was experimentally demonstrated using circularly polarized light excitation [Mak12a, Sallen12, Jones13]. By measuring the polarization of the emitted light, it was

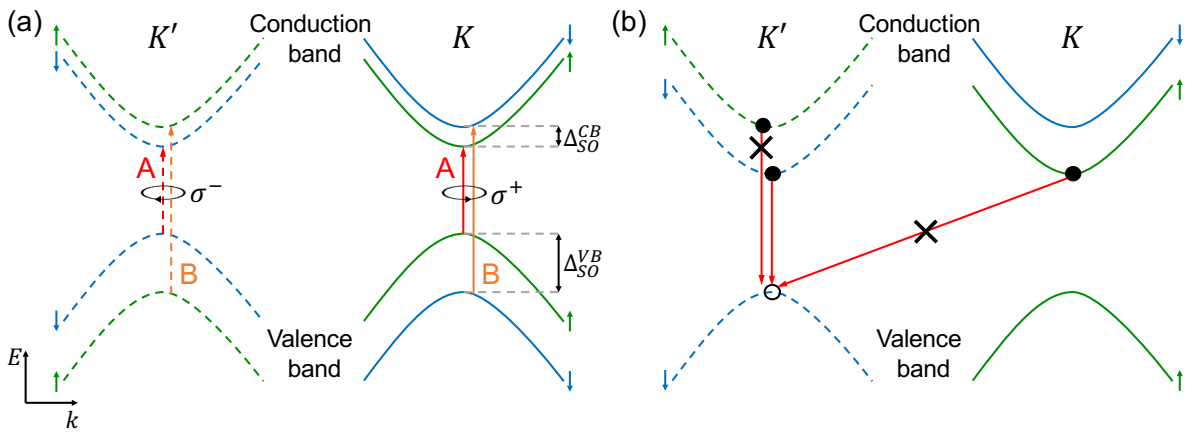

Figure 2.13 *– (a) One-dimensional band structure around K and K′ points of monolayers SCTMDs. The electronic spin states are labeled by small arrows and drawn in different colors. Spin-orbit coupling leads to the splittings of valence Δ_{SO}^{VB} and conduction bands Δ_{SO}^{CB}. Long vertical solid and dashed arrows show the allowed interband transitions giving rise to A and B excitons. The optical chiral selection rules are indicated. σ^+ (σ^-) denotes left (right) circularly polarized light. The order of conduction band states is displayed for Mo-based SCTMDs. The order is reverse for W-based SCTMDs. (b) Focus on the A excitonic transitions. Filled circles denote electrons and the open circle hole. One bright and two dark (crossed arrows) excitons are represented.*

proven that valley polarization was achieved and largely preserved during the exciton lifetime. The ability to manipulate the valley degree of freedom, together with unique properties such as the valley Hall effect [Mak14], paves the way towards the new field of **valleytronics** which exploits this degree of freedom for information processing. In this thesis, we will not further consider this degree of freedom since we are exciting the samples with linearly polarized light (see Chapter 4) and therefore excitons in both valleys are created.

Taking into account the electron spin, the spin-orbit interaction splits the valence bands by an energy $\Delta_{\mathrm{SO}}^{\mathrm{VB}}$ and the conduction band by $\Delta_{\mathrm{SO}}^{\mathrm{CB}}$ at each valley [Xu14, Glazov15]. The time-reversal symmetry ensures the splittings to be of opposite signs in the K and K' valley (see Fig. 2.13(a)). As a result, spin and valley pseudospin degrees of freedom are locked. The chiral selection rules are not changed by spin-orbit coupling [Glazov15]. However, because the dipole interaction with electromagnetic field conserves the spin, only two interband transitions at each valley are allowed. These transitions give rise to the aforementioned A and B excitons. As $\Delta_{\mathrm{SO}}^{\mathrm{VB}} \gg \Delta_{\mathrm{SO}}^{\mathrm{CB}}$ (see Tab. 2.1), the energy difference between the A and B excitons provides a direct measurement of the valence band splitting.

The conservation of spin for the interband transitions has very important consequences. Let us focus on the A exciton. Figure 2.13(b) illustrates the band structure in the case of Mo-based SCTMDs. In the case of W-based materials, the order of conduction band states is opposite (see Tab. 2.1). When an exciton is created, there are eight possibilities: two for the hole (the two valleys) and four for the electron (two valleys and two spins). Among them, there are only **two bright excitons** (corresponding to intravalley interband transitions that preserve the spin)[10] and six **dark excitons** (corresponding to all intervalley excitons and to

[10]These excitons are singlet like intravalley excitons.

not allowed intravalley interband transitions[11]). As an example, one bright exciton and two dark excitons are sketched in Fig. 2.13(b). An exciton can transit from a bright state to a dark state for instance by intravalley spin flip or intervalley scattering due to, e.g., thermal fluctuations. The energy difference between bright and dark excitons is determined (in first approximation) by the conduction band splitting Δ_{SO}^{CB} which is in the meV to tens of meV range (see Tab. 2.1). As a consequence, bright states in Mo-based materials are lower in energy than dark states and *vice-versa* in W-based materials. It qualitatively explains why MoS_2 and $MoSe_2$ are better emitters at low temperature than WS_2 and WSe_2 [Zhang15a]. It also explains why in time-resolved PL measurement at room-temperature at least two times are observed, one short and one long, which reflect competiting emission pathways from bright and dark excitons. In contrast only one time is observed at low temperature. However, to fully understand the exciton dynamics in monolayers SCTMDs, others mechanisms have to be taken into account.[12] For a recent review on this subject, see Ref. [Moody16].

	MoS_2	$MoSe_2$	$MoTe_2$	WS_2	WSe_2
E_X (eV)	2	1.7	1.1	2.1	1.8
E_b (meV)	300	600	580	550	400
Δ_{SO}^{VB} (meV)	150	180	250	430	470
Δ_{SO}^{CB} (meV)	3	20	?	-30	-35

Table 2.1 *– Basic optoelectronic properties of 2Hc monolayers TMDs. E_X denotes the optical bandgap (A-exciton energy), E_b the A-exciton binding energy, and Δ_{SO}^{VB} and Δ_{SO}^{CB} the spin-orbit splittings of the valence and conduction bands, respectively. The values are extracted from the review [Mak16], except for $MoTe_2$ for which the data are extracted from Refs. [Ruppert14, Yang15].*

2.2.5 Vibrational properties

Similarly to their optoelectronic properties, the vibrational properties of TMD critically depend on the number of layers. Raman spectroscopy emerges as the ideal tool to study these vibrational properties [Lee10]. Indeed, it offers a fast and unambiguous method to determine the number of layers and to probe the electron-phonon interactions [Zhang15b]. Figure 2.14 shows the calculated phonon dispersion relation for monolayer MoS_2. In contrast to graphene, there are no Kohn anomalies. Consequently, electron-phonon interactions are weaker than in graphene. However, such interactions are notably important for transport properties as they limit the carrier mobility in monolayers TMDs due to deformation potential and Fröhlich interactions [Kaasbjerg12]. Furthermore, compared to graphene, Raman spectroscopy of TMDs remains less known. Therefore, we have dedicated the whole Chapter 6 on the Raman spectroscopy of N-layer TMDs.

[11] These excitons are triplet like intravalley excitons.

[12] For instance, a bright exciton can be scattered to a dark exciton state with the same spin but located outside the light cone [Robert16a].

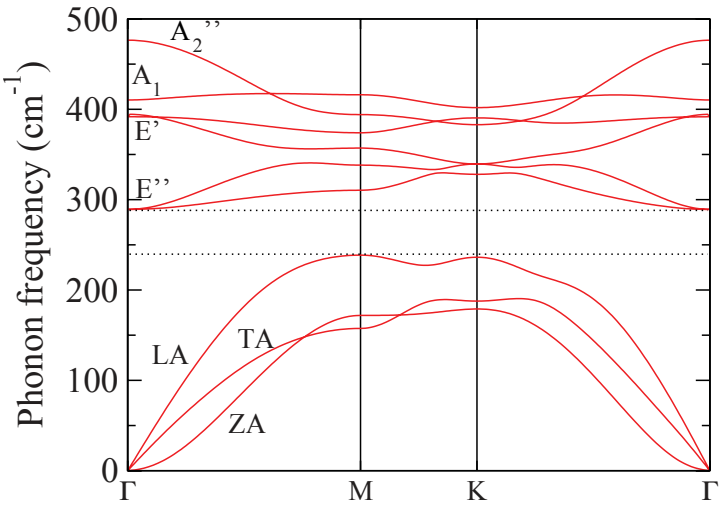

Figure 2.14 *– Calculated phonon dispersion relation of monolayer MoS_2. Figure extracted from [Molina-Sánchez11].*

2.2.6 Optoelectronic applications

SCTMDs-based optoelectronic devices have attracted tremendous attention due to their properties that complement those of graphene-based devices. Indeed, SCTMDs are advantageous for applications that require high sensitivity and low dark currents, and can operate in the visible and near-infrared spectrum. Up to now, mainly two groups of SCTMDs-based optoelectronic devices have been investigated: (i) SCTMDs-based FETs (i.e., lateral metal-TMD-metal devices) that are called phototransistors and (ii) in-plane p-n junction in SCTMDs where p-n junctions are created by local electrostatic gates. An example of each type of devices is depicted in Fig. 2.15.

Phototransistors Phototransistors are chiefly used for photodetection (see Fig. 2.15(a)), e.g. [Yin11, Lee12a, Lopez-Sanchez13]. Such devices consist in applying a source-drain voltage and monitoring the source-drain current under optical illumination which changes the sheet conductivity. The mechanisms that give rise to photoconductivity in SCTMDs-based transistors are carefully studied in Ref. [Furchi14a]. These devices have the advantage to be able to operate on homogeneous SCTMDs layers and do not need the introduction of a junction or a built-in field. On the other hand, they are rather slow and are thus only suitable for applications that do not require fast response times. Phototransistors can also be exploited for electrically driven light emission. Under high source-drain bias hot carrier processes can occur and light can be emitted [Sundaram13]. However, the efficency (ratio between the emitted optical power and electrical input power) of such devices was found to be $\sim 10^{-5}$ which is rather low compared to conventional devices based on p-n junctions (see below).

Lateral p-n junctions The second type of optoelectronic devices was achieved almost simultaneously by three independent groups [Pospischil14, Baugher14, Ross14]. They all used the same design: split-gate electrodes coupled to two different regions of a WSe_2 monolayer

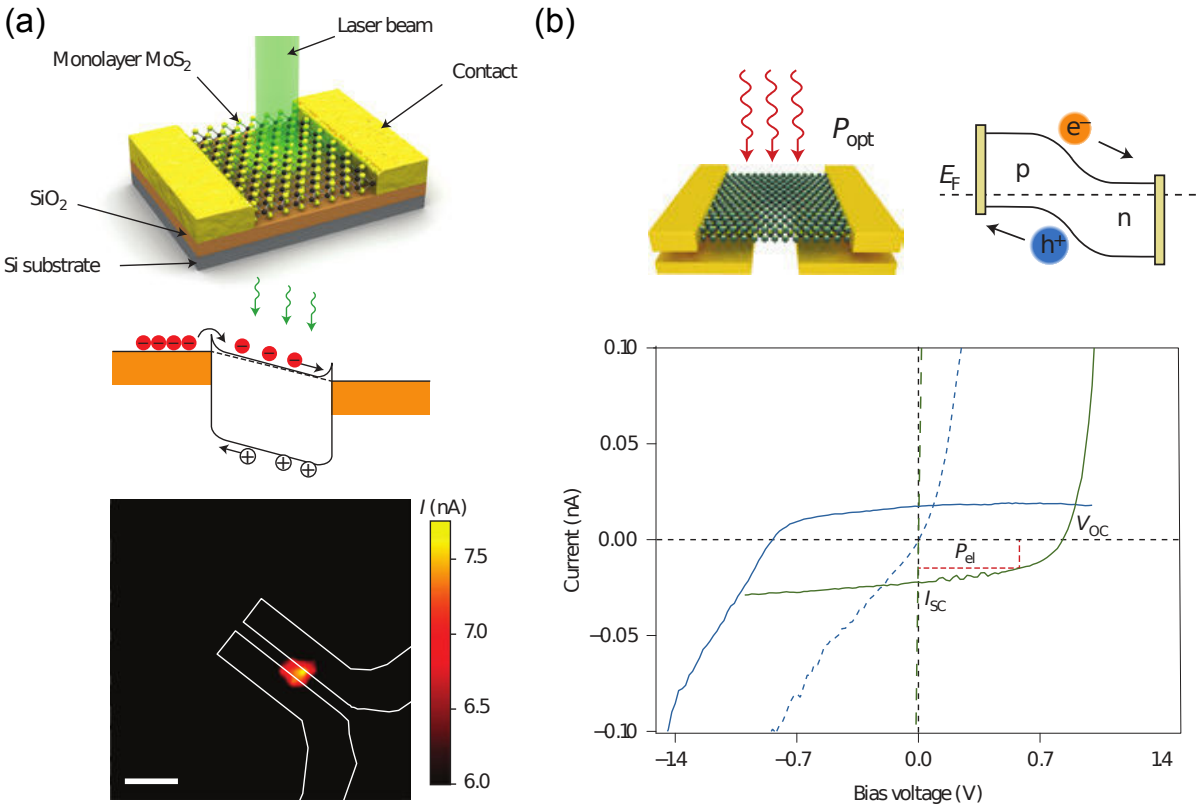

Figure 2.15 *– (a) Top: three-dimensional schematic view of a monolayer MoS_2 phototransistor. Middle: band diagram of the phototransistor under source-drain bias and optical illumination. Bottom: map of the photocurrent displaying a hot spot that corresponds to the monolayer MoS_2. Scale bar: 5 µm. Figures extracted from Ref. [Lopez-Sanchez13]. (b) Top left: three-dimensional schematic view of a WSe_2 devices with split-gate electrodes. P_{opt} is the optical power. Top right: band diagram of the device when operating as a p-n junction. Bottom: Photocurrent as a function of the bias voltage under different biasing conditions. The solid green line correspond to p-n junction,the solid blue line n-p, the dashed green line n-n, and the dashed blue line p-p. V_{OC} is the open-circuit voltage, I_{SC} is the short-circuit current, P_{el} is the electric power and E_F is the Fermi energy. Figures extracted from Refs. [Pospischil14, Mak16].*

(see Fig. 2.15(b)). By biasing one gate electrode with a negative voltage and the other with a positive voltage a lateral p-n junction is made. The main advantage, compared to traditional p-n junctions created with impurities, is that depending on the sign of the two gate voltages, p-n, n-p, p-p or n-n junctions can be obtained on the same device. Such devices exhibit the typical photodiode characteristic as shown in Fig. 2.15(b). Hence, they can operate as photodetector or photovoltaic devices. By driving a current through the electrostatically defined diode, electroluminescence was obtained with much better efficiency that for the hot carrier emission in phototransistors. However, for both detection and emission, these devices suffer from the fact that their active area are limited in space because of the lateral arrangement of the junction. This last point brings us to the next section where heterostructures based on 2D materials offer the possibility to build vertical junctions with larger active areas than lateral ones.

2.3 Heterostructures

In this section, we give a brief overview of heterostructures based on 2D materials. Broadly speaking these heterostructures can be separated into two groups: (i) **hybrid heterostructures** based on 2D materials and nano-objects such as quantum dots or plasmonic antennas and (ii) **van der Waals heterostructures** made by artificially stacking different 2D materials.[13] Compared to devices based on pristine layers, heterostructures offer the possibility to combine the advantages of different nanomaterials. Heterostructures are already used in the semiconductor industry in a variety of applications such as light emitting diodes (LED) or laser [Casey12]. However, compared to the existing technologies, heterostructures based on 2D materials offer flexibility, semi-transparency, better scalability and integrability at lower cost. We will first present the fabrication techniques and the coupling mechanisms. Then, we introduce selected examples of heterostructures.

2.3.1 Fabrication techniques

Hybrid heterostructures Hybrid heterostructures are usually fabricated following conventional micro-fabrication techniques [Houdy06]. The 2D material is either mechanically exfoliated or grown using chemical vapor deposition (CVD) or epitaxial methods. Then the nano-objects are deposited by drop-casting or spin-coating. In the case of plasmonic structures, they are patterned by standard fabrication techniques. Noteworthy, large-area hybrid heterostructures are in general easy to fabricate (especially compared to van der Waals heterostructures).

Van der Waals heterostructures On the other hand, van der Waals heterostructures (vdWHs) are fabricated using outlandish techniques. Currently, the most versatile technique is the direct assembly by micromechanical stacking (see Fig. 2.16(a)). This technique is possible owing to the van der Waals nature of the interlayer interactions. Because of this weak interlayer interactions, vdWHs have the major advantage of not requiring any lattice matching conditions contrary to traditional epitaxial semiconductor heterostructures. Consequently, any arbitrary sequence of layered materials is allowed and since there exists a library of avaiblable layered materials with distinct properties, a huge amount of novel heterostructures can be built showing unique properties [Geim13]. Unfortunately, such a fabrication technique is not suitable for large scale production. However for fundamental research, it is a practical tool that provides samples of unmatched quality. Meanwhile, alternative techniques (e.g., liquid exfoliation, CVD or epitaxial growth), that might be appropriate for large scale production, are under investigation but are currently in their infancy. For a recent review, see Ref. [Novoselov16].

Micromechanical assembly of layers can be divided into three methods:

[13] Note that in hybrid heterostructures, the different systems are usually also connected by van der Waals interactions. However, here van der Waals heterostructures refer exclusively to heterostructures made up of 2D materials.

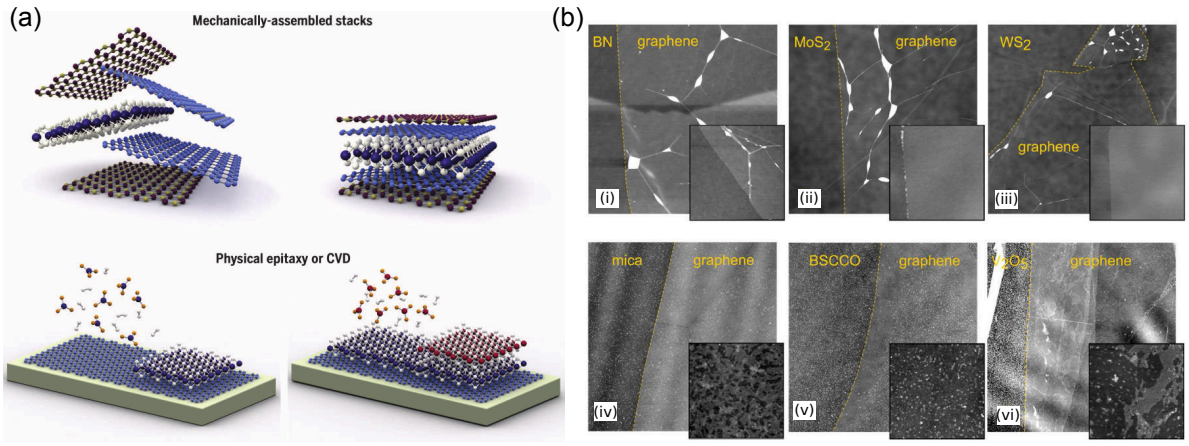

Figure 2.16 *– (a) Cartoon of the fabrication of van der Waals heterostucutres. The mechanical assembly (top) is suitable for research purposes, while large-scale growth by CVD or epitaxy (bottom) are promising for technological purposes. Figure extracted from Ref. [Novoselov16]. (b) Atomic force microscopy images of graphene transfered on various 2D crystals. A self-cleaning mechanism occurs for graphene on (i) hBN, (ii) MoS_2 and (iii) WS_2. In contrast for (iv) mica, (v) BSCCO and (vi) V_2O_5, no self-cleaning mechanism happens, instead contamination is spread uniformly across the whole interface. Insets:* $1.5\ \mu m \times 1.5\ \mu m$. *Pictures extracted from Ref. [Kretinin14].*

(i) The **'sacrificial'** method. This technique is based on exfoliating a flake on a sacrificial membrane, aligning and placing it on top of another flake and then removing the membrane with chemical treatments in liquid phase [Dean10]. This process is repeated to deposit further layers. Annealing is often performed to remove the contaminants and to improve the interface quality. As it involves at least one step with chemical treatments in liquid phase, it is referred to as a wet transfer.

(ii) The **'stamp'** method. This technique makes use of the viscoelastic properties of a polymer stamp like PDMS [Castellanos-Gomez14]. A flake is directly exfoliated onto the stamp, aligned and placed on top of another flake and then the flake is released by peeling off the stamp very slowly. This method is known as the **all-dry transfer technique** and results in cleaner samples. Although it is a method easy to implement, it is not a convenient technique to build vdWHs with a large number of layers. It is the method used in this thesis, see Chapter 4.

(iii) The **'pick-and-lift'** method. This technique is based on strong van der Waals interactions that exist between 2D crystals [Wang13]. A first flake is exfoliated on a membrane, aligned and placed on top of a second flake, and then brought into contact. The membrane is lifted up and the second crystal may stick to the first one. The process can be repeated several times and produces to very clean interfaces. At the end of the process, the entire stack is deposited onto a substrate and the membrane is washed away with chemical treatments in liquid phase. As there is a last step involving wet chemical processing, it is not a completely all-dry transfer but is often said to be because only the top layer might be contaminated by the membrane. Very recently, an improved version of this method came up which is called the **'hot pick-up'** technique [Pizzocchero16]. This

method utilizes a polypropylene carbonate (PPC) membrane to pick-up and release 2D crystals by playing with temperature and thus does not involve a sacrificial membrane. It can be viewed as a mix between the stamp and the pick-and-lift methods, and offer a much more precise control of the transfer.

Surprisingly, the interfaces between the different layers are free of contamination and are atomically flat due to the so-called **'self-cleaning'** mechanism [Haigh12, Kretinin14]. Figure 2.16(b) illustrates this mechanism: the affinity between 2D crystals is in general higher than the affinity between the crystals and contaminants, therefore it is energetically favorable to have the largest possible common interface between the two crystals; in consequence, the contaminants are pushed away. It results in the observed bubbles under transfered 2D crystals that correspond to pockets of contamination pushed away from the rest of the interface. Note that this mechanism works only for certain pairs of crystals.

2.3.2 Near-field coupling mechanisms

The physical properties of optoelectronic devices based on heterostructures are governed by the coupling mechanisms at the heterointerface. Uncovering and controlling these mechanisms is of scientific and technologic interest in order to improve the device performances or develop new devices. In this thesis, we choose to focus on the two main coupling mechanisms that are: **charge transfer** (CT) and **energy transfer** (ET). Before presenting charge and energy transfer, we have first to discuss how the electronic band structure of the different materials is changed in the heterostructure.

Band alignment

In conventional semiconductor heterostructures, the electronic bands of the different semiconductors deform to ensure the continuity of the band structure [Rosencher02]. However, in heterostructures based on 2D materials this situation is rather different especially in the case of monolayers. Indeed, the depletion region is often much larger than the atomically thin layers. Consequently, in first approximation, the band structure of the heterostructure can be considered as the superposition of the bands of the different materials [Kośmider13, Pierucci16a]. Figure 2.17(a) displays examples of calculated band alignments and bandgaps for II-VI semiconductors [Norris08], monolayer SCTMDs [Liang13] and monolayer graphene. The relative position of the bands is determined by the electronic affinity or the work function. These parameters can be experimentally measured using, for instance, scanning Kelvin probe microscopy [Yu09] or tranport measurements [Kim15a]. However, as illustrated in Fig. 2.17(b), calculated one-electron band structures provide a fair estimation of the bandgap and band alignment. Indeed, the single particle gap $E_{\mathrm{gap},0}$ is renormalized to E_{gap} by electron-electron interactions ($\delta E_{\mathrm{e\text{-}e}}$). The significant exciton binding energy (E_{b}) results in an optical transition (E_{opt}) that can be close to $E_{\mathrm{gap},0}$ [Ugeda14].

Interestingly, in Fig. 2.17(a) we can notice that it is possible to form type-II heterojunc-

tions where the lowest-energy electron states are spatially located in one component while the highest-energy hole states are in another. In type-II heterojunctions based on SCTMDs, optical excitation followed by charge separation may lead to the formation of **interlayer excitons** as as the interlayer separation is smaller than 1 nm. Such a charge separation can be harnessed in optoelectronic devices as depicted in Section 2.3.3.

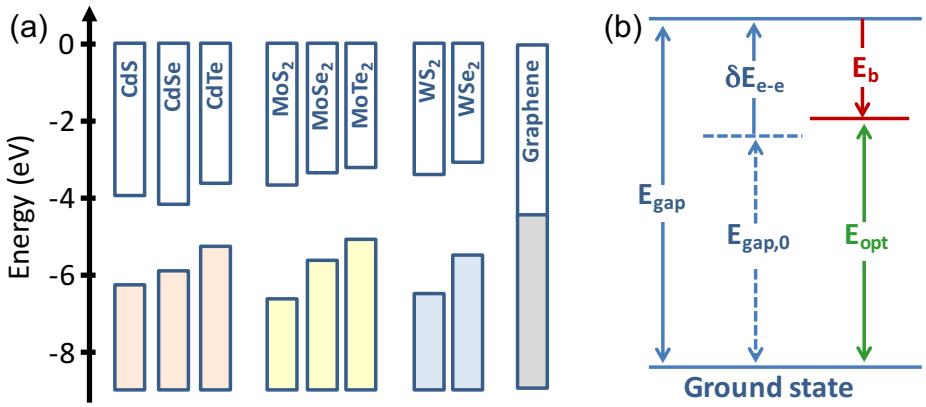

Figure 2.17 *– (a) Calculated band alignments and bandgaps for II-VI semiconductors [Norris08], monolayer SCTMDs [Liang13] and monolayer graphene [Yu09]. (b) Schematic of the relevant energy levels. The single particle gap $E_{gap,0}$ is renormalized to E_{gap} by electron-electron interactions ($\delta E_{e\text{-}e}$). The significant exciton binding energy (E_b) results in an optical transition (E_{opt}) that can be close to $E_{gap,0}$ [Ugeda14].*

Microscopic mechanisms

To present the microscopic mechanisms associated to the charge and energy transfer, we will use the example of a two-level system (which can correspond to the HOMO and LUMO of a molecule, the ground and excited state of a quantum dots, or the valence and conduction band edges) and a monolayer graphene. An electron is photoexcited in the two-level system which is the donor, while graphene plays the role of the acceptor. This example is of practical interest since in photodetectors graphene usually plays the role of the transparent electrode while the two-level system represents the photoactive material (see Section 2.3.3). From a more scientific point of view, graphene is an ideal acceptor because it is a semimetal, i.e., it offers a continuum of states covering the whole range of energies. However, these mechanisms can be generalized to other heterostructures.

Charge transfer The charge transfer corresponds to the spatial transfer of the photoexcited electron from the two-level system to an available state with equal or lower energy in the graphene sheet, as illustrated in Fig. 2.18(a). Since the electron is not in the two-level system anymore, CT leads to a **quenching** of the PL of the two-level system. The charge transfer can be evidenced by monitoring the doping level in the graphene flake. This is the approach that we will employ in Chapter 8 to study the CT between monolayers of $MoSe_2$ and graphene. Zhang *et al.* have followed a similar approach [Zhang14]. They have demonstrated and quantified a photoinduced electron transfer from a MoS_2 monolayer to graphene by monitoring the shift of the CNP in the electrical measurements as a function of the incident optical

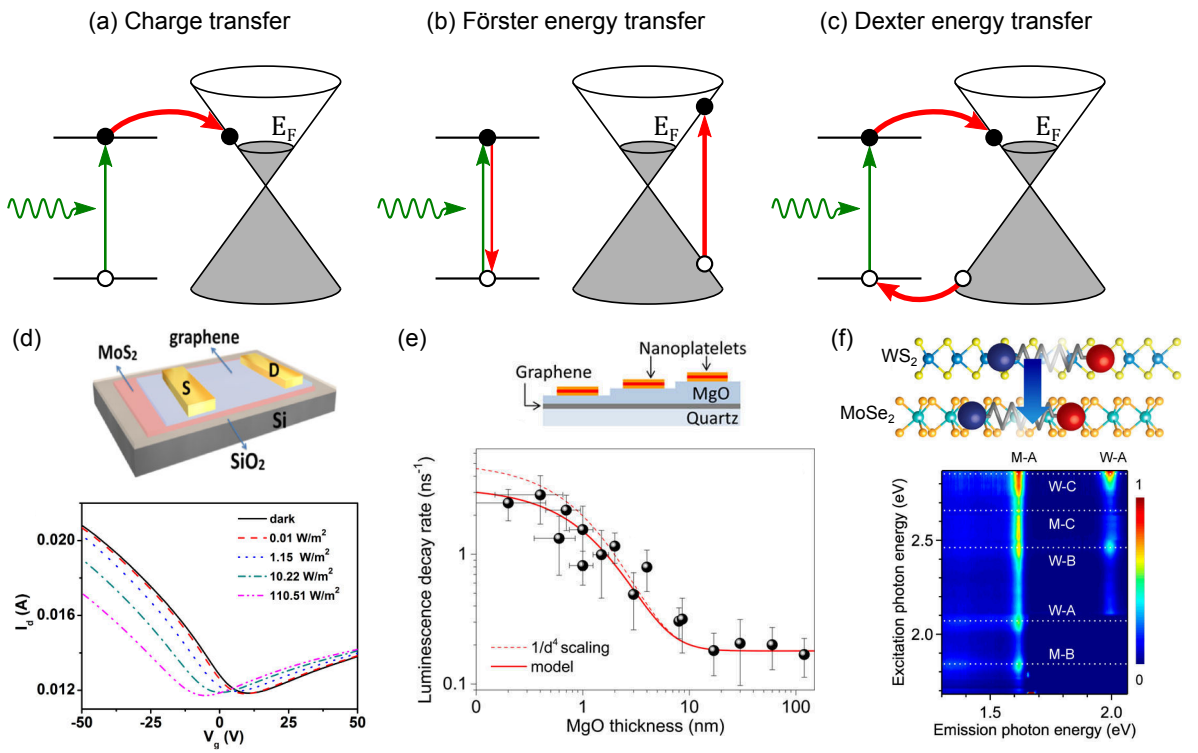

Figure 2.18 *– Schematic illustration of (a) charge transfer, (b) Förster energy transfer and (c) Dexter energy transfer between a two-level system and a graphene monolayer. (d) Top: three-dimensional schematic view of a vdWH device made of a monolayer graphene on top of a monolayer MoS_2. Bottom: transfer curves for the graphene sheet in the corresponding device under various incident optical densities. The CNP shifts with the optical density. Figures extracted from Ref. [Zhang14]. (e) Top: schematic diagram of a hybrid heterostucture based on semiconducting nanoplatelets and a monolayer graphene. The nanoplatelets are separated by a MgO spacer with various thicknesses. Bottom: measured decay rate of the nanoplatelets as a function of the thicknesses of the MgO spacer. The red solid and dashed lines are, respectively, a theoretical model which considers a thermal distribution of free excitons in a 2D quantum well, and a theoretical model in $1/d^4$ with d the distance between the middle of the nanoplatelets and the graphene sheet. This latter model is expected for Förster ET from a 0D donor to a 2D acceptor. Figures extracted from Ref. [Federspiel15b]. (f) Top: cartoon of the energy transfer from a monolayer WS_2 to a monolayer $MoSe_2$. Bottom: photoluminescence excitation intensity map of the corresponding vdWH. The color scale represents the emission intensity. Exciton energies of each material are indicated by the horizontal dotted line. M (W) denotes $MoSe_2$ (WS_2). Figures extracted from Ref. [Kozawa16].*

density (see Fig. 2.18(d)). Such a transfer was reported to happen on a timescale of 1 ps in monolayer graphene/monolayer WS_2 heterostructures [He14a].

Charge transfer also takes place in TMD/TMD vdWHs, especially in the case of interlayer excitons between two monolayers where electrons and holes can be transferred from one layer to the other [Ceballos14, Fang14, Hong14, Lee14a, Yu14, Ceballos15, Rivera15, Rivera16, Wang16a, Zhang16] (see Figs. 2.21(c) and (d)). Careful optical studies have revealed an ultrafast CT between the monolayers with a transfer time of the order of 100 fs [Ceballos14, Hong14, Ceballos15, Wang16a] event at room temperature. The observation of such a short charge transfer time is remarkable and may be due to the formation of interlayer excitons that are energetically favourable compared to excitons confined to only one layer [Hong14]. In addition, interlayer excitons can be electricaly tuned using electro-

static doping [Rivera15]. Remarkably, the interlayer exciton lifetime was found to be higher than the one in the pristine layers [Ceballos14, Ceballos15, Rivera15]. Lifetimes as high as 1.8 ns were reported [Rivera15] at low temperature. Furthermore, interlayer excitons can exhibit valley lifetime of 40 ns which is also higher than in pristine layers [Rivera16]. Surprisingly, the ultrafast CT does not show a strong dependence on the relative orientation of the two monolayers [Hong14, Lee14a, Rivera15, Wang16a]. However, the relative twist plays an important role in the direct or indirect nature of the interlayer excitons because of momentum conservation [Yu15]. Noteworthy, if the photoexcitation is done at an energy higher than the energy difference between the two levels, hot CT can occur, especially if the transfer time is similar to the relaxation time. Finally, let us precise that CT is a short-range mechanism which typically scales exponentially with the donor-acceptor distance.

Energy transfer Energy transfer can be divided into two mechanisms (as depicted in Figs. 2.18(b) and (c)):

(i) **Förster** energy transfer [Förster48] (usually denoted FRET for Förster Resonant Energy Transfer) which corresponds to direct transfer of energy from the photoexcited electron in the two-level system to graphene through dipole-dipole interaction. As it arises from near field Coulomb interaction, no photon is emitted during the process. The excited electron in graphene can further relax through electron-phonon coupling for instance. The ET rate typically follows a power law dependence on the donor-acceptor distance. However, for distances of the order of few Å, this dependence is not known.

(ii) **Dexter** energy transfer [Dexter53] (denoted DET) which corresponds to two opposite charge transfers leading to no macroscopic charge transfer. Indeed, the photoexcited electron in the two-level system is brought into its ground state and an electron in graphene is excited. It is a short-range transfer, as for CT, because it directly depends on the overlap of the orbital function or in other words on the band alignment.

Both mechanisms lead to a **quenching** of the PL of the two-level system since the energy of the photoexcited electron is transfered nonradiatively to the graphene. This quenching is of practical interest for imaging purposes, espcially in biology [Jares-Erijman03]. However, contrary to CT, there is no carrier density change in both systems. This makes ET much more difficult to quantified than CT since it cannot be monitored by the doping level in graphene. In general, ET is investigated using PL spectroscopy.

Charge versus energy transfer In the general case, CT and both ET mechanisms occur and quench the PL. Therefore, it is not always obvious to separate them. Nevertheless, it is possible to isolate the FRET by separating the donor and acceptor so that CT and DET are negligeable. Then by further studying the distance dependence of the ET process, the Förster nature can be demonstrated. FRET between semiconducting quantum dots [Chen10], molecules [Gaudreau13], NV (Nitrogen-Vacancy) color center in diamond [Tisler13] and semiconducting nanoplatelets [Federspiel15b], and a graphene sheet

was evidenced (see Fig. 2.18(e)). The latter study was perfomed in our group by a former PhD Student, François Federspiel with my collaboration. More information can be found in François' thesis [Federspiel15a]. Furthermore, FRET between semiconducting quantum dots and SCTMDs was also reported [Prins14, Raja16]. In our group, a PhD Student, Olivia Zill, has just started her PhD on the study of the FRET between semiconducting nanoplatelets and SCTMDs.

Up to now, no study on the ET in graphene/SCTMD vdWHs was performed. Such an experiment is very challenging because CT and ET are very strong and compete due to the subnanometer donor-acceptor distance. In this range of separations, the regimes of CT and ET remain poorly known. In addition, it is difficult to distinguish between Förster and Dexter processes. Temperature measurements might help to separate the two contributions since Förster and Dexter ET do not have the same temperature dependence [Lyo00]. However, very recently, interlayer ET (IET) was evidenced in vdWHs made of monolayers WS_2 and $MoSe_2$ [Kozawa16]. As shown in Fig. 2.18(f), for resonant excitation energies with the A, B and C excitons energy of WS_2, luminescence at the A exciton energy of the $MoSe_2$ is enhanced. Although the type-II heterojunction, the authors did not observe emission from interlayer exciton due to not very obvious reasons. Nevertheless, contrary to all the previous studies on TMD/TMD vdWHs (see above) where only the charge transfer was highlighted, the authors have suggested that the IET rate can be larger than the ICT one. In Chapter 8, we will demonstrate that in graphene/SCTMD vdWHs there is a charge transfer from the SCTMD to graphene but also show that there are strong hints for IET that may even dominate the PL quenching.

Electrical control of the transfer mechanisms Finally, let us discuss on the influence graphene's Fermi energy on the CT and ET. From the schematic diagrams in Figs. 2.18(a)-(b)-(c), it seems quite obvious that when the Fermi energy reaches the ground or excited state of the two-level system, the CT and DET are suppressed due to Pauli blocking. This shows the importance of band alignment in the heterostructures. In contrast, FRET processes are not sensitive to the relative position of the two-level system with respect to graphene's band, but to the energy of the transition. If E_0 is the energy difference between the two states, then FRET is suppressed for $|E_F| \geqslant E_0/2$ (the 2 comes from the electron-hole symmetry of graphene's dispersion relation). As a result for FRET, the bandgaps of the materials in the heterostructure are more important than the band alignment. Note that in any case hot CT or ET might still occur. Consequently, by tuning graphene's Fermi energy is it possible to electrically control the transfer mechanisms. For instance, experimental demonstration of the electical control of the FRET was already achieved by various groups for quantum dots/graphene [Lee14b], erbium ions/graphene [Tielrooij15] and quantum dots/MoS_2 [Prasai15] hybrid heterostructures. The electrical control of the transfer processes is of great interest for applications but also for studying different transfer regimes. Especially, in the case of vdWHs it could be used to separate CT and DET from FRET. In this context, it is particularly important to have a efficient and reliable method to tune graphene's Fermi energy, but also to accurately determine

it. This is the aim of the work presented in Chapter 5.

2.3.3 Optoelectronic applications

Hybrid heterostructures

Optoelectronic devices based on hybrid heterostructures have generally a FET geometry, where the layered material is employed as an electrode and the nano-objects as efficient light absorbers and/or emitters. Several studies have reported hybrid phototransistors based on graphene and various nano-objects such as quantum dots [Konstantatos12], plasmonic nanoantennas [Fang12], molecules [Chen13], or more recently nanoplatelets [Robin16] (see Fig. 2.19). In the work of Konstantatos *et al.* [Konstantatos12], a graphene FET was decorated with colloidal lead sulphide (PbS) quantum dots (see Fig. 2.19(a)). The illumination of the device leads to a modification of graphene's conductance due to charge transfer from the PbS quantum dots that absorb light, similarly to what happens in graphene/MoS_2 devices [Zhang14] (see the photocurrent map in Fig. 2.19(a)). However, these devices suffer from high dark currents and large power consumption due to the semimetallic nature of graphene. Therefore, in a next generation of hybrid phototransistors, the graphene channel was replaced by few layers of MoS_2 [Kufer15] whose semiconducting nature provides orders of magnitude lower dark current and high signal-to-noise ratio. Furthermore, SCTMDs can be strongly coupled [Liu16, Wang16b, Wang16c, Zhao16] to plasmonic structures and optical microcavities [Liu15b, Dufferwiel15] resulting in the formation of polaritons and paving the way towards new polaritonic devices. At the time of writing this thesis and to the best of our knowledge, no electrically driven light emission from hybrid heterostuctures have been observed.

Van der Waals heterostuctures

The first fabrication of vdWHs based on 2D systems was performed in 2010, by depositing graphene on nanometer thick terraces of hexagonal boron nitride [Dean10]. This landmark result has demonstrated that substrate engineering could greatly improve the electron transport properties of graphene. Since them, vdWHs have attracted much attention. In this subsection, we will focus on two types of vdWHs: (i) graphene/TMD and (ii) TMD/TMD.

Graphene/TMD based heterostructures Despite the recent emergence of vdWHs, a large variety of novel experiments and prototypes of optoelectronic devices have already been reported. Figure 2.20 presents examples of such devices that compared to lateral devices (see Section 2.2.6) offer larger area and easier scalability. In all these devices, graphene is employed as tunable work function electrodes and SCTMDs as photoactive material with strong light-matter interaction. Britnell *et al.* [Britnell13] and Yu *et al.* [Yu13] have reported the first vdWHs photodetectors displaying a graphene-SCTMD-graphene structure (see Fig. 2.20(a)). A bias between the two graphene electrodes is applied in order to separate and collect the

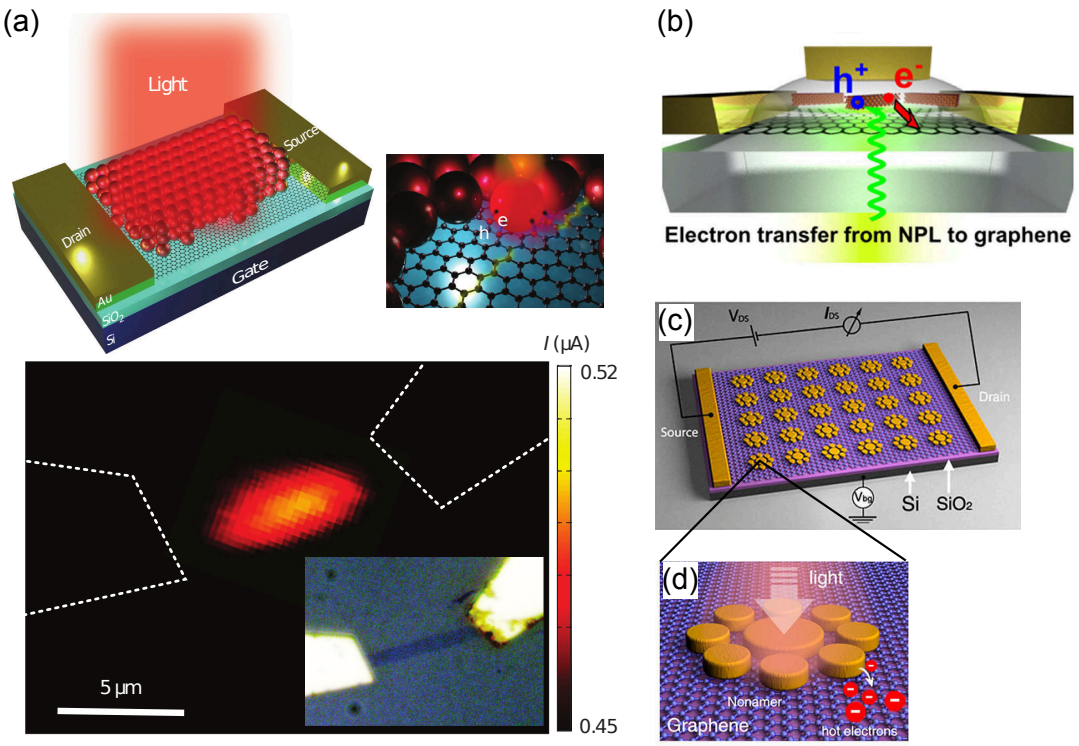

Figure 2.19 – *(a) Top right: three-dimensional schematic view of a hybrid phototransistor based on graphene and PbS quantum dots. Top left: cartoon of the electron-hole separation in the quantum dot. Bottom: map of the photocurrent displaying a hot spot that corresponds to the location of the overlap between graphene and quantum dots. Figures extracted from Ref. [Konstantatos12] (b) Three-dimensional schematic view of a hybrid electrochemically top-gated phototransistor based on graphene and CdSe nanoplatelets. Figure extracted from Ref. [Robin16]. (c) Three-dimensional schematic view of a hybrid phototransistor based on graphene and plasmonic nanoantennas. (d) Zoom on a nanoantennas showing the hot electron transfer to the graphene sheet. Figures extracted from Ref. [Fang12].*

photogenerated carriers in the TMD. Note that electrostatic doping of graphene layers can also create a built-in field even without applying a bias voltage. Furthermore, very recently Massicotte *et al.* [Massicotte16a] have demonstrated an intrinsic response time shorter than 10 ps in such devices (see Fig. 2.20(b)). They establish that this time is limited by the transfer at the heterointerface, proving the importance of the coupling at the heterointerlayer. Interestingly, they also show that monolayer WSe_2 does not give faster response than trilayer and that monolayer based devices are less efficient due to higher losses caused by direct electron-hole recombinations and presumably ET. This highlights the importance of N-layer SCTMDs for applications. Note that the same device was utilized to detect infrared light through photothermionic effect at the graphene/WSe_2 interface [Massicotte16b]. Light emitters were achieved as well. For instance, Withers *et al.* [Withers15] make use of a more complex vdWH (see Fig. 2.20(c)) to fabricate a vertical LED. In this LED, electrons and holes are injected into a monolayer TMD (they have used WS_2 or MoS_2) from the graphene electrodes. Few layers of hBN separated the graphene electrodes and the monolayer TMD in order to prevent direct tunneling between graphene sheets.

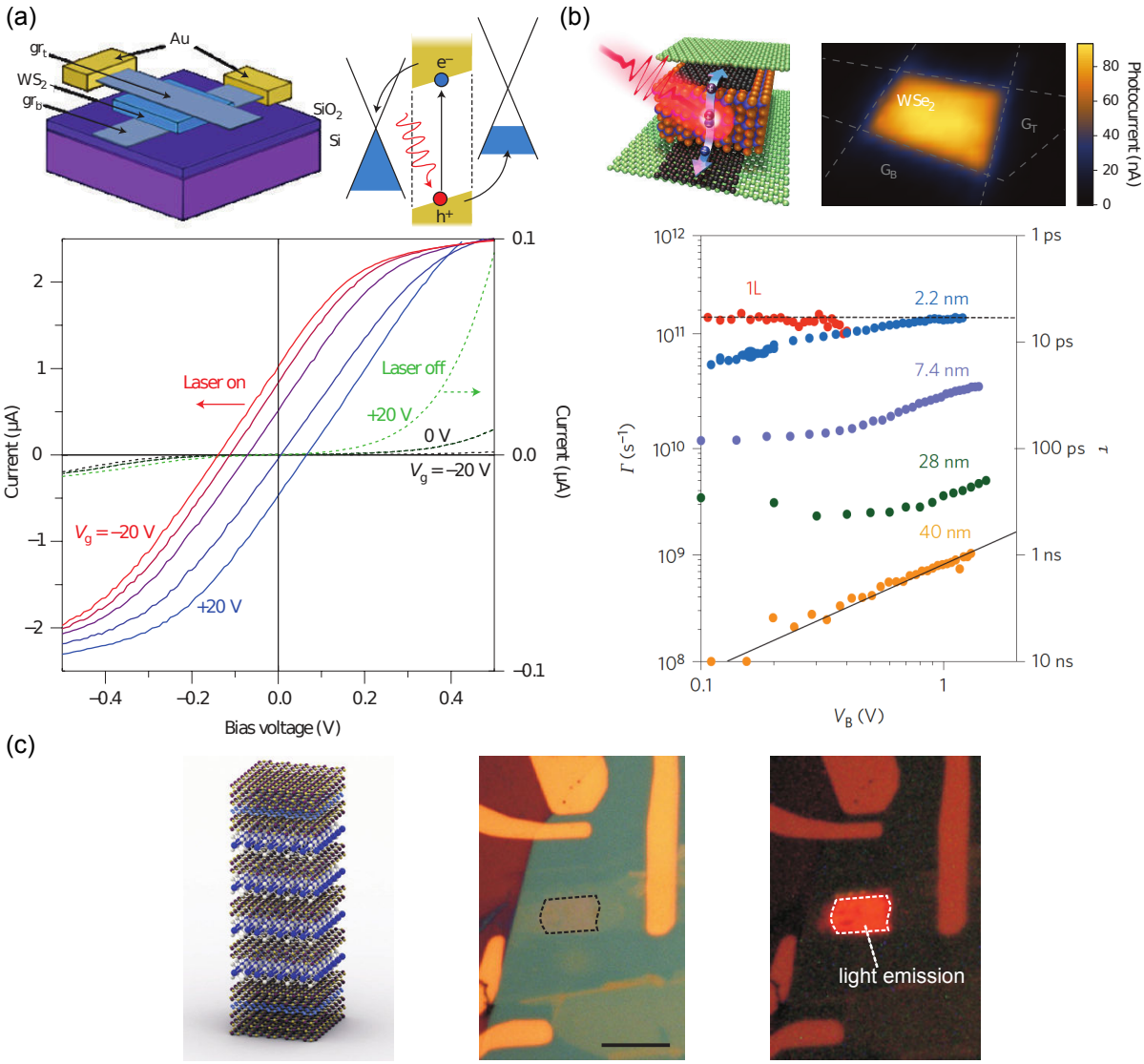

Figure 2.20 – *(a) Top left: three-dimensional schematic view of a vdWH photodetector. Top right: schematic band diagram with a built-in electric field to separate the photogenerated carriers. Bottom: gate dependent electrical characteristics taken under illumination (left axis) and in the dark (right). Figures extracted from Ref. [Britnell13]. (b) Top left: cartoon of a vdWH where a photogenerated electron-hole pair is separated and collected by the graphene sheets. Top right: photocurrent map displaying a photocurrent in the overlap region. Bottom: photoresponse rate Γ as a function of bias voltage V_B between graphene electrodes for various values thickness L of WSe_2. The solid black line corresponds to a linear relationship between Γ and V_B, whereas the dotted line shows the effective minimum response time τ = 5.5 ps. Figures extracted from Ref. [Massicotte16a]. (c) A vdWH LED. Left: cartoon of the heterostructure. Middle: optical image of the heterostructure. Scale bar, 10 μm. Right: optical image of electroluminescence from the sample. Figures extracted from Ref. [Withers15].*

TMD/TMD based heterostructures Several works have reported TMD/TMD based optoelectronic devices [Cheng14, Furchi14b, Lee14a]. All these devices consist in vertical p-n junction where one layer is n-type (e.g., MoS_2) and the other p-type (e.g., WSe_2). Figure 2.21(a) depicts such a structure with monolayers MoS_2 and WSe_2. In the overlap region, a type-II heterojunction is formed (see Fig. 2.21(c)). As a result interlayer excitons are created due to ultrafast and efficient interlayer CT (see Section 2.3.2). An unambigous

signature of this interlayer exciton appears in the PL spectrum of the overlap region at lower energy than the features of pristine layers as shown in Fig. 2.21(d) for monolayers $MoSe_2/WSe_2$ vdWHs [Rivera15]. Owing to the spatial charge separation, these devices display the typical characteristic of a photodiode indicating that they can be used as photodetectors or photovoltaic devices [Furchi14b, Lee14a]. Noteworthy, in these devices the coupling mechanisms at the heterointerface play a important role as charges are transferred from one layer to the other. These mechanisms are notably different from what happens in conventional epitaxial heterostructures in which charges are separated by an extended depletion region [Rosencher02]. Electroluminescence from this type of vdWHs was reported as well [Cheng14].

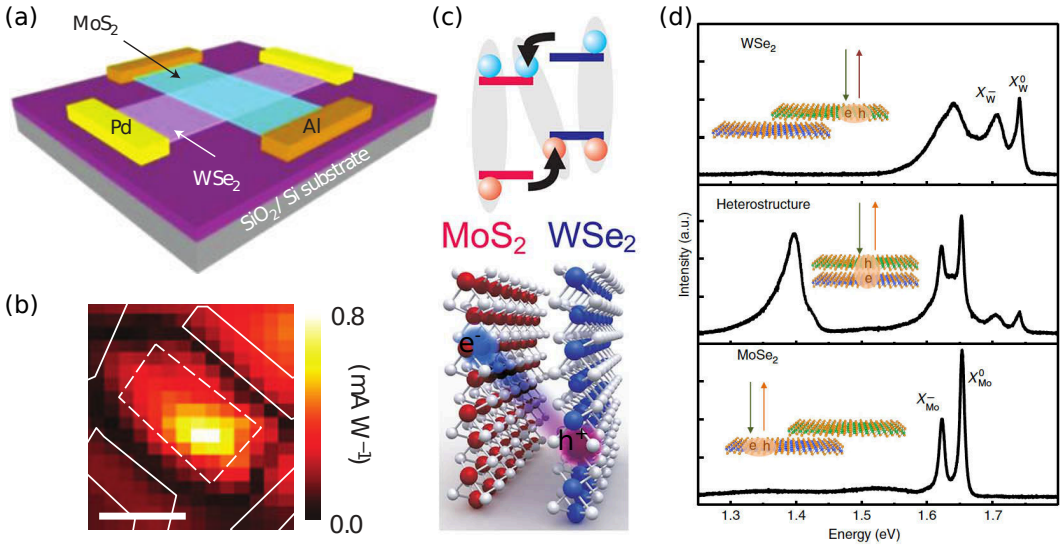

Figure 2.21 *– (a) Three-dimensional schematic view of a p-n vdWH made of a monolayer MoS_2 on top of a monolayer WSe_2. (b) Photocurrent map showing a hot spot in the overlapping region. Scale bar, 3 µm. Figures extracted from Ref. [Lee14a]. (c) Top: band diagram of the corresponding heterostructure displaying the charge transfer and the interlayer exciton. Bottom: cartoon of the same heterostructure illustrating the spatial separation of the electron and hole. Figures extracted from Ref. [Novoselov16]. (d) Photoluminescence of individual monolayers and the heterostructure recorded at 20 K. Figure extracted from Ref. [Rivera15].*

2.4 Conclusion

In this chapter, we have presented the crystal structure and basic properties of graphene and semiconducting transition metal dichalcogenides. We have also introduced heterostructures based on these layered materials, and presented the two main coupling mechanisms, namely charge and energy transfer, that govern the photophysics of these heterostuctures. Furthermore, for both pristine materials and heterostructures, we have shown several examples of optoelectronics devices to illustrate the broad range of possibilities. Many more examples can be found in the literature, for recent reviews see Refs. [Koppens14, Mak16, Mueller16]. All these devices exhibit very different figures of merit. For instance, the responsivity of the

photodetectors[14] shown in this chapter ranges from 10 mA W^{-1} for the device in Fig. 2.15(b) to 10^7 A W^{-1} for the one in Fig. 2.18(d). Such a huge discrepancy probably arises from different experimental conditions (e.g., different incoming photon energy, temperature), distinct geometry (e.g., surface of the detector) and method of calculations (internal *versus* external quantity[15]). Therefore, it is challenging and not necessarily meaningful to quantitatively compare the performance of these devices. However, from this comparison we can conclude that these optoelectronic devices hold great promise for various applications but remain for now proof-of-principle devices. Progresses are still needed in order to reach a level of maturity. In addition, large scale production of high-quality layered materials and heterostructures remains to be developed.

From a scientific point of view, most of these photodetectors are based on the dissociation of excitons followed by a separation and/or a charge transfer from one material to the other. In particular, van der Waals heterostructures are very interesting because the underlying microscopic mechanisms differ strongly from those of conventional epitaxial heterostructures. In particular, owing to the subnanometer interlayer distance, they provide a unique platform to investigate the competition between charge and energy transfer in regimes that remain unexplored. While energy transfer is usually seen as a negative aspect and remains mostly unexploited, it could be employed to inject electron-hole pairs into a emitter without contacting it [Achermann04]. In this context, developing model systems based on graphene and semiconducting transition metal dichalcogenides to study and control the interlayer charge and energy transfer is of great interest but remains challenging. To achieve this goal, it is essential

(i) to fabricate devices in which the doping level can be efficiently and finely tuned, and to develop method to accurately monitor it. This point will be presented in Chapter 5.

(ii) to precisely characterize the properties of N-layer semiconducting transition metal dichalcogenides since they potentially offer distinct advantages as a function of N. This point will be addressed in Chapters 6 and 7.

(iii) to fabricate elementary heterostructures to investigate the charge and energy transfer. This point will be considered in Chapter 8.

Take home messages

- Graphene and semiconducting transition metal dichalcogenides offer complementary properties which can be harnessed in heterostuctures.
- Heterostructures show very rich physics and hold great promises especially for opto-

[14] The responsitvity of a photodetector is the ratio between the electrical output current and the optical input power.

[15] In particular, the external quantum efficiency (EQE) is equal to the number of electron-hole pairs per second collected to produce the photocurrent divided by the incident photon flux, while the internal quantum efficiency (IQE) is calculated in a similar way except that the absorbed photon flux is considered.

electronic applications.

- Studying and controlling the coupling mechanisms, which govern the photophysics of these heterostructures, are of great interest for optoelectronics but remains challenging.

Related publication and communications

Paper

- F. Ferderpiel, G. Froehlicher, M. Nasilowski, S. Pedetti, A. Mahmood, B. Doudin, S. Park , J. Lee , D. Halley, B. Dubertret, P. Gilliot, and S. Berciaud, *Distance Dependence of the Energy Transfer Rate from a Single Semiconductor Nanostructure to Graphene*, Nano Letters **15**, 1252-1258 (2015).

Posters

- F. Ferderpiel, G. Froehlicher, M. Nasilowski, S. Pedetti, A. Mahmood, B. Doudin, S. Park , J. Lee , D. Halley, B. Dubertret, P. Gilliot, and S. Berciaud, D*istance Scaling of the Energy Transfer Rate from a Single Semiconductor Nanostructure and a Graphene Monolayer*, E-MRS Spring Meeting, May 2016, Lille, France
- François Federspiel, G. Froehlicher, David Halley, Michelangelo Romeo, Michel Nasilowski, Benoît Dubertret, Pierre Gilliot and Stéphane Berciaud, *Energy transfer from individual semiconductor quantum dots to graphene*, UFA-Winter School "Surface-Confined Synthesis of Nanostructures", February 2014, Baden-Baden, Germany.

Chapter 3

Introduction to group theory and Raman spectroscopy

This chapter introduces the common spectroscopic tool used throughout this work: Raman spectroscopy. As the interpretation of the experimental results often requires group theory analysis, we first recall the main principles and notations of group theory applied to phonons. For readers unfamiliar with group theory, corresponding basics are pedagogically introduced in Appendix A. Then group theory is applied to graphene, N-layer and bulk 2Hc transition metal dichalcogenides to derive the phonon symmetries. Finally, the theory of Raman scattering in the classical and quantum frameworks is outlined. This chapter is rather technical but contains essential elements for Chapters 5 and 6. However, the following chapters can be addressed without reading this chapter in detail.

3.1 A brief summary of group theory

For readers not familiar with group theory, a pedagogical introduction applied to phonons is presented in Appendix A. The statements are not demonstrated but they are illustrated using the very simple example of the water molecule. More detailed references on this subject include [Dresselhaus07, Yu10]. Here, we briefly recall the main notions and notations of group theory that are essential to understand the symmetry analysis performed in the following sections and used in Chapters 5 and 6.

The symmetry operations in a crystal are

E	identity;
C_n/C_n^{-1}	clockwise/anticlockwise rotation by $\frac{2\pi}{n}$ with $n \in \mathbb{N}$;
σ	reflection about a plane;
i	inversion;
S_n/S_n^{-1}	rotation C_n/C_n^{-1} followed by a reflection through a plane perpendicular to the rotation axis;

plus the combination of a rotation C_n/C_n^{-1} (screw axis) or a reflection σ (glide plane) plus a translation of a fractional lattice vector along the same axis or parallel to the plane of reflection, respectively.

The space group of a crystal is described by a Bravais lattice plus a point group. This crystal point group corresponds to the symmetry of the unit cell including the rotations and reflection of screw axis and glide plane. In the case of phonons, the determination of the crystal point group is sufficient since the symmetry of the Bravais lattice is included in the reciprocal space (i.e, in the space of wavevectors). These groups are labeled following the Schönflies notation [Schoenflies91] and their irreducible representations with the Mulliken one [Mulliken55, Mulliken56]. The meaning of Mulliken's symbols is presented in Tab. 3.1.

Symbols	symmetry property	with respect to	comments
A/B	sym/antisym	principal axis C_n	one-dimensional representations
subscript 1/2	sym/antisym	C_2 perpendicular to principal axis C_n or vertical plane σ_v or σ_d	
subscript u/g	sym/antisym	inversion center i	from German 'gerade'/'ungerade'
$'/''$	sym/antisym	horizontal plane σ_h	
E	two-dimensional representations		from German 'entartet' (degenerate)
T	three-dimensional representations		F is also used in spectroscopy

Table 3.1 *– Mulliken notation. Sym (antisym) means symmetric (antisymmetric).*

To find the symmetry of the phonons at a given point of the Brillouin zone, one first has to determine the group of the wavevector, which is always a subgroup of the crystal space group. This group corresponds to the set of space group operations, which transform the wavevector $\boldsymbol{q}$ into itself (possibly plus a reciprocal lattice vector). For zone-center phonons (i.e., $\boldsymbol{q} = 0$), the group of the wavevector is always the same as the space group of the crystal. Consequently, the symmetries of the phonons are described using the irreducible representation of the crystal point group. In the following, we will mostly study zone-center phonons. However, in the case of graphene, we will also find the irreducible representation of the phonons at the

edges of the Brillouin zone. The irreducible representation of all the phonon modes at a given point of the Brillouin zone can be deduced from the decomposition of the representation of the total vibration Γ^{vib} using the following relation [Dresselhaus07]

$$\Gamma^{\text{vib}} = \Gamma^{\text{eq}} \otimes \Gamma^{\text{vec}}, \tag{3.1}$$

where Γ^{vec} is the representation of a vector (x, y, z) and Γ^{eq} is the equivalence representation, in the group of the wavevector.

3.2 Group theory applied to graphene

In this section, we applied group theory to graphene to get the phonon symmetries at the Γ and $K^{(')}$ points.

3.2.1 Crystal symmetries

As shown in Chapter 2, the Bravais lattice of graphene is hexagonal. To determine the crystal point group, we must analyze the symmetry in the unit cell. This analysis leads to the following 24 rotation operations [Malard09a]

- E identity;
- $2C_6$ clockwise and anticlockwise rotations of 60 ° along the axis shown in Fig. 3.1;
- $2C_3$ clockwise and anticlockwise rotations of 120 ° along the axis shown in Fig. 3.1;
- C_2 rotation of 180 ° along the axis shown in Fig. 3.1;
- $3C_2'$ rotations of 180 ° along the axis shown in Fig. 3.1;
- $3C_2''$ rotations of 180 ° along the axis shown in Fig. 3.1;
- i inversion center shown as a red dot in Fig. 3.1;
- σ_h reflection with respect to the xy plane shown in Fig. 3.1;
- $2S_6$ clockwise and anticlockwise rotations of 60 ° along the axis shown in Fig. 3.1 followed by a σ_h reflection;
- $2S_3$ clockwise and anticlockwise rotations of 120 ° along the axis shown in Fig. 3.1 followed by a σ_h reflection;
- $3\sigma_d$ reflections with respect to the vertical planes shown in Fig. 3.1.
- $3\sigma_v$ reflections with respect to the vertical planes shown in Fig. 3.1.

Consequently, the point group is D_{6h} and the space group D_{6h}^1 [Malard09a]. The character table of this space group is displayed in Tab. A.6. Note that although graphene is two-dimensional, we need to consider a three dimensional space group to account for the out-of-plane phonons.

3.2.2 Irreducible representations of the phonons

The primitive unit cell has two atoms. Therefore, monolayer graphene exhibits six phonons: 3 acoustic and 3 optical modes. The irreducible representations of these phonon modes are

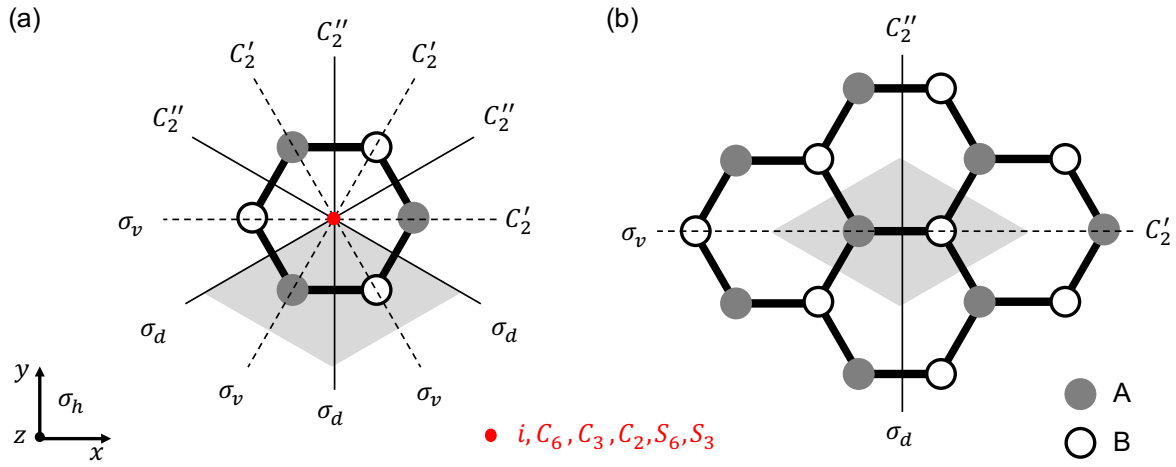

Figure 3.1 – *Symmetry operations of monolayer graphene. The primitive unit cell (gray diamond) contains two inequivalent atoms A (gray filled circle) and B (open black circle). (a) Top view of a monolayer graphene with six atoms (one hexagon) represented. The inversion center i and the axis (along z axis) of the C_6, C_3, C_2, S_6 and S_3 operations is illustrated as a red dot. The horizontal σ_h reflection is in the xy plane. The axis of the C_2' and C_2'' are illustrated in black dashed and solid lines, respectively. The vertical planes for the σ_v and σ_d reflections are demonstrated as black dashed and solid lines, respectively. (b) Top view of a monolayer graphene with more hexagons. The axis and planes of one C_3', C_3'', σ_v and σ_d operation are drawn. This sketch is useful to determine the characters of the equivalence representation.*

given by the direct product $\Gamma^{\text{vib}} = \Gamma^{\text{eq}} \otimes \Gamma^{\text{vec}}$, where Γ^{eq} denotes the equivalence representation for the atomic sites and Γ^{vec} is the representation for the x, y and z real space vectors. These representations have to be determined for the group of the wavevector.

Γ-point phonons

The group of the Γ-point is the same as the point group of the crystal, thus we need to consider the symmetry operations of D_{6h}. From the character table A.6, we see that

$$\Gamma^{\text{vec}} = A_{2u} \oplus E_{1u},$$

where z and (x, y) transform as A_{2u} and E_{1u}, respectively. To find Γ^{eq}, we have to consider the transformation of the two atoms in the unit cell under the symmetry operations of the group. With the help of Fig. 3.1, we obtain the character table 3.2. Following the procedure described in detail in Appendix A Section A.4 and using the character table of D_{6h}, we deduce the irreducible representation of the equivalence representation

$$\Gamma^{\text{eq}} = A_{1g} \oplus B_{1u}.$$

Finally, the irreducible representation of the six Γ-point phonon modes is

$$\Gamma^{\text{vib}} = A_{2u} \oplus B_{2g} \oplus E_{2g} \oplus E_{1u}. \tag{3.2}$$

E_{1u} and E_{2u} are doubly degenerate and correspond to the in-plane modes (in xy plane), while A_{2u} and B_{2g} correspond to the out-of-plane mode (along z axis). As we will explain in section 3.4, from the character table A.6, we see directly that only E_{2g} is Raman active (this mode is called the G mode), A_{2u} and E_{1u} IR active, and B_{2g} silent.

	E	$2C_6$	$2C_3$	C_2	$3C_2'$	$3C_2''$	i	$2S_3$	$2S_6$	σ_h	$3\sigma_d$	$3\sigma_v$
Γ^{eq}	2	0	2	0	2	0	0	2	0	2	0	2

***Table 3.2** – Characters for Γ^{eq} for monolayer graphene within the D_{6h} group. When the character is equal to zero, A and B atoms are exchange.*

Figure 3.2 sketches the atomic displacements of the six Γ-point phonons in monolayer graphene with the corresponding irreducible representation. We notice that the phonon modes with A_{2u} and E_{1g} symmetry correspond the acoustic modes, while E_{2g} and B_{2g} correspond to the optical ones.

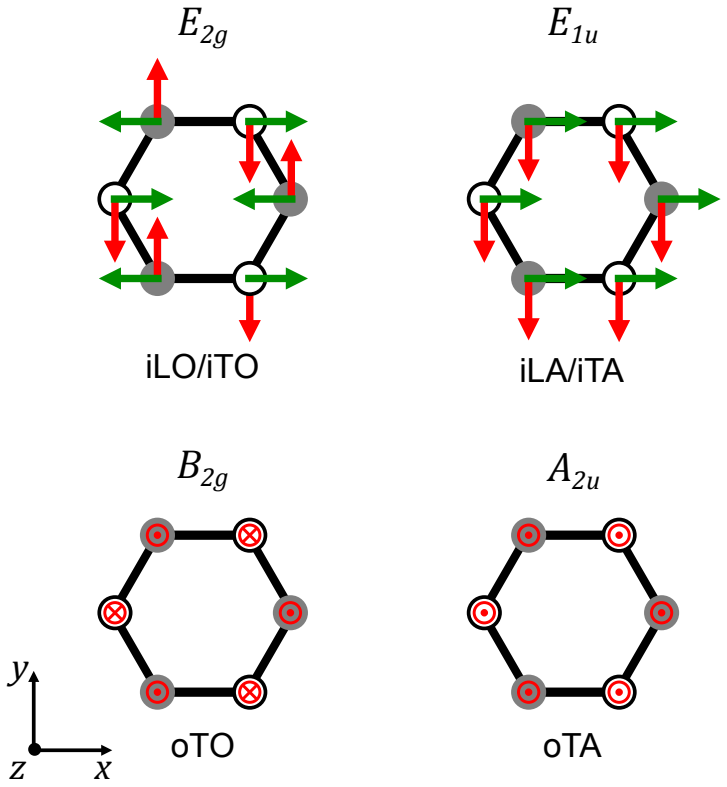

***Figure 3.2** – Atomic displacements and irreducible representations associated with the six Γ-point phonons in monolayer graphene. The solid and open circles indicate the A and B atoms, respectively. The corresponding phonon branch is indicated (see Fig. 2.4). E_{2g} and E_{1u} are doubly degenerated: red arrows corresponds to transverse modes (T) and green arrows to longitudinal modes. Crossed and dotted points represent vectors pointing in and out of the image plane. Only E_{2g} is Raman active, E_{1u} and A_{2u} are acoustic modes and have a zero frequency, and B_{2g} is optically inactive.*

$K^{(')}$-point phonons

Having studied the Γ-point phonons, we now turn to the $K^{(')}$-point phonons. We will focus on K-point phonons but the results are similar for K'-point phonons. The complete analysis

can be found in Ref. [Dresselhaus07]. As illustrated in Fig. 3.3(a), among the 24 symmetries of the crystal, only 12 are still symmetry operation for the K vector: E, σ_h, $2C_3$, $2S_3$, $3C_2$, $3\sigma_v$. Consequently, the group of the wavevector at the K point is D_{3h}. The character table of this group is displayed in Tab. A.7.

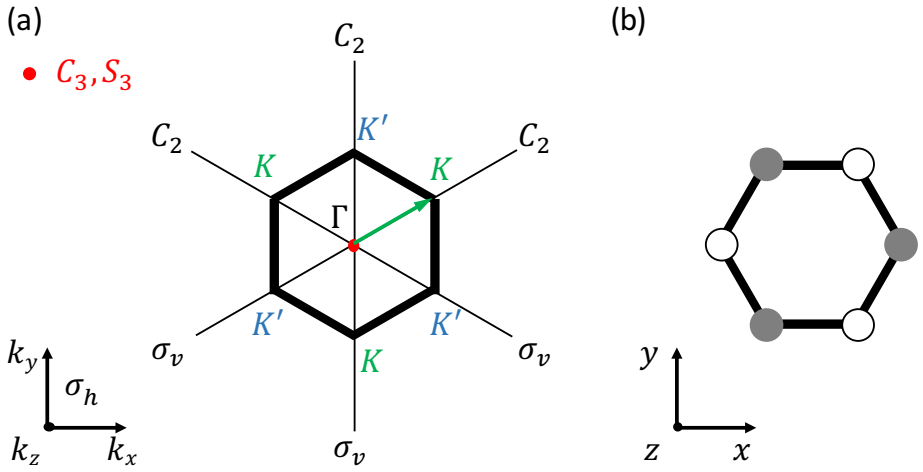

Figure 3.3 *– (a) Symmetry operation of the K vector in the Brillouin zone of monolayer graphene. The center of the Brillouin zone* Γ*, and the three equivalent K and K′ points, respectively, are indicated. The axis (along k_z axis) of the C_3 and S_3 operations is illustrated as a red dot. The horizontal σ_h reflection is in the $k_x k_y y$ plane. The axis of the C_2 and the planes of the σ_v reflections are illustrated in black solid lines. (b) Top view of the corresponding graphene monolayer with six atoms.*

From the character table A.7, we see that

$$\Gamma^{\text{vec}} = A_2'' \oplus E',$$

where z and (x,y) transform as A_2'' and E', respectively. To find Γ^{eq}, we have to consider the transformation of the two atoms in the unit cell under the symmetry operations of the group D_{3h}. To determine the characters of Γ^{eq} we can use the previous analysis made for the D_{6h} group. From Fig. 3.3, $3C_2$ and $3\sigma_v$ corresponds to the $3C_2''$ and $3\sigma_d$ in the crystal symmetry (see Fig. 3.1). Therefore, with the help of Tab. 3.2, the character of E and σ_h is 2, and 0 for C_2 and σ_v. However, the character of C_3 and S_3 is not 2 because under these rotations K is invariant only with the addition of a reciprocal lattice vector. Hence, the phase factor due to this reciprocal lattice vector has to be taken into account, and the character is -1 [Dresselhaus07]. From the character table of D_{3h}, we deduce immediately that the irreducible representation of the equivalence representation is

$$\Gamma^{\text{eq}} = E'.$$

Finally, the irreducible representation of the six K-point phonon modes is

$$\Gamma^{\text{vib}} = A_1' \oplus A_2' \oplus E' \oplus E''. \tag{3.3}$$

E' and E'' are doubly degenerate. The corresponding atomic displacements are drawn in

Fig. 3.4. Note that due to the wavevector K, the periodicity is described by a supercell of six carbon atoms.

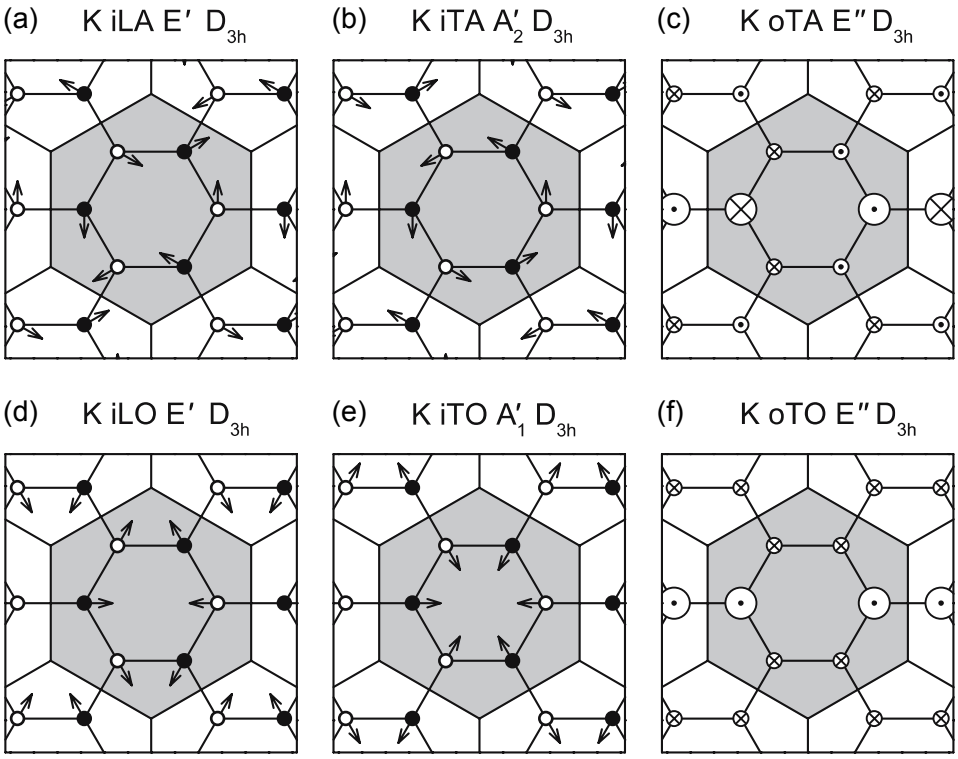

Figure 3.4 *– Atomic displacements and irreducible representation associated with the six K-point phonons. The solid and open circles indicate the A and B atoms, respectively. The corresponding phonon branch is indicated (see Fig. 2.4). The crossed and dotted points in (c) and (f) represent the vectors pointing in and out of the image plane. The large and small points indicate the magnitudes of the vectors. Figure from Ref. [Dresselhaus07].*

3.2.3 Generalization to graphite

Let us briefly discuss the case of graphite with AB Bernal stacking. Because of this stacking, graphite's unit cell is composed of four atoms: the two atoms of the unit cell of two layers. From the symmetry analysis, graphite belongs to the non-symmorphic D_{6h}^4 group [Ferrari13] which point group is D_{6h} as for the monolayer. The irreducible representation of the 12 Γ-point phonons is [Ferrari13]

$$\Gamma^{\text{vib}} = 2\left(A_{2u} \oplus B_{2g} \oplus E_{2g} \oplus E_{1u}\right). \tag{3.4}$$

Compared to Γ^{vib} for the monolayer (see Eq. (3.2)), we notice that the graphite phonons have the same irreducible representation. Indeed, the phonons in graphite can be deduced from the vibrational modes in the two monolayers. These modes can be either in-phase or out-of-phase [Nemanich77]. Therefore, the monolayer modes are said to become Davydov doublets (see chapter 6). Only the phonon modes with E_{2g} symmetry are Raman active. One is similar to the E_{2g} vibration in monolayer (in-phase combination of the E_{2g} mode in the two layers), the other corresponds to a rigid layer shear mode which is the out-of-phase combination of

the acoustic modes E_{1u} (see chapter 6 for more a detailed study of interlayer modes).

3.3 Group theory applied to 2Hc transition metal dichalcogenides

3.3.1 Bulk crystals

Symmetry analysis

As introduced in Chapter 2, this manuscript focuses only on 2Hc TMDs. The bulk primitive cell is composed of two layers and has six atoms. Top and lateral views of the primitive cell are highlighted in Figs. 3.5(a) and (b), respectively.

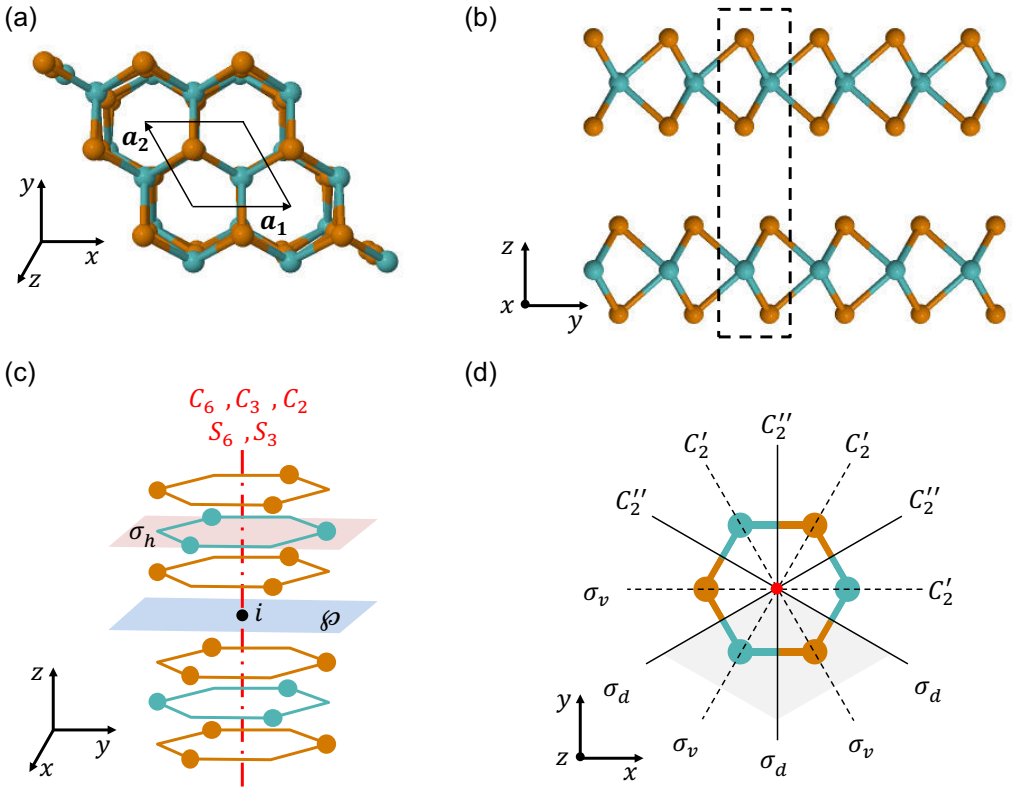

Figure 3.5 *– Symmetry operations of bulk 2Hc transition metal dichalcogenides. The primitive unit cell contains two layers. Blue spheres represent metal atoms and orange spheres chalcogen atoms. (a) Top view of the two layers.* $\boldsymbol{a_1}$ *and* $\boldsymbol{a_2}$ *are the in-plane primitive unit vectors. (b) Lateral view of the two layers. The unit cell is highlighted by a dashed rectangle. The unit cell comprises six atoms: two metal atoms and four chalcogen atoms. (c) Side view of the two layers. The axis of the* C_6*,* C_3*,* C_2*,* S_6 *and* S_3 *is illustrated as red dashed line. The horizontal* σ_h *reflection is shown as a light red plane. The light blue plane* $\mathcal{P}$ *alone is not a symmetry operation but is part of S operations. The inversion center is drawn as a black dot. (d) Top view of the layers. The unit cell is highlighted in gray. The axis of the* C_2' *and* C_2'' *are illustrated in black dashed and solid lines, respectively. The former axis are lying in the* σ_h *plane and the latter in the* $\mathcal{P}$ *one. The vertical planes for the* σ_v *and* σ_d *reflections are demonstrated as black dashed and solid lines, respectively. The red dot represents the red dashed line in (c).*

The Bravais lattice of the bulk crystal is hexagonal. To determine the crystal point group, rotations accompanied by a translation of one layer along the out-of-plane direction (z axis

in Fig. 3.5), namely screw axis and glide plane, also have to be taken into account. Note that this translation does not belong to the Bravais lattice, since it is a translation of half the c lattice parameter along the out-of-plane axis (z axis). Knowing this, there are 24 rotational symmetry operations [Wilson69, Ribeiro-Soares14] that can be divided into two categories. First, the rotations that belong to the space group (see Fig. 3.5): E, $2C_3$, $3C_2'$, $3C_2''$, i, $2S_6$, $2S_3$, σ_h and $3\sigma_v$. Second, the rotations that without the one layer translation do not belong to the space group (see Fig. 3.5): $2C_6$, C_2, $3\sigma_d$.

Consequently, the point group of bulk 2Hc TMDs is D_{6h} and thus the space group is the non-symmorphic D_{6h}^4 group [Wilson69, Ribeiro-Soares14]. The character table of this space group is displayed in Tab. A.6.

Irreductible representations of the Γ-point phonon modes

The primitive unit cell has six atoms. Therefore, bulk 2Hc TMDs exhibit 18 zone centrers (Γ) phonons: 3 acoustic and 15 optical modes. The irreducible representations of these phonon modes are given by the direct product $\Gamma^{\text{vib}} = \Gamma^{\text{eq}} \otimes \Gamma^{\text{vec}}$, where Γ^{eq} denotes the equivalence representation for the atomic sites and Γ^{vec} is the representation for the x, y and z real space vectors [Dresselhaus07]. Since the group of the Γ point is the same as the point group of the crystal, we need to consider the symmetry operations of D_{6h}. From the character table A.6, we see that

$$\Gamma^{\text{vec}} = A_{2u} \oplus E_{1u},$$

where z and x, y transform as A_{2u} and E_{1u}, respectively. To find Γ^{eq}, we have to consider the transformation of the six atoms in the unit cell under the symmetry operation of the group. We obtain the character table 3.3. From the character table of D_{6h}, we deduce the irreducible representation of the equivalence representation

$$\Gamma^{\text{eq}} = 2A_{1g} \oplus B_{2g} \oplus A_{2u} \oplus 2B_{1u}.$$

Finally, the irreducible representation of the 18 Γ-point phonon modes is

$$\Gamma^{\text{vib}} = A_{1g} \oplus 2A_{2u} \oplus B_{1u} \oplus 2B_{2g} \oplus E_{1g} \oplus 2E_{1u} \oplus E_{2u} \oplus 2E_{2g}. \tag{3.5}$$

E_{1g}, E_{1u}, E_{2u} and E_{2g} are doubly degenerate and correspond to the in-plane modes (in xy plane), whereas A_{1g}, A_{2u}, B_{1u} and B_{2g} correspond to the out-of-plane mode (along z axis). From the character table A.6, we see directly that A_{1g}, E_{1g} and E_{2g} are Raman active, A_{2u} and E_{1u} IR active, and B_{1u}, B_{2g} and E_{2u} silent.

3.3.2 N-layer crystals

In N-layer 2Hc TMDs, the stacking order is maintained. Due to the lack of translation invariance in the out-of-plane direction (z axis), the primitive unit cell of the N-layer crystal contains the N layers. Therefore, the symmetry operations are reduced from 24 in the bulk to

	E	$2C_6$	$2C_3$	C_2	$3C_2'$	$3C_2''$	i	$2S_3$	$2S_6$	σ_h	$3\sigma_d$	$3\sigma_v$
Γ^{eq}	6	0	6	0	2	0	0	2	0	2	0	6
	all		all		2 M			2 M		2 M		all

Table 3.3 *– Characters for Γ^{eq} for bulk 2Hc TMDs. The atoms that remain unchanged under each symmetry operation are indicated. M stands for the metal atom. Note that C_3 operations need a lattice vector and C_2', S_3 and σ_h can be done independently in the two planes of the metal atoms.*

12 in N-layer crystal, and the symmetry group of N-layer crystal is different from the bulk's one. Moreover, the symmetry groups of even and odd N are different. However, contrary to the bulk, the space groups of N-layer crystal are symmorphic, i.e., there are no screw axis or glide plane operations. To determine the crystal point group of N-layer crystals, we will use $N = 1$ and $N = 2$ as examples for odd and even N, respectively.

Odd N

To analyze the symmetries of odd N, we are using the simplest case of monolayer $N = 1$. This analysis can be easily generalized to any odd N. The 12 rotational symmetry operations are (see Fig. 3.6): E, σ_h, $2C_3$, $2S_3$, $3C_2$ and $3\sigma_v$. Consequently, the point group of monolayer and more generally odd N-layer 2Hc TMDs is D_{3h} and thus the space group is the symmorphic D_{3h}^1 [Ribeiro-Soares14]. The character table of this group is displayed in Tab. A.7.

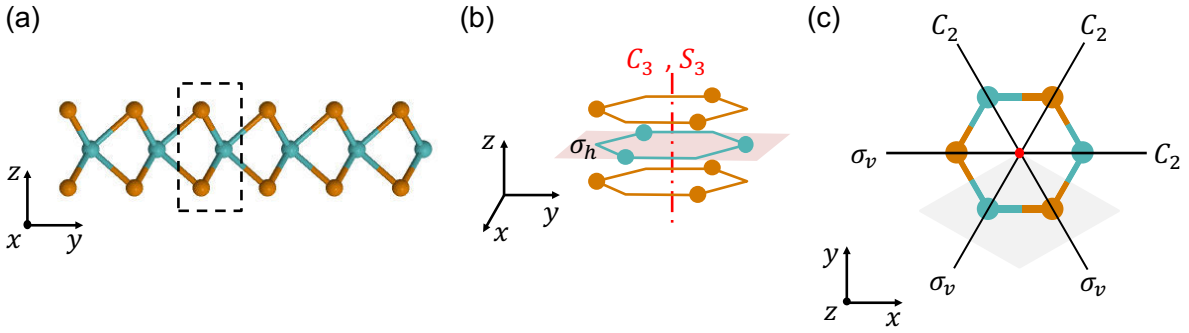

Figure 3.6 *– Symmetry operations of monolayer ($N = 1$) 2Hc transition metal dichalcogenides. Blue spheres represent metal atoms and orange spheres chalcogen atoms. (a) Lateral view of the monolayer. The unit cell is highlighted by a dashed rectangle. The unit cell comprises three atoms: one metal atoms and two chalcogen atoms. (b) Side view of the monolayer. The axis of C_3 and S_3 is illustrated as red dashed line. The horizontal σ_h reflection is shown as a light red plane. (c) Top view of the monolayer. The unit cell is highlighted in gray. The axis of the C_2 is drawn in black solid lines and is lying in the σ_h plane. The vertical planes for the σ_v reflections are demonstrated as black solid lines. The red dot presents the red dashed line in (b).*

Next, we find the irreducible representation of the Γ-point phonon modes. The primitive unit cell of the N-layer crystal has $3N$ atoms. Therefore, N-layer 2Hc TMDs exhibit $9N$ Γ-point phonons: 3 acoustic and $9N - 3$ optical modes. In the case of the monolayer, there are 9 modes. The irreducible representation of these modes is given by the direct product $\Gamma^{\text{vib}} = \Gamma^{\text{eq}} \otimes \Gamma^{\text{vec}}$. From the character table A.7, we see that

$$\Gamma^{\text{vec}} = E' \oplus A_2'',$$

where x, y and z transform as E' and A_2'', respectively. To find Γ^{eq}, we use the character table 3.4 of the equivalence representation of the atomic sites. From this table we get

$$\Gamma^{\text{eq}} = 2A_1' \oplus A_2''.$$

Finally, the irreducible representation of the 9 Γ-point phonon modes of the monolayer is

$$\Gamma^{\text{vib}} = A_1' \oplus E'' \oplus 2(A_2'' + E'). \tag{3.6}$$

E' and E'' are doubly degenerate and correspond to the in-plane modes (in xy plane), whereas A_1' and A_2'' correspond to the out-of-plane mode (along z axis). From the character table A.7, we see directly that A_1' and E'' are Raman active, A_2'' IR active, and E' both Raman and IR active.

	E	σ_h	$2C_3$	$2S_3$	$3C_2$	$3\sigma_v$
Γ^{eq}	3	1	3	1	1	3
	all	M	all	M	M	all

***Table 3.4** – Characters for Γ^{eq} for monolayer 2Hc TMDs. The atoms that remain unchanged under each symmetry operation are indicated. M stands for the metal atom.*

We can generalize this result to any odd N ($N = 1, 3, 5, ...$)

$$\Gamma^{\text{vib}} = \frac{3N-1}{2}(A_1' \oplus E'') + \frac{3N+1}{2}(A_2'' \oplus E'). \tag{3.7}$$

Note that we clearly observed the Davydov splitting in this equation (see Chapter 6).

Even N

To analyze the symmetries of even N, we are using the simplest case of bilayer $N = 2$. This analysis can be easily generalized to any even N. The 12 rotational symmetry operations are (see Fig. 3.7): E, $2C_3$, $3C_2$, i, $2S_6$ and $3\sigma_d$. Consequently, the point group of bilayer and more generally even N-layer 2Hc TMDs is D_{3d} and thus the space group is the symmorphic D_{3d}^3 [Ribeiro-Soares14]. The character table of this group is displayed in Tab. A.8.

As mentioned previously, in the case of the bilayer, there are 18 Γ-point modes. The irreducible representation of these modes is given by the direct product $\Gamma^{\text{vib}} = \Gamma^{\text{eq}} \otimes \Gamma^{\text{vec}}$. From the character table A.8, we see that

$$\Gamma^{\text{vec}} = A_{2u} \oplus E_u,$$

where z and x, y transform as A_{2u} and E_u, respectively. To find Γ^{eq}, we use the character table 3.5 of the equivalence representation of the atomic sites. From this table we get

$$\Gamma^{\text{eq}} = 3A_{1g} \oplus 3A_{2u}.$$

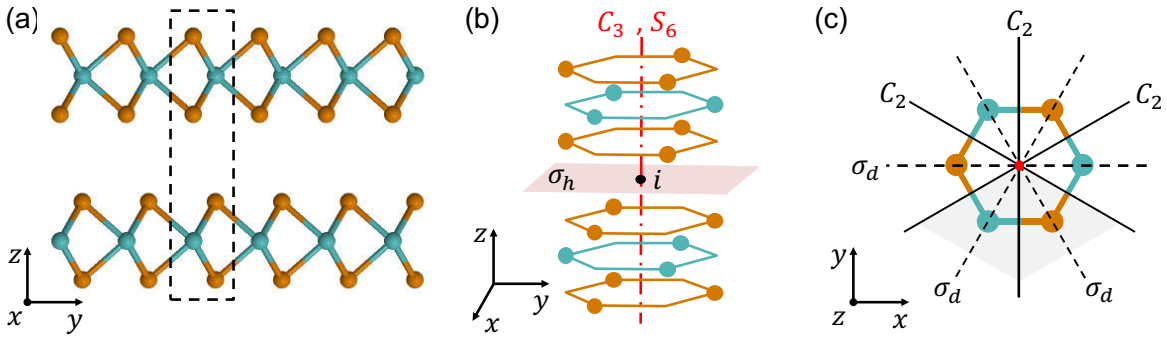

Figure 3.7 *– Symmetry operations of bilayer (N = 2) 2Hc transition metal dichalcogenides. Blue spheres represent metal atoms and orange spheres chalcogen atoms. (a) Lateral view of the bilayer. The unit cell is highlighted by a dashed rectangle. The unit cell comprises six atoms: two metal atoms and four chalcogen atoms. (b) Side view of the bilayer. The axis of C_3 and S_6 is illustrated as red dashed line. The horizontal σ_h reflection is shown as a light red plane. The inversion center is drawn as a black circle. (c) Top view of the bilayer. The unit cell is highlighted in gray. The axis of the C_2 is drawn in black solid lines and is lying in the σ_h plane. The vertical planes for the σ_d reflections are demonstrated as black dashed lines. The red dot presents the red dashed line in (b).*

Finally, the irreducible representation of the 18 Γ-point phonon modes of the bilayer is

$$\Gamma^{\text{vib}} = 3(A_{1g} \oplus A_{2u} \oplus E_g \oplus E_u). \tag{3.8}$$

E_g and E_u are doubly degenerate and correspond to the in-plane modes (in xy plane), whereas A_{1g} and A_{2u} correspond to the out-of-plane mode (along z axis). From the character table A.8, we see directly that A_{1g} and E_g are Raman active, and A_{2u} and E_u IR active.

	E	$2C_3$	$3C_2$	i	$2S_6$	$3\sigma_d$
Γ^{eq}	6	6	0	0	0	6
	all	all				all

Table 3.5 *– Characters for Γ^{eq} for bilayer 2Hc TMDs. The atoms that remain unchanged under each symmetry operation are indicated.*

We can generalize this result to any even N ($N = 2, 4, 6, \ldots$)

$$\Gamma^{\text{vib}} = \frac{3N}{2}(A_{1g} \oplus A_{2u} \oplus E_g \oplus E_u). \tag{3.9}$$

As for odd N, we explicitly observe the Davydov splitting in this equation.

3.4 Raman spectroscopy: generalities

When light propagates through a medium, most of it is either transmitted or absorbed, but a very tiny fraction is scattered in all directions due to inhomogeneities inside the medium. These inhomogeneities may be static such as defects in crystals, or dynamic like atomic vibrations or fluctuations in the charge or spin density in crystals. The former correspond to **elastic** scattering of light (i.e., without frequency change) and is called **Rayleigh scattering**,

while the latter correspond to **inelastic** scattering of light (i.e., with frequency change) and is called **Raman scattering** from the name of one of his discoverer C. V. Raman (Nobel prize in 1930).[1] Note that only a tiny fraction of the scattered light (typically one photon over ten millions) is scattered inelastically, which made this phenomenon difficult to observe before the invention of the laser. Nowadays, the spectroscopy based on the Raman scattering of light (known as Raman spectroscopy) is a widely used technique to study liquids, gases and solids.

In this section, we will focus on Raman scattering in crystals.[2] First we will give a classical picture of the light scattering (macroscopic approach) in crystals in order to obtain the basic properties of Raman scattering, then we will present the quantum approach (microscopic theory), and finally we will introduce the Raman activity and selection rules. This section is largely based on [Yu10].

3.4.1 Classical picture of light scattering (macroscopic theory)

In the classical framework, the incoming light induces microscopic dipole moments by disturbing the electronic charge distribution in the atoms of the crystal. The sum of all these induced dipole moments will act as a macroscopic polarization $\boldsymbol{P}$. This polarization is the source of a secondary electromagnetic field that corresponds to the scattered light [Jackson99].

Light scattering

Let us assume that the incident light is a monochromatic sinusoidal plane wave. The incident electric field is therefore equal to $\boldsymbol{E}_i(\boldsymbol{r},t) = \boldsymbol{E}_0(\boldsymbol{k}_i,\omega)\cos(\omega t - \boldsymbol{k}_i\cdot\boldsymbol{r})$ where $\boldsymbol{E}_0$ is the amplitude of the field, $\boldsymbol{k}_i$ is the wavevector and ω the frequency. For the sake of readability, in the following we will omit the dependencies of all the quantities. The polarization $\boldsymbol{P}$ is related to the incident electric field by

$$\boldsymbol{P} = \epsilon_0 \chi \boldsymbol{E}_i, \tag{3.10}$$

where χ is the electric susceptibility and represents the ability to disturb all the electronic clouds out of their equilibrium configurations and ϵ_0 is the vacuum permittivity. In general, χ is a second rank tensor but without changing the result, we assume that the crystal is isotropic so that χ can be represented by a scalar. Atomic vibrations act on χ because the electronic density adiabatically adjusts to the nuclear motion to minimize the energy of the system. χ is therefore a function of atomic vibrations. A given atomic vibration can be decomposed into a sum of normal modes (i.e., phonons) therefore without loss of generality, we can consider the atomic displacements $\boldsymbol{u}$ associated with one phonon of frequency Ω and wavevector $\boldsymbol{q}$:

$$\boldsymbol{u} = \boldsymbol{u}_0 \cos(\Omega t - \boldsymbol{q}\cdot\boldsymbol{r}). \tag{3.11}$$

[1] In the case of vibrations in crystals, one distinguishes scattering by optical and acoustic phonons. The latter is known as Brillouin scattering.

[2] However, the results are general and also apply to molecules.

As χ varies with $\boldsymbol{u}$, it can be expanded as a Taylor series with $\boldsymbol{u}$. The first order expansion reads

$$\chi = \chi_0 + \left(\frac{\partial \chi}{\partial \boldsymbol{u}}\right)_0 \cdot \boldsymbol{u}. \tag{3.12}$$

The subscript 0 stands for the equilibrium position of the atoms. The electric susceptibility splits into a static and a dynamic $\boldsymbol{u}$-dependent part. Inserting Eqs. (3.11) and (3.12) into Eq. (3.10) yields,

$$\boldsymbol{P} = \epsilon_0 \left[\chi_0 + \left(\frac{\partial \chi}{\partial \boldsymbol{u}}\right)_0 \cdot \boldsymbol{u}_0 \cos(\Omega t - \boldsymbol{q}\cdot\boldsymbol{r})\right] \boldsymbol{E}_0 \cos(\omega t - \boldsymbol{k}_i \cdot \boldsymbol{r}). \tag{3.13}$$

Finally,

$$\boldsymbol{P} = \epsilon_0 \chi_0 \boldsymbol{E}_0 \cos(\omega t - \boldsymbol{k}_i \cdot \boldsymbol{r}) + \frac{1}{2}\epsilon_0 \left(\frac{\partial \chi}{\partial \boldsymbol{u}}\right)_0 \cdot \boldsymbol{u}_0 \boldsymbol{E}_0 \Big\{ \cos[(\omega_i + \Omega)t - (\boldsymbol{k}_i + \boldsymbol{q})\cdot\boldsymbol{r}] + \cos[(\omega_i - \Omega)t - (\boldsymbol{k}_i - \boldsymbol{q})\cdot\boldsymbol{r}]\Big\}. \tag{3.14}$$

This equation constitutes the conceptual core of light scattering since $\boldsymbol{P}$ will act as a secondary source of scattered radiation. It contains three distinctive terms:

1. The first one oscillates at the same frequency ω_i as the incident light and has the same wavevector $\boldsymbol{k}_i$. As a results, this term is responsible for the elastic Rayleigh scattering. Note that this light does not give any information on the phonons.

2. The second one oscillates at a frequency $\omega_s = \omega_i + \Omega$ and has a wavevector $\boldsymbol{k}_s = \boldsymbol{k}_i + \boldsymbol{q}$. Therefore, this term represents inelastic light scattering. The scattered light is blue-shifted with respect to the incoming light, thus this process corresponds to the annihilation of a phonon of frequency Ω and wavevector $\boldsymbol{q}$. It is called **anti-Stokes** scattered light.

3. The third one oscillates at a frequency $\omega_s = \omega_i - \Omega$ and has a wavevector $\boldsymbol{k}_s = \boldsymbol{k}_i - \boldsymbol{q}$. It gives rise to inelastic scattered light which is red-shifted with respect to the incident light. This process corresponds to the creation of a phonon of frequency Ω and wavevector $\boldsymbol{q}$. It is known as the **Stokes** scattered light.

Note that in this classical approach, $\left(\frac{\partial \chi}{\partial \boldsymbol{u}}\right)_0$ represents the light-matter interaction. If this term is equal to zero, there is no light-matter interaction. This simple approach allows us to obtain the two fundamental relations for Raman scattering

$$\hbar\omega_i = \hbar\omega_s \pm \hbar\Omega, \tag{3.15}$$

$$\boldsymbol{k}_i = \boldsymbol{k}_s \pm \boldsymbol{q}, \tag{3.16}$$

where the + correspond to the Stokes process and the – to the anti-Stokes. The former relation expresses the conservation of energy while the latter corresponds to momentum conservation. The processes studied here correspond to first-order Raman processes because they involve

only one phonon. However, the expansion in Eq. (3.12) can be extended to higher orders in $\boldsymbol{u}$. This will give rise to multiple-phonon Raman scattering (e.g., second order give rise to two-phonon processes). In that case, Eqs. (3.15) and (3.16) still hold if Ω and $\boldsymbol{q}$ are the sum of all the phonon frequencies and wavevectors, respectively. At last, let us precise that in Raman experiments the incident light is usually in the visible range and that in the case of crystals the maximum phonon frequency is about $10^{12} - 10^{13}$ Hz [Fox10]. Therefore, from Eqs. (3.15) and (3.16), the maximum possible value of $|\boldsymbol{q}|$ is $\sim 10^7$ m^{-1}. This is very small compared to the typical size of the first Brillouin zone ($\sim 10^{10}$ m^{-1}). Hence, **one-phonon Raman scattering in crystals probes only zone-center phonons, i.e., phonons with $\boldsymbol{q} \approx 0$.** However, multiple-phonon Raman scattering can probe others points of the first Brillouin zone but the total phonon wavevector must be (almost) equal to zero. This is especially the case in graphene, as we will see in Chapter 5.

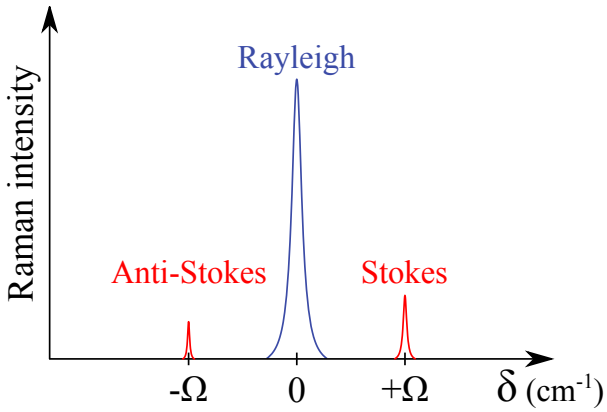

***Figure 3.8** – Schematic representation of a typical Raman spectrum showing the Rayleigh, Stokes and anti-Stokes lines. The spectrum is represented as a function of the Raman shift δ usually expressed in wavenumber (cm^{-1}).*

Typical spectrum

Figure 3.8 sketches the typical spectrum of the scattered light. It is composed of three features: the Stokes, anti-Stokes and Rayleigh lines.[3] The two first are symmetrically located from both sides of the Rayleigh line. Their positions with respect to the Rayleigh line do not depend on the position of the latter (i.e., the frequency of the incident light ω_i) but only on the material (i.e., the different possible value of the phonon frequency Ω). Therefore, it is more convenient to represent the spectrum of the scattered light as a function of the **Raman shift** δ defined as

$$\delta = \omega_i - \omega_s. \tag{3.17}$$

This quantity is generally express as a wavenumber in cm^{-1}. It is equal to 0 for the Rayleigh line, and to $+\Omega$ (positive) and $-\Omega$ (negative) for the Stokes and anti-Stokes lines, respectively (see Fig. 3.8). Note that every Raman process has a Stokes and anti-Stokes feature. Hence, if a line is present only in one side of the spectrum, it is an artifact (such as a cosmic ray).

[3] One can say that light scattering somehow looks alike the frequency modulation (FM) in radio transmission where the role of the carrier wave is played by the incident light.

Raman tensor

As mentioned previously, the polarization $\boldsymbol{P}$ acts as a secondary source for the scattered light. In fact, the microscopic oscillating induced dipoles serve as small antennas that emit the scattered field. From the total power emitted by an oscillating dipole [Jackson99], we deduce that the Raman scattered intensity is proportional to

$$I \propto \omega_s^4 \left| \boldsymbol{e}_s \cdot \left(\frac{\partial \chi}{\partial \boldsymbol{u}} \right)_0 \cdot \boldsymbol{u}_0 \boldsymbol{E}_0 \right|^2 = \omega_s^4 \left| \boldsymbol{e}_s \cdot \left(\frac{\partial \chi}{\partial \boldsymbol{u}} \right)_0 \cdot \frac{\boldsymbol{u}_0}{|\boldsymbol{u}_0|} \boldsymbol{e}_i \right|^2 |\boldsymbol{u}_0|^2 |\boldsymbol{E}_0|^2, \tag{3.18}$$

where $\boldsymbol{e}_i$ ($\boldsymbol{e}_s$) is the unit vector of the polarization of the incident (scattered) field. We notice that I is proportional to the intensity of the incident light $|\boldsymbol{E}_0|^2$ and to the square of the amplitude of vibration $|\boldsymbol{u}_0|^2$, i.e., there is no scattering if no vibrations are present. This is a direct consequence of the classical treatment and we will see later that it is not true. Note that, I depends on the fourth power of ω_s. Consequently, short wavelengths are scattered more efficiently than long wavelengths. Up to now for the sake of simplicity, we assumed that χ is a scalar. However, in general it is a second rank tensor. Therefore, $\left(\frac{\partial \chi}{\partial \boldsymbol{u}} \right)_0$ is also a tensor. The **Raman tensor** is defined as

$$\mathcal{R} = \left(\frac{\partial \chi}{\partial \boldsymbol{u}} \right)_0 \cdot \frac{\boldsymbol{u}_0}{|\boldsymbol{u}_0|}, \tag{3.19}$$

and the Raman intensity in Eq.(3.18) can be express as

$$I \propto \omega_s^4 |\boldsymbol{e}_s \cdot \mathcal{R} \cdot \boldsymbol{e}_i|^2 |\boldsymbol{u}_0|^2 |\boldsymbol{E}_0|^2. \tag{3.20}$$

The Raman tensor has the same symmetry as the corresponding phonon. It is worth mentioning that if the Raman tensor is null then the corresponding phonon is not observable in Raman experiments. On the other hand, if the phonon mode is visible, Eq. (3.20) can be used to predict if this mode is observable or not under a given experimental geometry, i.e., a certain choice for the polarizations $\boldsymbol{e}_i$ and $\boldsymbol{e}_s$. These are the so-called **Raman selections rules**. We will come back later in more detail on these rules.

3.4.2 The quantum approach (microscopic theory)

The classical approach allows us to deduce the two fundamental conservation laws of Raman scattering, to define the Raman tensor and to determine the dependence of the Raman intensity especially on the polarization of the incident and scattered light. But this description has some severe shortcomings. In particular, in this picture the incoming photon interacts directly with a phonon. As the frequency of the photons (at least in the visible range) is much higher than the one of the phonons, such direct interactions are very weak [Yu10]. However, the coupling of photons and electrons is much stronger. Therefore, even if electrons remain globally unchanged, they play a very important role in Raman scattering.

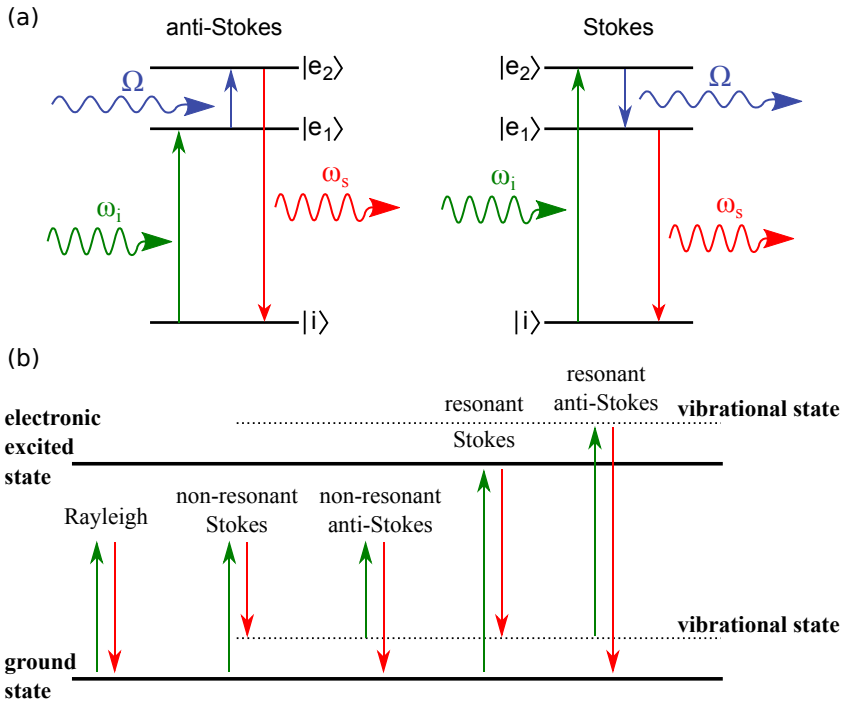

Figure 3.9 *– (a) Anti-Stokes (left) and Stokes (right) processes. ω_i, ω_s and Ω are the frequencies of the incident light, scattered light and phonon, respectively. The system is initially in state $|i\rangle$ and comes back to this state after the process. States $|e_1\rangle$ and $|e_2\rangle$ are intermediate states that can be either real or virtual. (b) Summary of Rayleigh and Raman scattering processes in resonant and non resonant conditions. Figure adapted from Ref. [Ferrari13].*

Microscopic description of the scattering process

In the quantum framework, the Raman scattering procces can be separated into three steps (see Fig. 3.9(a)):

1. The system is initially in the state $|i\rangle$. The incident photon ω_i excites an electron into an intermediate state $|e_1\rangle$ by creating an electron-hole pair (or an exciton). The electron-photon interaction is described by the Hamiltonian $\mathcal{H}_{\text{e-l}}$.

2. The electronic intermediate state $|e_1\rangle$ interacts with the lattice by emitting (Stokes) or absorbing (anti-Stokes) a phonon of frequency Ω and is converted into another intermediate state (or electron-hole pair) $|e_2\rangle$. The electron-phonon interaction Hamiltonian is $\mathcal{H}_{\text{e-v}}$.

3. The intermediate state $|e_2\rangle$ deexcites into the initial state $|i\rangle$ by recombining the electron-hole pair with the emission of the scattered photon ω_s. The electron-photon interaction is described by the Hamiltonian $\mathcal{H}_{\text{e-l}}$.

The intermediate states $|e_1\rangle$,$|e_2\rangle$ can be either real states (i.e., correspond to eigenstates of the system) or **virtual states** (i.e., do not correspond to eigenstates of the system).[4] Note that virtual transitions do not have to conserve energy, although they still have to conserve

[4] In the classical language, it corresponds to the driven oscillations of the electrons at ω_i or ω_s.

momentum.[5] If at least one of these two states is real, the process is said to be **resonant**. More precisely, if $|e_1\rangle$ ($|e_2\rangle$) is real the process is referred to as an incoming (outgoing) resonance. Rayleigh scattering is described similarly but with only one intermediate state since no phonon is involved. The different scattering processes are summed up in Fig. 3.9(b). One may wonder what is the difference between resonant scattering process and luminescence. First, luminescence process involves only real states. Second, if the scattering is fully resonant (i.e., all the states are real), luminescence differs from scattering because luminescence takes a finite time to occur, while scattering is an instantaneous phenomenon. In addition, luminescence is more efficient than scattering. Because scattering is instantaneous, the order of the interactions described above does not matter and all possible permutations of these interactions can describe the process. In total there are six possibilities [Yu10].

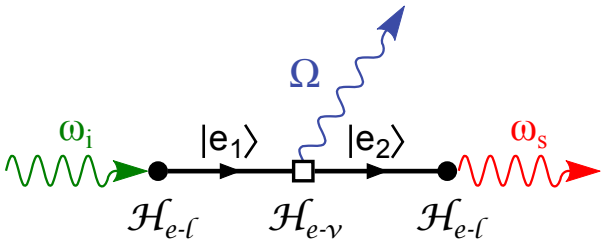

Figure 3.10 *– Feynman diagram of the Raman Stokes process described in the main text and in Fig. 3.9. The incident and scattered light have a frequency ω_i and ω_s, respectively. The emitted phonon has a frequency Ω. $|e_1\rangle$ and $|e_2\rangle$ are the two electronic intermediate states. The interaction Hamiltonian for the three vertex is denoted: $\mathcal{H}_{e\text{-}l}$ for the electron-photon interaction and $\mathcal{H}_{e\text{-}v}$ for the electron-phonon interaction. Due to time reversal invariance, this diagram can also be read from right to left. This order represents the anti-Stokes process.*

Feynman diagrams

The Raman intensity is proportional to the probability of the six possible processes described above. As long as the interactions are weak enough, the probability can be calculated using third-order perturbation theory. This is fundamentally different from the classical theory, where Raman is viewed as a one order perturbation because photons directly interact with phonons. However, in the quantum framework they interact through electrons. The calculation can be done with the help of **Feynman diagrams**. To simplify, let us focus on the Stokes process. Each of the six possibilities for the Raman process described above is represented by one Feynman diagram. Figure 3.10 shows one out of the six Feynman diagrams corresponding to the process depicted in detail previously (see also Fig. 3.9(a)). As a consequence of time invariance, the Feynman diagram can also be read from right to left. This case corresponds to the anti-Stokes process. The other five possible permutations of the interactions in the Raman process are presented in the Fig. 7.28 of Ref. [Yu10]. However, the order shown in Fig. 3.10 gives the strongest contribution, especially in the vicinity of electronic resonances. Therefore, we will only consider this term in the scattering probability. The Feynman diagram in

[5] This can be understood by the fact that this transitions are instantaneous. Therefore, from the uncertainty principle, the energy is not conserved. On the other hand, there no specific constrains on the position and thus momentum is conserved.

Fig. 3.10 can be translated into a scattering probability using the Fermi Golden rule [Yu10]

$$I_{\mathrm{S}} \propto \left| \sum_{|e_1\rangle,|e_2\rangle} \frac{\langle i|\mathcal{H}_{\text{e-l}}|e_2\rangle\langle e_2|\mathcal{H}_{\text{e-v}}|e_1\rangle\langle e_1|\mathcal{H}_{\text{e-l}}|i\rangle}{[\hbar\omega_i - (E_1 - E_i)][\hbar\omega_s - (E_2 - E_i)]} \right|^2 \quad \text{with } \hbar\omega_s = \hbar\omega_i - \hbar\Omega, \tag{3.21}$$

where E_i, E_1 and E_2 are the energy of the states $|i\rangle$, $|e_1\rangle$ and $|e_2\rangle$, respectively. The summation is on *all* the intermediate states $|e_1\rangle$ and $|e_2\rangle$. For simplicity, E_i is often taken to be equal to zero. To avoid any unphysical divergence in the scattering probability, one needs to take into account the damping constant Γ (or in other words the lifetime $\tau = \Gamma^{-1}$) of the intermediate states by replacing E_1 and E_2 by $E_1 - \mathrm{i}\Gamma_1$ and $E_1 - \mathrm{i}\Gamma_2$, respectively. But here, we will neglect this broadening. The rigorous scattering probability with the six Feynman diagrams is expressed in Eq. (7.50b) in Ref. [Yu10]. Note that Eq. (3.21) is generally not used to compute Raman intensity because the matrix elements in the numerator are often difficult to evaluate. However, under resonance conditions, it is common to assume that the numerator is constant and integrate over all possible intermediate states $|e_1\rangle$ and $|e_2\rangle$ [Reich08] (see Chapter 5 Section 5.1).

Stokes and anti-Stokes intensities

Since phonons are Bosons, at thermodynamic equilibrium, the average number of phonons of frequency Ω at a temperature T is given by the Bose-Einstein distribution

$$n_{\mathrm{v}} = \frac{1}{\exp(\hbar\Omega/k_{\mathrm{B}}T) - 1}, \tag{3.22}$$

where k_{B} is the Boltzmann constant. We recall that the Stokes (anti-Stokes) process involves the creation (annihilation) of a phonon. Therefore, the electron-phonon interaction Hamiltonian $\mathcal{H}_{\text{e-v}}$ in Eq. (3.21) includes the phonon creation and annihilation operator, respectively. Let us assume that initially there are n phonons in the crystal, i.e., $|e_1\rangle \propto |n_{\mathrm{v}}\rangle$. For a Stokes process, after the scattering there will be $n_{\mathrm{v}} + 1$ phonons, thus $|e_2\rangle \propto |n_{\mathrm{v}} + 1\rangle$ and $\langle e_2|\mathcal{H}_{\text{e-v}}|e_1\rangle \propto (n_{\mathrm{v}} + 1)^{1/2}$. Similarly, for an anti-Stokes process $|e_2\rangle \propto |n_{\mathrm{v}} - 1\rangle$ and $\langle e_2|\mathcal{H}_{\text{e-v}}|e_1\rangle \propto n_{\mathrm{v}}^{1/2}$ [Cohen-Tannoudji79]. As a consequence, I_{S} is proportional to $n_{\mathrm{v}} + 1$ and I_{AS} to n_{v} [Yu10]. To make the link with Eq.(3.20), one has to replace $|\boldsymbol{u}_0|^2$ by a term proportional to $n_{\mathrm{v}} + 1$ or n_{v} [Cardona83]. This has two important consequences. First, even in the absence of phonons (i.e., $n_{\mathrm{v}} = 0$) the Stokes intensity I_{S} is different from zero. Second, the ratio $I_{\mathrm{AS}}/I_{\mathrm{S}}$ is proportional to the Boltzmann factor $\exp(-\hbar\Omega/k_{\mathrm{B}}T)$. This is the reason why the anti-Stokes feature has, in general,[6] a lower intensity than the Stokes one, as drawn in Fig. 3.8. Finally, let us point out that the ratio of the Stokes to anti-Stokes intensities may be used to determine n_{v} and the temperature T.

3.4.3 Raman selection rules

[6] Due to resonance effect the anti-Stokes feature can be more intense than the Stokes one. For instance in N-layer $MoTe_2$ see Ref. [Goldstein16].

Raman selection rules on activity

To find out whether a particular vibrational normal mode is observable in Raman scattering (**Raman active**) or not (**Raman inactive**), we must examine the matrix element $\langle \psi_f | \mathcal{H}_{\text{Raman}} | \psi_i \rangle$, where ψ_i is the initial state of the crystal, ψ_f the normal mode that may be excited and $\mathcal{H}_{\text{Raman}}$ is the Hamiltonian of the Raman process [Dresselhaus07]. The vibrational mode is Raman active if this matrix element is non zero. Let Γ_i, Γ_f and Γ_{Raman} be the irreducible representations of ψ_i, ψ_f and $\mathcal{H}_{\text{Raman}}$, respectively. The matrix element does not vanish if the direct product $\Gamma_{\text{Raman}} \otimes \Gamma_i$ contains Γ_f [Dresselhaus07]. In general, $|\psi_i\rangle$ corresponds to the ground state of the crystal which is totally symmetric. Therefore, $\Gamma_{\text{Raman}} \otimes \Gamma_i = \Gamma_{\text{Raman}}$ and more simply a given vibration mode is Raman active if its irreducible representation is contained in the irreducible representation of $\mathcal{H}_{\text{Raman}}$. As $\mathcal{H}_{\text{Raman}}$ is proportional to the Raman tensor which is a symmetric second rank tensor,[7] it has the same transformation properties as a general quadratic form (e.g., x^2, y^2, z^2, xy, yz, zx, ...) [Dresselhaus07]. Hence, Γ_{Raman} is directly obtained by identifying the quadratic basis function in the character table. In conclusion, if a given normal mode has an irreducible representation with a quadratic basis function, it is Raman active, otherwise it is not. Let us precise that a similar rule apply for multi-phonon processes. For instance in a second-order Raman process, a combination of two modes Γ_{v1} and Γ_{v2} is Raman active if the irreducible decomposition of $\Gamma_{\text{v1}} \otimes \Gamma_{\text{v1}}$ contains at least one Raman-active irreducible representation [Dresselhaus07]. In particular, as the direct product of a representation with itself always contains the identity representation, which transforms as a combination of x^2, y^2, z^2, all second-harmonic modes at 2Ω (if Ω is the frequency of the mode) are Raman-active. Therefore, silent modes that cannot be observed in first-order spectrum may be observable in second-order spectrum.

Similarly, we can determine if a particular vibrational mode is **infrared (IR) active** following the same procedure. But in that case, $\mathcal{H}_{\text{IR}}$ transforms as a vector [Dresselhaus07] (because it corresponds to an electric dipole transition), i.e., $\Gamma_{\text{IR}} = \Gamma^{\text{vec}}$ (see Section A.4). In short, if a given normal mode has an irreducible representation with a linear basis function (e.g., x, y, z, (x, y), ...), it is IR active, otherwise it is not. Note that some modes are both Raman and IR active, while others are neither Raman active nor IR active. The latter are called **silent modes**. Raman and IR spectroscopies are complementary techniques since IR processes couple states with opposite parity, while Raman processes couple states with the same parity.

These rules were already applied in Sections 3.2 and 3.3 to determine the Raman or IR activity of the phonon modes.

Raman selection rules on polarizability

In practice, even if a given vibrational mode is Raman active, it not necessarily experimentally observable depending on the geometry of the setup. Indeed, as shown in Eq. (3.20), the Ra-

[7] Rigorously, it is only symmetric if we can neglect the frequency difference between ω_i and ω_s. However, this is the case for crystals and visible light.

man intensity depends on the polarization of the incident $\boldsymbol{e}_i$ and scattered $\boldsymbol{e}_s$ light following the relation

$$I \propto |\boldsymbol{e}_s \cdot \mathcal{R} \cdot \boldsymbol{e}_i|, \tag{3.23}$$

where $\mathcal{R}$ is the Raman tensor of a particular mode. Since, the Raman tensor has the same symmetry as the corresponding mode, one can deduce the general form of the tensor which can be represented as a 3×3 matrix. For the different crystallographic point group, R. Loudon has tabulated [Loudon64] the general form of the 3×3 matrices of the Raman tensors (assuming a symmetric tensor) for the Raman active modes. Note that there are as many tensors as the dimension of the irreducible representation.

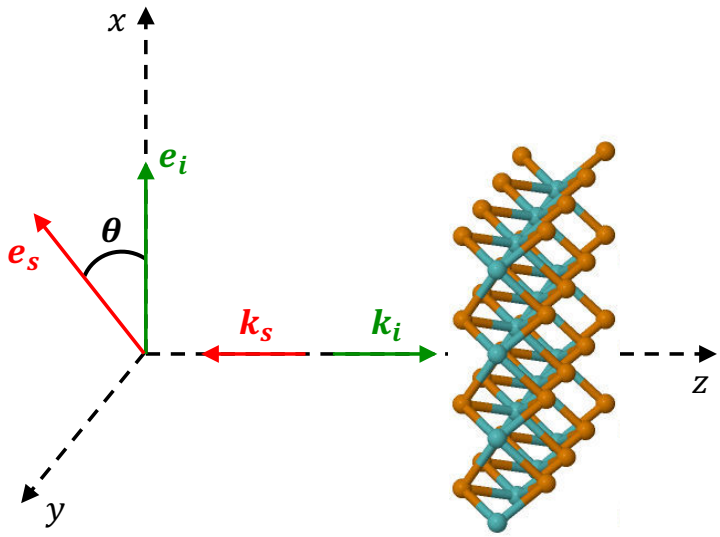

Figure 3.11 *– Scattering configuration used for all the Raman measurements in this thesis. $\mathbf{k}_i$ and $\mathbf{k}_s$ are the wavevectors of the incident and scattered light, respectively. As they are antiparallel, this geometry is said to be the backscattering one. $\boldsymbol{e}_i$ and $\boldsymbol{e}_s$ are the unity vectors of the polarization of the incident and scattered light, respectively. $\boldsymbol{e}_s$ is in the xy plane and makes a angle θ with x axis (or $\boldsymbol{e}_i$). The sample (here a monolayer TMDs) lies in the yz plane.*

To illustrate the Raman selection rules, let us take the example of the monolayer TMDs studied in Section 3.3.2. From Eq. (3.7), the irreducible representation of the Raman active modes at Γ are A_1', E'' and E'. The most common scattering geometry for studying 2D crystals is the **backscattering** one, i.e., $\boldsymbol{k}_i$ and $\boldsymbol{k}_s$ are antiparallel to each other. Let us assume that $\boldsymbol{k}_i$ and $\boldsymbol{k}_s$ are along the z axis, that the incident light is linearly polarized ($\boldsymbol{e}_i$) along the x axis, that the scattered light is chosen[8] to be linearly polarized ($\boldsymbol{e}_s$), in the xy plane, along an axis making an angle θ with the x axis, and that the monolayer lies in the yz plane (see Fig. 3.11). Note that a given scattering configuration is usually represented as $\boldsymbol{k}_i(\boldsymbol{e}_i, \boldsymbol{e}_s)\boldsymbol{k}_s$ [Yu10]. The

[8] In practice, a polarizer is used to select the linear polarization, see Chapter 4.

Raman tensor for this configuration are given by [Loudon64]

$$\mathcal{R}(A_1') = \begin{pmatrix} a & 0 & 0 \\ 0 & a & 0 \\ 0 & 0 & b \end{pmatrix},$$

$$\mathcal{R}(E')_x = \begin{pmatrix} 0 & d & 0 \\ d & 0 & 0 \\ 0 & 0 & 0 \end{pmatrix}, \quad \mathcal{R}(E')_y = \begin{pmatrix} d & O & 0 \\ 0 & -d & 0 \\ 0 & 0 & 0 \end{pmatrix},$$

$$\mathcal{R}(E'') = \begin{pmatrix} 0 & 0 & 0 \\ 0 & 0 & c \\ 0 & c & 0 \end{pmatrix}, \quad \mathcal{R}(E'') = \begin{pmatrix} 0 & 0 & -c \\ 0 & 0 & 0 \\ -c & 0 & 0 \end{pmatrix}, \tag{3.24}$$

where $a, b, c, d \in \mathbb{C}$. It is worth noticing that, as E' and E'' are representation of dimension two, there are two Raman tensors. Applying Eq.(3.23) yields to the following Raman selection rules

$$\left|\boldsymbol{e}_s \cdot \mathcal{R}(A_1') \cdot \boldsymbol{e}_i\right|^2 = |a|^2 \cos^2\theta, \tag{3.25}$$

$$\left|\boldsymbol{e}_s \cdot \mathcal{R}(E')_x \cdot \boldsymbol{e}_i\right|^2 = |d|^2 \sin^2\theta, \tag{3.26}$$

$$\left|\boldsymbol{e}_s \cdot \mathcal{R}(E')_y \cdot \boldsymbol{e}_i\right|^2 = |d|^2 \cos^2\theta, \tag{3.27}$$

$$\left|\boldsymbol{e}_s \cdot \mathcal{R}(E'') \cdot \boldsymbol{e}_i\right|^2 = 0. \tag{3.28}$$

Consequently, phonon modes with E'' symmetry are not observable in backscattering geometry. To be observable, these two modes require the polarization to have a non-zero component along z. For $\theta = 0$ (i.e., $\boldsymbol{e}_s = \boldsymbol{e}_i$), the phonon modes with A_1' and E' symmetry are observable. This configuration is usually denoted $z(x,x)\bar{z}$ or XX and is called the parallel configuration. For $\theta = \frac{\pi}{2}$ (i.e., $\boldsymbol{e}_s \perp \boldsymbol{e}_i$), only the phonon modes with E' symmetry are observable. This configuration is often denoted $z(x,y)\bar{z}$ or XY and is referred to as the perpendicular configuration. For $\theta \in]0, \frac{\pi}{2}[$, the phonon modes with A_1' and E' symmetry are observable. Interestingly, the intensity of the phonon modes with E' symmetry is constant since $\forall\theta, \cos^2\theta + \sin^2\theta = 1$. In conclusion, among the seven Raman active phonon modes at Γ only five are observable in this configuration including one which is not visible in the perpendicular configuration. Note that in principle, by measuring the Raman intensity for different θ it is possible to determine $|a|$. Inversely, by using different configurations, it is possible to identify the symmetry of the Raman tensor and thus the symmetry of the underlying phonon. For instance in the example above, the parallel and perpendicular configurations allow to distinguish between the A_1' and E' modes.

3.5 Conclusion

In conclusion, we have successfully applied group theory to graphene, and to N-layer and bulk 2Hc transition metal dichalcogenides in order to derive the phonon symmetries. In

addition, we have introduced Raman scattering in a classical and quantum framework. We have established the two fundamentals laws (energy and momentum conservation) and the expressions of the Raman intensity, defined the Raman tensor and given the Raman selection rules. All these results will be particularly useful for the Chapters 5 and 6.

Take home messages

- Group theory is an extremely powerful tool to predict the vibrational properties of layered materials.
- The Raman intensity is highly sensitive to the symmetry of the phonons and is directly related to the scattering probability.
- In graphene, there is only one Raman-active mode at Γ (see Chapter 5).
- Depending on the parity of N, N-layer 2Hc transition metal dichalcogenides belongs to different space groups. The irreducible representations of the phonons at Γ are given by Eqs. (3.7) and (3.9) for odd and even N, respectively. In particular, multiple phonons with same symmetry give birth to the Davydov splitting studied in detail in Chapter 6.

Chapter 4

Experimental methods

The experimental methods used in this thesis are described in this chapter. The first part presents the fabrication techniques used to prepare the different types of samples studied in this work, namely graphene, N-layer transition metal dichalcogenides, van der Waals heterostructures and electrochemically top-gated graphene field-effect transistors. The second part is dedicated to our experimental setup, with which Raman and photoluminescence measurements can be performed under ambient conditions with electrical access. Finally, the third part is devoted to the optical interference effects that occurs in quasi two-dimensional samples deposited onto layered substrate. However, the mathematical treatment of these effects is presented in Appendix C.

4.1 Sample fabrication

In this section, we introduce the techniques used to fabricate the three different types of samples. N-layer TMDs deposited onto silicon (Si) substrate covered with a ~ 100 nm-thick silicon oxide (SiO_2) epilayer are used for the Raman and PL studies in Chapters 6 and 7. Van der Waals heterostructures based on graphene and TMDs are exploited in Chapter 8 to investigate the heterolayer coupling by mean of Raman and PL spectroscopy. Dual-gated graphene FETs, with a solid state back gate and an electrochemical top gate, are used in Chapter 5 to study the electrical tuning of the optoelectronic properties of graphene by Raman scattering.

4.1.1 Mechanical exfoliation

Although, mechanical exfoliation of layered crystal using adhesive tape has been known for decades [Frindt66], this technique was popularized only recently by Geim and Novoselov [Novoselov04, Novoselov05b]. This method is commonly called 'Scotch-tape technique'. To date, it is the most utilized way to produce monolayers and few layers of graphene and TMDs. As surprising as it may sound, this technique has so far provided crystallites of unmatched quality.

All samples studied in this thesis were prepared by mechanical exfoliation following two slightly different protocols. The first one corresponds to the standard procedure and is used to exfoliate graphene. The the second one involves one supplementary step with a viscoelastic polymer and is used to exfoliate TMDs. The two protocols are described in detail below.

Graphene exfoliation

All graphene samples were obtained from natural graphite using the standard 'Scotch-tape technique'. This technique can be summarized in the following steps (see Fig. 4.1 for the illustration of each step):

1. Put a graphite piece on an adhesive tape.
2. Fold the adhesive tape and open it delicately to increase the surface.
3. Stick another adhesive tape to the first adhesive tape and press delicately on it.
4. Peel off slowly the two adhesive tapes and keep the first, repeat steps 2 and 3 with that adhesive tape until transparent zones appear.
5. Stick the adhesive tape with thin transparent graphite on a substrate and massage it with a finger by applying a moderate pressure, for a few minutes.
6. Peel off slowly the adhesive tape from the substrate.

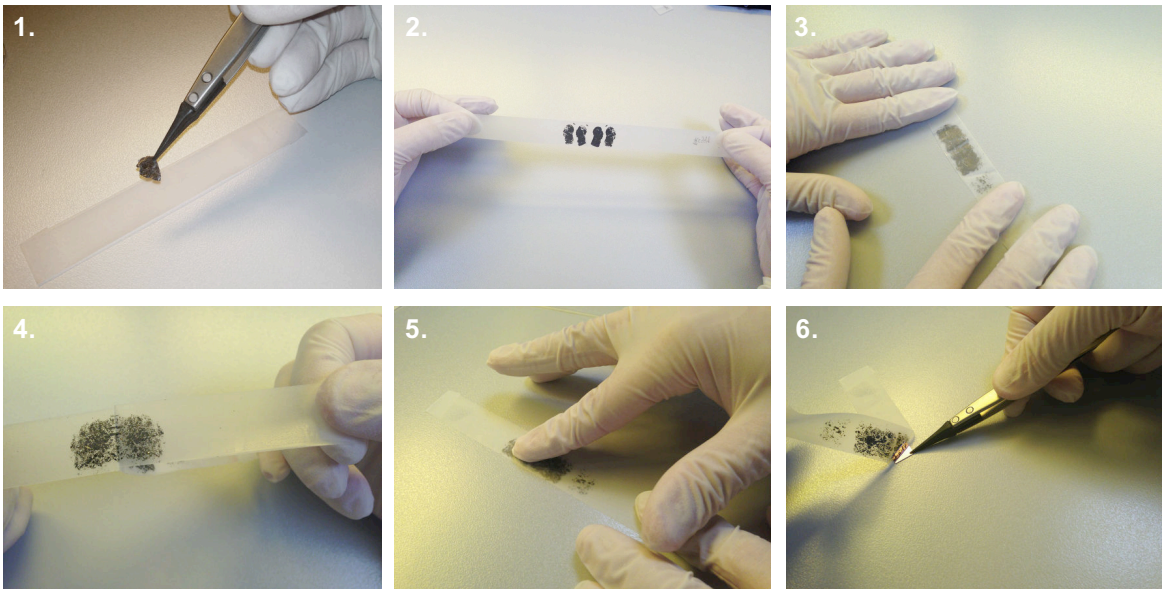

Figure 4.1 *– Photos of the six steps of the standard 'Scotch-tape technique' used to exfoliate graphene. The steps are described in the main text.*

The substrates used are highly *p*-doped Si substrates covered with a thermally grown 90-nm or 285-nm SiO_2 epilayer (these thicknesses are well-suited for optical microscope identification, see Section 4.3). The substrates are typically 1 cm × 1 cm. Prior to deposition (step

5), the substrates are cleaned with acetone, ethanol and isopropyl alcohol in an ultrasonic bath for 10 min each time. Then they are heated up to about 120 °C to remove residual solvent and water molecules. Finally, they are surface-activated by exposure to a 10 min oxygen plasma to improve the adhesion of the graphene flakes on the substrate. Since the surface activation remains for a few minutes, step 5 has to be done as quickly as possible after the oxygen plasma exposure.

This exfoliation technique produces flakes with different sizes and thicknesses randomly distributed over the sample substrate as it can be seen with the naked eyes. Among all these fragments only a small fraction are atomically thin. We can detect the interesting flakes under an optical microscope by using the optical contrast variation with the number of layers [Blake07, Roddaro07]. Indeed, one layer of graphene absorbs about 2.3 % of the visible light (see Chapter 2 Section 2.1) and in first approximation, the absorptance of few layers is proportional to the number of layers (see Appendix C Section C.2). In addition, this detection is made easier by a suitable choice of oxide thickness due to interference effects (see Section 4.3). The positions of the regions of interest are then located with respect to an origin (usually a corner of the substrate). A trained eye can easily identify monolayers from few layers. However, the exact number of layers is further confirmed by Raman (or AFM) measurements (see Chapter 5 Section 5.1).

Transition metal dichalcogenides exfoliation

All TMDs samples were obtained from synthetic bulk crystals purchased from *2D Semiconductors* or *HQ Graphene* using a slightly modified 'Scotch-tape technique'. This modified technique involves the use of a viscoelastic substrate. Viscoelastic materials exhibit both viscous and elastic properties: at short timescales it behaves as an elastic solid and at long timescales it flows slowly [Meitl06]. Here, we employ commercially available viscoelactic films (Gel-Pak 4) based on Polydimethylsiloxane (PDMS). We choose to work with commercial films and not with homemade PDMS films because they are flatter [Castellanos-Gomez14]. TMDs are exfoliated onto the same Si/SiO_2 substrates as graphene. These substrates are prepared following the same exact protocol.

This modified exfoliation technique can be summarized in the following steps (Fig. 4.2 for the illustration of each step):

1. to 4. Same steps as the standard 'Scotch-tape technique' (see description above and Fig. 4.1) but less one repetition of steps 2 and 3.

5. Stick the adhesive tape to the viscoelastic substrate and massage it with a finger by applying moderate pressure, for a few minutes. Let in contact for few more minutes an apply eventually a uniform pressure with a small weight.

6. Peel off very quickly the adhesive tape from the substrate. Peeling off with sufficiently high velocity leads to the adhesion of the flakes to the viscoelactic film [Meitl06].

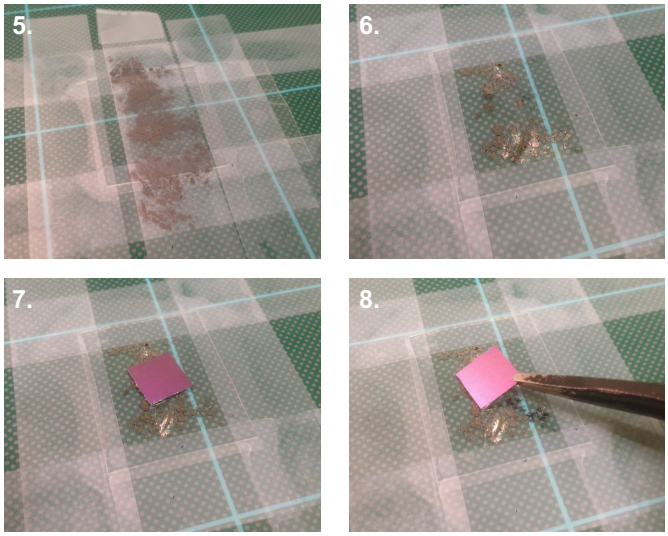

Figure 4.2 *– Photos of the four last steps of the modified 'Scotch-tape technique' used to exfoliate TMDs. The steps are described in the main text.*

7. Turn the Si/SiO_2 substrates upside down and press carefully against the viscoelastic film. Leave in contact for some minutes and facultatively apply a uniform pressure with a small weight.

8. Peel off very slowly the Si/SiO_2 substrate from the viscoelastic film. Peeling off with sufficiently low velocity causes the flakes to separate from the viscoelastic film and to adhere preferentially to the Si/SiO_2 substrate [Meitl06].

Compared to the standard 'Scotch-tape technique', this modified technique deposits less materials onto the Si/SiO_2 substrate. However, the size of the flakes is larger. Note that for graphene, standard exfoliation leads to better results. All the exfoliated TMDs were found to degrade over tens of days in ambient conditions [Qiu12, Tongay13, Nan14, Lee15a, Gao16]. Therefore, the samples were stored in vacuum. In the case of $MoTe_2$, the aging effects were found to be even faster (few days), especially for the $MoTe_2$ crystals provided by *HQ Graphene*. Consequently, all the data presented in this manuscript were obtained on freshly exfoliated samples.

4.1.2 All-dry transfer technique

To fabricate van der Waals heterostructures of 2D crystals, we have developed an all-dry transfer technique based on the work of A. Castellanos-Gomez [Castellanos-Gomez14]. This technique utilizes a viscoeleactic film as a stamp to deterministically transfer a given flake onto a user-defined location on an acceptor surface, like another 2D crystal or a pre-patterned substrate (e.g., with trenches to obtain freely suspended samples). Such deterministic transfer is possible owing to the viscoelastic properties of the stamp [Meitl06] and to the fact that 2D crystals adhere preferentially to the acceptor surface rather to the stamp [Castellanos-Gomez14]. Therefore, peeling off with low velocity causes the flakes to

be transferred.

In brief, this transfer technique is similar to the modified 'Scotch-tape technique' described above, except that the random transfer of the flakes is replaced by the positioning and transfer of a given flake to the target surface. This desired positioning is achieved using a Karl Suss MJB3 mask aligner. Such commercial system has the advantage to be optimized for accurate alignments at sub-micrometer resolution. The viscoelactic films employed are also the commercial PDMS Gel-Pak 4.

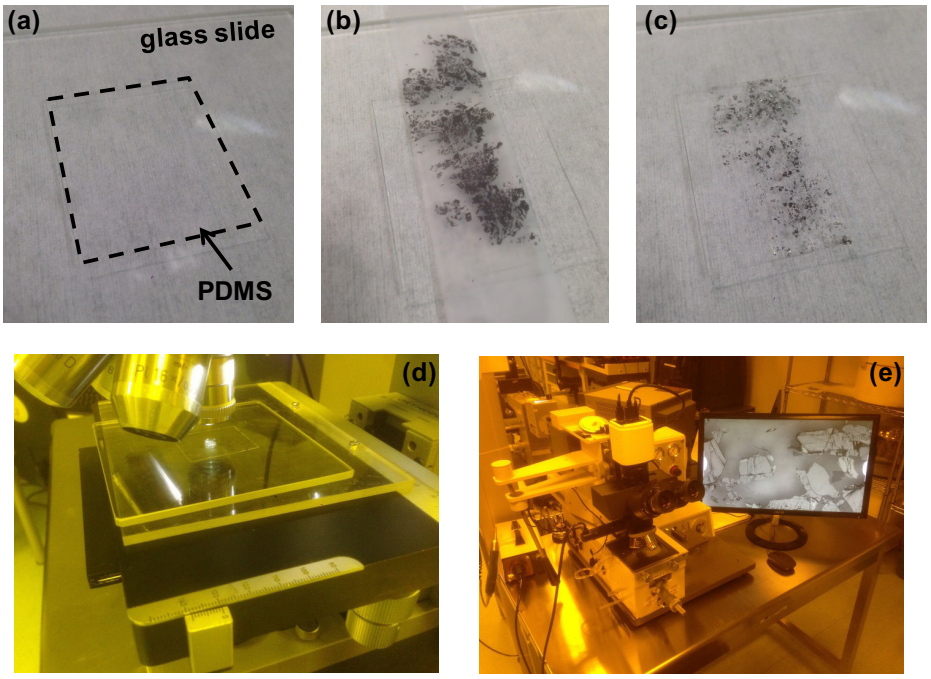

Figure 4.3 *– Photos of the all-dry transfer technique. (a), (b) and (c) illustrate the preparation of the viscoleslactic stamp on the mask glass slide (see Section 4.1.1). (d) An optical microscope is used to identify and locate the interesting flakes. (e) Photo of the Karl Suss MJB3 mask aligner employed to align the viscoelactic stamp with the target substrate and to bring them into contact.*

This all-dry transfer technique is illustrated in Fig. 4.3 and can be summarized in the following steps:

1. Exfoliate the desired 2D crystals onto the viscoelactic stamp following steps 1 to 6 of the modified 'Scotch-tape technique' (see Section 4.1.1). Prior to exfoliation, stick the viscoelactic film to a mask glass slide.

2. Identify and locate an interesting flakes at the surface of the stamp by optical contrast under a optical microscope.

3. Place the target substrate in the mask aligner by sticking it to the stage with double side adhesive tape. The acceptor substrate being first prepared for instance by exfoliating and detecting another 2D crsytals or by pre-patterning it.

4. Turn down the mask glass slide and put it in the mask aligner.

5. Carefully align the flake on top of the target substrate.

6. Cautiously bring the acceptor substrate and the viscoelastic film in contact. Once in contact, do not press further the stamp against the target substrate in order to not induce strain and bubbles in the transferred flake [Castellanos-Gomez14].

7. Peel off very slowly the stamp from the acceptor subtrate.

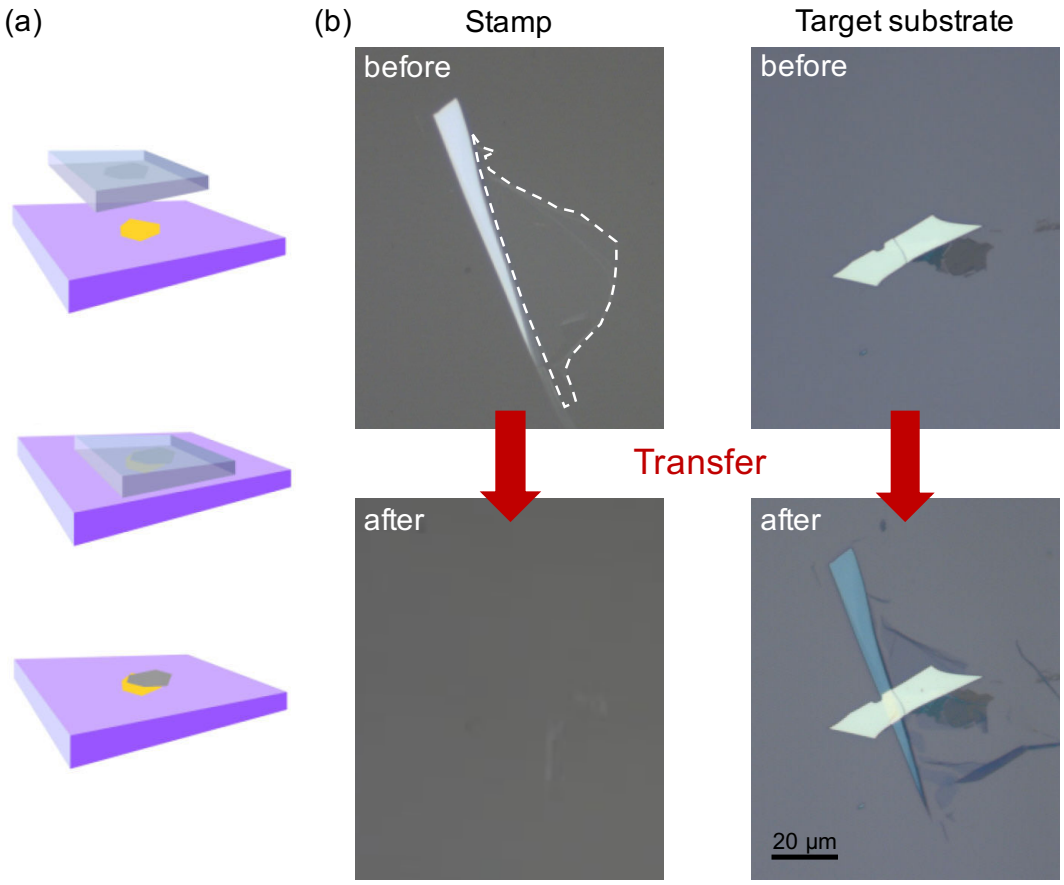

Figure 4.4 *– (a) Cartoon of the transfer process extracted from Ref. [Castellanos-Gomez14]. (b) Optical images of the surface of the PDMS stamp (left) and the target substrate (right). Before the transfer: a graphene flake was exfoliated and detected on a PDMS film. The flake is highlighted with a dashed line. A monolayer of $MoSe_2$ was exfoliated and detected onto a Si/SiO_2 substrate. After the transfer: almost all the graphene flake has disappeared on the PDMS stamp. Most of the graphene layer was transferred on top of the $MoSe_2$ sheet. Note that during the transfer process the graphene flake cracked.*

Figure 4.4 shows an example of a van der Waals heterostructure made by transferring a monolayer of graphene on top of a monolayer of molybdenum diselenide ($MoSe_2$). The top photos display the surface of the PDMS stamp and the surface of the acceptor substrate before the transfer. The $MoSe_2$ flakes was exfoliated with the modified 'Scotch-tape technique' and detected under an optical microscope. Then the bottom photos exhibit the same surfaces but after the transfer. We notice that almost all the graphene flake was transferred to the target substrate. But a part of graphene monolayer broke during the process. This happens sometimes especially for 'large' flakes. However, the graphene flake covers a part of the $MoSe_2$ sheet (see Chapter 8 for the characterization of this heterostructure). It is worth mentioning

that for such structures, the entire process, from the exfoliation on the target substrate to the transfer, is done in a clean room as quick as possible to avoid oxidation and contamination of the flakes. In practice, it can be done in 2 hours.

Finally, let us precise that this technique has the advantage not to involve any sacrificial layer. Therefore, the all-dry technique presented here is well adapted for the fabrication of clean suspended samples and is now widely used in the team to fabricate such samples. Let us precise that a dedicated transfer setup is currently being built in our group by Etienne Lorchat, PhD student. This setup will be more stable compare to the old MJB3 and also offer the possibility to heat the sample in order to improve the interface quality or to used the 'hot pick-up technique' [Pizzocchero16] (see Chapter 2 Section 2.3.1).

4.1.3 Fabrication of graphene field-effect transistors

The dual gated graphene field-effect transistors studied in Chapter 5 were fabricated following standard microfabrication processes in the STnano cleanroom. Source, drain and gate electrodes are made by photolithography, followed by metal deposition. A second photolithography step is performed to coat the source and drain electrodes with a thick resist. Then the electrochemical top gate is drop-casted. Finally, the metal contacts on the sample are connected to a chip carrier by thin gold wires glued to the contacts with silver epoxy. The main fabrication steps are summarized in Fig. 4.5 and described in more detail below.

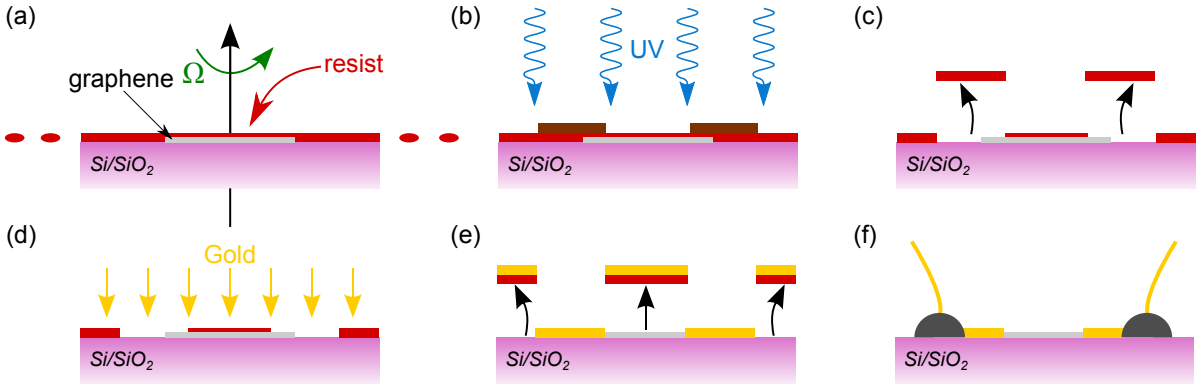

Figure 4.5 *– Schematic summary of the fabrication steps. (a) Spin-coating of the negative photo-sensitive resist. (b) Mask alignment and UV exposition. (c) Development of the sample. The non-expose resist is washed away by the developer solution. (d) Metal deposition. (e) Lift-off of the resist. (f) Manual wire bonding. Electrodes are connected to the chip carrier by means of thin gold wires glued with conductive silver epoxy.*

Photolithography Photolithography (or optical lithography) is a powerful technique to fabricate micrometer-sized structures. It consist in transferring a geometric pattern from a mask to a photo-sensitive resist. Standard optical lithography is limited by optical diffraction. To achieve the highest possible resolution, ultra-violet (UV) light at 365 nm is used allowing to obtain, for our setup (Karl Suss MJB4), a resolution of ≈ 4 μm. We first design a mask for the two lithography steps (see Fig 4.6.). The three main steps of photolithography are (see Figs. 4.5(a)-(b)-(c))

1. A photo-sensitive resist is spin-coated on the sample. This photoresist is used as a negative tone resist, i.e., the exposed area are modified in order to be washed away in the developer (see step 3).

2. The mask with source, drain and gate electrodes is align on top of the graphene flake with a Karl Suss MJB4 mask aligner. The mask is brought in contact with the sample and the non protected areas are exposed to UV light.

3. The sample is immersed in the developer solution[1] in order to dissolve the non exposed area. The sample is then rinsed with deionized water and dried with nitrogen. The resist acts then like a mask for following fabrication steps.

Metal deposition A metal film is deposited onto the sample by heating and evaporating solid metal under high vacuum at typically 10^{-7} bar (see Fig. 4.5(d)). The film thickness is controlled in the nanometer range. Different metals can be evaporated successively with one machine, the metal sources being placed in melting pots in a revolving disc. An electron beam heats the metal source to create an evaporation cone containing metal atoms which then deposit above the metal source. The sample to be covered is upside down within that cone, and the thickness is controlled by shutters and a quartz crystal micro-balance in a very accurate way. As gold does not stick very well to SiO_2, we first deposit a 3 nm-thick film of titanium (Ti) followed by a 47 nm-thick film of gold (Au). Finally, the sample is immersed in acetone to remove the resist covered with metal. This step is called lift-off (see Fig. 4.5(e)).

Second photolithography This second photolithography is not neccessary but was found to greatly improve the top gating efficiency of the sample. This photolithography is identical to the first one except that we use $\approx$ 4-μm-thick photoresist layer (MicroChem SU8 2005) and the second mask. This mask opens a windows above the graphene channel, gate electrode and parts of source and drain electrodes for wire bonding (see Fig. 4.6). Once this photolithography is done, the resist is hard backed to ensure it being insoluble in most of chemical solvent including acetone and methanol.

Wire bonding The source, drain and gate electrodes are connected to the chip carrier by a manual bonding procedure. First, the sample is glued with silver paste to the conductive bottom of the chip carrier since the highly p-doped Si substrate can be used as a back gate electrode for dual-gated geometry. Then, the electrodes on the sample are connected to the chip carrier with gold wires and conductive silver epoxy (see Fig. 4.5(f)). The conductive epoxy is dropped on the electrodes and the chip carrier, and before drying, these drops are connected by a thin gold wire.

Electrochemical top gate the electrochemical top-gate is formed by depositing a drop of polymer electrolyte with a micropipette. The polymer electrolyte is prepared by mixing lithium perchlorate ($LiClO_4$) and polyethylene oxide (PEO) in methanol at a weight

[1] A chemical solution, provided by the resist manufacturer, specially made for this step.

ratio[Das08, Lu04, Liu13] 0.012:1:4. The mixture is then heated at 45 °C and stirred until it becomes uniform. This suspension is filtered to get a clear solution. After dropcasting, the methanol evaporates and a thin film of transparent polymer electrolyte is formed. To remove residual moisture and solvent, the device is annealed at about 90 °C.

Figure 4.6(c)-(d) shows an example of a device prior deposition of the polymer electrolyte. The device geometry features a well-defined gated region and prevents the polymer electrolyte to be in contact with the source and drain electrodes.

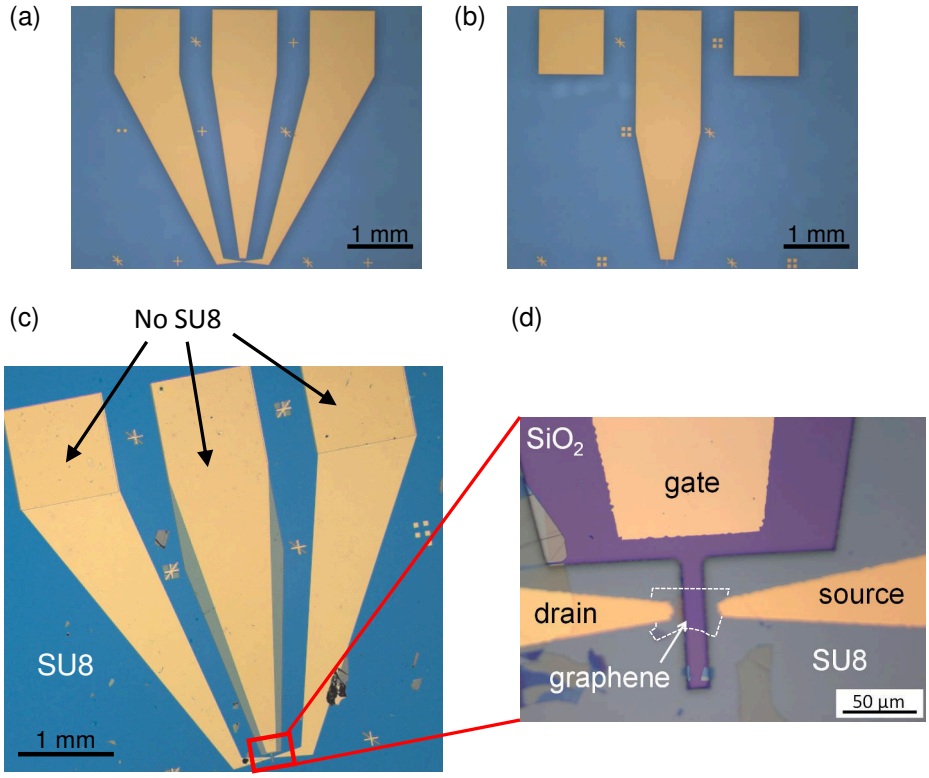

Figure 4.6 *– (a) and (b) Optical images of the mask used in the firt and second lithography, respectively. (c) and (d) Optical images of a graphene field-effect transistor prior deposition of the polymer electrolyte. The sample is covered with photoresist (SU8). Windows above the graphene channel, gate electrode and two squares on source and drain electrodes are opened. This photoresist prevents the source and drain to be in contact with the polymer electrolyte.*

4.2 Experimental setup

All the samples fabricated following the techniques described in the previous section were studied using photoluminescence and/or Raman measurements. These measurements were performed on the same setup. The core of this setup is a home-built **confocal microscope** used in backscattering geometry. This setup allows for spatially resolved micro-PL and micro-Raman measurements, and time-resolved PL under ambient conditions with electrical access. The setup is described in detail below with its main characteristics.

4.2.1 The setup

The principle of the experimental setup is sketched in Fig. 4.7. The heart of the setup is a backscattering commercial (Nikon) microscope. An infinity conjugated, enlarged, and spatially and spectrally filtered (F_1) laser beam (green line) is injected into the microscope and directed towards the sample by means of a dichroic mirror (DM) or 10/90[2] beam splitter (for ultralow Raman measurements[3]). Different optical paths allow to choose the laser beam among continuous wave (cw) lasers at photon energy E_L equal to 2.33 eV (532 nm), 1.96 eV (633 nm) and 1.58 eV (785 nm) for PL and Raman measurements, and a supercontinuum tunable laser (repetition rate between 1.96 – 78.05 Hz and pulsed width of $\sim$ 20 ps) for time-resolved PL. The spectral filter F_1 is a bandpass filter (Semrock MaxLine® or OptiGrate BragGrate™ bandpass filter for ultralow Raman measurements). The intensity of the laser beam can be adjusted with optical densities. The laser beam is focused on the sample via an objective, which can be chosen among objectives with different magnifications and numerical aperture (NA) (see Tab. 4.1). The sample holder is mounted on a xyz-piezoelectric stage allowing for a precise positioning. The range of the piezoelectric element is 100 μm in x- and y-direction and 20 μm in z-direction. To locate the region of interest on the sample, a white light (yellow line) can be focused on the sample by means of a removable 50/50 beam splitter, and the optical image can then be detected by a removable mirror (M_1) and a camera.

The backscattered and/or emitted light (orange line) is collected by the same objective and passes through the dichroic mirror or 10/90 beam splitter. In the case of the dichroic mirror, a first spectral separation of the residual excitation and PL or Raman scattered light is made. The subsequent beam is spatially filtered with the help of two lenses (L_1 and L_2) and a pinhole (P) of diameter 100 μm. The lens L_1 permits to focus the incident beam at the center of the hole and the lens L_2 to parallelize the outgoing beam. The pinhole is spatially conjugated with the laser spot on the sample, which ensures that the recorded signal originates from a well defined volume on the sample and further improves the signal to noise ratio.

Spectroscopy The light can then be sent on two different detection systems by means of a removable mirror (M_2). The first system is used for PL and Raman measurements. It consists in a spectrometer with a dispersive element (grating can be choose between 150, 300, 900 and 2400 grooves/mm) and a charged-coupled device (CCD) array. The CCD camera is either a liquid nitrogen cooled Si array of 1340×100 pixels (Princeton Instruments Spec-10) or a thermoelectrically cooled two-dimensional InGaAs array of 640×512 pixels (Princeton Instruments NIRvana®).[4] The former is used for Raman and visible PL measurements while the latter is used for NIR PL measurements. The second system is adapted to time-resolved PL measurements. The photons are detected by an avalanche photodiode (APD). The tunable pulsed laser and the APD are connected to a TCSPC board (PicoHarp 300) allowing to obtain

[2] 10 % of the light is reflected and 90 % transmitted.
[3] Indeed, the dichroic mirror is no spectrally steep enough.
[4] This camera was loaned by Philippe Bernhard at Roper Scientific.

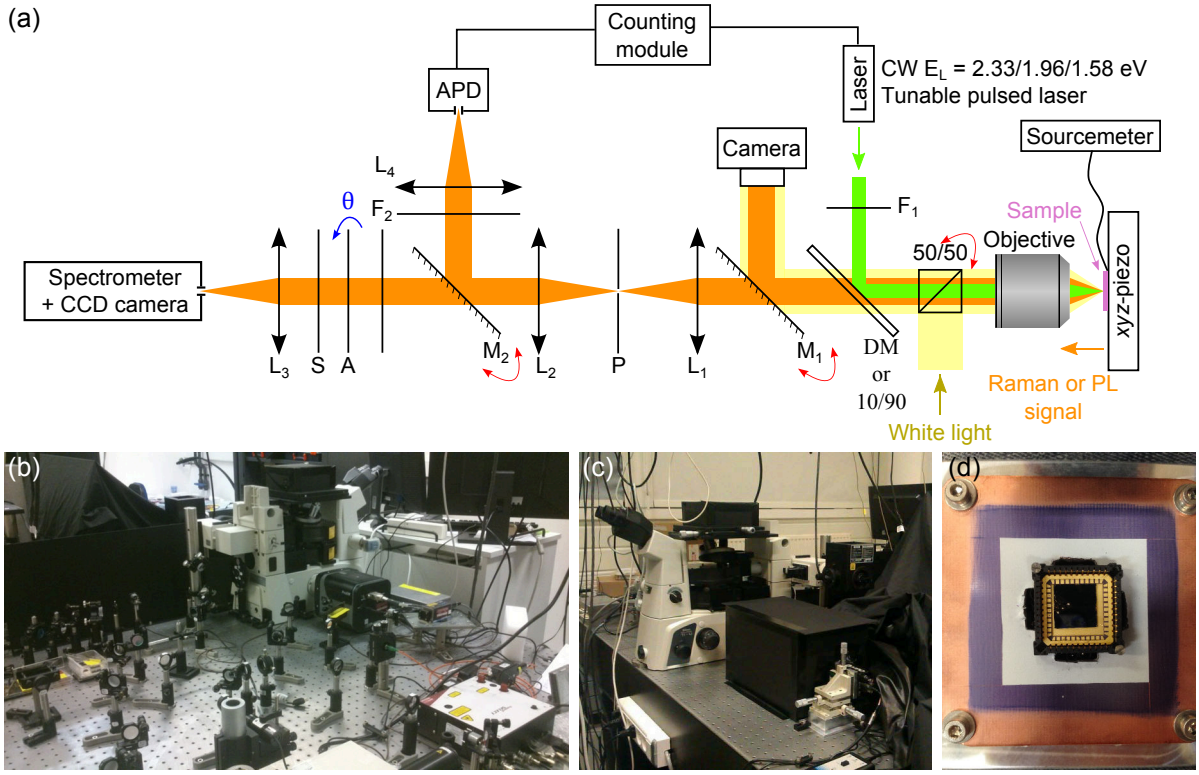

Figure 4.7 *– (a) Sketch of the confocal microscope setup in backscattering geometry. See main text for details. L_i lenses, F_i filters, M_i mirrors, P pinhole, DM dichroic mirror, A analyzer and S scrambler. The angle θ of the analyzer is adjustable (blue arrow). The red arrows indicate removable elements. The cw lasers are used for PL and Raman measurements and are all linearly polarized, while the tunable laser is only employed for PL measurements. The sample holder is electrically connected to a sourcemeter and mounted on a xyz-piezoelectric stage. The spectrometer, the CCD camera, the piezoelectric element and the sourcemeter are interfaced with a computer. (b) and (c) Photos of the experimental setup. (d) Photo of the home-built sample holder.*

photoluminescence decays. For both system, a spectral notch filter (F_2) blocks the reflected laser and Rayleigh signal, so that the PL or Raman signal can enter the detection system. For ultralow Raman measurements, F_2 is composed of two narrow notch filters (OptiGrate BragGrate™ notch filters). In combination with the narrow bandpass filter F_1 and after optimization, Raman features at frequencies as low as 4.5 cm^{-1} could be measured. For others measurements, F_2 is a Semrock StopLine® notch filter. The light is focused into the detection system with lenses L_3 and L_4.

Polarized measurements Polarization-dependent Raman studies were performed using the linearly polarized cw lasers and by placing an analyzer before the entrance of the spectrometer, followed by a polarization scrambler in order to avoid any artifacts due to polarization sensitive optics in the spectrometer. The angle θ (see Fig. 3.11) between the analyzer and the linear polarization of the excitation laser can take any values. However, in this thesis we use only two configurations: the parallel one XX ($\theta = 0$) and the perpedendicular one XY ($\theta = 90$ °). To avoid any artifacts due to polarization sensitive optics in the spectrometer, a polarization scrambler is placed at the entrance of the spectrometer.

Electrical access The sample holder is electrically connected to a Keithley 2612A SourceMeter®. The electrical sample holder was designed and fabricated with the help of Fabien Chevrier, technician at IPCMS. We chose to work with chip carriers of 44 pins (Spectrum Semiconductor LCC04420) to ensure compatibility with others experimental setup in the team. The corresponding socket is fixed onto an epoxy board and is is electrically connected to a matrix box, which itself is connected to the two channel sourcemeter. This box simplifies the connection. Note that we connected only 10 pins. The sourcemeter can be used to apply a source-drain bias and a gate voltage, and to measure the source-drain and gate currents.

Computer interfacing The piezoelectric stage, the sourcemeter, the spectrometer and the CCD camera are controlled by Labview interfaces. These interfaces were developed by Michelangelo Romeo, research engineer at IPCMS. One interface controls at the same time the spectrometer, the CCD camera and the piezoelectric element in order to record PL or Raman hyperspectral maps by spatially scanning the sample and recording spectrum at each point. The second interface commands simultaneously the CCD camera and the sourcemeter. This program permits to apply source-drain and gate voltages, to measure source-drain and gate currents and to trig the CCD camera. In particular, it allows a smooth gate voltage ramping with an adjustable delay time before starting the Raman measurement. For instance for the electrochemically top-gated measurements of Chapter 5, the gate bias is first applied for a settling time of $\sim$ 1 min (i.e., once a steady gate leak current, typically lower than 100 pA, is achieved), before recording each Raman spectrum. This procedure ensures that Raman spectra are recorded at constant charge carrier densities.

4.2.2 Incident photon flux Φ_{ph}

For the experimental measurements, one important quantity to know is the the incident photon flux denoted Φ_{ph}. This quantity is particularly useful for Chapters 7 and 8. The incident photon flux is given by $\Phi_{ph} = P_{opt}/(A_L E_L)$ where P_{opt} is the laser beam power at the objective, A_L is the laser spot area and E_L laser photon energy. The laser beam power at the objective is measured by focusing the laser beam onto the surface of a powermeter. Instead of repeating this measurement for every laser power, we calibrated the experimental setup by measuring the power of the infinity conjugated laser beam at the entrance of the microscope and the power at the objective. By repeating the measurement for few laser power, we have checked that these two quantities are proportional. The laser spot area A_L is measured by recording an optical image of the tightly focused laser spot on the surface of a substrate. An example a such a measurement is depicted in Appendix B. For the cw laser at 2.33 eV (which is the most used laser in this manuscript), Tab. 4.1 summarized the measured A_L and the corresponding Φ_{ph} for $P_{opt} = 1$ μW.

Objective	×100	×50	×40
NA	0.90	0.65	0.6
A_L (μm^2)	0.12	0.40	0.6
Φ_{ph} ($\times 10^{20} cm^2\ s^{-1}$)	22	6.7	4.5

Table 4.1 *– Measured spot area for the three objectives used in this thesis for the cw laser at 2.33 eV. Corresponding incident photon flux Φ_{ph} for a laser beam power at the objective $P_{opt} = 1\ \mu W$.*

4.2.3 Data acquisition and treatment

As mentioned previously, the setup is interfaced with a computer. The data are either recorded with the commercial software Winspec or with Labview interfaces developed by Michelangelo Romeo. In both cases, the result is exported to ASCII files to be further used with Origin® or MATLAB®.

In particular, I developed various MATLAB® scripts (non-exhaustive list) to analyze the PL and Raman maps, to calculate the optical interference in multilayered systems (see next section), and for various fitting procedure. For instance, the script to analyze the PL and Raman maps was used to obtain the hyperspectral maps shown in Chapters 6 and 8. The main steps of the script are:

- Interactive file selection.
- Loading and calibration of the spectra.
- Selection between 1. integration at a given frequency or photon energy or 2. fitting of the spectra.
- If choice 1: selection of the range of integration, integration, displaying and saving of the results.
- If choice 2: interactive selection of the feature(s) to fit, fitting, interactive display of the fitting results and saving.

4.3 Optical interference effects

N-layer crystals deposited onto given substrates (e.g.,the silicon substrates covered with a $\sim$ 100 nm-thick SiO_2 epilayer used in the fabrication of our samples, see Section 4.1) can be viewed as multilayered systems. Since the involved layer thicknesses are of the same order of magnitude as the wavelength of the light, interference effects appear due to multiple reflections at interfaces. The importance of these interference effects is well illustrated by the drastic variations in the optical visibility of N-layer crystals with the sub-

strate [Blake07, Roddaro07]. As an example, Fig. 4.8(a) shows the difference in graphene's visibility between silicon substrates covered with a (1) 300 nm and (3) 200 nm SiO_2 layer when illuminated with white light. In the case of 200 nm of silicon oxide, we do not see the graphene flake whereas it is clearly visible for a silicon oxide thickness of 300 nm. To further highlight that variations in the optical contrast are due to interference effects, the top and bottom panels in Fig. 4.8(a) show the same samples as in (1) and (3), respectively, but illuminated through different narrow bandpass filters (with a bandwidth of ≈ 10 nm). We notice that the flakes are clearly visible for given wavelengths and not for others. Finally, Fig. 4.8(b) presents a color plot for the expected optical contrast of graphene onto a Si/SiO_2 substrate as a function of the oxide thickness and the illumination wavelength. It turns out that Si/SiO_2 substrates with oxide thickness of 90 nm, 285 nm and 500 nm are the most suitable to identify few-layer graphene by optical means. These values are also appropriate to identify few-layer TMDs [Li12b], but only 90 nm is suitable to identify few-layer BN [Gorbachev11].

These optical interference effects strongly affect the optical absorption, as well as the Raman [Yoon09, Li12b] and PL [Buscema14] signal of layered materials. To quantitatively compare the absorptance, PL or Raman intensity of a layered material in different configurations (e.g., with varying number of layers N or for different incoming photon energy), it is mandatory to carefully calculate the amplitude of the electric field of the incident light and of the emitted (PL) or scattered (Raman) light within the layered materials. These calculations are summarized in one quantity called the **enhancement factor** F which reflects how the propagation of electric fields in the layered structure affects the absorptance, PL or Raman intensity as compared to a **interference-free** case. In practice, the measured absorptance, PL or Raman intensity are the product of the enhancement factor F (homogeneous to a length) and the interference-free quantity (homogeneous to the inverse of a length). The detail of the calculations of the absorptance of a layer in a multilayered system and of the PL and Raman enhacement factors can be found in Appendix C. The absorptance will be useful in Chapters 7 and 8 to compute the absorbed photon flux, the Raman enhancement factor is employed in Chapters 5 and 6 to deduce interference-free intensities and the PL enhancement factor is utilized in Chapter 7 to quantitatively compare the PL intensity of N-layer $MoTe_2$ as a function of N.

4.4 Conclusion

To conclude, we have shown the different fabrication technique used to prepare the samples studied in the following chapters. We have also presented the experimental setup that can be used for spatially-resolved micro-Raman and micro-photoluminescence, as well as for time-resolved, measurements under ambient conditions and with electrical access. The setup is fully computer-interfaced allowing for fast and reliable acquisitions. Furthermore, MATLAB®scripts were developed for data treatment. Finally, we have pointed out that optical interference can drastically affect the absorptance, Raman and photoluminescence signal of the different layers in a multilayered structure.

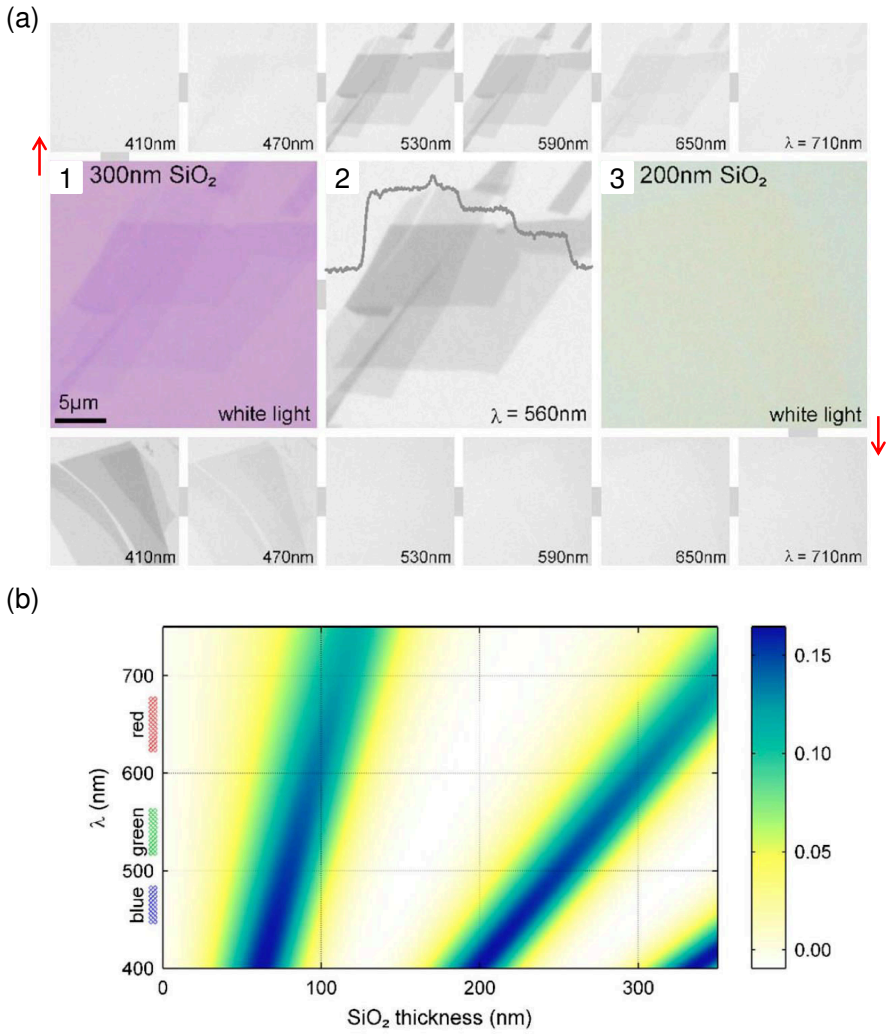

Figure 4.8 *– (a) Optical images of graphene sheets on silicon substrates covered with a (1)* 300 *nm- and (2)* 200 *nm-thick SiO_2 epilayer, and illuminated with white light. The graphene layers are visible in (1) whereas the optical contrast vanishes in (3). Top and bottom panels show the same flakes as in (1) and (3),respectively, but illuminated through different narrow bandpass filters (with a bandwidth of* $\approx$ *10 nm). (2) corresponds to the same sample as (1) but illuminated with green light. The trace shows steplike changes in the contrast. This measurement can be used as a quantitative tool for determining the number of layers on a given substrate. (b) Calculated optical contrast of graphene on a Si/SiO_2 substrate as a function of the oxide thickness and illumination wavelength. Figures are taken from Ref. [Blake07].*

Take home messages

- All the sample studied in this work were prepared by mechanical exfoliation using adhesive tape from bulk crystals.
- Van der Waals heterostructures were fabricated with an all-dry transfer technique.
- Raman and photoluminescence measurements can be performed on the same home-built experimental setup.
- Optical interference effects can drastically affect the absorptance, Raman and photo-

luminescence signal. These effects can be easily computed following the expressions depicted in Appendix C.

Chapter 5

Raman spectroscopy of electrochemically gated graphene transistors

This chapter is devoted to the study of electrochemically-gated graphene field-effect transistors by means of micro-Raman spectroscopy. In the first part, we discuss the microscopic mechanisms associated with the main Raman features in graphene, that were briefly introduced in Chapter 2 Section 2.1.4. In the second part, we carefully investigate the Raman response of graphene under electrostatic doping. By comparing the evolution of the two prominent Raman features with theoretical models, we are able to deduce the electron-phonon coupling for zone-center and zone-edge phonons. In the third part, we show that the linewidth and frequency of these two features in doped graphene follow sample-independent correlations that can be utilized for accurate estimations of the charge carrier density. Finally in the last part, we display that electrochemical reactions, occurring at large gate biases, can be harnessed to efficiently create defects in graphene.

5.1 Raman scattering in graphene

In this section, we provide more details on the main Raman features of graphene introduced in Chapter 2 Section 2.1.4. In particular, we focus on the underlying microscopic mechanisms.

5.1.1 The G mode

The G mode is associated with the only one-phonon Raman active process in graphene which involves the Γ-point phonon with E_{2g} symmetry. The representation of this vibrational mode in the real space is shown in Fig. 3.2. It corresponds to the out-of-phase vibration

of the sublattices A and B with respect to each other.[1] The atomic displacement can be along the carbon-carbon bond (iLO) or perpendicular to it (iTO). It is noteworthy to mention that the degeneracy can be broken by applying, for instance, a mechanical deformation to the graphene lattice which breaks the crystal symmetry. As a result, the G-mode feature splits [Mohiuddin09, Huang09, Mohr09, Polyzos15].

Experimentally, the G-mode feature is very well described by a Lorentzian profile [Ferrari13]

$$I(\Omega) = \frac{2I_G}{\pi} \frac{\Gamma_G}{4(\Omega - \Omega_G)^2 + \Gamma_G^2}, \tag{5.1}$$

where Ω_G is the center of the feature, Γ_G its FWHM and I_G its integrated intensity. The center Ω_G is assigned to the phonon frequency. The width Γ_G is related to the phonon damping or lifetime (e.g., phonons can decay into other phonons due to anharmonicity [Bonini07] or into electron-hole pairs due to electron-phonon coupling, see Section 5.3), but also contains the influence of the experimental setup such as the instrumental function response. The integrated intensity I_G corresponds to the intensity of the Raman mode, which is linked to the Raman tensor by Eq. (3.20) or to the scattering probability by Eq. (3.21).

In this work, we are using Raman spectroscopy as a very sensitive tool to probe the properties of graphene. Therefore, it is very important to know how Ω_G, Γ_G and I_G are affected by external perturbations, such as the energy of the incident photon or the doping level. As expected for a one-phonon Raman process, the G mode is not dispersive, i.e. Ω_G does not depend on the frequency of the incident photon ω_i [Malard09b, Ferrari13]. However, Ω_G and Γ_G are strongly affected by doping, see Section 5.2.1. In contrast, as long as the Fermi energy E_F is different from half of the incident photon energy ($\hbar\omega_i$), I_G remains constant. For E_F close to $\hbar\omega_i/2$ a drastic increase of I_G is observed [Kalbac10, Chen11]. These observations are quite surprising and need a close description of the Raman process to be fully understood.

First, let us precise that for phonons with E_{2g} symmetry [Loudon64], I_G is insensitive to the polarization of the incident and scattered light in our experimental geometry [Ferrari13]. In the quantum framework, the microscopic process associated with the G mode is well described by the diagram in Fig. 3.10: the system, initially in state $|i\rangle$, is excited by an incident photon ω_i into a first intermediate state $|e_1\rangle$, then the system goes to a second intermediate state $|e_2\rangle$ by emitting a phonon and finally deexcites to $|i\rangle$ by emitting a photon ω_s. In the momentum-energy space, this process is represented in Fig. 5.1. The intermediate states can be either real or virtual. Because transitions from an empty state or to a filled state are impossible due to Pauli blocking, some transition might be excluded (as the one crossed out in Fig. 5.1). In the case of neutral graphene ($E_F = 0$), regardless of the incident photon energy $\hbar\omega_i$, a resonant interband transition is always possible, and therefore the G mode process could be expected to be resonant. Counterintuitively, D. Basko has shown that destructive quantum interference leads to a non-resonant process [Basko09a]. In addition, this interfer-

[1] Note that all the A atoms and all the B atoms have exactly the same displacement, as expected this is a direct consequence of the zero phonon momentum.

ence can be controlled externally by changing the Fermi energy. This change suppresses the destructive interference and makes the G-mode intensity increases, as observed experimentally in [Kalbac10, Chen11].

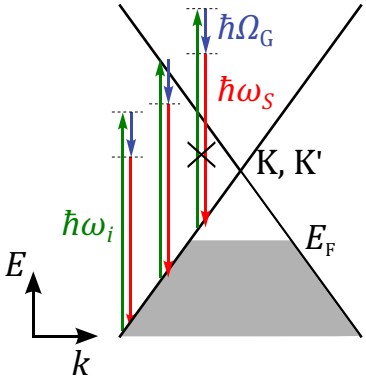

Figure 5.1 *– One-dimensional schematic representation of the G mode in graphene in the momentum-energy space. Occupied states are represented in gray. The green arrow illustrates the absorption of the incident photon ω_i, the blue one the emission of the phonon Ω_G and the red one the emission of the scattered photon ω_s. The horizontal dashed lines denote virtual states. Three different elementary processes are drawn. The G mode is a non-resonant process due to strong quantum interference between the different elementary processes. Some elementary processes can be suppressed by tuning the Fermi energy, such as the one that is crossed-out.*

These observations can be understood by a simplified version of the calculations. The intensity of the G-mode feature I_G is given by Eq. (3.21). Owing to the linear band structure of graphene (see Eq. (2.3)), each electronic energy is characterized by a wavevector $\boldsymbol{k}$ measured from the K or K' point. For the sake of simplicity, we will consider a one-dimensional problem. The energies of the initial E_i and intermediate states E_1 and E_2 are characterized by the wavevectors k_i, k_1 and k_2, respectively. Knowing that the phonon has zero momentum, momentum conservation imposes $k_i = k_1 = k_2 = k$, i.e., the transitions are vertical as depicted in Fig. 5.1. As a result, $E_1 - E_i = E_2 - E_i = 2\hbar v_F |k|$. Furthermore, the transition matrix elements in the numerator in Eq. (3.21) are assumed to be the same for all transitions. Finally, the sum over the continuum of states can be converted to an integral over k. Thus, I_G is given by

$$I_G \propto 2|M_{tot}|^2 \left| \int_{k_F}^{+\infty} \frac{dk}{(\hbar\omega_i - 2\hbar v_F k)(\hbar\omega_s - 2\hbar v_F k)} \right|^2 = 2\frac{|M_{tot}|^2}{(\hbar\Omega_G)^2} \left(\ln \left| \frac{\hbar\omega_i - 2|E_F|}{\hbar\omega_s - 2|E_F|} \right| \right)^2, \tag{5.2}$$

where M_{tot} is the total matrix elements (i.e., the product of the three transition matrix elements), $k_F = |E_F|/\hbar v_F$ and $\hbar\omega_s = \hbar\omega_i + \hbar\Omega_G$ (energy conservation) with $\Omega_G \approx 196$ meV. In the case of neutral graphene ($E_F = 0$), we notice that for visible light ($\sim 1.5 - 3\ eV$) there is no selection of a specific interband transition (i.e., a specific k). The logarithmic function in Eq. (5.2) is a slowly varying function of $\hbar\omega_i$ as shown in Fig. 5.2(a). Consequently, the Raman G mode is a non resonant process and can be represented by any of the allowed processes in the momentum-energy space (see for instance the two allowed processes in Fig. 5.1). For doped graphene ($E_F \neq 0$), the situation is rather different. For a given incident photon energy

$\hbar\omega_i$, there are two singularities at $|E_F| = \hbar\omega_i/2$ and $|E_F| = \hbar\omega_s/2$ (see Fig. 5.2(b)). Surprisingly, these two maxima occur when the incoming and outgoing resonances are blocked due to the Pauli principle. This is a direct manifestation of quantum interference. Indeed, each term in the sum of Eq. (5.2) can be viewed as the amplitude of the corresponding elementary process with given intermediate states. These amplitudes may add up in-phase or out-of-phase, which corresponds to constructive or destructive quantum interference. To make the interference explicit, let us focus on the terms close to the incoming and outgoing resonances. If we set the transition energies to the intermediate states to be $\hbar\omega_i - \hbar\Omega_G/2 + \epsilon$, the amplitude of the corresponding elementary process is

$$\frac{1}{\left[\hbar\omega_i - \left(\hbar\omega_i - \frac{\hbar\Omega_G}{2} + \epsilon\right)\right]\left[\hbar\omega_s - \left(\hbar\omega_i - \frac{\hbar\Omega_G}{2} + \epsilon\right)\right]} = \frac{1}{\left(\epsilon + \frac{\hbar\Omega_G}{2}\right)\left(\epsilon - \frac{\hbar\Omega_G}{2}\right)} \tag{5.3}$$

$$\underset{\epsilon \to \pm\frac{\hbar\Omega_G}{2}}{\sim} \frac{1}{\hbar\Omega_G\left(-\frac{\hbar\Omega_G}{2} \pm \epsilon\right)}. \tag{5.4}$$

Around $\pm\hbar\Omega_G/2$, this function is an odd function of ϵ. In consequence, in the sum over k of Eq. (5.2), the terms close to the incoming ($\epsilon \approx +\hbar\Omega_G/2$) and outgoing ($\epsilon \approx -\hbar\Omega_G/2$) resonances interfere desctructively and cancel each other. This destructive interference can be suppressed by tuning $|E_F|$ close to $\hbar\omega_i/2$ or $\hbar\omega_s/2$ in order to exclude some terms from contributing to the sum and hence increase I_G. Note that for $|E_F|$ much higher than $\hbar\omega_i/2$, the intensity I_G is approximately the same as for neutral graphene when all the elementary processes are allowed and that in Fig. 5.2 this condition is not really satisfied. However, in the full calculations one has also to take into account the matrix elements [Basko09b]. All these results show that the simple picture of G mode, in which only the on-resonance processes are considered, is invalid.

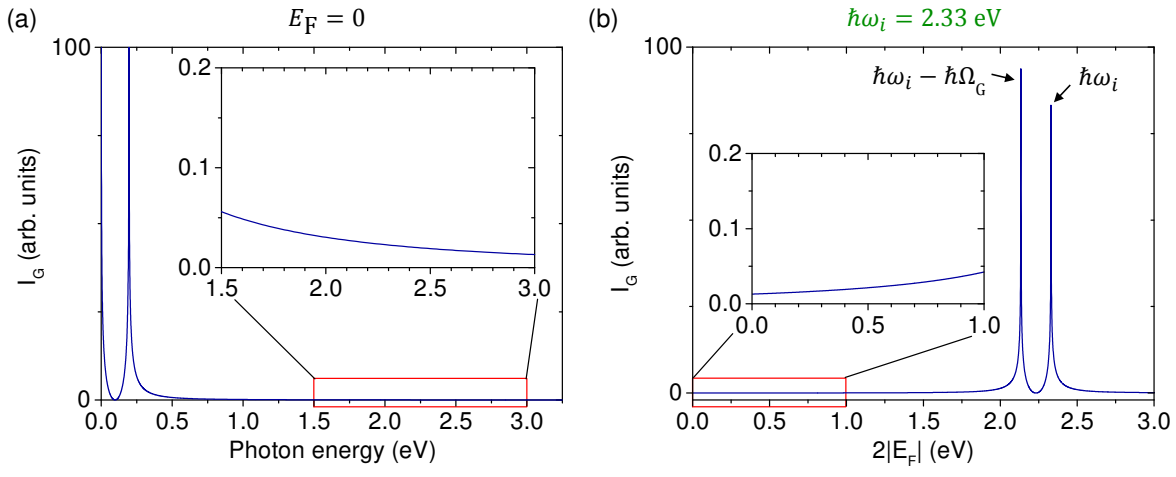

Figure 5.2 *– (a) Calculated intensity of the G-mode feature for neutral graphene as a function of the incident photon energy $\hbar\omega_i$. The insert shows a zoom in the visible range where the intensity varies slowly compared to the resonances at 0 and $\hbar\Omega_G$. (b) Calculated intensity of the G-mode feature for an incident photon energy $\hbar\omega_i = 2.33$ eV as a function of two times the Fermi energy E_F. Two singularities are observed at $\hbar\omega_i - \hbar\Omega_G$ and $\hbar\omega_i$. The insert shows a zoom in the typical range of Fermi energy reached in experiments. The intensity varies slowly as compared to the two singularities.*

In the rigorous calculations, the damping of the intermediate states has to be taken into account. This leads to the broadening of the two peaks at $\hbar\omega_i - \hbar\Omega_G$ and $\hbar\omega_i$ in Fig. 5.2(b). Qualitatively, assuming an identical damping constant $\gamma \approx \hbar\Omega_G \approx 0.2$ eV [Chen11] for each intermediate state, the two peaks will merge to form a broader peak centered at $\hbar\omega_i - \hbar\Omega_G/2$.[2]

5.1.2 The 2D mode

Surprisingly, the 2D-mode feature, observed at approximately 2675 cm^{-1} in the Raman spectrum (see Fig. 2.5), has an intensity somewhat larger than the G-mode one. Because of this unusual observation, the physical origin of the 2D-mode feature underwent a long period of discussion since the first Raman spectrum [Tuinstra70] had been observed. The complete story is summarized in the Supplementary Information of Ref. [Ferrari13]. Finally, it is only thirty years later that the first consensus on the mechanism of the 2D mode was achieved: Thomsen and Reich [Thomsen00] suggested a **double resonant** (DR) mechanism.[3] Note that DR was first proposed by Baranov in 1987 [Baranov87] but somehow went unnoticed.

As already mentioned in Chapter 2 Section 2.1.4, the 2D mode involves two phonons with opposite momentum from the iTO branch near K or K' points. These phonons have a A_1' symmetry and correspond to the breathing vibration of the six atoms of one hexagon (see Fig. 3.4). This process is illustrated in Fig. 5.3(a) and can be separated into four steps (the K and K' points can be exchanged and all wavevectors are expressed with respect to the Γ point):

1. An electron, around K, with wavevector $\boldsymbol{k}_i$ and energy $E_i = -\hbar v_F |\boldsymbol{k}_i - \boldsymbol{K}|$ is excited into a real state with wavevector $\boldsymbol{k}_1 = \boldsymbol{k}_i$ and energy $E_1 = \hbar v_F |\boldsymbol{k}_i - \boldsymbol{K}|$ by absorbing the incident photon ω_i and thus creating an electron-hole pair. This is the first resonance.

2. The excited electron is inelastically scattered by a phonon of wavevector $\boldsymbol{q}$ and frequency Ω_D to a second real state, around K', of wavevector $\boldsymbol{k}_2$ and energy $E_2 = \hbar v_F |\boldsymbol{k}_2 - \boldsymbol{K}'|$. This is the second resonance. Momentum conservation imposes $\boldsymbol{q} = \boldsymbol{k}_i + \boldsymbol{k}_2$.

3. The electron is inelastically back-scattered by a phonon of wavevector $-\boldsymbol{q}$ and frequency Ω_D to a virtual state, around K, of wavevector $\boldsymbol{k}_3 = \boldsymbol{k}_i$ due to momentum conservation.

4. The electon-hole pair in the K valley recombines with the emission of the scattered photon $\omega_s = \omega_i - 2\Omega_D$.

As the process connects points from the two inequivalent valleys, it is referred to as an **intervalley** process. Note that the process described here is in resonance with the incident photon,

[2] Rigorously, taking into account a constant broadening γ for each intermediate states, Eq. (5.2) becomes

$$I_G \propto 2\frac{|M_{tot}|^2}{(\hbar\Omega_G)^2}\left|\ln\left|\frac{\hbar\omega_i - 2|E_F| + i\gamma}{\hbar\omega_s - 2|E_F| + i\gamma}\right| + i\arg\left(\frac{\hbar\omega_i - 2|E_F| + i\gamma}{\hbar\omega_s - 2|E_F| + i\gamma}\right)\right|^2, \tag{5.5}$$

where arg is the argument of the complex number.

[3] Note that they suggested this mechanism for the D mode. However, as we will see later, the 2D mode is an overtone of the D mode. Thus, they are of the same physical origin.

but it can also be resonant with the scattered photon. In that case the first intermediate state is virtual and the last one real.

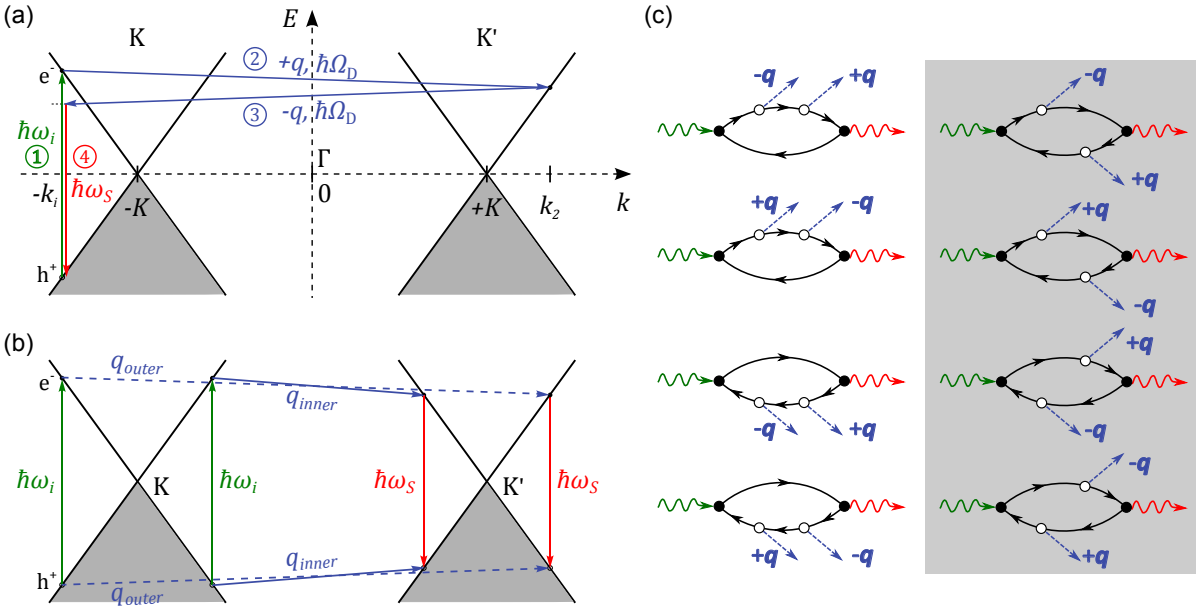

Figure 5.3 *– One-dimensional schematic representation of the 2D mode in graphene in the momentum-energy space. The green arrow illustrates the absorption of the incident photon ω_i, the blue one the emission of the phonon Ω_D with wavevector $\pm q$ and the red one the emission of the scattered photon ω_s. (a) A typical double-resonant process that involves two real intermediate states and one virtual (horizontal dashed line). See main text for details. (b) Typical fully-resonant processes, i.e., all intermediate states are real. One outer and one inner process are drawn. (c) Feynman's diagrams of all (double-resonant) processes that contribute to the 2D mode. Left column represents processes where the electron or hole scattered twice. Note that the process sketched in (a) corresponds to the second diagram. Right column displays the processes where the electron and the hole scattered one phonon each. Note that the two processes sketched in (b) correspond to the second diagram. This column, higlihted with the gray rectangle, corresponds to the dominant processes. (c) is adapted from Ref. [Venezuela11].*

To highlight the resonant nature of this process, let us calculate the intensity of the 2D-mode feature with Eq. (3.21). Note that since it is a second order process, there is one additional term in the numerator and denominator [Cardona83] in Eq. (3.21). As for the G mode, we consider a one-dimensional problem (see Fig. 5.3(a)) and assume that the four transition matrix elements in the numerator are constant. In addition, we suppose that $k_i, k_2 \geq K$ or $k_i, k_2 \leq K$, i.e., only electronic states with opposite slopes can be connected [Maultzsch04a] (see also below). In the first case $q \geq 2K$ and points from outer slopes are connected, thus the process is said to be an outer process. In the second case $q \leq 2K$ and the process is referred to as an inner process (see Fig. 5.3(a) and (b)) The sum over the continuum of states can be converted to an integral over k and thus the intensity of the process described above is given

by

$$I_{2D} \propto |M_{tot}|^2 \left| \frac{1}{\hbar\omega_i - \hbar\Omega_D - \hbar v_F(q-2K)} + \frac{1}{\hbar\omega_i - \hbar\Omega_D - \hbar v_F(2K-q)} \right|^2 \times \left| \int_{k_F}^{+\infty} \frac{dk}{(\hbar\omega_i - 2\hbar v_F k)(\hbar\omega_s - 2\hbar v_F k)} \right|^2, \quad (5.6)$$

where M_{tot} are the total matrix elements (i.e., the product of the four transition matrix elements), $k_F = |E_F|/\hbar v_F$ and $\hbar\omega_s = \hbar\omega_i + 2\hbar\Omega_D$ (energy conservation). Compared to the G-mode intensity in Eq. (5.2), the integral gives a similar logarithmic function but there are two additional terms which correspond to outer and inner processes, respectively. These two terms are important because if their denominator goes to zero, the intensity is drastically enhanced. Therefore, there is a double resonance when the following relation is satisfied

$$\hbar\omega_i - \hbar\Omega_D = \hbar v_F |q - 2K|. \quad (5.7)$$

As $\Omega_D \ll \omega_i$, this relation can be simplified to $2|k_i - K| \approx |q - 2K|$, where $|k_i - K| = \omega_i/2v_F$ is the wavevector of the first excited electron. This implies that the phonons with wavevector q couple preferentially to the electronic states with wavevector k_i. Accordingly, for a given incident photon frequency ω_i, it fixes the phonon wavevector q and its corresponding frequency $\Omega_D(q)$. The deduced variation of Ω_D with ω_i is in good agreement with measurements [Thomsen00], proving that the 2D mode arises from a DR mechanism.

When $k_i \geq K$ and $k_2 \leq K$ or when $k_i \leq K$ and $k_2 \geq K$ (i.e., points from parallel slopes are connected), a similar calculation leads, at first sight, to a double resonance when $q \approx 2K$. However, the full calculation shows that theses contributions cancel [Maultzsch04a] due to destructive interference. As a conclusion, the outer and inner processes contribute solely to the DR mechanism.

In the above calculation, we have considered only one possible DR for simplicity reasons. Indeed, both phonons can be emitted by the electron (as the above process), or by the hole, or one can be emitted by the electron and the other by the hole (see the Feynman's diagrams in Fig. 5.3(c)). In the latter case, all the involved states are real (see Fig. 5.3(b)). Therefore, this process is sometimes said to be triple-resonant (TR) [Malard09b] or fully-resonant [Ferrari13]. All these processes obey the relation of Eq. (5.7). In a rigorous calculation of the 2D-mode intensity, one has to take into account all these different possibilities. Venezuela *et al.* [Venezuela11] have performed the complete calculations (for a two-dimensional system) and found that the dominant processes are the fully-resonant ones because of destructive quantum interference that cancels out processes involving only electrons or only holes (see Fig. 5.3(c)). This conclusion can be easily understood by considering the Raman process in real space [Basko08a, Ferrari13]. For these processes, the electron and hole motion can be viewed in a quasi-classical manner. In the case of fully-resonant processes, the

real-space picture is illustrated in Fig. 5.4 and summarized in the following steps:

1. The incident photon ω_i creates an electron-hole pair. The electron and hole move in opposite directions so that their total momentum is zero (the momentum of the light is neglected). They also travel with the same speed because of the linear band structure of graphene.

2. At some point, the electron and hole are both scattered by a phonon of frequency Ω_D with opposite momentum $\pm\boldsymbol{q}$ such that the total phonon momentum is zero. The electron and hole move now towards each other.

3. The electron and hole meet and recombine to emit the scattered photon ω_s.

Obviously, if only the electron or the hole is scattered twice, one carrier has to travel for longer than the other in order to meet and recombine. However, this is in conflict with the fact that both electron and hole travel at the same speed. Therefore, such processes are prohibited in the quasi-classical picture. Moreover, the G mode is also classically forbidden because electron and hole cannot meet at the same point to recombine. Hence, care has to be taken when dealing with the classical picture. It might help to understand Raman processes, but strictly speaking they have to be treated in the quantum framework.

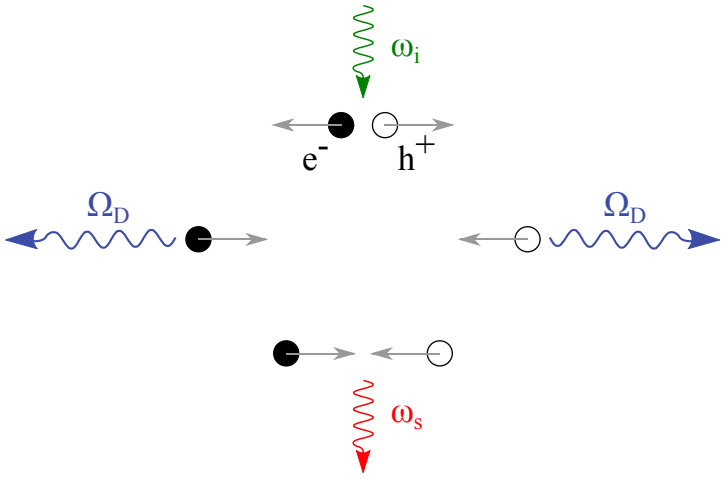

Figure 5.4 *– Real-space representation of the fully-resonant 2D-mode process. The horizontal gray arrows indicate the displacement of the electron e^- and hole h^+. The green, red an blue wavy arrows illustrates the incident photon ω_i, the scattered photon ω_s and the two scattered phonons of frequency Ω_D and opposite wavevector $\pm q$, respectively.*

Among the fully-resonant processes, the dominant contribution to the intensity of the 2D-mode feature has been first attributed to the outer loop [Kürti02, Ferrari06, Graf07], before a possible explanation by a dominant inner loop came up [Huang10, Mohr10, Frank11, Mafra11, Yoon11]. Again, Venezuela *et al.* [Venezuela11] have shown that the dominant contribution comes from the inner loop. Nevertheless, experimentally the 2D-mode feature is generally viewed as a single quasi-Lorentzian peak [Ferrari06, Graf07] and the distinction between inner and outer loop is challenging [Berciaud13], even if clear bimodal 2D-mode line shapes are observed experimentally on undoped ultra-clean graphene [Berciaud09, Luo12,

Berciaud13].

In practice, the 2D-mode feature in supported graphene (which is always the case in this manuscript) is phenomenologically well described by a modified Lorentzian profile proposed by Basko [Basko08a]

$$I_{2D}(\Omega) = I_{2D}\Gamma_{2D}^2 \left\{ 8(2^{2/3}-1)\left[(\Omega - \Omega_{2D})^2 + \frac{\Gamma_{2D}^2}{4(2^{2/3}-1)} \right]^{3/2} \right\}^{-1}, \tag{5.8}$$

where Ω_{2D} is the center of the feature, Γ_{2D} its FWHM and I_{2D} its integrated intensity. Note that we use this profile in a pure phenomenological manner. We have stated that this shape adjusts well the experimental data of the 2D-mode feature, in particular better than a pure Lorentzian profile, but not necessarily better than a Voigt profile. However, the latter requires more fitting parameters, whereas the modified Lorentzian profile comes along solely with the peak position and its linewidth.

In a nutshell, the 2D mode is a second order Raman process which is resonant. Therefore, the frequency of the 2D-mode feature depends on the energy of the incident photon, but also on the electronic dispersion that is directly related to the number of layers (see Fig. 2.6). It also explains why the intensity of the 2D-mode feature is comparable to the one of the G-mode feature which is a first-order process but is non-resonant. However, contrary to the intensity of G-mode feature, the intensity of the 2D-mode feature depends on E_F even for energies smaller than half the energy of the incoming photon, as we will see in Section 5.3.3.

5.1.3 The 2D′ mode

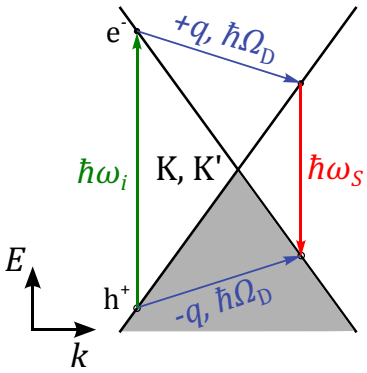

Figure 5.5 *– One-dimensional schematic representation, of the 2D′ mode in graphene in the momentum-energy space. The process is identical to the 2D mode (see Fig.5.3 except that it is intravalley and not intervalley.*

Let us briefly mention the existence of the 2D′ mode. This feature lies at approximately 3240 cm^{-1} [Ferrari13] and is not displayed in this manuscript but will be used in Section 5.3.3. The mechanism that gives rise to this mode is identical to the one of the 2D mode but instead being intervalley it is **intravalley**, i.e., the whole process takes place in the same valley (see Fig. 5.5). Therefore, it involves phonons from the iLO branch close

to the Γ-point (with E_{2g} symmetry) where a Kohn anomaly occurs [Piscanec04]. As the electron-phonon coupling is weaker at that point than at the K and K' points (see Section 5.3), the intensity of the 2D'-mode feature is smaller than the one of the 2D-mode feature [Basko08a, Venezuela11]. As for the 2D mode, the 2D'-mode feature is well described by the modified Lorentzian profile of Eq. (5.8).

5.1.4 The D mode and D′ mode

The D-mode and D'-mode features are only observable in defective graphene samples (see Fig. 2.5). Indeed, the mechanisms that give rise to the D and D' modes are identical to the ones of the 2D and 2D', respectively, except that one inelastic scattering by a phonon is replaced by one elastic scattering by a defect [Thomsen00] (see Fig. 5.6). Consequently, these two modes are one-phonon process that are forbidden in pristine graphene but become allowed in defective graphene.

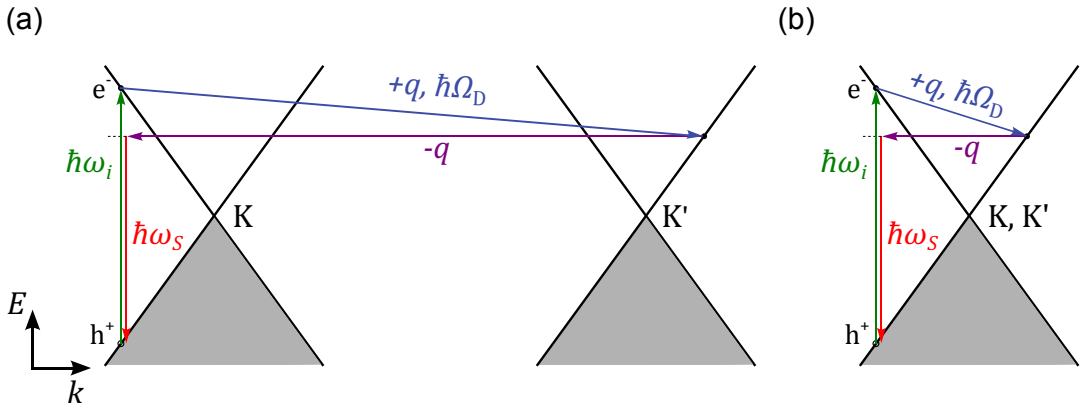

Figure 5.6 *– One-dimensional schematic representation of the (a) D mode and (b) D' mode in graphene in the momentum-energy space. The first one is an intervalley process, while the second one is intravalley. The green arrow illustrates the absorption of the incident photon ω_i, the blue one the emission of the phonon Ω_D with wavevector $+q$, the horizontal purple one the elastic scattering by a defect and the red one the emission of the scattered photon ω_s. Horizontal dashed lines correspond to virtual states.*

The D (D') mode is an intervalley (intravalley) process that involves phonons with A_1' (E_{2g}) symmetry from the iTO (iLO) branch close to the K or K' (Γ) point [Ferrari13], i.e., the same phonon as the 2D (2D') mode. Note that these modes cannot be fully resonant, there is at least one virtual state. However, as shown in Fig. 2.5, the intensity of the D-mode feature is comparable to the one of the 2D mode. Althought, the dominant contribution of the 2D-mode feature intensity is attributed to fully-resonant processes, the simple argument of being fully-resonant does not hold, it is more subtle than that [Venezuela11]. Note also that the intensity of the D'-mode feature is smaller than that of the D-mode one, as for the 2D' mode compared to the 2D mode. As the D and D' modes involve only one phonon, their frequency is twice as small as that of the 2D or 2D' mode, or in other words the 2D and 2D' mode can be viewed as overtones of the D and D' mode, respectively. This explains the name of the 2D and 2D' mode even if they are not defect induced. Finally, both D- and D'-mode feature are well described by the modified Lorentzian profile of Eq. (5.8).

Having described in detail the microscopic mechanisms of the main Raman features in graphene, we now turn to their experimental investigation in the next sections.

5.2 Electric field effect and geometrical capacitance

In Chapter 2 Section 2.1.5, we have shown that graphene's optoelectronic properties can be efficiently tune using the electric field effect. Here, we make use of this effect to study how the Raman spectrum is affected by graphene's Fermi energy. The dual-gated field-effect transistors used in this chapter were fabricated following the method described in Chapter 4 Section 4.1. Figures 5.7(a) and (b) show an optical image and a schematic cross-section of a device.

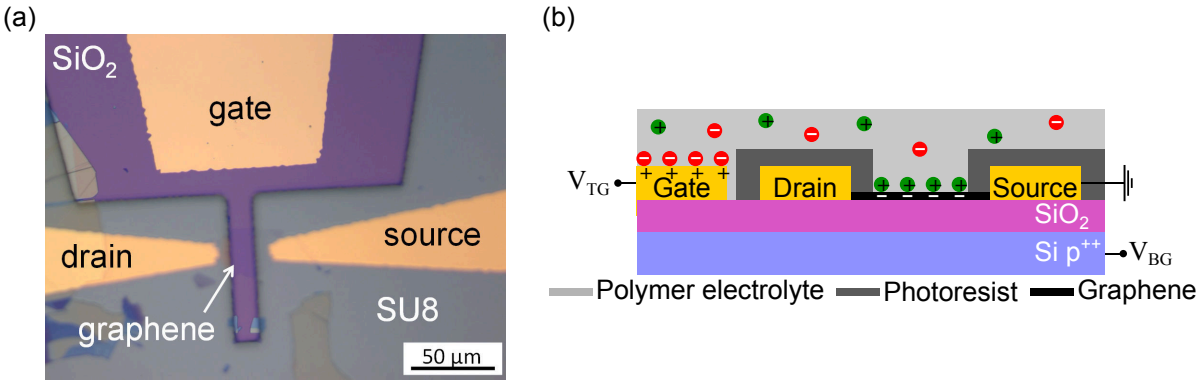

Figure 5.7 *– (a) Optical image of a dual-gated graphene field-effect transistor prior deposition of the polymer electrolyte. The source and drain electrodes are covered with photoresist (SU8) to prevent them to be in contact with the polymer electrolyte. (b) A schematic cross-section of our dual gated graphene field-effect transistor, with Li^+ (green) and ClO_4^- (red) ions and the electrical double layers near each electrode. The Si substrate is used as a back-gate.*

Micro-Raman scattering measurements were performed on these samples in the experimental setup presented in Chapter 4 Section 4.2 in ambient conditions. The laser power was maintained below 500 μW in order to avoid thermally induced spectral shifts or lineshape modifications of the Raman features [Calizo07], as well as photo-electrochemical reactions [Kalbac10, Efetov10, Bruna14]. Raman spectra were recorded as a function of the applied gate bias, once a steady gate leak current (typically lower than 100 pA in the electrochemically top-gated configuration) was achieved. For this purpose, the gate bias was first applied for a settling time of $\sim$ 1 min, before recording each Raman spectrum. This procedure ensures that Raman spectra were recorded at constant charge carrier densities. Raman spectra were also recorded during several forward and backward top-gate sweeps at the same spot on a given sample and very reproducible results, with no significant hysteresis, were observed. We find, however, that the geometrical capacitance of the top-gate, as well as the electron-phonon coupling constant may exhibit a certain degree of spatial inhomogeneity. Additionally, in ambient air, the gate capacitance may decrease over time, by up to one order of magnitude over a couple of days, due to a degradation of the polymer electrolyte. Such aging effects underscore the necessity of fast characterizations of electrochemically gated FETs

and may account for the fairly large spread in the gate capacitances reported in literature. In order to avoid sample aging effects, our measurements were performed immediately after deposition of the polymer electrolyte. Interestingly, the dispersions obtained from a set of measurements at several spots on a given graphene FET are very similar to the sample-to-sample dispersions observed by measuring at (single) random spots on a set of graphene FETs. This further highlights the interest of spatially resolved studies.

To study the influence of doping on Raman features of graphene, an accurate determination of the Fermi energy E_F (or equivalently the doping n) as a function of the gate voltage is a critical requirement. To this end, let us first present the effect of a gate bias on the Raman spectrum of graphene.

5.2.1 Electric field effect

Figure 5.8 shows typical Raman spectra recorded over a top-gate voltage sweep, with the two prominent Raman features in pristine graphene: the first order G-mode feature and the second-order resonant 2D-mode feature. Note that no defect-induced D-mode feature emerges from the background in our experimental conditions. This illustrates the high structural quality of the graphene sample. As expected [Das08], the G-mode frequency and linewidth vary significantly with the top-gate bias (V_{TG}). Similar trends are observed by applying a back-gate voltage (V_{BG}). The minimum value of the G-mode frequency Ω_G and the maximum value of its full width at half maximum (FWHM) Γ_G are reached at the same value of $V_{TG,0} = +0.5$ V. This value corresponds to the charge neutrality point (CNP), where $E_F = 0$. The CNP is reached at a finite $V_{TG,0}$, due to an unintentional doping of the graphene layer, induced by the substrate as well as the polymer electrolyte [Das08]. A finite value of $V_{TG} - V_{TG,0}$ results in a finite charge carrier density n. In this work, a positive (negative) gate voltage corresponds to electron (hole) injection. Qualitatively, for both positive and negative values of $V_{TG} - V_{TG,0}$, we observe a nearly symmetric increase of Ω_G accompanied by a symmetric decrease of Γ_G (see Section 5.3). In contrast, the 2D-mode feature is less sensitive to doping than the G-mode feature [Das08] (see Section 5.3).

In order to carefully study the G- and 2D-mode features as a function of E_F, one has to convert the gate voltage into E_F or, equivalently, n. This was done in Chapter 2 Section 2.1.5. Equation (2.9) can be rewritten:

$$V - V_0 = \frac{E_F}{e} + \mathrm{sgn}(E_F)\frac{eE_F^2}{\pi(\hbar v_F)^2 C_G}. \tag{5.9}$$

One may have noticed in Fig. 5.8, that compared to traditional SiO_2 solid state back-gate [Yan07, Pisana07], the applied voltages are much smaller. This can be easily understood by the estimation of the involved capacitances. For a typical SiO_2 back-gate insulator, the geometrical capacitance C_{BG} per unit area is simply given by $C_{BG} = \varepsilon_r\varepsilon_0/d_{BG}$, where $\varepsilon_r \approx 4$ is the relative permittivity of SiO_2, ε_0 the vacuum permittivity and d_{BG} is the SiO_2 thickness. In

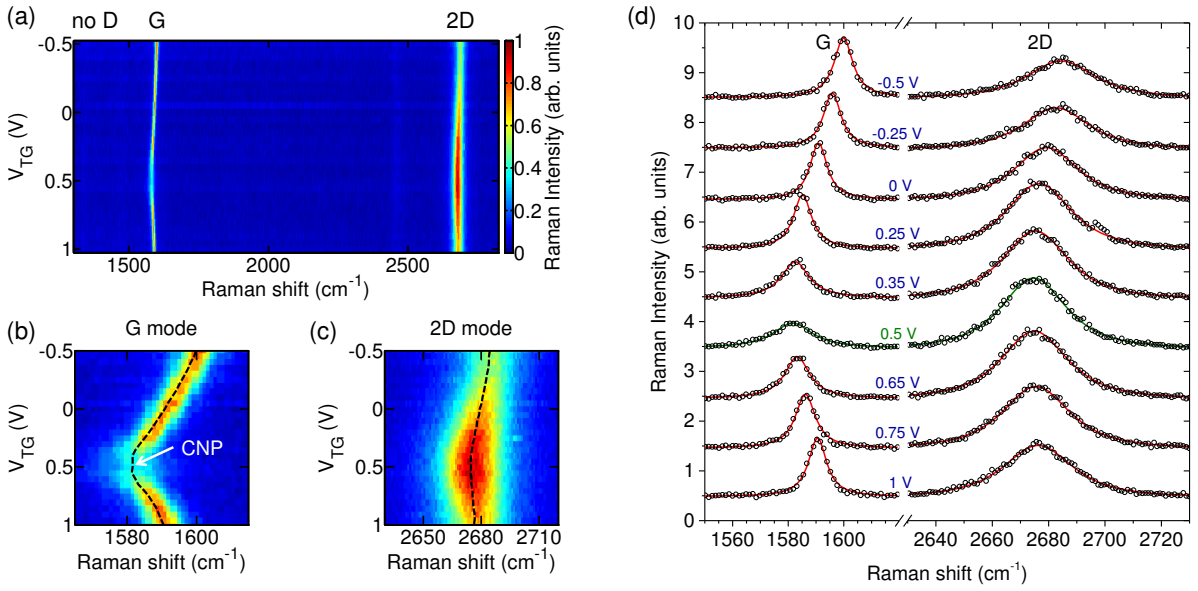

Figure 5.8 *– (a)-(c) Color maps of the Raman spectra of a pristine graphene monolayer (sample 1), measured using a 532 nm laser beam, as a function of the top-gate voltage V_{TG}. The G- and 2D-mode features appear prominently and no defect-induced D-mode feature is observed. Panels (b) and (c) show a clear evolution of the G- and 2D-mode features with varying V_{TG}. The black dashed lines correspond to the central frequency of each Raman feature. The charge neutrality point (CNP) is indicated by an arrow. (d) Raman spectra at values of V_{TG} between -0.5 V and +1 V. The circles are the experimental data and the solid lines are fits (see text for details). The CNP is reached at $V_{TG,0} = +0.5$ V (see green line).*

this work, $d_{BG} = (285 \pm 15)$ nm results in a back-gate capacitance $C_{BG} = (12.4 \pm 0.7)$ nF cm^{-2}. For a typical Fermi energy $E_F \sim 100$ meV, the quantity E_F/e is negligible as compared to the other term in Eq. (9.1).

The case of the polymer electrolyte top-gate is slightly more complicated. Indeed, when a voltage is applied between the gate and the SLG, Li^+ and ClO_4^- diffuse in the polymer to form electrical double layers (EDLs) at the interfaces as it is sketched in Fig. 5.7(b) [Das08]. These EDL can be modeled as parallel plate capacitors with a thickness given by the Debye length d_{TG}, and a geometrical capacitance per unit area $C_{TG} = \varepsilon_r \varepsilon_0 / d_{TG}$. The total geometrical capacitance of the polymer electrolyte is thus given by $C_{TG}\left(S_{p-gate}^{-1} + S_{p-graphene}^{-1}\right)^{-1}$, where S_{p-gate} (resp. $S_{p-graphene}$) is the contact area between the polymer electrolyte and the gate electrode (resp. the graphene monolayer). Since $S_{p-gate} \gg S_{p-graphene}$ (see Fig. 5.7(a)), one only needs to take into account the geometrical capacitance of the EDL at the graphene-polymer electrolyte interface. The Debye length is theoretically given by $d_{TG} = 2\mathcal{C}e^2/\varepsilon_0 \varepsilon_r k_B T$, where T is the temperature, k_B is Boltzmann's constant and $\mathcal{C}$ is the concentration of ions in the polymer electrolyte [Das08]. In practice, the exact value of $\mathcal{C}$ cannot be measured. One can nevertheless obtain an estimate of $C_{TG} \approx 4.4$ μF cm^{-2}, assuming a typical value of $d_{TG} \approx 1$ nm and $\varepsilon_r \approx 5$ for PEO [Das08]. This capacitance is more than two orders of magnitude larger than C_{BG} and becomes comparable to the quantum capacitance for $E_F \sim 100$ meV. As a result, the two terms in Eq. (9.1) are of the same order of magnitude and must be taken into account in the present study.

5.2.2 Geometrical capacitance of the electrical double layer

Our first objective is to precisely determine C_{TG}. Previous works on oxide dual-gated graphene FETs [Meric08, Xu11b] have shown that provided one geometrical capacitance is known, the other can be determined by monitoring the minimum (source-drain) conductivity point as a function of the bottom and top-gate biases. At steady state, our dual-gated graphene FETs have the same equivalent electrical circuit (see Fig. 5.9(c)) as the devices of Ref. [Xu11b]. Here, rather than using electron transport measurements, we apply micro-Raman scattering spectroscopy, which provides a local measurement. For a fixed V_{BG}, we sweep V_{TG} and record Raman spectra. Then, we extract Ω_G and Γ_G from Lorentzian fits (see Eq. (5.1)).

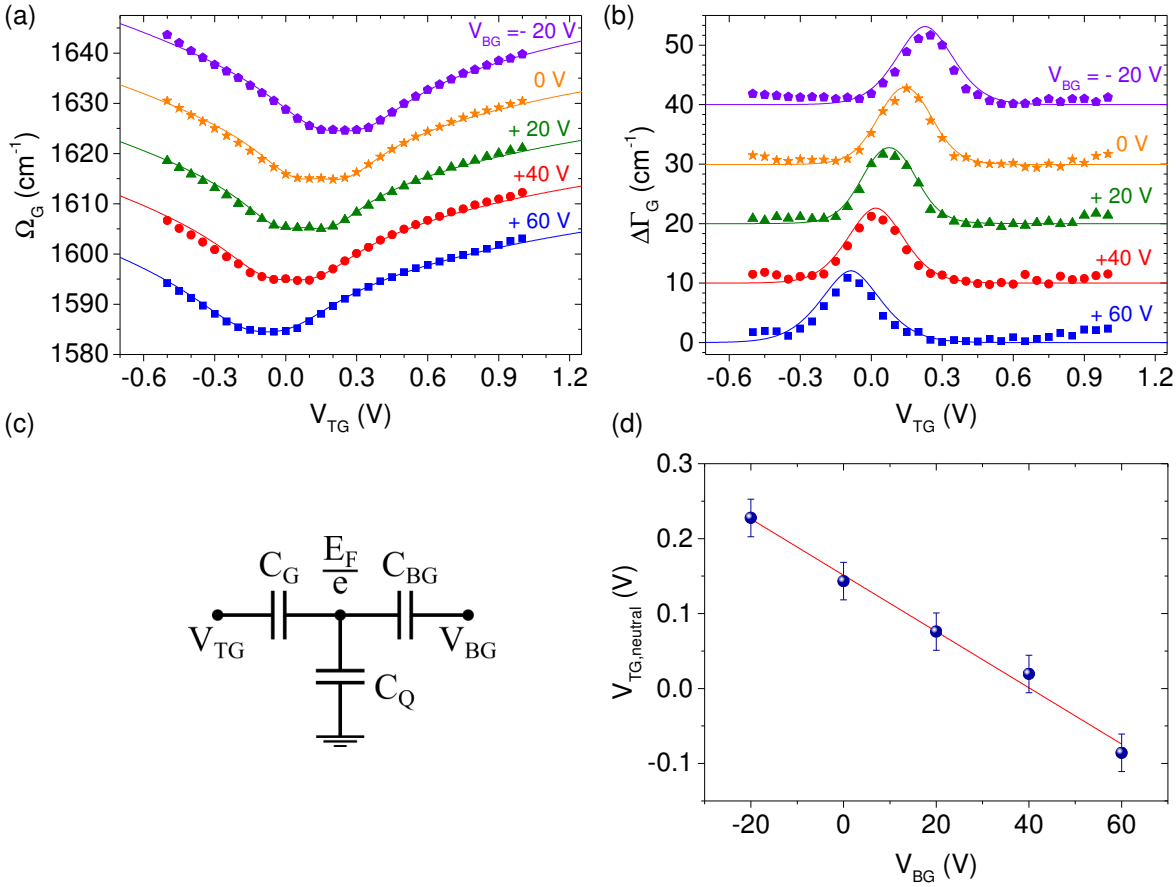

Figure 5.9 *– (a) Frequency Ω_G and (b) relative FWHM $\Delta\Gamma_G$ of the G-mode feature as a function of the top-gate voltage, recorded at various back-gate voltages on sample 1. The curves are vertically offset by 10 cm^{-1} for clarity. The symbols are experimental data. (C) Equivalent electrical circuit of our device at steady state. C_{BG} is the geometrical capacitance of the Si/SiO$_2$ back-gate, C_G is the geometrical capacitance of the electrical double layer at the graphene/polymer electrolyte interface and C_Q is the quantum capacitance of graphene. (d) Top-gate voltage $V_{TG,neutral}$, corresponding to the CNP in dual-gated graphene, as a function of the applied back-gate voltage V_{BG}. A top gate capacitance C_{TG} = 3.3 $\mu F\ cm^{-2}$ is deduced from a linear fit of the data (solid line). The solid lines in (a) and (b) are fits based on Eq. (5.12) and (5.13), respectively, with C_{TG} = 3.3 $\mu F\ cm^{-2}$.*

Figures 5.9(a) and 5.9(b) show these two quantities as a function of V_{TG} for five different values of V_{BG}. We observe a clear shift of the CNP, attained at $V_{TG,neutral}$, with V_{BG}. In

practice, $V_{TG,neutral}$ is extracted from the $\Gamma_G(V_{TG})$ curves, which, expectedly (see Section 5.3), exhibit a sharper extremum near neutrality than the $\Omega_G(V_{TG})$ curves. As shown in Fig. 5.9(d), $V_{TG,neutral}$ varies linearly with V_{BG}. Indeed, from the equivalent circuit in Fig. 5.9(c), the total charge density injected by top- and back-gates leads to [Xu11b]

$$ne = -C_{TG}\left(V_{TG} - V_{TG,0} - \frac{E_F}{e}\right) - C_{BG}\left(V_{BG} - V_{BG,0} - \frac{E_F}{e}\right). \tag{5.10}$$

At the CNP, $n = 0$ and $E_F = 0$. Therefore,

$$V_{TG,neutral} = V_{TG,0} - \frac{C_{BG}}{C_{TG}}(V_{BG} - V_{BG,0}). \tag{5.11}$$

Using Eq. (5.11), a linear fit of the data in Fig. 5.9(d) yields $C_{BG}/C_{TG} = (3.8 \pm 0.2) \times 10^{-3}$. Since $C_{BG} = (12.4 \pm 0.7)$ nF cm^{-2}, we deduce that $C_{TG} = (3.3 \pm 0.3)$ μF cm^{-2}, which is of the same order of magnitude as what was reported before for similar devices [Das08, Das09, Shimotani06, Efetov10, Bruna14]. We may now convert V_{TG} into E_F.

5.3 Electron-phonon coupling in pristine graphene

Having an accurate determination of E_F as a function of V_{TG}, we can focus on the doping-dependance of the G- and 2D-mode features. This study will allow us to quantitatively deduce the electron-phonon coupling at the Γ and $K^{(')}$ points, where Kohn anomalies strongly increase the electron-phonon coupling [Piscanec04].

5.3.1 Doping-dependence of the G-mode feature

Considering only lattice expansion, due to the addition of charge carriers, one may expect the G-mode frequency to increase (decrease) under hole (electron) doping [Lazzeri06]. Thus, the peculiar, nearly symmetric behaviors observed here and previously reported by others [Pisana07, Yan07, Das08, Kalbac10, Chen11, Chattrakun13] contrast strongly with the trends predicted if one only considers lattice expansion effects. This *anomalous* behavior has been originally predicted by Ando [Ando06] and by Lazzeri and Mauri [Lazzeri06] as a consequence of the strong coupling between zone-center optical phonons and low-energy electronic excitations across the gapless bands of graphene. Related effects occur in metallic carbon nanotubes [Piscanec07]. The anomalous doping dependence of the G-mode can be described using the **phonon self-energy** [Taylor02, Ando06, Lazzeri06, Pisana07, Yan07, Yan08b, Araujo12], the real part of which give the correction to the phonon frequency Ω_G due to electron-phonon interaction and the imaginary part is equal to Γ_G. As a result, the evolution of Ω_G and Γ_G are deeply connected. Note that these renormalizations can also be obtained without defining the self-energy, by calculating the change in phonon energy caused by electron-phonon interaction with second-order perturbation theory [Taylor02] and by applying Fermi's golden rule [Lazzeri06], respectively.

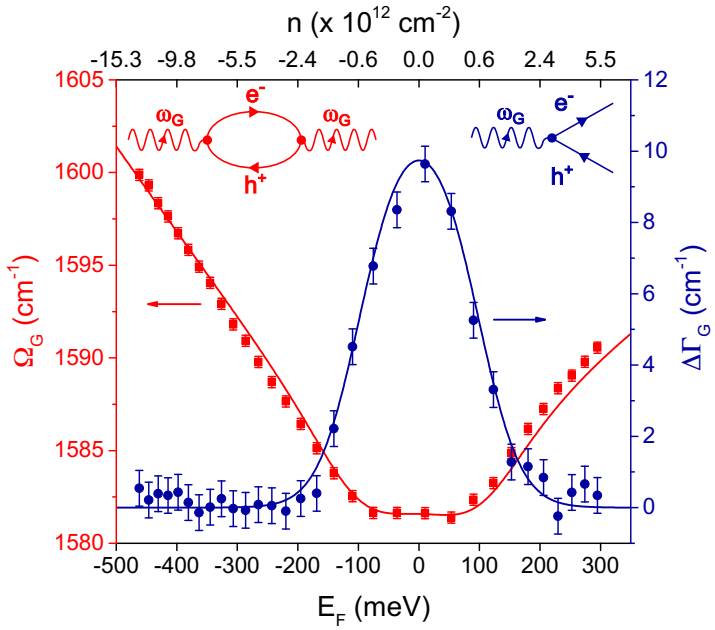

Figure 5.10 *– Frequency Ω_G (red squares, left axis) and relative FWHM $\Delta\Gamma_G$ (blue circles, right axis) of the G-mode phonon, extracted from the measurements in Fig. 5.8, as a function of Fermi energy or doping. The corresponding Feynman diagrams are shown as insets. The left inset represents the renormalization of the G-mode phonon frequency due to interactions with virtual electron-hole pairs. The right inset represents lifetime broadening due to the resonant decay of a G-mode phonon into an electron-hole pair. The solid blue and red lines are fits based on Eqs. (5.12) and (5.13), respectively. The fitting parameters are $C_{TG} = 3.9\ \mu F\ cm^{-2}$, $\lambda_\Gamma = 0.027$ and $\delta E_F = 35\ meV$.*

G-mode linewidth The variation of Γ_G is due to the decay of the G phonon into an electron-hole pair (see right inset in Fig. 5.10) and can be deduced from Fermi's golden rule[4]

$$\Delta\Gamma_G = \Gamma_G - \Gamma_0 = \frac{\lambda_\Gamma}{4}\Omega_G^0 \times \left[f\left(-\frac{\hbar\Omega_G^0}{2} - E_F\right) - f\left(\frac{\hbar\Omega_G^0}{2} - E_F\right)\right], \tag{5.12}$$

where Ω_G^0 is the phonon frequency at $E_F = 0$, $f(E) = [1 + \exp(E/k_B T)]^{-1}$ is the Fermi-Dirac distribution at a temperature T and λ_Γ is a dimensionless coefficient corresponding to the electron-phonon coupling strength[5] at the Γ point. Γ_0 contains all other sources of broadening that are independent on the carrier density (anharmonic coupling [Bonini07], disorder, instrument response function). For $|E_F| > \hbar\Omega_G^0/2$, $\Delta\Gamma_G$ vanishes due to Pauli blocking.

G-mode frequency The evolution of Ω_G with E_F is the sum of two contributions. The first one corresponds to the modification of the carbon-carbon bond strength (or equivalently to the modification of the equilibrium lattice parameter) due to the addition of charges. Indeed, electron doping adds electrons to the antibonding orbitals which leads to a softening of the

[4] In detail, $\Delta\Gamma_G = \Gamma_{ph\to e\text{-}h} - \Gamma_{e\text{-}h\to ph}$, where $\Gamma_{ph\to e\text{-}h}$ and $\Gamma_{e\text{-}h\to ph}$ are computed using Fermi's golden rule and correspond, respectively, to the transition probability of the phonon decay into an electron-hole pair (see right insert in Fig. 5.10, read left to right) and of the the electron-hole pair decay into a phonon (see right insert in Fig. 5.10, read right to left).

[5] Here, we choose to use the coupling constant λ_Γ as defined by Basko in Ref. [Basko08a]. In Refs. [Lazzeri06, Pisana07] the dimensionless electron-phonon coupling constant is denoted α' and is defined as $\alpha' = \lambda_\Gamma/2\pi$

carbon-carbon bond, whereas removing electrons leads to a hardening [Lazzeri06, Kalbac10]. This contribution can be computed within the standard textbook Born-Oppenheimer approximation, which states that the lighter electrons adjust adiabatically to the motion of the heavier nuclei, remaining at any time in their instantaneous ground state. Thus, this term is referred to as the **adiabatic** contribution $\Omega_{\mathrm{G}}^{\mathrm{A}}$. The second one corresponds to the renormalization of the G-mode phonon energy due to interactions with virtual electron-hole pairs [Ando06, Lazzeri06]. Indeed, due to strong electron-phonon coupling a phonon spends part of its time as a virtual electron-hole pair as suggested by the left insert in Fig. 5.10. This causes a change in the phonon energy (that can be described with the phonon self-energy). However, this change cannot be deduced within the adiabatic Born-Oppenheimer approximation because due to interactions with phonons, the electrons do not have enough time to relax to the instantaneous adiabatic ground state. Hence, this correction is referred to as the **nonadiabatic** contribution $\Omega_{\mathrm{G}}^{\mathrm{NA}}$ and is responsible of the anomalous G-mode frequency shift. Note that without a strong electron-phonon coupling, this contribution is negligible and is therefore directly related to the Kohn anomaly [Lazzeri06].[6] Finally, the frequency shift with respect to the Ω_{G}^{0} (the phonon frequency for neutral graphene) is given by [Lazzeri06, Pisana07]

$$\Delta\Omega_{\mathrm{G}} = \Omega_{\mathrm{G}} - \Omega_{\mathrm{G}}^{0} = \Delta\Omega_{\mathrm{G}}^{\mathrm{A}} + \Delta\Omega_{\mathrm{G}}^{\mathrm{NA}}. \tag{5.13}$$

At a finite temperature T, the adiabatic contribution $\Delta\Omega_{\mathrm{G}}^{\mathrm{A}}$ is accurately described by the analytic expression obtained by Lazzeri and Mauri [Lazzeri06]:

$$\Delta\Omega_{\mathrm{G}}^{\mathrm{A}} = -2.13n - 0.0360n^2 - 0.00329n^3 - 0.226|n|^{3/2}, \tag{5.14}$$

where $\Delta\Omega_{\mathrm{G}}^{\mathrm{A}}$ is in cm^{-1} and the charge carrier density n in 10^{13} cm^{-2}. Note that this expression is independent of the temperature T. The nonadiabatic contribution $\Delta\Omega_{\mathrm{G}}^{\mathrm{NA}}$ is given by [Lazzeri06, Pisana07]

$$\Delta\Omega_{\mathrm{G}}^{\mathrm{NA}} = \frac{\lambda_{\Gamma}}{2\pi\hbar} \fint_{-\infty}^{+\infty} \frac{[f(E-E_{\mathrm{F}}) - f(E)]E^2 \operatorname{sgn}(E)}{E^2 - (\hbar\Omega_{\mathrm{G}}^{0})^2/4} \,\mathrm{d}E, \tag{5.15}$$

where $\fint$ denotes the Cauchy principal value. This expression is obtained from the difference between the renormalized phonon frequency for a given E_{F} ($f(E-E_{\mathrm{F}})$ term) and for $E_{\mathrm{F}} = 0$ ($f(E)$ term). Because of the difference of the Fermi-Dirac distributions $f(E-E_{\mathrm{F}}) - f(E)$, the integration is restricted approximately to the range $[0, |E_{\mathrm{F}}|]$. As a consequence, there are *a priori* two singularities when $E_{\mathrm{F}} = \pm\hbar\Omega_{\mathrm{G}}^{0}/2$, which are known as the two phonon anomalies [Ando06, Lazzeri06, Yan08b]. For $T = 0$, one can obtain an analytic expression of $\Delta\Omega_{\mathrm{G}}^{\mathrm{NA}}$ and notice that these two divergences are logarithmic [Ando06, Lazzeri06, Yan07]. However, because the typical width of Fermi-Dirac distribution is $k_{\mathrm{B}}T$ and because $\hbar\Omega_{\mathrm{G}}/2 \approx 98$ meV,

[6] In fact, Kohn anamolies occur for phonon wavevector $\boldsymbol{q}$ such that $\boldsymbol{q} = 2\boldsymbol{k}_{\mathrm{F}}$ where $\boldsymbol{k}_{\mathrm{F}}$ is a Fermi-surface wavevector [Kohn59]. Thus, varying E_{F} causes the Kohn anomaly at Γ to shift away from Γ. This shift is reflected in $\Omega_{\mathrm{G}}^{\mathrm{NA}}$.

these singularities are smeared out with increasing T. In fact, one can see this as an upper integral limit slightly higher than $|E_F|$ resulting in smaller divergences. These phonon anomalies can also be understood more physically. The renormalization of the phonon frequency is due to the interaction with virtual electron-holes pairs. As it involves transitions to virtual states, energy conservation is not required. Consequently, the phonon interacts with all the virtual electron-hole pairs allowed by Pauli principle, with higher, lower or the same energy as the phonon (this is mathematically done in Eq. (5.15) by summing on all the allowed energy). The coupling of the phonon with an electronic state at an energy between $-\hbar\Omega_G/2$ and $+\hbar\Omega_G/2$ tends to increase the phonon frequency. In return, the coupling with an electronic state at higher energy than $|\hbar\Omega_G|/2$ tends to decrease the phonon frequency. Hence, for neutral graphene the phonon frequency is given by the equilibrium between this two contributions. Let us assume that $T = 0$ for simplicity. When increasing $|E_F|$, the coupling with electronic states at absolute energies lower than $|E_F|$ is forbidden due to Pauli principle. In this way, when increasing $|E_F|$ from 0, we first decrease the number of states that increase the phonon frequency. Consequently, the phonon frequency decrease. For $|E_F| = \hbar\Omega_G/2$, there are no states that increase the phonon frequency anymore, therefore the phonon frequency diverges. When $|E_F| > \hbar\Omega_G/2$, the number of states that descrease the phonon frequency is reduced and thus the phonon frquency increase. Finally, one should note that $\Delta\Gamma_G$ and $\Delta\omega_G$ are proportional to λ_Γ.

Charge inhomogeneity Furthermore, to accurately describe the experimental evolution of the G mode, one also has to take into account random spatial fluctuations of the Fermi energy [Casiraghi07, Martin08, Xu11a, Li11]. As a result, the measured Ω_G and Γ_G are average values of the fluctuating quantities under the laser spot. To calculate these average quantities, we assume that the graphene layer under the laser spot can be divided into N small cells of the same area. If the cells are small enough, we can suppose that the Fermi energy and thus Ω_G and Γ_G are uniform across each cell. If the Fermi energy of the i^{th} cell is E_F^i and if N tends to infinite, the average Ω_G and Γ_G are given by:

$$\Omega_G(E_F) = \frac{1}{N}\sum_{i=1}^{N}\Omega_G(E_F^i) = \int_{-\infty}^{+\infty}\Omega_G(E)P(E,E_F)\,dE, \tag{5.16}$$

$$\Gamma_G(E_F) = \frac{1}{N}\sum_{i=1}^{N}\Gamma_G(E_F^i) = \int_{-\infty}^{+\infty}\Gamma_G(E)P(E,E_F)\,dE, \tag{5.17}$$

where P is the statistical distribution function of the Fermi energy and E_F is the average value of the Fermi energy. It is reasonable to assume that P follows a Gaussian distribution [Martin08, Xu11a, Li11] center on the average value of the Fermi energy E_F and with a standard deviation (or in other words a Fermi energy fluctuation) δE_F :

$$P(E,E_F) = \frac{1}{\delta E_F\sqrt{2\pi}}\exp\left[-\frac{(E-E_F)^2}{2{\delta E_F}^2}\right]. \tag{5.18}$$

Thereafter, the computed $\Delta\Omega_G(E_F)$ and $\Delta\Gamma_G(E_F)$ used to fit our data are given by the convolution of this Gaussian distribution with Eq. (5.12) and (5.13).

Results of the simultaneous fit Figure 5.9 displays the results of **simultaneous** fits of $\Delta\Omega_G(V_{TG})$ and $\Delta\Gamma_G(V_{TG})$ for five top-gate sweeps at different V_{BG}. We used $v_F = 1.1 \times 10^6$ m s^{-1} and the values of C_{TG}, $V_{TG,neutral}$ and Ω_G^0 obtained previously (see subsection 5.2.2). Thus, the fitting parameters are λ_Γ, δE_F and Γ_0. The experimental data are remarkably well fitted by the theoretical model. Interestingly, although the two phonon anomalies [Ando06, Lazzeri06, Yan08b] predicted at $E_F = \pm\hbar\Omega_G^0/2$ by Eq. (5.13) are largely smeared out at room temperature, one can still notice a hint of their presence in Fig. 5.9(a) and 5.10. From these five fits, we get $\lambda_\Gamma = 0.036$ and $\delta E_F = 40$ meV. Since $\delta E_F \approx 50$ meV on bare SiO_2 without an electrochemical top-gate [Martin08, Xue11], we conclude that charge inhomogeneity does not have a major effect on our analysis. DFT calculations [Lazzeri06, Pisana07] have predicted $\lambda_\Gamma = 0.028$, which is slightly smaller, but consistent with our measurement.

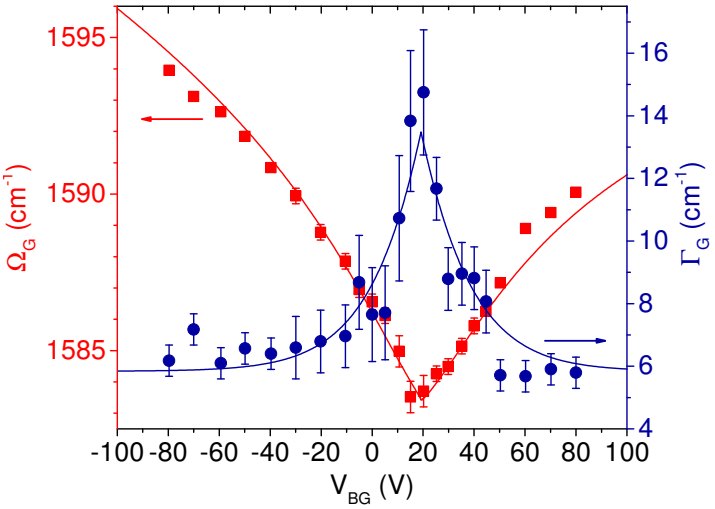

Figure 5.11 *– Frequency Ω_G (red squares, left axis) and FWHM Γ_G (blue circles, right axis) of the G-mode phonon, extracted from Fig. 3 of Ref. [Yan07], as a function of back gate voltage. The solid blue and red lines are fits based on Eqs. (5.12) and (5.13), respectively. The fitting parameters are $C_{BG} = 10.8$ nF cm^{-2}, $\lambda_\Gamma = 0.025$ and $\delta E_F = 80$ meV.*

Another way to further compare the experimental data and theory is to set C_{TG} as adjustable parameter when fitting $\Delta\Omega_G(V_{TG})$ and $\Delta\Gamma_G(V_{TG})$. This yields $C_{TG} = 3.9$ μF cm^{-2}, $\lambda_\Gamma = 0.034$ and $\delta E_F = 35$ meV. These values are very consistent with the more constrained fits discussed above. Similar studies were repeated on more than five samples, with similar conclusions. Additionally, to show the generality of this procedure, we fit the data measured on a conventional solid state graphene FET using a SiO_2 epilayer as a gate dielectric. These data were extracted from Fig. 3 of Ref. [Yan07]. The result of the fit is shown in Fig. 5.11 and is in good agreement with the experimental data. The deduced fitting parameters are $C_{BG} = (10.8 \pm 1.4)$ nF cm^{-2}, $\lambda_\Gamma = 0.025 \pm 0.003$ and $\delta E_F = (80 \pm 10)$ meV. In particular, C_{BG} is in excellent agreement with the value determined theoretically from the thickness of the SiO_2 epilayer $C_{BG} = 11.5$ nF cm^{-2} [Yan07].

In conclusion, this demonstrates that a direct fit of $\Delta\Omega_G(V_{TG})$ and $\Delta\Gamma_G(V_{TG})$ can be used to get an accurate measurement of C_{TG}, which allows to convert V_{TG} into E_F through Eq. (9.1). This is a much faster approach to determine C_{TG}, which does not require a dual-gated device. As an example, a fit of the data in Fig. 5.8 is shown in Fig. 5.10, and shows a very good agreement between experiment and theory. More generally, our fitting procedure allows us to estimate C_{TG} and λ_Γ with relative uncertainties of approximately 20% and 10%, respectively. In return, these results show also that the theoretical evolution of $\Delta\Omega_G(V_{TG})$ and $\Delta\Gamma_G(V_{TG})$ can be used to determine the doping level (see Chapter 8).

To better understand the importance to fit simultaneously $\Delta\Omega_G(V_{TG})$ and $\Delta\Gamma_G(V_{TG})$, we have fit these quantities separately for the measurements shown in Fig. 2.6. From the fit of $\Delta\Omega_G(V_{TG})$, we obtain $C_{TG} = 2.3$ μF cm^{-2}, $\lambda_\Gamma = 0.042$ and $\delta E_F = 50$ meV. Except the large value of λ_Γ, the two parameters are reasonable. From the fit of $\Delta\Gamma_G$, we obtain $\lambda_\Gamma = 0.033$ and $\delta E_F \approx 40$ meV and an unrealistically large $C_{TG} \sim 100$ μF cm^{-2}. The latter value suggests that the behavior of $\Delta\Gamma_G$ can be rationalized using solely the quantum capacitance of graphene. This is understandable, since the variations of $\Delta\Gamma_G$ occur near $E_F = 0$, where the contribution of the quantum capacitance dominates in Eq. (9.1). However, the value of $\Delta\Gamma_G$ near $E_F = 0$ is directly proportional to λ_Γ and is not influenced by C_{TG}, while $\Delta\omega_G$ varies mostly away from the CNP. Hence, its evolution with V_{TG} is influenced by both λ_Γ and C_{TG}. Consequently, a simultaneous fit allows for a reliable estimation of λ_Γ (through the doping dependence of $\Delta\Gamma_G(V_{TG})$), and, in turn of C_{TG} (through the slope of $\Delta\Omega_G(V_{TG})$ curve, having λ_Γ constrained by $\Delta\Gamma_G(V_{TG})$).

Comparison between different samples Let us now compare the results obtained on different samples. Figure 5.12 shows the evolution of E_F as a function of $\Delta\Omega_G$ for five different graphene FETs (denoted sample 1 to 5) in which C_{TG} and λ_Γ have been previously determined by the simultaneous fit of $\Delta\Omega_G(V_{TG})$ and $\Delta\Gamma_G(V_{TG})$. For these five samples, we found an average of $\langle C_{TG}\rangle = (4.5 \pm 1.5)$ μF cm^{-2} and $\langle\lambda_\Gamma\rangle = 0.032 \pm 0.004$ (see also Table 5.2). This translates into an average relative G-mode FWHM (see Eq. (5.12)) of $\Delta\Gamma_G = (12.6 \pm 1.6)$ cm^{-1} (at $T = 0$, $E_F = 0$ and $\delta E_F = 0$) that is consistent with the value of $\Gamma_G \approx 15$ cm^{-1} recorded on quasi-undoped suspended graphene at low temperature [Berciaud13]. Remarkably, and in spite of the different values of C_{TG}, the data for these five devices shown in Fig. 5.12 collapse onto a same curve. In practice, this very reproducible behavior can be used to evaluate E_F knowing $\Delta\Omega_G$, which is of broad interest in graphene science. For this purpose, we consider the asymptotic behavior of $\Delta\Omega_G(E_F)$. When $|E_F| \gg \hbar\Omega_G^0/2$, Eq. (5.15) becomes

$$\Delta\Omega_G^{NA} \approx \frac{\lambda_\Gamma}{2\pi\hbar}|E_F|. \tag{5.19}$$

Assuming that the adiabatic contribution $\Delta\Omega_G^A$ is negligible compared to $\Delta\Omega_G^{NA}$, $\Delta\Omega_G$ should be linear with $|E_F|$. Indeed, in Fig. 5.12 for the five different samples, $\Omega_G(E_F)$ clearly scales linearly for $|E_F| \gtrsim 100$ meV. The slightly different slopes observed for electron and hole

doping arise from the opposite sign of the adiabatic corrections. For $|E_F| \gtrsim 100$ meV, we find

$$E_F \gtrsim +100 \text{ meV}, \qquad E_F = +21\Delta\Omega_G + 75, \tag{5.20}$$

$$E_F \lesssim -100 \text{ meV}, \qquad E_F = -18\Delta\Omega_G - 83, \tag{5.21}$$

where E_F is expressed in meV and $\Delta\Omega_G$ in cm^{-1}. However, it should be noted that this linear scaling only holds for $|E_F| \lesssim 500 - 600$ meV. In fact, for higher $|E_F|$, $\Delta\Omega_G$ no longer scales linearly with $|E_F|$ since $\Delta\Omega_G^A$ can no longer be neglected compared to $\Delta\Omega_G^{NA}$. Moreover, Eqs. (5.20) and (5.21) can be applied provided the shift in $\Delta\Omega_G$ is exclusively due to doping, i.e., other extrinsic factors, such as mechanical strain do not contribute. If this is not the case, one has to separate the various contributions, using, e.g., the G- and 2D-mode frequency correlations [Lee12c] (see Section 5.4).

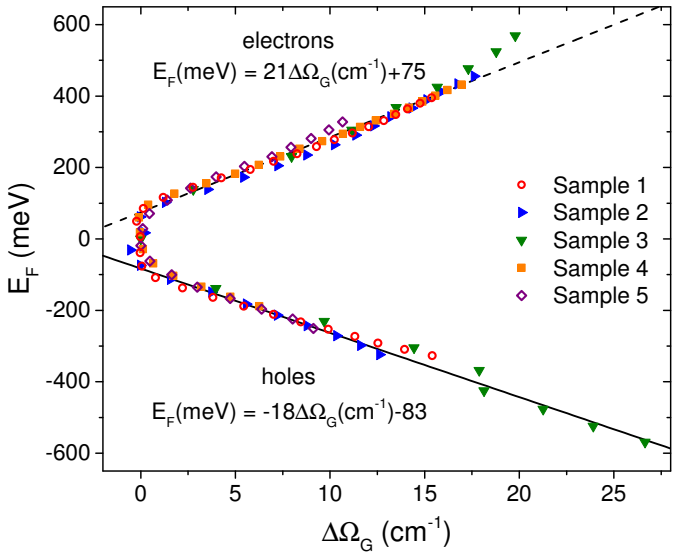

Figure 5.12 *– Fermi energy E_F as a function of the relative frequency of the G mode $\Delta\omega_G$. Measurements on five different devices are represented with different symbols. The dashed and solid lines correspond to Eq. (5.20) and (5.21), respectively.*

5.3.2 Doping-dependence of the 2D-mode feature

We now briefly comment on the 2D-mode feature. Figure 5.13 shows the evolution of the frequency Ω_{2D} and FWHM Γ_{2D} of the 2D-mode feature with E_F for sample 2 (2D mode spectra are also shown for sample 1 in Fig. 5.8). As expected for supported graphene, the 2D-mode feature exhibits a quasi-symmetric lineshape that can be phenomenologically fit to the modified Lorentzian profile of Eq. (5.8). We find that Γ_{2D} does not vary significantly with E_F, while Ω_{2D} varies little at moderate doping ($|E_F| \lesssim 200$ meV), but tends to stiffen (soften) significantly for stronger hole (electron) doping. The observation of an almost constant Ω_{2D} can be understood from the fact that, contrary to the G-mode phonon, the resonant decay of the 2D-mode phonon into an electron-hole pair is not possible since the phonon momentum $\boldsymbol{q}$ is fixed by Eq. (5.7). The observed evolution of Ω_{2D} outlined in Fig. 5.13 (see also Fig. 5.8) can

be qualitatively understood as the sum of a dominant adiabatic contribution and a weaker non-adiabatic contribution. The latter is reduced as compared to the case of the G-mode feature, likely because the 2D-mode feature involves phonons that are significantly away from the Kohn anomalies at the edges of the Brillouin zone [Das08].

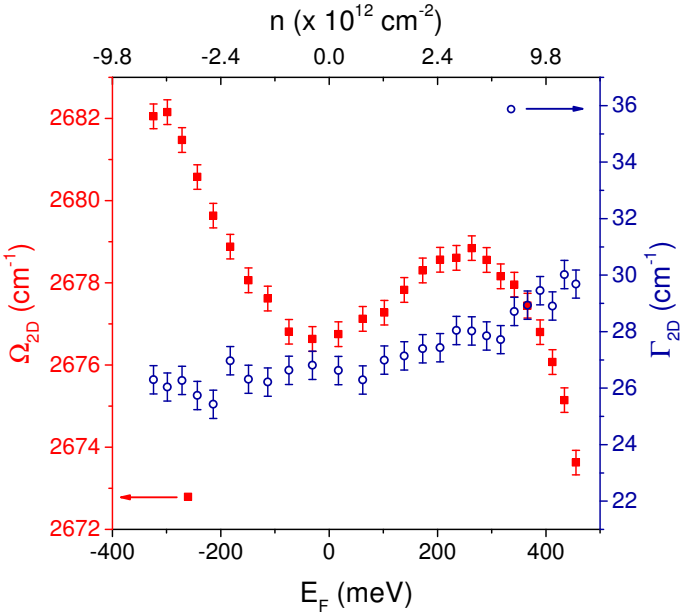

Figure 5.13 *– Doping dependence of the frequency (red squares, left axis) and FWHM (blue open circle, right axis) of the 2D mode (sample 2 without defect).*

5.3.3 Integrated intensity of the G- and 2D-mode features: electron-electron and electron-phonon scattering

Up to now, we did not discuss the integrated intensity of the G- and 2D-mode features. In Chapter 3 Section 3.4, we have stated that this integrated intensity is proportional to the total probability of the Raman process (see Eq. (3.21)). The integrated intensity of the 2D-mode feature (I_{2D}) depends on E_F [Das08, Das09, Basko09b], while previously in this chapter (see Fig. 5.2(b)), we have shown that as long as $|E_F| \ll \hbar\omega_L/2$, where $\hbar\omega_L$ is the energy of the incident laser, I_G is almost constant [Basko09a, Kalbac10, Chen11].

In Fig. 5.14, we consider the ratio I_{2D}/I_G, which is maximum for $E_F = 0$ and decreases almost symmetrically for increasing $|E_F|$. Following [Basko08a, Basko09b], the integrated intensity of the 2D-mode feature writes

$$I_{2D} \propto \left(\frac{\gamma_K}{\gamma_{e-ph} + \gamma_D + \gamma_{ee}} \right)^2, \tag{5.22}$$

where $\gamma_{e-ph} + \gamma_D + \gamma_{ee}$ is the total electron scattering rate, with γ_{e-ph} the electron-phonon scattering rate, γ_D the electron-defect scattering rate, and γ_{ee} the electron-electron scattering rate. The electron-phonon scattering rate can be approximated as $\gamma_{e-ph} = \gamma_K + \gamma_\Gamma$, where γ_K and γ_Γ are the scattering rates for zone-edge and zone-center optical phonons, respec-

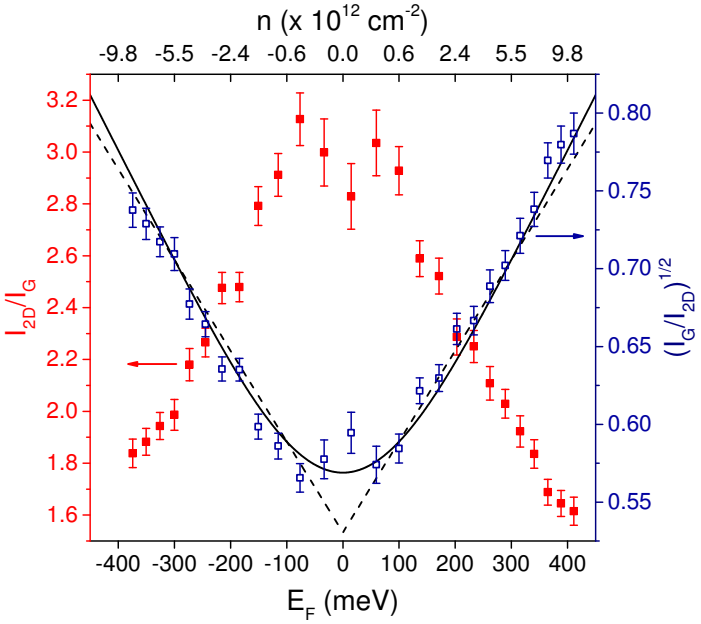

Figure 5.14 – *Left axis: doping dependence of the ratio between the integrated intensity of the 2D-mode feature and that of the G-mode feature (red squares). Right axis: doping dependence of the square root of the ratio between the integrated intensity of the G mode and that of the 2D mode (blue open squares). The dashed and solid lines are fits based on Eq. (5.23), without and with Fermi energy fluctuations, respectively. A value of $\gamma_{e\text{-}ph} = 51$ meV is deduced from the fit. The measurements are performed on sample 2.*

tively. Note that Eq. (5.22) is obtained under the assumption of a fully resonant process (see Fig. 5.3), and that trigonal warping effects leading to momentum-dependent scattering rates are neglected [Basko08a, Basko09b, Venezuela11, Basko13]. While γ_D and $\gamma_{e\text{-ph}}$ do not depend on E_F, γ_{ee} has been predicted to scale linearly with $|E_F|$. For $|E_F| \ll \hbar\omega_L/2$, Basko *et al.* calculated [Basko09b]

$$\sqrt{\frac{I_G}{I_{2D}}} = \frac{\left.\sqrt{\frac{I_G}{I_{2D}}}\right|_0}{\gamma_{e\text{-ph}} + \gamma_D}(\gamma_{e\text{-ph}} + \gamma_D + 0.06|E_F|), \tag{5.23}$$

where $\left.\sqrt{\frac{I_G}{I_{2D}}}\right|_0$ corresponds to the value at $E_F = 0$.

In this section, we are considering pristine graphene, in which $\gamma_D \ll \gamma_{e\text{-ph}}$. As illustrated by the dashed line in Fig. 5.14, our experimental data agree well with a fit based on Eq. (5.23) for $|E_F| \gtrsim 100$ meV. However, we observe a deviation from Eq. (5.23) near the CNP, likely due to Fermi energy fluctuations. As for the G-mode frequency and linewidth (see Eqs. (5.16) to (5.18)), we therefore fit the experimental data with the Gaussian convolution of Eq. (5.23), resulting in the solid line in Fig. 5.14. The agreement between theory and experiment is very good and more compelling than in the seminal study in Ref. [Basko09b]. The fitting parameters are $\left.\frac{I_{2D}}{I_G}\right|_0 = 3.6$, $\gamma_{e\text{-ph}} = 51$ meV and $\delta E_F = 110$ meV. We repeated this analysis on three pristine samples and found average values of $\langle\gamma_{e\text{-ph}}\rangle = (47 \pm 7)$ meV, $\langle\delta E_F\rangle = (120 \pm 10)$ meV and $\left\langle\left.\frac{I_{2D}}{I_G}\right|_0\right\rangle = 4.2 \pm 0.6$ (see Tab. 5.2). Note that the dispersion of the measurements on these

three devices is very similar to the dispersion observed when measuring on several spots on the same sample. The value of $\gamma_{\text{e-ph}}$ is in good agreement with the estimate in [Basko09b]. The Fermi energy fluctuation δE_F obtained here is more realistic than the lower values estimated from the simultaneous fit of $\Delta\omega_G(V_{TG})$ and $\Delta\Gamma_G(V_{TG})$. It corresponds to a charge inhomogeneity of $\delta n \lesssim 10^{12}$ cm^{-2}, in line with previous scanning tunneling microscopy measurements [Martin08, Xue11].

Interestingly, in Ref. [Basko09b], the authors claim that the **intrinsic** value of $\left.\frac{I_{2D}}{I_G}\right|_0$ for undoped graphene is in the range 12-17 (using a 2.4 eV excitation laser). However, this estimation is based on Raman measurements on quasi-undoped suspended graphene [Berciaud09] and does not take into account the effect of optical interferences, which occur in graphene-based multilayer structures and may critically affect the intensity of the Raman features (see Chapter 4 Section 4.3 and Appendix C). An intrinsic value corrected from interference effects of $\left.\frac{I_{2D}}{I_G}\right|_{intr} = 5 \pm 1$ was estimated for freely suspended, undoped graphene, using a 2.33 eV excitation laser, as in the present study [Metten15]. Considering the distinct Raman enhancement factors for the G- and 2D-mode features in the PEO/graphene/SiO_2 (285 nm)/Si multilayer structure, the average value of $\left\langle \left.\frac{I_{2D}}{I_G}\right|_0 \right\rangle = 4.2 \pm 0.6$ translates into an average intrinsic value of $\left\langle \left.\frac{I_{2D}}{I_G}\right|_{intr} \right\rangle = 4.9 \pm 0.7$ (see Tab. 5.2), which is in excellent agreement with the measurements on suspended graphene.

As outlined in Refs. [Basko08a, Basko09b, Basko08b], the scattering rate $\gamma_{\text{e-ph}}$ is linked to the dimensionless electron-phonon coupling constants λ_Γ and λ_K through

$$\gamma_{\text{e-ph}} = \gamma_K + \gamma_\Gamma = \frac{\lambda_K}{4}\left(\frac{\hbar\omega_L}{2} - \hbar\Omega_K\right) + \frac{\lambda_\Gamma}{4}\left(\frac{\hbar\omega_L}{2} - \hbar\Omega_\Gamma\right), \tag{5.24}$$

where $\hbar\Omega_K \approx 1210$ cm^{-1} = 150 meV is the in-plane transverse optical (TO) phonon energy at the $K^{(')}$ point, $\hbar\Omega_\Gamma := \hbar\Omega_G \approx 1580$ cm^{-1} = 196 meV is the in-plane optical phonon energy at Γ (i.e., the G-mode frequency) and $\hbar\omega_L = 2.33$ eV is the laser photon energy.

For sample 2 (see Fig. 5.14 and Tab. 5.2), a value of $\lambda_\Gamma = 0.034$ is deduced from the simultaneous fits of $\Delta\Omega_G$ and $\Delta\Gamma_G$. Then, using Eq. (5.24), we can estimate[7] $\lambda_K = 0.17$. Overall, for the three pristine samples studied here, we obtained average values of $\langle\lambda_\Gamma\rangle = 0.031 \pm 0.004$, $\langle\lambda_K\rangle = 0.15 \pm 0.03$ and $\left\langle\frac{\lambda_K}{\lambda_\Gamma}\right\rangle = 5.1 \pm 1.2$ (see Tab. 5.2).

To close this section, we compare the average ratio $\left\langle\frac{\lambda_K}{\lambda_\Gamma}\right\rangle$ deduced from the doping-dependent Raman study to a direct estimate derived from the measured ratio of the integrated intensities of the intravalley (2D' mode) and intervalley (2D mode) resonant two-phonon features. This ratio is expected to be independent of E_F [Basko08a, Basko09b] and writes $\frac{I_{2D}}{I_{2D'}} = 2\left(\frac{\lambda_K}{\lambda_\Gamma}\right)^2$. In our experimental conditions, we obtain $\frac{I_{2D}}{I_{2D'}} = 40 \pm 2$. Thus, by considering

[7] Following [Basko09b, Basko08b], the value of λ_K deduced from Eq. (5.24) corresponds to the electron-phonon coupling constant at a carrier energy of $\hbar\omega_L/2$. To obtain the coupling constant exactly at the K point $\lambda_K(\hbar\omega_K)$, we can use the relation $\lambda_K(\hbar\omega_K)/\lambda_K(\hbar\omega_L/2) \approx 1.2$ that is valid for a polymer electrolyte with a relative permittivity $\varepsilon_r \approx 5$. In this manuscript, λ_K implicitly denotes $\lambda_K(\hbar\omega_L/2)$.

one more time the different Raman enhancement factors for the 2D- and 2D'-mode features in the PEO/graphene/SiO_2 (285 nm)/Si multilayer system, we deduce $\frac{\lambda_K}{\lambda_\Gamma} \approx 4.2$. This value is consistent with the analysis outlined above.

5.4 Correlations

In the previous section, we have successfully compared our measurements to theoretical calculations and, in particular, estimated the electron-phonon coupling constants. In this section, we present correlations between the frequencies and linewidths of the G- and 2D-mode features in doped graphene, with the aim to extract universal behaviors that could be useful for sample characterization.[8]

5.4.1 G-mode frequency and linewidth

Figure 5.15 shows $\Delta\Gamma_G$ as a function of $\Delta\Omega_G$ for the five different samples already shown in Fig. 5.12. We observe a universal behavior and the experimental data are in good agreement with the theoretical calculations, although the very slight difference expected for electron and hole doping (due to $\Delta\Omega_G^A$, see Eq. (5.13)) is not resolved experimentally, likely due to Fermi energy fluctuations. We also note that in the high-doping regime, $\Delta\Gamma_G$ tends to increase somewhat. This increase, also observed by others [Bruna14] is presumably due to the increasing inhomogeneity of the charge distribution at high top-gate biases. The correlation displayed in Fig. 5.15 may be used to estimate E_F, in particular in the low doping regime $\left(|E_F| \lesssim \hbar\Omega_G^0\right)$.

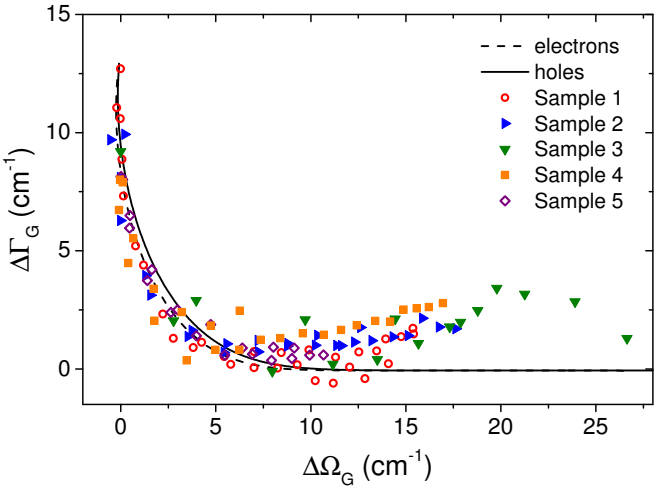

Figure 5.15 *– Correlation between the relative FWHM $\Delta\Gamma_G$ and relative frequency $\Delta\Omega_G$ of the G-mode feature in doped graphene, for the five samples introduced in Fig. 5.12. The solid and dashed lines correspond to theoretical calculations (based on Eqs. (5.12) and (5.13)), for electron and hole doping, respectively.*

[8] Based on the conclusions of next section 5.5, the correlations discussed in the following will also hold in weakly defective graphene.

5.4.2 G- and 2D-mode frequencies

Figure 5.16 represents the evolution of Ω_{2D} as a function of Ω_G for the same five samples. A clear correlation is observed between these two quantities. For hole doping, the correlation is quasi-linear in the range of E_F studied here (-500 meV $\lesssim E_F < 0$). In contrast, for electron doping, a quasi-linear scaling, again with a (much smaller) positive slope is also observed at low doping ($0 < E_F \lesssim 250$ meV), until Ω_{2D} levels off and ultimately decreases, leading to a non-linear scaling. This behavior was observed on every sample either for electrolyte-gated or conventional back-gated FETs and has been also observed in chemically doped graphene [Lee12c].

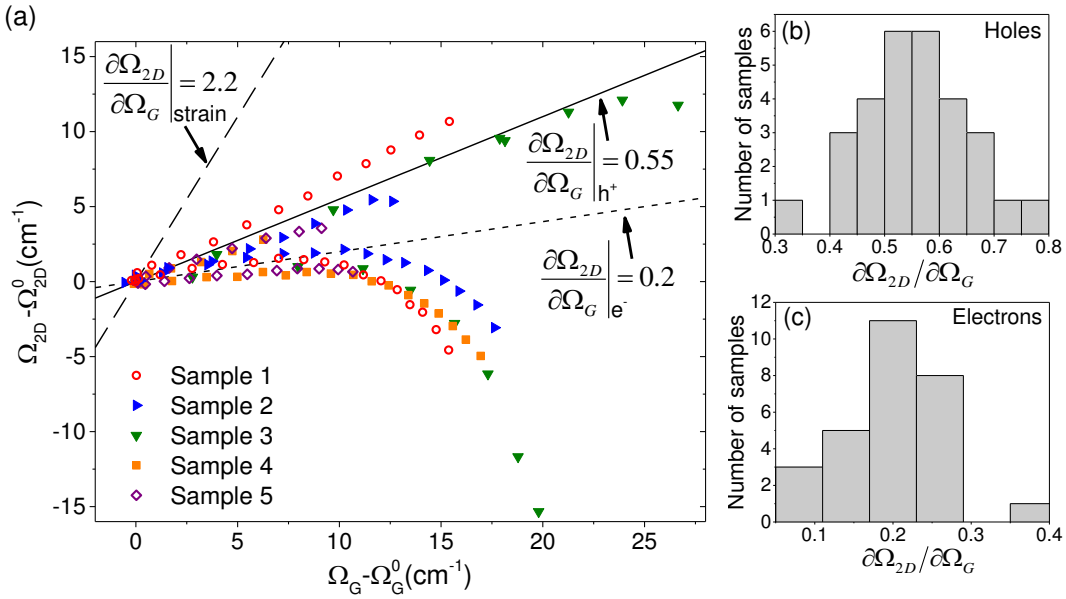

Figure 5.16 *– (a) Correlation between the frequencies of the 2D- and G-mode features (relative to their values near the charge neutrality point) in doped graphene, for the five samples introduced in Fig. 5.12. The continuous and short-dashed lines are global fits performed on the linear portions of the hole doping and electron doping branches, respectively. The dashed line corresponds to the evolution of Ω_{2D} versus Ω_G under pure strain [Lee12c, Metten14]. Statistical distribution of the measured slopes $\frac{\partial\Omega_{2D}}{\partial\Omega_G}$ under hole and electron doping are shown in (b) and (c), respectively.*

From the slopes $\frac{\partial\Omega_{2D}}{\partial\Omega_G}$ extracted on thirty samples (see Fig. 5.16(b)-(c)), we find an average of (0.55 ± 0.2) for hole doping and of (0.2 ± 0.13) for electron doping, respectively. These values agree with the slopes reported previously [Lee12c, Fromm13, Tiberj13]. However, we provide a much more accurate statistical study. From this statistical study, we note that the correlation between Ω_{2D} and Ω_G is more dispersed than the correlation between $\Delta\Gamma_G$ and $\Delta\Omega_G$. This is chiefly due to the dependence of Ω_{2D} on E_F, which is not as universal as that of Ω_G. In addition, it is rather challenging to extract a well-defined correlation for electron doping due to the small variations of Ω_{2D} at moderate doping.

Noteworthy, estimations of E_F based on the frequency and/or linewidth of the Raman features may only be reliable if graphene is not subjected to significant strains. Indeed, as

mentioned before, strain also affects the Raman features. However, for biaxial strains[9] below 1 % [Metten14], Γ_G is marginally affected and Ω_G soften (stiffen) under tensile (compressive) strain. Thus, a linear correlation between Ω_{2D} and Ω_G has been measured in strained graphene [Lee12c, Zabel11, Lee12b, Metten13, Metten14]. Since the measured slopes ($\frac{\partial\Omega_{2D}}{\partial\Omega_G} \approx 2.2$, for undoped, strained graphene [Metten14]) are appreciably larger than the slopes measured in doped graphene (presumably under a small but constant built-in strain), Lee *et al.* have proposed to use the correlation between ω_{2D} and ω_G as a robust tool to optically separate strain from charge doping [Lee12c].

This optical separation of mechanical strain from charge doping is based on a vector decomposition model in the Ω_G-Ω_{2D}-plane, reliably up to certain limiting conditions, which will be discussed hereafter. The complete decomposition method is described in Appendix D. In this method, three basis vectors are defined corresponding to the slopes $\frac{\partial\Omega_{2D}}{\partial\Omega_G}$, under strain, hole and electron doping, respectively (see Fig. 5.16). For each vector, a coefficient is defined in order to deduce the absolute levels of strain and/or doping (in Appendix D, these coefficient are denoted $\mathcal{C}_s$ and $\mathcal{C}_d$, respectively). Moreover, one also has to know the 2D- and G-mode frequencies that correspond to an undoped and unstrained graphene sample. For clarity, in Fig. 5.16, the 2D- and G-mode frequencies are shown relative to the measurements at $E_F \approx 0$. These origin points, denoted $(\Omega_G^0, \Omega_{2D}^0)$ might differ from the reference point corresponding to undoped and unstrained graphene, since an undetermined amount of native strain may be present and induce a shift along the strain vector. Furthermore, Ω_{2D}^0 depends on the photon energy of the excitation laser and on the nature of the substrate (see Chapter 8).

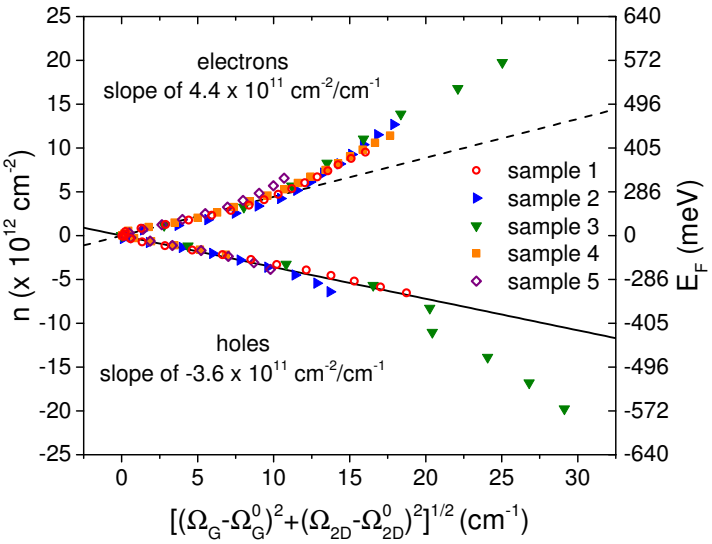

Figure 5.17 *– Charge carrier density n as a function of the shift* $\left[(\Omega_G - \Omega_G^0)^2 + (\Omega_{2D} - \Omega_{2D}^0)^2\right]^{1/2}$ *from the reference point corresponding to undoped graphene. Data are shown for the five samples introduced in Fig. 5.12. The continuous and dashed lines are global linear fits, performed in the low doping regime on the electron and hole branches, respectively.*

[9] We assume that biaxial strain is the most common type of strain present in exfoliated graphene.

The data in Fig. 5.17 allows an estimation of the coefficient which connects $\left[(\Omega_G - \Omega_G^0)^2 + (\Omega_{2D} - \Omega_{2D}^0)^2\right]^{1/2}$, the measured distance from the zero doping point, to a given doping level (see Fig. 5.17). We chose to consider n instead of E_F because it is a more relevant quantity as far as graphene characterization is concerned. Although the curves displayed in Fig. 5.17 are not expected to exhibit a linear scaling (as opposed to the data shown in Fig. 5.12), we observe a quasi-linear scaling for sufficiently small doping ($|n| \lesssim 7 \times 10^{12} \text{cm}^{-2}$). We therefore fit the linear part for both electron- and hole-doping with a line intercepting the zero doping point. We find slopes of 4.4×10^{11} cm^{-1} for electrons and -3.6×10^{11} cm^{-1} for holes, respectively.

Finally, considering the Grüneisen parameters of 1.8 and 2.4 for the Raman G- and 2D-modes under biaxial strain Ref. [Metten14], we can estimate a slope of 7.1×10^{-3} % strain/cm^{-1} to connect $\left[(\Omega_G - \Omega_G^0)^2 + (\Omega_{2D} - \Omega_{2D}^0)^2\right]^{1/2}$ to an applied biaxial strain. In practice, the strain field may be anisotropic, depending on the sample and on the experimental conditions, leading to a different slope.

In summary, the value of the slopes and coefficients that can be used in the decomposition method, described in Appendix D, are listed in Tab. 5.1. For a 2.33 eV excitation laser and supported graphene on Si/SiO_2, the statistical analysis on the thirty samples leads to a reference point for undoped and unstrained graphene of (1581 ± 0.5 cm^{-1}, 2673.6 ± 1 cm^{-1}). Note that the polymer electrolyte seems to induce no significant changes as compared to devices without top gate. All these values can be used for a reliable estimation of doping and strain in graphene samples and devices. In particular, it can be used to identify the nature of the doping (see Chapter 8) or to study the spatial variations of strain and doping within a sample using hyperspectral imaging. One must keep in mind that this method is only valid up to charge densities of approximately 7×10^{12} cm^{-2} for electron doping and 10^{13} cm^{-2} for hole doping.

	slope $\frac{\partial \Omega_{2D}}{\partial \Omega_G}$	Coefficients
Electron	0.2 ± 0.13	$+4.4 \times 10^{11}$ cm^{-1}
Hole	0.55 ± 0.2	-3.6×10^{11} cm^{-1}
Strain	2.2 ± 0.1	7.1×10^{-3} %/cm^{-1}

Table 5.1 *– Summary of the extracted values, from this work and [Metten14], that can be used to separate strain from electron and hole doping following the decomposition method described in Appendix D.*

5.5 Defective graphene

In Chapter 2, Fig. 2.5 shows the typical Raman spectrum of pristine and defective graphene. These two spectra were recorded at zero gate bias on the same point of the sample 1 before and after the creation of defects. Indeed, when an electrochemically gated graphene FET is subjected to a sufficiently high gate bias, electrochemical reactions may occur [Kalbac10, Efetov10, Bruna14] and create defects in the graphene channel. In our devices, a reaction

systematically occurs at negative gate biases ($V_{TG} \approx -1$ V to -2 V). The threshold voltage depends on the sample and on the gate capacitance. Electrochemical reactions result in an increase of the gate leak current above 1 nA, and in the emergence of defect-induced features in the Raman spectrum. Figure 5.18 illustrates this *in-situ* creation of defects during a sweep gate from +4 V to −3 V. Close to -1.7 V, we observe the emergence of an intense D-mode feature, a deformation and an increase of the intensity of the G-mode feature, and a drastic decrease of the intensity of the 2D-mode feature. At this point, the Raman spectrum resemble that of amorphous carbon [Ferrari00]. These observations suggest that sp3 bonds are probably formed. However, after a couple of hours at $V_{TG} = 0$, one obtains a spectrum similar to the one of defective graphene shown in Fig. 2.5.

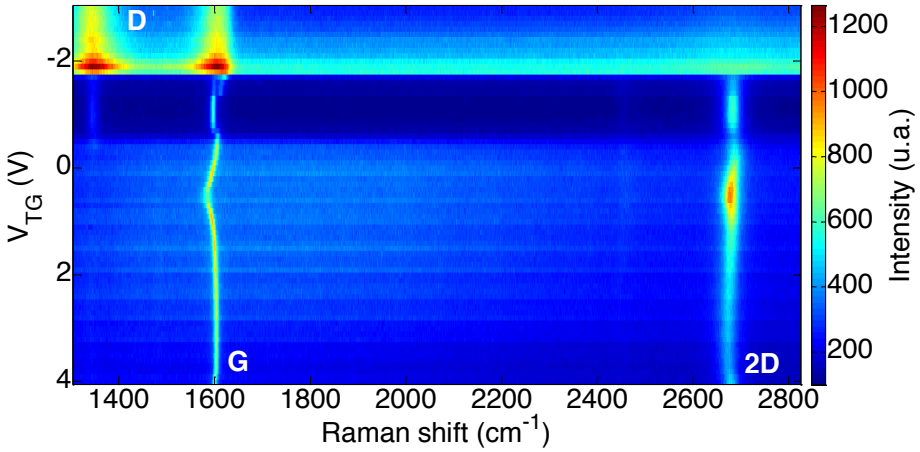

Figure 5.18 *– Color map of the Raman spectra of graphene monolayer (sample 1), measured using a 532 nm laser beam, as a function of the top-gate voltage V_{TG}. The top gate voltage was decreased from +4 V to −3 V.*

We took advantage of the created defects to investigate their effects on the G- and 2D-mode features. This comprehensive study is published in Physical Review B [Froehlicher15] and will not be detailed here. However, let us sum up the main results of this study. The defect concentration n_D can be estimated, independently of the type of defect, using the relation

$$n_D \approx 1.8 \times 10^{10} (\hbar\omega_L)^4 \left(\frac{I_D}{I_G}\right)_0, \tag{5.25}$$

where n_D is the concentration of defects in cm^{-2}, $\hbar\omega_L$ is the laser photon energy in eV and $\left(\frac{I_D}{I_G}\right)_0$ is taken at $|E_F| \lesssim 100$ meV. For defect concentration up to 1.4×10^{12} cm^{-2}, the evolution of the G- and 2D-mode features upon doping remain unaffected by the presence of defects and the doping dependence of the D mode closely follows that of its two-phonon (2D mode) overtone. Finally, at such defect concentrations, we estimate that the electron-defect scattering γ_D (see Eq. (5.22)) rate remains much smaller than the electron-phonon scattering rate. Consequently, in defective graphene, the ratio between the integrated intensity of the G- and 2D-mode features provides a fair estimate of $\gamma_{e\text{-}ph}$ from which λ_K can be extracted knowing λ_Γ. Table 5.2 summarizes the results obtained on the 5 samples studied here.

Sample	$\left.\frac{I_{2D}}{I_G}\right\|_{intr}$	$\left(\frac{I_D}{I_G}\right)_0$	n_D ($\times 10^{12}$ cm^{-2})	$\gamma_{e\text{-}ph} + \gamma_D$ (meV)	λ_Γ	λ_K
1 (w.o. D)	5.6	< 0.05	-	50	0.027	0.17
1 (w. D)	4.6	1.7	0.9	57	0.031	$\lesssim 0.20$
2 (w.o. D)	4.2	< 0.05	-	51	0.034	0.17
2 (w. D)	3.3	1.3	0.7	69	0.031	$\lesssim 0.24$
3	5.0	< 0.05	-	39	0.031	0.12
4	4.4	2.6	1.4	53	0.037	$\lesssim 0.18$
5	4.3	1.4	0.7	72	0.031	$\lesssim 0.25$

***Table 5.2** – Intrinsic integrated intensity ratio (corrected from interference effects, see Appendix C) $\left.\frac{I_{2D}}{I_G}\right|_{intr}$ at $E_F = 0$, measured integrated intensity ratio $\left(\frac{I_D}{I_G}\right)_0$ at $E_F = 0$, estimated defect concentration n_D, sum of the electron-phonon and electron-defect scattering rates, and dimensionless electron-phonon coupling constants at Γ and near $K^{(\prime)}$, for five different electrochemically gated graphene transistors. w. D and w.o. D stand for with without defects, respectively.*

5.6 Conclusion

In conclusion, we have presented a quantitative analysis of the doping dependence of the frequency, linewidth and integrated intensity of the main Raman features in pristine and defective graphene. The anomalous doping dependence of the G-mode phonons is well captured by theoretical models over a broad range of Fermi energies above or below the Dirac point, and provides an experimental measurement of the electron-phonon coupling constant at the Γ point of the Brillouin zone. We have then exploited the peculiar doping dependence of the integrated intensity of the resonant 2D-mode feature to estimate the electron-phonon coupling constant at the edges ($K^{(\prime)}$) of the Brillouin zone. We find that the electron-phonon coupling strength at Γ is five times weaker than at $K^{(\prime)}$.

This study provides useful guidelines for the characterization of graphene samples. We have, in particular, considered the correlation between the frequency and width of the G-mode feature, as well as between the frequencies of the 2D- and G-mode features. These correlations reveal **universal** behaviors that can therefore be applied to evaluate doping in a variety of experimental situations. We have also demonstrated that defects can be efficiently created *in-situ* in electrochemically gated graphene field effect transistors with concentrations up to approximately 1.4×10^{12} cm^{-2}. At such defect concentrations, we notice that the evolution of the G- and 2D-mode features upon doping remain unaffected by the presence of defects.

Finally, this work demonstrate that Raman spectroscopy can be accurately utilized to **locally** estimate the doping level in graphene. This technique will therefore be employed in Chapter 8 to monitor the charge transfer in graphene/transition metal dichalcogenides van der Waals heterostructures. In addition, we conservatively estimate that Fermi energies as

high as ≈ 700 meV above the Dirac point can be achieved in ambient conditions, without damaging graphene. This naturally opens exciting perspectives for the electrical control of the interlayer charge and energy transfer (see Chapter 2 Section 2.3.2) in optoelectronic devices.

Take home messages

- We developed very robust and efficient electrochemically-gated graphene field-effect transistors.
- Raman spectroscopy is a powerful tool to monitor the evolution of the quality of a sample.
- Raman spectroscopy is a highly sensitive tool to precisely estimate the doping level:
  - the measurements are quantitatively described by theoretical models,
  - universal correlations are very useful for advanced characterizations.

  Chapter 8 depicts an original utilization of this tool.

Related publications and communications

Papers

- D. Metten, G. Froehlicher and S. Berciaud, *Monitoring Electrostatically-Induced Deflection, Strain and Doping in Suspended Graphene using Raman Spectroscopy*, 2D Materials **4**, 014004 (2017).
- D. Metten, G. Froehlicher and S. Berciaud, *Doping- and interference-free measurement of I_{2D}/I_G in suspended monolayer graphene blisters*, pssb **252**, 2390-2394 (2015)
- G. Froehlicher, and S. Berciaud, *Raman spectroscopy of electrochemically gated graphene transistors: Geometrical capacitance, electron-phonon, electron-electron, and electron-defect scattering*, Phys. Rev. B **91**, 205413 (2015) - Editor's Suggestion.

Posters

- G. Froehlicher and S. Berciaud, *Electrochemically-gated graphene field effect transistors for optoelectronics*, GDRI Graphene and Nanotubes Annual meeting 2014, September 2014, Strasbourg, France.
- G. Froehlicher and S. Berciaud, *Electrochemically-gated graphene field effect transistors for optoelectronics*, Cargèse International School - Frontier Research in Graphene-based Systems, April 2014, Cargèse, France.

Chapter 6

Raman spectroscopy of N-layer transition metal dichalcogenides

In this chapter, we focus on the Raman response of N-layer transition metal dichalcogenides. These systems provide a unique platform to investigate the evolution of the physical properties between the bulk (three-dimensional) and the monolayer (quasi two-dimensional) limits. The evolution of these properties are of great interest for the applications as illustrated in Chapter 2. The results of the group theory analysis performed in Chapter 3 are fully utilized in this chapter. In a first part (Section 6.1), we investigate the Davydov splitting of all the Γ-point optical phonons in N-layer $MoTe_2$ and introduce a unified description of all these modes based on a force constant model that includes interactions up to the second nearest neighbor. To show the generality of this model, we also present the results obtained on N-layer $MoSe_2$. In a second part (Section 6.2), we show that a simplified force constant model accurately describes the low-frequency modes in any layered materials and provides a measurement of the strength of the van der Waals interlayer interactions. In a third part (Section 6.3), we give an alternative description of the frequency of the phonons by deriving it from the bulk phonon dispersion. In a last part (Section 6.4), we discuss the possible influence of resonance effects in all the measurements presented in the chapter. Note that this work was done in collaboration with the group of Ludger Wirtz *at the University of Luxembourg.*

6.1 Unified description of the phonon modes in N-layer transition metal dichalcogenides

In Chapter 3, we have introduced group theory and applied it to unveil the symmetry of the zone-center phonons in N-layer 2Hc TMDs. Interestingly, Eqs. (3.7) and (3.9) show that multiple phonons in N-layer TMDs have the same symmetry but different frequencies. All these different phonon modes with the same symmetry arise from the same monolayer mode. This observation is known as the **Davydov splitting**. The Davydov splitting (or factor-group splitting) is "the splitting of bands in the electronic or vibrational spectra

of crystals due to the presence of more than one (interacting) equivalent molecular entity in the unit cell" [Davydov71, McNaught97]. Such effect has been studied in polyaromatic molecules [Khelladi75] and thin films [Aroca87]. N-layer TMDs provide an ideal platform to investigate this splitting. Indeed, the unit cell contains N equivalent MX_2 entities (the three atoms of one layer) that are coupled via van der Waals interactions.

As shown in Chapter 3, Raman spectroscopy is an ideal technique to study such a splitting in N-layer TMDs. Up to now, the Davydov splitting has mainly been reported for the low-frequency modes in N-layer MoS_2 [Plechinger12, Zeng12, Zhao13, Zhang13, Boukhicha13] and WSe_2 [Zhang13]. These modes correspond to interlayer shear (LSM) and breathing (LBM) modes, which arise from the Davydov splitting of the zero frequency acoustic modes. Related splittings of the higher frequency modes involving intralayer atomic displacements have been reported in $N \leq 5$-layer $MoSe_2$ [Tonndorf13, Chen15] and WS_2 [Staiger15]. However, these splittings solely involve the out-of-plane Raman-active phonon with A_{1g} symmetry in the bulk, while other high-frequency modes, such as the in-plane phonon with E_{2g} symmetry in the bulk, exhibit anomalous N-dependent frequency shifts [Lee10, Li12a, Molina-Sánchez11, Luo13a, Luo13b, Tonndorf13, Berkdemir13, Yamamoto14], but no splitting.

In this section, we quantitatively investigate the Davydov splitting of all the Γ-point optical phonon modes, over the range $4-300$ cm^{-1}, in N-layer 2H $MoTe_2$, and provide a unified description of this splitting. This analysis can be generalized to other TMDs as we will show for $MoSe_2$.

6.1.1 Identification of the one phonon modes in N-layer $MoTe_2$

Using the symmetry analysis done in Chapter 3 Section 3.3, we have summarized in Table 6.1 the irreducible representations of the phonon modes for single-, bi-, N- layer and bulk $MoTe_2$. Taking into account the backscattering geometry of our experimental setup (see Chapter 3 Section 3.4.3), the bold characters denote Raman-active modes which in theory are observable.

Figure 6.1(a) shows the micro-Raman spectra of monolayer, bilayer and bulk $MoTe_2$ recorded at $E_L = 2.33$ eV for $\theta = 0$ (parallel configuration, XX) and $\theta = \pi/2$ (cross-polarized configuration, XY). We recall that polarized measurements allow to identify the in- and out-of-plane phonon modes (see Chapter 4 Section 3.4.3) since here out-of-plane modes are not visible in XY configuration.

We first address the **low-frequency** range below 40 cm^{-1}. In bulk $MoTe_2$, we observe only a single feature at 26 cm^{-1} that shows similar intensities in the XX and XY configurations. The latter is assigned to the in-plane interlayer shear mode (LSM) with E_{2g} symmetry [Wieting80]. For $N = 2$, we observe a prominent feature at 28 cm^{-1} that shows strong extinction in the XY polarization and a fainter feature at 18 cm^{-1} whose intensity is similar in the XX and XY configurations. The former is thus assigned to the out-of-plane layer breathing mode (LBM) with A_{1g} symmetry, while the latter is assigned to the LSM with E_g symmetry. The LBM has

Number of layers	LSM $\leqslant 30$ cm^{-1}	LBM $\leqslant 40$ cm^{-1}	iX ~ 120 cm^{-1}	oX ~ 170 cm^{-1}	iMX ~ 235 cm^{-1}	oMX ~ 290 cm^{-1}
1	–	–	E''	$\boldsymbol{A_1'}$	$\boldsymbol{E'}$	A_2''
2	$\boldsymbol{E_g}$	$\boldsymbol{A_{1g}}$	$\boldsymbol{E_g}$	$\boldsymbol{A_{1g}}$	$\boldsymbol{E_g}$	$\boldsymbol{A_{1g}}$
–	–	–	E_u	A_{2u}	E_u	A_{2u}
odd N	$\frac{N-1}{2}\boldsymbol{E'}$	$\frac{N-1}{2}\boldsymbol{A_1'}$	$\frac{N-1}{2}\boldsymbol{E'}$	$\frac{N+1}{2}\boldsymbol{A_1'}$	$\frac{N+1}{2}\boldsymbol{E'}$	$\frac{N-1}{2}\boldsymbol{A_1'}$
–	$\frac{N-1}{2}E''$	$\frac{N-1}{2}A_2''$	$\frac{N+1}{2}E''$	$\frac{N-1}{2}A_2''$	$\frac{N-1}{2}E''$	$\frac{N+1}{2}A_2''$
even N	$\frac{N}{2}\boldsymbol{E_g}$	$\frac{N}{2}\boldsymbol{A_{1g}}$	$\frac{N}{2}\boldsymbol{E_g}$	$\frac{N}{2}\boldsymbol{A_{1g}}$	$\frac{N}{2}\boldsymbol{E_g}$	$\frac{N}{2}\boldsymbol{A_{1g}}$
–	$\left(\frac{N}{2}-1\right)E_u$	$\left(\frac{N}{2}-1\right)A_{2u}$	$\frac{N}{2}E_u$	$\frac{N}{2}A_{2u}$	$\frac{N}{2}E_u$	$\frac{N}{2}A_{2u}$
bulk	$\boldsymbol{E_{2g}}$	B_{2g} ★	E_{1g}	$\boldsymbol{A_{1g}}$	$\boldsymbol{E_{2g}}$	B_{2g} ★
–	–	–	E_{2u} ★	B_{1u} ★	E_{1u}	A_{2u}

Table 6.1 *– Irreducible representations of the optical phonon modes at Γ for single-, bi-, N- layer and bulk $MoTe_2$. Bold characters denote Raman-active modes in a backscattering geometry. Note that modes with E_{1g} and E'' symmetry are Raman-active but not observable in a backscattering geometry [Loudon64] and that modes with E' are Raman- and infrared-active. Stars (★) denote silent modes. All the other modes are infrared active.*

B_{2g} symmetry in the bulk and is silent. As expected, we do not observe any interlayer mode for $N = 1$.

In the **mid-** (100–200 cm^{-1}) and **high-frequency** (200–300 cm^{-1}) ranges, the Raman spectra of bilayer $MoTe_2$ displays four one-phonon features, which have previously been identified as originating from the following intralayer displacements [Wieting80, Yamamoto14, Guo15a]:

(i) The in-plane, out-of-phase vibration of the Te planes, with E_{1g} symmetry in the bulk (iX mode, near 120 cm^{-1}).

(ii) The out-of-plane, out-of-phase vibration of the Te planes, with A_{1g} symmetry in the bulk (oX mode, near 170 cm^{-1}).

(iii) The in-plane vibration of the Mo and Te planes against each other, with E_{2g} symmetry in the bulk (iMX mode, near 230 cm^{-1}).

(iv) The out-of-plane vibration of the Mo and Te planes against each other, with B_{2g} symmetry in the bulk, (oMX mode, near 290 cm^{-1}).

The bulk iX and oMX modes are predicted to be Raman inactive in a backscattering geometry and silent (see Tab. 6.1), respectively. However, both modes appear as faint features in thick $MoTe_2$ flakes (considered as a bulk reference). This surprising observation, also reported

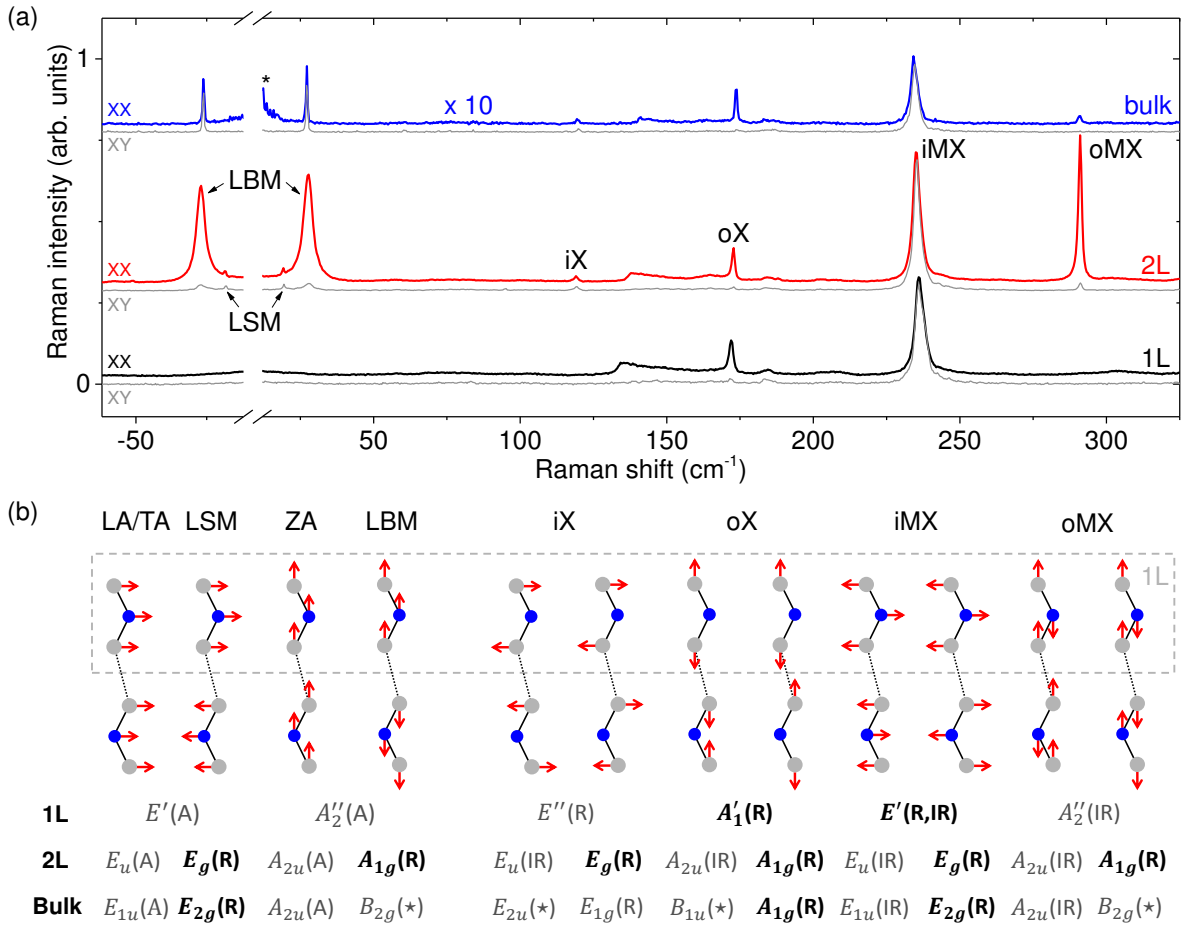

Figure 6.1 *– (a) Raman spectra of monolayer, bilayer and bulk $MoTe_2$ in the parallel (XX, thick colored solid lines) and perpendicular (XY, thin gray lines) polarization configuration. The spectra are vertically offset for clarity and the asterisk highlights residual contributions from the exciting laser beam. (b) Atomic displacements and irreducible representations associated with the Γ point phonon modes in monolayer, bilayer and bulk $MoTe_2$. The Raman (R) and/or infrared (IR) activity are indicated, and stars denote silent modes. The zero frequency acoustic modes (LA, TA, ZA) and their irreducible representations are also shown for clarity.*

recently on other TMDs might be a consequence of the finite penetration depth of our laser due to the strong optical absorption of $MoTe_2$ (see Appendix C Section C.2). As predicted, the iX and oMX modes are not observed in monolayer $MoTe_2$ and can thus be used as a robust criterion to identify MoTe2 monolayers. We verified that the oX and oMX features nearly vanish in the XY configuration, while the integrated intensities of the iX and iMX features do not change.

Finally, Fig. 6.1(b) illustrates the atomic displacements of these phonon modes in monolayer, bilayer and bulk. The Davydov splitting is clearly evidenced: one monolayer phonon mode gives rise to two bilayer phonon modes, in which the relative motion of equivalent atoms belonging to two adjacent layers is either in-phase or out-of-phase. This observation can be generalized to any number of layers: in a N-layer system each monolayer mode (LSM, LBM, iX, oX, iMX, oMX) gives rise to N modes with different optical activity (see Tab. 6.1). Note that since acoustic modes have a zero frequency, there are $N-1$ LSM and LBM.

6.1.2 Experimental spectra

Low-frequency modes

Figure 6.2 shows the evolution of the low-frequency modes (LSM and LBM) from $N = 2$ to $N =$ 12-layer $MoTe_2$. As previously reported in multilayer graphene [Tan12, Lui14] and recently in other TMDs, [Plechinger12, Zeng12, Zhao13, Boukhicha13, Zhang13, Chen15], a set of N-dependent low-frequency Stokes and anti-Stokes peaks appears for $N \geq 2$. The number of detected peaks increases with N and the peaks can be separated into branches that seemingly stiffen or soften with increasing N (see the dashed lines in Fig 6.2(a)). Interestingly, compared to a reference recorded in the XX configuration, the integrated intensity of peaks belonging to a branch that softens with increasing N drops by more than one order of magnitude in the XY configuration, while the integrated intensity of the peaks that belong to a branch that stiffens with increasing N is marginally affected (see Figs 6.2(b) and (c)). Therefore, the branches that soften (stiffen) with increasing N are assigned to the LBM (LSM). We are able to resolve two branches of LSM and, remarkably, five branches of LBM, i.e., the complete manifold of Raman-active LBM up to N=11 (see Tab. 6.1).

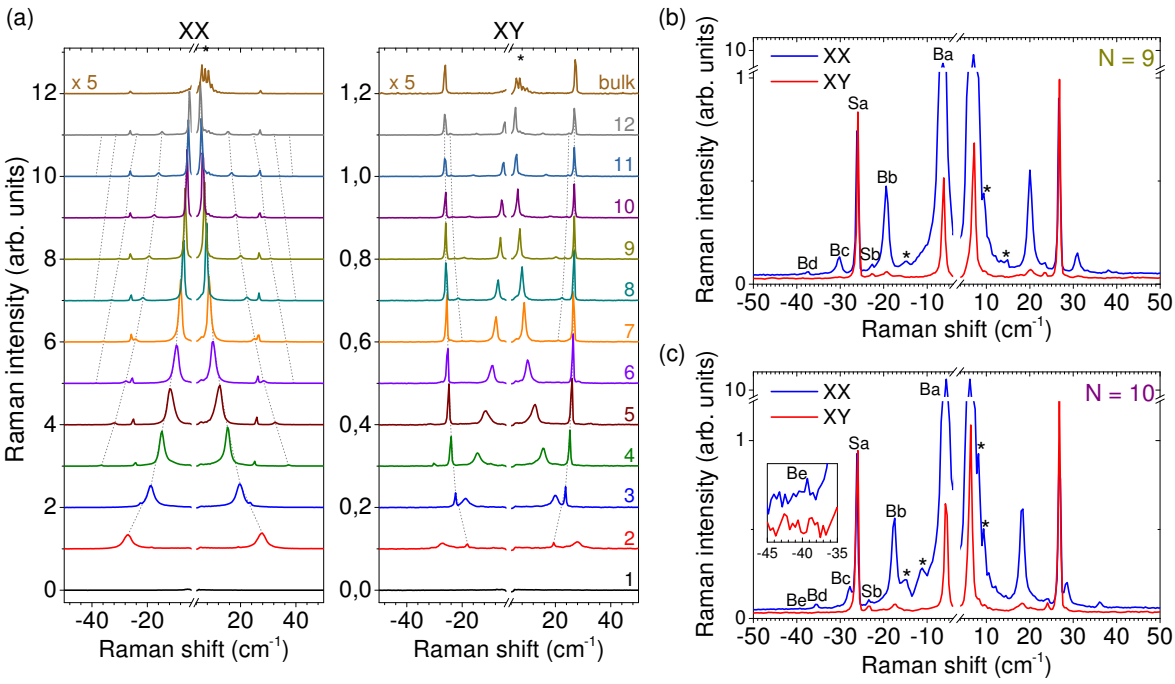

Figure 6.2 *– (a) Polarization-resolved low-frequency Raman spectra of $N = 1$ to $N = 12$-layer and of bulk $MoTe_2$, in the parallel (XX) and transverse (XY) configuration recorded at $E_L = 2.33$ eV. The interlayer breathing modes (LBM) largely dominate the spectra in the XX configuration and their intensity is reduced by more than one order of magnitude in the XY configuration. The shear modes (LSM) are not sensitive to the polarization configuration. The dashed lines follow the frequencies of each LSM and LBM. (b-c) Polarization-resolved low-frequency micro-Raman spectra of (b) $N = 9$ and (c) $N = 10$ layer $MoTe_2$ in the parallel (XX) and transverse (XY) configuration. The four (five) expected Raman-active LBM denoted Ba to Bd (Ba to Be) for $N = 9$ ($N = 10$) and two LSM denoted Sa and Sb are observed. The asterisks highlight residual contributions from the exciting laser beam.*

Mid- and hig-frequency modes

The Raman spectra of the mid- (iX, oX) and high-frequency (iMX and oMX) modes in N-layer $MoTe_2$ are shown in Fig. 6.3. For $N \geq 3$-layer $MoTe_2$, we observe a prominent splitting of the oX-mode feature (see Fig. 6.3(b)), while in the bulk limit, one recovers a single symmetric feature (assigned to the Raman-active A_{1g} mode). Interestingly, as shown in Fig. 6.3(a), the iX-mode feature also splits, but only for $N \geq 4$. We can resolve up to three subfeatures for $N = 6$ and 7, but the Raman signal in $N \geq 8$-layer $MoTe_2$ becomes too small to perform a quantitative analysis. At $E_L = 1.96$ eV, the oMX-mode feature also exhibits a modest splitting, on the order of 1 cm^{-1}, for $N \geq 4$. Two subpeaks can be distinguished. However, the evolution of their frequencies does not follow a specific trend as a function of N (see Fig. 6.3(d)). In contrast, the iMX-mode feature exhibits a faint shoulder on its high-energy side (see Fig. 6.3(c)), but no appreciable splitting can be resolved. However, the iMX feature downshifts as N increases, consistently with previous reports on N-layer TMDs [Lee10, Li12a, Molina-Sánchez11, Luo13a, Luo13b, Berkdemir13, Tonndorf13, Zhao13, Yamamoto14, Ruppert14].

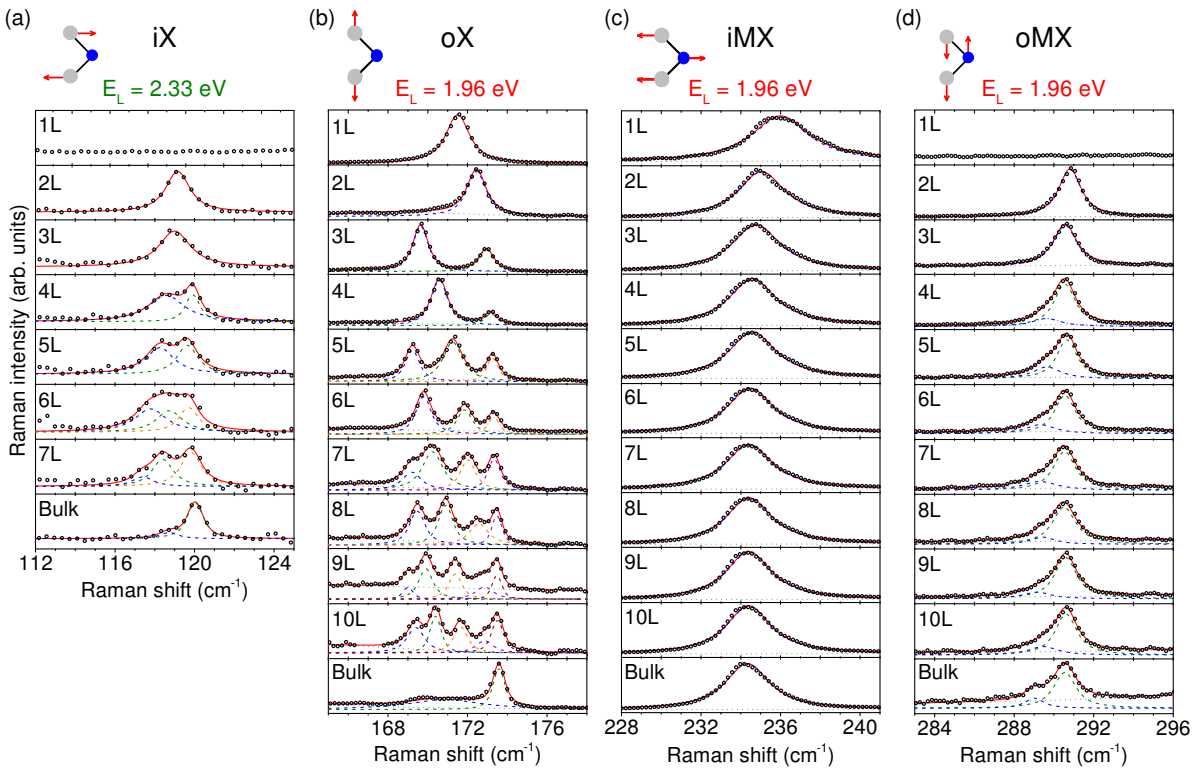

Figure 6.3 *– Normalized micro-Raman spectra of the (a) iX, (b) oX, (c) iMX, and (d) oMX mode-features in N-layer $MoTe_2$. The laser phonon energy E_L and the elementary intralayer displacements are indicated. The measured Raman features (symbols) are fit to Voigt profiles (solid lines). For the modes that show a Davydov splitting, each subpeak is represented with a colored dashed line. A featureless background (gray dashed line) has been considered when necessary.*

To sum up, in agreement with predicted Davydov splittings, the Raman measurements reveal that

(i) secondary LSM and LBM features appear for $N \geq 4$;

(ii) the oX feature splits for $N \geq 3$ and we observe $\lceil N/2 \rceil$ Raman active subfeatures in N-layer $MoTe_2$;

(iii) the splitting of the iX feature into $\lfloor N/2 \rfloor$ Raman active subfeatures is observed from $N \geq 4$;

(iv) a splitting of the oMX feature appears for $N \geq 4$.

The frequencies of all the measured Raman features, extracted from Voigt fits (see Figs. 6.2 and 6.3) are reported in Fig. 6.5. The Gaussian component is fixed in order to take into account our spectral resolution.

6.1.3 Force constant model

The model

To describe the observed splittings and frequency shifts of the phonon modes with increasing number of layers, we now introduce a semiempirical model. N-layer $MoTe_2$ is modeled as a **finite linear chain** composed of $2N$ Te atoms of mass per unit area μ_X and N Mo atoms of mass per unit area μ_M (see Fig. 6.4) [Luo13b]. Within one $MoTe_2$ unit nearest neighbor Mo and Te atoms and the pair of second nearest neighbor Te atoms are connected by springs with force constants per unit area α and δ respectively [Luo13b] (see Fig. 6.4). Interlayer interactions are then described by two force constants per unit area, β and γ, between nearest neighbor Te atoms belonging to adjacent layers and between second nearest neighbor Mo and Te atoms, respectively. In addition, finite size effects are known to lead to a slight reduction of the metal-chalcogen bond length on the outer layers (these effects are called **'surface effects'**) [Luo13b]. As a result, to improve our model, effective values $\alpha_e > \alpha$ and $\delta_e > \delta$ are phenomenologically considered for the first and N^{th} layer. We note that our choice of using the same value of α_e at both ends of the chain is consistent with the fact that no significant substrate-induced frequency shifts have been observed on the Raman response of $MoTe_2$ and other TMDs [Lee10, Yamamoto14, Luo13a, Luo13b, Zhao13].

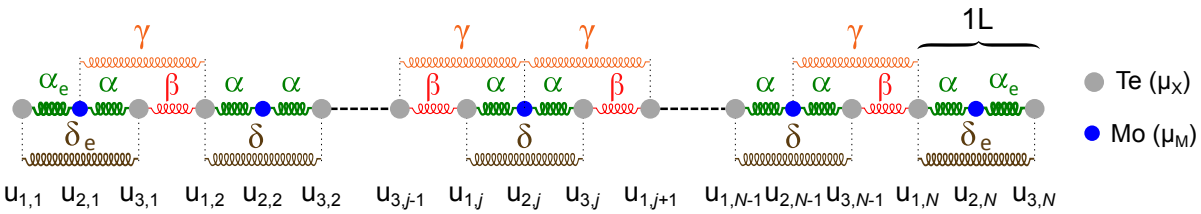

Figure 6.4 *– Schematic of the finite linear chain model. μ_X (μ_M) is the mass per unit area of the Mo (Te) atom. α and β are the force constants that connect the first nearest neighbor atoms. γ and δ are the force constants that connect the second nearest neighbor atoms. $u_{i,j}$ the displacement, with respect to the equilibrium position, of the i^{th} atom ($i = 1, 3$ for Te and $i = 2$ for Mo) in the j^{th} $MoTe_2$ layer ($j \in [\![1, N]\!]$).*

We define $u_{i,j}$ the displacement, with respect to the equilibrium position, of the i^{th} atom

($i = 1,3$ for Te and $i = 2$ for Mo) in the j^{th} $MoTe_2$ layer ($j \in [\![1,N]\!]$). From Newton's and Hooke's law, we can write $3N$ coupled differential equations which can be rewritten in matrix form

$$\frac{\mathrm{d}^2\mathcal{U}}{\mathrm{d}t^2} = -\mathcal{C}\,\mathcal{U}, \tag{6.1}$$

with the displacement vector $\mathcal{U} = \left(u_{1,1},\ u_{2,1},\ u_{3,1},\ \ldots,\ u_{i,j},\ \ldots,\ u_{1,N},\ u_{2,N},\ u_{3,N}\right)$ and the $3N \times 3N$ force constant matrix

$$\mathcal{C} = \begin{pmatrix}
\frac{\alpha_e+\delta e}{\mu_X} & -\frac{\alpha_e}{\mu_M} & -\frac{\delta_e}{\mu_X} & \cdots & 0 & 0 & 0 & 0 & 0 & \cdots & 0 & 0 & 0 \\
-\frac{\alpha_e}{\mu_X} & \frac{\alpha_e+\alpha+\gamma}{\mu_M} & -\frac{\alpha}{\mu_X} & \ddots & \vdots & \vdots & \vdots & \vdots & \vdots & \ddots & \vdots & \vdots & \vdots \\
-\frac{\delta_e}{\mu_X} & -\frac{\alpha}{\mu_M} & \frac{\alpha+\beta+\gamma+\delta_e}{\mu_X} & \ddots & \vdots & \vdots & \vdots & \vdots & \vdots & \ddots & \vdots & \vdots & \vdots \\
0 & -\frac{\gamma}{\mu_M} & -\frac{\beta}{\mu_X} & \ddots & \vdots & \vdots & \vdots & \vdots & \vdots & \ddots & \vdots & \vdots & \vdots \\
\vdots & 0 & -\frac{\gamma}{\mu_X} & \ddots & \vdots & \vdots & \vdots & \vdots & \vdots & \ddots & \vdots & \vdots & \vdots \\
\vdots & \vdots & 0 & \ddots & \vdots & \vdots & \vdots & \vdots & \vdots & \ddots & \vdots & \vdots & \vdots \\
\vdots & \vdots & \vdots & \ddots & 0 & \vdots & \vdots & \vdots & \vdots & \ddots & \vdots & \vdots & \vdots \\
\vdots & \vdots & \vdots & \ddots & -\frac{\delta}{\mu_X} & 0 & \vdots & \vdots & \vdots & \ddots & \vdots & \vdots & \vdots \\
\vdots & \vdots & \vdots & \ddots & -\frac{\alpha}{\mu_X} & -\frac{\gamma}{\mu_X} & 0 & \vdots & \vdots & \ddots & \vdots & \vdots & \vdots \\
\vdots & \vdots & \vdots & \ddots & \frac{\alpha+\beta+\gamma+\delta}{\mu_X} & -\frac{\beta}{\mu_X} & -\frac{\gamma}{\mu_M} & 0 & \vdots & \ddots & \vdots & \vdots & \vdots \\
\vdots & \vdots & \vdots & \ddots & -\frac{\beta}{\mu_X} & \frac{\alpha+\beta+\gamma+\delta}{\mu_X} & -\frac{\alpha}{\mu_M} & -\frac{\delta}{\mu_X} & 0 & \ddots & \vdots & \vdots & \vdots \\
\vdots & \vdots & \vdots & \ddots & -\frac{\gamma}{\mu_X} & -\frac{\alpha}{\mu_X} & 2\frac{\alpha+\gamma}{\mu_M} & -\frac{\alpha}{\mu_X} & -\frac{\gamma}{\mu_X} & \ddots & \vdots & \vdots & \vdots \\
\vdots & \vdots & \vdots & \ddots & 0 & -\frac{\delta}{\mu_X} & -\frac{\alpha}{\mu_M} & \frac{\alpha+\beta+\gamma+\delta}{\mu_X} & -\frac{\beta}{\mu_X} & \ddots & \vdots & \vdots & \vdots \\
\vdots & \vdots & \vdots & \ddots & \vdots & 0 & -\frac{\gamma}{\mu_M} & -\frac{\beta}{\mu_X} & \frac{\alpha+\beta+\gamma+\delta}{\mu_X} & \ddots & \vdots & \vdots & \vdots \\
\vdots & \vdots & \vdots & \ddots & \vdots & \vdots & 0 & -\frac{\gamma}{\mu_X} & -\frac{\alpha}{\mu_X} & \ddots & \vdots & \vdots & \vdots \\
\vdots & \vdots & \vdots & \ddots & \vdots & \vdots & \vdots & 0 & -\frac{\delta}{\mu_X} & \ddots & \vdots & \vdots & \vdots \\
\vdots & \vdots & \vdots & \ddots & \vdots & \vdots & \vdots & \vdots & 0 & \ddots & \vdots & \vdots & \vdots \\
\vdots & \vdots & \vdots & \ddots & \vdots & \vdots & \vdots & \vdots & \vdots & \ddots & 0 & \vdots & \vdots \\
\vdots & \vdots & \vdots & \ddots & \vdots & \vdots & \vdots & \vdots & \vdots & \ddots & -\frac{\delta}{\mu_X} & 0 & \vdots \\
\vdots & \vdots & \vdots & \ddots & \vdots & \vdots & \vdots & \vdots & \vdots & \ddots & -\frac{\beta}{\mu_X} & -\frac{\gamma}{\mu_M} & 0 \\
\vdots & \vdots & \vdots & \ddots & \vdots & \vdots & \vdots & \vdots & \vdots & \ddots & \frac{\alpha+\beta+\gamma+\delta}{\mu_X} & -\frac{\alpha}{\mu_M} & -\frac{\delta_e}{\mu_X} \\
\vdots & \vdots & \vdots & \ddots & \vdots & \vdots & \vdots & \vdots & \vdots & \ddots & -\frac{\alpha}{\mu_X} & \frac{\alpha_e+\alpha+\gamma}{\mu_M} & -\frac{\alpha_e}{\mu_X} \\
0 & 0 & 0 & \cdots & 0 & 0 & 0 & 0 & 0 & \cdots & -\frac{\delta_e}{\mu_X} & -\frac{\alpha_e}{\mu_M} & \frac{\alpha_e+\delta_e}{\mu_X}
\end{pmatrix}.$$

To find the zone-center (Γ) normal modes, one has to seek for sinusoidal solutions in the form $u_{i,j} = \varepsilon_{i,j}\mathrm{e}^{-\mathrm{i}\Omega t}$. For this kind of solutions, Eq. (6.1) becomes

$$\mathcal{D}\,\mathcal{E} = \Omega^2\,\mathcal{E}, \tag{6.2}$$

where $\mathcal{E} = \left(\varepsilon_{1,1}, \varepsilon_{2,1}, \varepsilon_{3,1}, \ldots, \varepsilon_{i,j}, \ldots, \varepsilon_{1,N}, \varepsilon_{2,N}, \varepsilon_{3,N}\right)$ is known as the **polarization vector** of the normal mode and $\mathcal{D} = \mathcal{C}$ is the **dynamical matrix** [Ashcroft76]. It is noteworthy that the dynamical matrix is equal to the force constants matrix only for zone-center (Γ) normal modes. The $3N$ normal modes of the finite linear chain, with eigenfrequencies Ω_p and normal displacements $\mathcal{E}_p$ ($p \in [\![1, 3N]\!]$), are obtained by diagonalizing the matrix $\mathcal{D}$.

Equation. (6.2) can be generalized to any wavevector q of the Brillouin zone. If $u_{i,j} = \varepsilon_{i,j} e^{-i(\Omega t - q x_{i,j})}$, the eigenvalue problem becomes [Ashcroft76]

$$\mathcal{D}(q)\,\mathcal{E} = \Omega(q)^2\,\mathcal{E}, \tag{6.3}$$

where $x_{i,j}$ is the equilibrium position of the i^{th} atom within the j^{th} layer and the dynamical matrix $\mathcal{D}(q)$ can be viewed as the representation of the force constant matrix in reciprocal space, since $\mathcal{C}$ implicitly depends on the equilibrium positions $x_{i,j}$. Knowing the force constant matrix $\mathcal{C}$, the dynamical matrix $\mathcal{D}(q)$ is given by

$$\mathcal{D}_{n,m}(q) = \mathcal{C}_{n,m} e^{ik(q_{k,l} - x_{i,j})}, \tag{6.4}$$

with $n = 3(j-1)+i$, $m = 3(l-1)+k$, and $i,k \in [\![1,3]\!]$ and $j,l \in [\![1,N]\!]$.

The in-plane and out-of-plane displacements are both described by Eq. (6.2) using two different set of force constants. Indeed, for in-plane (out-of-plane) displacements, Eq. (6.2) predicts three manifolds of N normal modes that correspond to (i) the low frequency LSM (LBM) (including the zero frequency acoustic mode) (ii) the mid-frequency iX (oX) modes and (iii) the high-frequency iMX (oMX) modes. Note that the in-plane phonon modes are doubly degenerate, thus only one set of parameters is enough to describe the $6N$ modes. Furthermore, except for the zero acoustic mode, one has

$$\sum_{j=1}^{N} \sum_{i=1}^{3} \mu_i\, \varepsilon_{i,j} = 0, \tag{6.5}$$

where $\mu_1 = \mu_3 = \mu_{\text{X}}$ and $\mu_2 = \mu_{\text{M}}$. This relation means that the center of mass of the N-layer system stays at rest [Michel12].

Bulk frequencies

Contrary to a finite number of layers, the frequencies of the bulk normal modes have a simple analytic expression. To take into account the infinite size of the crystal, we apply the Born von Kármán periodic boundary conditions. In this case, the unit cell of the one-dimensional Bravais lattice of this linear chain contains **the three atoms of one layer**.

For the n^{th} layer, we suppose that the equilibrium positions are nc for the Mo atom and $nc - d$ and $nc + d$ for the two Te atoms. Thus, Mo atoms belonging to adjacent layers are

separated by a distance c which is the lattice parameter of the linear chain.[1] We seek for solutions in the form of a plane wave with frequency Ω and wavevector q: $u_{j,n} = A_j e^{-i(\Omega t - qnc)}$ where $j = 1, 3$ for Te and $j = 2$ for Mo, and A_j are constants to be determined, whose ratio specify the relative amplitude and phase of vibration of the atoms within each layer. We emphasize that we are seeking for solutions not limited to zone center phonons (i.e., $q = 0$) for a reason that will become clearer below. By substituting $u_{j,n}$ into the equations of motion, we obtain three homogeneous equations in terms of A_j. These equations will have a non-zero solution provided that the determinant of the coefficients vanishes. This yields

$$\begin{aligned}\Big[\mu_X\Omega^2 - (\alpha+\beta+\gamma+\delta)\Big]^2\Big[\mu_M\Omega^2 - 2(\alpha+\gamma)\Big] \\ + (\alpha+\gamma e^{iqc})^2(\delta+\beta e^{-iqc}) + (\alpha+\gamma e^{-iqc})^2(\delta+\beta e^{iqc}) \\ - \Big[\mu_M\Omega^2 - 2(\alpha+\gamma)\Big](\delta+\beta e^{iqc})(\delta+\beta e^{-iqc}) \\ - 2\Big[\mu_X\Omega^2 - (\alpha+\beta+\gamma+\delta)\Big](\alpha+\gamma e^{iqc})(\alpha+\gamma e^{-iqc}) = 0. \quad (6.6)\end{aligned}$$

The Born von Karman boundary condition leads to N nonequivalent values of q given by $q = \frac{2\pi}{c}\frac{p}{N}$ with p an integer. In addition all the information is contained in the Brillouin zone, i.e. we can consider only wavevectors such that $q \in [-\frac{\pi}{c}, \frac{\pi}{c}]$. Eq. (6.6) does not need be solved for every q since we are only interested in phonons with $q = 0$. However, the real unit cell of the bulk crystal contains the six atoms of two layers and not the three atoms of one layer, i.e., the arrangement has a repeat distance $2c$ instead of c. Consequently, the reciprocal lattice changes from $c^*_{\text{old}} = \frac{2\pi}{c}$ to $c^*_{\text{new}} = \frac{\pi}{c}$. In the former lattice the border of the Brillouin zone was at $\frac{\pi}{c}$, now it is at half that distance. We must translate the pieces of dispersion relation for $|q| \in [\frac{\pi}{2c}, \frac{\pi}{a}]$, through a reciprocal lattice vector c^*_{new}. Hence, the frequencies of the six bulk normal modes are obtained by solving Eq. (6.6) for $q = 0$ and $q = \frac{\pi}{c}$. For $q = 0$ ($q = \frac{\pi}{c}$) the displacements of the three atoms within one layer are in-phase (out-of-phase) with the displacements of the atoms of adjacent layers. Using the symmetry of the atomic displacements, we can get the expression of the six bulk frequencies [Luo13b] associated with the low-frequency modes (LSM, LBM)

$$\Omega^-_{\text{low}} = 0, \quad (6.7)$$

$$\Omega^+_{\text{low}} = \frac{\alpha+\gamma+2\beta}{2\mu_X} + \frac{\alpha+\gamma}{\mu_M} - \sqrt{\left(\frac{\alpha+\gamma+2\beta}{2\mu_X} - \frac{\alpha+\gamma}{\mu_M}\right)^2 + 2\frac{(\alpha-\gamma)^2}{\mu_X\mu_M}}, \quad (6.8)$$

the mid-frequency modes (iX, oX)

$$\Omega^-_{\text{mid}} = \frac{\alpha+\gamma+2\delta}{\mu_X}, \quad (6.9)$$

$$\Omega^+_{\text{mid}} = \frac{\alpha+\gamma+2\delta+2\beta}{\mu_X}, \quad (6.10)$$

[1] Note that c is here the distance between two adjacent planes and not the lattice parameter of the bulk crystal.

and high-frequency (iMX, oMX) modes

$$\Omega^{-}_{\text{high}} = \frac{(2\mu_X + \mu_M)(\alpha+\gamma)}{\mu_X \mu_M}, \tag{6.11}$$

$$\Omega^{+}_{\text{high}} = \frac{\alpha+\gamma+2\beta}{2\mu_X} + \frac{\alpha+\gamma}{\mu_M} + \sqrt{\left(\frac{\alpha+\gamma+2\beta}{2\mu_X} - \frac{\alpha+\gamma}{\mu_M}\right)^2 + 2\frac{(\alpha-\gamma)^2}{\mu_X\mu_M}}. \tag{6.12}$$

It is striking to notice that these expressions give the force-constant dependence of the phonon modes: (i) the low-frequency modes depend on β and γ, (ii) the mid-frequency modes depend on α (α_e), β, γ and δ (δ_e), and (iii) the high-frequency modes depend on α (α_e), β and γ.

Since α is the only force constant that describes covalent bonds, its value is expected to be higher than the others. Thus assuming $|\alpha| \gg |\beta|, |\gamma|, |\delta|$, we can perform Taylor developments of Eqs. (6.8) and (6.12) to get more convenient expressions

$$\Omega^{+}_{\text{low}} \approx 4\frac{\beta+2\gamma}{\mu}, \tag{6.13}$$

$$\Omega^{+}_{\text{high}} \approx \frac{\alpha\mu^2 + 2\beta\mu_M^2 + \gamma(2\mu_X - \mu_M)^2}{\mu\mu_X\mu_M}, \tag{6.14}$$

where $\mu = 2\mu_X + \mu_M$ is the mass per unit area of the unit cell. The relative difference between the results of Eqs. (6.13)/(6.14) and the exact values obtained using Eqs. (6.8)/(6.12), respectively, is lower than 1 ‰for the parameters in Tab. 6.2.

An interesting quantity than can be deduced from the expressions of the bulk frequencies, for low-, mid- and high-frequency modes, is the bulk Davydov splitting $\Delta\Omega = \Omega^{+} - \Omega^{-}$. Again by performing Taylor expansions, we get the following expressions for the Davydov splitting

$$\Delta\Omega_{\text{low}} \approx 2\sqrt{\frac{\beta+2\gamma}{\mu}}, \tag{6.15}$$

$$\Delta\Omega_{\text{mid}} \approx \frac{\beta}{\alpha}\left(1 - \frac{\gamma+2\delta}{2\alpha}\right)\sqrt{\frac{\alpha}{\mu_X}}, \tag{6.16}$$

$$\Delta\Omega_{\text{high}} \approx \left(\frac{\mu_M^2}{\mu^2}\frac{\beta}{\alpha} - \frac{4\mu_X\mu_M}{\mu^2}\frac{\gamma}{\alpha}\right)\sqrt{\frac{\alpha\mu}{\mu_X\mu_M}}. \tag{6.17}$$

The deviation of the results of Eqs. (6.15) and (6.16) from the exact values deduced from Eqs. (6.7)-(6.10) is lower than 1%, and the deviation of the results of Eqs. (6.17) from the exact values deduced from Eqs. (6.11) and (6.12) is lower than 10 % for the parameters in Tab. 6.2.

Interestingly, the high-frequency Davydov splitting (Eq. (6.17)) is the only one that can be negative since $|\alpha| \gg |\beta|, |\gamma|, |\delta|$. If $\frac{\mu_M}{4\mu_X}\frac{\beta}{\gamma} \geq 1$, the splitting is normal and the bulk high-frequency in-phase mode has a lower frequency than the bulk high-frequency out-of-phase mode. Otherwise, the splitting is anomalous, as it has been reported for the iMX mode in bulk transition metal dichalcogenides [Wieting80].

Fitting procedure

The force constants are determined by fitting the experimental data. Since Eq. (6.2) gives the frequency of all the phonon modes, one has to sort the proper frequencies. First, the acoustic mode is easily identified. Second, using the eigenvectors and symmetry arguments, we can find the Raman-active modes in a backscattering geometry. For a N-layer system, the criteria are the following:

- For in-plane modes
  - if N is **even** then $\forall j \in \left[\!\left[1, \frac{N}{2}\right]\!\right]$ and $i \in [\![1,3]\!]$,

$$\varepsilon_{i,j} + \varepsilon_{4-i,N+1-j} = 0; \tag{6.18}$$

  - if N is **odd** then $\forall j \in \left[\!\left[1, \frac{N+1}{2}\right]\!\right]$ and $i \in [\![1,3]\!]$,

$$\varepsilon_{i,j} - \varepsilon_{4-i,N+1-j} = 0; \tag{6.19}$$

- For out-of-plane modes
  - if N is **even** then $\forall j \in \left[\!\left[1, \frac{N}{2}\right]\!\right]$ and $i \in [\![1,3]\!]$,

$$\varepsilon_{i,j} + \varepsilon_{4-i,N+1-j} = 0; \tag{6.20}$$

  - if N is **odd** then $\forall j \in \left[\!\left[1, \frac{N+1}{2}\right]\!\right]$ and $i \in [\![1,3]\!]$,

$$\varepsilon_{i,j} + \varepsilon_{4-i,N+1-j} = 0. \tag{6.21}$$

Third, since not all Raman-active modes are experimentally observed (e.g, we observe no splitting for the iMX feature), we have to select manually the observed frequencies within the Raman-active modes. Once the frequencies are selected, we use a least squares method to obtain the force constants.

6.1.4 Results of the fits

Force constants

The fan diagrams in Fig. 6.5 associated with the in-plane LSM, iX- and iMX-mode frequencies on the one hand, and out-of-plane LBM, oX- and oMX-mode frequencies on the other hand, are very well described by the force-constant model (red connected symbols in Fig. 6.5). The force constants (per unit area) used as fitting parameters are reported in Tab 6.2. We find that all the force constants correspond to a restoring force, except for the in-plane second nearest neighbor force constant between Te pairs. The values obtained here are qualitatively

similar to the values that Luo *et al.* reported for MoS_2 by fitting the bulk frequencies (obtained from calculations based on the local density approximation (LDA)) to a force constant model [Luo13b]. From a quantitative point of view, two important remarks have to be made:

(i) As supposed to obtain Eqs. (6.13)-(6.17), $|\alpha| \gg |\beta|, |\gamma|, |\delta|$.

(ii) A force constant model restricted to the first nearest neighbor interactions (i.e., $\gamma = \delta = 0$) suffices to fit the frequencies of the low- and mid-frequency modes, but would then fail to predict the frequencies of the oMX and iMX modes. Indeed, the second nearest neighbor interlayer (γ) and intralayer (δ) force constants are of the same order of magnitude and larger than the nearest neighbor interlayer force constant β, respectively.

	in-plane	**out-of-plane**
$\alpha(10^{19}\ \mathrm{N/m^3})$	105	159
$\alpha_e(10^{19}\ \mathrm{N/m^3})$	107	163
$\beta(10^{19}\ \mathrm{N/m^3})$	2.28	5.61
$\gamma(10^{19}\ \mathrm{N/m^3})$	0.585	1.11
$\delta(10^{19}\ \mathrm{N/m^3})$	-4.53	19.8
$\delta_e(10^{19}\ \mathrm{N/m^3})$	-4.22	20.4

***Table 6.2** – Force constants per unit area extracted from the fit of the experimental data to the finite linear chain model (see Eq. (6.2) and Fig. 6.5).*

Phonon frequencies and atomic displacements

Using the deduced force constants in Tab. 6.2, we were able to calculate **all** phonon modes (see Fig. 6.5) and the corresponding atomic displacements. Figure 6.6 represents the calculated displacements for $N = 4$ and $N = 5$ (see Appendix F for $N = 1$ to $N = 6$). Note that these displacements satisfy Eq. (6.5). In addition, we computed the bulk frequencies using Eqs.(6.7)-(6.12) (see gray dashed lines in Fig. 6.5). The non-zero low- and mid-frequency of the bulk modes are reported in Tab 6.3. We emphasize that we deduced the frequency of optical phonons that are silent in bulk crystals, namely the low-frequency interlayer breathing mode (LBM) with B_{2g} symmetry, and the mid-frequency in-plane (iX) and out-of-plane (oX) modes with E_{2u} and B_{1u} symmetry, respectively. The deduced bulk frequencies are in good agreement with frequencies obtained from *ab-initio* calculations (see Tab 6.3). These calculations were done by our collaborators at the University of Luxembourg. They used density functional perturbation theory (DFPT) [Baroni01] as implemented in the Quantum Espresso code [Giannozzi09], with the local-density approximation (LDA) which does not properly take into account van der Waals interaction between the layers. Nevertheless it gives decent results for the phonons of many layered systems because it overestimates the weak covalent part of the interlayer bonding.

We now discuss more carefully the results for the low-, mid- and high-frequency modes.

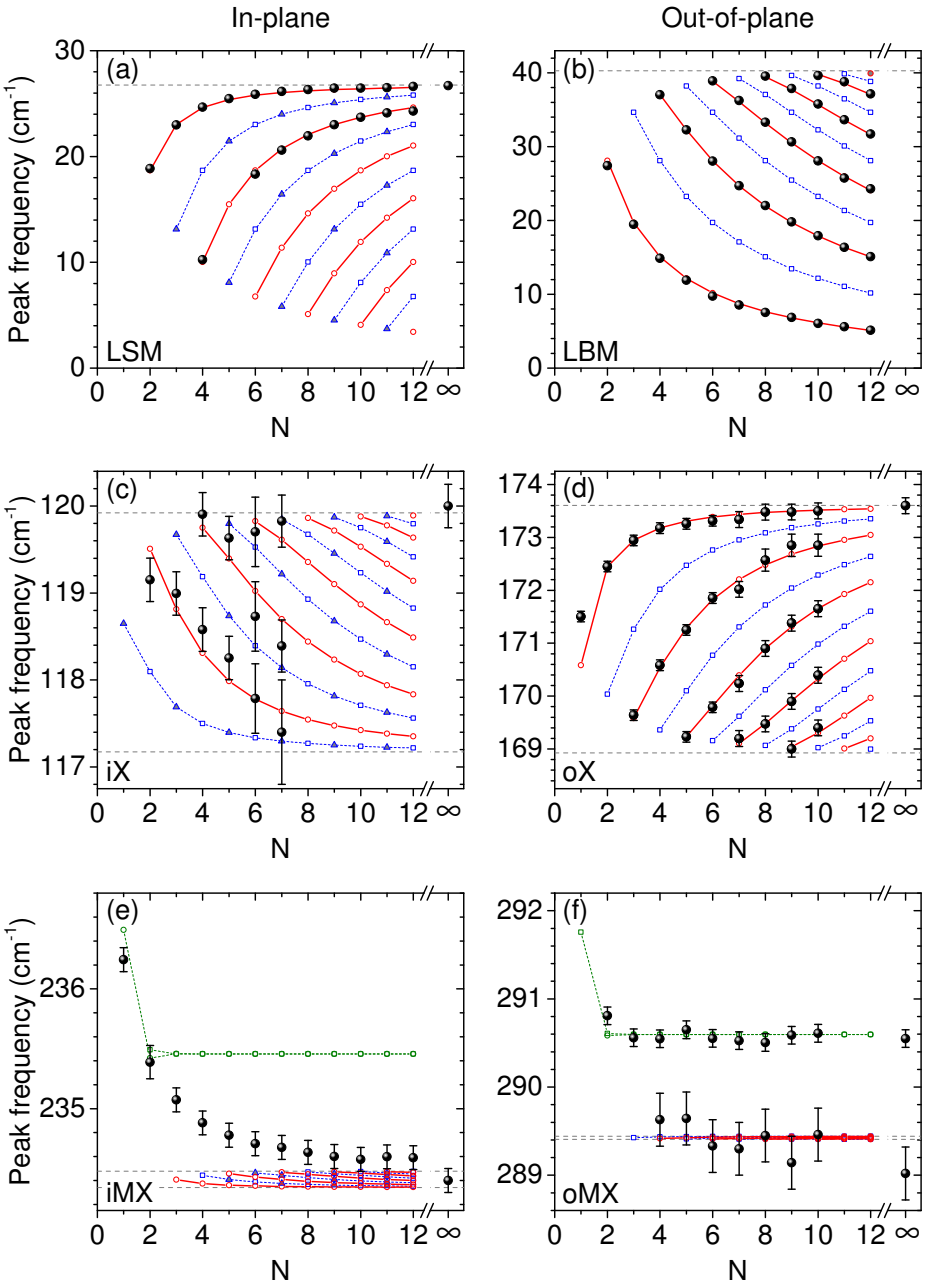

Figure 6.5 *– Frequencies of the (a) LSM (b) LBM (c) iX, (d) oX, (e) iMX, (f) oMX modes extracted from fits of the spectra displayed in Figs 6.2-6.3 (black circles) as a function of the number of layers N. The red open cirles in (a)-(f) are the frequencies of the Raman-active modes calculated by solving Eq.(6.2) with the fitting parameters in Tab. 6.2. The gray-filled triangles in (a), (c), (f) (resp. the open squares in (a)-(f)) are the frequencies of the E″ modes that are not Raman active in a backscattering geometry (resp. of the infrared-active modes) also predicted by Eq. (6.2) using the same fitting parameters. The solid and dashed lines connect the calculated frequencies and are guides to the eye. The upper and lower horizontal dotted lines in (a)-(b), (c)-(d), and (e)-(f) correspond to the bulk frequencies $\omega^{\pm}_{low}$, $\omega^{\pm}_{mid}$, and $\omega^{\pm}_{high}$, respectively (see also Tab. 6.2). The green open circles (squares) in (e) and (f) correspond to the Raman-active (infrared-active) surface modes (see also Fig. 6.6).*

Low-frequency modes The low-frequency branches of LSM and LBM are very well fit by this force constant model and that the LSM and LBM branches have opposite trends with

	in-plane		out-of-plane	
	exp.	**DFT**	**exp.**	**DFT**
$\omega^{+}_{\text{low}}(\text{cm}^{-1})$	26.755	27.2 (E_{2g})	40.289	37.5 (B_{2g}) ★
$\omega^{-}_{\text{mid}}(\text{cm}^{-1})$	117.17	116.4 (E_{2u}) ★	168.93	171.2 (B_{1u}) ★
$\omega^{+}_{\text{mid}}(\text{cm}^{-1})$	119.92	118.5 (E_{1g})	173.60	174.5 (A_{1g})
$\omega^{-}_{\text{high}}(\text{cm}^{-1})$	234.48	233.3 (E_{1u})	289.44	281.5 (A_{2u})
$\omega^{+}_{\text{high}}(\text{cm}^{-1})$	234.34	233.2 (E_{2g})	289.41	287.3 (B_{2g}) ★

Table 6.3 *– Bulk frequencies extracted from the fit of the experimental data (exp.) to the finite linear chain model (see dashed lines in Fig. 6.5) and from DFT calculations. Note that $\omega^{-}_{\text{low}} = 0$ for both in- and out-of-plane modes. The irreducible representations of the bulk phonon modes are indicated. Stars (★) denote silent modes.*

increasing N. These distinct trends can be weel understood using symmetry arguments. The eigenfrequencies increase (decrease) as the layers exhibit more out-of-phase (in-phase) relative motion, up to the limit of the highest- (lowest-) frequency mode, which corresponds to an out-of-phase (in-phase) oscillation for all layers.[2] From this analysis, we can readily conclude that the dominant LBM feature (Ba) corresponds, for even N to the out-of-phase oscillation of two blocks composed of $N/2$ layers that vibrate in-phase; for odd N to the out-of-phase oscillations of two blocks composed of $(N-1)/2$ layers that vibrate in-phase, while the central layer stays at rest. In contrast, the dominant LSM feature (Sa) corresponds to an out-of-phase displacement of adjacent layers as in bulk crystals [Michel12, Zhao13] (see Fig. 6.6).

Mid-frequency modes The mid-frequency Raman-active modes that are observable in our backscattering experiments correspond to the second-lowest, fourth-lowest,... frequency mode for the iX phonons and to the highest, third-highest,... frequency mode for the oX phonons. These distinct symmetry properties result in a set of **softening** and **stiffening** branches in the experimentally measured fan diagrams in Fig. 6.5(c) and 6.5(d), respectively. A remarkable validation of this symmetry analysis is that the highest frequency iX mode that can be observed has the highest frequency (E_g symmetry) for even N and the second highest frequency (E' symmetry) for odd N (see Fig. 6.6). As a result, the iX-mode frequency for $N = 3$ is lower than for $N = 2$, and the two observed iX-mode subfeatures for $N = 4$ are slightly upshifted relative to their counterparts recorded for $N = 5$ (see Figs. 6.3 and 6.5).

The bulk Davydov splitting is given by Eq. (6.16) which leads to the values of 2.7 cm^{-1} and 4.7 cm^{-1} for the iX and oX modes, respectively. These Davydov splittings are in good agreement with the ones deduced from *ab-initio* calculations. However, they are typically one order of magnitude smaller than the splittings of low-frequency modes. This is partly why Davydov splittings of mid-frequency modes have been scarcely studied. We also note that our model predicts a somewhat lower frequency for the oX (A'_1) mode in monolayer $MoTe_2$

[2] This trend is as expected from classical theories of coupled oscillators.

(see Fig. 6.5(d)). This discrepancy is due to a stronger bond length contraction in the limit of a monolayer [Luo13b], as compared to the bilayer or to the outer layers in $N \geq 2$-layer samples. That is why we do not fit the frequency of the monolayer.

High-frequency modes For iMX and oMX modes, the force constant model predicts very small **anomalous** Davydov splittings (below 0.2 cm^{-1}), which are consistent with previous studies of the iMX mode in bulk TMDs [Wieting80, Ghosh83, Molina-Sánchez11, Luo13b], and a critical influence of surface effects. Indeed we find that among the N iMX and oMX normal displacements, two modes predominantly involve atomic displacement of the first and/or N^{th} layer and can be regarded as **surface modes**. Such surface modes are not predicted for the iX and oX displacements (see Fig. 6.6). As a result, the surface terms α_e and δ_e, will only bring a small correction to the fan diagrams associated with the mid-frequency modes, but will shape the manifold of high-frequency phonon modes. For $N \geq 3$, the force constant model predicts a fan diagram for $N-2$ quasi-degenerate iMX and oMX modes, where atomic displacement chiefly occurs in the inner layers, and two surface modes (see Fig. 6.6 and Fig. 6.5). The strength of the surface effects will set the frequencies of the surface modes relative to that of the other modes.

iMX mode A tentative explanation for the pronounced downshift observed for the iMX mode is that the surface mode dominates for small N and that the modes arising from the inner layers provide most of the Raman intensity as N increases. To confirm this scenario our collaborators at the University of Luxembourg has performed calculations based on a bond polarizability model [Umari01], which was also recently used for layered BN and BN nanotubes [Wirtz05]. Such model can assign a Raman intensity to each Raman frequency obtained with the force constant model. The result of their calculations is that for the iMX mode there are two close peaks for $N \geq 3$. The lower in frequency corresponds to the quasi-degenerate inner mode and the higher being the surface mode. For increasing N, the absolute intensity of the quasi-degenerate inner mode increases almost linearly, as there are more modes, whereas the absolute intensity of the surface mode is independent of N, as only the outer layers are vibrating. In addition, the iMX-mode feature in N-layer $MoTe_2$ is appreciably broader (with a FWHM decreasing from 3.5 cm^{-1} for $N = 1$ down to 2.6 cm^{-1} in the bulk) than the iX, oX and oMX peaks, whose FWHM are approximately 1 cm^{-1}. This broadening prevents us from unveiling any splitting of the iMX-mode feature in N-layer $MoTe_2$, even between surface and inner modes where the frequency difference is smaller than 1 cm^{-1}. As a result, the relative intensity of the surface mode drops as N increases, and thus the maximum of the combined peak shifts to smaller frequencies as N increases. Therefore, for the fit of iMX, we have used the average frequency of all the Raman active mode. In that case, for increasing N, the number of quasi-degenerate inner modes increases, and thus their weight in the average increases. Finally, the Davydov splitting is anomalous and equal to 0.14 cm^{-1} according to the force-constant fit and to Eq. (6.17). *Ab initio* calculations (see Tab. 6.3) yield also a minimal anomalous Davydov splitting of 0.1 cm^{-1}.

oMX mode For the oMX mode, we also find that the surface modes have a slightly higher frequency than the modes localized on the inner layers. The bond polarizability model predicts that the surface mode has a much larger intensity than the inner modes irrespective of N. Supported by these results, we assign the dominant high-energy oMX subfeature to the surface mode, while the faint lower-energy shoulder is assigned to the quasi-degenerate inner modes. This is the criteria used to fit the oMX features to the force constant model. The deduced Davydov splitting is also anomalous and is equal to 0.04 cm^{-1}. *Ab-initio* calculations (see Tab. 6.3) yield a sizable (normal) Davydov splitting of 5.8 cm^{-1} between the bulk A_{2u} and B_{2g} frequencies. In order to reproduce this splitting, an additional force-constant between Mo atoms of neighboring layers should be introduced (which would not modify the splitting between the oX modes B_{1u} and A_{1g} modes because those modes do not involve motion of the Mo atoms). Since the resulting fan-diagram is not visible in the experimental spectra of the oMX mode, we did not include this additional force constant here.

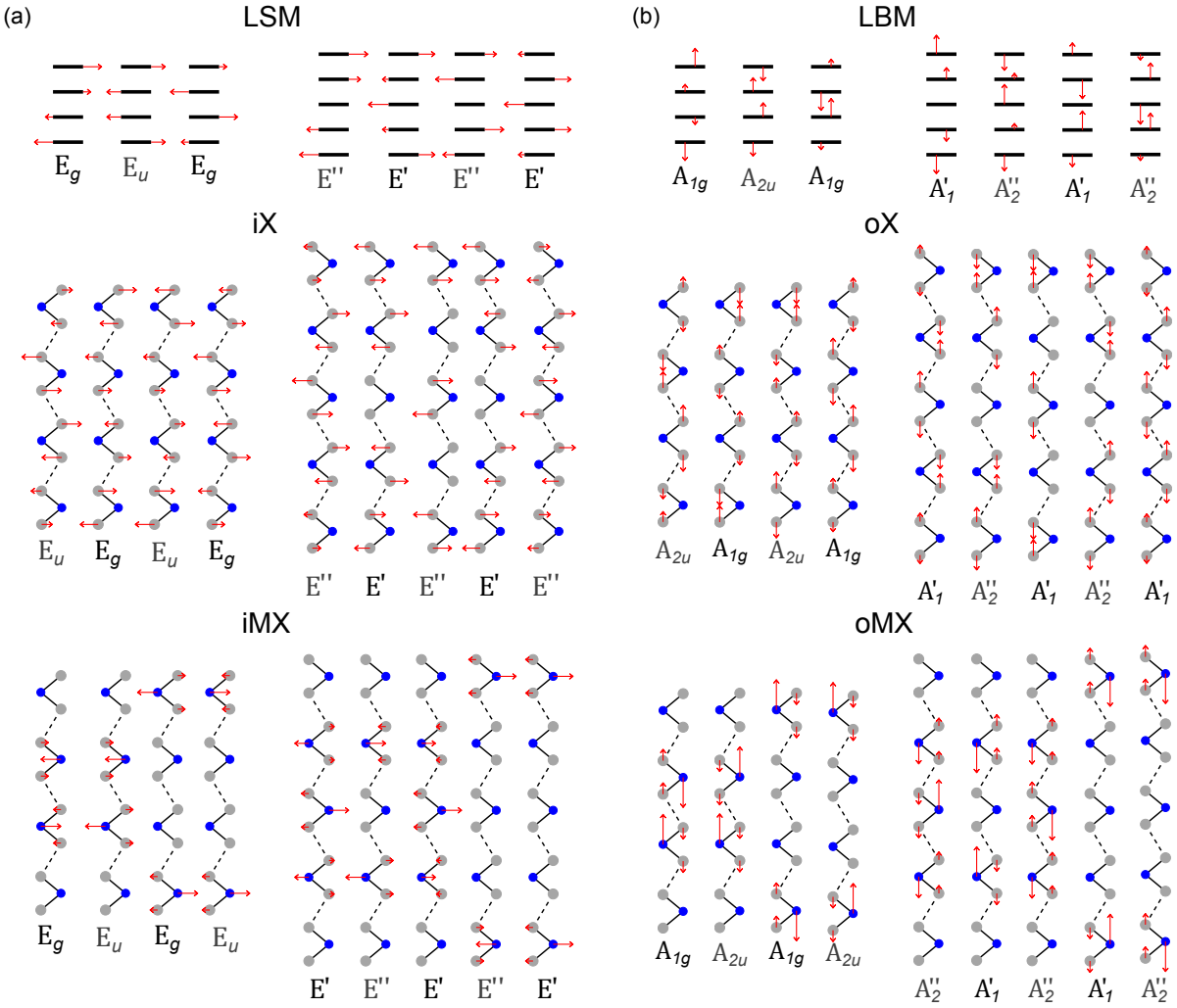

Figure 6.6 *– Calculated normal displacements associated with all the in-plane (a) and out-of-plane (b) optical phonon modes in $N = 4$ and $N = 5$ layer $MoTe_2$. The size of the arrows is proportional to the amplitude $\varepsilon^p_{i,j}$ of the normal displacement obtained from the solution of Eq. (6.2). At a given N, the mode frequencies increase from left to right. The irreducible representation of each normal mode is indicated.*

6.1.5 Generalization: the case of $MoSe_2$

To show the generality of our model, we have also studied N-layer $MoSe_2$. The results were analyzed with the help of two Master 1 students under my supervision: Edurne Iriondo and Minghao Li. As already mentioned at the beginning of this section, Davydov splittings of mid-frequency modes have been previously reported in N-layer $MoSe_2$ [Tonndorf13, Chen15]. Very recently, following our work on $MoTe_2$, Kim *et al.* have reported a unified description of the optical phonons in N-layer $MoSe_2$ [Kim16] which can be compared to our results.

Raman spectra of $N = 1$ to $N = 8$ layer $MoSe_2$ and of bulk $MoSe_2$ were recorded in similar conditions as N-layer $MoTe_2$ at the two same photon energies: $E_L = 1.96$ eV and $E_L = 2.33$ eV. However, the result presented here were all obtained at $E_L = 2.33$ eV as Davydov splitting are more visible at this energy (see Section 6.4).

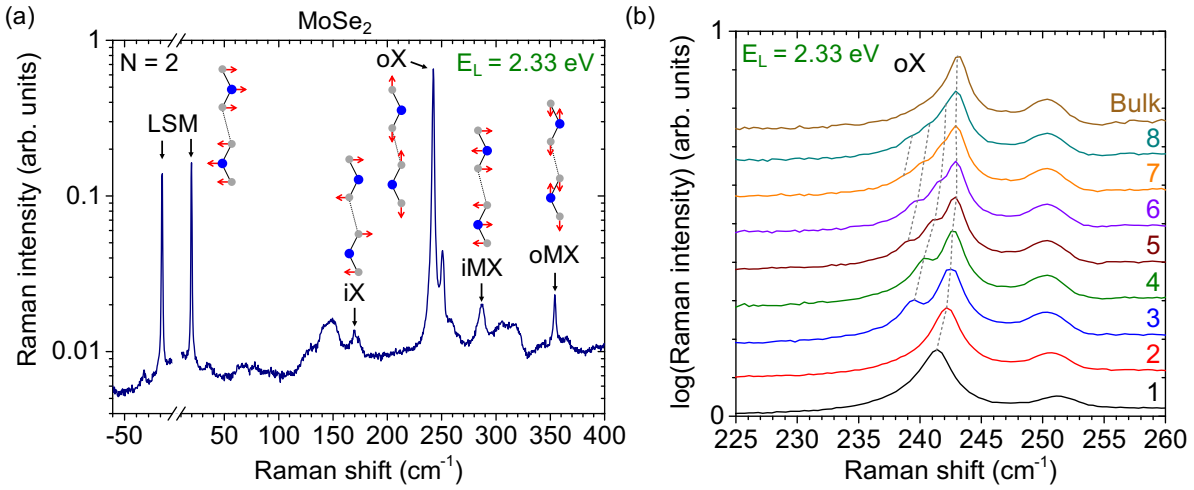

Figure 6.7 *– (a) Raman spectrum of bilayer $MoSe_2$. The one-phonon modes are identified and labeled (except the LBM). The corresponding atomic displacement are sketched. (b) Raman spectra of the oX-mode features of $N = 1$ to $N = 8$ layer $MoSe_2$ and of bulk $MoSe_2$. The gray dashed lines are guide to the eye to distinguish the subfeatures. Note that we have plotted the* log *of the spectra to highlight the subpeaks. The spectra are vertically offset for clarity.*

Figure 6.7(a) shows the Raman spectrum of a bilayer $MoSe_2$. We identified the one-phonon modes with the help of Ref. [Soubelet16] and labeled them with the same notation as for N-layer $MoTe_2$. We observe the same modes but with some discrepancies:

(i) We identified only one LBM branch (and no LBM for $N = 2$) while we observed three LSM branches (i.e., all the LSM except the lowest one for $N = 7$).

(ii) The iX mode is only visible for $N = 2$ and $N = 3$ but we observed all the oX subfeatures as displayed in Fig. 6.7(b).

(iii) We noticed no splitting for the high-frequency modes.

The frequencies of all the measured Raman features, extracted from Voigt are reported in

Fig. 6.8.

We use the force constant model developed previously to fit these frequencies. As for N-layer $MoTe_2$ (see Fig. 6.5), the fan diagrams are very well described by the force-constant model. The force constants (per unit area) used as fitting parameters are reported in Tab 6.4 and should be compared to the values in Tab 6.2 for N-layer $MoTe_2$. We find comparable values for both materials. In particular, the in-plane second nearest neighbor force constant between Se pairs (δ) is also negative. Note that for the iMX and oMX modes, we used the average of all the Raman-active modes, and that for the in-plane modes we did not use δ_e as there are only two points which might not be enough to obtain a significant value of δ_e. The deduced bulk frequencies are in very good agreement with the measured one and the Davydov splittings are similar to $MoTe_2$. Interestingly, the Davydov splitting of the high-frequency modes of $MoSe_2$ is found to be normal while it is anomalous in $MoTe_2$ and no clear surface modes were identified. A direct consequence is that the frequency trends of iMX and oMX subfeatures are the opposite of $MoTe_2$.

The results obtained by Kim *et al.* [Kim16] are also displayed in Tab 6.4. We notice that all values very consistent with ours. In particular, they also observe a normal Davydov splitting for the high-frequency modes. However, the frequency difference is obviously too small to draw a clear conclusion.

	in-plane		out-of-plane	
	This work	**[Kim16]**	**This work**	**[Kim16]**
$\alpha(10^{19}\ \mathrm{N/m^3})$	152	152	232	229
$\alpha_e(10^{19}\ \mathrm{N/m^3})$	154	155	234	235
$\beta(10^{19}\ \mathrm{N/m^3})$	2.34	1.82	5.24	5.47
$\gamma(10^{19}\ \mathrm{N/m^3})$	0.324	0.55	1.43	1.63
$\delta(10^{19}\ \mathrm{N/m^3})$	-6.88	-6.80	24.0	25.3
$\delta_e(10^{19}\ \mathrm{N/m^3})$	-6.88	-6.70	25.5	25.3
$\omega^+_{low}(\mathrm{cm^{-1}})$	27.40	27.09 (E_{2g})	45.09	46.80 (B_{2g}) ★
$\omega^-_{mid}(\mathrm{cm^{-1}})$	167.7	167.7 (E_{2u}) ★	238.7	238.5 (B_{1u}) ★
$\omega^+_{mid}(\mathrm{cm^{-1}})$	170.5	169.9 (E_{1g})	243.1	243.1 (A_{1g})
$\omega^-_{high}(\mathrm{cm^{-1}})$	289.0	285.8 (E_{1u})	353.7	351.4 (A_{2u})
$\omega^+_{high}(\mathrm{cm^{-1}})$	286.3	285.8 (E_{2g})	353.8	351.4 (B_{2g}) ★

Table 6.4 *– Force constants per unit area and corresponding bulk frequencies extracted from the fit of the experimental data to the finite linear chain model (see Eq. (6.2) and dashed lines in Fig. 6.8) for $MoSe_2$. Note that $\omega^-_{low} = 0$ for both in- and out-of-plane modes. The irreducible representations of the bulk phonon modes are indicated. Stars (★) denote silent modes.*

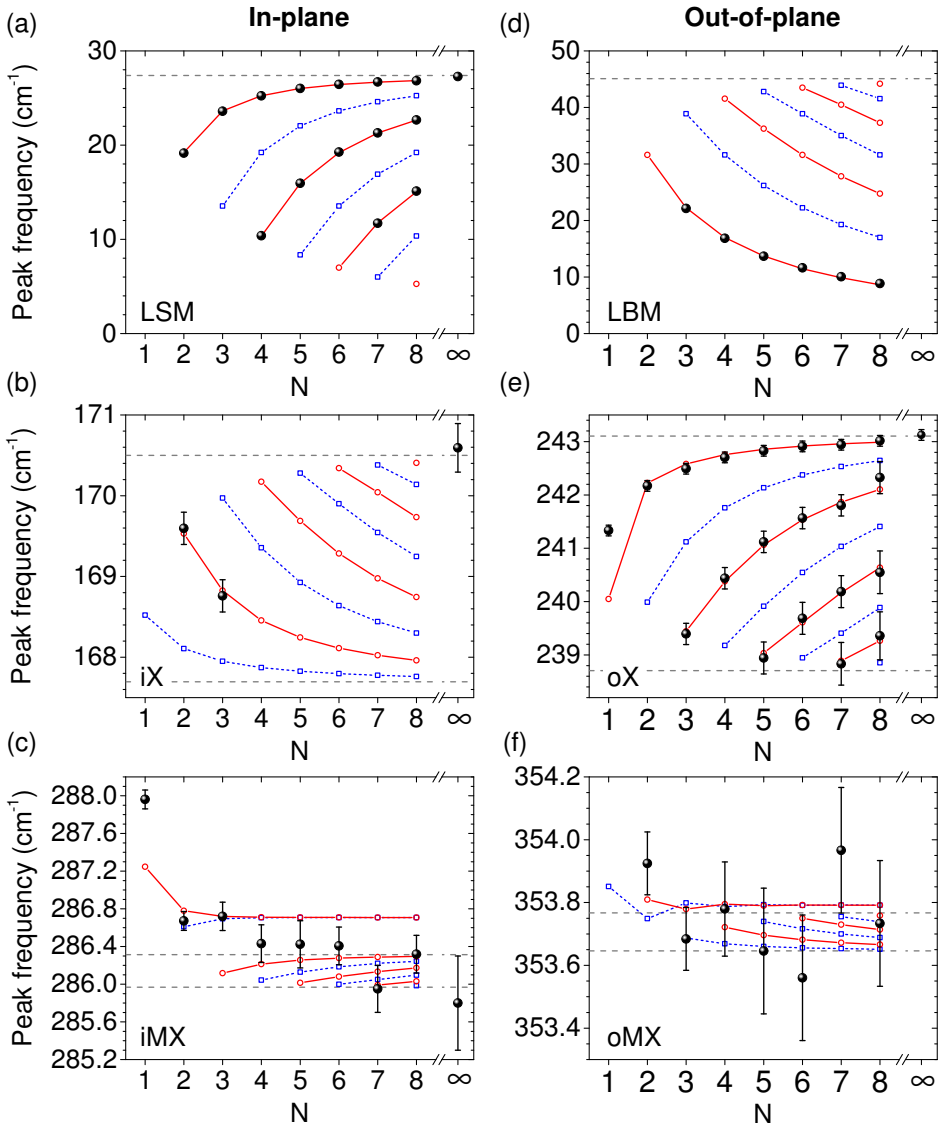

Figure 6.8 *– Frequencies of the (a) LSM (b) LBM (c) iX, (d) oX, (e) iMX, (f) oMX modes extracted from fits of the N-layer $MoSe_2$ spectra (black circles) as a function of the number of layers N. The red open cirles in (a)-(f) are the frequencies of the Raman-active modes calculated by solving Eq.(6.2) with the fitting parameters in Tab. 6.4. The open-squares in (a)-(f) are the frequencies of the E'' modes that are not Raman active in a backscattering geometry and the infrared-active modes also predicted by Eq. (6.2) using the same fitting parameters. The solid and dashed lines connect the calculated frequencies and are guides to the eye. The upper and lower horizontal dotted lines in (a)-(b), (c)-(d), and (e)-(f) correspond to the bulk frequencies $\omega^{\pm}_{low}$, $\omega^{\pm}_{mid}$, and $\omega^{\pm}_{high}$, respectively (see also Tab. 6.4).*

6.2 A simplified description of the low-frequency modes

In this section, we present a simplified description of the low-frequency modes that can be employed for any layered materials. This simplified description opens very interesting perspectives to accurately determine the number of layers and to easily extract the strength of the van der Waals interlayer interactions. To shed light on the universality of this model, we will compare the results obtained in our group on different materials: 2Hc $MoTe_2$, $MoSe_2$,

WS_2 and WSe_2, and distorted octahedral 1T' phase ReS_2 and $ReSe_2$. The latter two display much lower symmetry and significant in-plane anisotropy due to covalent bonding between Re atoms leading to quasi one-dimensional Re chains [Ho97, Ho98, Ho04, Tiong99].

6.2.1 Frequency of the LSM and LBM

As for N-layer $MoTe_2$, the frequencies of the LSM and LBM were extracted from fits with Voigt profiles and are displayed in Fig. 6.10. Note that the branches have been identified by polarized measurements for the 2H materials and by the fact that the LSM are split for the 1T' ReX_2 due to the in-plane anisotropy [Lorchat16]. The LBM and LSM branches are denoted by Ba, Bb,... and Sa, Sb,..., respectively. First of all, we notice that the frequencies of the different crystals have the same order of magnitude. We observe that for ReX_2 both LSM and LBM decrease as N increases, in contrast to the case of MoX_2 and WX_2. This observation can be explained by a simple symmetry analysis knowing that the 1T' structure has no mirror symmetry plane but preserves an inversion center for any value of N. Consequently, for both LSM and LBM, the frequency modes that can be observed have the highest frequency, with A_g symmetry, for $N = 2$ and the second highest frequency, with also A_g symmetry, for $N = 3$. As a result, the LSM and LBM frequencies for $N = 3$ are lower than for $N = 2$, and so on for increasing N [Lorchat16]. In contrast, N-layer 2H compounds exhibit a mirror symmetry plane (but no inversion center) for odd N and an inversion center (but no mirror symmetry plane) for even N (see Chapter 3 Section 3.3). Therefore, for the LSM (LBM), the frequency modes that can be observed have the highest frequency, with E_g (A_{1g}) symmetry, for $N = 2$ and the (second) highest frequency, with E' (A_2''), for $N = 3$. In consequence, the LSM (LBM) frequency for $N = 3$ is higher (lower) than for $N = 2$ (see Tab. 6.1 and Fig. 6.6).

6.2.2 Hyperspectal Raman imaging

The observation of a well-defined, N-dependent series of LBM and LSM opens very interesting perspectives for hyperspectral Raman imaging. In Fig. 6.9(a), we present an optical image of a $MoTe_2$ crystal containing domains with N ranging from $N = 2$ to $N = 13$. The number of layers is readily identified by atomic force microscopy (Fig. 6.9(b)) and the height difference between two $MoTe_2$ layers is measured to be ~ 0.6 nm, in agreement with previous studies [Böker01, Ruppert14, Yamamoto14, Lezama15]. Note that the step between the Si/SiO_2 substrate and $N = 2$ might be due to changes in the tip-surface interaction between the substrate and the sample [Nemes-Incze08] or to the presence of adsorbates under the sample [Lee10]. In Fig. 6.9(c), we plot the hyperspectral map of the frequency ω_{Ba} of the lowest energy and most intense LBM (see Fig. 6.2). This map readily allows one to distinguish N-layer domains, up to $N \approx 10$ with a high contrast. One can also map out the Raman scattering intensity at a given shift. By selecting the Raman shifts that correspond to the Ba mode frequency of a N-layer specimen, we can then selectively image all the N-layer domains with an unprecedented contrast as illustrated in Fig. 6.9(d)-(o). Such a high contrast arises chiefly from the strong enhancement of the LBM features (especially for the Ba branch) and to the

fact that the Ba branch is spectrally well separated from the other LBM and LSM modes. In principle, such hyperspectral imaging can be applied to any TMDs providing that there is a spectrally well separated and intense enough branch. Note that it may also be possible to combine different branches.

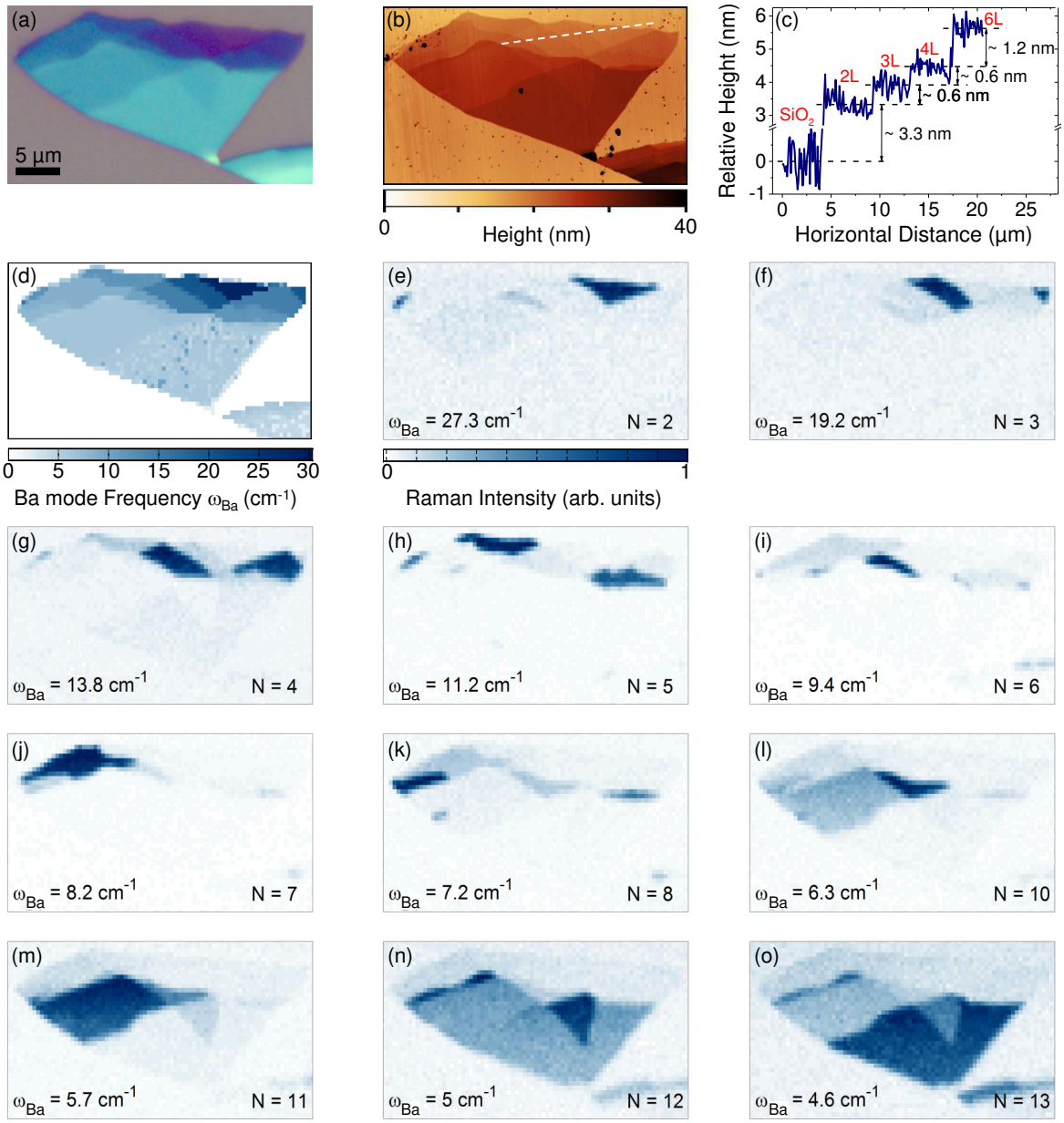

Figure 6.9 *– Optical (a) and atomic force microscopy (AFM) (b) images of a $MoTe_2$ flake. A height profile along the white dashed-line shown in the AFM image is shown in (c). (d) Hyperspectral map of the frequency of the most prominent interlayer breathing mode feature (denoted Ba in Fig.6.2). (e-o) Hyperspectral maps of the integrated Raman intensity at selected frequencies that correspond to the frequency of the Ba feature at a given value of N.*

6.2.3 A simplified force constant model

For the low-frequency modes, the displacements of the atoms within one layer are the same. Consequently, the bond lengths within one layer remain unchanged and the LSM and LBM can be modeled using a linear chain of N-oscillators, where one layer is treated as a rigid mass unit with a mass $\mu = 2\mu_X + \mu_M$, where μ_X is the mass per unit area of the chalcogen atom and μ_M of the metal atom. In other words, van der Waals interactions between adjacent layers are, in first approximation, sufficient to accurately describe the series of interlayer modes without further consideration of the in-plane crystal structure and intralayer force constants [Tan12, Michel12, Zhao13, Zhang13, Boukhicha13].

Contrary to the full force constant model developed in subsection 6.1.3, this simpler model has analytic expressions for the eigenfrequencies and eigenvectors. Let us consider a finite linear chain of N identical masses μ (numbered from 1 to N) connected to each other by identical springs of force constant κ. The normal modes, such that the displacement of the i^{th} mass is $u_i^p = \varepsilon_i^p e^{-i\Omega_p t}$, can be calculated analytically (see Appendix E) and yield

$$\Omega_p = \sqrt{\frac{2\kappa}{\mu}\left[1 - \cos\left(\frac{(p-1)\pi}{N}\right)\right]} \text{ with } p \in [\![1, N]\!], \tag{6.22}$$

$$\varepsilon_i^p = \begin{cases} \frac{1}{\sqrt{N}} & \text{if } p = 1, \\ \sqrt{\frac{2}{N}} \cos\left(\frac{(p-1)(2i-1)\pi}{2N}\right) & \text{if } p \in [\![2, N]\!], \end{cases} \tag{6.23}$$

Note that ε_i^p is normalized to unity since the eigenvectors are defined up to a constant multiplier. $p = 1$ corresponds to the acoustic mode with a zero frequency and a center of mass not at rest. For $N = 2$, the non-zero frequency is $\Omega = \sqrt{\frac{2\kappa}{\mu}}$ and the non-zero bulk frequency is $\Omega^+ = \sqrt{\frac{4\kappa}{\mu}}$. These two expressions can be deduced from simple considerations. For $N = 2$, the problem is equivalent to a spring-mass system with a reduced mass $\mu/2$ and a spring κ. Such oscillator has a frequency $\Omega = \sqrt{\frac{2\kappa}{\mu}}$. For the bulk, the two masses are connected by two springs of force constant κ because of the boundary condition. This system is equivalent to one oscillator with a reduced mass $\mu/2$ and a spring 2κ which frequency is $\Omega = \sqrt{\frac{4\kappa}{\mu}}$.

We use this simplified model to describe the observed frequencies. Using Eq. (6.23), we globally fit the LSM and LBM branches with the shear (κ_S) and breathing (κ_B) force constants as the only fitting parameter. The observed Raman-active modes correspond to branches with (i) $p = N,\ N-2,\ N-4, \ldots$ for the LSM Sa, Sb, Sc, ... and (ii) $p = 2,\ 4,\ 6, \ldots$ for the LBM Ba, Bb, Bc, ... We obtain excellent agreement for all the materials we consider here (see Fig. 6.10). The resulting force constants are reported in Tab. 6.5 and compared to measurements on other layered materials found in the literature. Despite different compounds and crystal structure, we notice that the interlayer force constant are all very close. As a result, the low-frequency phonon modes can be viewed as vibrations of **rigid** layers, independent of their composition and structure. In addition, in all these layered materials, the van der Waals

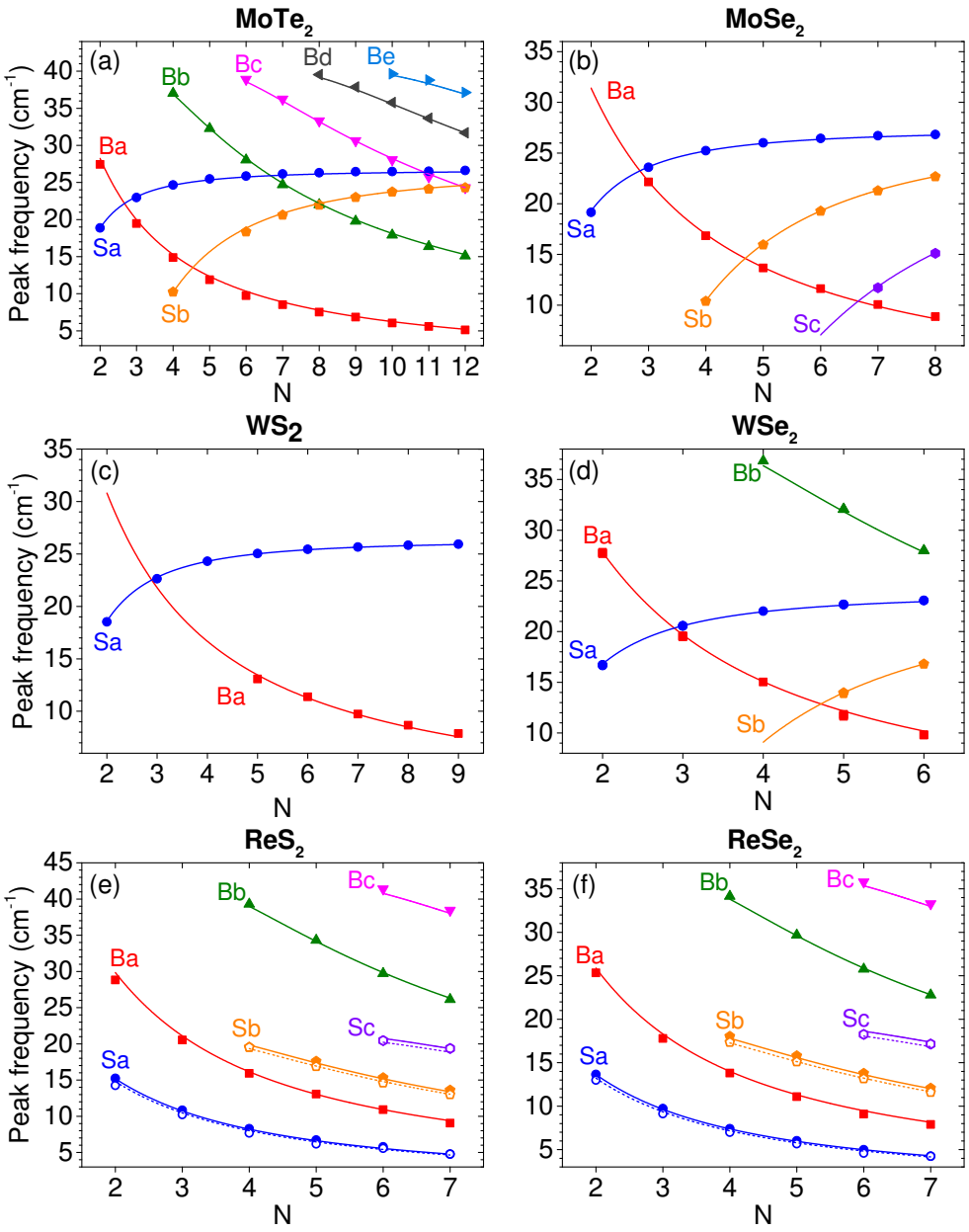

Figure 6.10 – *Frequencies (symbols) of the interlayer shear (Sa, Sb,...,) and breathing (Ba, Bb,...) modes as a function of N for N-layer (a) $MoTe_2$, (b) $MoSe_2$, (c) WS_2, (d) WSe_2, (e) ReS_2 and (f) $ReSe_2$. The measured frequencies are globally fit to Eq. (6.23) (lines). The theoretical curves are plotted in the range of N where the corresponding mode is observable. Due to in-plane anisotropy, each LSM branches of ReS_2 and $ReSe_2$ is split into a lowest- (open symbols and dashed lines) and a highest-frequency branch (filled symbols and solid lines), leading to two shear (κ_S) force constants. The extracted force constants are summarized in Tab. 6.5. WX_2 measurements were done by Olivia Zill and ReX_2 by Etienne Lorchat.*

interaction between the layers are similar. This explains why all of them can be cleaved in the same manner and whey they can be stacked artificially to form van der Waals heterostructures (see Chapter 2 Section2.3).

To finish this section, let us explain why this simplified model describes the low-frequency modes as good as the full force constant model. If layers are treated as rigid planes, it means

Material	κ_S (10^{18} N/m^3)	κ_B (10^{18} N/m^3)
$MoTe_2$	34.2	76.9
$MoTe_2$ [Grzeszczyk16, Song16]	36.0, 42.5	75.0, 91.2
$MoSe_2$	29.6	78.4
$MoSe_2$ [Kim16]	29.2	87.3
WS_2	29.4	80.6
WSe_2	30.5	83.7
WSe_2 [Zhao13]	30.7	86.3
ReS_2	17.1/18.9	69.3
$ReSe_2$	17.8/19.4	69.2
MoS_2 [Boukhicha13, Zhang13, Zhao13]	28.1, 28.2, 27.2	88.1, 89.0, 86.2
Graphite [Tan12, Lui14]	12.8	88.0

Table 6.5 *– Force constants per unit area extracted from the fit of the experimental data to the finite linear chain model (see Fig. 6.10) and from the literature. For ReS_2 and $ReSe_2$, the shear force constants κ_S correspond to the lowest-/highest-frequency branch, respectively.*

that the force constant α in the complete model (see Fig. 6.4) is infinite $|\alpha| \gg |\beta|, |\gamma|, |\delta|$. However, as shown in Tab. 6.2, this relation is verified. In that case, the non-zero bulk frequency is given by Eq. (6.13). By comparing with the non-zero bulk frequency obtained from the simplified model, we deduce that $\kappa \approx \beta + 2\gamma$. As expected, this relation involves the two interlayer force constants. This relation is experimentally very well verified (see Tab. 6.2 and Tab. 6.5). Therefore, the use of a simplified model for the low-frequency mode is justified. Note that surface effects only affect intralayer force constants and have therefore a negligible influence on the rigid layer modes.

6.3 Deriving the phonon frequency in N-layer TMDs from the bulk phonon dispersion

In this section, we give an alternative description of the phonon modes in N-layer crystals using the phonon bulk dispersion [Karssemeijer11, Michel12]. Note that this description can be viewed as a 'top-down' approach, while the description of Section 6.1 can be viewed as a 'bottom-up' approach. As for rest of this chapter, we will use N-layer $MoTe_2$ as an example but this description can be generalized to any TMDs.

6.3.1 Low-frequency modes

To demonstrate that the phonon modes can be deduced from the bulk dispersion, we will use the simplified model established in Section 6.2 that accurately depicts the low-frequency modes in any layered crystals. The dispersion relation of an infinite monoatomic linear chain can be found in e.g., [Ashcroft76]. Using the same notation as previously, the dispersion relation is

$$\Omega(q) = \sqrt{\frac{2\kappa}{\mu}(1 - \cos qc)}, \tag{6.24}$$

where $q \in \left[-\frac{\pi}{c}, \frac{\pi}{c}\right]$ is the phonon wavevector taken in the Brillouin zone of the monoatomic linear chain. But Eq. (6.24) is not the dispersion relation of the bulk crystal since the unit cell contains two layers. However, as explained previously (see section 6.1.3), the dispersion relation of the bulk crystal can be deduced from the one with one layer in the unit cell. Therefore using Eq. (6.24), we obtain

$$\Omega(q) = \sqrt{\frac{2\kappa}{\mu}(1 \pm \cos qc)}, \tag{6.25}$$

with $q \in \left[-\frac{\pi}{2c}, \frac{\pi}{2c}\right]$. The phonon branch with the + (−) corresponds to the optical (acoustic) branch. Note that $q = 0$ gives the two frequencies of the bulk zone center phonon modes. For non-zero wavevector q and $N \geq 2$[3], by comparing Eqs. (6.23) and (6.25), and using the trigonometric formula $\forall\theta \in \mathbb{R}\ \cos(\pi - \theta) = -\cos(\theta)$, we infer

$$q(\nu) = \frac{\pi}{c}\frac{\nu}{N}, \tag{6.26}$$

with $\nu \in [\![1, \left\lfloor \frac{N}{2} \right\rfloor]\!]$ and $N \geq 2$. Thus, we find that the $N-1$ LSM and LBM of the N-layer system are obtained as the intersections of the bulk phonon branches and vertical lines located at q given by Eq. (6.26), in the range $\left[0, \frac{\pi}{2c}\right]$.[4] To recover the complete low-frequency modes, one has to add the lowest frequency obtained at $q = 0$, i.e. the zero frequency $\Omega = 0$ of the acoustic mode. Interestingly, Eq. (6.26) suggests that the modes are confined to an effective thickness of Nc. Extrapolating to the single layer gives an effective thickness of c (i.e., an interplanar distance) for one layer, as we have assumed in the calculations of the enhancement factors in Appendix C.

[3] For $N = 1$, $q = 0$ and thus the only mode is the acoustic one.

[4] Similar results could be obtain in the range $\left[-\frac{\pi}{2c}, 0\right]$ since the dispersion relation is an even function of q.

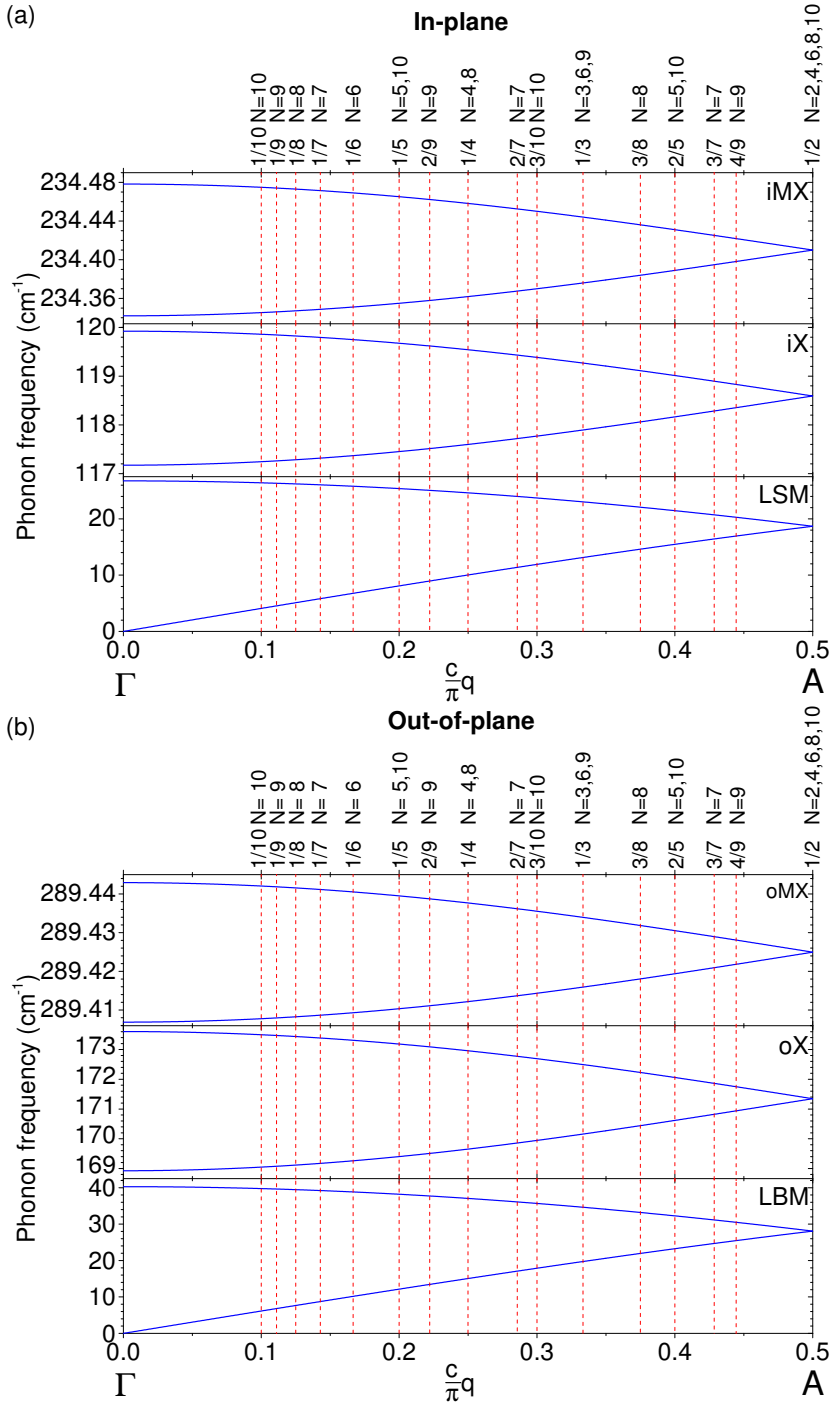

Figure 6.11 – *Calculated phonon dispersion along* $\Gamma - A$ ($\boldsymbol{q} = (0, 0, q)$) *for (a) in-plane and (b) out-of-plane phonon modes in bulk* $MoTe_2$. *The relations were computed using Eq.* (6.6). c *is the interplanar distance. Cuts at values of* q *defined by Eq.* (6.26) *(marked by vertical red dashed lines and labeled at the top horizontal axis) yield the* Γ*-point phonon frequencies of the* N*-layer system.*

6.3.2 Deriving the phonon frequency from the bulk

This simple analysis can be extended to the mid- and high-frequency modes. The bulk dispersion relation along the $\Gamma - A$ line in the 3D Brillouin zone can be computed using Eq. (6.6) and the values of the force constants in Tab. 6.2. The calculated bulk dispersion relation is plotted in Fig. 6.11. The frequencies all phonon modes in the N-layer system are obtained as the intersections of these plots and vertical lines given by Eq. (6.26), plus the lowest frequencies of the mid- and high-frequency modes at $q = 0$ (namely Ω^{-}_{mid} and Ω^{+}_{high}). These two frequencies correspond to $q = \frac{\pi}{c}$ in Eq. (6.6), i.e., the displacements of the three atoms within one layer are out-of-phase with the displacements of the atoms of adjacent layers. This is in agreement with the displacements drawn on Fig. 6.6 and in Appendix F, where the mid- and high-frequency mode with the lowest frequency has out-of-phase displacements of atoms of two adjacent layers.

The extracted frequencies are plotted in Fig. 6.12. We obtain well-defined fan diagrams delimited by the two bulk frequencies Ω^{-} and Ω^{+}. The in- and out-of-plane fan diagrams are qualitatively similar (as the dispersion relation in Fig. 6.11) since the in-plane and out-of-plane vibrations are described by the same force constant model but with two different sets of force constants. For N even, the value $\nu = \frac{N}{2}$ corresponds to $q = \frac{\pi}{2c}$, i.e., the A-point in the 3D Brillouin zone. This value gives rise to the series of central points with the same frequency in the fan diagrams. More generally, the frequencies present for N are also present for all multiples of N. Comparing these extracted frequencies with the frequencies obtained from the diagonalization of the dynamical matrix (see Fig. 6.5), we notice that (i) the low-frequency modes are in excellent agreement, (ii) the mid-frequency are in qualitative agreement but do not correspond exactly, and (iii) the quasi-degenerate high-frequency modes are in good agreement but there are no surface modes. Indeed, surface effects are not present in the bulk since it is infinite and the low-frequency modes are not sensitive to such effects whereas the mid- and high-frequency are. To illustrate more precisely these differences, we focus on the oX mode in Fig. 6.13. We observe first that the constant frequencies at ω^{-}_{mid} are not constant for the frequencies obtained by the diagonalization, because of the renormalized α_{e} and δ_{e} for the two outer layers. The differences are also due to the fact that the two outer layers are only connected by two γ-springs while the inner layers are all connected by four γ-springs. As expected, when increasing N the differences become smaller since the surface effects have a smaller influence. Finally, even if there are slight differences, the extraction of the frequencies from the bulk dispersion relation is an easy way to qualitatively describe and quantitatively estimate the frequency of all the modes of the N-layer system.

6.4 Resonance effects?

At this point, we could ask why we observe more modes in N-layer $MoTe_2$ than in N-layer $MoSe_2$ (compare Figs. 6.3 and 6.7)? More generally, one may wonder why the Davydov splitting was reported only on $MoTe_2$ [Grzeszczyk16, Song16], $MoSe_2$ [Tonndorf13, Chen15,

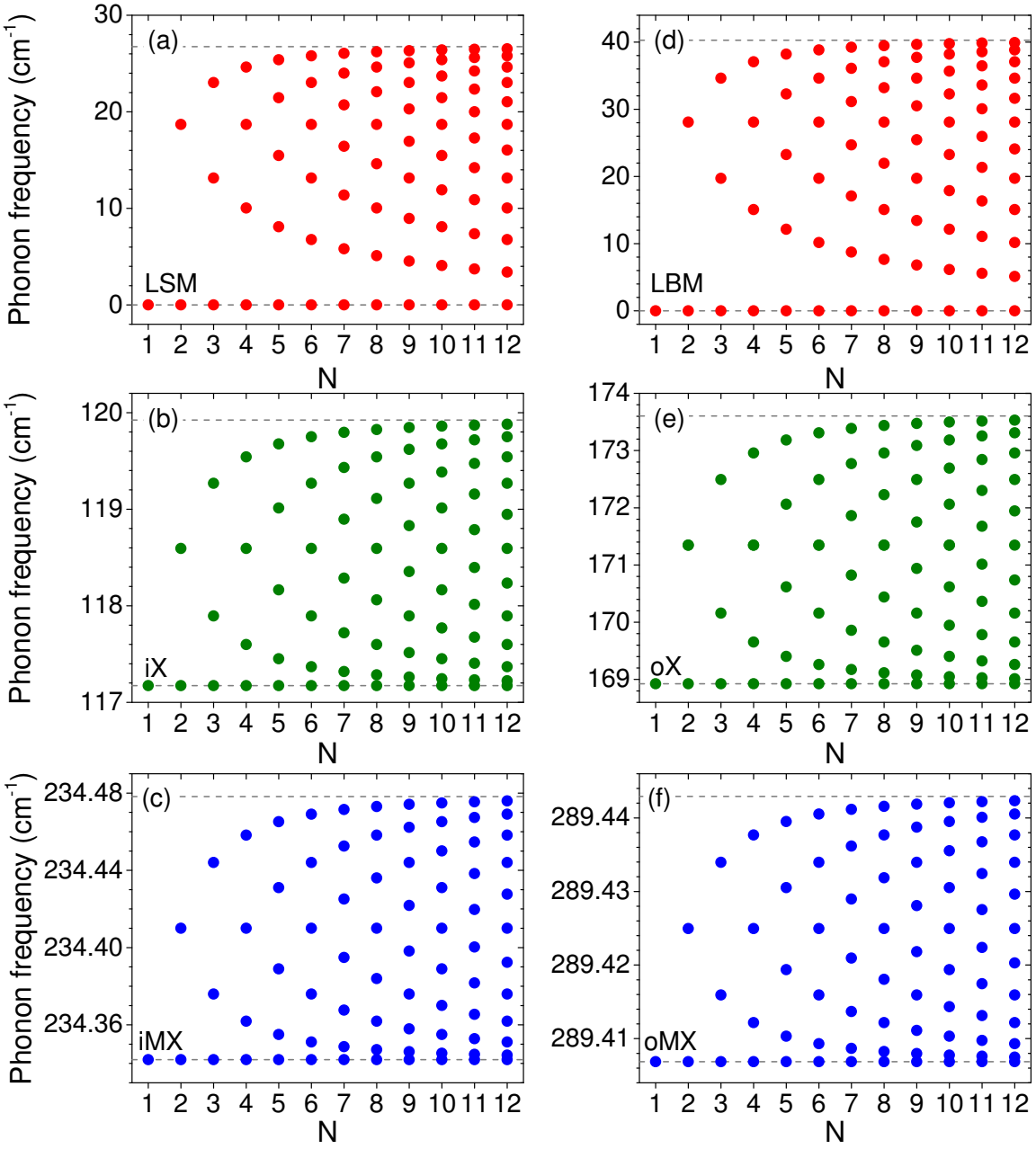

Figure 6.12 *– Frequencies (symbols) of the (a) LSM (b) LBM (c) iX, (d) oX, (e) iMX, (f) oMX modes extracted from cuts in the bulk dispersion relation displayed in Fig. 6.11 as a function of the number of layers N. The upper and lower horizontal gray dotted lines in (a)-(b), (c)-(d), and (e)-(f) correspond to the bulk frequencies* $\Omega^{\pm}_{low}$, $\Omega^{\pm}_{mid}$, *and* $\Omega^{\pm}_{high}$, *respectively.*

Kim16] and WS_2 [Staiger15], while group theory (see Chapter 3 Section 3.3) predicts a Davydov splitting for all N-layer 2Hc TMDs? For instance, no splittings have seen in numerous studies on MoS_2 using visible photon energies [Lee10, Li12a, Luo13b, Lee15b, Zhang15b]. Obviously, distinct TMDs can have different inter- and intralayer force constants leading to more or less important Davydov splitting. However, by comparing the results obtained for $MoTe_2$ and $MoSe_2$ (see Tabs. 6.2 and 6.4) the force constants seem to be of the same order

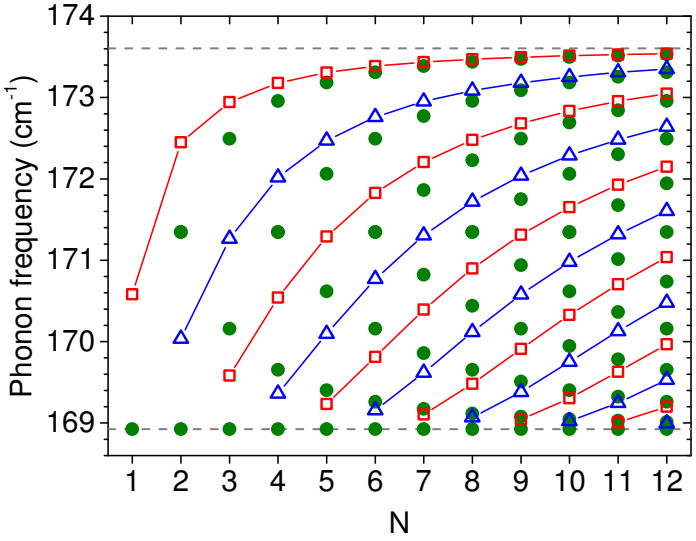

Figure 6.13 *– oX mode frequencies extracted from the bulk dispersion (green filled circles) and from the diagonalization of the dynamical matrix (red open squares and blue open triangles) as a function of the number of layers N (same data as Figs. 6.12 and 6.5, respectively). The solid lines are guide for the eye. The red open squares (blue open triangles) are the frequency of the Raman-active (Infrared-active) modes. The gray dashed lines correspond to the bulk frequencies* $\Omega^{\pm}_{mid}$.

of magnitude. Consequently, this assumption seems to be unlikely. Another explanation is that resonance effects can affect the measurements. The possible influence of these effects are discussed in this section.

6.4.1 Raman measurements at 2.33 eV and 1.96 eV in N-layer $MoTe_2$

The Raman results presented on N-layer $MoTe_2$ were recorded at two photon energies: E_L = 2.33 eV for LSM, LBM and iX, and E_L = 1.96 eV for oX, iMX and oMX. Each time, we choose to use the data at the photon energy where we observe more modes. However, we recorded the entire spectra at both photon energies. Figure 6.14 shows the raw Raman spectra of N-layer $MoTe_2$ recorded at E_L = 2.33 eV and E_L = 1.96 eV. Note that the iX mode is not shown at 1.96 eV because its intensity is too weak.

First, at low-frequency, we observe the same modes at both photon energies. As expected, these phonon modes have the same frequency. However, we notice that the integrated intensity of the LSM compared to LBM is higher at E_L = 1.96 eV than at E_L = 2.33 eV. In particular, the intensity of the first LBM branch E_L = 1.96 eV is not as intense as at E_L = 2.33 eV. Second at mid- and high-frequency, we identify the same features at both photon energies. Even for the iX mode, we were able to observe a faint feature at E_L = 1.96 eV but almost one order of magnitude less intense. Since at E_L = 1.96 eV its Raman signal is already small compared to the other modes, we do not display this feature in Fig. 6.14. Figure 6.15 shows more precisely the Raman spectra of the oX, iMX and oMX modes in N-layer $MoTe_2$ recorded at E_L = 2.33 eV. The results have to be compared to Fig. 6.3. At E_L = 2.33 eV, the Davydov splitting also appears clearly for the oX feature, although the highest energy subfeature contains most of the

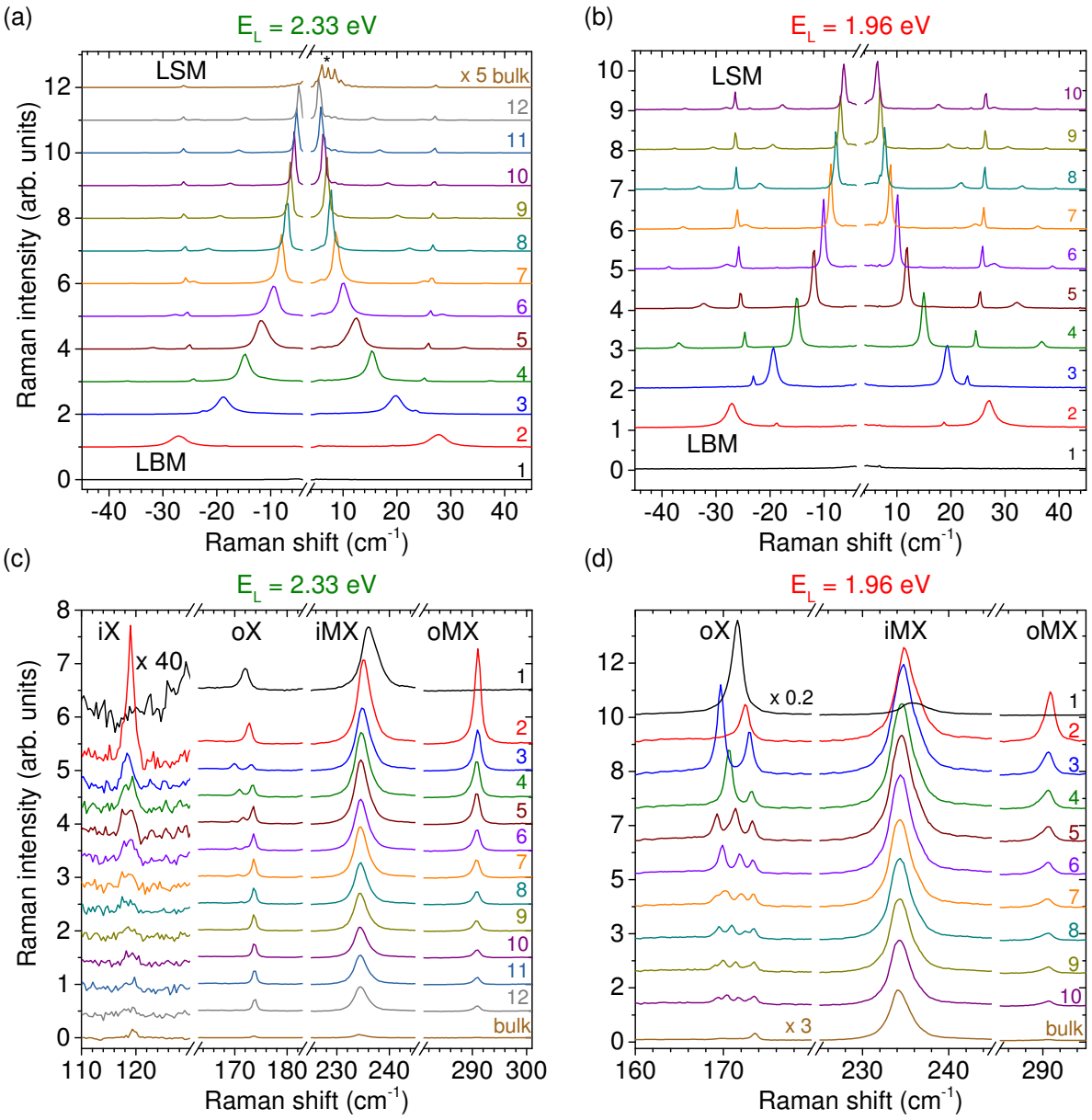

Figure 6.14 – *Raman spectra of N–layer $MoTe_2$ recorded under the same conditions at a photon energy of (a)-(c) 2.33 eV and (b)-(d) 1.96 eV. The spectra are vertically offset for clarity. At 1.96 eV, the intensity of the iX mode is too weak to be observable.*

oscillator strength for $N \geq 6$. The iMX feature also downshifts as N increases and no appreciable splitting can be resolved. However, in contrast with our results at $E_L = 1.96$ eV, the oMX feature does not exhibit any measurable splitting at $E_L = 2.33$ eV.

The frequency of the oX-, iMX- and oMX-mode recorded at $E_L = 2.33$ eV can be extracted and compared to the ones measured at $E_L = 1.96$ eV. These two sets of data (not shown) are very consistent with each other. Still, there is a small rigid shift of approximately 0.2 cm^{-1} which is smaller than the resolution of the experimental setup. This shift presumably arises from uncertainties (below our spectral resolution) in the calibration of our spectrometer. This is further confirmed by the fact that the fan diagrams associated with the LSM and LBM are

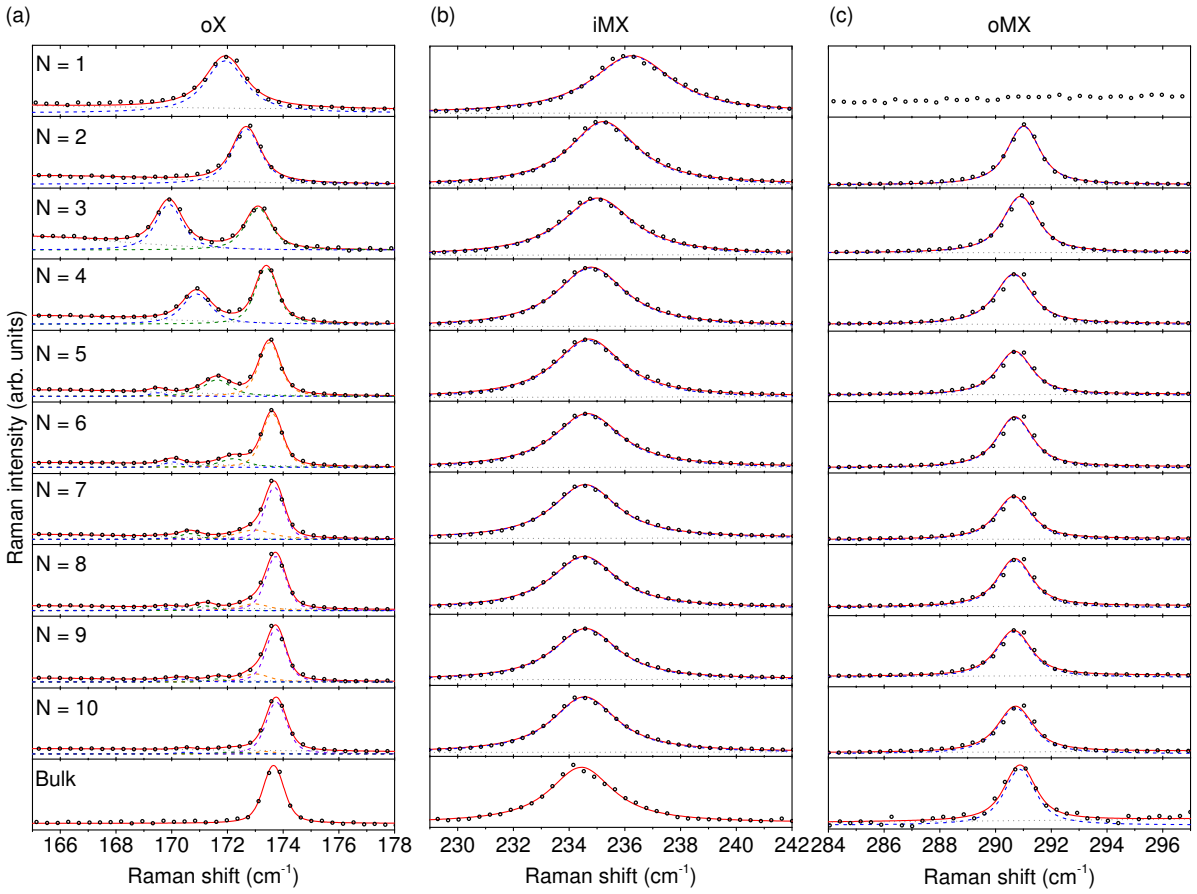

Figure 6.15 *– Normalized micro-Raman spectra of the (a) oX, (b) iMX, and (c) oMX mode-features in N–layer $MoTe_2$ recorded at $E_L = 2.33$ eV. The measured Raman features (symbols) are fit to Voigt profiles (solid lines). For the modes that show a Davydov splitting, each subpeak is represented with a colored dashed line. A featureless background (gray dashed line) has been considered when necessary.*

the same. Indeed, for such modes the frequency is deduced from the difference between the Stokes and anti-Stokes features which is supposed to be independent of any systematic error due to the calibration. Importantly, such a small shift has a negligible influence on the determination of the force constants. Indeed, the latter vary by less than 1.5 % if one uses the oX, oMX and iMX frequencies recorded at $E_L = 2.33$ eV instead of their values recorded at $E_L = 1.96$ eV in the global fitting procedure described previously.

Finally to conclude, the Γ-point phonon frequencies are not affected by E_L, although the integrated intensity of one given Raman feature and the repartition of the spectral weight within a given subfeature are affected by E_L. Similar conclusions hold for other TMDs. In particular, recent experiments [Soubelet16, Kim16] on N-layer $MoSe_2$ different excitation energies have shown that the Raman intensity strongly depends on the excitation energies. For instance at $E_L = 2.5 - 2.6$ eV, the mid-frequency modes are more visible. Unfortunately, we cannot measure at such photon energies on our experimental setup, this is why less modes were observed in N-layer $MoSe_2$ than in $MoTe_2$.

6.4.2 Bond polarizability model

To explain these observations, our collaborators at the University of Luxembourg performed calculations based on a bond polarizability model to assign a Raman intensity to each iX and oX subfeatures in N-layer $MoTe_2$. The results of their calculations are described in the following. For the iX mode, the bond polarizability model predicts spectral weights that are in-line with group theory predictions and the experimental results at $E_L = 2.33$ eV. However, the same model predicts that the highest frequency oX mode should have a much larger oscillator strength than its lower energy counterparts. This prediction is clearly in contradiction with the observations at $E_L = 1.96$ eV (see Fig. 6.3(b)), where the oX-mode subfeatures have comparable integrated intensities, but is closer to the observations at $E_L = 2.33$ eV (see Fig. 6.15(a)).

Let us focus more precisely on the oX mode for the trilayer. Figure 6.16 shows the three spectra recorded at 1.58 eV, 1.96 eV and 2.33 eV. As already observed at 1.96 eV and 2.33 eV, there are two subfeatures at almost the same Raman shift. However, the intensity ratio of the two subfeatures is rather different and is in agreement with the bond polarizability model only at 1.58 eV.

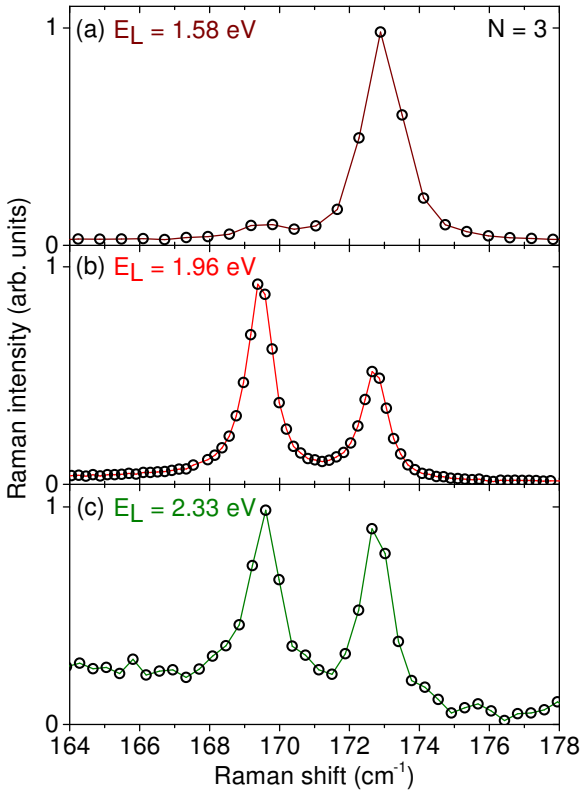

Figure 6.16 *– Normalized Raman spectra of the oX-mode features in $N = 3$ layers $MoTe_2$ recorded at (a) $E_L = 1.58$ eV, (b) $E_L = 1.96$ eV and (c) $E_L = 2.33$ eV.*

Very recently, Song *et al.* [Song16] have measured the oX mode of a trilayer at ten photon energies from 1.58 eV to 2.54 eV. The measured Raman spectra are displayed in Fig. 6.17(a).

These spectra were recorded on quartz substrates to minimize the optical interference effects. They were further normalized by the intensity of the A_3 modes in quartz at ~ 465 cm^{-1} to eliminate the difference of CCD efficiencies at different excitation energies. The two subfeatures are observed at every photon energies (R_1 (R_2) denotes the high- (low-) frequency subfeature) but with distinct intensity ratios. The extracted intensity for the two subfeatures are plotted in Fig. 6.17(b) with the reflectance spectra ($\Delta R/R$) which is in first approximation proportional to the absorptance [McIntyre71, Buckley77]. We observe that the high-frequency subfeature (R_1) is considerably enhanced at 1.58 eV and 1.71 eV. This energy range corresponds to the A' exciton. The low-frequency subfeature (R_2) shows a strong intensity enhancement at 1.83 eV, which is between the A' (~ 1.73 eV) and B' (~ 1.96 eV) exciton. Our measurements at three different photon energies (see Fig. 6.16) are in agreement with this conclusion. However, further investigations are needed to unveil the underlying physics behind these resonant exciton-phonon couplings. We are currently working on these resonance effects with our collaborators at the University of Luxembourg (see Chapter 9).

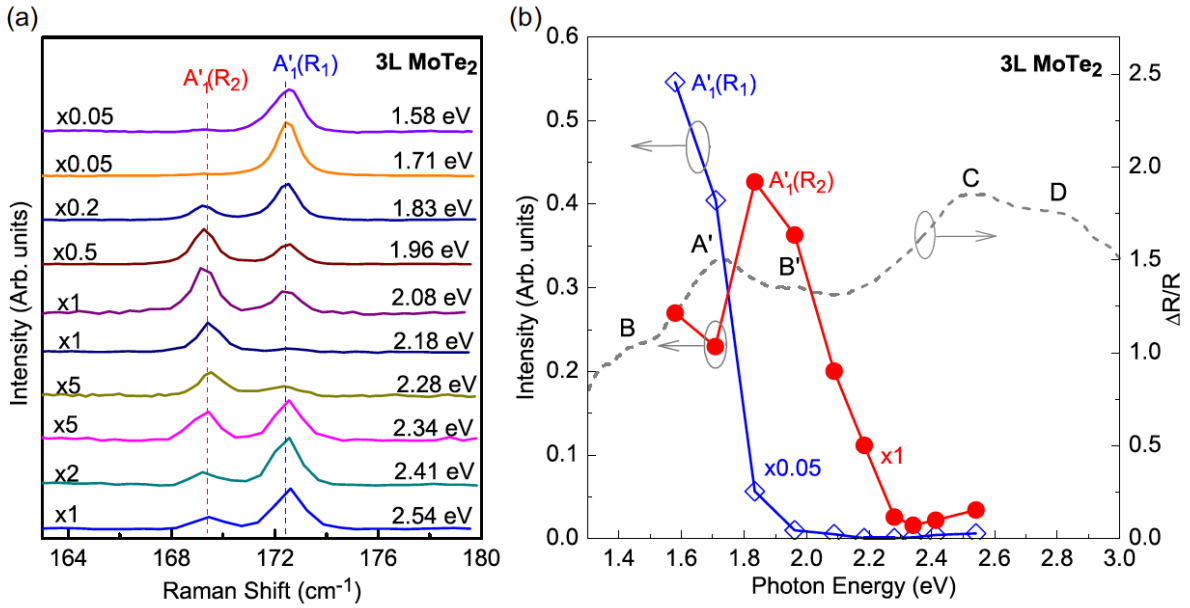

Figure 6.17 *– (a) Raman spectra of the oX-mode features in $N = 3$ layers $MoTe_2$ recorded at ten laser excitation energies. The Raman intensity is normalized to the A_3 mode in quartz at about ~ 465 cm^{-1}. The spectra are vertically offset for clarity. (b) The intensity of the high-frequency subfeature $A'_1(R_1)$ (blue open diamonds) and low-frequency subfeature $A'_1(R_2)$ (red solid circles) as a function of the excitation energy. The dashed gray line is the reflectance contrast spectrum (R/R) of $N = 3$ layers $MoTe_2$. Figure from Ref. [Song16].*

6.5 Conclusion

In this chapter, we have reported a unified description of the optical phonon modes in N-layer 2Hc transition metal dichalcogenide crystals (more precisely $MoTe_2$ and $MoSe_2$), between the bulk and monolayer limits. The manifolds of low-frequency interlayer shear and breathing modes, and of the mid-frequency modes involving out-of-phase intralayer motion of the chalcogen atoms are well understood using classical theories of coupled oscillators.

Especially, the low-frequency modes of any N-layer materials are well described by rigid-plane modes. In contrast, the behavior of the high-frequency modes that involve out-of phase motion of the metal and chalcogen planes is largely influenced by surface effects. We have introduced a global fitting procedure based on linear chain model to derive the force constants up to the second nearest neighbor and to assess the strength of the surface effects. This model allows us to deduce the frequency of optical phonons that are silent in bulk crystals, namely the low-frequency interlayer breathing mode (LBM) with B_{2g} symmetry, and the mid-frequency in-plane (iX) and out-of-plane (oX) modes with E_{2u} and B_{1u} symmetry, respectively. We have also shown that the phonon frequencies can be deduced reasonably from the bulk phonon dispersion relation. Finally, this work shed light on resonant effects in layered materials and has already motivated multiple studies of the Davydov splitting in other TMDs [Grzeszczyk16, Song16, Kim16].

Take home messages

- Raman spectroscopy is an extremely sensitive technique to probe the influence of interlayer coupling and the surface effects.
- The complete manifold of all the Γ-point phonons in N-layer transition metal dichalcogenides is well captured by a simple force constant model which includes interactions up to the second nearest neighbor and surface effects.
- The low-frequency modes correspond to rigid layer modes and are accurately described by a simplified force constant model which includes only the interlayer force constant in spite of the crystal structure and composition.
- Resonant exciton-phonon couplings play a major role in the observations of very clear Davydov splittings.

Related publications and communications

Papers

- H. P. C. Miranda, S. Reichardt, G. Froehlicher, A. Monlina-Sánchez, S. Berciaud and L. Wirtz, *Quantum interference effects in resonant Raman spectroscopy of single- and triple-layer $MoTe_2$ from first principles*, Nano Letters, Just Accepted Manuscript
- E. Lorchat, G. Froehlicher and S. Berciaud, *Splitting of interlayer shear modes and photon energy dependent anisotropic Raman response in N-layer $ReSe_2$ and ReS_2*, ACS Nano **10**, 2752-2760 (2016).
- G. Froehlicher, E. Lorchat, F. Fernique, C. Joshi, A. Monlina-Sánchez, L. Wirtz and S. Berciaud, *Unified Description of the Optical Phonon Modes in N-Layer $MoTe_2$*, Nano Letters **15**, 6481-6489 (2015).

Oral

- G. Froehlicher, E. Lorchat, F. Fernique, C. Joshi, A. Monlina-Sánchez, L. Wirtz and S. Berciaud, *Unified Description of the Optical Phonon Modes in N-Layer $MoTe_2$*, APS March Meeting, March 2016, Baltimore, USA
- E. Lorchat, G. Froehlicher and S. Berciaud, *Probing in-plane anisotropy and interlayer interactions in N-layer $ReSe_2$ and ReS_2 by Raman spectroscopy*, APS March Meeting, March 2016, Baltimore, USA.
- G. Froehlicher, E. Lorchat, F. Fernique and S. Berciaud, *From the bulk to the monolayer: Evolution of the optical properties of N-Layer $MoTe_2$*, Congrès général de la Société Française de Physique, August 2015, Strasbourg, France.

Posters

- G. Froehlicher, E. Lorchat, F. Fernique and S. Berciaud, *Photoluminescence and Raman spectroscopy of N-Layer $MoTe_2$*, International Winterschool on Electronic Properties of Novel Materials (IWEPNM), March 2015, Kirchberg in Tirol, Austria.

Award

- **The Ovshinsky Student Travel Grant Award** for the talk *Unified Description of the Optical Phonon Modes in N-Layer $MoTe_2$* at the 2016 APS March Meeting, American Physical Society – Division of Materials Physics

Chapter 7

Photoluminescence spectroscopy of N-layer semiconducting transition metal dichalcogenides

The present chapter is devoted to the study of the photoluminescence properties of N-layer semiconducting transition metal dichalcogenides. We first recall the main theoretical concepts of photoluminescence spectroscopy that are essential to understand the experimental results. Then, we thoroughly investigate the room temperature photoluminescence of N-layer transition metal dichalcogenides using the example of $MoTe_2$. Finally, the evolution of the photoluminescence intensity in monolayer $MoTe_2$ as a function of the absorbed photon flux is presented and an elementary rate equation model is introduced to describe the observed sub-linear scaling of the photoluminescence intensity with the incoming photon flux.

7.1 Photoluminescence spectroscopy: generalities

"**Luminescence** is the general name given to the process of spontaneous emission of light by excited atoms in a solid state material" [Fox10]. Atoms can be promoted to excited states by, for instance, absorbing light (photoluminescence), electrical excitation (electroluminescence), heat (thermoluminescence), chemical reactions (chemiluminescence), friction (triboluminescence), ... In all cases, the light is emitted in all directions. In this work, we are studying the PL of SCTMDs. Therefore, we will focus on the PL of semiconductors, first with a direct bandgap and then with an indirect one.

Direct bandgap

Light absorption The fraction of absorbed light is quantified by the absorptance $\mathcal{A}$ which is defined and calculated in Appendix C Section C.2. In semiconductors, optical absorption is dominated by **interband absorption**, i.e., electrons are excited from the valence band to

the conduction band as sketched in Fig. 7.1. The excited electron leaves an unoccupied state in the valence band which is described as a hole. Hence, the interband absorption process creates an **electron-hole pair**. The energy conservation and momentum conservation in this process imply that

$$E_f = E_i + \hbar\omega, \tag{7.1}$$

$$\boldsymbol{k}_f = \boldsymbol{k}_i \pm \boldsymbol{k}, \tag{7.2}$$

where E_i (E_f) is the energy of the electron in the valence (conduction) band, $\hbar\omega$ is the incoming photon energy, $\boldsymbol{k}_i$ ($\boldsymbol{k}_f$) is the wavevector of the electron in the valence (conduction) band and $\boldsymbol{k}$ is the wavevector of the incoming photon. Because there are no states in the gap (we do not consider the possible defect states and we will consider the effect of the attractive force between the electron and hole later), there is a threshold: interband transitions are only possible if $\hbar\omega = E_f - E_i \geq E_g$, where E_g is the energy of the gap. Thus, the absorption spectrum is continuous from the energy threshold at E_g to an upper value set by the extreme limits of the participating bands. As for Raman spectroscopy (see Chapter 3), in the visible range the photon wavevector in Eq. (7.2) can be neglected

$$\boldsymbol{k}_f = \boldsymbol{k}_i. \tag{7.3}$$

Equation (7.3) implies that the interband absorption processes correspond to vertical transitions and are represented by vertical arrows in diagrams such as the one in Fig. 7.1.

Emission of light The PL phenomenon in semiconductors is dominated by the interband luminescence that occurs when an electron excited into the conduction band drops back to the valence band by the emission of a photon. This process corresponds to a radiative electron-hole recombination and is the opposite process of interband absorption. However, this recombination is not necessarily radiative. For example, the electron-hole pair can recombine non-radiatively by emitting phonons or by transferring its energy to impurities or defects. As for the interband absorption, interband luminescence follows Eqs. (7.1) and (7.3). To understand the basic concepts, let us take a very simple picture where at a time $t = 0$, a number $N(0)$ of electron-hole pairs is created by the absorption of light. The evolution of the number of electron-hole pairs $N(t)$ for $t > 0$ is governed by

$$\frac{\mathrm{d}N}{\mathrm{d}t} = -\Gamma_\mathrm{r} N - \Gamma_\mathrm{nr} N = \Gamma N, \tag{7.4}$$

where Γ_r (Γ_nr) is the radiative (non-radiative) recombination rate and $\Gamma = \Gamma_\mathrm{r} + \Gamma_\mathrm{nr}$ is the total recombination (or deexcitation) rate. $\Gamma_\mathrm{r} N$ is the radiative emission rate and $\Gamma_\mathrm{nr} N$ is the non-radiative recombination rate. Note that non-linear processes in N, such as the mutual annihilation of two electron-hole pairs which is proportional to N^2, might also occur but are not considered in this simple picture. Therefore, Γ is usually referred as the linear recombi-

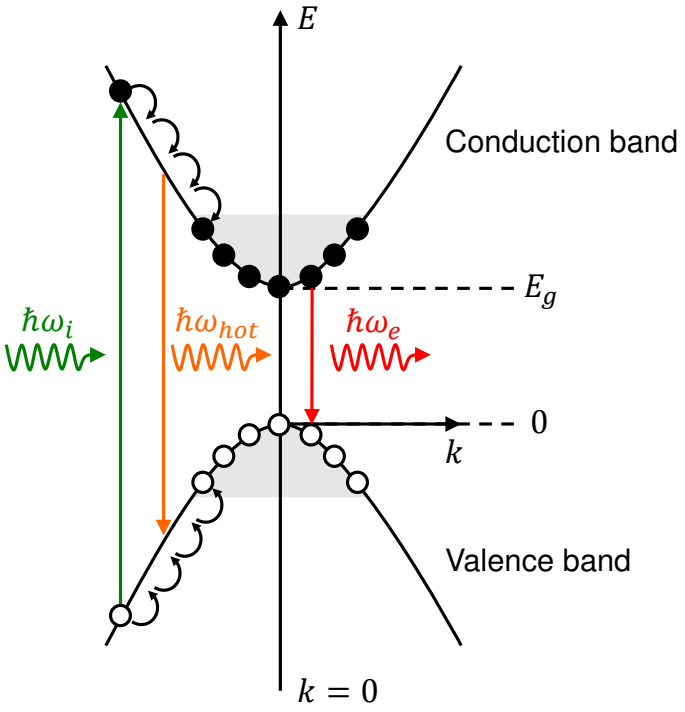

Figure 7.1 *– Schematic band diagram of the photoluminescence processes in a semiconductor with a direct bandgap. An electron-hole pair is created by the absorption of a photon of energy $\hbar\omega_i$. The electron and hole rapidly relax, by emission of phonons, to the bottom and top, respectively, of their band. The occupied states are indicated in gray and follow a statistical distribution of width $\sim k_B T$. Electron hole pairs from these occupied states can recombine by emitting a photon $\hbar\omega_e$ close to E_g. If the electron hole pair recombine before reaching the bottom of the conduction band and the top of the valence band, the emitted photon has an energy $\hbar\omega_{hot}$ higher than E_g. Such process is said to be hot luminescence because the electron and hole are not in a thermal equilibrium.*

nation rate. This rate equation can be solved to give

$$N(t) = N(0)\exp(-\Gamma t) = N(0)\exp(-t/\tau), \tag{7.5}$$

where $\tau = \Gamma^{-1}$ is the lifetime of the electron-hole pair. One can also define the radiative and non-radiative lifetime of the electron-hole pair $\tau_r = \Gamma_r^{-1}$ and $\tau_{nr} = \Gamma_{nr}^{-1}$, respectively. The **luminescence efficiency** η is given by the ratio of the radiative rate to the total recombination rate

$$\eta = \frac{\Gamma_r}{\Gamma_r + \Gamma_{nr}}. \tag{7.6}$$

If $\Gamma_r \gg \Gamma_{nr}$ then η approaches unity and the maximum possible amount of light is emitted. On the other hand, if $\Gamma_r \ll \Gamma_{nr}$ then the light emission is poor. In other words, efficient luminescence requires that the radiative lifetime is much smaller than the non-radiative one.

Photoluminescence In general, the incoming photon has a much higher energy than the bangap $\hbar\omega > E_g$ so that the excited electrons (holes) are promoted in states well above (below) the conduction (valence) band edges (see Fig. 7.1). However, they do not remain in these

states for long. Indeed, they rapidly lose energy by emitting phonons. In Fig. 7.1, this process is illustrated by the cascade of transitions within the conduction (or valence band) band. The typical timescale of this process is of the order of 100 fs [Fox10] while the typical radiative lifetime of electron-hole pairs is of the order of ns. Consequently, the electrons (the holes) relax to the bottom (top) of the conduction (valence) band before radiatively recombine, and form a thermal distribution with a width of $\sim k_B T$. The radiative recombination takes place within $\sim k_B T$ of the bottom and top of the conduction and valence band, respectively. As a result, the PL spectrum consists in a peak at an energy E_g with a width $\sim k_B T$.[1] Hence, PL spectroscopy is a technique to measure the bandgap of a semiconductor. The PL intensity is proportional to ηN. In the case of continuous wave excitation, η is also equal to the **quantum yield** which is the ratio of the number of emitted photons to the number of absorbed ones. Recombination outside the range of energy close to the conduction and valence band edges is also possible and is called **hot photoluminescence** because the electrons and holes do not have the time to thermalize to the bottom of the conduction band and top of the valence band. In this case, the emission energy is always higher than E_g. Emission at energies lower than E_g might occurs if states exist in the gap. Such states are associated to impurities or defects. Photoluminescence from these states is usually low and will not be considered here. To differentiate between this PL and the one described previously, the latter is said to be **intrinsic** while the former is said to be **extrinsic**. However even if there are no impurities or defects states in the gap, PL at lower energies than E_g is observable due to **excitonic effects**. Finally, let us briefly mention that the carrier dynamics (i.e., Γ in the simple picture described in the previous paragraph) can be obtained using time-resolved PL spectroscopy. In this measurements, the sample is excited with a very short light pulse and the emitted light is recorded as a function of time after the pulse arrives. In practice, we use the TCSPC configuration of the experimental setup described in Chapter 4.

Excitonic effects Up to now, we have neglected the attractive force between the negative electron and the positive hole. In fact, the oppositely charged particles are created at the same point in space and can attract each other through Coulomb interactions. Such interactions can lead to the formation of a bounded electron-hole pair which is called **exciton**. This neutral particle can be viewed as a hydrogenic system. Its energy levels lay in the gap and are characterized by the binding energy $E_X^{(n)}$ where $n = 1, 2, 3, \ldots, \infty$ (see Fig. 7.2). These energies follow a Rydberg-like series. As the formation of excitons is energetically favorable, features at energies equal to $E_g - E_X^{(n)}$ appear in the absorption and emission spectra (see Fig. 2.12). In mono and few layers SCTMDs, Coulomb interactions are so high (see Chapter 2 Section 2.2) that each electron-hole pair created forms a tightly bound excitons. The PL spectrum is therefore dominated by the lowest excitonic feature at $E_g - E_X^{(1)}$. To avoid any confusion with the **electronic bandgap** E_g, the energy $E_g - E_X^{(1)}$ is referred as the **optical bandgap**. For SCTMDs, PL spectroscopy always probe the optical bandgap. Note that by measuring the electronic

[1] In practice, the peak is larger because of broadening due for instance to electron-phonon coupling, especially at room temperature.

and optical bandgaps, one can deduce the exciton binding energy $E_b = E_X^{(1)}$.

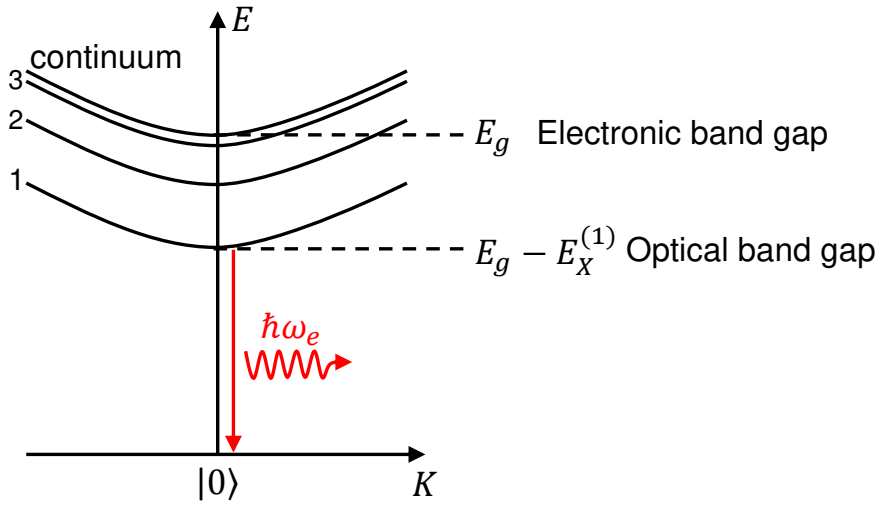

***Figure 7.2** – Exciton dispersion relation. $\boldsymbol{K}$ is the wavevector of the exciton center of mass. Photoluminescence corresponds to the recombinations from excitons in the lowest excitonic state (1). Emitted photons have an energy $\hbar\omega_e$ close to the optical bandgap $E_g - E_X^{(1)}$. Note that exciton concept goes beyond the one-electron approximation used to compute the band structure such as the one drawn in Fig. 7.1. Therefore $\boldsymbol{K} = |0\rangle$ cannot be identified with the top of the valence band, it represents the ground state of the whole crystal.*

Indirect bandgap

Indirect bandgap semiconductors have their conduction band minimum at a different wavevector than their valence band maximum (see Fig. 7.3). Therefore, transitions at the band edges need an additional momentum. This momentum can be provided by a phonon of energy $\hbar\Omega$ and wavevector $\boldsymbol{q}$. Energy and momentum conservation impose

$$E_f = E_i + \hbar\omega \pm \hbar\Omega, \tag{7.7}$$

$$\boldsymbol{k}_f = \boldsymbol{k}_i \pm \boldsymbol{q}, \tag{7.8}$$

where, $(E_i, \boldsymbol{k}_i)$ and $(E_f, \boldsymbol{k}_f)$ are the initial and final states, $\hbar\Omega$ is the phonon energy, and the $\pm$ stands for the creation or annihilation of a phonon. Note that the photon momentum is neglected as in Eq. (7.3). The phonon energy $\hbar\Omega$ is often negligible compared to the other energies. Such indirect transition is a second-order process contrary to the direct transition discussed above which is a first-order process. As a result, it is much less probable than direct transitions. Note that higher processes involving multiple phonons are possible but even less likely. Light absorption at energies close to E_g is therefore weak in indirect bangap semiconductors compared to the case of direct bandgap ones. However in PL measurements, the creation of electron-hole pairs usually corresponds to a direct transition at much higher energy than E_g. In that case, the efficiency of the process is similar for direct and indirect semiconductors. As for direct semiconductors, the created electron-hole pairs rapidly relax to the bottom and top of their bands. Radiative recombination of electron-hole pairs also

happens in the vicinity of the minimum of the conduction band and maximum of the valence band, and needs an additional momentum as sketched in Fig. 7.3. In consequence, the PL intensity of an indirect bandgap semiconductors is much weaker than the one of a direct bandgap. As for the direct bandgap semiconductor, the emission feature is also close to E_g but is generally broader due to the energy of the involved phonon in the process. In addition, hot PL can occur, especially from direct recombination at the wavevector of the top of the valence band ($\boldsymbol{k} = 0$ in Fig. 7.3). Note that excitonic effects also play a role but they are more difficult to conceptualize since electron and holes have different wavevectors. As for direct bandgap SCTMDs, PL spectroscopy also probes the optical bandgap in the case of indirect bandgap SCTMDs.

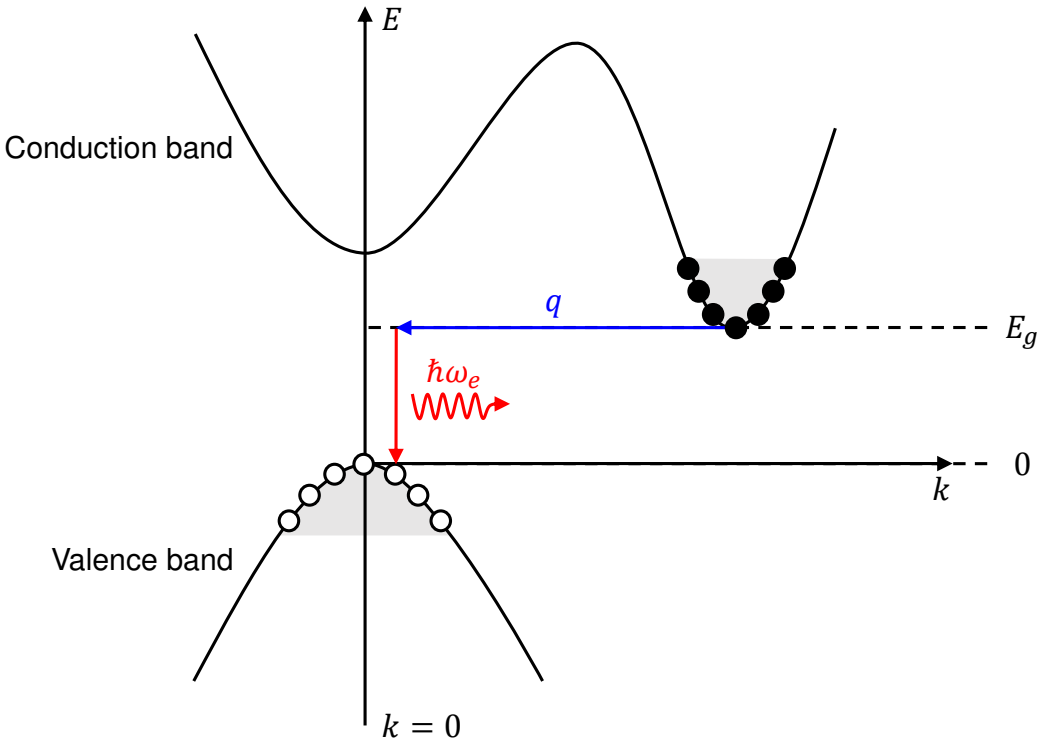

Figure 7.3 *– Schematic diagram of the photoluminescence processes in a indirect semiconductor. The bottom of the conduction band and the top of the valence band are not located at the same wavevector. As for the direct semiconductor, electron-hole pair are created at an energy well above the gap and relax rapidly to the bottom and the top of their bands (not shown, see Fig. 7.1). The occupied states are indicated in gray. To recombine electron-hole pairs need a supplementary momentum* $\boldsymbol{q}$ *provided by phonons. The emitted photon has an energy* $\hbar\omega_e$ *close to* E_g*.*

Finally, let us precise that the dimensionality of the system plays a very important role in the PL properties. Indeed, the reduction of dimensionality, induced by confinement effects, can lead to drastic changes in the density of states and thus in the PL properties. Such changes are responsible of the indirect-to-direct bandgap transition observed in 2Hc SCTMDs.

7.2 Photoluminescence of N-layer $MoTe_2$

In the previous section, we have shown that PL spectroscopy is a powerful technique to study semiconductors, as it gives information on the band structure and on the charge carrier dynamics. In Chapter 2 Section 2.2, we have mentioned that N-layer TMDs are model systems to study the effects of dimensionality. The most prominent manifestation of these effects is the drastic enhancement of the PL intensity of MoS_2, shown in Fig. 2.11, when the number of layers is decreased [Mak10, Splendiani10]. This change in the PL demonstrates a transition from an indirect bandgap in the bulk to a direct bangap in the monolayer limit. Such transition also occurs in others 2Hc SCTMDs like $MoTe_2$, $MoSe_2$, WS_2 and WSe_2 [Zhao12, Tonndorf13, Ruppert14] (see Fig. 7.4). In addition to the PL intensity, the PL lineshape also depends on the number of layers and provides more information on the band structure. In this section, we will address the room temperature PL properties of N-layer $MoTe_2$. Compared to others SCTMDs, a detailed analysis of the PL lineshape in N-layer $MoTe_2$ is still lacking[2] and the exact value of N at which the crossover occurs is a matter of debate [Lezama15].

7.2.1 Photoluminescence spectra of N-layer $MoTe_2$

N-layer $MoTe_2$ were prepared by the slightly modified 'Scotch-tape technique' described in Chapter 4 Section 4.1.1 and deposited onto Si wafers covered with a 90 nm-thick SiO_2 epilayer. In that case, we have shown in Chapter 4 Section 4.3 that interference effects strongly affect the absorbed photon flux, as well as the PL response. In order to take these phenomena into account, **interference-free** PL spectra were obtained by normalizing the raw spectra by the enhancement factor calculated with Eq. (C.19) in Appendix C using the refractive index extracted from the measurements in Ref. [Lezama14]. This allows us to quantitatively compare the interference-free PL quantum yields, which are proportional to the integrated intensity of the interference-free PL spectra. Note that the enhancement factor takes into account the number of layers and is thus homogeneous to a length. Therefore, the interference-free PL quantum yields are given per unit length and one would expect to observe the same value for every N if there were no intrinsic changes in the PL quantum yields with N. Contrary to what was reported in Ref. [Yang15], the PL background from the Si substrate is negligible in our experiments.

Figure 7.5(a) displays the interference-free PL spectra for $N = 1$ to $N = 7$ and for the bulk. Note that N was determined using Raman spectroscopy (see Chapter 6). As N increases, we directly notice that

(i) the integrated PL intensity decreases monotonically and is three (resp. forty) times smaller in bilayer (resp. bulk) $MoTe_2$ than in the monolayer limit (see Fig. 7.5(b));

(ii) the PL peak energy redshifts from 1.10 eV for the monolayer down to 0.94 eV in the

[2] Likely because $MoTe_2$ emits in the near-infrared and thus requires specific detectors.

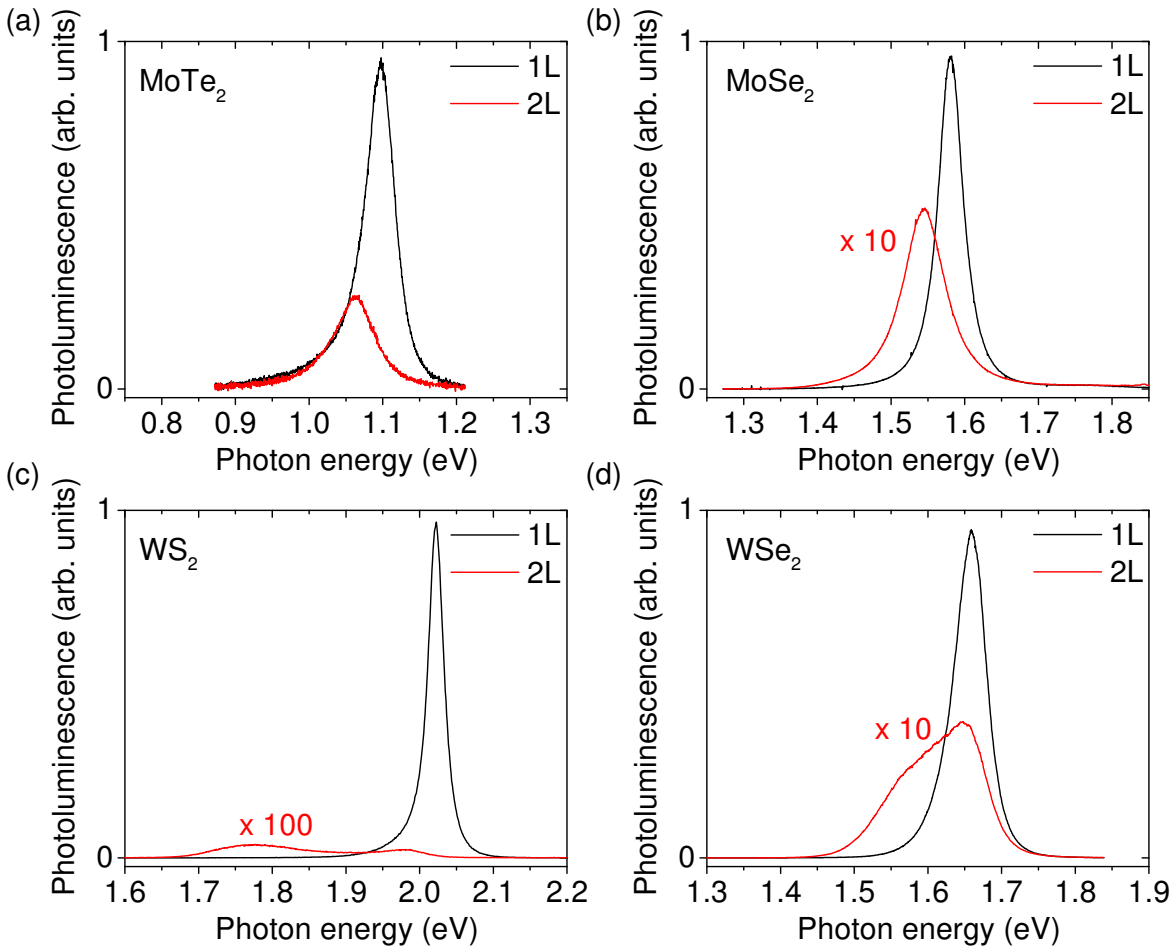

Figure 7.4 *– Photoluminescence spectra of monolayer and bilayer (a) $MoTe_2$, (b) $MoSe_2$, (c) WS_2 and (d) WSe_2 recorded at an excitation energy of 2.33 eV in ambient conditions. The data on WS_2 and WSe_2 were recorded by Olivia Zill. For each crystal, we observe a greater (from a few times to two order of magnitude) PL intensity when decreasing the number of layers, in agreement with a transition from an indirect bandgap in the bilayer to a direct bandgap in the monolayer. Bilayer Mo based materials exhibit a single prominent feature whereas W based exhibit two distinct features. he high energy feature is attributed to the direct optical bandgap and the low energy to the indirect one.*

bulk limit;

(iii) the PL lineshapes are slightly asymmetric for $N = 1, 2$ and clearly bimodal for $N \geq 3$.

The first two observations are consistent with a transition from an indirect optical bandgap in the bulk limit to a direct optical bandgap for $N = 1$ [Ruppert14]. The increase in PL quantum yield as N decreases is moderate (see Fig. 7.5(b)), as compared to recent observations in MoS_2, $MoSe_2$, WS_2, and WSe_2 [Mak10, Tonndorf13, Zhao12]. This behavior is due to the smaller energy difference between the bulk emission from the indirect optical bandgap and from the direct optical bandgap. For instance, this difference is approximately 0.6 eV in MoS_2 [Mak10], 0.5 eV in $MoSe_2$ [Tonndorf13] and WS_2 [Zhao12, Zeng13], and 0.3 eV in WSe_2 [Zhao12, Zeng13].

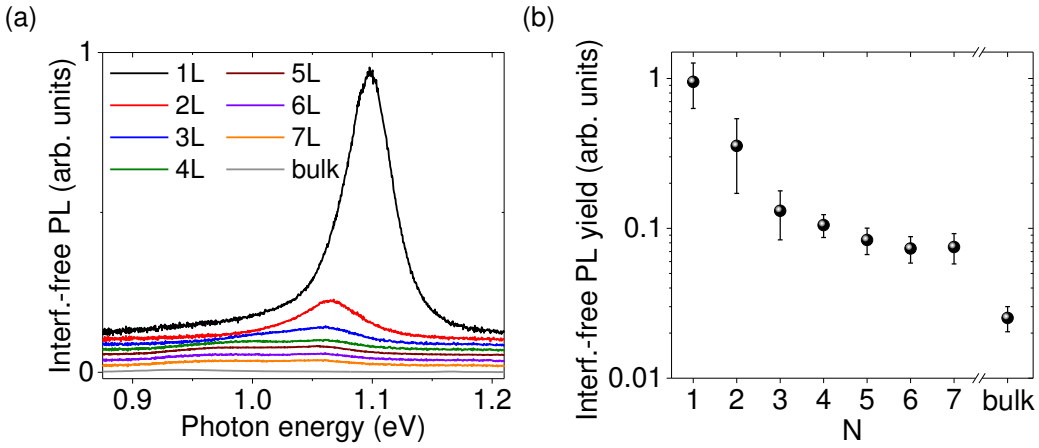

Figure 7.5 *– (a) Interference-free PL spectra of $N = 1$ to $N = 7$ layer $MoTe_2$ and of bulk $MoTe_2$ deposited on a Si/SiO_2 substrate. (b) Average total integrated intensities of the interference-free PL spectra as a function of N obtained on three samples (except for $N = 5$ and $N = 6$, for which only one sample was studied).*

7.2.2 Indirect-to-direct optical bandgap crossover

The exact value of N at which the crossover, from indirect to direct optical bandgap, occurs is still debated. Ruppert *et al.* [Ruppert14] have suggested a crossover when reaching the monolayer limit, while Lezama *et al.* [Lezama15] concluded that the crossover occurs between $N = 3$ and $N = 2$. However, there is no apparent contradiction between these claims since the two experiments were done at room and low (4 – 180 K) temperature, respectively, and it is well known that temperature might affect the crossover [Tongay12]. Furthermore, recently Robert *et al.* [Robert16b] have studied the PL of mono- and bilayer $MoTe_2$ at 10 K and 200 K and performed time-resolved measurements at 10 K. Their results are compatible with a direct or indirect optical bandgap for the bilayer. From DFT calculations, they obtained an indirect electronic bandgap for the bilayer that lies only 60 meV above the energy of the direct electronic bandgap. Taking into account the excitonic effects (binding energy of $\sim$ 500 meV), this energy difference is very small. Unfortunately, they were not able to conclude on the direct or indirect nature of the optical bandgap, since calculations are quite difficult and were beyond the scope of their study.

Here, we could clearly identify two subfeatures within each PL spectrum, as illustrated in Fig. 7.6(a). We may now wonder whether these two contributions may be associated with the direct and indirect optical bandgaps. To answer this question, we have systematically fitted the PL spectra with a double Voigt profile (see Fig. 7.6(a)) and extracted the high- (PL^+) and low-energy (PL^-) contributions. We choose a Voigt profile because it phenomenologically fits better and because there are no apparent reasons that at room temperature the PL lineshape is purely Lorentzian or Gaussian. Figure 7.6(b) displays the peak positions PL^+_{max} and PL^-_{max}.

First, the PL spectrum of monolayer $MoTe_2$ exhibits an almost symmetric lineshape dominated by a relatively narrow PL^+ feature with a full width at half maximum (FWHM) of approximately 50 meV. The peak position PL^+_{max} matches the energy of the A exciton mea-

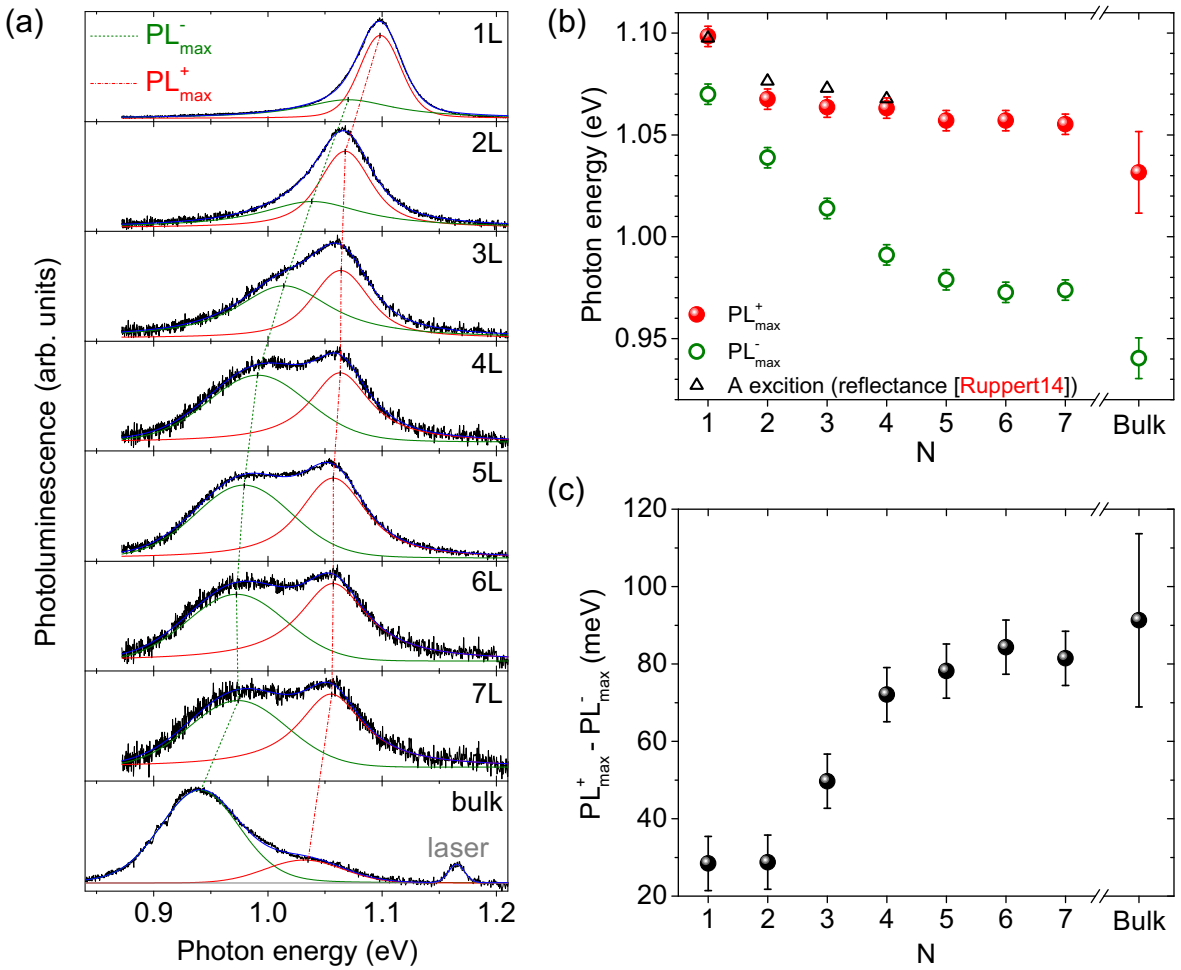

Figure 7.6 *– (a) Normalized interference-free photoluminescence spectra of $N = 1$ to $N = 7$ layer $MoTe_2$ and of bulk $MoTe_2$. The spectra are the same as in Fig. 7.5 and fit to Voigt profiles. The high (low) photoluminescence peak energy is denoted PL^{+}_{max} (PL^{-}_{max}). (b) Energy of the photoluminescence peaks PL^{-}_{max} (green open circles) and PL^{+}_{max} (red circles) as a function of the number of layers N. Our experimental measurements are compared to the reflectance (open black triangles) measurements from Ref. [Ruppert14]. (b) Energy difference between the two photoluminescence peaks as a function of the number of layers N.*

sured by room temperature differential reflectance spectroscopy by Ruppert *et al.* [Ruppert14] (see Fig. 7.6(b)) and PL^{+}_{max} is therefore identified as the direct optical bandgap energy. The PL^{-} shoulder is much broader (FWHM of approximately 100 meV) and has lower integrated intensity than the PL^{+} peak. Assuming that monolayer $MoTe_2$ is a direct bandgap semiconductor, the PL^{-} feature cannot arise from the indirect optical bandgap. Since the energy difference between the $PL^{\pm}$ features is approximately 30 meV (see Fig. 7.6(c)), the PL^{-} peak can tentatively be assigned to emission from charged A excitons (i.e., trions [Lezama15, Yang15, Robert16b]) or to exciton-phonon sidebands involving the coupling of A excitons with Γ-point optical phonons (whose energies lie in the range 15-35 meV see Chapter 6).

Second, the PL spectrum of bilayer $MoTe_2$ is slightly redshifted (by about 30 meV) with respect to the monolayer case, with a normalized PL quantum yield about three times smaller

than that of monolayer $MoTe_2$, suggesting that bilayer $MoTe_2$ is not a direct bandgap semiconductor. However, although the bilayer PL spectrum is appreciably broader than that of the monolayer PL spectrum (FWHM of approximately 65 meV), the spectra are similar. Indeed, PL^+_{max} also matches the energy of the A exciton for $N = 2$ [Ruppert14] (see Fig. 7.6(b)). In addition, the PL^+ peak is more intense than the PL^- peak, and the energy difference between the peak positions of these two features remains approximately 30 meV (see Fig. 7.6(c)), as in monolayer $MoTe_2$. We cannot attribute the PL^- peak to a trion signature as no charge tunable device based on bilayer has been reported yet. These observations indicate that the room temperature PL in mono- and bilayer $MoTe_2$ likely originates from similar mechanisms. However, the reduced PL quantum yield of bilayer $MoTe_2$ suggests that the indirect optical bandgap is slightly smaller than the direct optical bandgap such that phonon-assisted emission across the indirect optical bandgap may contribute to the broadening of the PL spectrum in bilayer $MoTe_2$. Overall, we conclude that direct optical bandgap emission dominates the room temperature PL response of bilayer $MoTe_2$.

Third, the PL spectra of $N \geq 3$-layer $MoTe_2$ differ markedly from the mono- and bilayer cases. We observe (i) a broad and prominent PL^- feature (with a FHWM of approximately 100 meV), which, as N increases, progressively dominates the narrower PL^+ feature (with a FWHM in the range 60-70 meV), and (ii), as N increases, PL^-_{max} downshifts significantly, while PL^+_{max} remains almost constant and very close to the energy of the A exciton [Ruppert14] (see Fig. 7.6(b)). In the bulk limit, the PL^- peak is centered at 0.94 eV and is followed by a much fainter feature near 1.03 eV. Note that following [Cappelluti13, Brumme15] the difference between the values of the integrated PL intensities recorded in bulk and few-layer flakes ($N = 6, 7$) (see Fig. 7.6) may arise from the fact that the bulk conduction band minimum occurs at a point in momentum space that lies halfway between the K and and the Γ points, while the conduction band minimum is reached at the Γ point in the few-layer limit. Thus, the PL^+ and PL^- peaks can tentatively be assigned to competing emission pathways, associated with hot luminescence from the A exciton and with phonon-assisted emission from the indirect excitons, respectively. Note that the PL^- peak is broader than the PL^+ peak, presumably due to the phonons involved in the indirect emission process. Finally, our conclusions are further confirmed by the fact that the bulk values of PL^+_{max} and PL^-_{max} are in fair agreement with previous measurements of the bulk direct and indirect optical bandgaps obtained from optical transmission spectroscopy [Lezama14].

7.3 Exciton-exciton annihilation in monolayer $MoTe_2$

Having studied the photoluminescence of N-layer $MoTe_2$ as a function of the number of layers N and shown that monolayer $MoTe_2$ has a direct optical bandgap, we now focus on the monolayer which optical properties are important in the perspective to develop novel optoelectronic devices (see Chapter 2). In Chapter 2, we have shown that the PL properties, and more generally the photophysics, of SCTMDs is dominated by excitonic effects due to the reduced screening of the Coulomb interaction and the relatively large effective

masses [Mak16]. Interestingly, these enhanced Coulomb interactions result in exceptionally strong exciton-exciton interactions and thus efficient Auger-type processes [Moody16]. Although, Auger-type processes are common in semiconductor physics, SCTMDs are ideal systems to study such processes. **Exciton-exciton annihilation** (EEA) has been experimentally observed at high exciton density in monolayers MoS_2 [Sun14, Yu16], $MoSe_2$ [Kumar14], WSe_2 [Mouri14, Zhu15, Yu16], and WS_2 [Yuan15, Zhu15, Yu16] through changes in the PL or absorption or in the exciton decays. However, the evolution of the PL spectrum and integrated PL intensity of monolayer $MoTe_2$ with increasing exciton density n_x remains unexplored so far. Therefore, in this section, we will focus on the influence of the absorbed photon flux $\mathcal{A}\Phi_{ph}$ on its PL quantum yield and PL spectral lineshape under continuous wave laser excitation

7.3.1 Photoluminescence spectra as a function of $\mathcal{A}\Phi_{ph}$

Absorbed photon flux $\mathcal{A}\Phi_{ph}$ The absorbed photon flux is given by $\mathcal{A}\Phi_{ph}$, where $\mathcal{A}$ is the absorptance of monolayer $MoTe_2$ in the Air/$MoTe_2$/SiO_2/Si layered structure and Φ_{ph} the incident photon flux. The former is calculated using the expressions presented in Appendix C Section C.2. For a laser photon energy of 2.33 eV, we calculated an absorptance of $\mathcal{A} \approx 16.5$ % for monolayer $MoTe_2$. This value is in line with the absorptance of MoS_2, $MoSe_2$ and WSe_2 monolayers measured on SiO_2/Si [Tonndorf13]. The latter is computed by measuring the laser beam power at the objective and by taking into account the size of the tightly focused laser spot (see Chapter 4 Section 4.2.2). The absorbed photon fluxes investigated here range from $\mathcal{A}\Phi_{ph} \approx 1 \times 10^{19}$ cm^{-2} s^{-1} up to 3.6×10^{22} cm^{-2} s^{-1}.

Photoluminescence spectra Figure 7.7(a) shows PL spectra recorded on the same monolayer for increasing values of $\mathcal{A}\Phi_{ph}$. The spectra have been normalized by the absorbed photon flux $\mathcal{A}\Phi_{ph}$ and by the integration time. We clearly observe a non-linear decrease of the normalized PL intensity suggesting that the raw integrated PL intensity levels off with increasing $\mathcal{A}\Phi_{ph}$. We have checked that this non-linear behavior was not due to irreversible photo-induced damage of the sample by monitoring the PL intenisty when cycling $\mathcal{A}\Phi_{ph}$. As illustrated in Fig. 7.7(b), we notice that the linewidth of the PL spectra is independent of $\mathcal{A}\Phi_{ph}$ and that the PL spectra downshift very slightly (by only 3 meV) only when $\mathcal{A}\Phi_{ph}$ reaches 3.6×10^{22} cm^{-2} s^{-1}. We may thus conclude that biexciton emission [You15] and photothermally-induced modifications of the PL spectra can be neglected for the range of exciton densities explored here. Note that we have checked that the PL background from the Si substrate remains negligible in our experiments.

Photoluminescence intensity In order to quantitatively study this non-linear increase of the PL intensity with $\mathcal{A}\Phi_{ph}$, we fit the PL spectra with a Voigt profile and extract the integrated intensity. The results are presented in Fig. 7.8 for two different samples. We observe comparable sub-linear rises of the integrated PL intensity for both samples. Such non-linear rises are typical of EEA, as previously reported in other SCTMDs monolayers [Mouri14, Zhu15, Yu16]. However, at low $\mathcal{A}\Phi_{ph}$ (see insert in Fig. 7.8), the PL intensity is

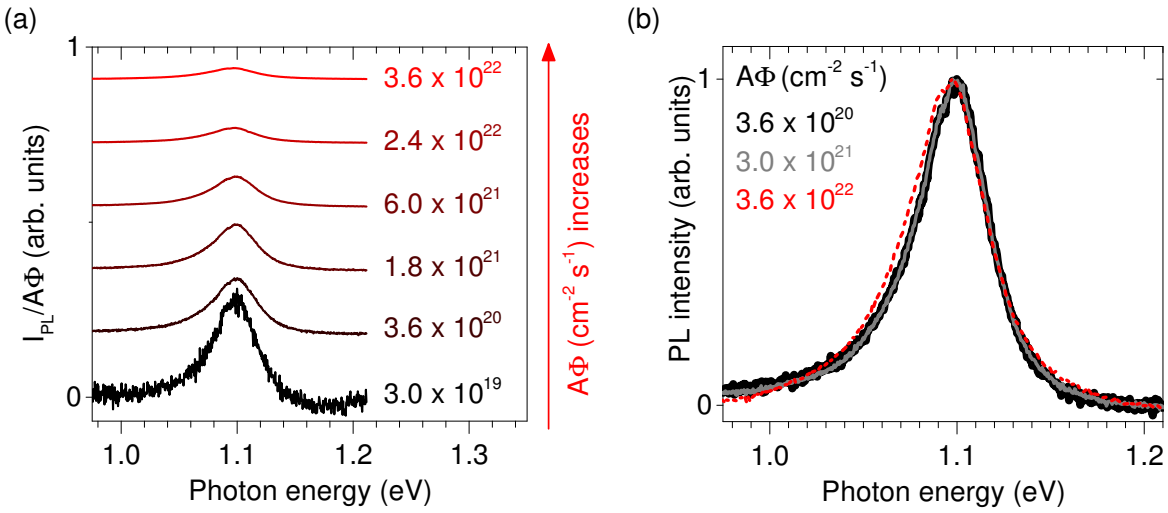

Figure 7.7 *– (a) Photoluminescence spectra of a monolayer $MoTe_2$ sample at different absorbed photon fluxes $\mathcal{A}\Phi_{ph}$. The spectra are normalized by $\mathcal{A}\Phi_{ph}$ and by the integration time, and are vertically offset for clarity. (b) Photoluminescence spectra of monolayer $MoTe_2$ for three different absorbed photon fluxes. The spectra have been normalized to unity.*

almost linear because the exciton density is not high enough to observe EEA processes. Such low $\mathcal{A}\Phi_{\mathrm{ph}}$ were used to record the N-layer spectra presented in Section 7.2. The transition between the linear and non-linear regimes occurs at approximately $\mathcal{A}\Phi_{\mathrm{ph}} \approx 10^{21}$ cm^{-2} s^{-1}. Note that the Raman measurements in Chapter 6 were done at $\mathcal{A}\Phi_{\mathrm{ph}} \sim 10^{23}$ cm^{-2} s^{-1}, i.e., in the non-linear regime where EEA are non negligible.

7.3.2 Rate equation model

In order to further demonstrate the observation of EEA in monolayer $MoTe_2$, we make use of a simple rate equation model [Yu16]. In the continuous wave regime, the integrated PL intensity is proportional to the steady state exciton density $\langle n_{\mathrm{x}} \rangle$. The proportionality factor contains the product of the radiative decay rate and the detection efficiency of the experimental setup. Assuming, that the time dependence of the exciton density n_{x} is essentially governed by the interplay between exciton formation (at a rate per unit area $\mathcal{A}\Phi_{\mathrm{ph}}$), linear recombination (at a rate Γ_{x}) and excition-exciton annihilation (EEA) (at a rate γ_{eea}), one obtains

$$\frac{\mathrm{d}n_{\mathrm{x}}}{\mathrm{d}t} = \mathcal{A}\Phi_{\mathrm{ph}} - \Gamma_{\mathrm{x}} n_{\mathrm{x}} - \gamma_{\mathrm{eea}} n_{\mathrm{x}}^2. \tag{7.9}$$

Note that we have assumed that one absorbed photon gives rise to one exciton since excitonic effects are very strong. The EEA term in this equation scales quadratically with n_{x} since the annihilation process involves Coulomb interaction between two excitons. The steady state exciton density is

$$\langle n_{\mathrm{x}} \rangle = \frac{\Gamma_{\mathrm{x}}}{2\gamma_{\mathrm{eea}}} \left(\sqrt{1 + \frac{4\gamma_{\mathrm{eea}}}{\Gamma_{\mathrm{x}}^2} \mathcal{A}\Phi_{\mathrm{ph}}} - 1 \right). \tag{7.10}$$

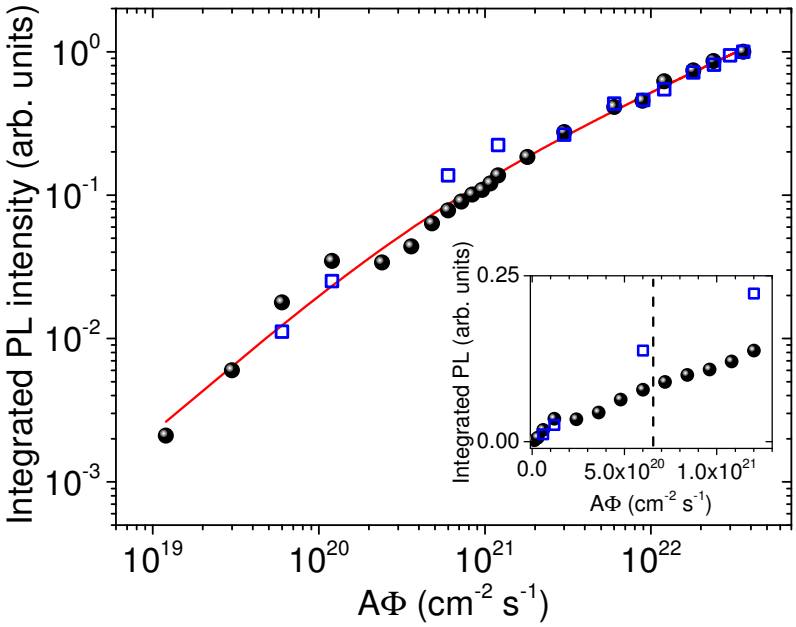

Figure 7.8 *– Integrated photoluminescence intensity as a function of the absorbed photon flux $\mathcal{A}\Phi_{ph}$ for two different monolayer samples $MoTe_2$. The black-filled circles are data from the same sample as Fig.7.7 (sample 1). The solid red line is the fit to this data using Eq.(7.10). The raw PL intensity from the second sample has been multiplied by a factor of 2.4 (open blue squares) to show a clearer comparison with the data from sample 1. The normalized PL intensity from sample 2 scales very similarly as the PL intensity from sample 1, suggesting similar exciton-exciton annihilation rates and linear exciton decay rates for both samples. The inset shows the same data at low absorbed photon fluxes $\mathcal{A}\Phi_{ph}$, on a linear scale. The vertical dashed line indicates the absorbed photon flux at which the measurements on N-layer $MoTe_2$ shown in Section 7.2 have been performed. The error bars are smaller than the symbols size.*

The experimental data of sample 1 in Fig. 7.8 are very well fit by Eq. (7.10). From the fit, we extract $\gamma_{eea}/\Gamma_x^2 \approx 1.4 \times 10^{-21}$ cm^2 s. Assuming a reasonable value of $\gamma_{eea} \sim 0.1$ cm^2 s^{-1}, similar to previous estimates in substrate-supported SCTMDs monolayers [Kumar14, Sun14, Yu16, Mouri14, Yuan15], one obtains a linear exciton recombination rate of $\Gamma_x \sim 8.5 \times 10^9$ s^{-1}, that is an exciton lifetime of ~ 120 ps at room temperature. Although additional near-infrared time-resolved measurements or transient absorption studies on monolayer $MoTe_2$ are needed to separately determine the exact values of γ_{eea} and Γ_x, our simple analysis provides values that are in-line with recent room-temperature studies on other SCTMDs [Yu16]. Very recently, Robert *et al.* [Robert16a] have measured an intrinsic exciton lifetime of 4 ps at 10 K. However, it is well known [Moody16] that exciton lifetime increase with temperature due to, for instance, the presence of dark states [Zhang15a] (see Chapter 2 Section 2.2) or exciton-phonon coupling [Korn11]. Previously, we have mentioned that EEA dominates for $\mathcal{A}\Phi_{ph}$ higher than approximately 10^{21} cm^{-2} s^{-1}, while linear recombination dominates for lower rates. Using the estimations of γ_{eea} and Γ_x, we can deduce that this value corresponds to an average exciton-exciton distance of $1/\sqrt{\langle n_x \rangle} \approx 40$ nm, which seems to be a reasonable value knowing that micrometer-long exciton diffusion lengths were reported for monolayers WSe_2 [Mouri14].

7.4 Conclusion

To conclude, we have first recalled some generalities on photoluminescence spectroscopy. Then, we have performed a detailed analysis of the room temperature photoluminescence of N-layer $MoTe_2$. Monolayer $MoTe_2$ displays a direct optical bandgap, with sharp emission at 1.10 eV. The crossover from a dominant direct excitonic emission (as observed in monolayers) to a dominant phonon-assisted indirect emission (in the bulk limit) occurs more smoothly than in other transition metal dichalcogenides, such as MoS_2, $MoSe_2$, WS_2 and WSe_2. As a result, the difference between the bulk indirect optical bandgap and the monolayer direct optical bandgap is found to be only about 160 meV. This observation of close-lying direct and indirect emission lines invites further calculations of exciton-phonon coupling in $MoTe_2$ and related systems, in order to correlate the values of the one-particle indirect bandgap to the energy of the emission lines arising from indirect exciton recombination. In addition, we have unveiled a sub-linear scaling of the photoluminescence intensity of monolayer $MoTe_2$ with increasing absorbed photon flux, which can be rationalized using a simple model based on exciton-exciton annihilation. This model also allowed us to obtain an order of magnitude estimate for the exciton lifetime in the linear regime that needs to be quantitatively confirmed by time-resolved photoluminescence measurements in the near-infrared range. Note that EEA in monolayers transition metal dichalcogenides is much more efficient than related processes in conventional quantum wells [Haug92, Taylor96, Sun14] and that this reflects the strongly enhanced Coulomb interactions in these materials.

Take home messages

- Monolayer $MoTe_2$ exhibits a direct optical bangap 1.10 eV at room temperature.
- N-layer semiconducting transition metal dichalcogenides display a very rich photophysics.
- The photoluminescence of monolayers semiconducting transition metal dichalcogenides presents strong nonlinearities.

Related publication

Papers

- G. Froehlicher, E. Lorchat, and S. Berciaud, *Direct versus indirect band gap emission and exciton-exciton annihilation in atomically thin molybdenum ditelluride ($MoTe_2$)*, Phys. Rev. B **94**, 085429 (2016).

Chapter 8

Monolayer graphene/monolayer transition metal dichalcogenides van der Waals heterostructures

In this chapter, we study the interlayer coupling in monolayer graphene/monolayer transition metal dichalcogenides van der Waals heterostructures by means of micro-photoluminescence and micro-Raman spectroscopy. As an example, we focus on monolayer graphene/monolayer $MoSe_2$ heterostructures. Importantly, the results of Chapters 5 and 7 will be used in this chapter. We first highlight the strong interlayer coupling by atomic force microscopy, by photoluminescence and by Raman mapping. Then, from Raman measurements in graphene, we demonstrate and quantify the transfer of photoexcited electrons from $MoSe_2$ to graphene. Next, we investigate the photoluminescence response of $MoSe_2$ in the heterostructure and show that its massive quenching cannot be solely explained by charge transfer, suggesting that energy transfer plays a significant role. Finally, the influence of the environmental conditions is discussed and a toy model based on rate equations, that qualitatively reproduces our observations, is presented.

8.1 Characterization of the heterostructures

8.1.1 Context

In Chapter 2, we have shown that van der Waals heterostuctures (vdWHs) are very promising for optoelectronic applications. In such structures, the behavior of photoexcited carriers and excitons is largely affected by interlayer coupling. Interlayer charge transfer (ICT) and energy transfer (IET) may lead to drastic changes in the photophysical and optoelectronic properties. Charge transfer can be efficiently harvested in optoelectonic devices [Zhang14, Massicotte16a]. However, the performances of such devices are limited by the interlayer interactions: IET leads to losses and thus limits the gain, and ICT limits the

response time of the detectors. Therefore, a good understanding, as well as a precise control, of these mechanisms is crucial for the improvement of the efficiency of optoelectronic devices. So far, few essential points are still missing: (i) what is the relative weight of ICT and IET, (ii) what are the associated microscopic mechanisms, (iii) what are their respective efficency and (iv) how changes in the environment and in Fermi energies affect these two mechanisms? To try to answer to these questions, we choose to investigate the basic unit monolayer graphene/monolayer TMDs by means of Raman and PL. spectroscopy. Indeed, the previous chapters have demonstrated the efficiency of these techniques to study 2D materials. In particular, in Chapter 5, we have shown that Raman spectroscopy is an accurate tool to quantitatively measure the charge carrier density in graphene. Hence, it can be used to demonstrate and quantify the ICT. Moreover, PL spectroscopy is a powerful technique to address the carrier dynamics as evidenced in Chapter 7.

8.1.2 The samples

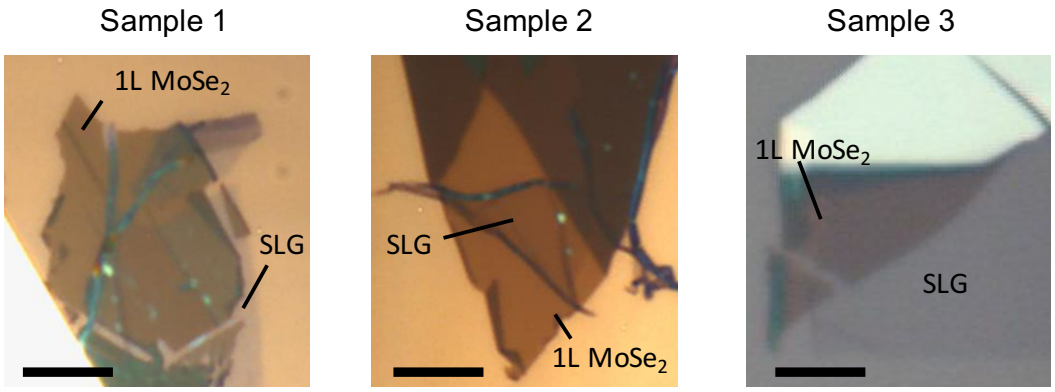

Figure 8.1 *– Optical image of three single layer graphene (SLG)/monolayer (1L) $MoSe_2$ van der Waals heterostructures (deposited onto a Si/90 nm SiO_2 substrate). Sample 2 and 3 were annealed at low pressure. Scale bar: 5 µm.*

Our first intention was to build monolayer graphene/monolayer $MoTe_2$ vdWHs because the smaller bandgap of $MoTe_2$ should make the study of the influence of graphene's Fermi energy on the interlayer transfer (IT) easier. Unfortunately due to technical reasons (we did not have the proper detector[1]) but also for improved environment stability, we started by working with monolayer graphene/monolayer $MoSe_2$ vdWHs (hereafter denoted SLG/$MoSe_2$) prepared using the transfer technique detailed in Chapter 4 Section 4.1.2. Note that during the fabrication, we did not pay attention to the twist angle between the two monolayers which is probably different for each sample. No strong effects were observed, suggesting that the twist angle is probably not an essential parameter. Among the fabricated structures, we have mainly studied three samples denoted sample 1, 2 and 3. These samples are displayed in Fig. 8.1. Contrary to sample 1, samples 2 and 3 were annealed at low pressure ($\sim 10^{-6}$ mbar) at 150 °C for 1 hour and 200 °C for 2 hours in order to improve the interlayer

[1] As outlined in Chapter 4, the InGaAs detector used to obtain the results of Chapter 7 was loaned by the manufacturer.

coupling [Lui15]. For all samples, the SLG is on the top of $MoSe_2$ layer and is not covering it entirely. Therefore, the PL of pristine $MoSe_2$ can be recorded on the same flake as for the vdWH. The part of the SLG lying in SiO_2 can be used as a reference for Raman measurements. Most of the results presented in this chapter were obtained on sample 1 but very similar results were observed on the two others samples (see Section 8.2.5).

8.1.3 Atomic Force Microscopy

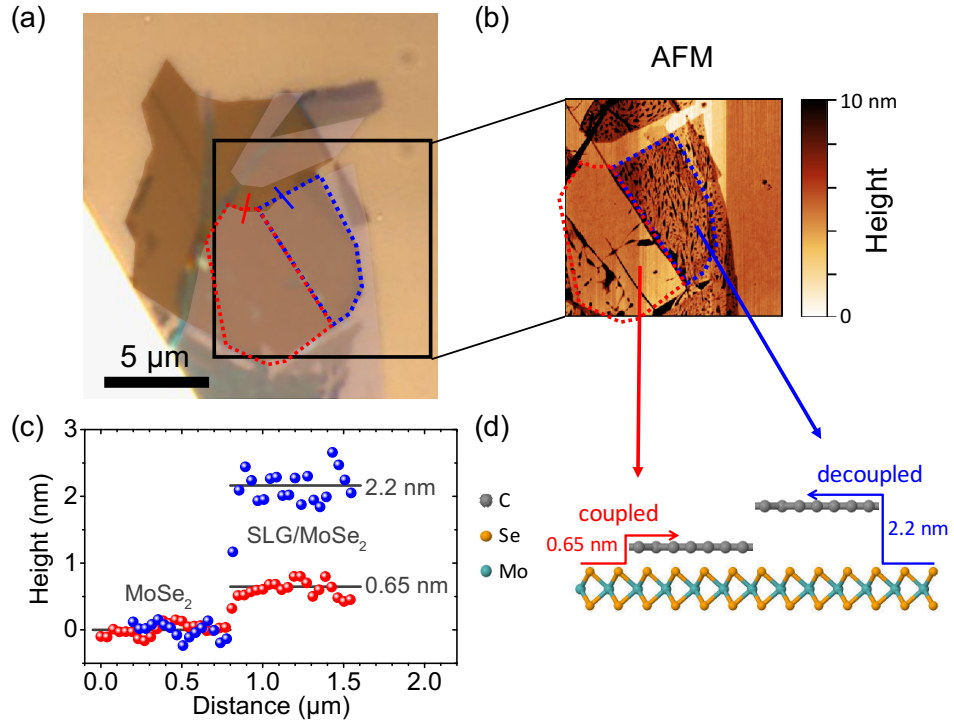

Figure 8.2 *– (a) Optical image of sample 1. The two different layers have been highlighted with colors. (b) Atomic force microscopy image of the black square in (a). (c) Height profiles, measured by atomic force microscopy, along the blue and red lines drawn in (a). (d) Side view of the heterostructure showing the coupled and decoupled regions. These two particular regions are highlighted with red and blue dashed lines, respectively, in (a) and (b).*

The heterostructures were first characterized by atomic force microscopy (AFM). Figure 8.2(b) shows an AFM image of sample 1. We distinguish two regions in the heterostructure. The region delimited by the red dashed line display a very clean interface, while the other delimited by the blue dashed line shows lots of small 'pockets'. As explained in Chapter 2 Section 2.3, these small pockets corresponds to contaminants and are pushed away when the two layers are well coupled (see also Fig. 2.16). Consequently, from this observation, we conclude that in the former region the two layers are well **coupled**, while in the latter they are not and thus said to be '**decoupled**'[2] (see Fig. 8.2(d)). Note that this is why sample 1 is particularly interesting because one can compare a coupled and decoupled heterostructure on the same sample. Furthermore, interlayer coupling is confirmed by the measured height difference between the two layers. The height profile for the two regions is displayed in Fig. 8.2(c).

[2]Note that this part may be not fully decoupled as we will see later.

For the coupled region, we measure a step of 0.65 nm. Knowing that the typical thickness of a monolayer graphene is 0.33 nm, we can estimate that the interlayer distance is approximately 0.3 nm. For the other region, we measure a step of 2.2 nm, i.e., an interlayer distance of around 1.9 nm.

8.1.4 Photoluminescence mapping of $MoSe_2$

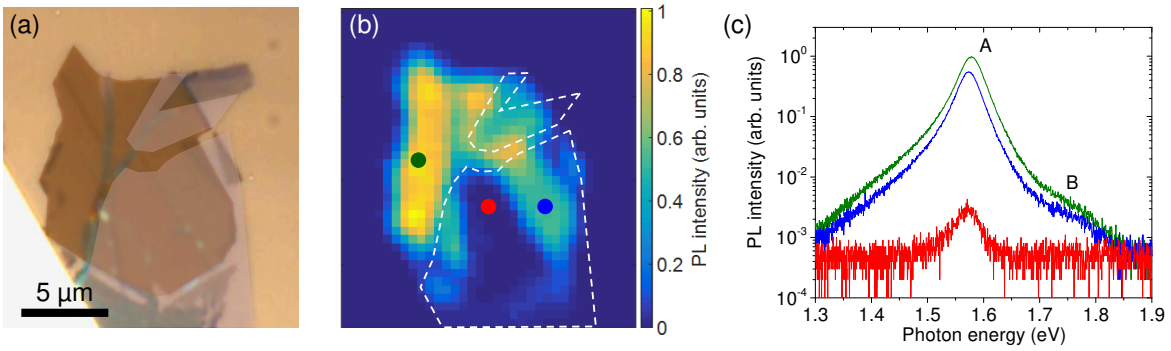

Figure 8.3 *– (a) Optical image of sample 1. (b) Photoluminescence map of sample 1 (same dimensions as the optical image in (a)) recorded in ambient conditions with an excitation energy of $E_L = 2.33$ eV and an incident photon flux $\Phi_{ph} = 2 \times 10^{19}$ cm^{-2} s^{-1}. The SLG is highlighted by white dashed lines. (c) Photoluminescence spectra of the three points defined in (b). The spectra are plotted with the same color as the dots in (b).*

Figure 8.3(b) displays the photoluminescence map of sample 1 recorded in ambient conditions with an excitation energy of $E_L = 2.33$ eV and an incident photon flux $\Phi_{ph} = 2 \times 10^{19}$ cm^{-2} s^{-1}. We can clearly recognize the shape of the $MoSe_2$ layer and can distinguish three parts: pristine $MoSe_2$, coupled and decoupled SLG/$MoSe_2$. For each part, Fig. 8.3(c) displays a PL spectrum. On these spectra, we observe the typical PL features of monolayer $MoSe_2$ [Tonndorf13, Ross13, Wang15a, Wang15c] (see also Fig. 7.4(b)) i.e., the A exciton at around 1.570 eV and the B exciton at around 1.755 eV (not visible for coupled SLG/$MoSe_2$). However, the intensities are different for the three parts. For decoupled SLG/$MoSe_2$, there is only a slight decrease (factor ~ 2) of the PL intensity compared to bare $MoSe_2$, whereas for the coupled part, the PL intensity is ~ 300 times weaker than on pristine $MoSe_2$. Such a significant quenching indicates a **strong interlayer coupling**. Similar PL quenching was observed for graphene/TMD [He14a, Shim14, Massicotte16a, Pierucci16b] and TMD/TMD [Furchi14b, Cheng14, Fang14, Lee14a, Hong14, Yu14, Rivera15] vdWHs. However, our quenching factor is higher than the reported ones in the literature. A possible explanation is that the incident photon flux, used to record the reference on pristine TMD, was too high in the other studies. Indeed, as evidenced in Chapter 7, the increase of the PL intensity with Φ_{ph} is sub-linear. In addition, not all the measurements were done at the same temperature while temperature is known to affect the PL intensity because of the presence of dark states [Zhang15a] or electron-phonon coupling [Korn11]. One may wonder if optical interference effects could explain the reduction of the PL intensity in the heterostructure, at least for the decoupled region. Using Appendix C, we calculated that the PL intensity for

SLG/$MoSe_2$ (assuming no gap between the two layers) is decreased by approximately 5 % compared to pristine $MoSe_2$. This value is too low to explain the observed difference in the PL intensity, even for the decoupled region.

8.1.5 Raman mapping of graphene

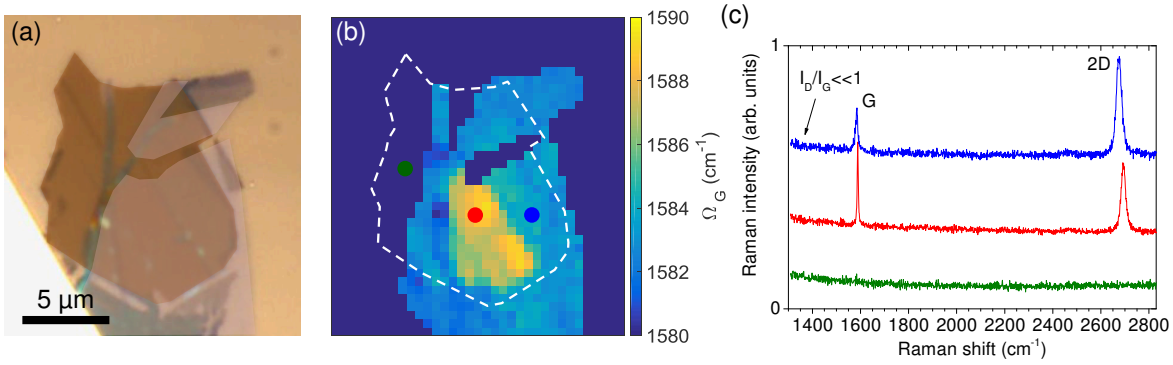

Figure 8.4 *– (a) Optical image of sample 1. (b) G-mode frequency map of the sample 1 (same dimensions as the optical image in (a)) recorded in ambient conditions with an excitation energy of E_L = 2.33 eV and an incident photon flux $\Phi_{ph} = 2\times10^{22}\ cm^{-2}\ s^{-1}$. An increase in the G-mode frequency indicates an increase of doping level (see Chapter 5). The monolayer $MoSe_2$ is highlighted by white dashed lines. (c) Raman spectra of the three points defined in (b). The spectra are plotted with the same color as the dots in (b) and are vertically offset for clarity.*

Figure 8.4(b) shows graphene G-mode frequency map of sample 1 recorded in ambient conditions with an excitation energy of E_L = 2.33 eV and an incident photon flux $\Phi_{ph} = 2\times10^{22}$ cm^{-2} s^{-1}. We can readily recognize the graphene shape (including the multilayer in the upper right part of the heterostructure and the two pieces of rolled graphene probably induced during the fabrication process). For the three same parts and points as previously, Fig. 8.4(c) displays the corresponding Raman spectrum. We observe the two main Raman features of pristine graphene (see Chapter 5), the G- and 2D- mode features, in the coupled and decoupled SLG/$MoSe_2$, but of course not for individual $MoSe_2$. Note that no defect-induced D-mode feature emerges from the background showing the very good quality of the sample. However, the spectrum of the coupled and decoupled regions are different. To study in detail these disparities, we have plotted the map of the frequency and FWHM of the G- and 2D-mode feature, and the ratio between their integrated intensity in Fig. 8.5.

First, in all maps, we can immediately identify the coupled part of the heterostructure. Indeed, we observe major spectral modifications compared to the others regions (pristine $MoSe_2$ and graphene, and decoupled SLG/$MoSe_2$). In particular, we notice an upshift of Ω_G and Ω_{2D}, a decrease of Γ_G and Γ_{2D} and of the I_{2D}/I_G ratio. Based on the results in Chapter 5, we can readily conclude that these variations are robust signatures of changes in the doping level of graphene. Such changes also demonstrate the strong interlayer coupling which induce an **interlayer charge transfer** (ICT). Furthermore, the decoupled region exhibits similar values as the rest of the graphene sheet laying on SiO_2 or on multilayer $MoSe_2$. Hence, no change of doping level is observed for decoupled SLG/$MoSe_2$ confirming the weak interlayer coupling

of this part of the heterostructure.

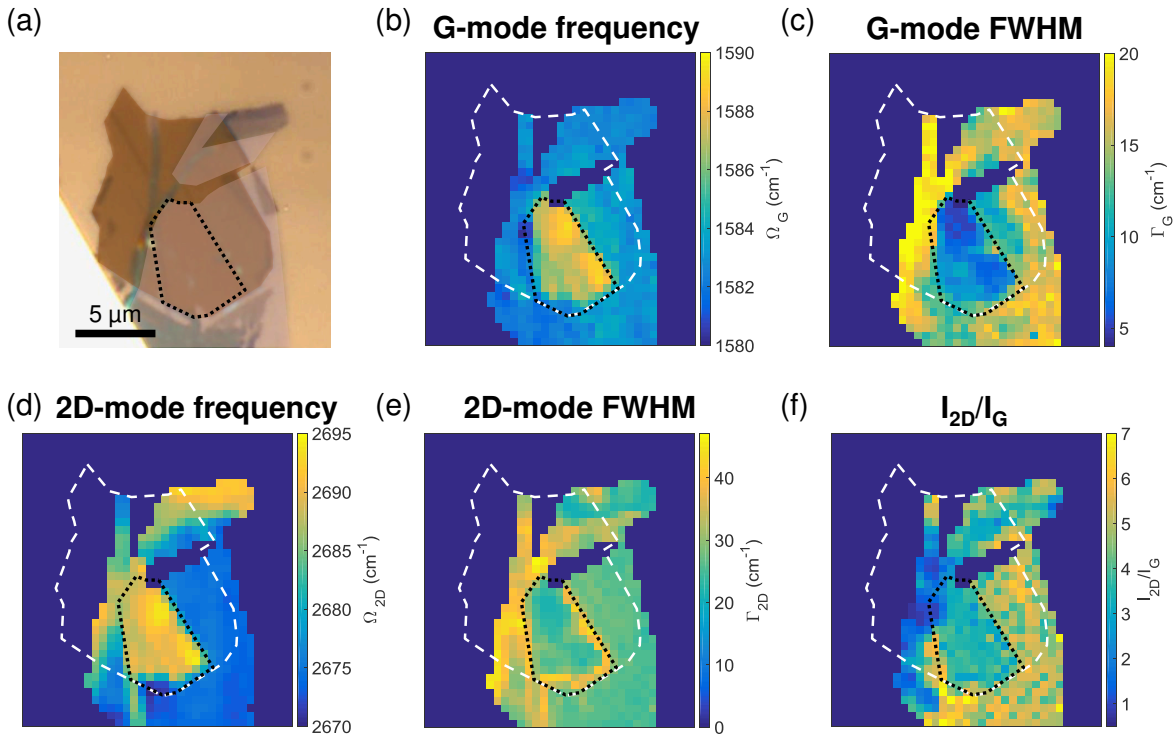

Figure 8.5 *– (a) Optical image of sample 1. Raman map of graphene (b) G-mode frequency, (c) G-mode FWHM, (d) 2D-mode frequency, (e) 2D-mode FWHM and (f) ratio between the integrated intensity of the 2D-mode feature and that of the G-mode feature I_{2D}/I_G. In (b)-(f) the monolayer $MoSe_2$ is highlighted with white dashed lines and the coupled part of the heterostructure with black dotted lines. These maps were recorded in ambient conditions with an excitation energy of $E_L = 2.33$ eV and an incident photon flux $\Phi_{ph} = 2 \times 10^{22}$ cm^{-2} s^{-1}.*

8.1.6 Conclusion

To conclude this section, we have reported a strong interlayer coupling in a well-defined part of the SLG/$MoSe_2$ heterostructure in sample 1. Similar results were observed on the two other samples. Such strong interlayer coupling gives rise to a massive quenching of $MoSe_2$ photoluminescenc and a clear ICT. However, at this stage, IET cannot be excluded as it may significantly contribute to the large PL quenching factors that we observed.

In the following, we are going to study the Raman spectrum of the SLG and the PL of $MoSe_2$ as a function of the incident photon flux (Φ_{ph}) to (i) confirm the photoinduced ICT, (ii) identify the nature of the ICT, (iii) quantify the ICT and (iv) try to evidence an IET.

8.2 Raman spectroscopy as a function Φ_{ph}

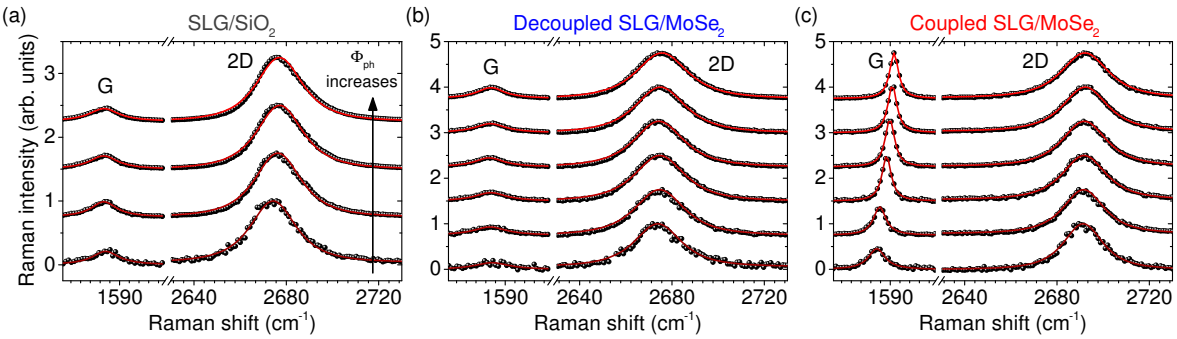

Figure 8.6 *– Raman spectra recorded at $E_L = 2.33$ eV in ambient conditions for increasing values of incident photon flux (Φ_{ph}), between 3.3×10^{20} cm^{-2} s^{-1} and 4.2×10^{23} cm^{-2} s^{-1}, for (a) SLG/SiO_2, (b) decoupled and (c) coupled SLG/$MoSe_2$ heterostructures. The spectra are vertically offset for clarity. Symbols are the experimental data and the solid lines are fits. A Lorentzian background have been subtracted for the G band due to residual PL of the $MoSe_2$.*

8.2.1 Raman spectrum of graphene

We first study the Raman spectrum of graphene for increasing Φ_{ph} at three fixed points of sample 1: one on the coupled part of the heterostructure, one on the decoupled part and one on graphene on SiO_2 (located in the lower right part of the sample in Fig. 8.1(a)). The latter serves as a reference. Note that in general Raman spectrum are measured at $\Phi_{ph} \gtrsim 10^{22}$ cm^{-2} s^{-1}, but in this study we have also measured at much lower flux. Figure 8.6 shows the G- and 2D- mode features for some of the recorded spectra. While the Raman spectra of SLG/SiO_2 and decoupled SLG/$MoSe_2$ remain mostly not affected by the increase of Φ_{ph}, the Raman spectra of coupled SLG/$MoSe_2$ are strongly affected. To quantitatively compare and investigate these changes, we fit the G- and 2D-mode features and extracted the frequency, linewidth and ratio of the integrated intensity. The results of the fit are displayed in Fig. 8.7.

On the one hand, for SLG/SiO_2 and decoupled SLG/$MoSe_2$, we observe that the G- and 2D-mode frequency, linewidth and integrated intensity are almost constant and equal to $\Omega_G \approx 1583$ cm^{-1}, $\Gamma_G \approx 16$ cm^{-1}, $\Omega_{2D} \approx 2674$ cm^{-1} and $I_{2D}/I_G \approx 6.5$. These values correspond to very weakly doped graphene ($|n| \sim 10^{11}$ cm^{-2} or $|E_F| \lesssim 100$ meV). This is further confirmed by the slightly asymmetric line shape of the 2D-mode feature in Figs. 8.6(a) and (b) [Berciaud09, Luo12, Berciaud13]. Noteworthy, we calculated that I_{2D}/I_G is enhanced by a negligible factor of about 4 % compared to SLG/SiO_2 due to optical interference effects. On the other hand, for coupled SLG/$MoSe_2$, the G- and 2D-mode features distinctly evolve with increasing Φ_{ph} in agreement with a change of doping (see Chapter 5). Since there are no changes for SLG/SiO_2 and decoupled SLG/$MoSe_2$, we conclude that this doping is in fact a signature of a **photoinduced ICT from $MoSe_2$ to graphene**. Moreover, at low Φ_{ph}, the value of Ω_G, Γ_G and I_{2D}/I_G get closer to the values of weakly doped graphene, suggesting that by extrapolating at $\Phi_{ph} = 0$ the graphene is weakly doped. Consequently, if there is a **static** (i.e., not photoinduced) ICT between the two monolayers, it is negligible as compared to the photoinduced one.

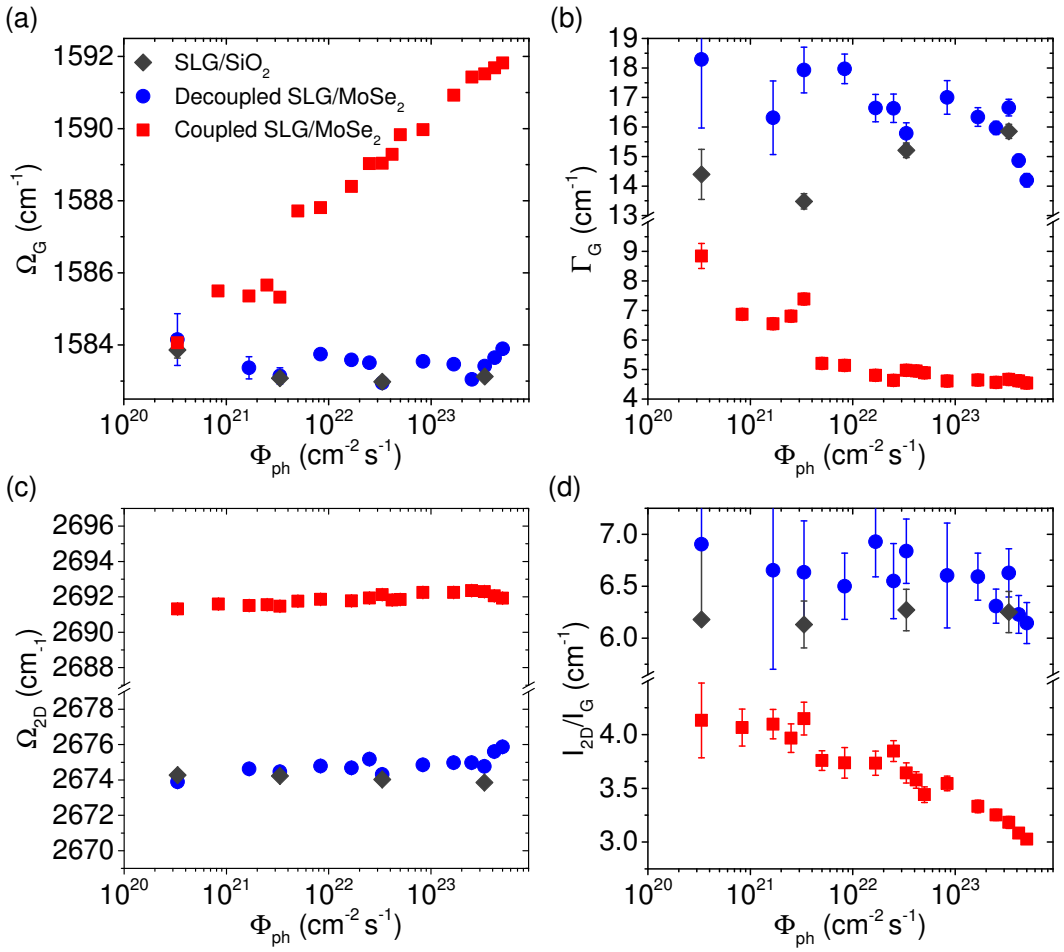

Figure 8.7 *– (a) G-mode frequency Ω_G, (b) full width at half maximum Γ_G, (c) 2D-mode frequency Ω_{2D} and (d) ratio between the integrated intensity of the 2D-mode feature and that of the G-mode feature I_{2D}/I_G, extracted from the fits in Fig. 8.6(a)-(c).*

Let us now briefly comment on the 2D-mode frequency. In Fig. 8.7(c), we notice that there is a rigid upshift of ≈ 17 cm^{-1} in coupled SLG/$MoSe_2$ compared to SLG/SiO_2 and decoupled SLG/$MoSe_2$. This upshift cannot be explained by a change of doping or strain. Indeed, the 2D mode is less sensitive to doping than the G mode but is more sensitive to strain. However, an upshift of the 2D-mode frequency of around 17 cm^{-1} caused by strain would also lead to an upshift of the G-mode frequency of around 8 cm^{-1} [Metten14] (see Chapter 5 Section 5.4). Such a shift is clearly not observed. Interestingly, a similar upshift of the 2D-mode feature has been observed in SLG/thick hBN [Ahn13, Forster13, Neumann15] and SLG/monolayer MoS_2 heterostructures [McCreary14]. For SLG/hBN, this shift has been explained by the screening of the thick hBN substrate, which reduces the electron-phonon coupling at the K and K' points. It is not obvious that a similar explanation could work for SLG/monolayer TMD because of the atomic thickness of the TMD. Another possible explanation could be the modification of the band structure due to the interaction. However, in the case of MoS_2/SLG, it has been calculated that the effects of the interaction on graphene band structure at Γ, K and K' can be neglected [Komsa13, Pierucci16a]. This observation will need further theoretical

investigations to be fully understood.

8.2.2 Nature of the ICT

We can make use of the extracted frequencies and linewidths to identify the nature of the ICT using the universal correlations shown in Chapter 5 Section 5.4. For this, we assume that these correlations hold for SLG/$MoSe_2$. Figure 8.8(a) shows Γ_G as a function of Ω_G and Fig. 8.8(b) represents the evolution of Ω_{2D} as a function of Ω_G for the three same points of sample 1 as in Fig. 8.7.

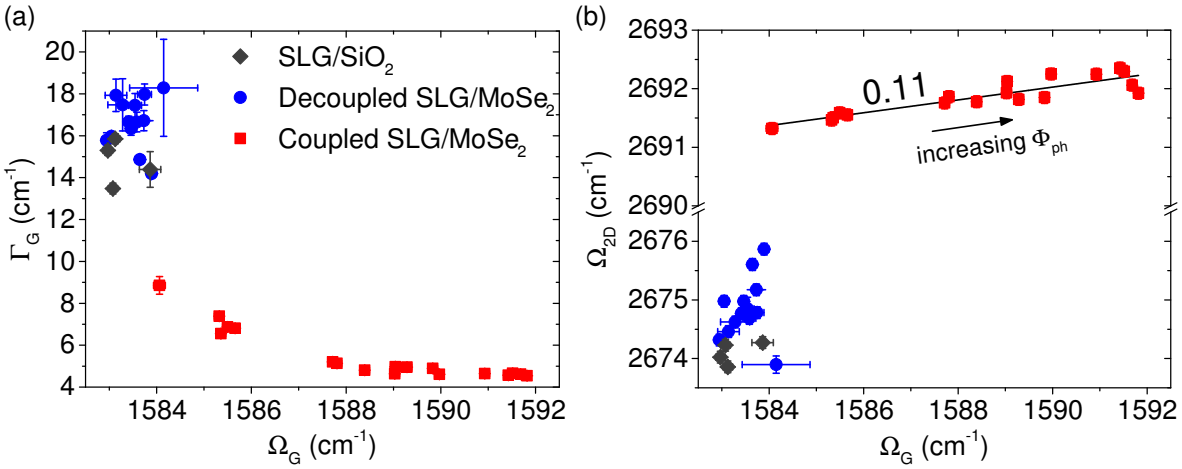

Figure 8.8 *– Correlations between (a) the FWHM and frequency of the G-mode feature, (b) the frequencies of 2D- and G- mode features under increasing photon flux Φ_{ph} for the three same fixed points of sample 1 as in Figs. 8.6-8.7.*

We observe that the $\Gamma_G(\Omega_G)$ follows the curve of doped graphene (see Fig. 8.7). The SLG/SiO_2 and decoupled SLG/$MoSe_2$ points are close to the CNP (1583.5 cm^{-1}, 17 cm^{-1}), while the coupled SLG/$MoSe_2$ points are spread along the doping curve. Unfortunately, this correlation cannot be used to differentiate electron and hole doping since the slight difference expected between the two curves cannot be resolved experimentally. However, it confirms again the photoinduced ICT and that be extrapolating at $\Phi_{ph} = 0$ the SLG coupled with $MoSe_2$ is weakly doped.

On the other hand, the 2D- and G-mode frequencies correlation can be used to separate strain from hole and electron doping. When increasing Φ_{ph}, the data for SLG/SiO_2 and decoupled SLG/$MoSe_2$ cluster around (1583.5 cm^{-1}, 2674.5 cm^{-1}) and show no clear correlations indicating that for the range of Φ_{ph} studied here heating effects can be neglected. On the contrary, the measured frequencies on coupled SLG/$MoSe_2$ follow a linear correlation with a slope of about 0.11. This value indicates electron doping in graphene (see Fig. 5.16). Consequently, **photoexcited electrons** generated in $MoSe_2$ transfer to graphene. This is in agreement with previous studies made on SLG/MoS_2 [Zhang14, Shim14, De Fazio16, Pierucci16b] and SLG/WS_2 [He14a] heterostructures. However, here, we unambiguously demonstrate the nature of the ICT. Noteworthy, the electron transfer is an agreement with the band alignments

(see Chapter 2 Fig. 2.17).

8.2.3 Spatial variations

We now focus on the spatial variation of the ICT. Instead of recording Raman maps, we choose to perform line scans because it is faster and gives similar information.

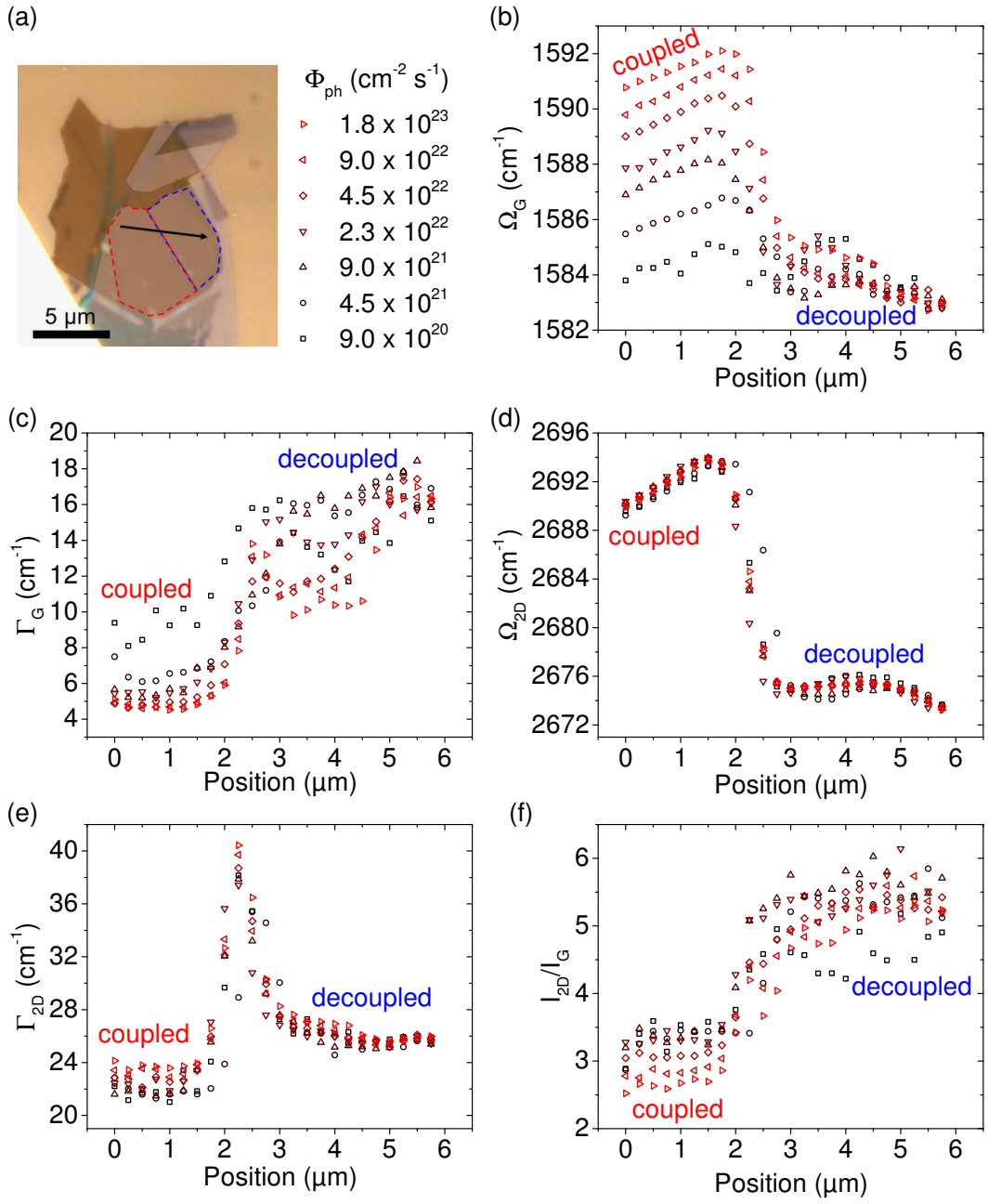

Figure 8.9 *– (a) Optical image of sample 1. The red (blue) dashed line delimits the coupled (decoupled) part of the heterostructure. The line scans were recored along the black arrow. The incident photon flux Φ_{ph} are indicated. (b) G-mode frequency Ω_G, (c) G-mode FWHM Γ_G, (d) 2D-mode frequency Ω_{2D}, (e) 2D-mode FWHM Γ_{2D} and (f) ratio between the integrated intensity of the 2D-mode feature and that of the G-mode feature I_{2D}/I_G along the line scan.*

Figure 8.9 presents the extracted frequency, linewidth and ratio between the integrated intensities of the G- and 2D- mode features as a function of the position along the line scan for various Φ_{ph}. We can clearly observe the transition from coupled to decoupled SLG/$MoSe_2$ in all quantities. Their evolution with Φ_{ph} is in good agreement with the previous observations. Note that the rigid shift of the 2D-mode frequency between coupled and decoupled SLG/$MoSe_2$ is obvious in Fig. 8.9(d). Furthermore, Γ_{2D} is approximately 3 cm^{-1} lower in the coupled heterostructure than in the decoupled one. Such narrowing of the 2D-mode feature was also observed in SLG/thick hBN [Ahn13, Forster13, Neumann15] and qualitatively explained with the same arguments as the frequency shift. Interestingly, $\Gamma_{2D} \approx 22 - 23$ cm^{-1} corresponds to the value measured for SLG/hBN [Forster13, Neumann15] and suspended graphene [Berciaud09] suggesting that $MoSe_2$ can also be viewed as a high quality substrate. The increase of Γ_{2D} by almost a factor 2 in the transition between coupled and decoupled heterostructure can be understood by the combined effects of the rigid frequency shift of Ω_{2D} and of the size of the focused laser beam.

For a given Φ_{ph} along the line scan, Ω_G and Ω_{2D} slightly upshift (downshift) in the coupled (decoupled) part. Such changes can be induced by strain and/or, in the case of coupled SLG/$MoSe_2$, by spatial differences in the ICT efficency. In decoupled SLG/$MoSe_2$, Γ_G and I_G/I_{2D} are more dispersed than in coupled SLG/$MoSe_2$. However, since for this part the graphene is weakly doped, these quantities are more sensitive to small doping variations (see Chapter 5). Therefore, the dispersion could be caused by spatial charge inhomogeneities.

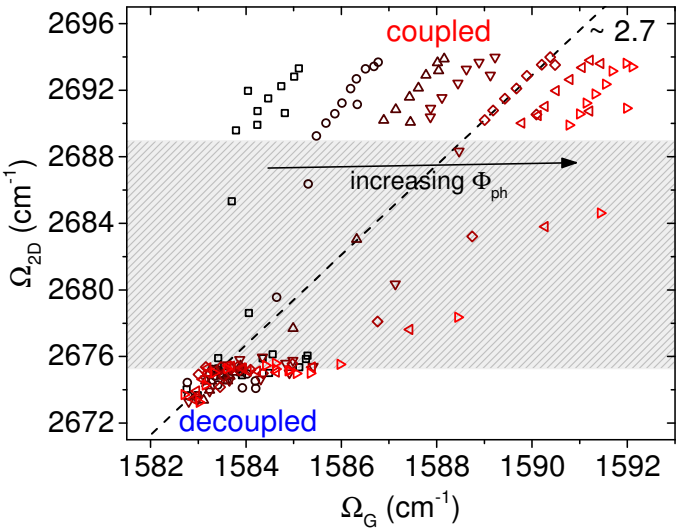

Figure 8.10 – *Correlations between the 2D- and G-mode frequencies for the same line scans as in Fig. 8.9.*

To study the spatial variations in more detail, Fig. 8.10 shows the 2D- and G-mode frequencies correlations for the data shown in Fig. 8.9. We notice that for the decoupled part, the frequencies collapse onto the same line of slope ~ 2.7 for all Φ_{ph}, while in the coupled region, they are correlated along lines of same slope (~ 2.7) but horizontally shifted to higher Ω_G for increasing Φ_{ph}. This horizontal shift corresponds to the increase of doping with Φ_{ph}. The slope of ~ 2.7 is approximately in agreement with the typical slope of 2.2 measured

for biaxial strain [Metten14] (see Chapter 5 Section 5.4). Assuming a strain coefficient of 7.1×10^{-3} % strain/cm^{-1} [Metten14], we deduced a variation of around 0.01% for decoupled SLG/$MoSe_2$ and around 0.03% for coupled SLG/$MoSe_2$. Interestingly, the strain variations are slightly higher in coupled SLG/$MoSe_2$ most likely because of the coupling. The fact that the slopes are similar for the two parts of the heterostructure tends to show that doping variations due to spatial fluctuations of the ICT are negligible. Finally, for all Φ_{ph} the slopes and the strain variations are similar in the coupled region, therefore heating effects are negligible in the range of Φ_{ph} studied here.

8.2.4 Quantitative measurement of the ICT

In Chapter 5, we have shown that the behavior of the G-mode phonon in doped graphene is universal and can be utilized to accurately determine the charge carrier density. In this model, $\Gamma_G(E_F)$ and $\Omega_G(E_F)$ are given by Eq. (5.12) and Eq. (5.13), respectively. To calculate these two quantities, we use the electron-phonon coupling $\lambda_\Gamma = 0.031$ deduced from the average of the three non-defective graphene samples measured in Tab. 5.2. In contrast, the two constants Γ_0 and Ω_0 in the G-mode linewidth and frequency as well as the spatial fluctuations of the Fermi energy δE_F are sample dependent and therefore need to be determined for each sample. This can be done using the correlation $\Gamma_G(\Omega_G)$. In this correlation, the adiabatic contribution Ω_G^A can be neglected. Therefore, using Eqs. (5.12) and (5.15), we fit $\Gamma_G(\Omega_G)$ and obtained the very good agreement depicted in Fig. 8.11(a) with $\Omega_0 = 1582.9$ cm^{-1}, $\Gamma_0 = 4.53$ cm^{-1} and $\delta E_F = 31$ meV. Note that the value of Ω_0 is in agreement with the measured value of Ω_G on SLG/SiO_2 and decoupled SLG/$MoSe_2$ (see Fig. 8.7).

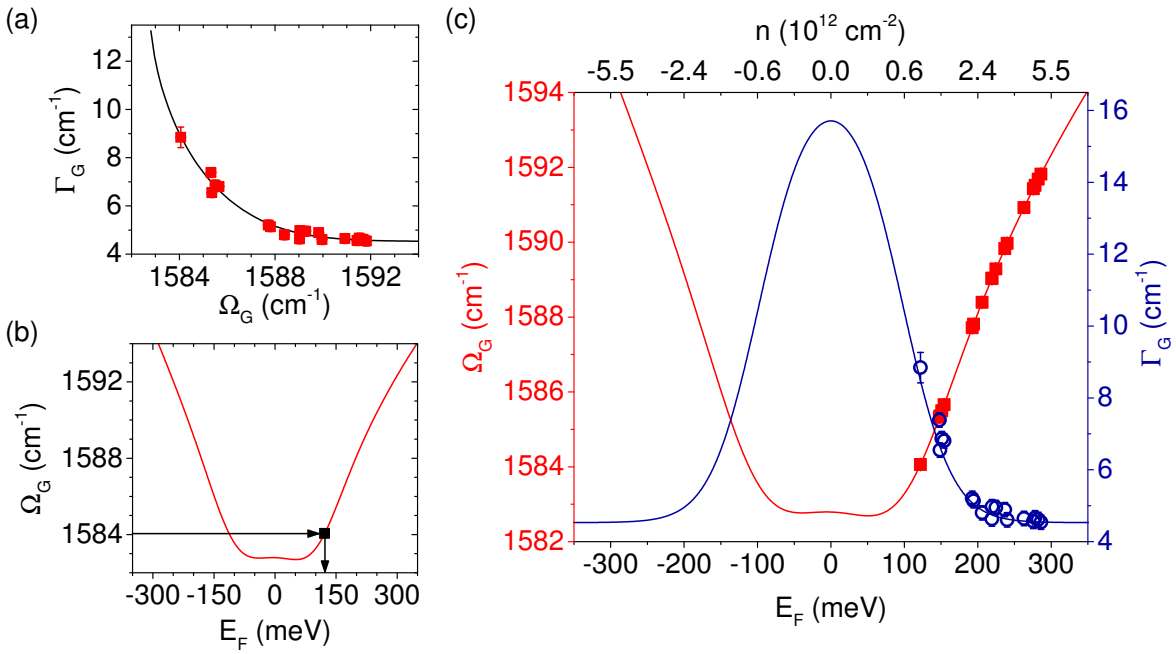

Figure 8.11 *– (c) Frequency Ω_G (red square, left axis) and full width at half maximum Γ_G (blue circle, right axis) of the G-mode feature. The solid lines are theoretical calculations.*

We have now all the values needed to compute the theoretical evolution of Ω_G (with both adiabatic and non-adiabatic contributions) and Γ_G with E_F. Since the measured Ω_G varies more than Γ_G, we utilize the theoretical variation of Ω_G to deduce E_F. Note that in these calculation, we have assumed that the Ω_G^A, λ_Γ and v_F have the same expression or value as for graphene on SiO_2. As sketched in Fig. 8.11(b), for a given Raman shift, one can simply read the corresponding Fermi energy E_F in the range (positive or negative) determined by the correlations $\Omega_{2D}(\Omega_G)$. In the case of sample 1, there is only electron doping, i.e., $E_F > 0$. Note that the typical uncertainty associated with this determination is of order of 10meV. Finally, we plot the Ω_G and Γ_G as a function of the extracted E_F together with the theoretical curves in Fig. 8.11(c). We obtain a excellent agreement for Γ_G as expected. The deduced doping level in graphene n_G is plotted in Fig. 8.12 as a function of Φ_{ph}. We clearly observe a sub-linear rise of n_G (phenomenologically, $n_G \propto \Phi_{ph}^{1/5}$), which suggests that the ICT is not constant as Φ_{ph} (and therefore E_F or n_G) increases (see insert in Fig 8.12). As previously noticed, at $\Phi_{ph} = 0$ the graphene flake is weakly doped ($\lesssim 10^{11}$ cm^{-2}). Consequently, n_G is also the density Δn of transferred electrons from $MoSe_2$ to graphene.

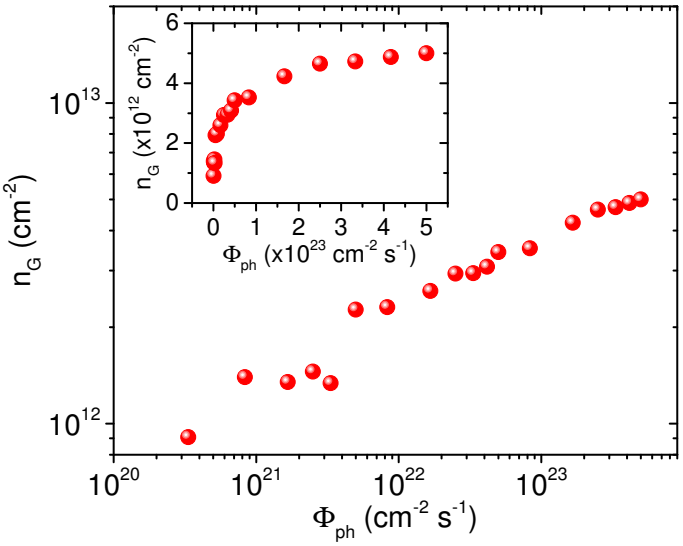

Figure 8.12 *– Deduced density of electrons n_G in graphene as a function of Φ_{ph}. The error bars are smaller than the symbol size. The insert shows the same points but on a linear scale. We can clearly observe a saturation behavior.*

8.2.5 Comparison with samples 2 and 3

We have performed similar measurements and analysis on samples 2 and 3, and have found comparable results. For instance, for sample 2, Fig. 8.13(a) displays Ω_G and Γ_G as a function of Φ_{ph}. We observe that at low Φ_{ph} the frequency (1591.5 cm^{-1}) and the linewidth (9.7 cm^{-1}) of the G-mode feature indicate weakly doped graphene. Therefore, on the contrary to sample 1, the graphene sheet is not neutral at $\Phi_{ph} = 0$. This initial doping might be due to the annealing done on the sample as it is well-known that such treatment can affect the doping level [Ryu10]. Ω_G and Γ_G vary significantly with Φ_{ph}: the minimum value of Ω_G and the maximum value of Γ_G are reached at the same value of Φ_{ph}. This value correspond to

the CNP. Such variations are similar to what we observed on gated graphene (see Fig. 5.10). Figure 8.13(b) shows the correlations between Ω_{2D} and Ω_G. We observe a clear linear correlation along two lines with different slope. Before the CNP, the frequencies follow a line of slope 0.56 corresponding to hole doping, while after the CNP, the frequencies are aligned along a quasi-horizontal line corresponding to electron doping (see Fig. 5.16). As a result, the graphene flake is initially doped by holes and, as for sample 1, photoexcited electrons are transferred from $MoSe_2$ to graphene. A similar behavior was observed on sample 3.

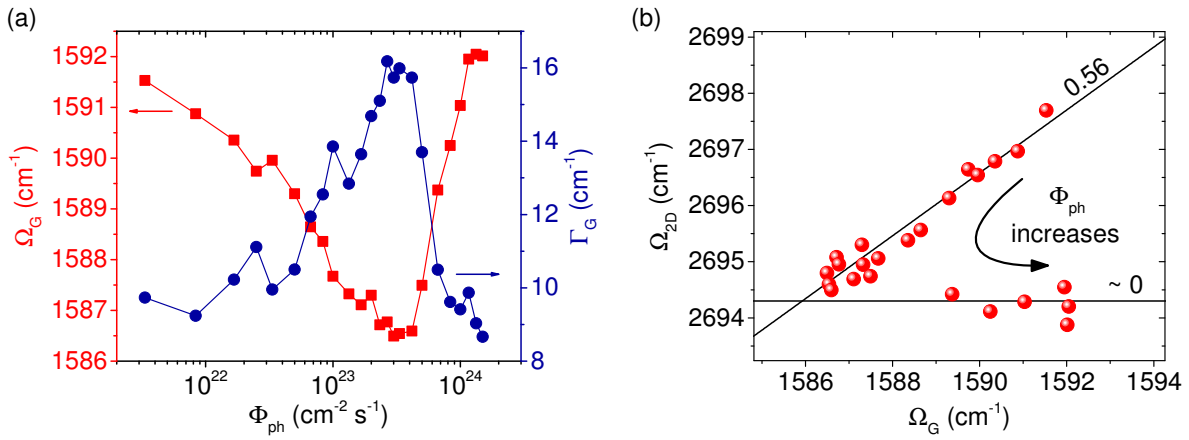

Figure 8.13 *– (a) Frequency Ω_G (red circles and lines, left axis) and FWHM Γ_G (blue circles and lines, right axis) of the G-mode feature measured on sample 2 at 2.33 eV under ambient conditions as a function of the incident photon flux Φ_{ph}. Lines are guides for the eye. (b) Correlations between the frequencies of 2D- and G-mode features under increasing photon flux Φ_{ph} for sample 2.*

Furthermore, we can apply the same procedure as for sample 1 to deduce the doping level n_G (or equivalently E_F) in samples 2 and 3. The results are shown in Fig. 8.14 together with the result of sample 1. Let us recall that $\Omega_G \approx \Omega_G^0$ corresponds to Fermi energies such as $|E_F| \lesssim 100$ meV (i.e, $|n_G| \lesssim 6\times10^{11}$ cm^{-2}). Consequently, in this range of energy it is difficult to use the theoretical evolution of Ω_G to deduce an accurate E_F. One can than use Γ_G which show steeper variations in the vicinity of the CNP. However, in this range of E_F, the correlation $\Omega_{2D}(\Omega_G)$ is close to the origin and it is therefore not obvious to identify between electron and hole doping (see Fig. 5.10). As a result, for $|E_F| \lesssim 100$ meV there is an uncertainty on the sign. For instance, the first point of sample 3 can corresponds to electron or hole doping as reflected by the large vertical error bar in Fig. 8.14. Knowing all this, we can now compare the results obtained on these three samples. We observe that (i) the samples do not have the same initial doping, (ii) they do not show the same sub-linear variations with Φ_{ph}, suggesting different ICT rate and (iii) they all seem to tend to a maximum Fermi energy E_F^{max} around 250 – 300 meV (i.e., $4-5\times10^{12}$ cm^{-2}). Note that on other samples, we typically measured a shift of $\Delta\Omega_G \approx 8$ cm^{-1} which, using Eq. (5.20), corresponds to $E_F \approx 250$ meV. The different ICT rate may arise from different near field couplings between the two layers. Indeed, AFM measurements on samples 2 and 3 have revealed a slightly higher interlayer distance which may be due to different twisting angle between monolayers or to an imperfect transfer during the fabrication process. For further comparison, we have summarized in Tab. 8.1 the maxi-

mum measured E_F with the corresponding Φ_{ph} and the initial E_F. In the case of sample 2 and 3, for $\Phi_{ph} \gtrsim 10^{24}$ cm^{-2} s^{-1} we start to observe thermal effects since the correlation $\Omega_{2D}(\Omega_G)$ displays a slope suggesting influence of mechanical strain (see Fig. 5.16). Hence, for these points we have not deduced E_F as we could not use the method of the previous subsection to do it. As a conclusion of the comparison of the three samples, **the ICT rate seemingly decreases with the increase of the doping level in graphene**.

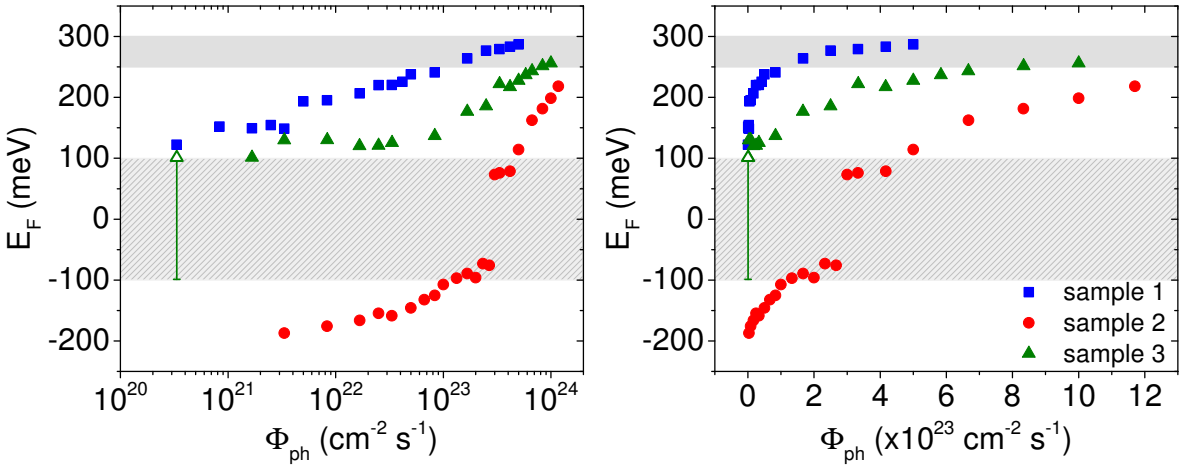

Figure 8.14 *– Fermi energy E_F in graphene as a function of the incident photon flux Φ_{ph}. Left: semi-logarithmic scale. Right: linear scale. Measurements on the three samples are represented with different symbols. The hatched region denotes the range of E_F close to the charge neutrality point where there is an uncertainty on the sign and on the exact value of E_F. We have represented this uncertainty with an error bar for the first point (open triangle) of sample 3. The gray rectangle illustrates the maximum attainable Fermi level in graphene through ICT.*

	$\Phi_{photons}^{max}$ (cm^{-2} s^{-1})	E_F^{max} (meV)	E_F^0 (meV)
Sample 1	5.0×10^{23}	290	$\lesssim 100$
Sample 2	1.2×10^{24}	220	−190
Sample 3	1.0×10^{24}	260	$\lesssim 100$

Table 8.1 *– Comparison of the maximum measured Fermi energy E_F^{max} with the corresponding incident photon flux Φ_{ph}^{max} and the initial Fermi energy E_F^0.*

8.2.6 Raman spectrum of $MoSe_2$

Up to now, we have focused only on the Raman spectrum of graphene. In this subsection, let us briefly address the Raman spectrum of $MoSe_2$. Figure 8.15(a) displays the oX mode with A_1' symmetry (see Chapter 6 and Fig. 6.7) of the Raman spectrum of $MoSe_2$ recorded on sample 1 for pristine $MoSe_2$, decoupled and coupled SLG/$MoSe_2$. We observe that the feature of individual $MoSe_2$ and decoupled SLG/$MoSe_2$ are very similar, while the one of coupled SLG/$MoSe_2$ is blueshifted by approximately 0.5 cm^{-1} and narrower.

On the one hand, such changes may be due to the modification of the dielectric envi-

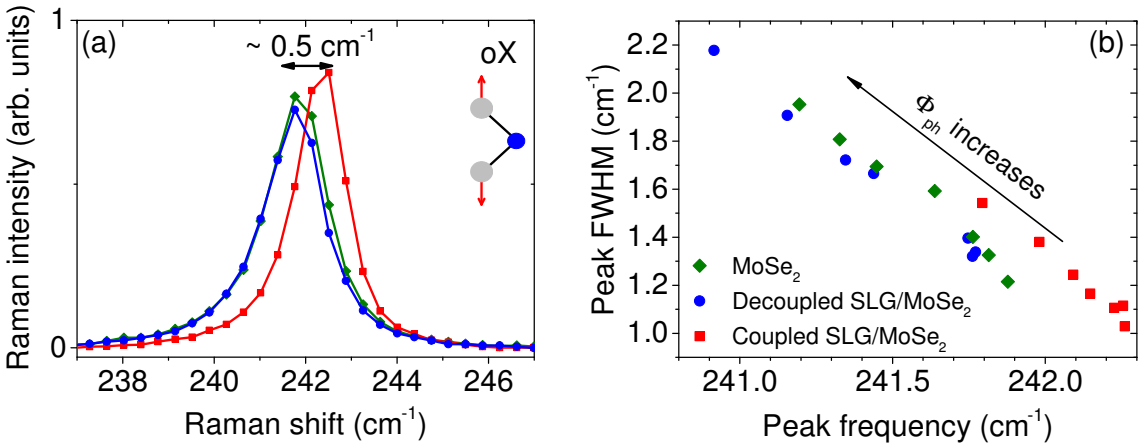

Figure 8.15 *– (a) Raman spectra of the oX-mode feature (the corresponding atomic displacements are sketched) of $MoSe_2$ recorded at $E_L = 2.33\ eV$ and $\Phi_{ph} \approx 3.3\times10^{20}\ cm^{-2}\ s^{-1}$ under ambient conditions. (b) Correlation between the linewidth and the frequency of the oX-mode feature for Φ_{ph} from $3.3\times10^{20}\ cm^{-2}\ s^{-1}$ to $6.7\times10^{23}\ cm^{-2}\ s^{-1}$ (i.e., the same range as for the Raman measurements on graphene). Note that we observe clear changes only for $\Phi_{ph} > 3.3\times10^{22}\ cm^{-2}\ s^{-1}$.*

ronment as for the 2D-mode feature in graphene. On the other hand, it has been observed in MoS_2 that the oX-mode phonon is sensitive to the doping level due to phonon renormalization (as for the G-mode phonon in graphene, see Chapter 5) [Chakraborty12, Miller15]. More precisely, for increasing electron doping, the phonon frequency is redshifted and the linewidth becomes larger [Chakraborty12, Miller15]. Figure 8.15(b) shows the correlation between the linewidth and frequency of the oX-mode feature for increasing Φ_{ph}. We observe a correlation that phenomenologically agrees with changes in the carrier densities. The points recorded on the coupled region have a higher frequency and a smaller width than the ones obtained on bare $MoSe_2$ and on the decoupled part, for all Φ_{ph}. Note that bare $MoSe_2$ was found to be initially *n*-doped [Larentis12]. **This observation suggests that the electron density in $MoSe_2$ is smaller in the coupled heterostructure which is in good agreement with the previous conclusion of an electron transfer from $MoSe_2$ to graphene**.

Furthermore, for the three parts of the sample, we observe a linear correlation with increasing Φ_{ph}. Similar changes were reported on MoS_2 [Miller15] and attributed to the desorption of molecules (e.g., H_2O or O_2) from the surface of MoS_2 causes by the laser heating. These molecules trap electrons and therefore removing them favors electron doping in MoS_2. The same argument should explain the observed variations for bare $MoSe_2$ and decoupled SLG/$MoSe_2$. In the latter case, trapped molecules between graphene and $MoSe_2$ are still mobile. In the case of coupled SLG/$MoSe_2$, the graphene layer prevents the physisorption of molecules on the top surface of $MoSe_2$. Consequently, these observations cannot be assigned to a change of doping. However, it has been observed that such variations can be caused by heating effects [Late14]. By assuming that the observed changes are only due to heating, we deduce from Ref. [Late14], that there is an increase of the temperature of approximately 83 °C for bare $MoSe_2$, 93 °C for decoupled SLG/$MoSe_2$ and 65 °C for decoupled SLG/$MoSe_2$. These values seem to be reasonable. We notice that for individual $MoSe_2$ and decoupled

SLG/$MoSe_2$, the increase is higher most likely because the variations in the peak frequency and width are due to a combination of heating and desorption of molecules. To conclude, these observations are in qualitative agreement with the previous conclusions.

8.3 Photoluminescence spectroscopy as a function of Φ_{ph}

In the previous section, we demonstrated and quantified a photoinduced electron transfer form $MoSe_2$ to graphene using Raman spectroscopy. In this section, by means of photoluminescence spectroscopy, we will study the excitons dynamics in $MoSe_2$ as a function of the incident photon flux with the aim to further unravel the consequences of the interlayer coupling on the photophysics of $MoSe_2$.

8.3.1 Photoluminescence spectra

Figures 8.16(a), (b) and (c) show the PL spectra, recorded respectively on bare $MoSe_2$, decoupled and coupled SLG/$MoSe_2$, for increasing Φ_{ph}. The spectra have been normalized using the product of the integration time by Φ_{ph}. All the spectra have a similar shape for the three regions of interest. We can clearly discern the A and B excitons at an energy around 1.570 eV and 1.755 eV, respectively. Interestingly, the excitons energies slightly decrease by a few meV with increasing Φ_{ph}. This shift most likely arise from the laser heating and/or from the increase of the exciton density. Furthermore, in coupled SLG/$MoSe_2$, there is a redshift of ~ 10 meV compared to individual $MoSe_2$ and decoupled SLG/$MoSe_2$. This shift is probably due to a different dielectric environment caused by the close presence of the graphene sheet [Ugeda14, He14a]. Such a modification of the dielectric environment can induce a change of the exciton binding energy and thus of the optical bandgap (see Chapter 2 Section 2.2). In addition, the energy difference between the A and B excitons is about 185 meV in all regions of the sample and does not vary with Φ_{ph}. This value is in good agreement with previous observations [Ross13, Li14, Wang15c, Wang15a].

Figures 8.16(d), (e) and (f) display one PL spectrum for each region recorded at a given Φ_{ph}. The spectra were fit using Voigt profiles. The PL spectrum of pristine $MoSe_2$ and decoupled SLG/$MoSe_2$ are well fit with two Voigt profiles: one for the A exciton and one for the B. Surprisingly, the PL spectrum of coupled SLG/$MoSe_2$ needs two additional features between the A and B excitons to be well described, at around 1.59 eV and 1.67 eV. At the moment, we do not fully understand the origin of these peaks. A tentative explanation is that the former peak corresponds to a slight asymmetry of the A exciton peak, while the latter is assigned to the emission from an excited excitonic state of the A exciton (see Chapter 2 Fig. 2.12 and Chapter 7 Section 7.1). However, further investigations are needed to confirm this statement. Actually, these two features were only observed on sample 1. On sample 2 and 3, only the feature at the lowest energy was observed.

Finally, when increasing Φ_{ph} by three orders of magnitude, the PL signal normalized using the product of the integration time by Φ_{ph} clearly decreases for bare $MoSe_2$ and decoupled

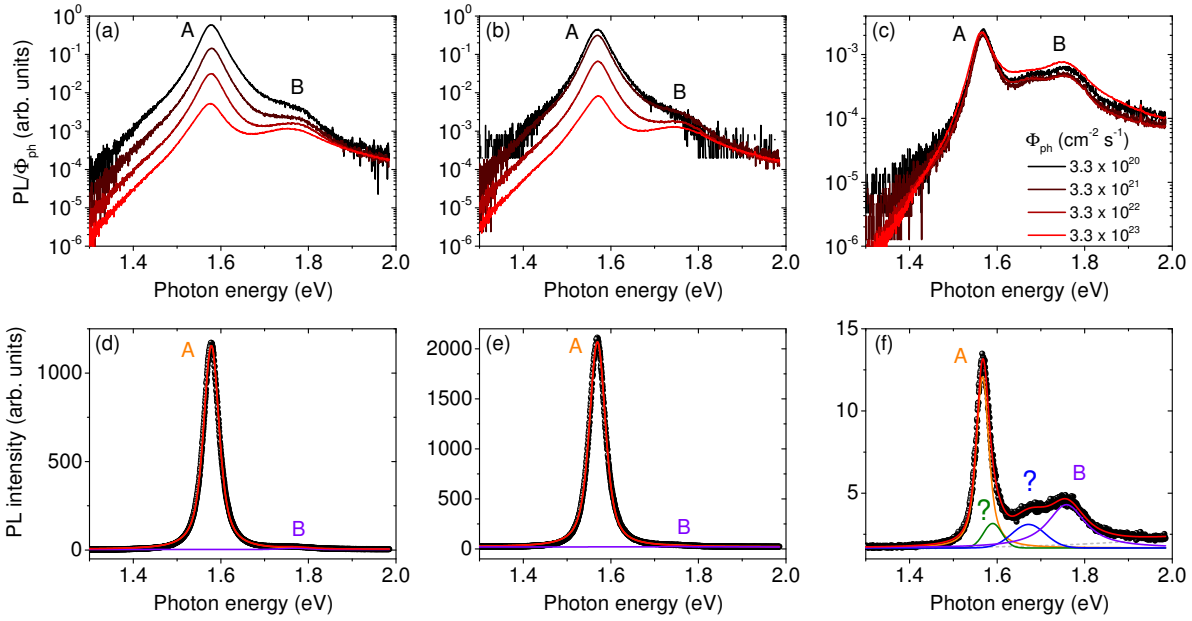

Figure 8.16 *– (a)-(c) Photoluminescence spectra, normalized by the integration time and the incident photon flux (Φ_{ph}), of (a) bare $MoSe_2$, (b) decoupled SLG/$MoSe_2$ and (c) coupled SLG/$MoSe_2$ at different Φ_{ph}. One can clearly distinct the A and B excitons. (d)-(f) Photoluminescence spectra (black symbols) recorded at $\Phi_{ph} \approx 1.7\times10^{21}$ cm^{-2} s^{-1} and normalized by the integration time of (d) bare $MoSe_2$, (e) decoupled SLG/$MoSe_2$ and (f) coupled SLG/$MoSe_2$. Solid lines are fits with Voigt profiles. In (f), there are two unidentified features.*

SLG/$MoSe_2$, but is almost constant for coupled SLG/$MoSe_2$. To quantitatively analyze this behavior, we extracted the integrated intensity of A and B excitons from the fits.

8.3.2 Photoluminsecence intensity

Figure 8.17(a) displays the integrated intensity of the A exciton, normalized using the product of the integration time by Φ_{ph}, as a function of Φ_{ph}. For individual $MoSe_2$ and decoupled SLG/$MoSe_2$, we observe a clear sub-linear evolution of the normalized intensity, consistent with exciton-exciton annihilation as previously discussed in Chapter 7 Section 7.3. On the contrary to the PL map in Fig. 8.3, the PL intensity in decoupled SLG/$MoSe_2$ is higher than pristine $MoSe_2$. A possible explanation is that PL intensity decreased due to aging effects since the PL map was acquired just after the fabrication on the sample, while the measurements in Fig. 8.17 were done after few days in air. Aging effects such as oxidation or adsorption of contaminants can quench the PL [Gao16]. In the case of decoupled SLG/$MoSe_2$ the graphene layer encapsulate $MoSe_2$ and slow down aging effects. In the case of coupled SLG/$MoSe_2$, the normalized PL intensity is almost constant (see the gray dashed line in Fig. 8.17(a)), i.e., the raw PL intensity increases linearly with Φ_{ph}. This behavior reveals a **drastic reduction of A exciton lifetime** compared to pristine $MoSe_2$ and decoupled SLG/$MoSe_2$. This reduction provides evidence of a very efficient coupling which serves as a fast decay channel. The ICT demonstrated in the previous section offers such a decay channel. However, at this stage, we cannot exclude the possibility of IET. Remarkably, because of the dramatic reduction of the lifetime, exciton-exciton annihilation can be neglected in coupled

SLG/$MoSe_2$.

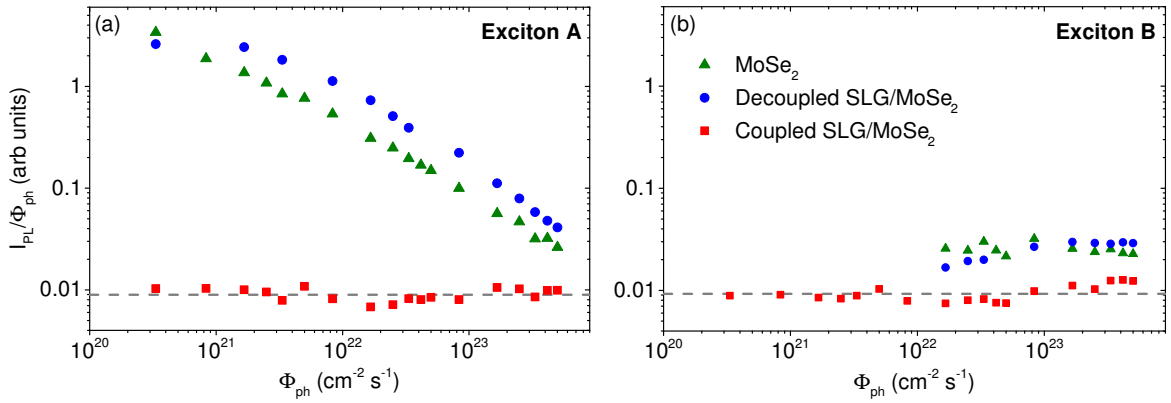

Figure 8.17 *– Integrated PL intensity of (a) A exciton and (b) B exciton as a function of Φ_{ph}. The PL intensity has been normalized by the integration time and Φ_{ph}. The gray dashed line is a guide for the eye. The error bars are smaller than symbol size.*

Furthermore, Fig. 8.17(b) shows the integrated intensity of the B exciton, normalized using the product of the integration time by Φ_{ph}, as a function of Φ_{ph}. For the three parts of the heterostructure, the normalized PL intensity of B exciton is of the same order of magnitude and is almost constant with Φ_{ph}. However, in the coupled region, the normalized intensity is approximately two times smaller than in the two other regions. Thus, the interlayer coupling has a minor effect, yet not negligible, on the B exciton. Note that for low Φ_{ph}, the intensity of the B exciton in pristine $MoSe_2$ and decoupled SLG/$MoSe_2$ is too weak to deduce a reliable value, therefore we did not plot this points in Fig. 8.17(b). Since PL from the B exciton corresponds to hot photoluminescence, the B exciton has a shorter lifetime than the A exciton. The effect of an additional fast decay channel is therefore less important. We deduce that the B exciton recombination is on the same timescale as the transfer process between $MoSe_2$ and graphene. Interestingly, for coupled SLG/$MoSe_2$, the integrated intensity of the A and B exciton are of the same order of magnitude. Consequently, the A and B exciton lifetimes in the coupled heterostructure are comparable.

8.4 Discussion

In the previous section, we have evidenced that the interlayer coupling induces a dramatic reduction of the A exciton lifetime and thus a quenching of the PL of the A exciton. The A and B exciton lifetimes are comparable and are of the order of a few picoseconds. We have also demonstrated that a photoinduced electron transfer from $MoSe_2$ to graphene occurs consistently with the reduction of the A exciton lifetime. Indeed, the ICT offers an additional non-radiative decay channel. In addition, we have noticed that this ICT seemingly saturates at Fermi energies around 250 – 300 meV. This latter point is obviously not consistent with the linear increase of the PL intensity with Φ_{ph} suggesting that IET also plays a role. As an attempt to explain this important point, we will first present the influence of the environmental conditions and then, we will propose a simple model that qualitatively reproduce our

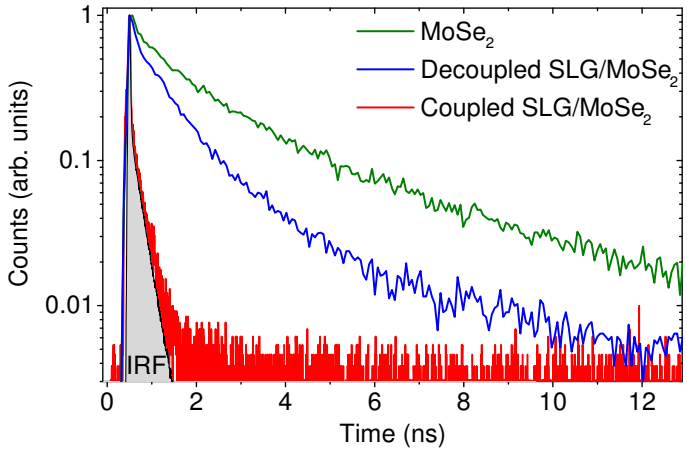

Figure 8.18 *– Photoluminenscence decays recorded for bare $MoSe_2$, decoupled and coupled SLG/$MoSe_2$. All data were recorded using a pulsed laser at 1.96 eV with $\Phi_{ph} \approx 8.6 \times 10^{17}$ cm^{-2} s^{-1} for pristine $MoSe_2$ and decoupled SLG/$MoSe_2$, and $\Phi_{ph} \approx 1.7 \times 10^{19}$ cm^{-2} s^{-1} for coupled SLG/$MoSe_2$. The gray area corresponds to the instrumental function response (IRF). These data were acquired after those of Fig. 8.3 and before those of Fig. 8.17.*

observations.

8.4.1 Sensitivity to environmental conditions

Influence of the increase and decrease of Φ_{ph}

Figure 8.19 shows the frequency of the G-mode feature and the PL intensity of the A exciton for increasing and then decreasing Φ_{ph}. We notice that the frequency of the G-mode feature does not follow the same curve, while there is almost no changes in the PL intensity. Clearly, the modifications in the G-mode frequency indicates that the graphene, which was initially weakly doped, is clearly *p*-doped after the increase and decrease of Φ_{ph}. Such a behavior was found to be very reproducible: if one waits a couple of minutes and redo the experiment, similar results will be obtained. A tentative explanation is that increasing Φ_{ph} favors the adsorption of electron-trapping molecules such as oxygen [Mitoma13]. Interestingly, as previously observed, regardless the initial doping of the graphene layer, the final $\Delta\Omega_G \approx 7$ cm^{-1} which corresponds to $E_F \approx 220$ meV. Furthermore, the fact that there is almost no variations in the PL intensity suggests that the PL quenching is insensitive to the modification of the ICT and therefore to graphene's Fermi energy (at least in the range of E_F reached here). Importantly, the most pronouced hysteretic behaviors were observed on annealed samples.

Measurements in air and under vaccum

Up to now, all the measurements were performed under ambient conditions. Figure 8.20 displays Ω_G and Γ_G as a function of Φ_{ph} recorded under ambient condition and under vacuum (at room temperature) on sample 1. Under vacuum, we observe that Ω_G and Γ_G varies much less than in air. They both show a variation of approximately 1 cm^{-1}. Remarkably, their val-

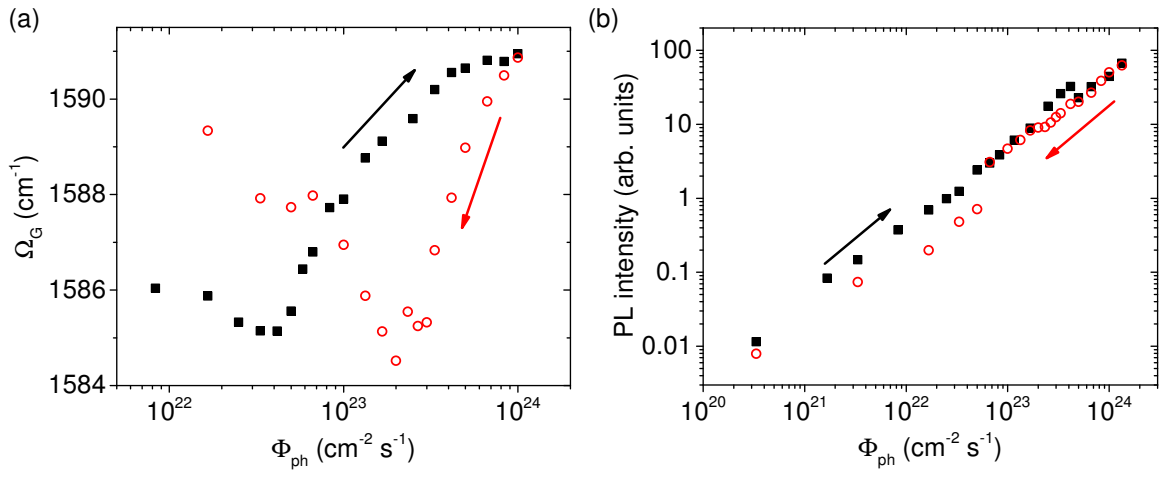

Figure 8.19 *– (a) Frequency of the G-mode feature and (b) integrated PL intensity of the A exciton as a function of the incident photon flux Φ_{ph} for first increasing Φ_{ph} (black squares) and then decreasing Φ_{ph} (open red circles). Measurements recorded on sample 3.*

ues correspond to the values measured at high Φ_{ph} in air suggesting that graphene's Fermi energy E_F is already around 250 – 300 meV even at low Φ_{ph}. Note that Γ_0 is slightly larger under vacuum probably due to different experimental conditions. On the other hand, under vacuum, we observe only small changes (~ 1 cm^{-1}) on decoupled SLG/$MoSe_2$ and SLG/SiO_2 compared to air. In conclusion, these observations indicate that **under vacuum the ICT is much more efficient than in air** and saturates even at low Φ_{ph}. At the same time, the PL intensity is linear with Φ_{ph} but is approximately two times smaller under vacuum than in air. This observation is in agreement with the previous assumption that the ICT has only a minor contribution to the quenching of the PL. As for the increasing and decreasing Φ_{ph}, the modification of the ICT are probably related to the adsorbates as vacumm removes H_2O and O_2 molecules which are known to trap electrons due to the electronegativity of the oxygen. Interestingly, changes in the ICT were also reported from electrical measurements on SLG/MoS_2 vdWH but with the opposite conclusion [Zhang14], i.e., ICT seems to be reduced under vacuum compared to ambient conditions.

8.4.2 Toy model

Summary of the observations

Let us summarize all the observations and conclusions made up to this point:

(i) Regardless of the initial doping in graphene or the efficiency of the photoinduced electron transfer, the graphene's Fermi energy seems to tends to a maximum value of $E_F \approx 250 - 300$ meV (i.e., a doping level of $n_G^{max} \approx 5 \times 10^{12}$ cm^{-2}). As sketched in Fig. 8.21, this observation can be well understood from band alignment considerations (see Chapter 2 Section 2.3.2). When the Fermi level in graphene reaches the bottom of the conduction band of $MoSe_2$, the ICT stops occuring (at least from a macroscopic

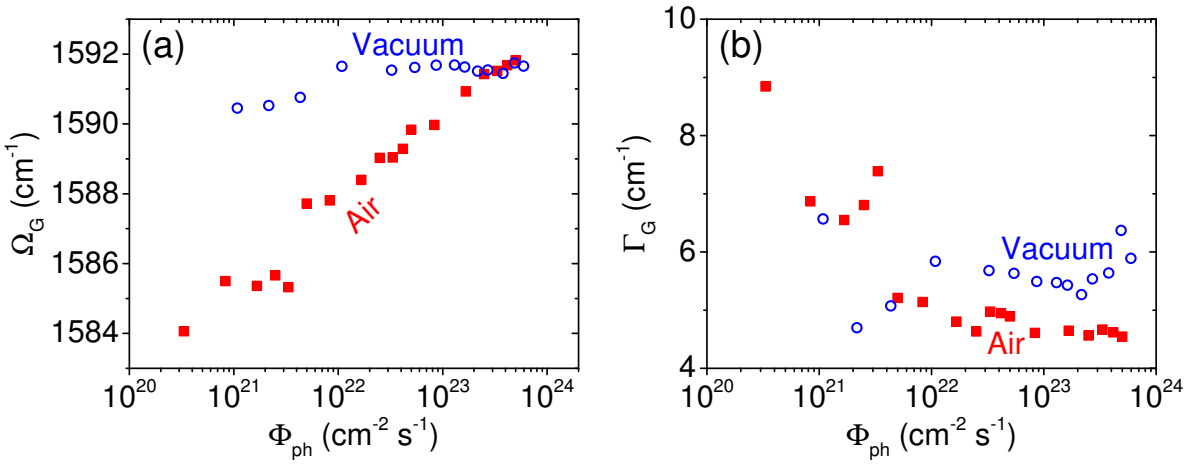

Figure 8.20 *– (a) Frequency Ω_G and (b) FWHM Γ_G of the G-mode feature as a function of the incident photon flux Φ_{ph} recorded under ambient conditions (red filled squares) and under vacuum (blue open circles).*

point of view). A similar behavior was observed in WSe_2/graphene vdWHs by means of electrical measurements and an electronic affinity of $\chi_M \approx 4.06$ eV for WSe_2 was deduced [Kim15a]. From our observations and knowing that graphene's work function is equal to $W_G = 4.57$ eV [Yu09], we deduce an electronic affinity of $\chi_M \approx 4.3$ eV for $MoSe_2$. This value seems reasonable knowing that a difference of 0.3 eV was theoretically calculated for χ_M between $MoSe_2$ and WSe_2 [Liang13]. However, very importantly, in this reasoning we did not take into account excitonic effects. Indeed, prior to the charge transfer, the exciton has to be dissociated. Consequently, we have assumed than when the CT happens the electron is at the bottom of the conduction band.

(ii) The environment, and most likely absorbates at the surface of the heterostructure, drastically affects the ICT. A very small (or reduced) electron transfer can be observed even at low Φ_{ph} if graphene is sufficiently *p*-doped.

(iii) Although all these modifications of the ICT, the PL intensity of $MoSe_2$ remains poorly affected. Especially, when the ICT rate is reduced due to the increase of doping level in graphene, the PL intensity still scales linearly with Φ_{ph}. This suggests that a non-radiative decay channel governs the carrier dynamics in the heterostructure on a shorter timescale than the ICT. We propose that fast IET is responsible for this non-radiative decay channel. If one thinks about the fact that ICT requires exciton dissociation prior to the transfer, whereas IET does not, it seems to be a reasonable assumption knowing that graphene is an ideal acceptor (see Chapter 2 Section 2.3.2) and that such transfer, with almost 100 % efficiency, was evidenced in molecules/carbon nanotubes [Roquelet10]. Assuming that IET dominates the interlayer transfers, it is insensitive to the doping level reached here and happens on a picosecond timescale (from the estimation of the exciton lifetime done in Section 8.3). As a result, ICT occurs on a longer timescale. This is rather different from the subpicosecond ICT observed in TMD/TMD vdWHs (see Chapter 2 Section 2.3.2). However, in these systems, there is presumably no exciton dissociation

and the formation of interlayer excitons is energetically more favorable. On the other hand, He *et al.* [He14a] have measured an ICT between monolayer WSe_2 and graphene on a picosecond timescale. Nevertheless, the authors of this study did not prove that there is indeed an ICT and not a IET. Noteworthy, all these measurements were done using pump-probe techniques, while we have estimated the exciton lifetime from cw measurements, i.e., at a steady state. Therefore, this may lead to some discrepancy since the regimes of measurement are rather different.

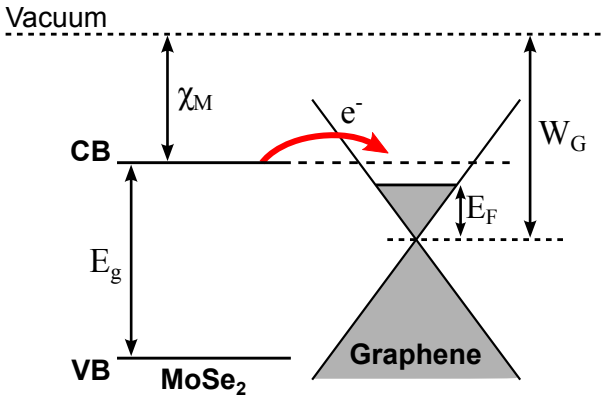

Figure 8.21 *– Schematic band structure of $MoSe_2$/graphene heterostructure. The conduction (BC) and valence (VB) band edges of $MoSe_2$ are represented by horizontal lines separated by the bandgap E_g. Their position in energy is determined by the electron affinity χ_M. The position of graphene's band structure is fixed by the work function W_G. Occupied states are represented in gray. When graphene's Fermi energy E_F reaches the bottom of $MoSe_2$ conduction band, the electron transfer from this state in $MoSe_2$ to graphene is forbidden by the Pauli principle.*

The model

Using all these ingredients, we can propose a toy model based on rate equations to qualitatively reproduce our observations. This model is illustrated in Fig. 8.22(a). n_M describes the photoexcited electrons density in $MoSe_2$ (more precisely the exciton density) and n_G the electrons density in graphene. $\mathcal{A}\Phi_{ph}$ is the absorbed photon flux in $MoSe_2$. The absorptance $\mathcal{A}$ of $MoSe_2$ in the air/SLG/$MoSe_2$/SiO_2/Si layered structure is calculated using the procedure explained in Appendix C Section C.2.2 and found to be $\mathcal{A} \approx 20.8$ %. Note that graphene's absorptance of 2.3 % can be neglected. We assume that if $\Phi_{ph} = 0$ then $n_M = 0$ and $n_G = 0$ (i.e., we neglect the initial doping of graphene, see below). $\Gamma_M = \Gamma_r + \Gamma_{nr}$ is the linear recombination rate, where Γ_r (Γ_{nr}) is the (non) radiative recombination rate of the A exciton. Note that we assume that Γ_M is the same for bare $MoSe_2$ and $MoSe_2$ in the heterostructure. Γ_{IET} is the IET rate and Γ_{ICT} the ICT rate from $MoSe_2$ to graphene. Our measurements were performed using cw excitation. Therefore, the measured doping level in graphene corresponds to a steady state and not all the electrons that are transferred to graphene may participate in the increase of the doping level. Indeed, some of them might be trapped by adsorbates, impurities or defects, or some of them can also be retransferred to lower states in $MoSe_2$. All these possibilities are accounted for a 'leaks' rate Γ_{leaks}.

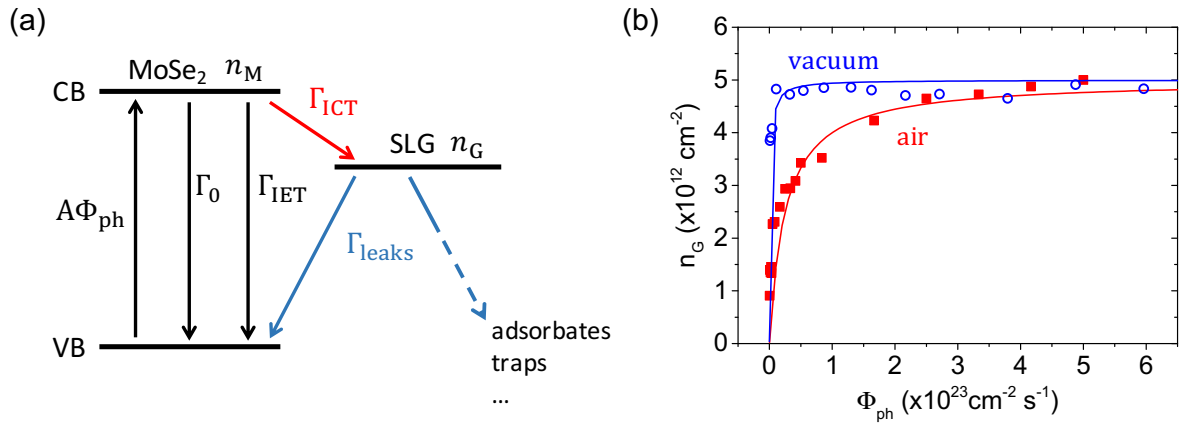

Figure 8.22 – *(a) Rate equation model. n_M and n_G are the densities of photoexcited electrons (or excitons) in $MoSe_2$ and the density of electrons in graphene, respectively. $\mathcal{A}\Phi_{ph}$ is the absorbed photon flux. Γ_M is the linear recombination rate. Γ_{IET} and Γ_{ICT} are the IET and ICT rate from $MoSe_2$ to graphene, respectively. Γ_{leaks} is the electron transfer rate from graphene to adsorbates, impurities, defects of to lower states in $MoSe_2$. (b) Density of electron in graphene n_G under ambient conditions (red filled squares and line) and vacuum (blue open circles and line). Symbols are measurement values. Lines are calculations using Eqs. (8.2) and (8.3) with $\mathcal{A} \approx 0.2$, $\Gamma_{IET} \sim 10^{12}\ s^{-1}$, $n_G^{max} \approx 5\times10^{12}\ cm^{-2}$, and $\Gamma_{leaks}/\Gamma_{ICT}^0 \sim 10^{-3}$ in air and 5×10^{-5} under vacuum.*

The time dependence of n_M and n_G are given by

$$\frac{dn_M}{dt} = \mathcal{A}\Phi_{ph} - \Gamma_M n_M - \Gamma_{IET} n_M - \Gamma_{ICT} n_M, \tag{8.1a}$$

$$\frac{dn_G}{dt} = \Gamma_{ICT} n_M - \Gamma_{leaks} n_G. \tag{8.1b}$$

Note that we have neglected the exciton-exciton annihilation in $MoSe_2$, i.e., we have assumed that $\mathcal{A}\Phi_{ph}\times\gamma_{eea} \ll (\Gamma_M+\Gamma_{IET}+\Gamma_{ICT})^2$. To a first approximation, Γ_{ICT} can be described by $\Gamma_{ICT}(n_G) = \Gamma_{ICT}^0\left(1 - n_G/n_G^{max}\right)$, where Γ_{ICT}^0 is a constant. At steady state the carrier densities are

$$\langle n_M \rangle = \frac{\mathcal{A}\Phi_{ph}}{\Gamma_M + \Gamma_{IET} + \Gamma_{ICT}} \approx \frac{\mathcal{A}\Phi_{ph}}{\Gamma_{IET}}, \tag{8.2}$$

$$\langle n_G \rangle = \frac{\langle n_M \rangle}{\Gamma_{leaks}/\Gamma_{ICT}^0 + \langle n_M \rangle / n_G^{max}}, \tag{8.3}$$

where we have assumed that $\Gamma_{IET} \sim 10^{12}\ s^{-1} \gg \Gamma_{ICT}^0, \Gamma_M$. This is a strong assumption but seems to experimentally verified since the PL intensity of $MoSe_2$ (which is proportional to $\langle n_M \rangle$) is linear with Φ_{ph} (see Fig. 8.17). Interestingly, the fact that Γ_{IET} is constant seems to indicate that the associated mechanism is of Förster-type since Dexter-type energy transfer should vanish as would the ICT (see Chapter 2 Section 2.3).

We can then use Eq. (8.3) to describe the measured $\langle n_G \rangle$ as a function of Φ_{ph}. Note that Eq. (8.3) corresponds to a saturation curve. In Section 8.2, we have deduced that $n_G^{max} \approx 5\times10^{12}\ cm^{-2}$. Figure 8.22(b) shows the experimental and the theoretical evolution of n_G as a function of Φ_{ph} for measurements under ambient conditions and under vacuum. The experimental data are qualitatively well described by Eq. (8.3) with $\Gamma_{leaks}/\Gamma_{ICT}^0$ equal to 10^{-3}

and 5×10^{-5}, respectively. Note that we have neglected the initial doping as sample 1 is weakly doped. However, if the initial doping is not negligible (as for sample 2), one has to add the initial doping n_0 to Eq. (8.3). Remarkably, this result is in good agreement with the fact that under vacuum the desorption of adsorbates decreases Γ_{leaks}. Furthermore, these observations are also in excellent agreement with the ones of Zhang *et al.* [Zhang14].

Overall, this toy model reproduces qualitatively our observations without the need of a microscopic description of the interlayer charge and energy transfer. In particular, for the ICT, we did not take into account the dissociation of the tightly bound excitons and how this affects the band alignment sketched in Fig. 8.21. Furthermore, this model, which only deals with electrons, does not consider the created holes in $MoSe_2$ and the possibility of hot IET and ICT. Especially, the latter does not require any exciton dissociation. All these comments provide strong impetus for further experiments that will be discussed in Chapter 9.

8.5 Conclusion

In this chapter, we have studied the interlayer coupling in monolayer graphene/monolayer $MoSe_2$ heterostructure by means of optical spectroscopy. The photoluminescence measurements reveal a drastic quenching of two orders of magnitude of the photoluminescence of $MoSe_2$. Using the results of Chapter 5, the Raman measurements demonstrate a photoinduced electron transfer from $MoSe_2$ to graphene that have been quantified. Interestingly, this charge transfer seems to saturate for graphene's Fermi energy around $250-300$ meV (i.e., doping level of approximatively 5×10^{12} cm^{-2}). This saturation may be explained by band alignment. In contrast, the photoluminescence intensity is linear with the incident photon flux suggesting that a fast interlayer energy transfer occurs and may dominate. Indeed, the energy transfer may be favored compared to the charge transfer as the latter requires the exciton dissociation. This energy transfer was evaluated to happen on a picosecond timescale, while the charge transfer occurs on a longer timescale. This is rather different from the ultrafast charge transfer, leading to the formation of interlayer excitons, observed in type-II heterojunctions made of transition metal dichalcogenides (see Chapter 2 Section 2.3.2. Furthermore, the environment, presumably the adsorbates at the surface of the heterostructure, influences the charge transfer. All these observations are qualitatively well described by a toy model based on rate equations. However, additional experiments are still needed to fully justify this simple model and unveil the underlying microscopic mechanisms associated with the charge transfer (exciton dissociation, influence of the adsorbates,...) and the energy transfer (Förster or Dexter). Finally, this work opens interesting perspectives for local photogating of graphene since doping levels similar to conventional gate dielectric, such as SiO_2 can be reached.

Take home messages

- A massive quenching of ~ 300 of $MoSe_2$ photoluminescence is observed.

- A photoinduced electron transfer from $MoSe_2$ to graphene occurs and saturates for graphene's Fermi energy around 250 – 300 meV presumably due to band alignment.
- The fast interlayer energy transfer ($\sim$ 1 ps) may be responsible for the large photoluminescence quenching and may be more efficient than the interlayer charge transfer.
- The photoinduced charge transfer is sensitive to the presence of adsorbates at the surface of the heterostructure.

Related communication

Oral

- G. Froehlicher, E. Lorchat, and S. Berciaud, *Photoinduced charge transfer in a $MoSe_2$/graphene van der Waals heterostructure*, E-MRS Spring Meeting, May 2016, Lille, France

Award

- **Young Scientist Award** for the talk *Photoinduced charge transfer in a $MoSe_2$/graphene van der Waals heterostructure* at the 2016 E-MRS Spring Meeting, European Materials Research Society

Chapter 9

Conclusion and perspectives

General conclusion

To conclude this thesis, I can say that the aim to build optoelectronic devices based on van derWaals heterostructures, made of graphene and transition metal dichalcogenides, to study and electrically control the interlayer interactions that govern their photophysics is nearly achieved. To reach this goal, we have carefully addressed the three milestones defined in Chapter 1.

First (Chapter 5), we have developed robust and efficient electrochemically-gated graphene transistors, where the properties of graphene can be finely tuned by the electric field effect. Using these devices, we have shown that Raman spectroscopy is an extremely sensitive tool for advanced characterization of graphene samples. In particular, graphene's Fermi energy can be precisely determined and the evolution of the crystalline quality can be monitored. For a more fundamental aspect, it has also allowed us to measure the electron-phonon coupling constants for zone-center and zone-edge optical phonons, where the interactions are particularly strong due to Kohn anomalies.

Second (Chapters 6 and 7), we have carefully investigated the evolution of the physical properties of semiconducting transition metal dichalcogenides between the three-dimensional (bulk) and the (quasi) two-dimensional (monolayer) limits. We have demonstrated that high-resolution Raman spectroscopy is a powerful technique to probe the Davydov splitting of all the zone-center optical phonon modes in N-layer $MoTe_2$ but more generally in all layered materials. Furthermore, the complete manifold of phonon modes associated with the in-plane and out-of-plane displacements are remarkably well described by a 'textbook' force constant model, including interactions up to the second nearest neighbor and surface effects as fitting parameters. The latter were found to play a major role in the evolution of the phonon frequencies. This study is an original example of the application of group theory and also sheds light on phonon coupling in transition metal dichalcogenides [Jones16].

Next, we have demonstrated that N-layer semiconducting transition metal dichalcogenides exhibit a very rich photophysics and that photoluminescnece intensity of monolayers present strong nonlinearities that reflects the strongly enhanced Coulomb interactions and reduced dielectric screening in these atomically thin two-dimensional materials.

Third (Chapter 8), we have fabricated van der Waals heterostructures made of monolayers graphene and $MoSe_2$ using a simple all-dry transfer technique. We have then made use of the results obtained in the previous chapters to characterize, in an original way, these heterostructures. In particular, using the highly accurate methods and powerful tools developed in Chapter 5, we were able to demonstrate and quantify the photoinduced electron transfer from $MoSe_2$ to graphene. Remarkably, we have found that the rate of this charge transfer decreases as graphene's Fermi energy increases. In contrast, the massive quenching of two order of magnitude of $MoSe_2$ photoluminescence was found to scale linearly with the incoming photon flux and thus to be insensitive to graphene's Fermi energy. Such a behavior cannot solely be explained by charge transfer and we have suggested that a fast energy transfer is responsible for the photoluminescence quenching. This is a major assumption which provides a strong impetus for quantitative investigations of the energy transfer in van der Waals heterostructures, that up to now has been mostly overlooked.

Finally, although the optoelectronic devices were ultimately not fabricated during my thesis, all the ingredients are now available together very efficient methods to analyze and model the measurements, and a better understanding of key phenomena in these devices. My work opens multiple interesting perspectives, especially for our group. In the short term, many questions directly related to my work remain open and provide strong impetus for further experiments. In the long term, more sophisticated fabrication techniques have to be developed so that more advanced heterostructures and more complex optoelectronic devices can be investigated.

Perspectives

In the following, I discuss few perspectives related to my work. The two first subsections present work directly related to my thesis, while the last subsection is a proposition to study heterostructures based on transition metal dichalcogenides with a large in-plane anisotropy.

Resonant exciton-phonon coupling in N-layer transition metal dichalcogenides

Our measurements on N-layer $MoTe_2$ have revealed that the Davydov splitting of the phonon modes appear prominently for a certain incoming photon energy. This is in agreement with recent observations of resonant effects in the Raman scattering of N-layer transition metal dichalcogenides [Chakraborty13, Luo13a, Carvalho15, Scheuschner15, Lee15b, Grzeszczyk16, Kim16, Song16, Soubelet16]. The collaboration with the group of Ludger Wirtz at the University of Luxembourg, which started for the work presented in Chapter 6; now continues on the importance of resonant exciton-phonon coupling on our measurements.

We have provided them with carefully normalized measurements on N-layer $MoTe_2$ at three different photon energies. Henrique Miranda (PhD student) is working on *ab initio* calculations that would reproduce our observations. The results of his calculations and the comparison with the experiment has just been accepted to Nano Letters (see List of Publications page 235). In brief, the intensity of the Davydov-split modes is governed by quantum interference effects. However, the quantitative agreement with the experimental data requires the proper inclusion of excitonic effects.

Monolayer graphene/monolayer transition metal dichalcogenides

The points presented in this subsection are already or will be addressed in our group, especially by Etienne Lorchat, a PhD Student, who has started in early 2016 to work on heterostructures.

Two-color measurements The main disadvantage of the Raman measurements performed in Chapter 8 is that the same laser beam is used to photogenerate excitons in $MoSe_2$ and to probe the Raman scattering in graphene. Hence, it is impossible to investigate a static non-photoinduced charge transfer arising from the near field interaction between $MoSe_2$ and graphene. Moreover, interlayer charge transfer under incident photon flux lower than 10^{20} cm^{-2} s^{-1} cannot be investigated because the Raman signal becomes too weak to be exploited. One solution to overcome these difficulties is to use two laser beams focused onto the same point of the sample (see Fig. 9.1(a)): one with with a photon energy higher than the A exciton to generate excitons in the TMD and the other with a photon energy lower than the A exciton to record the Raman spectrum of graphene. Unfortunately, in monolayer $MoSe_2$ the A exciton has an energy around 1.57 eV which requires the utilization of a laser in the near-infrared that is currently not available in the lab and that makes Raman measurements more challenging. However, in monolayer tungsten disulfide (WS_2) the A exciton is around 2 eV. Therefore, we can use the laser at 2.33 eV to generate excitons in WS_2 and the one at 1.58 eV to probe the Raman spectrum of graphene (see Fig. 9.1(b)). This type of heterostructure have been already fabricated and studied in our group by Etienne Lorchat, Jérémie Chretien (Master student) and me, showing very similar behaviors as graphene/$MoSe_2$ heterostructures. However, this measurement is more challenging as the Raman features are in the near-infrared range, but all the required equipment are available in the lab. This experiment is particularly interesting to confirm that under vacuum the observed high doping level in graphene, even at low incident photon flux, is photoinduced and that the saturation is reached at lower flux than in the air (see Fig. 8.22).

Monolayer $MoSe_2$/monolayer graphene heterostructure A simple method to study the effect of the surrounding atmosphere, especially of the vacuum, is to fabricate van der Waals heterostructures with the monolayer $MoSe_2$ on top of the graphene sheet as depicted in Fig. 9.2(b). In this configuration, the $MoSe_2$ layer prevents the adsorption of molecules at the surface of graphene. Thus, comparing the results obtained with this kind of heterostruc-

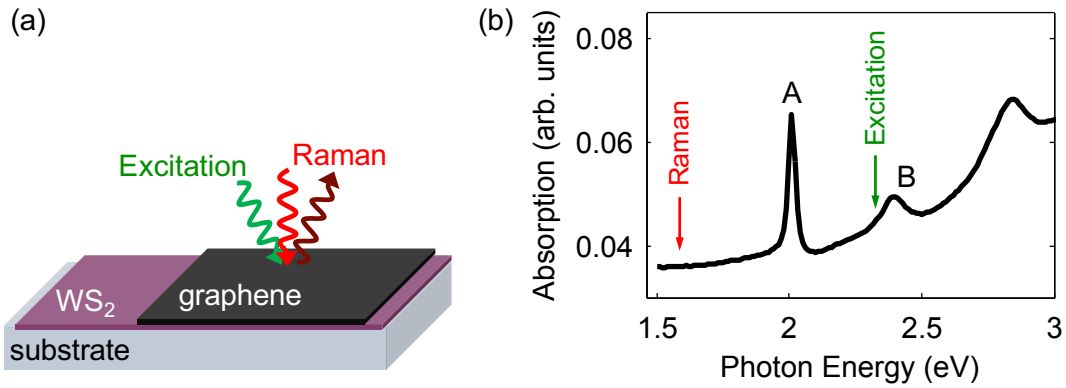

Figure 9.1 *– (a) Three-dimensional schematic view of a monolayer graphene/monolayer WS_2 heterostructure probed using a two-beam experiment. The excitation laser is used to generate excitons in WS_2 while the second laser is used to record the Raman spectrum of graphene wihout generating excitons in WS_2. (b) Absorption spectrum of a monolayer WS_2 extracted from Ref. [Li14]. The photon energy of the two lasers are indicated.*

tures and the one presented in Chapter 8 will probably help to understand the role played by the adsorbates at the surface of graphene and their possible effect on the 'leaks' rate Γ_{leaks} defined in the toy model.

Band alignment A promising way to study the interlayer interaction in heterostructures is to incorporate them into electric field-effect transistors. In particular, it is a relevant manner to study the saturation of the charge transfer. Indeed, this saturation is observed for graphene's Fermi energy around 250 – 300 meV which corresponds to the typical energies achievable with traditional solid state transistors. Therefore, by integrating the heterostucture into back-gated transistors where only the graphene flake is contacted, as illustrated in Fig. 9.2(a), it is possible to tune graphene's Fermi energy and then to study its effect on the charge transfer. Such a geometry can also be used to experimentally determine the band alignment (see Fig. 8.21) from electrical measurements (assuming that source and drain electrodes are contacting the graphene flake) [Kim15a]. Comparing these results with the ones obtained from Raman measurements for the photoinduced charge transfer in Chapter 8 will help to understand better the influence of the excitonic effects, especially the role of the exciton dissociation. Finally, let us mention that studying $MoSe_2$ field-effect transistor is necessary to confirm the supposed behavior of the oX-mode phonon under doping (see Fig. 8.15).

Electrical control of interlayer interactions To reach higher Fermi energies, conventional solid state back-gated transitors are not relevant. One can make use of the top-gated transistor developed in Chapter 5. Or one can also use the recent technique called *Space Charge Doping* introduced by Paradisi *et al.* [Paradisi15]. The principle of this technique is similar to electrochemically gated transistor but instead using a polymer electrolyte, it exploits the presence of mobile ions in glass (see Fig. 9.2(b)). Compared to polymer electrolyte, it has the major advantage of avoiding electrochemical reactions (see Chapter 5 Section 5.5). Consequently, extremely high doping levels higher than 10^{14} cm^{-2} (i.e., $E_F \gtrsim 1$ eV) can be reached

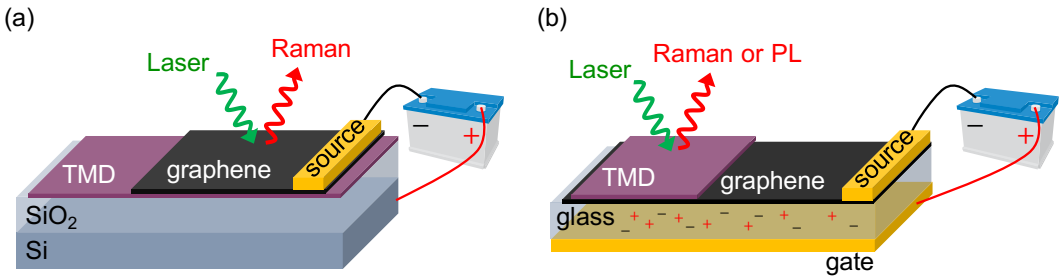

Figure 9.2 *– (a) Three-dimensional schematic view of a monolayer graphene/monolayer TMD heterostructure integrated in a back-gate transistor. Only the graphene flake is contacted and the Si substrate is used as a back gate. (b) Three-dimensional schematic view of a monolayer graphene/monolayer TMD heterostructure incorporated into a field-effect transistor based on the space charge doping technique introduced in [Paradisi15]. The mobile ions in the glass are used to create an electrical double layer and thus to efficiently dope graphene.*

with reversibility and without damaging graphene. This technique can also be extended to other layered materials. For instance, superconductivity in few-layer MoS_2 have been studied using space charge doping [Biscaras15]. However, to activate the mobility of the ions the sample has to be heated to more than 340 K. We have therefore developed a new heating sample holder for the experimental setup that will soon be operational. The possibility to achieve such high doping level opens very interesting perspectives to study the effect of the Fermi energy on the energy transfer and to achieve an electrical control of the interactions. In fact, Pauli blocking is expected to occur for $|E_F| \geq E_g/2$ where E_g is the optical bandgap of the TMD [Lee14b, Tielrooij15]. For such experiments, $MoTe_2$ might be more appropriate since the bandgap is smaller making the condition $|E_F| \geq E_g/2$ easier to reach.

Distance dependence of the interlayer energy transfer An interesting point to address would be to investigate the variation of the interlayer energy transfer as a function of the interlayer distance. Van der Waals heterostructures are particularly appealing because they provide systems with interlayer distance of few Ångströms. In order to unravel the nature of the energy transfer (Förster or Dexter), one solution is to study its distance dependence. From the observations on the decoupled part of the heterostructure studied in Chapter 8, we can get a first idea of this dependence since for interlayer distance of approximately 2 nm the photoluminescence quenching is drastically reduced, but not negligible as suggested by the photoluminescence map in Fig. 8.3. The natural dielectric spacer to use is hexagonal boron nitride because it is the most common two-dimensional insulator. Unfortunately, due to the presence of defects in boron nitride, a photoinduced charge transfer from boron nitride to graphene also occurs [Ju14], which may complicate the interpretation of the observations. Another solution is to use MgO grown by molecular beam epitaxy as successfully employed to study the distance dependence of the energy transfer between colloidal quantum dots or nanoplatelets and graphene [Federspiel15b]. However, preliminary tests have shown that the photoluminescence of $MoSe_2$ is strongly quenched in the presence of MgO. As a result, further investigations are needed to find a proper way to investigate the distance dependence

of the interlayer energy transfer. Furthermore, we have estimated that the energy transfer happens at a picosecond timescale in graphene/$MoSe_2$ heterostructures. Therefore, it would be very interesting to have the possibility to perform time-resolved measurements with a picosecond resolution in order to measure precisely this timescale.

Low-temperature photoluminescence measurements Last but not least, an interesting point to explore is the low-temperature photoluminescence of $MoSe_2$. Such an experiment will be presumably useful to identify the two unknown features observed in the PL spectrum displayed in Fig. 8.16. The highest one in energy was tentatively been assigned to highest excitonic states of the A exciton. Furthermore, at low-temperature, one can distinguish the emission from the neutral excitons and the charged ones. The intensity of these two features provides information on the doping level of $MoSe_2$ [Ross13]. Finally, low-temperature measurements will allow us to study the temperature dependence of the interlayer transfer. Knowing that Förster- and Dexter-type energy transfer are supposed to show different temperature dependence [Lyo00], it could also be a way to pinpoint the nature of the energy transfer. Note that preliminary experiment were already performed with our liquid helium cryostat on sample 1 discussed in Chapter 8.

Heterostructures based on anisotropic transition metal dichalcogenides

A promising perspective of this work is to study heterostructures based on anisotropic transition metal dichalcogenides. In particular, rhenium disulfide (ReS_2) and rhenium diselenide ($ReSe_2$) exhibit significant in-plane anisotropy and can be viewed as a distorted 1T phase due to the formation of a quasi one-dimensional chains of Re atoms [Wilson69, Ho97, Ho98, Ho04, Tiong99]. This anisotropy was mainly probed using optical spectroscopy [Wolverson14, Aslan15, Chenet15, Cui15, Feng15, Nagler15, Zhao15] and electrical measurements [Liu15a]. We have also investigated these materials using ultralow-frequency Raman spectroscopy [Lorchat16] (see Chapter 6). In particular, we have shown that although a complex angular dependence of the intensity of all Raman modes, low-frequency rigid layer modes can be empirically utilized to determine the crystal orientation (i.e., the direction of the Re chains) as depicted in Figs. 9.3(a) and (b). To further complicate the study of these materials, different stacking orders with nearly equal stability (i.e., polytypism) exist. We have also demonstrated that the angular dependence of the Raman response drastically depends on the incoming photon energy (Fig. 9.3(b)), again shedding light on the importance of resonant exciton-phonon coupling in these materials. Unfortunately, in contrast to the exciton-phonon coupling mentioned previously in N-layer $MoTe_2$, the theoretical calculations in such materials remain, up to now, out of reach due to the very complicated structure. Furthermore, several groups have observed that ReS_2 shows a anisotropic excitonic absorption [Aslan15, Cui15]. In our group, Etienne Lorchat has performed similar measurements on $ReSe_2$ and found a similar behavior. Consequently, van der Waals heterostructures based on graphene and ReS_2 or $ReSe_2$ should exhibit polarization-dependent interlayer interaction. As illustrated in Fig. 9.3(c), we could perform a similar study as in Chapter 8

but as a function of the angle θ between the linear polarization of the incoming laser and the direction of the Re chains. Althought, ReS_2 and $ReSe_2$ exhibit poor emission properties [Tongay14, Zhao15], such heterostructures offer exciting perspectives for anisotropic optoelectronic devices [Tiong99, Liu15a, Lin15], especially for polarization-sensitive photodetectors.

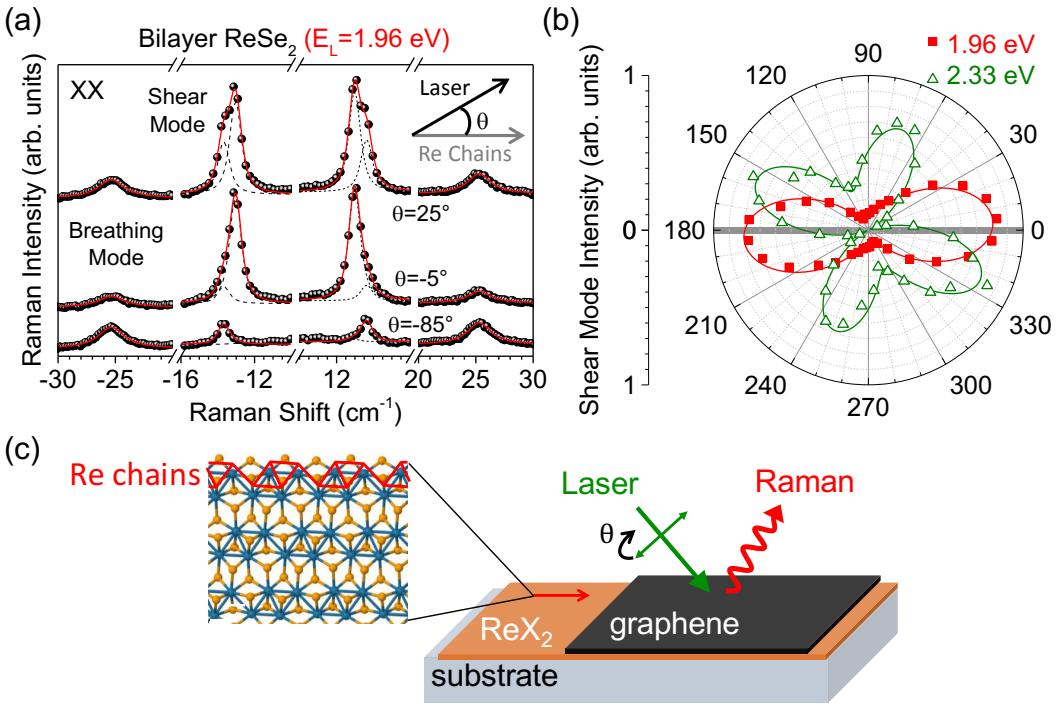

Figure 9.3 *– (a) Ultralow frequency Raman spectra of a bilayer $ReSe_2$ recorded at E_L = 1.96 eV in the parallel (XX) configuration. The different spectra correspond to distinct angle θ between the linear polarization of the incoming laser and the direction of the Re chains. We observed a splitting of the layer shear modes due to the anisotropy. See also Chapter 6 Section 6.2. (b) Polar plots of the integrated Raman intensity of shear modes recorded as a function of the angle θ, at two different photon energies E_L = 1.96 eV (red squares) and E_L = 2.33 eV (open green triangles) in the parallel (XX) configuration on the $ReSe_2$ bilayer. Figure extracted from Ref. [Lorchat16]. (c) Three-dimensional schematic view of a monolayer rhenium TMD (ReX_2) and a monolayer graphene heterostructure. A top view of a 1T'-ReX_2 monolayer (the rhenium chains are highlighted in red) is depicted. The incoming laser is linearly polarized and the Raman spectrum of graphene can be recorded as a function of the angle θ to investigate the interlayer charge transfer.*

Résumé détaillé

Introduction

En 1959, au cours d'une conférence intitulée *Il y a plein de place en bas* [Feynman60], le célèbre physicien Richard Feynman se demanda « que pourrions-nous faire avec des structures en couches ayant juste les bonnes couches ? ». Plus d'un demi-siècle plus tard, son intuition « nous aurons un éventail extrêmement large de propriétés possibles » semble bel et bien se confirmer.

Les matériaux lamellaires sont composés de couches d'atomes empilées les unes sur les autres. Ces couches sont qualifiées de matériaux bidimensionnels (M2D) car elles ne sont épaisses que d'un ou quelques atomes. Ces véritables plans d'atomes sont reliés entre eux par des interactions de van der Waals bien plus faibles que les liaisons covalentes qui assurent la cohésion des atomes au sein d'une même couche. Il est donc possible « d'exfolier mécaniquement », c'est-à-dire de séparer, les différentes couches sans les endommager. Bien qu'étudiés et utilisés depuis de très nombreuses années, ces matériaux ont connu un regain d'intérêt très important à partir de 2004 lorsque Geim et Novoselov (prix Nobel de physique en 2010) ont popularisé une méthode simple d'exfoliation mécanique utilisant du ruban adhésif et permettant d'isoler une monochouche ou plus généralement un système de N couches de M2D [Novoselov04, Novoselov05b].[1] Dès lors, ces systèmes ont suscité un engouement scientifique sans précédent. En effet, il a été très vite découvert que les propriétés physiques de ces matériaux évoluaient drastiquement avec le nombre de couches et que du fait de leur épaisseur atomique, ils étaient particulièrement sensibles à l'environnement. En outre, selon leur composition chimique et leur structure, ces matériaux possèdent des propriétés très variées et complémentaires (voi Fig. 9.4).

Parmi le vaste catalogue de M2D disponibles, le graphène et les dichalcogénures de métaux de transition (DMTs) sont les systèmes les plus étudiés. D'un côté, le graphène correspond à une seule couche d'épaisseur monoatomique de graphite. C'est un matériau qui possède des propriétés électriques [Novoselov04, Zhang05, Novoselov05a], op-

[1] Etonnamment, quelques décennies plus tôt Frindt et ses collaborateurs avaient déjà démontré qu'il était possible d'exfolier mécaniquement ces matériaux lamellaires à l'aide d'un ruban adhésif et ainsi d'isoler un système de quelques couches [Frindt66], voire d'une seule [Joensen86]. Malheureusement, leur travaux n'ont pas été remarqué par la communauté scientifique.

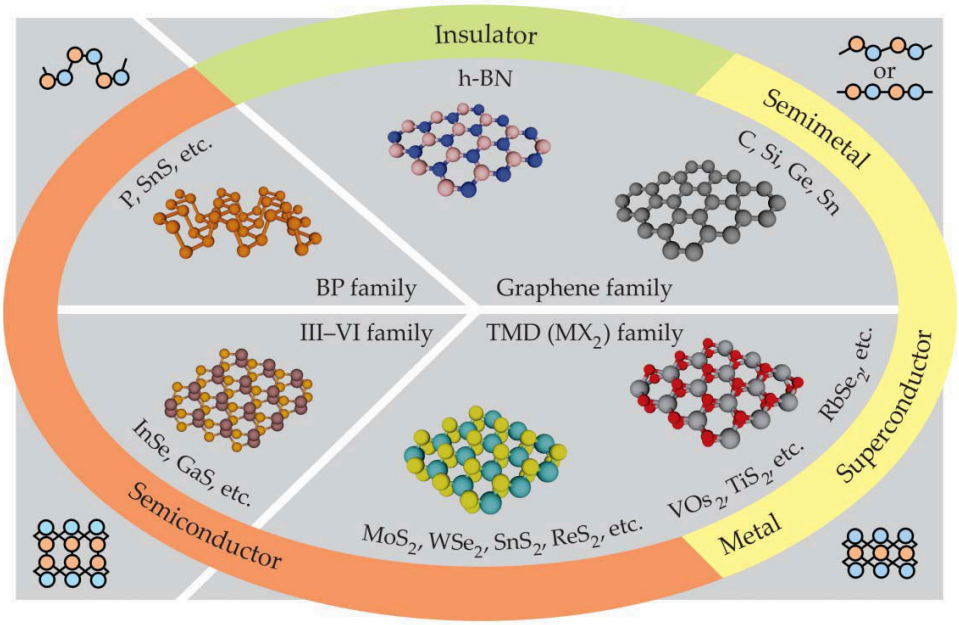

Figure 9.4 – *Le monde des matériaux bidimensionnels. Ce monde est composé du graphène et de ses analogues, notamment du nitrure de bore héxagonal ; du noir de phosphore (BP) et ses analogues ; de la famille des semi-conducteurs III-VI ; et ces dichalcogénures de métaux de transition (TMD). Les propriétés de ces matériaux sont très variées, certains sont métalliques ou semi-métalliques, d'autres sont semi-conducteurs ou isolants. Une coupe transversale des différent matériaux est représentée aux quatre coins. Remarquez que la plupart ne sont pas planaires. La figure est extraite de la Réf. [Ajayan16].*

tiques [Mak08, Nair08, Mak12b], thermiques [Ghosh10] et mécaniques [Lee08] remarquables et relativement facilement accordables par effet de champ notamment. D'un autre côté les DMTs, de formule chimique MX_2 avec M un métal de transition et X un chalcogène, offrent un éventail très large de propriétés physiques dont des semi-conducteurs émettant dans le visible et le proche infrarouge. En particulier, la monocouche (épaisse de trois atomes) des DMTs semi-conducteurs possède des propriétés optoélectroniques très intéressantes [Wang12, Xia14, Mak16], ainsi qu'un pseudospin de vallée pouvant être exploité pour processer de l'information [Xu14].

De plus, en raison de l'absence de liaisons pendantes et du fait que les différentes couches sont liées par des interactions de van der Waals, il est possible d'empiler artificiellement des M2D pour former des « **hétérostructure de van der Waals** » [Geim13]. Comparées aux hétérostructures traditionnelles obtenues par épitaxie et actuellement très largement répandues dans l'industrie [Alferov01], les hétérostructures de van der Waals (HvdW) présentent l'avantage de ne pas être limitées par le désaccord des paramètres de maille. Ainsi, ces structures sont très intéressantes d'un point de vue scientifique pour étudier de nouveaux phénomènes physiques, tel que le papillon de Hofstadter [Hofstadter76, Dean13, Hunt13, Ponomarenko13], mais aussi d'un point de vue technologique pour développer de nouvelles applications dans des domaines variés [Ferrari15]. En particulier, le graphène et les DMTs semi-conducteurs ont des propriétés complémentaires qui peuvent être combinées pour former de nouveaux dispositifs optoélectroniques fonctionnant dans le visible et le proche

infrarouge [Koppens14, Xia14, Mak16, Mueller16]. Comparés aux technologies actuelles, telles que le silicium, ces matériaux possèdent de nombreux avantages comme une semi-transparence, un faible poids, une grande surface, une grande résistance mécanique, ce qui ouvre la voie au développement de dispositifs flexibles, moins energivores et potentiellement à faible coût. Néanmoins, les recherches dans ce domaine n'en sont qu'à leur début, de nombreuses questions fondamentales restent encore sans réponses et de nouvelles techniques de fabrication à grande échelle doivent encore être développées. A noter, qu'en plus des HvdW, il est possible de combiner des M2D avec d'autres nano-objets tels que des boîtes quantiques ou des structures plasmoniques pour former des hétérostructures hybrides.

C'est dans ce contexte que s'insère les travaux de cette thèse. L'objectif de ce projet est de fabriquer des dispositifs optoélectroniques à base d'hétérostructures de van der Waals composées de graphène et de dichalcogénures de métaux de transition, pour étudier et contrôler électriquement les interactions inter-couche qui gouvernent la photophysique de ces structures. Ces systèmes sont étudiés par micro-spectroscopie optique, qui comparée à d'autres techniques présente l'avantage d'être une méthode non invasive, sans contact, locale et rapide pour sonder les propriétés physiques. La technique commune employée tout au long de ce projet de thèse est la **spectroscopie Raman** [Ferrari13, Zhang15b]. Cette technique fournie généralement des informations telles que la qualité cristalline ou la densité de charge mais est utilisée ici d'une manière originale pour étudier le couplage inter-couche. La deuxième technique employée au cours de ce projet est la **spectroscopie de photoluminescence** (PL) résolue spatialement et temporellement [Kolobov16] qui permet de sonder les dynamiques des porteurs de charge, ainsi que les effets excitoniques qui sont affectés pour le couplage inter-couche.

Pour atteindre le but de ce travail de thèse, j'ai défini trois objectifs intermédiaires :

1. Fabriquer des dispositifs robustes et efficaces pour contrôler précisément le niveau de Fermi du graphène, et développer une méthode permettant de déterminer ce niveau.

2. Caractériser des dichalcogénures de métaux de transition semi-conducteurs en fonction du nombre de couche. Parmi la vaste famille de ces matériaux, j'ai sélectionné le ditellurure de molybdène ($MoTe_2$) car il possède un gap optique dans le proche infrarouge (autour de 1 eV) ce qui devrait rendre le contrôle électrique des interactions inter-couches plus simple.

3. Fabriquer des hétérostructures de van der Waals et les intégrer dans les dispositifs développés lors de la première étape.

Pratiquement tous ces objectifs ont été atteints et sont décrits en détail dans ce manuscrit avec en plus une introduction des propriétés des M2D et de leur hétérostructures, des éléments théoriques sur la théorie des groupes, la spectroscopie Raman et de photoluminescence, les effets d'interférences optiques, ainsi qu'une description des méthodes expérimentales. Néanmoins dans ce résumé en français, nous nous focaliserons sur les résultats expérimentaux

correspondant à chacun des trois objectifs définis ci-dessus. Plus concrètement, la première partie résume le Chapitre 5, la deuxième les Chapitres 6 et 7 et la troisième le Chapitre 8.

Spectroscopie Raman de transistors au graphène munis d'une grille électrochimique

Dans cette partie sont présentés les résultats de l'étude par spectroscopie Raman de transistors à effet de champ à base de monocouches de graphène munis d'une grille électrochimique « par le haut ». De tels dispositifs permettent de contrôler électriquement, par effet de champ, les propriétés optoélectroniques du graphène via le niveau de dopage du graphène.

Fabrication des transistors

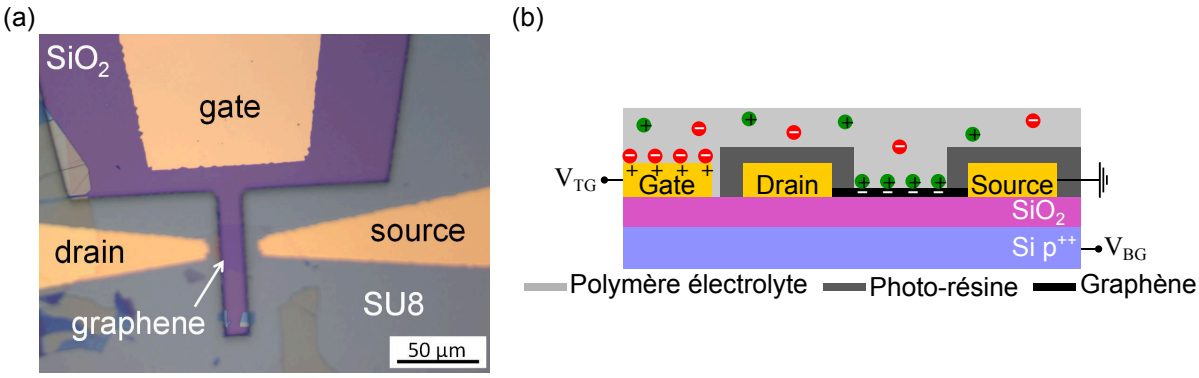

Figure 9.5 – *(a) Image optique d'un transistor à effet de champ à base de graphène avant le dépôt du polymère électrolyte. La source et le drain sont recouverts d'une photo-résine (SU8) pour les empêcher d'être en contact avec le polymère électrolyte. Au contraire, l'électrode de grille (gate) est laissée libre. (b) Schéma en coupe d'un transistor à effet de champ muni d'une grille « par le haut » et « par le bas ». La grille « par le haut » est constituée d'ions Li^+ (vert) and ClO_4^- (rouge) qui forment des doubles couches électriques à la surface des électrodes.*

Ces transistors ont été fabriqués par des techniques de photolithographie standards dans la salle blanche de la plateforme STnano. Dans un premier temps, des monocouches de graphène sont exfoliées mécaniquement à partir de graphite naturel, en utilisant du ruban adhésif, sur des substrats de silicium (Si) recouverts d'une fine couche d'oxyde de silicium (SiO_2) épaisse de 285 ± 15 nm. Les monocouches de graphène ont été repérées par microscope optique et par des mesures de spectroscopie Raman [Malard09b, Ferrari13]. Dans un deuxième temps, deux étapes de photolithographie ont été réalisées. La première étape consiste à contacter le graphène avec deux électrodes d'or (source et drain) et à déposer une troisième électrode (la grille) sur le côté. La deuxième étape permet de recouvrir la source et le drain d'une résine isolante (SU8) afin que la grille électrochimique ne contacte que le graphène et l'électrode de grille. Cette géométrie permet de réduire les réactions électrochimiques parasites. Une fois ces processus achevés, on obtient un dispositif similaire à celui de la Fig. 9.5(a). Enfin dans un troisième temps, une goutte d'une solution de polymère électrolyte est déposée sur l'échantillon grâce à une micropipette. Le polymère utilisé est un mélange de perchlorate de lithium ($LiClO_4$) et d'oxyde de polyéthylène (PEO) dans du méthanol avec un ratio en masse 0,012:1:4 [Das08, Lu04, Liu13]. C'est un polymère électrolyte fréquemment utilisé en électrochimie, tout particulièrement pour réaliser ce type de structure. Après dépôt, le mé-

thanol s'évapore et un fin film de polymère électrolyte transparent se forme, c'est la grille électrochimique.

Effet de champ

Une fois les transistors fabriqués, le spectre Raman du graphène en fonction de la tension de grille « par le haut » (V_{TG}) appliquée entre le graphène et l'électrode de grille a été mesuré. Les spectres obtenus sont présentés sur la Fig. 9.6

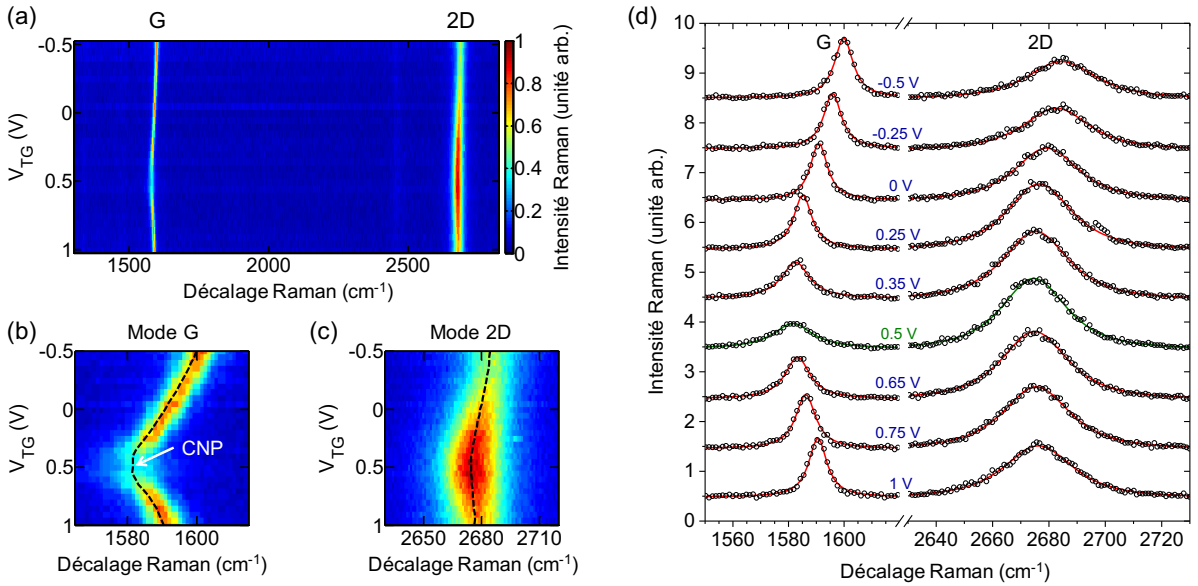

Figure 9.6 – *(a)-(c) Cartes des spectres Raman d'une monocouche de graphène, mesurées à 2,33 eV, en fonction de la tension de grille « par le haut » V_{TG}. On distingue les modes G et 2D, alors le mode D induit par les défauts n'est pas visible. (b) et (c) montrent une évolution claire des modes G et 2D avec V_{TG}. Les lignes pointillées noires correspondent à la fréquence centrale de chacun des pics Raman. Le point de neutralité (CNP) est indiqué par une flèche sur (b). (d) Spectres Raman à différentes valeurs de V_{TG} entre -0.5 V et +1 V. Les symboles correspondent aux données expérimentales et les lignes continues les ajustements. Le point de neutralité est atteint pour une tension $V_{TG,0}$ = +0.5 V (voir la courbe verte).*

On y observe les deux principaux modes Raman du graphène: le mode G et le mode 2D. On constate que ces deux modes évoluent clairement avec V_{TG} pour des tensions de l'ordre de 1 V seulement. En particulier, le mode G (correspondant à la création d'un phonon de quantité de mouvement nulle, c'est-à-dire au centre de la première zone de Brillouin) se translate vers des fréquences plus élevées et devient plus fin lorsque V_{TG} augmente en valeur absolue. C'est une signature claire d'un changement de dopage dans le graphène. On remarquera que la position de neutralité est atteinte pour un tension $V_{TG,0}$ non nulle, ce qui traduit un dopage initial de l'échantillon. On peut alors se demander comment relier V_{TG} et le niveau de Fermi E_F dans le graphène ? Pour répondre à cette question, il faut regarder ce qui se passe lorsqu'une tension V_{TG} est appliquée. Lorsqu'une différence de potentiel est appliquée entre la grille et le graphène les ions se déplacent dans la matrice de polymère sous l'effet du champ électrique créé. Des doubles couches électriques se forment aux interfaces grille/polymère et polymère/graphène, comme illustré sur la Fig. 9.5(b). Une double couche électrique peut être

modélisée par un condensateur plan dont la distance entre les couches de charges opposées est donnée par la longueur de Debye typiquement de l'ordre de 1 nm. En plus de cette capacité, il faut tenir compte de la capacité quantique (C_Q) qui rend compte du déplacement du niveau de Fermi dans le graphène. En tenant compte de ces deux contributions, il est possible de relier la tension V_{TG} au niveau de Fermi E_F dans le graphène :

$$V - V_0 = \frac{E_F}{e} + \mathrm{sgn}(E_F)\frac{eE_F^2}{\pi(\hbar v_F)^2 C_G}, \tag{9.1}$$

e est la charge élémentaire, $v_F \approx 1,1.10^6$ m s^{-1} est la vitesse de Fermi dans le graphène supporté sur SiO_2 [Knox08], $\hbar$ est la constante de Planck réduite et C_G la capacité géométrique de la double couche électrique. Or il est difficile d'évaluer la longueur de Debye et donc de connaître précisément C_G, c'est pourquoi j'ai cherché à mesurer directement C_G.

Pour ce faire, j'ai utilisé des dispositifs possédant une grille électrochimique « par le haut » et une autre grille « par le bas », tel que schématisé sur la Fig. 9.5(b). Le silicium fortement dopé est employé comme électrode de grille « par le bas » et la couche d'oxyde comme diélectrique. Contrairement à C_G, la capacité géométrique C_{BG} de ce dispositif est très bien connue puique l'épaisseur de la couche d'oxyde est elle-même précisément connue. Pour une tension de grille V_{BG} donnée, on balaye la tension V_{TG} en enregistrant les spectres Raman de manière à déterminer le point de neutralité $V_{TG,neutre}$. D'après la Ref. [Xu11b], $V_{TG,neutre}$ est linéaire avec V_{BG} et le coefficient directeur de la droite est donné par le rapport C_{BG}/C_G, ce qui permet d'en déduire que $C_G = 3,3 \pm 0,3$ μF cm^{-2} pour l'échantillon présenté ici (Figs. 9.5 et 9.6). Cette valeur est en bon accord avec ce qui a été reporté pour des dispositifs similaires [Das08, Das09, Shimotani06, Efetov10, Bruna14]. Ainsi, V_{TG} peut être convertie précisément en E_F. Remarquons qu'il est important de déterminer rigoureusement cette valeur car elle varie d'un dispositif à l'autre, spatialement sur un même échantillon mais également au cours du temps. En effet, après quelques jours passés à l'air libre, la capacité peut être réduite d'un ordre de grandeur.

Couplage électron-phonon

Une fois E_F précisément déterminé en fonction de V_{TG}, il est possible de comparer l'évolution expérimentale des modes de phonons avec des modèles théoriques. Le processus associé au mode 2D étant plus complexe que celui du mode G (voir Chapitre 5 pour plus de précision), nous nous concentrerons dans un premier temps uniquement sur les variations de la fréquence et de la largeur du mode G, puis dans un second temps nous nous focaliserons sur l'évolution du rapport entre les intensités intégrées des modes 2D et G.

Fréquence et largeur du mode G Une fois le phonon du mode G créé, celui-ci va interagir avec le système électronique ce qui va induire une **renormalisation**. Cette interaction peut correspondre (voir les diagrammes de Feynman de la Fig. 9.7) soit à une transition réelle qui fixe la durée de vie du phonon (et donc la largeur du pic Raman), soit

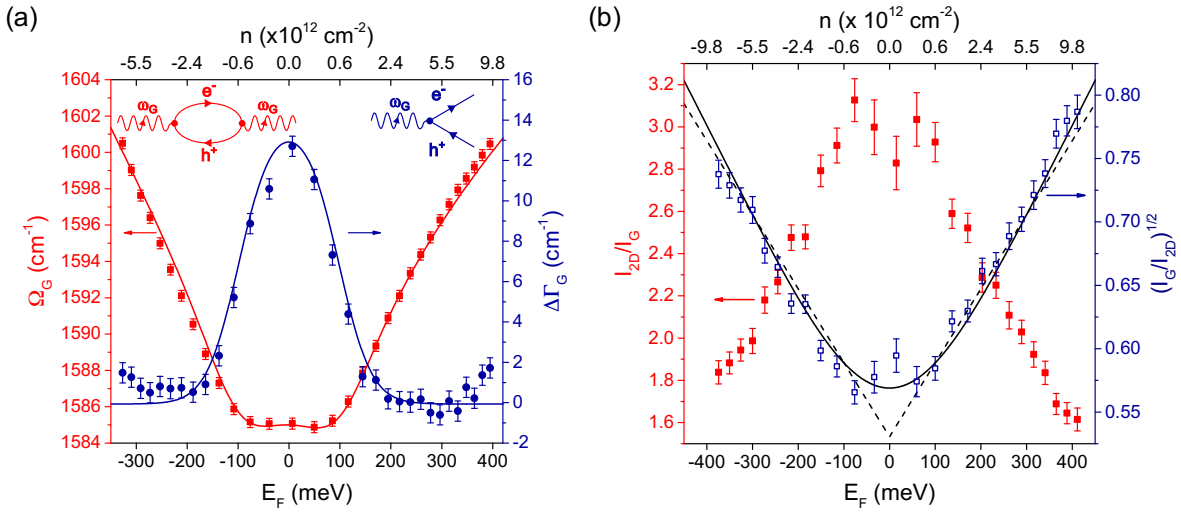

Figure 9.7 – *(a) Fréquence Ω_G (carrés rouges, axe gauche) et largeur Γ_G (cercles bleus, axe droit) du mode G. Les courbes rouges et bleues correspondent à l'ajustement avec le modèle théorique des Refs. [Lazzeri06, Pisana07]. Le diagramme de Feynman de gauche représente la renormalisation de la fréquence du phonon du mode G due à l'interaction avec des paires électron-trou virtuelles. En d'autres termes, le phonon passe un partie de sa vie sous forme de paires électron-trou. Le diagramme de Feynman de droite illustre le déclin du phonon du mode G en une paire electron-trou réelle. Ce processus fixe la durée de vie du phonon et donc la largeur du pic Raman correspondant. (b) Axe de gauche: variation du rapport des intensités intégrées entre les modes 2D et G avec le niveau de dopage (carrés rouges). Axe de droite: évolution de la racine carré du rapport des intensités intégrées entre les modes G et 2D avec le dopage (carrés ouverts bleus). Les courbes noires en pointillés et ligne continue correspondent aux ajustements, respectivement sans et avec une inhomogénéité de charge, fondés sur le modèle de Ref. [Basko09b].*

à une transition virtuelle qui fixe l'énergie du phonon (et donc la fréquence du pic Raman). Cette évolution théorique du pic Raman associée au mode G a notamment été mise en équation par Lazzeri et Mauri [Lazzeri06, Pisana07]. En convoluant leur modèle théorique avec une gaussienne de largeur δE_F afin de tenir compte de l'inhomogénéité de charge [Casiraghi07, Martin08, Xu11a, Li11], on peut alors ajuster simultanément l'évolution expérimentale de la fréquence et de la largeur du mode G avec comme seul paramètre d'ajustement le couplage électron-phonon au centre de la première zone de Brillouin λ_Γ et l'inhomogénéité de charge δE_F. Comme illustré sur la Fig. 9.7(a), l'accord expérience-théorie est excellent avec une valeur de λ_Γ cohérente avec les calculs DFT [Lazzeri06, Pisana07] et une inhomogénéité de charge raisonnable [Martin08, Xue11]. Ce très bon accord permet d'utiliser l'évolution théorique du mode G pour déterminer le niveau de Fermi dans le graphène (voir la troisième partie de ce résumé). En particulier, plutôt que d'utiliser une géométrie avec une grille « par le haut » et « par le bas » pour déterminer C_G, il est possible de l'inclure comme paramètre d'ajustement. On obtient alors une valeur de C_G sensiblement identique à celle obtenue avec la méthode des deux grilles. Notons que la renormalisation du mode G est particulièrement importante car il y a une anomalie de Kohn [Piscanec04] au centre de la première zone de Brillouin.

Intensité des modes 2D et G En plus des variations de fréquence et de largeur des modes Raman avec E_F, l'intensité intégrée des pics associés au mode Raman peut également dé-

pendre de E_F. En particulier, le rapport des intensités intégrées des modes 2D et G présente une variation claire avec E_F: le ratio I_{2D}/I_G est maximal à neutralité et décroit lorsque le dopage augmente. Cette variation est plus complexe à décrire que celle de la fréquence et de la largeur du mode G. Néanmoins, Basko a développé une modèle théorique pour décrire cette évolution [Basko09b]. En utilisant ce modèle, on obtient un très bon accord expérience-théorie (voir Fig. 9.7(b)). On peut alors déduire à l'aide de la valeur de λ_Γ déterminée précédemment, une valeur de couplage électron-phonon au bord de la première zone de Brillouin λ_K. On constate que λ_K est environ cinq fois plus important que λ_Γ, en accord avec le fait que le couplage au bord de la première zone de Brillouin est plus fort qu'au centre.

Corrélation entre la fréquence des modes G et 2D

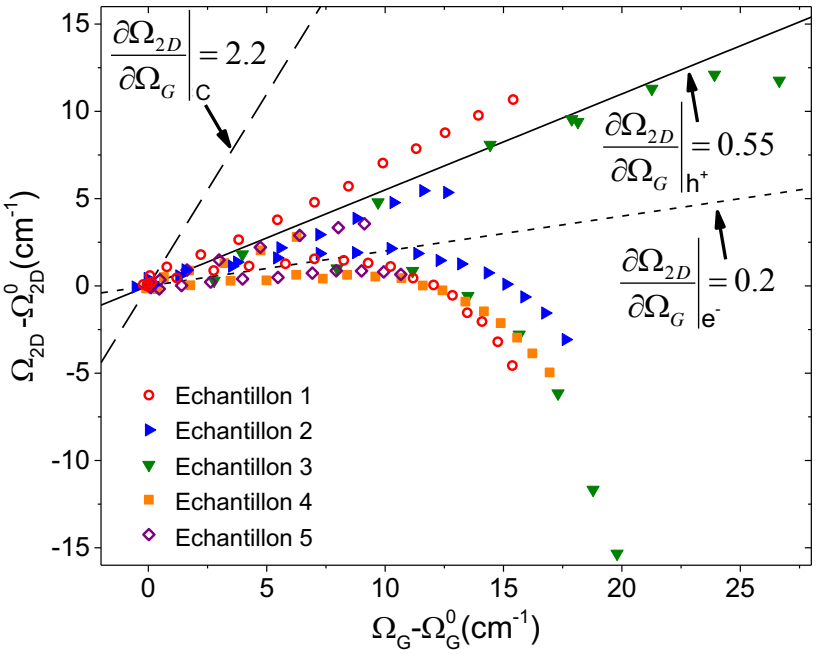

Figure 9.8 – *Corrélation entre les fréquences relatives, par rapport au point de neutralité, des modes 2D et G dans une monocouche de graphène dopée pour cinq échantillons différents. La ligne continue et en tirets courts sont des ajustements globaux des portions linéaires pour le dopage par des trous et des électrons respectivement. La ligne en tirets longs correspond à l'évolution de Ω_{2D} et Ω_G sous contrainte uniquement [Lee12c, Metten16].*

Comme mentionné précédemment, l'évolution théorique de la fréquence et de la largeur du mode G (voir du ratio I_{2D}/I_G) en fonction du niveau de Fermi E_F peut être utilisée pour déterminer précisément E_F dans un échantillon de graphène quelconque. Néanmoins, comme ces variations théoriques sont quasi identiques pour un dopage par des électrons ou par des trous, il est difficile de connaître la nature du dopage. Une solution est d'utiliser la corrélation entre la fréquence des modes G et 2D. En effet, comme illustré sur la Fig. 9.8, la corrélation $\Omega_{2D}(\Omega_G)$ est quasi linéaire de pente environ 0,55 pour une dopage par des trous et est quasi linéaire de pente environ 0,2 pour un faible dopage par des électrons, et cela indépendement de la valeur de C_G, des coulages électron-phonon ou encore de l'inhomogénéité de charge.

De plus, cette corrélation est également connue pour permettre de séparer les contraintes du dopage [Lee12c]. Au cours de ce projet, je ne me suis pas intéressé à l'effet des contraintes sur le spectre Raman du graphène. Cependant, Dominik Metten a réalisé un travail de thèse complet sur ce sujet [Metten16]. En particulier, il a été observé que pour des contraintes biaxiales, la corrélation $\Omega_{2D}(\Omega_G)$ est quasi linéaire de pente environ 2,2. Ces corrélations seront très utiles dans la troisième partie de ce résumé.

Conclusion

En conclusion de cette première partie, les transistors à effet de champ munis d'une grille électrochimique « par le haut » développés au cours de ce projet de thèse, sont des dispositifs très efficaces et robustse pour doper le graphène. Des niveaux de l'ordre de 700 meV sont atteignables dans des conditions ambiantes, ce qui ouvre des perpectives très intéressantes dans l'optique de contrôler les interactions inter-couches dans des hétérostructures. Cette étude a également permis de montrer que la spectroscopie Raman est une technique extrêmement puissante pour caractériser des échantillons de graphène, et notamment pour déterminer la nature et le niveau de dopage. Cet outil sera pleinement exploité dans la troisième partie de ce résumé. Enfin au cours des mesures, j'ai remarqué qu'il était possible de créer des défauts dans le feuillet de graphène *in-situ* en appliquant une tension de grille suffisamment élevée. L'influence de ces défauts sur la réponse Raman du graphène en fonction du dopage a alors été étudiée mais n'est pas présentée dans ce manuscrit. Malgré des concentrations de défauts supérieures à 10^{12} cm^{-2}, aucune influence sur les modes G et 2D n'a été constatée.

Du cristal massif à la monocouche : évolution des propriétés optiques d'un empilement de N couches d'un semi-conducteur lamellaire

Cette deuxième partie s'intéresse à l'évolution des propriétés optiques d'un semi-conducteur lamellaire en fonction du nombre de couches N. Le ditellurure de molybdène ($MoTe_2$) qui appartient à la famille des dichalcogénures de métaux de transition est utilisé comme exemple, il est complètement caractérisé pour $N = 1$ à $N = 12$ par des mesures de micro-spectroscopie Raman et de micro-photoluminescence.

Une description unifiée des phonons optiques dans un semi-conducteur lamellaire

Commençons par les modes de phonon dans les N couches de 2Hc $MoTe_2$ (voir Fig. 9.9(a) pour la structure cristalline). Dans un système de N couches de M2D, le couplage via des interactions de van der Waals entre couches donne naissance à une levée de dégénérescence de tous les modes de phonons existant dans une monocouche. Cet effet est connu sous le nom de « splitting (séparation) de Davydov » [Davydov64, Davydov71]. Ainsi, à chaque déplacement élémentaire présent dans la monocouche est associé N modes dans un système de N couches. Graphiquement, les fréquences de ces modes peuvent être représentées sous la forme d'un diagramme « en éventail ». C'est ce diagramme que j'ai cherché à mesurer expérimentalement et à modéliser théoriquement.

En pratique, j'ai mesuré systématiquement le spectre Raman en fonction de N. Les échantillons de N couches de $MoTe_2$ ont été obtenus par exfoliation mécanique d'un cristal synthétique de $MoTe_2$ acheté chez 2D Semiconductors et déposés sur des substrats de Si recouverts d'une couche de SiO_2 de 90 nm.

Sur les spectres obtenus, des séries de pics apparaissent (voir Fig. 9.9(b)). Le dispositif expérimental a été optimisé afin d'avoir accès à des décalages Raman dans la gamme 4 – 40 cm^{-1}. Les modes observés sur les spectres Raman ont été distingués, selon qu'ils soient dans le plan ou hors du plan, puis selon leur fréquence (ou énergie) [Wieting80, Yamamoto14, Guo15a] :

- à basse fréquence (< 40 cm^{-1}), les modes observés correspondent à des mouvements de « plaque rigide » (cisaillement dans le plan et respiration hors du plan), issus des modes acoustiques à fréquence nulle de la monocouche;
- à des fréquences intermédiaires (100 – 200 cm^{-1}), les modes observés impliquent un déplacement intra-couche des atomes de tellure;
- à des fréquences plus haute (200 – 300 cm^{-1}), les modes observés font intervenir un déplacement intra-couche des atomes de molybdène vis-à-vis des atomes de tellure.

En augmentant le nombre de couches N, on observe l'évolution de ces différents modes et notamment le « splitting de Davydov ». Par exemple dans le cas du mode hors du plan de fréquence intermédiaire (mode noté oX), on peut clairement distinguer sur la Fig. 9.9(c) ce « splitting de Davydov ».

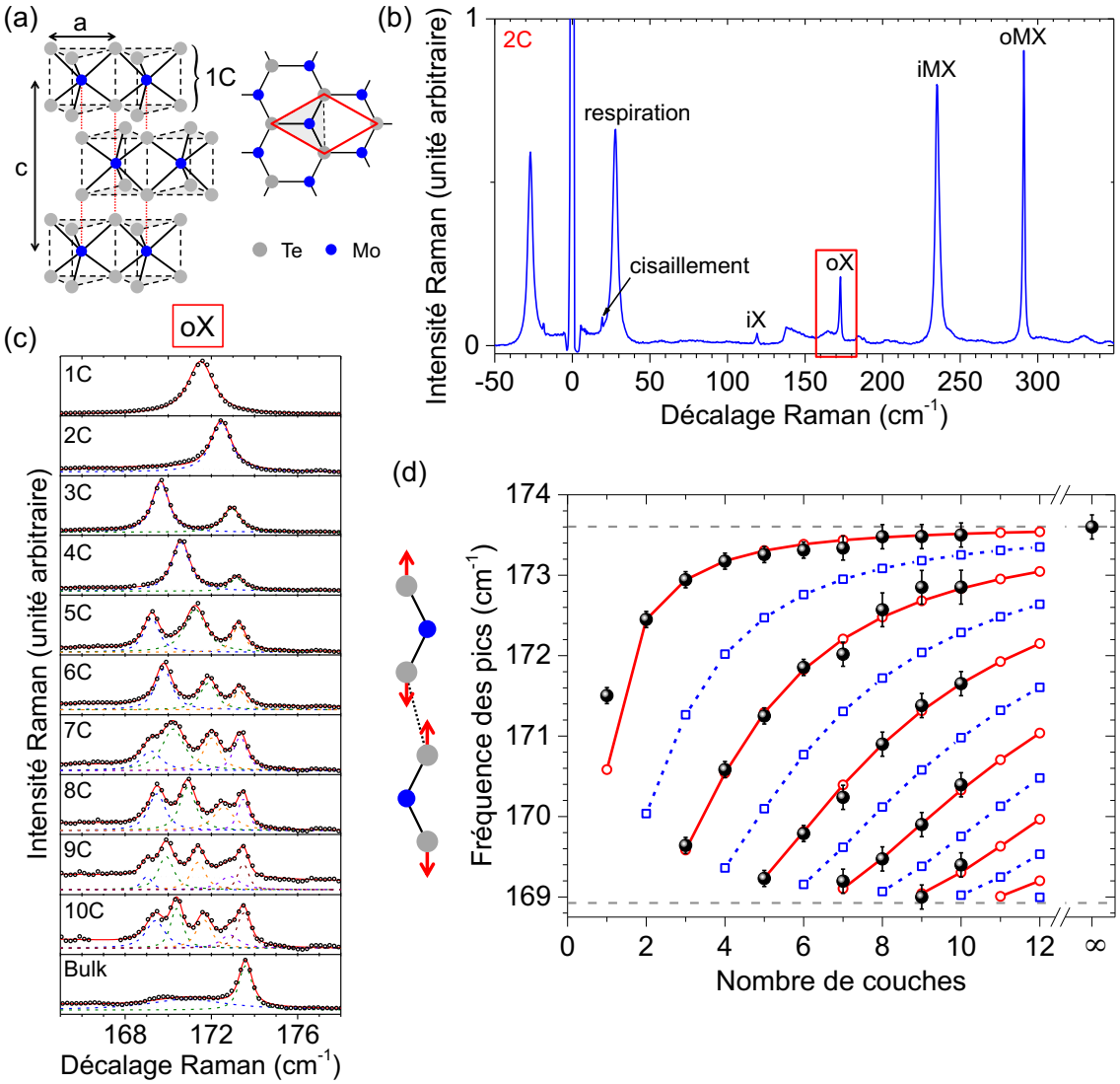

Figure 9.9 – *(a) Vue de côté et de dessus de la structure cristalline 2Hc du $MoTe_2$. Le losange rouge représente la maille élémentaire. (b) Spectre Raman d'une bicouche de $MoTe_2$ obtenu à une excitation de 2,33 eV dans des conditions ambiantes. Les modes de phonon étudiés sont marqués. (c) Spectres Raman de $N = 1$ à $N = 10$ et pour le cristal massif montrant le mode oX correspondant à un déplacement de atomes de tellure uniquement (les atomes de molybdène sont fixes). On observe clairement une séparation de Davydov lors que N augmente. (d) Fréquences (cercles noirs) du mode oX extraites des ajustements des spectres de (c) en fonction du nombre de couches N. Les cercles rouges ouverts (carrés bleus ouverts) correspondent aux fréquences des modes Raman (infrarouge) actifs calculés à l'aide du modèle de chaîne linéaire finie. Les lignes reliant ces points sont des guides pour les yeux. Les lignes horizontales en pointillé gris indiquent les fréquences des modes du cristal massif.*

L'ensemble de ces modes de phonons a ensuite été décrit à l'aide d'un modèle de chaîne linéaire finie dans lequel les interactions entre atomes sont décrites jusqu'aux second plus

proches voisins et où les effets de surface au niveau des deux couches externes sont pris en compte [Luo13b]. Les modes propres et fréquences propres de cette chaine linéaire donnent des résultats en excellent accord avec les mesures et permettent de déduire les constantes de forces microscopiques associées aux interactions interatomiques et de comprendre l'activité des modes observés en regard de leurs symétries. En outre, cela permet également d'obtenir les fréquences de tous les modes du cristal massif et notamment les modes silencieux.

Ces résultats sont importants d'un point de vue pratique car pour un grand nombre d'applications, il serait préférable d'opter pour des dispositifs dont le canal contient N couches de DMTs plutôt qu'une monocouche qui est intrinsèquement plus fragile et sensible aux perturbations extérieures. En outre, une compréhension détaillée du couplage électron-phonon, en particulier avec les modes de basse énergie, est indispensable pour comprendre les limitations et/ou optimiser les performances des nouveaux dispositifs à base de M2D.

D'un point de vue fondamental, ces travaux soulèvent aussi une nouvelle question importante. Jusqu'à présent, les séries de modes de basse énergie (respiration et cisaillement) typiques d'un échantillon de N couches ont été observées sur des systèmes similaires (MoS_2, WSe_2) [Plechinger12, Zeng12, Zhao13, Zhang13, Boukhicha13]. En revanche, la séparation de Davydov n'a été que très sporadiquement observée pour les modes à plus haute énergie car le mode Raman similaire à celui du matériau massif domine très largement par rapport aux autres modes issus de la séparation de Davydov [Tonndorf13, Chen15, Staiger15]. Comment se fait-il que cette séparation soit visible de façon aussi nette pour $MoTe_2$? La réponse à cette question nécessite une étude détaillée du couplage entre les modes de phonons et les fortes résonances excitoniques dans les DMTs, ainsi que de l'effet des symétries des fonctions d'ondes excitoniques et des modes de phonon sur le couplage exciton-phonon à résonance. Cette étude est en cours avec nos collaborateurs et théoriciens du groupe de Ludger Wirtz de l'Université de Luxembourg et tout particulièrement par Henrique Miranda dont ces travaux constitue son projet de thèse.

Photoluminescence d'un semi-conducteur lamellaire

Une fois le nombre de couches des échantillons de $MoTe_2$ déterminé, je me suis focalisé sur l'évolution des propriétés de photoluminescence (PL) en fonction de N. La Fig. 9.10(a) montre les spectres de PL mesurés en fonction de N pour N couches de $MoTe_2$. Comme pour les autres DMTs à base de molybdène [Mak10, Splendiani10, Tonndorf13], un fort décalage vers le bleu ainsi qu'une forte augmentation de l'intenisté de PL sont observés pour les monocouches. Ces résultats suggèrent une transition d'un gap optique indirect (d'environ 0.94 eV) en massif à un gap direct (d'environ 1.1 eV) pour $N = 1$ [Ruppert14]. Néanmoins, l'augmentation de l'intensité de PL lorsque N diminue est plus faible que pour les autres DMTs à base de molybdène. En effet, la différence d'énergie entre le gap optique direct et indirect est sensiblement plus faible pour $MoTe_2$ (0,16 eV) que pour MoS_2 (0,6 eV) ou $MoSe_2$ (0,5 eV).

Après avoir étudié la PL de N couches de $MoTe_2$, nous pouvons nous concentrer sur

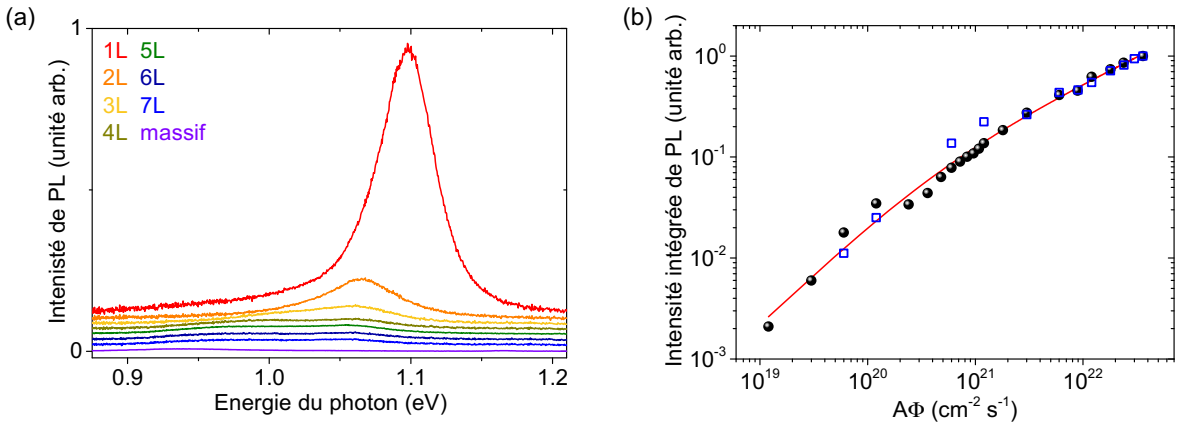

Figure 9.10 – *(a) Spectres de photoluminescence de $N = 1$ à $N = 7$ couches et pour le cristal massif de $MoTe_2$. Les spectres ont été corrigés des effets d'interférences optiques (voir Annexe C). (b) Intensité de photoluminescence d'une monocouche de $MoTe_2$ en fonction du flux de photons absorbés $\mathcal{A}\Phi_{ph}$. Les symboles correspondent aux mesures expérimentales faites sur deux monocouches différentes. La courbe en trait plein correspond à l'ajustement des points expérimentaux à l'aide du modèle de l'équatioon de taux (9.2).*

l'évolution de la PL d'une monocouche de $MoTe_2$ en fonction du flux de photons absorbés $\mathcal{A}\Phi_{\text{ph}}$, où $\mathcal{A}$ est le facteur d'absorption de la monocouche de $MoTe_2$ dans le système air/$MoTe_2$/SiO_2/Si ($\mathcal{A} \approx 16,5$ %) et Φ_{ph} le flux de photons incident. La Fig. 9.10(b) présente les variations de l'intensité intégrée de PL pour deux monocouches de $MoTe_2$. On observe distinctement une évolution sous-linéaire de l'intensité de PL avec le flux de photons absorbés. Une telle variation est caractéristique de phénomènes non-linéaires de type Auger tel que les annihilations exciton-exciton (AEE). En effet, les interactions de Coulomb sont exaltées dans les DMTs semi-conducteurs du fait de l'écrantage réduit et de larges masses effectives [Glazov15, Mak16], ce qui a pour conséquence des effets excitoniques importants et des processus non-linéaires de type Auger efficaces [Moody16]. Des manifestations d'AEE dans des monocouches de MoS_2 [Sun14, Yu16], $MoSe_2$ [Kumar14], WSe_2 [Mouri14, Zhu15, Yu16], et WS_2 [Yuan15, Zhu15, Yu16] ont été observées expérimentalement. Pour démontrer que les variations de PL de la monocouche de $MoTe_2$ sont également dominées par des AEE, nous avons utilisé un modèle simple d'équation de taux qui repose sur l'équation suivante :

$$\frac{\mathrm{d}n_{\text{x}}}{\mathrm{d}t} = \mathcal{A}\Phi_{\text{ph}} - \Gamma_{\text{x}} n_{\text{x}} - \gamma_{\text{aee}} n_{\text{x}}^2, \tag{9.2}$$

où n_{x} est la densité d'exciton, Γ_{x} le taux de recombinaison linéaire et γ_{aee} le taux d'AEE. En résolvant cette équation en régime permanent (puisque les mesures sont effectuées sous excitation laser continue) et en utilisant l'expression obtenue pour ajuster l'intensité de PL (qui est proportionnelle à n_{x}), on obtient le très bon accord de la Fig. 9.10(b).

Conclusion

En conclusion, la spectroscopie Raman est une technique extrêmement puissante pour sonder l'influence du couplage inter-couche et des effets de surface. **Tous** les phonons du centre de la première zone de Brillouin d'un système de N couches de $MoTe_2$ ont pu être décrits de

manière unifiée à l'aide d'un modèle de chaîne linéaire finie dans lequel sont pris en compte les interactions entre atomes jusqu'aux second plus proches voisins et les effets de surface au niveau des deux couches externes. De plus, le rôle majeur joué pour les couplages exciton-phonon à résonance sur l'observation de « splittings de Davydov » a été mis en évidence. Dans un second temps, la photoluminescence de N couches de $MoTe_2$ a été présentée. Comme ses cousins MoS_2 et $MoSe_2$, $MoTe_2$, on observe une transition d'un gap optique indirect (d'environ 0,94 eV) dans le cristal massif vers un gap optique direct (d'environ 1,1 eV) dans la limite d'une monocouche. De plus, la monocouche de $MoTe_2$ présente des non-linéarités caractéristiques de processus de type Auger (tel que des annihilations exciton-exciton) qui reflètent la forte exaltation des interactions de Coulomb dans ces matériaux. Enfin, bien que ces mesures ont été effectuées sur $MoTe_2$, elles sont parfaitement généralisable à d'autres DMTs semiconducteurs. En particulier, le modèle de chaine linaire finie sur N couches de diséléniure de molybdène ($MoSe_2$) a été employé avec succès (voir Chapitre 6).

Une étude toute optique d'hétérostructures de van der Waals graphène/dichalcogénure de métaux de transition

Cette troisième et dernière partie se focalise sur la fabrication et l'étude toute optique d'hétérostructures de van der Waals monocouche de graphène/monocouche de diséléniure de molybdène ($MoSe_2$).

Fabrication des hétérostructures

Pour fabriquer les hétérostructures, j'ai utilisé la technique de transfert sec (c'est-à-dire n'impliquant aucune étape avec une phase liquide) mise au point par Castellanos-Gomez [Castellanos-Gomez14]. Brièvement, dans une première étape on exfolie $MoSe_2$ à partir de cristaux massifs synthétiques achetés chez HQ Graphene sur des substrats de Si recouverts d'une couche de 90 nm de SiO_2. Puis, on repère au microscope optique les monocouches. Dans une seconde étape, on exfolie des monocouches de graphène à partir de graphite naturel sur des substrats de PDMS commerciaux (Gel-Pak 4). Les monocouches sont également identifiées au microscope optique. Dans une troisième étape, les monocouches de $MoSe_2$ et de graphène sont alignées et mise délicatement en contact à l'aide de l'aligneur de masque Karl Suss MJB3 de la salle blanche STnano. Enfin dans une dernière étape, le tampon de PDMS est décollé lentement. La monocouche de graphène est transférée sur la monocouche de $MoSe_2$. La Fig. 9.11(a) montre un exemple de structure obtenue avec cette technique.

Caractérisation des hétérostructures

Une fois les hétérostructures fabriquées, j'ai commencé par les caractériser en réalisant des cartographie AFM, de photoluminescence et de spectroscopie Raman. Les résultats obtenus sont présentés sur la Fig. 9.11.

Une image optique de l'hétérostructure étudiée ici est visible sur la Fig. 9.11(a). Sur cette image les deux monocouches ont été mises en évidence à l'aide de couleurs. On constate que la monocouche de graphène ne recouvre pas toute celle de $MoSe_2$. Sur les mesures de microscopie de force atomique, on distingue une zone particulière de l'hétérostructure délimitée par les pointillés blanc sur la Fig. 9.11(a). Pour cette zone, on mesure une hauteur d'environ 0.65 nm entre la surface de $MoSe_2$ et celle du graphène (voir Fig. 9.11(b)). Or pour le reste de l'hétérostructure cette distance est plutôt de 2-3 nm. De plus, pour cette même zone l'interface entre les deux couches est bien plus propre que pour le reste de l'échantillon à cause du mécanisme « d'auto-nettoyage » des couches bien couplées [Kretinin14]. Pour la suite et pour distinguer ces deux zones de l'hétéreostructure, nous dirons que pour la première les couches sont couplées alors que pour la deuxième elles sont découplées (voir Fig. 9.11(c)).

Les Figs. 9.11(d) et 9.11(e) montrent les cartes d'intensité de PL et de fréquence du mode G pour l'échantillon complet. Sur la première carte, on distingue clairement la forme de la monocouche de $MoSe_2$, ainsi que la partie couplée de l'hétérostructure. En effet, pour cette

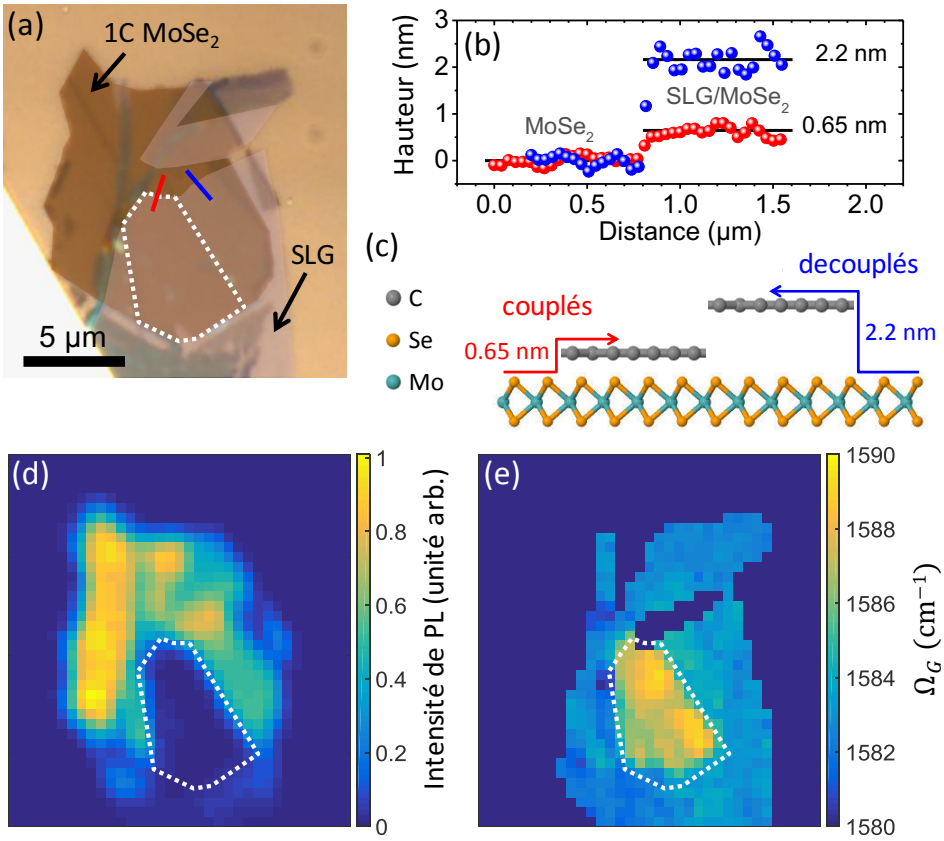

Figure 9.11 – *(a) Image optique d'une hétérostructure. Les monocouches de $MoSe_2$ et de graphène (SLG) sont mise en évidence avec des couleurs. La partie couplée de l'hétérostructure est délimitée par les pointillés blancs. (b) Profiles de hauteur mesurés par microscopie de force atomique le long des lignes bleues et rouges de (a). (c) Vue de côté de l'hétérostructure avec les parties couplées et découplées. (d) Carte de photoluminescence de $MoSe_2$. (e) Carte de la fréquence du mode G du graphène. Les deux cartes ont été enregistrées à 2,33 eV dans les conditions ambiantes, à un flux de photons de d'environ 2.10^{19} cm^{-2} s^{-1} pour la première et 2.10^{22} cm^{-2} s^{-1} pour la seconde.*

dernière zone, l'intensité de PL est diminuée d'environ 300 comparé à $MoSe_2$ seul, alors que pour le reste de l'hétérostructure l'intensité n'est réduite que d'un facteur deux. Une telle inhibition de l'intensité de PL est une signature manifeste d'un couplage inter-couche fort. Sur la seconde carte, on observe la forme de la monocouche de graphène[2] et une augmentation de la fréquence du mode G pour la zone couplée. De plus, on constate également une diminution de la largeur du mode G pour cette même zone (non montré ici, voir Chapitre 8). De tels changements sont des signatures claires d'une modification du dopage dans le graphène. Ainsi, cette observation tend à montrer qu'il y aurait un transfert de charge photoinduit entre $MoSe_2$ et la monocouche de graphène dans le cas où elles sont couplées. Afin de démontrer cette affirmation, j'ai réalisé des mesures Raman du graphène en fonction du flux incident de photons Φ_{ph}.

[2]Noter que l'extrémité haut droit correspond à un morceau de multicouche de graphène.

Spectres Raman du graphène en fonction de Φ_{ph}

Les spectres Raman du graphène en fonction de Φ_{ph} sont présentés sur les Figs. 9.12(a)-(c). Comme référence, j'ai mesuré les spectres Raman d'une partie de la monocouche de graphène sur SiO_2 (SLG/SiO_2). On observe que les spectres mesurés sur SLG/SiO_2 et sur SLG/$MoSe_2$ découplés sont semblables et ne changent quasiment pas avec Φ_{ph}. En revanche, les spectres de SLG/$MoSe_2$ couplés évoluent très distinctement avec Φ_{ph}. La fréquence et la largeur du mode G, ainsi que le rapport entre l'intensité intégrée du mode 2D et du mode G sont extraits des spectres et tracés sur les Figs. 9.12(d)-(f). On constate que les valeurs de ces paramètres pour SLG/$MoSe_2$ et SLG/$MoSe_2$ découplés sont quasi constante avec Φ_{ph} et correspondent à un graphène proche de la neutralité (voir Fig. 9.7(a)). Inversement pour la zone couplée, l'évolution de ces paramètres montre une augmentation du dopage avec Φ_{ph}. On en conclut qu'il y a bien un transfert de charge de $MoSe_2$ vers le graphène et que celui-ci est photoinduit.

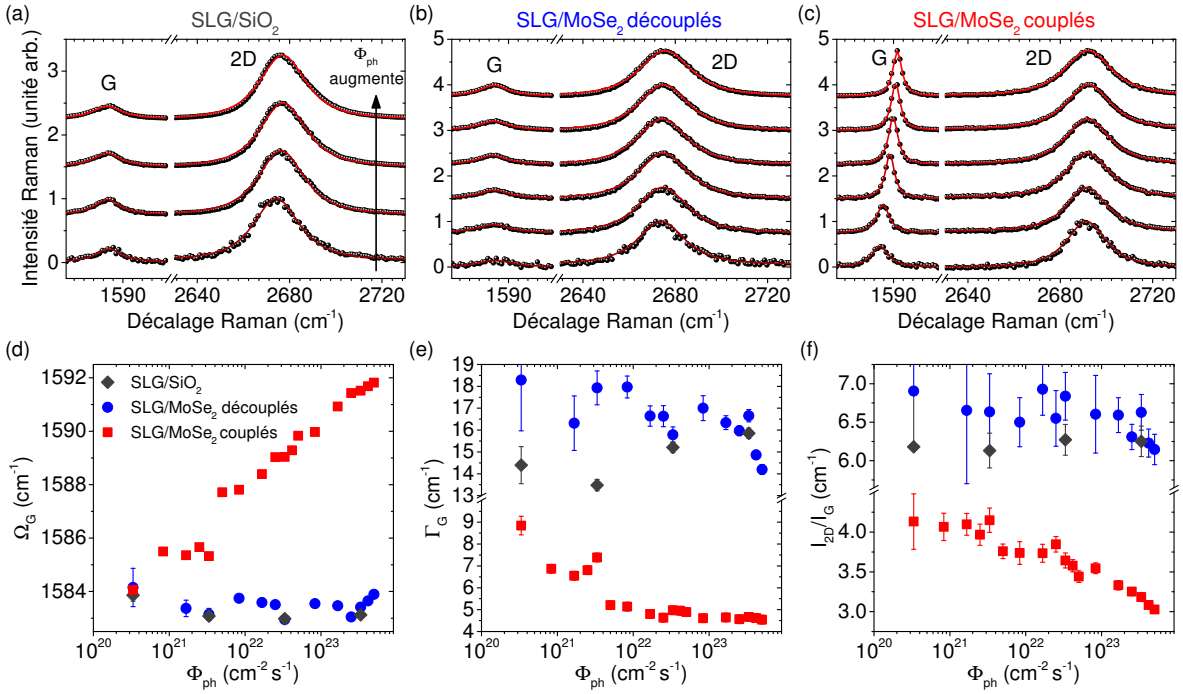

Figure 9.12 – *(a) Spectres Raman du graphène enregistrés à 2,33 eV dans des conditions ambiantes en fonction du flux de photons incidents Φ_{ph} pour (a) graphène sur SiO2, (b) graphène/MoSe2 découplés et (c) graphène/MoSe2 couplés. (d) Fréquence Ω_G du mode G, (e) largeur Γ_G du mode G et (f) ratio I_{2D}/I_G entre l'intensité intégrée du mode 2D et celle du mode G en fonction de Φ_{ph}*

.

On peut alors utiliser la corrélation des fréquences des modes G et 2D pour déterminer la nature de ce transfert (voir Fig. 9.8). La Fig. 9.13(a) montre cette corrélation $\Omega_{2D}(\Omega_G)$ pour les mesures de la Fig. 9.12. On observe une corrélation linéaire de pente environ 0,1 pour la partie couplée de l'hétérostructure, alors qu'il n'y a pas de corrélation claire pour le reste de l'échantillon. D'après les résultats obtenus dans la première partie, une telle corrélation correspond à un dopage par des électrons. Ainsi, on en conclut qu'il y a un **transfert d'électrons photoexcités du $MoSe_2$ vers le graphène**. De plus, en utilisant les courbes théoriques

de $\Omega_G(E_F)$ et $\Gamma_G(E_F)$ (voir Fig. 9.7(a)), il est possible d'en déduire le niveau de dopage dans le graphène. En effet, il suffit de lire le niveau de Fermi correspondant à un couple (Ω_G, Γ_G) sur les courbes théoriques pour un dopage par des électrons (d'après la corrélation $\Omega_{2D}(\Omega_G)$), comme illustré sur la Fig. 9.13(b). Une fois les niveaux de Fermi ou de manière équivalente la densité de porteur de charge n_G (ici des électrons) extraite, on peut tracer, par exemple, n_G en fonction de Φ_{ph} (voir Fig. 9.13(c)). On remarque pour cet échantillon que (i) n_G augmente de manière sous-linéaire avec Φ_{ph} (phénoménologiquement $n_G \propto \Phi_{ph}1/5$) et (ii) n_G tend à saturer autour d'une valeur maximale d'environ 5.10^{12} cm^{-2} (soit $E_F \approx 290$ meV). Un comportement similaire sur d'autres hétérostructures a été observé et ce indépendamment du niveau de dopage initial. Ces observations montrent que lorsque Φ_{ph} augmente, l'efficacité du transfert de charge diminue et que celui-ci devient même nul pour un flux de photons incidents suffisamment grand.

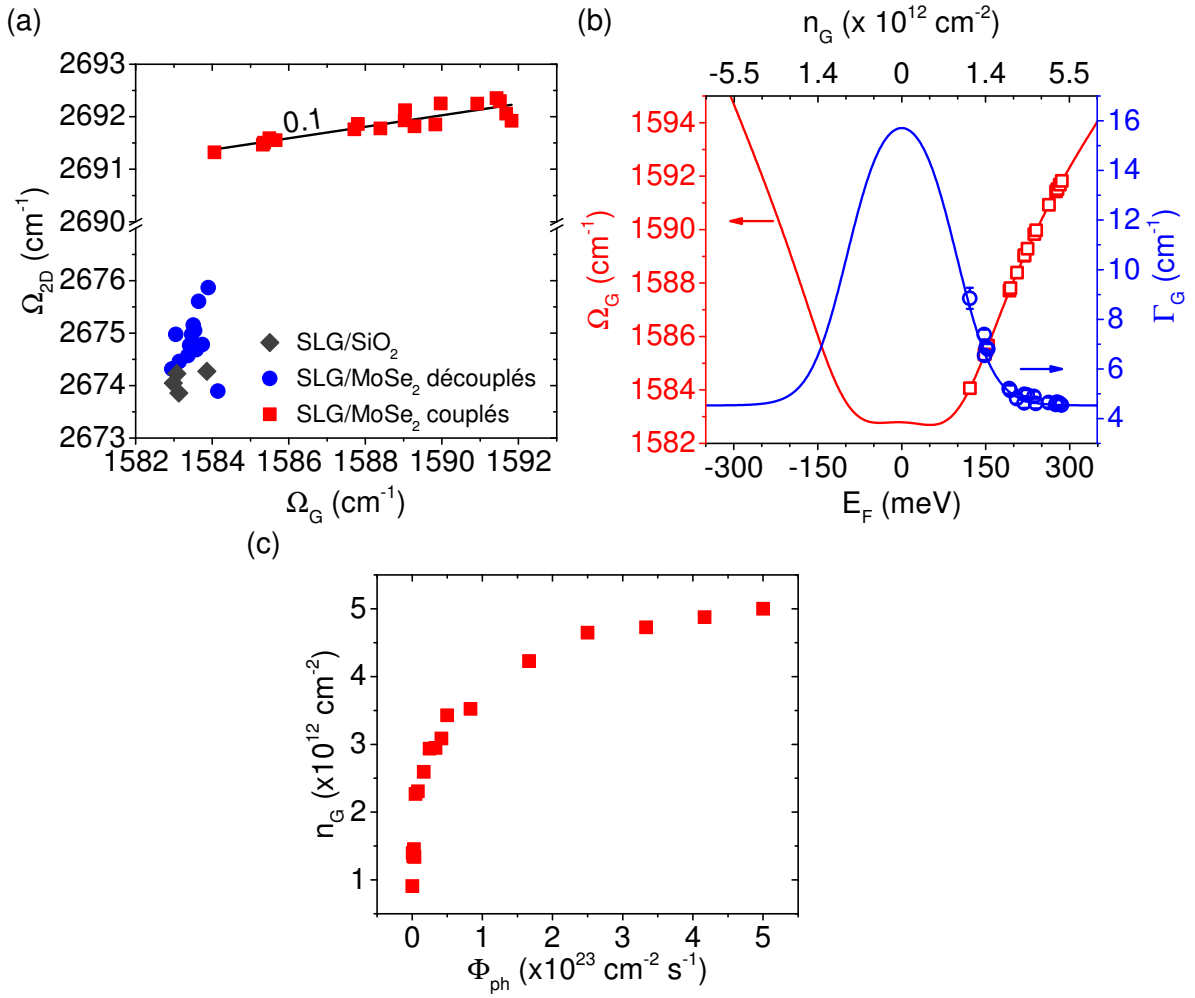

Figure 9.13 – *(a) Corrélations entre les fréquences du mode 2D et G pour différent photons. (b) Fréquence (carrés rouges, axe gauche) et largeur (cercles bleus, axe droit) du mode G pour différent photons. Les courbes rouges et bleues correspondent au modèle théorique de la première partie (voir Fig. 9.7(a)). Le niveau de dopage est extrait à partir de ces courbes. (c) Densité d'électrons dans la monocouche de graphène en fonction de flux de photons incidents Φ_{ph}.*

.

Spectres de photoluminescence de $MoSe_2$ en fonction de Φ_{ph}

De la même manière que pour le spectre Raman du graphène, j'ai ensuite étudié le spectre de photoluminescence de $MoSe_2$ en fonction du flux de photons incidents Φ_{ph}. Le spectre de PL de la monouche de $MoSe_2$ présentent deux pics [Tonndorf13] : le plus bas en énergie et plus intense correspond à l'exciton A, alors que le plus haut en énergie et le moins intense est l'exciton B. Nous nous intéresserons ici uniquement à l'exciton A. En enregistrant les spectres de PL en fonction de Φ_{ph}, puis en extrayant l'intensité intégrée de l'exciton A pour $MoSe_2$ seul, SLG/$MoSe_2$ découplés et SLG/$MoSe_2$ couplés, on obtient le graphique de la Fig. 9.14. Sur cette figure, les intensités en été normées par le produit du temps d'acquisition et de Φ_{ph}. On constate que pour $MoSe_2$ seul et pour la partie découplée de l'hétérostructure, l'intensité normée de l'exciton A décroit avec Φ_{ph}. Cette décroissance est en accord avec des annihilations exciton-exciton telles qu'observées également pour la monocouche de $MoTe_2$ (voir la deuxième partie de ce résumé). En revanche, l'intensité normée de l'exciton A est constante avec Φ_{ph}. En d'autres termes l'intensité non normée est proportionnelle à Φ_{ph}. Un tel comportement révèle **une réduction drastique de la durée de vie de l'exciton A** pour la partie couplée comparé à $MoSe_2$ seul et à la partie découplée. Cette réduction est due au fort couplage inter-couche qui offre un canal de désexcitation non radiatif supplémentaire. On remarquera que pour l'intervalle de Φ_{ph} étudié ici, l'efficacité de ce canal de désexcitation est constante.

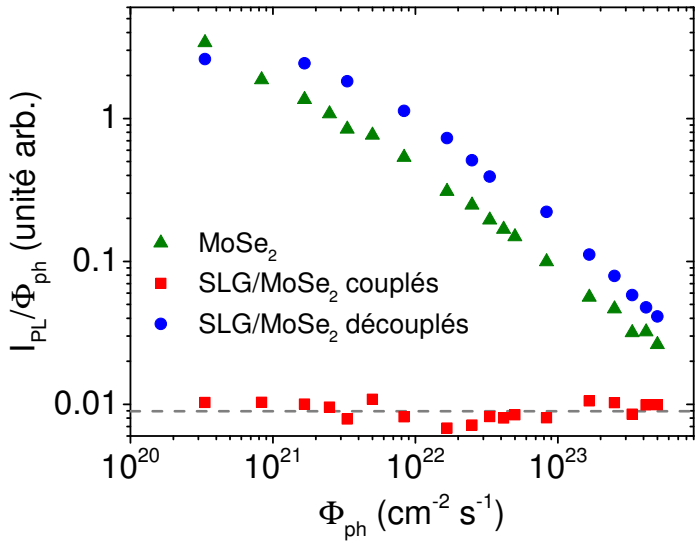

Figure 9.14 – *Intensité intégrée de l'exciton A en fonction du flux de photons incident Φ_{ph}. Les intensités ont été normées par le produit du temps d'intégration et de Φ_{ph}. La ligne horizontale en pointillés gris correspond à la moyenne des points de la partie couplée de l'hétérostructure.*

.

Comparaison des résultats Raman *versus* photoluminescence

A première vue, la réduction drastique de la durée de vie de l'exciton A (et donc de l'intensité de PL) est compatible avec un transfert de charge de $MoSe_2$ vers le graphène. Néan-

moins, l'efficacité du transfert de charge diminue lorsque Φ_{ph} augmente alors que parallèlement l'efficacité du canal de désexcitation non radiatif ne varie pas. Il y a donc un mécanisme supplémentaire au transfert de charge qui est responsable de l'inhibition de la PL. Nous suggérons que ce mécanisme corresponde à un **transfert d'énergie**. En effet, un tel transfert a déjà été étudié entre des nano-objets et un feuillet de graphène (voir par exemple [Chen10, Gaudreau13, Tisler13, Federspiel15b]) ou entre des molécules et des nanotubes de carbone (voir par exemple [Roquelet10]) avec des efficacités de transfert proche de 100 %. Plus récemment, un transfert d'énergie inter-couche, plus efficace que le transfert de charge, entre deux monocouches de DMTs dans un hétérostructure de van der Waals a été mis en évidence [Kozawa16]. Il paraît donc naturel qu'un transfert d'énergie inter-couche dans des hétérostructures de van der Waals graphène/DMT ait également lieu.

Conclusion

En conclusion, cette étude montrent qu'un fort couplage inter-couche entre les monocouches de graphène et de $MoSe_2$ conduit à une importante inhibition de la PL de $MoSe_2$ et à un transfert d'électrons photoinduit de $MoSe_2$ vers le graphène. Ces travaux démontrent également qu'il est possible de sonder localement les interactions inter-couches de manière tout optique, et même de quantifier le transfert de charge. De plus, ils mettent également en lumière la possibilité qu'il y ait, en plus du transfert de charge, un transfert d'énergie inter-couche. Cependant, il reste encore à élucider les mécanismes microscopiques associés à ces transferts et tout particulièrement comprendre le rôle joué par l'environnement qui semble fortement influencer les interactions inter-couches. Enfin, d'un point de vue plus pratique, ce travail ouvre la voie au dopage photoinduit réversible et local du graphène.

Conclusion et perspectives

En conclusion, au cours de ce projet de thèse, je me suis intéressé aussi bien aux propriétés de base des briques élémentaires d'hétérostructures de van der Waals, à savoir le graphène et les dichalcogénures de métaux de transition, qu'à leur couplage dans de telles structures. Toutes les études ont été menées à l'aide de techniques exclusivement optiques qui présentent l'avantage d'être non invasives, rapides et locales.

L'objectif de ce projet, qui consiste en la fabrication de dispositifs optoélectroniques à base de HvdWs, composés de graphène et de dichalcogénures de métaux de transition, pour étudier et contrôler électriquement les interactions inter-couche qui gouvernent la photophysique de ces structures, est quasiment atteint. Les méthodes ainsi que les outils, à la fois de fabrication et de caractérisation, sont maintenant disponibles pour réaliser la dernière étape : incorporer les hétérostructures dans les transistors développés dans la première partie avec l'espoir de pouvoir contrôler électriquement les transferts inter-couches.

Ce travail ouvre de très nombreuses perspectives de recherche, tout particulièrement parce qu'il constitue les premières études de matériaux bidimensionnels autre que le graphène, ainsi que de HvdWs dans le groupe. A court terme, de nombreuses questions concernant l'étude des hétérostructure graphène/$MoSe_2$ restent encore en suspend, principalement au sujet des mécanismes microscopiques associés aux différents transferts et à l'influence de l'environnement. Etienne Lorchat, qui reprend la suite de mon travail de thèse, réalise actuellement des expériences complémentaires pour tenter de répondre à ces questions. A plus long terme, d'autres hétérostructures à base d'autres matériaux bidimensionnels et/ou plus complexes peuvent être envisagées. Par exemple, utiliser des matériaux anisotrope, tels que le rhénium disulfure (ReS_2) ou le rhénium diséléniure ($ReSe_2$) qui ont déjà été étudié par notre groupe [Lorchat16], afin de sonder les transfert inter-couches en fonction de l'angle entre la polarisation linéaire du laser et la direction d'anisotropie du matériaux. En pratique, de telles structures permettraient notamment de créer des détecteurs sensibles à la polarisation de la lumière.

List of publications

Papers related to the work of this thesis

- H. P. C. Miranda, S. Reichardt, G. Froehlicher, A. Monlina-Sánchez, S. Berciaud and L. Wirtz, *Quantum interference effects in resonant Raman spectroscopy of single- and triple-layer $MoTe_2$ from first principles*, Nano Letters, Just Accepted Manuscript

- D. Metten, G. Froehlicher and S. Berciaud, *Monitoring Electrostatically-Induced Deflection, Strain and Doping in Suspended Graphene using Raman Spectroscopy*, 2D Materials **4**, 014004 (2017)

- G. Froehlicher, E. Lorchat, and S. Berciaud, *Direct versus indirect band gap emission and exciton-exciton annihilation in atomically thin molybdenum ditelluride ($MoTe_2$)*, Phys. Rev. B **94**, 085429 (2016)

- E. Lorchat, G. Froehlicher and S. Berciaud, *Splitting of interlayer shear modes and photon energy dependent anisotropic Raman response in N-layer $ReSe_2$ and ReS_2*, ACS Nano **10**, 2752-2760 (2016)

- G. Froehlicher, E. Lorchat, F. Fernique, C. Joshi, A. Monlina-Sánchez, L. Wirtz and S. Berciaud, *Unified Description of the Optical Phonon Modes in N-Layer $MoTe_2$*, Nano Letters **15**, 6481-6489 (2015)

- D. Metten, G. Froehlicher and S. Berciaud, *Doping- and interference-free measurement of I_{2D}/I_G in suspended monolayer graphene blisters*, pssb **252**, 2390-2394 (2015)

- G. Froehlicher, and S. Berciaud, Raman spectroscopy of electrochemically gated graphene transistors: Geometrical capacitance, electron-phonon, electron-electron, and electron-defect scattering, Phys. Rev. B **91**, 205413 (2015) - Editor's Suggestion

- F. Federspiel, G. Froehlicher, M. Nasilowski, S. Pedetti, A. Mahmood, B. Doudin, S. Park , J. Lee , D. Halley, B. Dubertret, P. Gilliot, and S. Berciaud, *Distance Dependence of the Energy Transfer Rate from a Single Semiconductor Nanostructure to Graphene*, Nano Letters **15**, 1252-1258 (2015)

Papers related to other works done during my PhD

- L. D. N. Mouafo, F. Godel, G. Froehlicher, S. Berciaud, B. Doudin, M. Venkata Kamalakar and J.-F. Dayen, *Tuning contact transport mechanisms in high on/off ratio bilayer $MoSe_2$ transistors*, 2D Materials **4**, 015037 (2017)
- F. Godel, L. D. N. Mouafo, G. Froehlicher, B. Doudin, S. Berciaud, Y. Henry, J.-F. Dayen and D. Halley, *Conductance oscillations in graphene/nanoclusters hybrid material: towards large area single electron devices*, Advanced Materials **2016**

Papers related to other works done before my PhD

- A. Hemmerle, G. Froehlicher, V. Bergeron, T. Charitat and J. Farago, Worm-like instability of a vibrated sessile drop, EPL **111**, 24003 (2015)
- B. Tavakol, M. Bozlar, C. Punckt, G. Froehlicher, H. A. Stone, I. A. Aksay and D. P. Holmes, Buckling of dielectric elastomeric plates for soft, electrically active microfluidic pumps, Soft Matter **10**, 4789-4794 (2014)
- D. P. Holmes, B. Tavakol, G. Froehlicher and H. A. Stone, Control and manipulation of microfluidic flow via elastic deformation, Soft Matter **9**, 7049-7053 (2013)

Chapter A

A brief introduction to group theory

In 1894, Pierre Curie noticed that the properties of matter are linked to its symmetries and formulated a principle that bears his name [Curie94]. In particular, vibrational properties are closely related to the molecule or crystal symmetries. The mathematical tool for studying symmetries is **group theory**. The purpose of this section is to give a brief introduction to group theory applied to molecules and crystals. No effort will be made to prove the statements, however they will be illustrated with the simple example of the water molecule. Rigorous proofs can be found in Ref. [Dresselhaus07]. This section is largely inspired from the pedestrian introduction to group theory in Ref. [Yu10] and from a lecture (in French) available on the internet [Symmo].

A.1 Symmetry operations

A.1.1 Molecular symmetry

The symmetry operations in a molecule with the Schönflies notation [Schoenflies91] are

E	identity;
C_n/C_n^{-1}	clockwise/anticlockwise rotation by $\frac{2\pi}{n}$ with $n \in \mathbb{N}$;
σ	reflection about a plane;
i	inversion;
S_n/S_n^{-1}	rotation C_n/C_n^{-1} followed by a reflection through a plane perpendicular to the rotation axis.

For simplicity, the above operations are denoted **rotations**. To distinguish between conventional rotations (C_n/C_n^{-1}) from other operations, the former are referred to as **proper rotations** and the latter to as **improper rotations**. The axis of the highest order proper rotation (i.e., highest n) is called the principal axis. Usually, σ_h denotes the reflection about a horizontal plane perpendicular to the principal axis and σ_v or σ_d a reflection about a vertical plane including the principal axis. Note that it is possible (e.g., for linear molecules) to find an infinity

of rotations along the axis of the bond(s). In that case the symmetry operation is written C_∞.

As an illustration, we will consider the molecule of water H_2O. The structure of the molecule is shown in Fig. A.1. The symmetry operations of this molecule are (see Fig. A.1)

- E identity;
- C_2 rotation by π along the z axis;
- σ_1 reflection about the yz plane;
- σ_2 reflection about the xz plane.

E and σ_1 leave the atoms of the molecules unchanged, while C_2 and σ_2 switch the two hydrogen atoms.

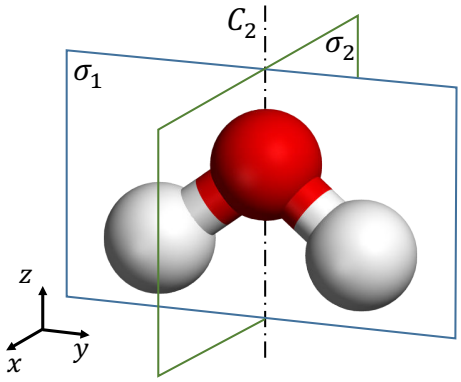

Figure A.1 *– Symmetry operations of a water molecule H_2O. The red sphere represents the oxygen atom and the two white spheres hydrogen atoms. The axis of the C_2 is illustrated as a black dashed line. The reflection plane of σ_1 and σ_2 are shown as a blue and green delimited plane, respectively.*

A.1.2 Crystal symmetry

A crystal is built up by the repetitive translation of a unit cell. The repeating unit cells are located at the points that form a lattice. Therefore, the symmetries of a crystal result from the one of the lattice and from the unit cell. The symmetry operations of a crystal are the translation of a lattice vector, the proper and improper rotations and the combination of a rotation and a translation of a fractional lattice vector. Such operations are called screw axis and glide plane. The former corresponds to a rotation C_n/C_n^{-1} plus a translation along the same axis. The latter is a reflection σ plus a translation parallel to the plane of reflection.

A.2 Symmetry group

The symmetry operations of a molecule or a crystal form a group in the mathematical sense. In the case of a molecule, this group is called **point group** because all the operations in the group leave at least one point fixed and unchanged in space. In the case of a crystal, it is called **space group**. Note that for both, we will use the Schönflies notation [Schoenflies91]

since it is the most common notation used in spectroscopy.[1]

A.2.1 Point group

Let us take again the example of the water molecule. The water molecule belongs to the C_{2v} group which has four elements presented in Fig. A.1. Since the product of two elements from the group belongs also to the group, one can create a multiplication table of dimension 4×4. The multiplication table of the C_{2v} group is displayed in Tab. A.1.

	$\boldsymbol{E}$	$\boldsymbol{C_2}$	$\boldsymbol{\sigma_1}$	$\boldsymbol{\sigma_2}$
$\boldsymbol{E}$	E	C_2	σ_1	σ_2
$\boldsymbol{C_2}$	C_2	E	σ_2	σ_1
$\boldsymbol{\sigma_1}$	σ_1	σ_2	E	C_2
$\boldsymbol{\sigma_2}$	σ_2	σ_1	C_2	E

Table A.1 *– Multiplication table of the C_{2v} group.*

A.2.2 Space group

The space group of a crystal is formed by translation symmetry operations, rotations (proper or improper) operations, and screw-axis and glide-plane operations. If there is no screw-axis or glide-plane operation, the space group is said to be **symmorphic** otherwise (i.e., there is at least one screw axis or one glide plane) it is said to be **non-symmorphic**.

The translational symmetry operations are obtained by analyzing the symmetries of the lattice. These operations form a subgroup of the space group, called the Bravais lattice. In three dimensions, there are 14 Bravais lattices. The rotations, screw-axis and glide-plane operations are determined by studying the symmetries of the unit cell. In the case of a symmorphic space group, these operations (i.e., the rotations) form a subgroup of the space group, but not in the case of a non-symmorphic space group because of screw axis or glide plane. However, one can define the **factor group** of the space group with respect to the subgroup of translation operations. Such factor group has several important properties. First, it contains all symmetry operations that occur in the unit cell of both symmorphic and non-symmorphic space group. Second, it is isomorphic to a point group which is made of the rotational part of all symmetry operations (including possibly screw axis and glide plane) of the space group. This isomorphism makes point group analysis directly applicable to factor group. Therefore, the factor group is usually referred as simply the point group of the crystal.

To sum up, the space groups are described by a Bravais lattice plus a point group. Note that the point group is a subgroup of the space group only in the case of symmorphic space

[1] The standard notation, adopted by the *International Tables For Crystallography*, is the Hermann–Mauguin notation. This notation is more accurate for space groups.

groups. Hence, special care must be taken when analyzing the symmetries of the unit cell to determine the point group of the crystal (one has always to keep in mind that the crystal is infinite and that screw axis and glide plane are possible). Not all molecular point groups are compatible with crytals. In three dimensions, there are only 32 compatible point groups because the space filling condition can only be met for $n = 1, 2, 3, 4, 6$ in C_n/C_n^{-1} and S_n/S_n^{-1} operations. These groups are called **crystallographic point groups**.[2] The combination of 14 Bravais lattices and 32 crystallographic point groups gives rise to 230 space groups among which 73 are symmorphic and 153 non-symmorphic. In spectroscopy, only the symmetries of the unit cell matter.[3] As a result, the determination of the crystallographic point group is sufficient.

A.3 Representations and character tables

A.3.1 Definition of a representation

A convenient way to study symmetry groups is to use **representations**. A representation of a group G (often denoted by Γ) is another group G' (with its own group law) which elements can be substituted to the one of group G without changing the multiplication table. The dimension of G' can be equal or smaller than the dimension of G.

Let us consider again the water molecule. The symmetry operations of the water molecule can be represented by square 3×3 matrices in the three dimensional Euclidean space. This set of matrices forms a representation Γ of the C_{2v} point group. The dimension of this representation is 3 because matrices are 3×3. Of course, these matrices depend on the choice of a basis. With the basis sketched in Fig. A.1, the four matrices representing the four symmetry operation are diagonal

$$\Gamma(E) = \begin{pmatrix} 1 & 0 & 0 \\ 0 & 1 & 0 \\ 0 & 0 & 1 \end{pmatrix}, \quad \Gamma(C_2) = \begin{pmatrix} -1 & 0 & 0 \\ 0 & -1 & 0 \\ 0 & 0 & 1 \end{pmatrix}, \quad \Gamma(\sigma_1) = \begin{pmatrix} -1 & 0 & 0 \\ 0 & 1 & 0 \\ 0 & 0 & 1 \end{pmatrix}, \quad \Gamma(\sigma_2) = \begin{pmatrix} 1 & 0 & 0 \\ 0 & -1 & 0 \\ 0 & 0 & 1 \end{pmatrix}. \tag{A.1}$$

One can easily verify that these four matrices have the same multiplication table as the one in Tab. A.1. As they are diagonal, the product of two of these matrices consists simply in multiplying corresponding diagonal elements together. Consequently, the four square matrices 1×1 made of the elements in position $(1,1)$ in the four matrices in Eq. (A.1) is another representation. Similarly, the matrices built up with the elements in position $(2,2)$ and $(3,3)$ are two others representations. These three representations are of dimension 1 and are labeled Γ_1, Γ_2 and Γ_3 respectively. In addition, there is a fourth one dimensional representation

[2] The crystallographic point groups are O_h, O, T_h, T_d, T, D_{4h}, D_4, D_{2d}, C_{4h}, C_{4v}, C_4, S_4, D_{2h}, D_2, C_{2v}, C_{2h}, C_s, C_2, C_i, C_1, D_{6h}, D_6, D_{3h}, C_{6v}, C_{6h}, C_6, C_{3h}, D_{3d}, D_3, S_6, C_{3v}, C_3.

[3] This comes from the fact that the Bravais lattice gives rise to the reciprocal lattice. Thus all the physics is given by the wavevector in the reciprocal space and the symmetries in the unit cell. See the application to phonons in Section A.4.

Γ_4 which cannot be deduced from geometry arguments in the three dimensional Euclidean space. These four one-dimensional representations are

	E	C_2	σ_1	σ_2
Γ_1	(1)	(-1)	(-1)	(1)
Γ_2	(1)	(-1)	(1)	(-1)
Γ_3	(1)	(1)	(1)	(1)
Γ_4	(1)	(1)	(-1)	(-1)

One can easily verify that Γ_4 is also compatible with the multiplication table A.1. These four representations of dimension 1 are said to be **irreducible**. They are also said to be inequivalent, since no change of basis on the set of matrices of one representation can generate the set of matrices of another one. We will see later that there are not more than four inequivalent irreducible representations for the C_{2v} group. In contrast, representations of dimension 3, like Γ, are **reducible** because they can be decomposed into irreducible representations. Note that irreducible representations are not necessary of dimension 1 but have the smallest possible dimension.

To decompose Γ into irreducible representations, we first recall the definition of the direct sum of two matrices. For any arbitrary matrices A (of size $m \times n$) and B (of size $p \times q$), the direct sum of A and B, denoted by $A \oplus B$, is a block diagonal matrix (of size $(m+p) \times (n+p)$) defined as

$$A \oplus B = \begin{pmatrix} (A) & 0 \\ 0 & (B) \end{pmatrix}. \tag{A.2}$$

With this definition, we readily deduce that

$$\Gamma = \Gamma_1 \oplus \Gamma_2 \oplus \Gamma_3. \tag{A.3}$$

In other words, by an appropriate choice of basis the matrices of a representation can be all written as diagonal block matrices. These block matrices being the matrices of an irreducible representation.

A.3.2 Character and character tables

As already pointed out, the choice of matrices to form a representation (either reducible or irreducible) is not unique. Indeed, on can make a change of basis and obtain a different set of matrices that is also a representation. These two sets are said to be equivalent. However, the trace of a matrix is independent of the choice of basis, thus it suggests that the set of equivalent representations can be specified uniquely by their traces. These traces are called **characters** and are usually denoted by χ. Obviously, the representation contains more information than their characters. However, the determination of the irreducible representations of a given group and of their characters is sufficient for many applications.

For a given symmetry group, because of the uniqueness of the characters of each irre-

ducible representation, the characters can be tabulated in what is called a **character table**. The character table of the C_{2v} group is presented in Tab. A.2. The top row labels the symmetry operations, the left-hand column lists the irreducible representations and the intersections give the characters χ of the operations for the different irreducible representations. In the case the C_{2v} group, all the irreducible representations are of dimension 1 so that the characters are equal to the unique element of the 1×1 matrices determined above. These characters are equal to +1 or −1 depending on whether the object is symmetric or antisymmetric, respectively, under the symmetry operation. The right-hand side column provides the **basis functions**. These functions are usually expressed in terms of space coordinates (x, y, z) and can be used to generate the corresponding representation by applying the symmetry operations on them. From the construction of the irreducible representations Γ_1, Γ_2 and Γ_3, it is obvious that these representations are generated by the basis functions x, y and z, respectively. Clearly, the choice of basis functions is not unique an this is why another set of basis functions is given in the character table A.2. Sometimes, the basis functions are expressed in terms of the angular momentum component R_x, R_y and R_z around the x, y and z axis, respectively. These components transform as pseudovectors. However, these basis functions are only relevant for molecules and will not be displayed for crystals.

	E	C_2	σ_1	σ_2	Basis functions
Γ_1	1	−1	−1	1	x; xz
Γ_2	1	−1	1	−1	y; yz
Γ_3	1	1	1	1	z; x^2; y^2; z^2
Γ_4	1	1	−1	−1	xy

Table A.2 *– Character table of the C_{2v} group. Different basis functions are separated by a semicolon.*

Let us take another example of character table. The ammonia molecule NH_3 has 6 symmetry operations: the identity E, clockwise and anticlockwise rotation C_3 and C_3^{-1}, and reflections σ_1, σ_2 and σ_3 about vertical planes. The symmetry group is C_{3v} and the corresponding character table is displayed in Tab. A.3.

	E	$2C_3$	$3\sigma_v$	Basis functions
Γ_1	1	1	1	z; x^2+y^2; z^2
Γ_2	1	1	−1	
Γ_3	2	−1	0	(x, y); (x^2-y^2, xy); (xz, yz)

Table A.3 *– Character table of the C_{3v} group. Different basis functions are separated by a semicolon.*

First, we notice that the character table A.3 has only 3 columns while there are 6 symmetry operations. The two C_3 rotations and the three vertical reflections were grouped together into **classes** in the mathematical sense. Elements in a class have the same character, therefore they can be grouped in the character table. In practice, rotations (either clockwise or anticlockwise) by the same angle around equivalent axis belong to the same class and reflections about equivalent planes also belong to the same class. The number written before the symme-

try operation corresponds to the number of elements in the class. Note that in the C_{2v} group, there are four classes of one element. Second, we observe that there are three inequivalent irreducible representations. In fact, **the number of inequivalent irreducible representations of a group is equal to the number of classes**. Third, the Γ_3 representation has characters different from ±1. This is due to the fact that the dimension of the representation is 2. Indeed, the identity operation E can always be represented by the identity matrix whose trace is equal to the dimension of the representation. So, the character of the identity $\chi(E)$ is always equal to the dimension of the representation. Since, the dimension is 2, the basis functions have two terms written in brackets. Furthermore, note that for a given representation, if the character of a symmetry operation is different from ±1, it is not possible to deduce the symmetric or antisymmetric nature of the operation. Finally, there is no basis function specified for the Γ_2 representation because it is not relevant. In general, only the most interesting basis functions are specified as we will see later.

Character tables are very useful to decompose a representation into irreducible representations. It can also be used to determine the direct product of irreducible representations. Nevertheless, these products are tabulated in product tables on the internet (e.g., [Moleca] or [Molecb]).

A.3.3 Setting up a character table

Setting up a character table is often not necessary since they can be found in books (e.g. [Dresselhaus07]), articles or on the internet (e.g., [Moleca] or [Molecb]). However, if one needs to build up a character table it is not necessary to find all the matrices of the irreducible representations, as we did for C_{2v} group. In most cases, to set up the character table, one can use the following two orthogonality relations [Dresselhaus07]

$$\sum_k \chi_i(C_k)^* \chi_j(C_k) N_k = h\delta_{ij}, \tag{A.4}$$

$$\sum_i \chi_i(C_k)^* \chi_i(C_l) = \frac{h}{N_l}\delta_{kl}, \tag{A.5}$$

where * denotes the complex conjugate, h is the order of the group (i.e., the number of elements in the group, here the number of symmetries), N_k is the number of elements of class C_k, $\chi_i(C_k)$ is the character of class C_k in the Γ_i irreducible representation and δ_{ij} is the Kronecker delta. Note that $\sum_k N_k = h$. Equation (A.4) can be viewed as a orthogonality relation on the rows of the character table and Eq. (A.5) on the columns. One can easily check that these two relations are verified for the characters tables A.1 and A.3. As mentioned earlier, the character of the identity $\chi(E)$ is always equal to the dimension of the representation, i.e. to a positive integer. Applying Eq. (A.5) to the identity, we obtain

$$\sum_i \chi_i(E)^2 = h. \tag{A.6}$$

In general, this equation is easy to solve. Note that the trivial identity representation, whose characters are all unity, is always an irreducible representation of a symmetry group. Without any effort, one row of the character table is determined. In general, this row is written first in the table. With all these ingredients, most of the character tables can be set up.

A.3.4 Notation for the irreducible representations

Up to now, we have labeled the irreducible representations following an arbitrary notation (Γ_1, Γ_2, ...) that does not give any information on the representation itself. To give information on the symmetry of the irreducible representations, we will use the Mulliken notation [Mulliken55, Mulliken56], which is mostly used in spectroscopy. The meaning of the symbols is presented in Tab. A.4. Note that the subscript 1 or 2 does not always have a specific meaning, especially for representation of dimension higher than one. Even for one-dimensional representation, in some groups, such as D_{2h}, a subscript 3 is used. In that case, these numbers are just used to distinguish different representations.

Symbols	symmetry property	with respect to	comments
A/B	sym/antisym	principal axis C_n	one-dimensional representations
subscript 1/2	sym/antisym	C_2 perpendicular to principal axis C_n or vertical plane σ_v or σ_d	
subscript u/g	sym/antisym	inversion center i	from German 'gerade'/'ungerade'
$'/''$	sym/antisym	horizontal plane σ_h	
E	two-dimensional representations		from German 'entartet' (degenerate)
T	three-dimensional representations		F is also used in spectroscopy

Table A.4 *– Mulliken notation. Sym (antisym) means symmetric (antisymmetric).*

Using this notation, the irreducible representations of the water molecule (see Tab. A.2) are labeled $\Gamma_1 = B_2$, $\Gamma_2 = B_1$, $\Gamma_3 = A_1$, and $\Gamma_4 = A_2$. σ_1 was chosen as the vertical plane for the subscript 1/2.

A.4 Application to phonons in crystals

In this subsection, we will apply group theory to vibrations (phonons) in crystals. Lattice vibrations are characterized by their displacement vectors in real space and by their wavevectors $\boldsymbol{q}$ in reciprocal space. Hence, symmetry operations on both vectors need to be taken into account in order to determine the symmetry of a phonon. The set of space group operations

which transform $\boldsymbol{q}$ into itself (possibly plus a reciprocal lattice vector) forms the group of the wavevector. Obviously, this group is a subgroup of the space group. The symmetry of the vibration is then given by the symmetries of the displacement vectors in the unit cell for the group of the wavevector. Clearly, the group of the wavevector for the Γ point (i.e., $\boldsymbol{q} = 0$) is always the same as the space group of the crystals. Physically, $\boldsymbol{q} \approx 0$ means a long wavelength vibration and therefore nearly uniform displacements of identical atoms in the different unit cells. In the following, we will mostly study phonons at the Γ-point, so that we only have to analyze the symmetry of displacement vectors in the unit cell for the crystal point group. However, in the case of graphene, we will also consider the irreducible representation of the phonons at the edges of the Brillouin zone. The approach is identical except that the crystal point group is replaced by the group of the wavevector.

To find the normal modes at the Γ-point, we need to find the representation of the total vibration Γ^{vib}. In general, this representation is reducible and can be decomposed into irreducible representations. Each irreducible representation corresponds to a normal mode and give its symmetry properties and degeneracy (dimensionality of the representation). If the same irreducible representation appears many times in the decomposition, it means that there are multiple modes with the same symmetry but with different energy (or frequency).

The representation of the total vibration Γ^{vib} and its irreducible decomposition can be obtained using the following relation [Dresselhaus07]

$$\Gamma^{\text{vib}} = \Gamma^{\text{eq}} \otimes \Gamma^{\text{vec}}, \tag{A.7}$$

where Γ^{vec} is the representation of a vector (x, y, z) and Γ^{eq} is the equivalence representation. This latter representation describes the invariance of the atoms under the symmetry operations of the group. We will not prove this relation but we can understand it. A vibration involves the symmetry of a vector (Γ^{vec}) but only the vectors of atoms which are invariant under the symmetry operations (Γ^{eq}) contribute to the character (otherwise it corresponds to non-diagonal terms which do not contribute in the trace).

Γ^{vec} is obtained by summing the irreducible representations to which the x, y, and z basis functions belongs. In the case of two- or three-dimensional representations, pairs such as (x, y), are counted only once. Γ^{eq} is determined by finding the characters and then by reducing it into irreducible representations. For Γ-point phonons, these characters are equal to the number of atoms in the unit cell that are invariant, modulo a lattice vector, under the symmetry operations of the group. Note that the character of product operations in non-symmorphic groups is always equal to 0.

To illustrate this procedure, we use the example of the water molecule. Note that we will not determine the normal modes of the water molecule[4] but instead treat it as it were a hypothetical unit cell of a crystal with point group C_{2v}. From the character table, x, y and z

[4] To determine the normal modes of a molecule, one needs to subtract the representations for the simple translations Γ^{trans} and rotations Γ^{rot} of the molecule about its center of mass in Eq. (A.7).

transform as B_2, B_1 and A_1, respectively. Thus

$$\Gamma^{\text{vec}} = A_1 \oplus B_1 \oplus B_2. \tag{A.8}$$

Next, we have to the study the transformation of the three atoms under the symmetry operations to deduce the equivalence representation. As explained previously, we apply the four symmetry operations on the molecule, and each site that is invariant under an operation add a contribution +1 to the character of that operation. We obtain the character table A.5 for Γ^{eq}.

	E	C_2	σ_1	σ_2
Γ^{eq}	3	1	3	1
	all	O	all	O

Table A.5 *– Characters for Γ^{eq} for the water molecule within the C_{2v} group. The atoms that remain unchanged under each symmetry operation are indicated.*

We need to reduce Γ^{eq} because it does not correspond to any of the irreducible representations of C_{2v}. To do it, we can use the following systematic procedure using the character table A.2. Let us assume that the reducible representation Γ^{r} is decomposed into irreducible representations Γ_i^{ir}

$$\Gamma^{\text{r}} = \bigoplus_i n_i \Gamma_i^{\text{ir}}, \tag{A.9}$$

where $n_i \in \mathbb{N}$. Therefore, the characters of Γ^{r} and Γ_i^{ir} for a given class C_k are linked by $\chi^{\text{r}}(C_k) = \sum_i n_i \chi_i^{\text{ir}}(C_k)$. By multiplying by the complex conjugate $\chi_i^{\text{ir}*}(C_k)$, summming on k and using the orthogonality relation (A.4), we deduce that

$$n_i = \frac{1}{h} \sum_k N_k \chi^{\text{r}}(C_k) \chi_i^{\text{ir}*}(C_k). \tag{A.10}$$

Applying this relation to Γ^{eq}, we have

$$\begin{aligned}
n_{A_1} &= \frac{1}{4}[3\times 1 + 1\times 1 + 3\times 1 + 1\times 1] = 2;\\
n_{A_2} &= \frac{1}{4}[3\times 1 + 1\times 1 + 3\times (-1) + 1\times (-1)] = 0;\\
n_{B_1} &= \frac{1}{4}[3\times 1 + 1\times (-1) + 3\times 1 + 1\times (-1)] = 1;\\
n_{B_2} &= \frac{1}{4}[3\times 1 + 1\times (-1) + 3\times (-1) + 1\times 1] = 0.
\end{aligned}$$

Thus,

$$\Gamma^{\text{eq}} = 2A_1 \oplus B_1. \tag{A.11}$$

Finally, we have to calculate the direct product of Eq. (A.7). We can use the character table A.2 and multiply the rows and then decompose into irreducible representation following the procedure described just below. Or, more easily, we can use the tabulated product tables

for the different point groups (e.g., [Moleca] or [Molecb]). We conclude that

$$\Gamma^{\text{vib}} = (2A_1 \oplus B_1) \otimes (A_1 \oplus B_1 \oplus B_2) = 3A_1 \oplus A_2 \oplus 3B_1 \oplus 2B_2. \tag{A.12}$$

So, there are three normal modes (with different frequencies) with A_1 symmetry (i.e., completely symmetric), one with A_2, three with B_1 and two with B_2. In total, there are nine modes which agree with three atoms in the unit cell. The atomic displacements associated with these modes are the same as the ones of the monolayer SCTMDs depicted in Fig. 6.1. Again, we recall that these modes are not the normal modes of the water molecule since one needs to subtract the translational and rotational degrees of freedom.

A.5 Character tables

This section presents the character table of D_{6h}, D_{3h} and D_{3d} point groups [Moleca, Molecb].

	E	$2C_6$	$2C_3$	C_2	$3C_2'$	$3C_2''$	i	$2S_3$	$2S_6$	σ_h	$3\sigma_d$	$3\sigma_v$	Basis functions
A_{1g}	1	1	1	1	1	1	1	1	1	1	1	1	x^2+y^2, z^2
A_{2g}	1	1	1	1	−1	−1	1	1	1	1	−1	−1	
B_{1g}	1	−1	1	−1	1	−1	1	−1	1	−1	1	−1	
B_{2g}	1	−1	1	−1	−1	1	1	−1	1	−1	−1	1	
E_{1g}	2	1	−1	−2	0	0	2	1	−1	−2	0	0	(yz, zx)
E_{2g}	2	−1	−1	2	0	0	2	−1	−1	2	0	0	(x^2-y^2, xy)
A_{1u}	1	1	1	1	1	1	−1	−1	−1	−1	−1	−1	
A_{2u}	1	1	1	1	−1	−1	−1	−1	−1	−1	1	1	z
B_{1u}	1	−1	1	−1	1	−1	−1	1	−1	1	−1	1	
B_{2u}	1	−1	1	−1	−1	1	−1	1	−1	1	1	−1	
E_{1u}	2	1	−1	−2	0	0	−2	−1	1	2	0	0	(x, y)
E_{2u}	2	−1	−1	2	0	0	−2	1	1	−2	0	0	

Table A.6 – *Character table of the D_{6h} group with relevant basis functions.*

	E	σ_h	$2C_3$	$2S_3$	$3C_2$	$3\sigma_v$	Basis functions
A_1'	1	1	1	1	1	1	x^2+y^2, z^2
A_2'	1	1	1	1	−1	−1	
E'	2	2	−1	−1	0	0	$(x, y), (x^2-y^2, xy)$
A_1''	1	−1	1	−1	1	−1	
A_2''	1	−1	1	−1	−1	1	z
E''	2	−2	−1	1	0	0	$(x, y), (xz, yz)$

Table A.7 – *Character table of the D_{3h} group with relevant basis functions.*

	E	$2C_3$	$3C_2$	i	$2S_6$	$3\sigma_d$	Basis functions
A_{1g}	1	1	1	1	1	1	x^2+y^2, z^2
A_{2g}	1	1	−1	1	1	−1	
E_g	2	−1	0	2	−1	0	(x^2-y^2, xy) , (yz, zx)
A_{1u}	1	1	1	−1	−1	−1	
A_{2u}	1	1	−1	−1	−1	1	z
E_u	2	−1	0	−2	1	0	(x, y)

Table A.8 – *Character table of the D_{3d} group with relevant basis functions.*

Chapter B

Measurement of the laser spot area

In this appendix, we show an example of how to measure the laser spot area A_L. It is measured by recording an optical image of the tightly focused laser spot on the surface of a substrate. The camera is calibrated with a optical image of a sample with a known distance. The intensity of the pixels are proportional to the intensity of the laser beam.[1] Assuming a Gaussian beam, we fit the intensity of the image with a two-dimensional Gaussian function

$$f(x,y) = A\exp\left(-\frac{(x-x_o)^2+(y-y_o)^2}{2\sigma^2}\right), \tag{B.1}$$

where A is the amplitude of the Gaussian, (x_0, y_0) are the coordinates of the center and σ is the standard deviation (we assumed that the standard deviation is the same for the two dimensions). For an excitation laser at 2.33 eV and a ×100 NA=0.90 objective, we obtained the results in Fig. B.1 and a standard deviation of $\sigma = 138$ nm. The surface spot area is given by $2\pi\sigma^2$. Table B.1 summarizes the spot sizes and area used in this thesis.

	σ (nm)	A (μm^2)
×100 NA = 0.90	138	0.12
×50 NA = 0.65	253	0.40
×40 NA = 0.60	310	0.60

Table B.1 *– Measured spot size (σ standard deviation), and calculated area for the cw laser at 2.33 eV.*

[1] Only for a sufficiently low intensity.

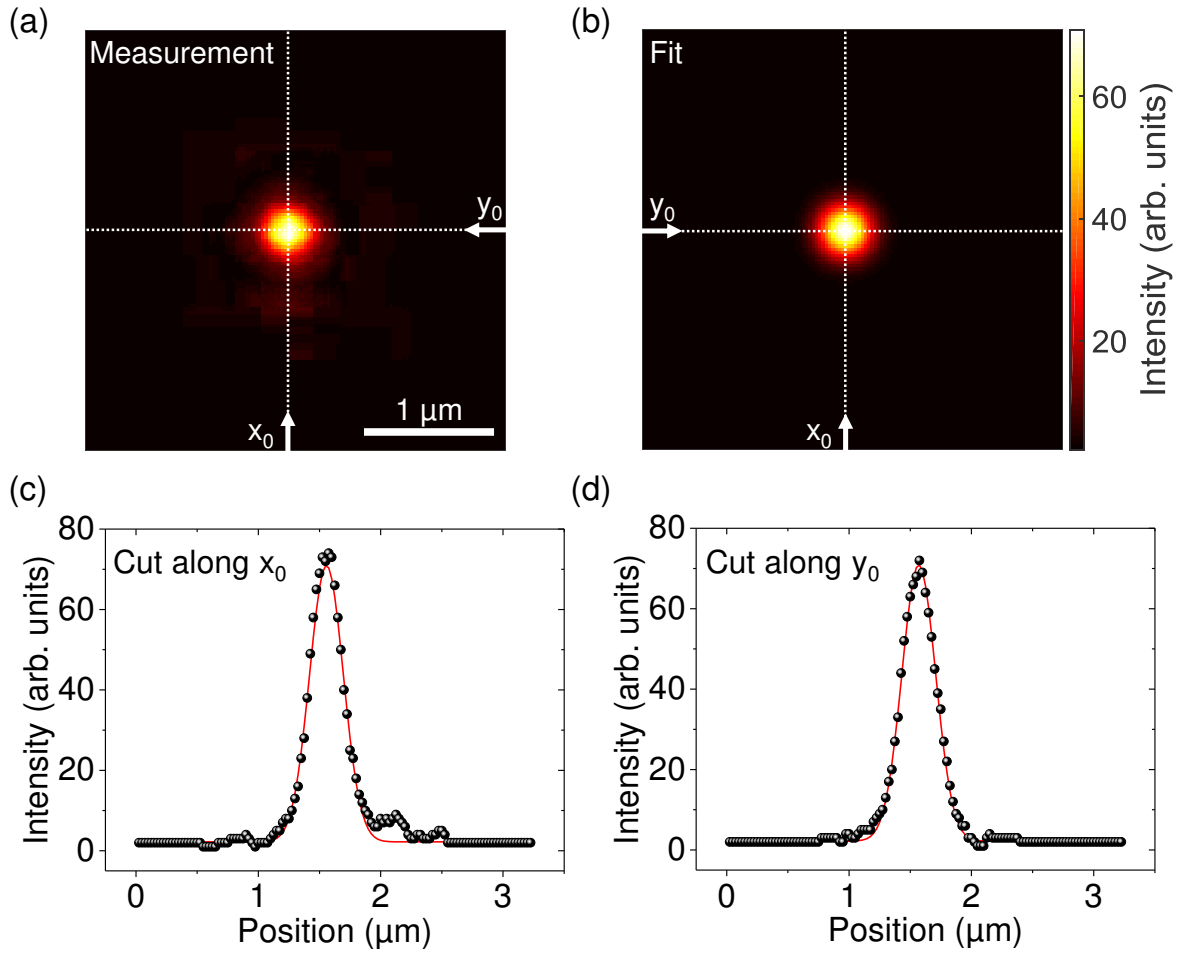

Figure B.1 *– (a) Optical image of the focused laser spot on the surface of a substrate. (b) Two-dimensional fit of the optical image. Cuts along (c) x_0 and (d) y_0. The solid lines are the fit to the experimental data (symbols).*

Chapter C

Optical interference effects

In this appendix, we will calculate the enhancement factor F defined in Chapter 4 Section 4.3. We will restrict the calculation to the case of normal incident light. This simplification is valid because, even if the NA of the objective lens is large, the majority of light is close to normal incidence provided that the laser beam is Gaussian and the focused beam hits the sample surface at the beam waist [Yoon09, Li12b]. The full calculation can be found in Ref. [Yoon09]. It only shows slight differences, that can be neglected here providing we are using objective lens with NA=0.6 or NA=0.65.

The calculations are performed as follows: first we calculate the effective reflection and transmission coefficients of one layer in two semi-infinite media, second we use this result to recursively obtain the equivalent coefficients for a multilayered structure, third we compute the absorptance of one layer in a multilayered system, and finally we calculate the enhancement factor for the PL or Raman intensity.

C.1 Equivalent coefficients

C.1.1 One layer interference

Let us suppose that one layer of medium (1) with complex refractive index n_1 is encapsulated in two semi-infinite media (0) and (2) with complex refractive indexes n_0 and n_2, respectively (see Fig.C.1(a)). Such geometry is similar to a Fabry-Pérot interferometer. The purpose of this subsection is to calculate the equivalent reflection ρ and transmission τ coefficients such that the problem is equivalent to Fig. C.1(b) where there is only one interface separating medium (2) and (0).

We first assume that a monochromatic light is coming from the top (medium (2)) and propagates along the z-axis, and that no light is coming from the bottom (medium (0)). In addition, the light is linearly polarized along the x-axis. Thus, the expression of the electric field is $E_0(z,t) = E\exp\left(-\mathrm{i}\left(\omega t - \frac{2\pi n}{\lambda}z\right)\right)$, where E is the amplitude of the field, ω and λ are the

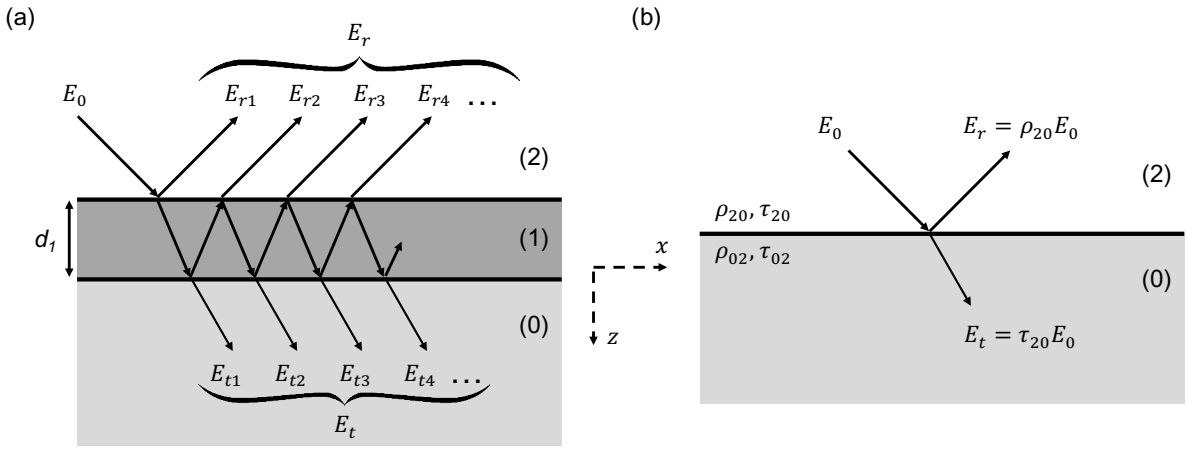

Figure C.1 – *(a) Multiple-beam interference from a one layer of medium (1) and thickness d_1 encapsulated in semi-infinite media (0) and (2). E_0 is the incident electric field and E_r (E_t) is the total reflected (transmitted) electric field. (b) Equivalent representation of the problem where medium (1) is represented as an interface separating media (2) and (0) with reflection ρ and transmission τ coefficients. Note that the beams are drawn with an angle for better illustration but the calculations are done for normal incidence.*

pulsation and wavelength of the light in vacuum, respectively, and n is the (complex) refractive index of the medium. For the sake of readability, in the following we will omit the (z,t) dependence of electric fields. To determine the equivalent reflection and transmission coefficients, we have to compute the total reflected E_r and transmitted E_t electric fields. The total reflected and transmitted electric fields are equal to the sum all the reflected and transmitted fields, respectively. Thus using the notation in Fig. C.1(a), we have

$$E_r = \sum_{q=0}^{+\infty} E_{rq} \quad \text{and} \quad E_t = \sum_{q=0}^{+\infty} E_{tq}. \tag{C.1}$$

The Fresnel reflection and transmission coefficients at $(i)/(j)$ interface for a normal incident beam that propagates from medium (i) to (j) are respectively [Hecht01]

$$r_{ij} = \frac{n_i - n_j}{n_i + n_j} \quad \text{and} \quad t_{ij} = \frac{2n_i}{n_i + n_j}. \tag{C.2}$$

It is obvious that $r_{ji} = -r_{ij}$ and easy to verify that $t_{ij}t_{ji} - r_{ij}r_{ji} = 1$. These expressions are the consequence of the optical reversibility principle at the $(i)/(j)$ interface [Hecht01]. Providing these coefficients, we deduce

$$\begin{aligned}
E_{r1} &= r_{21}E_0, \\
E_{r2} &= t_{21}\mathrm{e}^{\mathrm{i}\beta_1}r_{10}\mathrm{e}^{\mathrm{i}\beta_1}t_{12}E_0 = t_{21}r_{10}t_{12}\mathrm{e}^{\mathrm{i}2\beta_1}E_0, \\
E_{r3} &= t_{21}\mathrm{e}^{\mathrm{i}\beta_1}r_{10}\mathrm{e}^{\mathrm{i}\beta_1}r_{12}\mathrm{e}^{\mathrm{i}\beta_1}r_{10}\mathrm{e}^{\mathrm{i}\beta_1}t_{12}E_0 = E_{r2}(r_{12}r_{10}\mathrm{e}^{\mathrm{i}2\beta_1}), \\
&\vdots \\
E_{rq} &= E_{r2}(r_{12}r_{10}\mathrm{e}^{\mathrm{i}2\beta_1})^{q-2},
\end{aligned}$$

where $q \geq 2$ and $\beta_1 = \frac{2\pi n_1 d_1}{\lambda}$ is the phase difference due to the propagation in medium (1). Since $|n_0|, |n_1|, |n_2| \geq 1$, $\left|r_{12} r_{10} \mathrm{e}^{\mathrm{i}2\beta_1}\right| < 1$ and the total reflected electric field is

$$E_r = r_{21} E_0 + t_{21} r_{10} t_{12} \mathrm{e}^{\mathrm{i}2\beta_1} E_0 \sum_{q=0}^{+\infty} (r_{12} r_{10} \mathrm{e}^{\mathrm{i}2\beta_1})^q = r_{21} E_0 + \frac{t_{21} r_{10} t_{12} \mathrm{e}^{\mathrm{i}2\beta_1}}{1 - r_{12} r_{10} \mathrm{e}^{\mathrm{i}2\beta_1}} E_0 \tag{C.3}$$

By applying the relationships $r_{12} = -r_{21}$ and $t_{12} t_{21} - r_{12} r_{21} = 1$, the equivalent reflection coefficient is

$$\rho_{20} = \frac{E_r}{E_0} = \frac{r_{21} + r_{10} \mathrm{e}^{\mathrm{i}2\beta_1}}{1 + r_{10} r_{21} \mathrm{e}^{\mathrm{i}2\beta_1}}. \tag{C.4}$$

Similarly for the transmitted electric field, we have

$$E_t = \sum_{q=0}^{+\infty} t_{21} \mathrm{e}^{\mathrm{i}\beta_1} t_{10} E_0 (r_{10} r_{12} \mathrm{e}^{\mathrm{i}2\beta_1})^q = \frac{t_{21} t_{10} \mathrm{e}^{\mathrm{i}\beta_1}}{1 + r_{10} r_{21} \mathrm{e}^{\mathrm{i}2\beta_1}} E_0 \quad \text{and} \quad \tau_{20} = \frac{E_t}{E_0} = \frac{t_{21} t_{10} \mathrm{e}^{\mathrm{i}\beta_1}}{1 + r_{10} r_{21} \mathrm{e}^{\mathrm{i}2\beta_1}} \tag{C.5}$$

We can follow a similar procedure to determine ρ_{02} and τ_{02}, or more easily we can permute 0 and 2 subscripts in Eqs. (C.4) and (C.5), respectively. In either case, we obtain

$$\rho_{02} = \frac{r_{01} + r_{12} \mathrm{e}^{\mathrm{i}2\beta_1}}{1 + r_{10} r_{21} \mathrm{e}^{\mathrm{i}2\beta_1}} \quad \text{and} \quad \tau_{02} = \frac{t_{01} t_{12} \mathrm{e}^{\mathrm{i}\beta_1}}{1 + r_{10} r_{21} \mathrm{e}^{\mathrm{i}2\beta_1}}. \tag{C.6}$$

It is important to note that $\tau_{02}\tau_{20} - \rho_{02}\rho_{20} \neq 1$. Also if $d_1 = 0$, one recovers $\rho_{02} = -\rho_{20} = r_{02}$, $\tau_{02} = t_{02}$ and $\tau_{20} = t_{20}$.

C.1.2 Multilayer interference

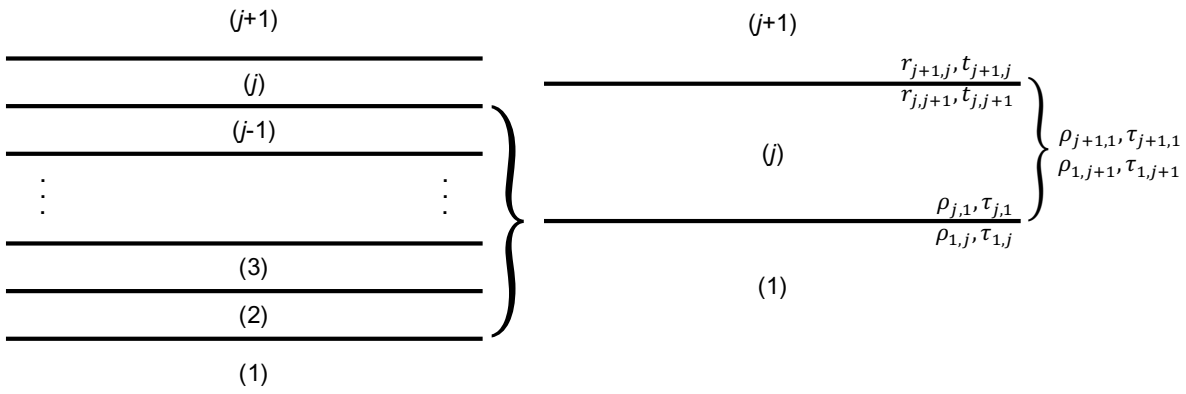

Figure C.2 – *Schematic diagram of a layered structure. Media (1) and (j+1) are supposed to be semi-infinite. $\rho_{j,1}$, $\tau_{j,1}$, $\rho_{1,j}$ and $\tau_{1,j}$ are the equivalent coefficients of the structure from (1) to (j). Using these coefficients, the equivalence coefficients $\rho_{j+1,1}$, $\tau_{j+1,1}$, $\rho_{1,j+1}$ and $\tau_{1,j+1}$ can be computed.*

For a multilayered structure, we can calculate the equivalent reflection and transmission coefficients recursively. Let us consider the j^{th} layer and assume that we have already compute $\rho_{j,1}$, $\tau_{j,1}$, $\rho_{1,j}$ and $\tau_{1,j}$ (see Fig. C.2). We therefore recover a structure similar to the one of the previous subsection (the 1^{st} and $j+1^{\text{th}}$ layers are supposed to be semi-infinite). Thus,

we can deduce the equivalent coefficients

$$\rho_{j+1,1} = \frac{r_{j+1,j} + \rho_{j,1} e^{i2\beta_j}}{1 + r_{j+1,j}\rho_{j,1} e^{i2\beta_j}} \quad \text{and} \quad \tau_{j+1,1} = \frac{t_{j+1,j}\tau_{j,1} e^{i\beta_j}}{1 + r_{j+1,j}\rho_{j,1} e^{i2\beta_j}}, \tag{C.7}$$

$$\rho_{1,j+1} = \frac{\rho_{1,j} + r_{j,j+1}(\tau_{j,1}\tau_{1,j} - \rho_{j,1}\rho_{1,j}) e^{i2\beta_j}}{1 + r_{j+1,j}\rho_{j,1} e^{i2\beta_j}} \quad \text{and} \quad \tau_{1,j+1} = \frac{\tau_{1,j} t_{j,j+1} e^{i\beta_j}}{1 + r_{j+1,j}\rho_{j,1} e^{i2\beta_j}}. \tag{C.8}$$

C.2 Absorptance in a multilayer system

The fraction of absorbed light in the layered structure plays an important role in its photophysics. This quantity will be needed for the study of the PL of SCTMDs in Chapter 7 and for the investigation of the interlayer coupling in van der Waals heterostructures in Chapter 8. When light is shined into a given medium, a fraction $\mathcal{R}$ of the density flux is reflected, a fraction $\mathcal{T}$ is transmitted and a fraction $\mathcal{A}$ is absorbed. These three fractions are called [Hecht01] **reflectance**, **transmittance** and **absorptance**, respectively. The conservation of energy imposes

$$\mathcal{R} + \mathcal{T} + \mathcal{A} = 1. \tag{C.9}$$

Note that the absorption of a medium is taken into account in the imaginary part of the refractive index (called the extinction coefficient). Equation (C.9) shows that $\mathcal{A}$ can be deduced from the determination of $\mathcal{R}$ and $\mathcal{T}$ which are linked to the reflection and transmission coefficients, respectively.

Let us consider a system composed of a stack of N layers sandwiched in two semi-infinite media (t) and (b). Light is coming from medium (t) at normal incidence. The object of this section is to calculate the absorptance of the whole N-layer structure and of each layer.

C.2.1 Absorptance of the whole multilayered structure

The absorptance of the whole structure can be easily computed using the equivalent coefficients ρ_{tb}, τ_{tb}, ρ_{bt} and τ_{bt} determined with Eqs. (C.7) and (C.8). Indeed, the reflectance and transmittance of the multilayered structure are given by [Hecht01]

$$\mathcal{R} = \left|\rho_{tb}\right|^2 \text{ and } \mathcal{T} = |\tau_{tb}\tau_{bt}|, \tag{C.10}$$

and thus from Eq. (C.9)

$$\mathcal{A} = 1 - \left|\rho_{tb}\right|^2 - |\tau_{tb}\tau_{bt}|. \tag{C.11}$$

C.2.2 Absorptance of one layer

The absorptance $\mathcal{A}$ of one layer encapsulated in two media can be notably enhanced compared to the **interference-free** case. Indeed, multiple reflections at interfaces increase the

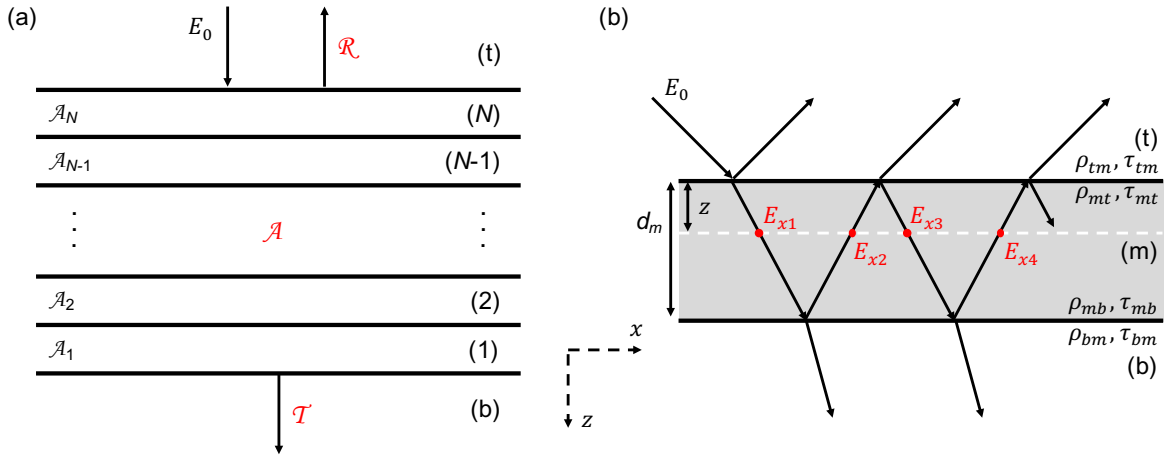

Figure C.3 – *(a) A N-layer structure sandwiched in two semi-infinite media (t) and (b). The incident light (E_0) is coming from the top. The reflectance, transmittance, and absorptance of the whole N-layer structure are $\mathcal{R}$, $\mathcal{T}$, and $\mathcal{A}$, respectively. The m^{th} layer has an absorptance $\mathcal{A}_m$. (b) m^{th} layer encapsulated in media (t) and (b) with equivalent reflection and transmission coefficient. The incoming light undergoes multiple reflections and interacts several times ($E_{z1}, E_{z2}, ...$) at a depth z. Note that the light has been drawn with an angle for clarity but is considered to be normal to the plane in the calculations.*

chances for the light to be absorbed. This enhancement depends on the surrounding media and on the thickness of the layer. First of all, one should precisely define the **interference-free reference**. There are two situations where no interference occurs in the layer: (i) the layer is thicker than the penetration length of the electric field therefore there are no reflections, and (ii) the sample conditions are such that there are no coherent reflections [Buckley77]. Obviously, only the first situation can be used as the interference-free reference. In this case, the problem is equivalent to two semi-infinite media separated by one interface. In order to compare to non-infinite media, one can define an interference-free absorptance per unit length $\mathfrak{a}$, which only depends on these two media.

Let us consider the m^{th} layer in the N-layer system in Fig. C.3(a), which has a thickness d_m and a refractive index $n_m = n'_m + \mathrm{i}n''_m$. The absorptance $\mathcal{A}_m$ of the layer is affected by the interference effects in the layer and in the neighboring layers. On the contrary by definition, the interference-free absorptance per unit length $\mathfrak{a}_m$ depends only on the m^{th} layer and on the top medium (t). The equivalent reflection and transmission coefficients for the top and bottom interfaces are computed applying Eqs. (C.7) and (C.8). The problem is then equivalent to Fig. C.3(b). To calculate $\mathcal{A}_m$, we assume that the layer can be divided into layers of thickness δ such that the electric field E is uniformed within each layers. The light intensity absorbed by one of these layers is given by $|E|^2\,\mathfrak{a}_m\delta$. The total absorbed intensity $|E_0|^2\,\mathcal{A}_m$ is equal to the sum of all these absorbed intensities. If the thickness δ tends to zero, we have

$$\mathcal{A}_m = \frac{1}{|E_0|^2}\int_0^{d_m} |E_z|^2\,\mathfrak{a}_m \mathrm{d}z = \mathfrak{a}_m \underbrace{\int_0^{d_m} \frac{|E_z|^2}{|E_0|^2}\mathrm{d}z}_{F_{\text{ab}}}, \tag{C.12}$$

where E_z is the electric field at a distance $z \leq d_m$ and F_{ab} is the enhancement factor which is homogeneous to a length. Hence to obtain $\mathcal{A}_m$, we have to determine the electric field E_z (i.e., F_{ab}) within the layer and $\mathfrak{a}_m$.

According to the notations in Fig. C.3(b), the different components of the electric field at point $z \leq d_m$ are

$$\begin{aligned}
E_{z1} &= \tau_{tm} e^{i\beta_z} E_0, \\
E_{z2} &= \tau_{tm} e^{i\beta_m} \rho_{mb} e^{i(\beta_m - \beta_z)} E_0 = \tau_{tm} \rho_{mb} e^{i(2\beta_m - \beta_z)} E_0, \\
E_{z3} &= \tau_{tm} e^{i\beta_m} \rho_{mb} e^{i\beta_m} \rho_{mt} e^{i\beta_z} E_0 = E_{z1} (\rho_{mb} \rho_{mt} e^{i2\beta_m}), \\
E_{z4} &= \tau_{tm} e^{i\beta_m} \rho_{mb} e^{i\beta_m} \rho_{mt} e^{i\beta_m} \rho_{mb} e^{i(\beta_m - \beta_z)} E_0 = E_{z2} (\rho_{mb} \rho_{mt} e^{i2\beta_m}), \\
&\vdots \\
E_{z2q+1} &= E_{z1} (\rho_{mb} \rho_{mt} e^{i2\beta_m})^q, \\
E_{z2q+2} &= E_{z2} (\rho_{mb} \rho_{mt} e^{i2\beta_m})^q,
\end{aligned}$$

where $q \geq 0$, $\beta_z = \frac{2\pi n_m z}{\lambda}$ and $\beta_m = \frac{2\pi n_m d_m}{\lambda}$ are the phase differences arising from propagation to z and the whole layer, respectively, and λ is the wavelength in vacuum of the incident light. The total electric field at z is

$$E_z = \sum_{q=0}^{+\infty} (E_{z1} + E_{z2}) (\rho_{mb} \rho_{mt} e^{i2\beta_m})^q = \tau_{tm} \frac{e^{i\beta_z} + \rho_{mb} e^{i(2\beta_m - \beta_z)}}{1 - \rho_{mb} \rho_{mt} e^{i2\beta_m}} E_0, \tag{C.13}$$

owing to $\left| \rho_{mb} \rho_{mt} e^{i2\beta_m} \right| < 1$. Finally, the enhancement factor is equal to

$$F_{ab} = \int_0^{d_m} \left| \tau_{tm} \frac{e^{i\beta_z} + \rho_{mb} e^{i(2\beta_m - \beta_z)}}{1 - \rho_{mb} \rho_{mt} e^{i2\beta_m}} \right|^2 dz \tag{C.14}$$

Note that if $d_m \gg \frac{\lambda}{4\pi n''_m}$ (the attenuation length in the m^{th} layer), $F_{ab} = \frac{|\tau_{tm}|^2 \lambda}{4\pi n''_m}$ and if $d_m \ll \frac{\lambda}{4\pi n''_m}$, $F_{ab} \propto d_m$.

Since $\mathfrak{a}_m$ depends only on the top medium (t), we have to consider that the m^{th} layer is encapsulated in medium (t) to determine $\mathfrak{a}_m$. Since the top medium is air, for usual experiments, this configuration is usually referred to as **free-standing**. Let $\mathcal{A}^0_m$ be the corresponding absorptance and F^0_{ab} the enhancement factor. For any thickness d_m, we have the relation $\mathfrak{a}_m = \mathcal{A}^0_m / F^0_{ab}$. If $d_m \to +\infty$, from Eqs. (C.11) and (C.14) we deduce

$$\mathfrak{a}_m = \frac{4\pi n''_m}{\lambda} \frac{1 - |r_{tm}|^2}{|t_{tm}|^2} = \frac{4\pi n''_m}{\lambda} \left[\frac{n'_t n'_m + n''_t n''_m}{n'^2_t + n''^2_t} \right]. \tag{C.15}$$

Note that $\mathfrak{a}_m$ is proportional to the **attenuation coefficient** $4\pi n''_m / \lambda$ of the m^{th} layer. In the case where the top medium is air ($n_t = 1$), $\mathfrak{a}_m = 4\pi n'_m n''_m / \lambda$ and we recover the results of

Ref. [Buckley77] for free-standing thin films.

We now have all the ingredients to calculate the absorptance of the different layers in the multilayered structure. One can of course check that the sum of all layer absorptance give the total absorptance of the structure calculated directly with Eq. (C.11). It is noteworthy to mention that, in practice, $\mathfrak{a}_m$ is not directly measurable quantity whereas $\mathcal{A}^0_m$ is. Consequently, the free-standing configuration can also be used as a reference

$$\mathcal{A}_m = \frac{F_{\mathrm{ab}}}{F^0_{\mathrm{ab}}}\mathcal{A}^0_m \tag{C.16}$$

where $F_{\mathrm{ab}}/F^0_{\mathrm{ab}}$ can be viewed as the enhancement factor compared to the free-standing case.

C.3 Photoluminescence and Raman enhancement factor

As already mentioned, PL [Buscema14] and Raman [Yoon09, Li12b] intensities from one layer in the N-layer structure can be drastically affected by optical interference. Although these two processes are fundamentally different, they are changed in the same way by optical interference. As for the absorptance, we can define an enhancement factor F_{x} and an interference-free intensity per unit length $\mathfrak{i}_{\mathrm{x}}$ such that the PL or Raman intensity of one layer is

$$I_{\mathrm{x}} = F_{\mathrm{x}}\mathfrak{i}_{\mathrm{x}}, \tag{C.17}$$

where x stands for PL or Raman. Note that contrary to the absorptance, we will not give an expression for $\mathfrak{i}_{\mathrm{x}}$. Here, the idea is to deduce $\mathfrak{i}_{\mathrm{x}}$ from the measurement of I_{x} in order to quantitatively compare experimental results obtain under different conditions (e.g., graphene or TMDs on various substrates or with different number of layers). Therefore, we need to calculate the enhancement factor F_{x}.

Let us consider the m^{th} layer in the N-layer system which has a thickness d_m and a refractive index $n_m = n'_m + \mathrm{i}n''_m$ (see Fig. C.3). The enhancement factor contains two contributions: (i) the excitation light E_{ex} at one point within the layer and (ii) the emitted (or scattered) light E_{em} coming from the same point, which are both modified by the multiple reflections at the boundaries (see Fig. C.4). The enhancement factor is then given by

$$F_{\mathrm{x}}(\lambda_{\mathrm{ex}}, \lambda_{\mathrm{em}}) = \int_0^{d_m} \left| \frac{E_{\mathrm{ex}}}{E_0}(\lambda_{\mathrm{ex}}) \times \frac{E_{\mathrm{em}}}{E_{\mathrm{c}}}(\lambda_{\mathrm{em}}) \right|^2 \mathrm{d}z, \tag{C.18}$$

where E_0 is the incident light, E_{c} the light created at a point z within the layer and λ_{ex} (λ_{em}) the wavelength in vacuum of the incident light E_0 (created light E_{c}). At point $z \leq d_m$ within the layer, the excitation electric field E_{ex} is given by Eq. (C.13). The emitted electric field E_{em} is computed following exactly the same method as E_z for the absorptance (see Section C.2.2). One would notice that E_{ex} and E_{em} have almost the same expression but at different wave-

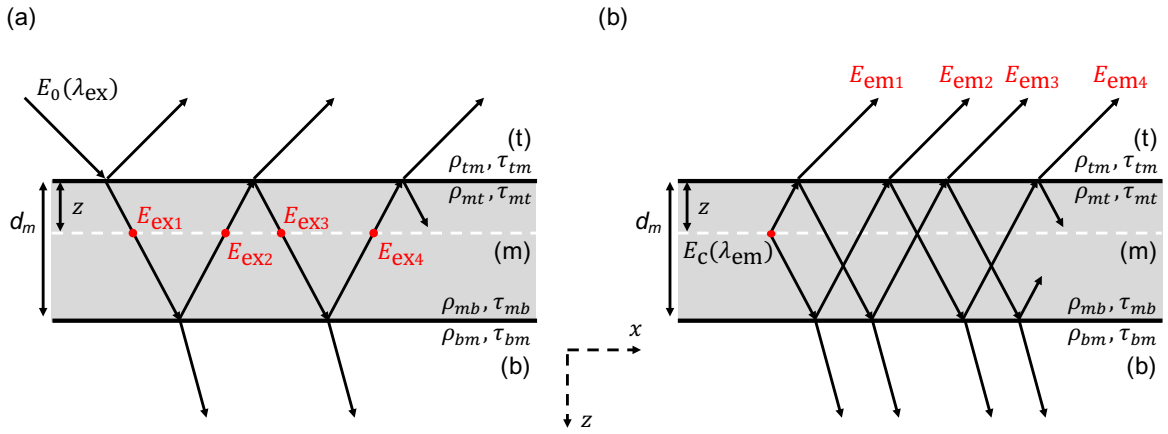

Figure C.4 – *m^{th} layer encapsulated in media (t) and (b) with equivalent reflection and transmission coefficients (a) The incident light E_0 with a wavelength λ_{ex} undergoes multiple reflections and interacts several times ($E_{ex1}, E_{ex2}, ...$) at a depth z. (b) The total emitted light $E_{em} = E_{em1} + E_{em2} + ...$ coming from a point at depth z also undergoes multiple reflections. Note that the light has been drawn with an angle for clarity but the calculations are done for normal incidence.*

lengths. Finally the enhancement factor is

$$F_x(\lambda_{ex}, \lambda_{em}) = \int_0^{d_m} \left| \left(\tau_{tm} \frac{e^{i\beta_z} + \rho_{mb} e^{i(2\beta_m - \beta_z)}}{1 - \rho_{mb}\rho_{mt} e^{i2\beta_m}} \right)_{ex} \times \left(\tau_{mt} \frac{e^{i\beta_z} + \rho_{mb} e^{i(2\beta_m - \beta_z)}}{1 - \rho_{mb}\rho_{mt} e^{i2\beta_m}} \right)_{em} \right|^2 dz, \qquad (C.19)$$

where $\beta_z = \frac{2\pi n_m z}{\lambda}$ and $\beta_m = \frac{2\pi n_m d_m}{\lambda}$ are the phase differences arising from propagation to z and the whole layer, respectively, and ρ and τ are the equivalent reflection and transmission coefficients. $(\,)_{ex}$ and $(\,)_{em}$ indicate the wavelength (λ_{ex} or λ_{em}) at which all quantities are calculated.

Chapter D

Optical separation of strain and doping

In this appendix, we show how strain and doping can be separated using the frequency correlations of the G- and 2D-mode feature. This method was proposed by Lee *et al.* [Lee12c] and is based on a vector decomposition model in the Ω_G-Ω_{2D}-plane.

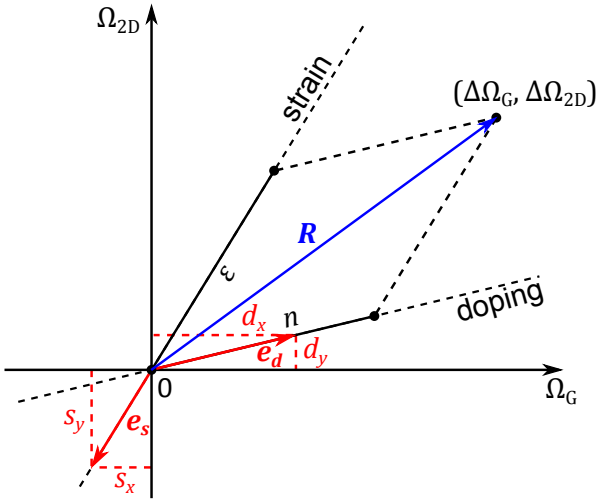

***Figure D.1** – Schematic of the vector decomposition of the strain and doping component in the ω_G-ω_{2D}-plane. The point $(\Delta\omega_G, \Delta\omega_{2D})$ defines a vector **R** which can be projected on the vectors $\boldsymbol{e}_s$ and $\boldsymbol{e}_d$ which form the coordinate system of strain and doping.*

The aim is to be able to attribute every measured pair of Ω_G and Ω_{2D} to a value of strain ϵ and doping n. Let $\boldsymbol{R}$ be a a vector of Raman shifts $(\Delta\Omega_G,\Delta\Omega_{2D})$ in the ω_G-ω_{2D}-plane (see blue vector in Fig. D.1). $\boldsymbol{R}$ can be expressed in a coordinate system with $\boldsymbol{e}_s$ and $\boldsymbol{e}_d$ as unity basis vectors, where $\boldsymbol{e}_s$ is a vector along the strain shift rate

$$\boldsymbol{e}_s = \begin{bmatrix} s_x \\ s_y \end{bmatrix}, \qquad \left.\frac{\partial\Omega_{2D}}{\partial\Omega_G}\right|_{strain} = \frac{s_y}{s_x} \tag{D.1}$$

and $\boldsymbol{e}_\mathrm{d}$ is a vector along the doping shift rate

$$\boldsymbol{e}_\mathrm{d} = \begin{bmatrix} d_\mathrm{x} \\ d_\mathrm{y} \end{bmatrix}, \qquad \left.\frac{\partial \Omega_{2\mathrm{D}}}{\partial \Omega_\mathrm{G}}\right|_{\mathrm{doping}} = \frac{d_\mathrm{y}}{d_\mathrm{x}}. \tag{D.2}$$

The vector $\boldsymbol{R}$ in the new coordinate system is then

$$\boldsymbol{R} = n \begin{bmatrix} d_\mathrm{x} \\ d_\mathrm{y} \end{bmatrix} + \epsilon \begin{bmatrix} s_\mathrm{x} \\ s_\mathrm{y} \end{bmatrix} = \begin{bmatrix} n \\ \epsilon \end{bmatrix}, \tag{D.3}$$

where n and ϵ are the projections on the doping and the strain axis in the new coordinate system. Solving Eq. (D.3) with respect to n and ϵ yields

$$\begin{aligned} n &= \mathcal{C}_\mathrm{d} \frac{\Delta\Omega_\mathrm{G} s_\mathrm{y} - \Delta\Omega_{2\mathrm{D}} s_\mathrm{x}}{s_\mathrm{y} d_\mathrm{x} - s_\mathrm{x} d_\mathrm{y}}, \\ \epsilon &= \mathcal{C}_\mathrm{s} \frac{\Delta\Omega_{2\mathrm{D}} d_\mathrm{x} - \Delta\Omega_\mathrm{G} d_\mathrm{y}}{s_\mathrm{y} d_\mathrm{x} - s_\mathrm{x} d_\mathrm{y}}, \end{aligned} \tag{D.4}$$

where $\mathcal{C}_\mathrm{d}$ and $\mathcal{C}_\mathrm{s}$ are the doping and strain coefficients, respectively. The coordinates are the basis vectors can be expressed in terms of the corresponding slopes

$$\begin{aligned} s_\mathrm{x} &= \cos\left[\arctan\left(\left.\frac{\partial \Omega_{2\mathrm{D}}}{\partial \Omega_\mathrm{G}}\right|_{\mathrm{strain}}\right)\right], \\ s_\mathrm{y} &= \sin\left[\arctan\left(\left.\frac{\partial \Omega_{2\mathrm{D}}}{\partial \Omega_\mathrm{G}}\right|_{\mathrm{strain}}\right)\right], \\ d_\mathrm{x} &= \cos\left[\arctan\left(\left.\frac{\partial \Omega_{2\mathrm{D}}}{\partial \Omega_\mathrm{G}}\right|_{\mathrm{doping}}\right)\right], \\ d_\mathrm{y} &= \sin\left[\arctan\left(\left.\frac{\partial \Omega_{2\mathrm{D}}}{\partial \Omega_\mathrm{G}}\right|_{\mathrm{doping}}\right)\right]. \end{aligned} \tag{D.5}$$

Finally, using Eqs. (D.4) and (D.5) and the value of the coefficients and the slopes displayed in Tab. 5.1, one can accurately estimate the strain and doping for any pair of Ω_G and $\Omega_{2\mathrm{D}}$. However, these method is only valid up to a certain doping level as shown in the main text.

Chapter E

Finite Linear Chain Model

Let us consider a chain of N identical masses μ (numbered from 1 to N) connected to each other by identical springs of force constant κ (see Fig. E.1). We assume that the two extreme masses are free, i.e., they are only connected to one spring.

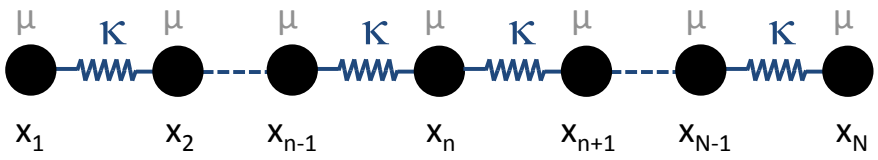

Figure E.1 *– A linear chain of N identical masses μ (numbered from 1 to N) connected to each other by identical springs of force constant κ. The two extreme masses (1 and N) are free. x_n is the displacement of the n^{th} mass with respect to the equilibrium position.*

If x_n is the displacement of the n^{th} mass with respect to the equilibrium position, the equations of motion are

$$\text{if } n = 1, \ \frac{\mathrm{d}^2 x_1}{\mathrm{d}t^2} = -\Omega_0^2 (x_1 - x_2), \tag{E.1}$$

$$\text{if } n = N, \ \frac{\mathrm{d}^2 x_N}{\mathrm{d}t^2} = -\Omega_0^2 (x_N - x_{N-1},) \tag{E.2}$$

$$\text{else}, \ \frac{\mathrm{d}^2 x_n}{\mathrm{d}t^2} = -\Omega_0^2 (2x_n - x_{n+1} - x_{n-1}), \tag{E.3}$$

where $\omega_0 = \sqrt{\frac{\kappa}{\mu}}$. These equation form a system of N coupled differential equations that can be rewritten using matrix

$$\frac{\mathrm{d}^2 X}{\mathrm{d}t^2} = -\Omega_0^2 M X, \tag{E.4}$$

$$\text{with } M = \begin{pmatrix} 1 & -1 & 0 & 0 & \dots & 0 & 0 \\ -1 & 2 & -1 & 0 & \dots & 0 & 0 \\ 0 & -1 & 2 & -1 & \dots & 0 & 0 \\ 0 & 0 & -1 & 2 & \dots & 0 & 0 \\ \dots & \dots & \dots & \dots & \dots & -1 & 0 \\ \dots & \dots & \dots & \dots & \dots & 2 & -1 \\ 0 & 0 & \dots & \dots & \dots & -1 & 1 \end{pmatrix}_{(N,N)} \quad \text{and } X = \begin{pmatrix} x_1 \\ x_2 \\ x_3 \\ \dots \\ \dots \\ x_{N-1} \\ x_N \end{pmatrix}.$$

To find the normal modes of this chain, one has to search for sinusoidal solutions. For this kind of solution, Eq. (E.4) becomes

$$MX = \left(\frac{\Omega}{\Omega_0}\right)^2 X. \tag{E.5}$$

Therefore, the normal modes are obtained by diagonalizing matrix M. Solving this problem leads to the eigenvalues

$$\lambda_p = 2\left[1 - \cos\left(\frac{(p-1)\pi}{N}\right)\right], \text{ with } p \in [\![1, N]\!], \tag{E.6}$$

and eigenvectors

$$\text{if } p = 1, \; x_{p,n} = \frac{1}{\sqrt{N}} \tag{E.7}$$

$$\text{if } p \in [\![2, N]\!], \; x_{p,n} = \sqrt{\frac{2}{N}} \cos\left(\frac{(p-1)(2n-1)\pi}{2N}\right). \tag{E.8}$$

The frequency Ω_p of each normal mode is linked to the eigenvalue λ_p by $\Omega_p = \Omega_0\sqrt{\lambda_p}$. The displacement $x_{p,j}$ of the n^{th} mass for each normal mode corresponds to the components of the eigenvector X_p. As these components are defined up to a constant multiplier, we choose to norm the eigenvectors, i.e., $\forall p, X_p \cdot X_p = \sum_{j=1}^{N} x_{p,j}^2 = 1$. Thus, the eigenvectors form a orthonormal basis of the solutions.

Chapter F

Normal mode displacements for N-layer $MoTe_2$

Figures F.1 to F.6 show the normal mode displacements associated with the LSM, iX, iMX, LBM, oX, and oMX modes in N-layer $MoTe_2$.

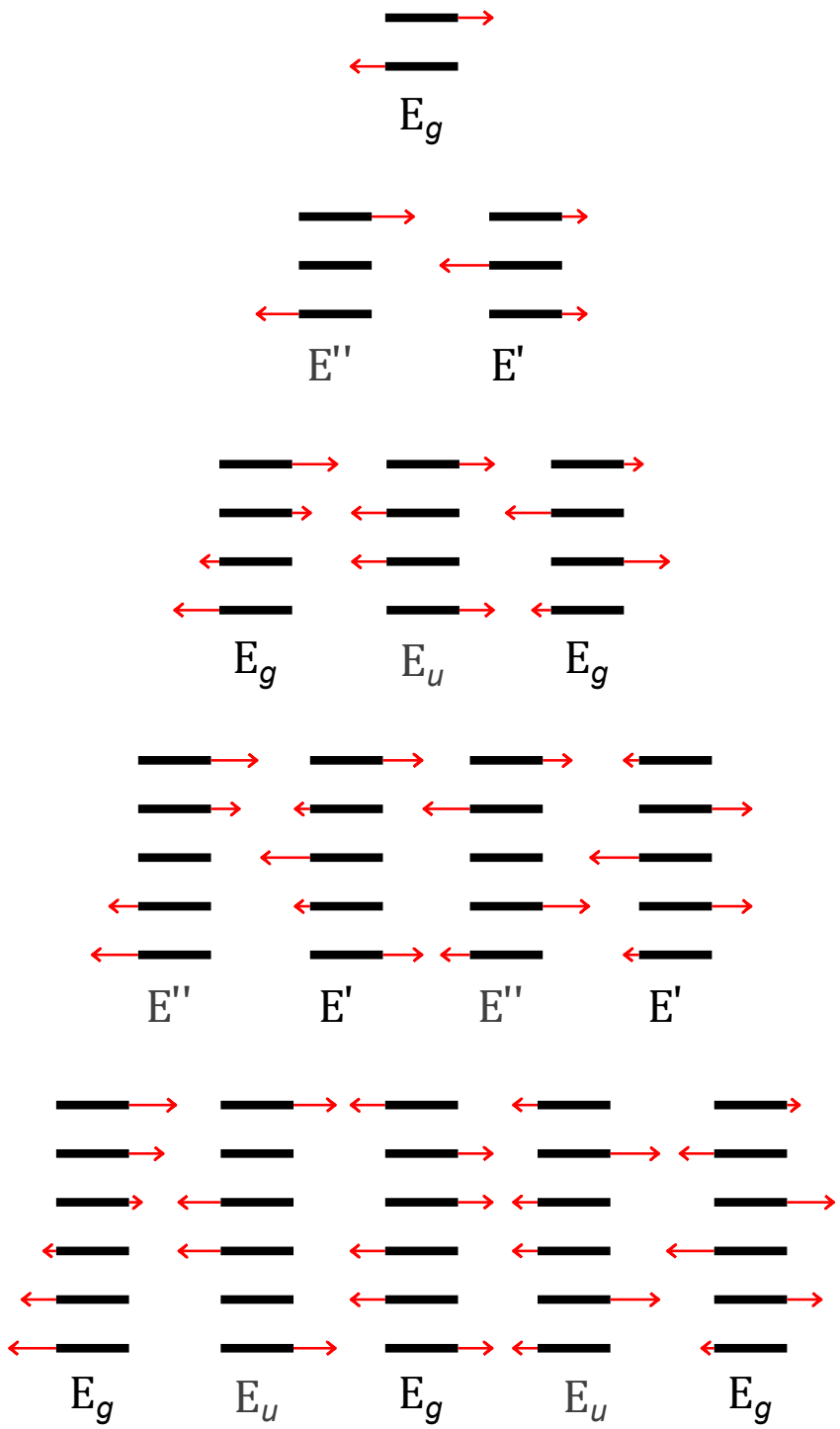

Figure F.1 *– Calculated normal displacements associated with the LSM in $N = 1$ to $N = 6$ layers $MoTe_2$. The size of the arrows is proportional to the amplitude of $\varepsilon^k_{i,j}$ of the normal displacement obtained from the solution of Eq. (6.1). The frequencies of the modes increase from left to right. The irreductible representation of each normal mode is indicated. The modes that are Raman-active in our geometry appear in black. The other modes appear in grey.*

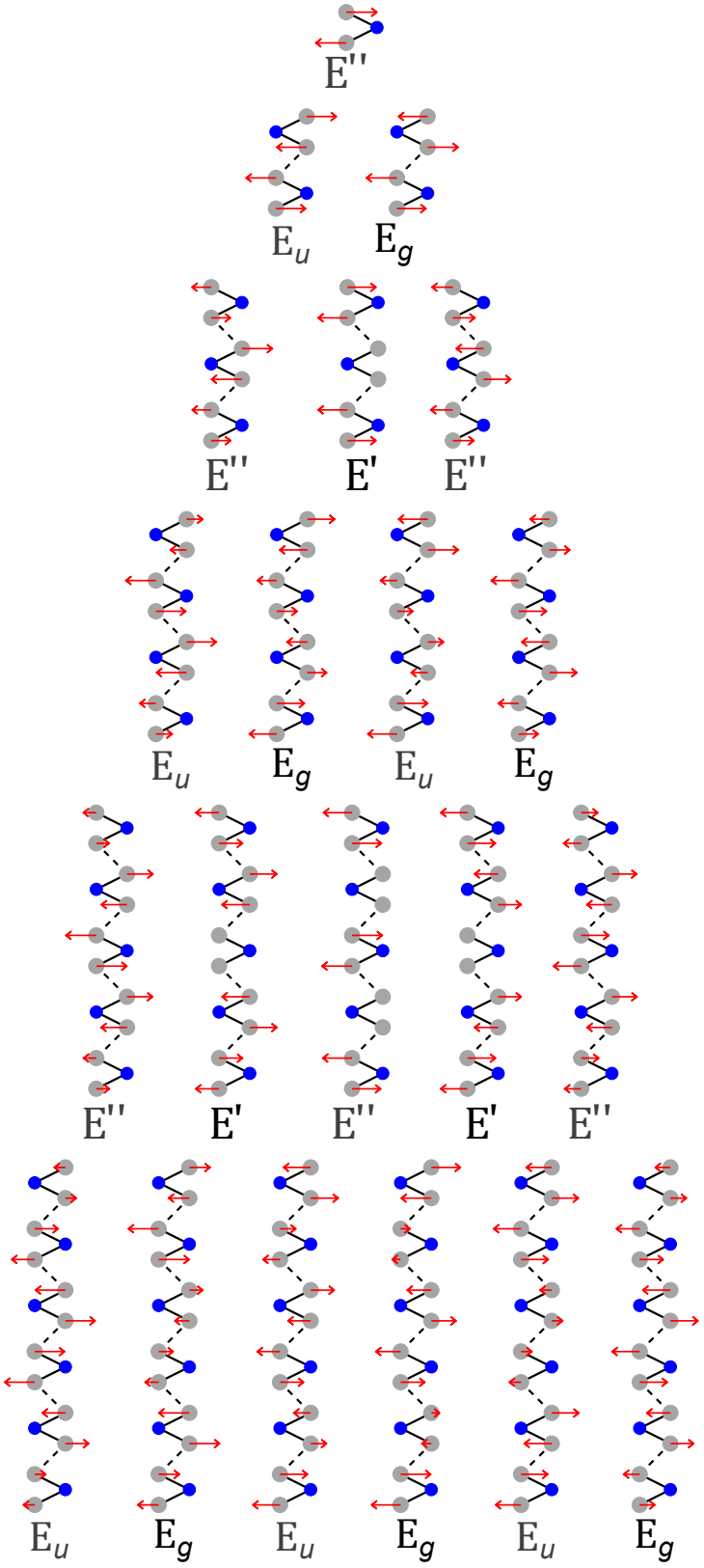

Figure F.2 – *Same as Fig. F.1 for the iX modes in $N = 1$ to $N = 6$ layers $MoTe_2$.*

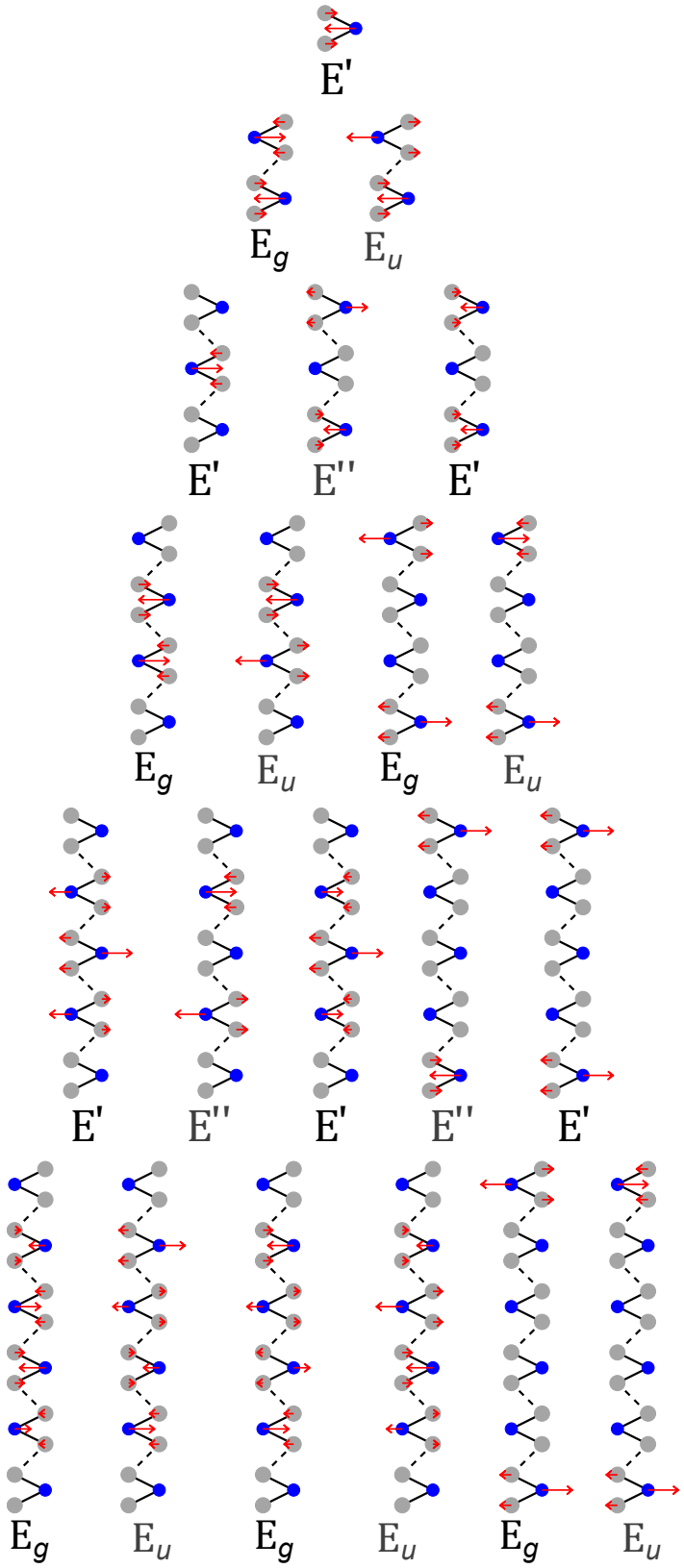

Figure F.3 – *Same as Fig. F.1 for the iMX modes in $N = 1$ to $N = 6$ layers $MoTe_2$.*

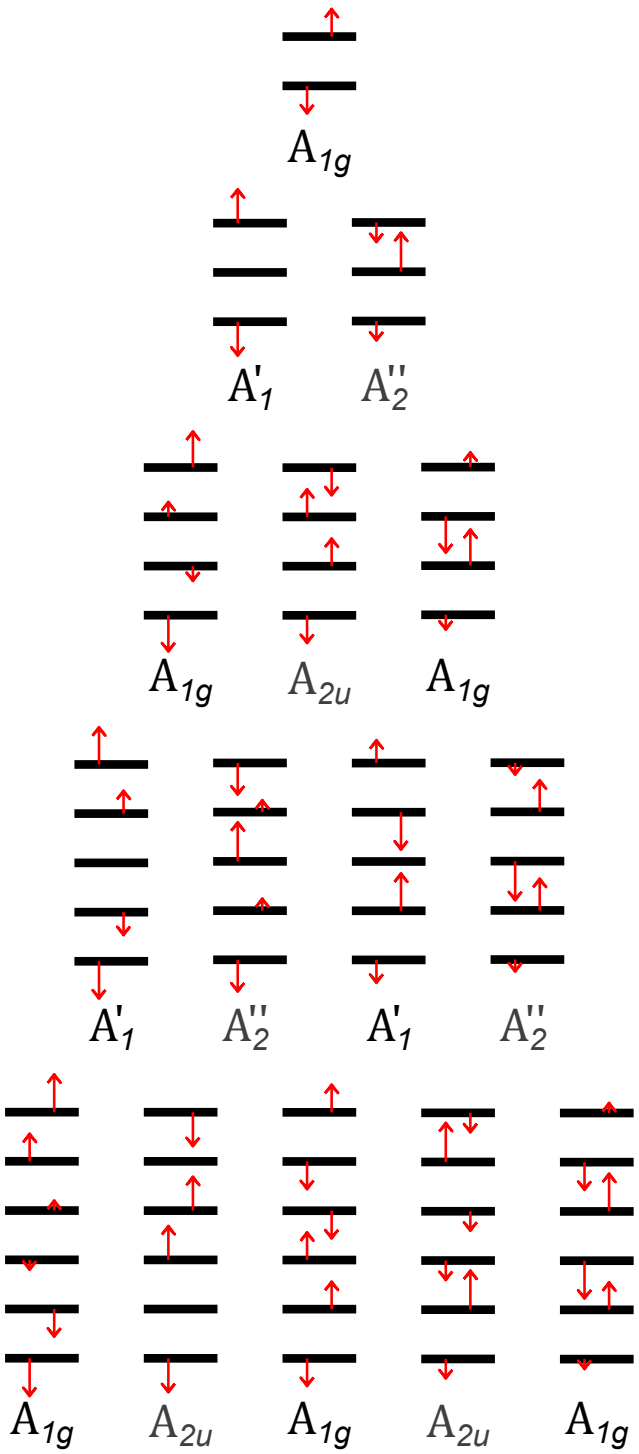

Figure F.4 *– Same as Fig. F.1 for the LBM in $N = 1$ to $N = 6$ layers $MoTe_2$.*

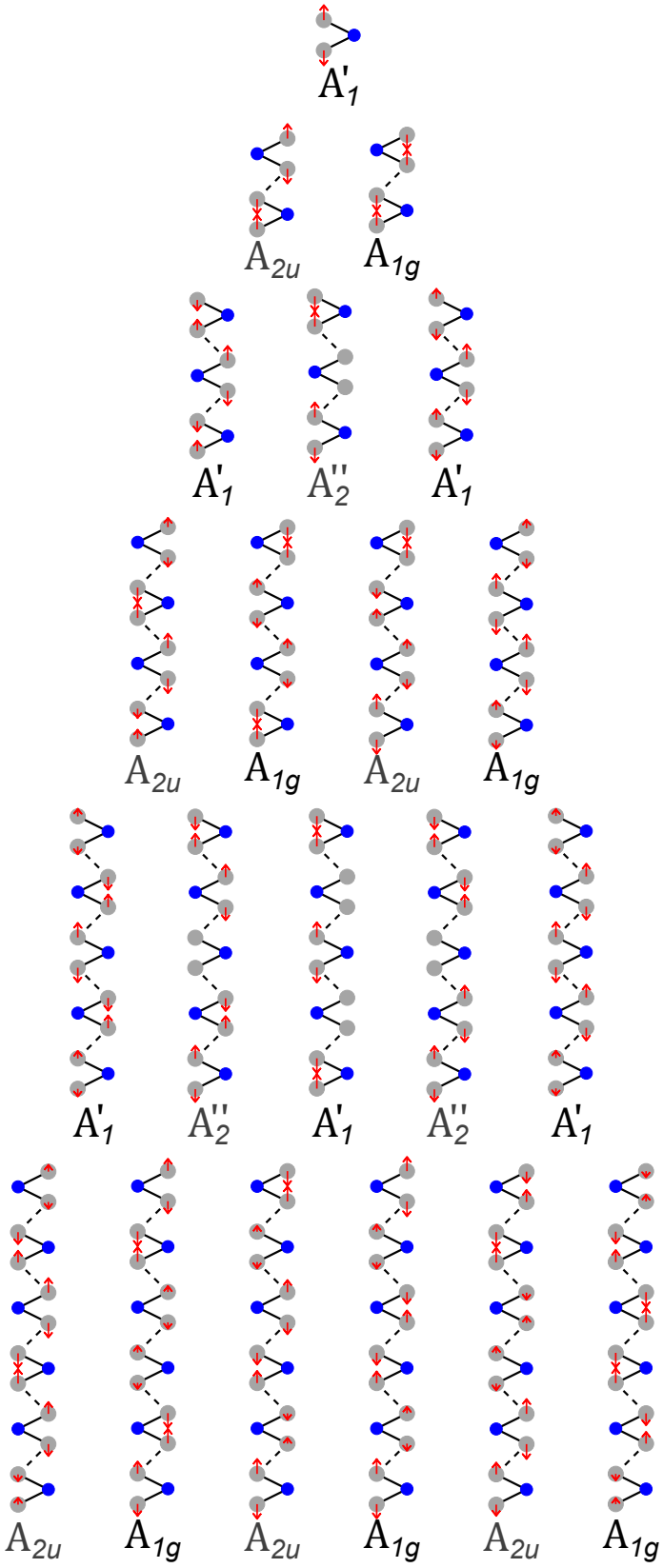

Figure F.5 – *Same as Fig. F.1 for the oX modes in $N = 1$ to $N = 6$ layers $MoTe_2$.*

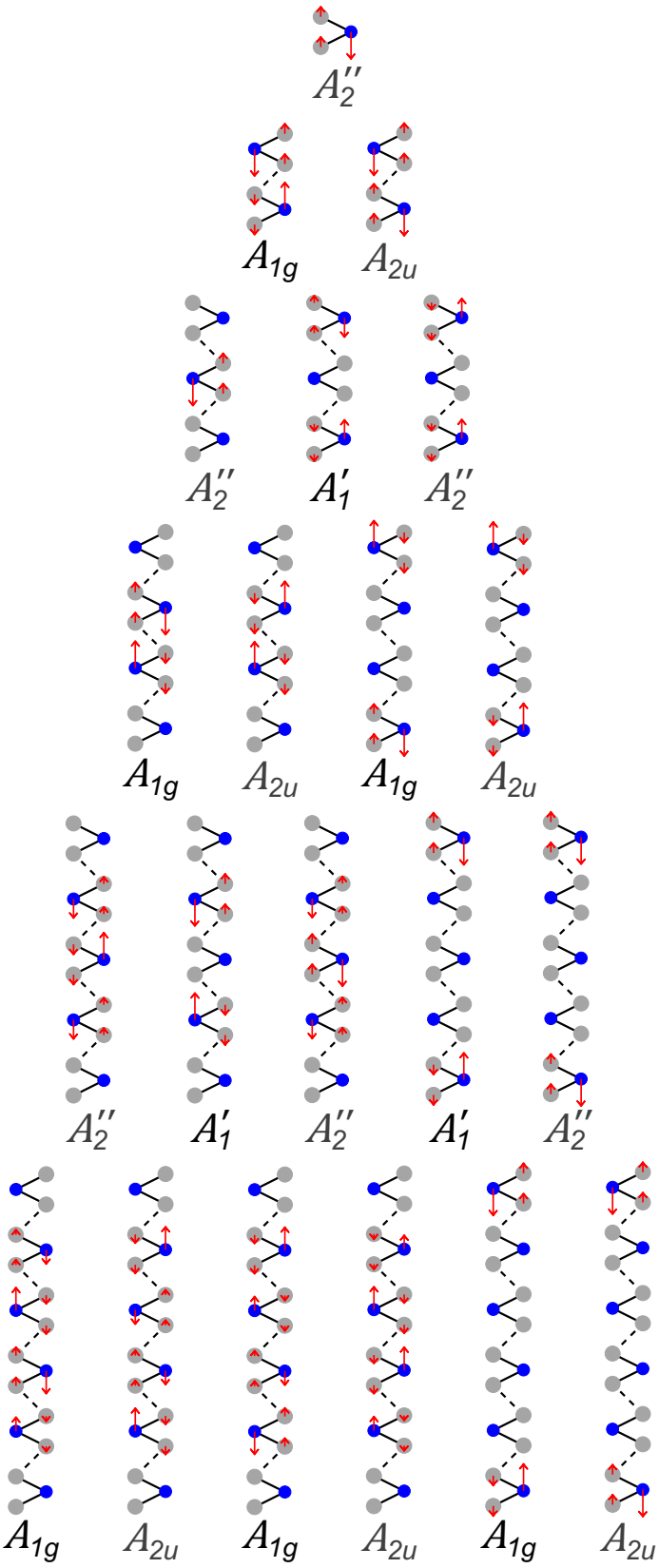

Figure F.6 *– Same as Fig. F.1 for the oMX modes in $N = 1$ to $N = 6$ layers $MoTe_2$.*

Bibliography

[Achermann04] M. Achermann, M. A. Petruska, S. Kos, D. L. Smith, D. D. Koleske, and V. I. Klimov. *Energy-transfer pumping of semiconductor nanocrystals using an epitaxial quantum well*. Nature **429** (6992), 642–646 (2004). 53

[Ahn13] G. Ahn, H. R. Kim, T. Y. Ko, K. Choi, K. Watanabe, T. Taniguchi, B. H. Hong, and S. Ryu. *Optical probing of the electronic interaction between graphene and hexagonal boron nitride*. ACS Nano **7** (2), 1533–1541 (2013). 186, 189

[Ajayan16] P. M. Ajayan, P. Kim, and K. Banerjee. *Two-dimensional van der Waals materials*. Phys. Today **69** (9), 38-44 (2016). 12, 214

[Al-Jishi82] R. Al-Jishi and G. Dresselhaus. *Lattice-dynamical model for graphite*. Phys. Rev. B **26**, 4514–4522 (1982). 23

[Alferov01] Z. I. Alferov. *Nobel Lecture: The double heterostructure concept and its applications in physics, electronics, and technology*. Rev. Mod. Phys. **73**, 767–782 (2001). 12, 214

[Amani15] M. Amani, D.-H. Lien, D. Kiriya, J. Xiao, A. Azcatl, J. Noh, S. R. Madhvapathy, R. Addou, K. Santosh, M. Dubey, et al. *Near-unity photoluminescence quantum yield in MoS2*. Science **350** (6264), 1065–1068 (2015). 35

[Ando02] T. Ando, Y. Zheng, and H. Suzuura. *Dynamical conductivity and zero-mode anomaly in honeycomb lattices*. J. Phys. Soc. Jpn. **71** (5), 1318–1324 (2002). 29

[Ando06] T. Ando. *Anomaly of Optical Phonon in Monolayer Graphene*. J. Phys. Soc. Jpn. **75** (12), 124701 (2006). 109, 111, 113

[Araujo12] P. T. Araujo, D. L. Mafra, K. Sato, R. Saito, J. Kong, and M. S. Dresselhaus. *Phonon Self-Energy Corrections to Nonzero Wave-Vector Phonon Modes in Single-Layer Graphene*. Phys. Rev. Lett. **109**, 046801 (2012). 109

[Aroca87] R. Aroca, C. Jennings, R. O. Loutfy, and A.-M. Hor. *Raman spectra of thin solid films—VI. Davydov splitting*. Spectrochim. Acta, Part A: **43** (6), 725–730 (1987). 128

[Ashcroft76] N. W. Ashcroft and N. D. Mermin. *Solid state physics*. Holt, Rinehart and Winston, 1976. 27, 135, 152

[Aslan15] O. B. Aslan, D. A. Chenet, A. M. van der Zande, J. C. Hone, and T. F. Heinz. *Linearly Polarized Excitons in Single- and Few-Layer ReS2 Crystals*. ACS Photonics **0** (ja) (2015). 210

[Baranov87] A. Baranov, A. Bekhterev, Y. S. Bobovich, and V. Petrov. *Interpretation of certain characteristics in Raman spectra of graphite and glassy carbon*. Opt. Spektrosk **62**, 1036 (1987). 99

[Baroni01] S. Baroni, S. de Gironcoli, A. Dal Corso, and P. Giannozzi. *Phonons and related crystal properties from density-functional perturbation theory*. Rev. Mod. Phys. **73**, 515–562 (2001). 139

[Basko08a] D. M. Basko. *Theory of resonant multiphonon Raman scattering in graphene*. Phys. Rev. B **78** (12), 125418 (2008). 101, 103, 104, 110, 116, 117, 118

[Basko08b] D. M. Basko and I. L. Aleiner. *Interplay of Coulomb and electron-phonon interactions in graphene*. Phys. Rev. B **77**, 041409 (2008). 118

[Basko09a] D. M. Basko. *Calculation of the Raman G peak intensity in monolayer graphene: role of Ward identities*. New J. Phys. **11** (9), 095011 (2009). 96, 116

[Basko09b] D. M. Basko, S. Piscanec, and A. C. Ferrari. *Electron-electron interactions and doping dependence of the two-phonon Raman intensity in graphene*. Phys. Rev. B **80** (16), 165413 (2009). 98, 116, 117, 118, 220, 221

[Basko13] D. M. Basko. *Effect of anisotropic band curvature on carrier multiplication in graphene*. Phys. Rev. B **87**, 165437 (2013). 117

[Baugher14] B. W. H. Baugher, H. O. H. Churchill, Y. Yang, and P. Jarillo-Herrero. *Optoelectronic devices based on electrically tunable p-n diodes in a monolayer dichalcogenide*. Nat. Nanotechnol. **advance online publication** (2014). 40

[Berciaud09] S. Berciaud, S. Ryu, L. E. Brus, and T. F. Heinz. *Probing the Intrinsic Properties of Exfoliated Graphene: Raman Spectroscopy of Free-Standing Monolayers*. Nano Lett. **9** (1), 346–352 (2009). 103, 118, 185, 189

[Berciaud10] S. Berciaud, M. Y. Han, K. F. Mak, L. E. Brus, P. Kim, and T. F. Heinz. *Electron and Optical Phonon Temperatures in Electrically Biased Graphene*. Phys. Rev. Lett. **104** (22), 227401 (2010). 22, 30

[Berciaud13] S. Berciaud, X. Li, H. Htoon, L. E. Brus, S. K. Doorn, and T. F. Heinz. *Intrinsic Line Shape of the Raman 2D-Mode in Freestanding Graphene Monolayers*. Nano Lett. **13** (8), 3517 (2013). 102, 103, 114, 185

[Berkdemir13] A. Berkdemir, H. R. Gutiérrez, A. R. Botello-Méndez, N. Perea-López, A. L. Elías, C.-I. Chia, B. Wang, V. H. Crespi, F. López-Urías, J.-C. Charlier, et al. *Identification of individual and few layers of WS_2 using Raman Spectroscopy*. Sci. Rep. **3** (2013). 128, 132

[Berkelbach13] T. C. Berkelbach, M. S. Hybertsen, and D. R. Reichman. *Theory of neutral and charged excitons in monolayer transition metal dichalcogenides*. Phys. Rev. B **88**, 045318 (2013). 37

[Biscaras15] J. Biscaras, Z. Chen, A. Paradisi, and A. Shukla. *Onset of two-dimensional superconductivity in space charge doped few-layer molybdenum disulfide*. Nat. Commun. **6** (2015). 209

[Blake07] P. Blake, E. W. Hill, A. H. Castro Neto, K. S. Novoselov, D. Jiang, R. Yang, T. J. Booth, and A. K. Geim. *Making graphene visible*. Appl. Phys. Lett. **91** (6) (2007). 81, 92, 93

[Böker01] T. Böker, R. Severin, A. Müller, C. Janowitz, R. Manzke, D. Voß, P. Krüger, A. Mazur, and J. Pollmann. *Band structure of MoS_2, $MoSe_2$, and α-$MoTe_2$: Angle-resolved photoelectron spectroscopy and ab initio calculations*. Phys. Rev. B **64**, 235305 (2001). 147

[Bonaccorso10] F. Bonaccorso, Z. Sun, T. Hasan, and A. C. Ferrari. *Graphene photonics and optoelectronics*. Nat. Photonics **4** (9), 611–622 (2010). 22

[Bonini07] N. Bonini, M. Lazzeri, N. Marzari, and F. Mauri. *Phonon Anharmonicities in Graphite and Graphene*. Phys. Rev. Lett. **99**, 176802 (2007). 23, 96, 110

[Boukhicha13] M. Boukhicha, M. Calandra, M.-A. Measson, O. Lancry, and A. Shukla. *Anharmonic phonons in few-layer MoS_2: Raman spectroscopy of ultralow energy compression and shear modes*. Phys. Rev. B **87**, 195316 (2013). 128, 131, 149, 151, 225

[Britnell13] L. Britnell, R. Ribeiro, A. Eckmann, R. Jalil, B. Belle, A. Mishchenko, Y.-J. Kim, R. Gorbachev, T. Georgiou, S. Morozov, et al. *Strong light-matter interactions in heterostructures of atomically thin films*. Science **340** (6138), 1311–1314 (2013). 49, 51

[Brumme15] T. Brumme, M. Calandra, and F. Mauri. *First-principles theory of field-effect doping in transition-metal dichalcogenides: Structural properties, electronic structure, Hall coefficient, and electrical conductivity*. Phys. Rev. B **91**, 155436 (2015). 173

[Bruna14] M. Bruna, A. K. Ott, M. Ijäs, D. Yoon, U. Sassi, and A. C. Ferrari. *Doping Dependence of the Raman Spectrum of Defected Graphene*. ACS Nano **8** (7), 7432–7441 (2014). 105, 109, 119, 122, 219

[Buckley77] R. G. Buckley and D. Beaglehole. *Absorptance of thin films*. Appl. Opt. **16** (9), 2495–2499 (1977). 35, 160, 255, 257

[Buscema14] M. Buscema, G. A. Steele, H. S. van der Zant, and A. Castellanos-Gomez. *The effect of the substrate on the Raman and photoluminescence emission of single-layer MoS_2*. Nano Res. **7** (4), 561–571 (2014). 92, 257

[Calizo07] I. Calizo, A. A. Balandin, W. Bao, F. Miao, and C. N. Lau. *Temperature Dependence of the Raman Spectra of Graphene and Graphene Multilayers*. Nano Lett. **7** (9), 2645–2649 (2007). 105

[Cappelluti13] E. Cappelluti, R. Roldán, J. A. Silva-Guillén, P. Ordejón, and F. Guinea. *Tight-binding model and direct-gap/indirect-gap transition in single-layer and multilayer MoS_2*. Phys. Rev. B **88**, 075409 (2013). 173

[Cardona83] M. E. Cardona. *Light scattering in solids I*. Light Scattering in Solids I: Introductory Concepts **8** (1983). 73, 100

[Carvalho15] B. R. Carvalho, L. M. Malard, J. M. Alves, C. Fantini, and M. A. Pimenta. *Symmetry-Dependent Exciton-Phonon Coupling in 2D and Bulk MoS_2 Observed by Resonance Raman Scattering*. Phys. Rev. Lett. **114**, 136403 (2015). 206

[Casey12] H. J. Casey. *Heterostructure lasers*. Elsevier, 2012. 42

[Casiraghi07] C. Casiraghi, S. Pisana, K. S. Novoselov, A. K. Geim, and A. C. Ferrari. *Raman fingerprint of charged impurities in graphene*. Appl. Phys. Lett. **91** (23), 233108 (2007). 112, 220

[Castellanos-Gomez14] A. Castellanos-Gomez, M. Buscema, R. Molenaar, V. Singh, L. Janssen, H. S. J. van der Zant, and G. A. Steele. *Deterministic transfer of two-dimensional materials by all-dry viscoelastic stamping*. 2D Mater. **1** (1), 011002 (2014). 43, 81, 82, 84, 228

[Castro Neto09] A. H. Castro Neto, F. Guinea, N. M. R. Peres, K. S. Novoselov, and A. K. Geim. *The electronic properties of graphene*. Rev. Mod. Phys. **81**, 109–162 (2009). 20, 21

[Ceballos14] F. Ceballos, M. Z. Bellus, H.-Y. Chiu, and H. Zhao. *Ultrafast charge separation and indirect exciton formation in a MoS2–MoSe2 van der Waals heterostructure*. ACS Nano **8** (12), 12717–12724 (2014). 46, 47

[Ceballos15] F. Ceballos, M. Z. Bellus, H.-Y. Chiu, and H. Zhao. *Probing charge transfer excitons in a MoSe 2–WS 2 van der Waals heterostructure*. Nanoscale **7** (41), 17523–17528 (2015). 46, 47

[Chakraborty12] B. Chakraborty, A. Bera, D. V. S. Muthu, S. Bhowmick, U. V. Waghmare, and A. K. Sood. *Symmetry-dependent phonon renormalization in monolayer MoS_2 transistor*. Phys. Rev. B **85** (16), 161403 (2012). 194

[Chakraborty13] B. Chakraborty, H. Matte, A. Sood, and C. Rao. *Layer-dependent resonant Raman scattering of a few layer MoS2*. J. Raman Spectrosc. **44** (1), 92–96 (2013). 206

[Chattrakun13] K. Chattrakun, S. Huang, K. Watanabe, T. Taniguchi, A. Sandhu, and B. J. LeRoy. *Gate dependent Raman spectroscopy of graphene on hexagonal boron nitride*. J. Phys.: Condens. Matter **25** (50), 505304 (2013). 109

[Cheiwchanchamnangij12] T. Cheiwchanchamnangij and W. R. L. Lambrecht. *Quasiparticle band structure calculation of monolayer, bilayer, and bulk MoS_2*. Phys. Rev. B **85**, 205302 (2012). 35

[Chen10] Z. Chen, S. Berciaud, C. Nuckolls, T. F. Heinz, and L. E. Brus. *Energy transfer from individual semiconductor nanocrystals to graphene*. ACS Nano **4** (5), 2964–2968 (2010). 47, 233

[Chen11] C.-F. Chen, C.-H. Park, B. W. Boudouris, J. Horng, B. Geng, C. Girit, A. Zettl, M. F. Crommie, R. A. Segalman, S. G. Louie, and F. Wang. *Controlling inelastic light scattering quantum pathways in graphene*. Nature **471** (7340), 617–620 (2011). 96, 97, 99, 109, 116

[Chen13] S.-Y. Chen, Y.-Y. Lu, F.-Y. Shih, P.-H. Ho, Y.-F. Chen, C.-W. Chen, Y.-T. Chen, and W.-H. Wang. *Biologically inspired graphene-chlorophyll phototransistors with high gain*. Carbon **63**, 23–29 (2013). 49

[Chen15] S.-Y. Chen, C. Zheng, M. S. Fuhrer, and J. Yan. *Helicity-resolved Raman scattering of MoS2, MoSe2, WS2, and WSe2 atomic layers*. Nano Lett. **15** (4), 2526–2532 (2015). 128, 131, 144, 155, 225

[Chenet15] D. A. Chenet, O. B. Aslan, P. Y. Huang, C. Fan, A. M. van der Zande, T. F. Heinz, and J. C. Hone. *In-Plane Anisotropy in Mono- and Few-Layer ReS2 Probed by Raman Spectroscopy and Scanning Transmission Electron Microscopy*. Nano Lett. **15** (9), 5667-5672 (2015). 210

[Cheng14] R. Cheng, D. Li, H. Zhou, C. Wang, A. Yin, S. Jiang, Y. Liu, Y. Chen, Y. Huang, and X. Duan. *Electroluminescence and Photocurrent Generation from Atomically Sharp WSe_2/MoS_2 Heterojunction p–n Diodes*. Nano Lett. **14** (10), 5590–5597 (2014). 51, 52, 182

[Chernikov14] A. Chernikov, T. C. Berkelbach, H. M. Hill, A. Rigosi, Y. Li, O. B. Aslan, D. R. Reichman, M. S. Hybertsen, and T. F. Heinz. *Exciton Binding Energy and Non-*

hydrogenic Rydberg Series in Monolayer WS_2. Phys. Rev. Lett. **113** (7), 076802 (2014). 35, 36

[Chhowalla13] M. Chhowalla, H. S. Shin, G. Eda, L.-J. Li, K. P. Loh, and H. Zhang. *The chemistry of two-dimensional layered transition metal dichalcogenide nanosheets*. Nat. Chem. **5** (4), 263–275 (2013). 12, 32

[Cohen-Tannoudji79] C. Cohen-Tannoudji, B. Diu, F. Laloë, and B. Crasemann. *Quantum mechanics*, (1979). 73

[Cui15] Q. Cui, J. He, M. Z. Bellus, M. Mirzokarimov, T. Hofmann, H.-Y. Chiu, M. Antonik, D. He, Y. Wang, and H. Zhao. *Transient absorption measurements on anisotropic monolayer ReS2*. Small **11** (41), 5565–5571 (2015). 210

[Curie94] P. Curie. *Sur la symétrie dans les phénomènes physiques, symétrie d'un champ électrique et d'un champ magnétique*. J. Phys. **3** (1), 393–416 (1894). 237

[Das08] A. Das, S. Pisana, B. Chakraborty, S. Piscanec, S. K. Saha, U. V. Waghmare, K. S. Novoselov, H. R. Krishnamurthy, A. K. Geim, A. C. Ferrari, and A. K. Sood. *Monitoring dopants by Raman scattering in an electrochemically top-gated graphene transistor*. Nat. Nanotechnol. **3** (4), 210–215 (2008). 29, 87, 106, 107, 109, 116, 217, 219

[Das09] A. Das, B. Chakraborty, S. Piscanec, S. Pisana, A. K. Sood, and A. C. Ferrari. *Phonon renormalization in doped bilayer graphene*. Phys. Rev. B **79** (15), 155417 (2009). 29, 109, 116, 219

[Davydov64] A. S. Davydov. *THE THEORY OF MOLECULAR EXCITONS*. Sov. Phys. Usp. **7** (2), 145 (1964). 223

[Davydov71] A. S. Davydov. *Theory of molecular excitons*. In *Theory of Molecular Excitons*. Springer US, (1971). 128, 223

[De Fazio16] D. De Fazio, I. Goykhman, D. Yoon, M. Bruna, A. Eiden, S. Milana, U. Sassi, M. Barbone, D. Dumcenco, K. Marinov, A. Kis, and A. C. Ferrari. *High Responsivity, Large-Area Graphene/MoS2 Flexible Photodetectors*. ACS Nano **10** (9), 8252-8262 (2016). 187

[Dean10] C. R. Dean, A. F. Young, I. Meric, C. Lee, L. Wang, S. Sorgenfrei, K. Watanabe, T. Taniguchi, P. Kim, K. Shepard, et al. *Boron nitride substrates for high-quality graphene electronics*. Nat. Nanotechnol. **5** (10), 722–726 (2010). 43, 49

[Dean13] C. Dean, L. Wang, P. Maher, C. Forsythe, F. Ghahari, Y. Gao, J. Katoch, M. Ishigami, P. Moon, M. Koshino, et al. *Hofstadter/'s butterfly and the fractal quantum Hall effect in moire superlattices*. Nature **497** (7451), 598–602 (2013). 12, 214

[Dexter53] D. L. Dexter. *A theory of sensitized luminescence in solids*. The Journal of Chemical Physics **21** (5), 836–850 (1953). 47

[Dresselhaus99] M. Dresselhaus. *Solid State Physics Part II Optical Properties of Solids*. Lecture Notes (1999). 21

[Dresselhaus07] M. S. Dresselhaus, G. Dresselhaus, and A. Jorio. *Group theory: application to the physics of condensed matter*. Springer Science & Business Media, 2007. 55, 57, 60, 61, 63, 74, 237, 243, 245

[Dubay03] O. Dubay and G. Kresse. *Accurate density functional calculations for the phonon dispersion relations of graphite layer and carbon nanotubes*. Phys. Rev. B **67**, 035401 (2003). 23

[Dufferwiel15] S. Dufferwiel, S. Schwarz, F. Withers, A. Trichet, F. Li, M. Sich, O. Del Pozo-Zamudio, C. Clark, A. Nalitov, D. Solnyshkov, et al. *Exciton-polaritons in van der Waals heterostructures embedded in tunable microcavities*. Nat. Commun. **6** (2015). 49

[Efetov10] D. K. Efetov and P. Kim. *Controlling Electron-Phonon Interactions in Graphene at Ultrahigh Carrier Densities*. Phys. Rev. Lett. **105** (25), 256805 (2010). 105, 109, 122, 219

[Elias11] D. Elias, R. Gorbachev, A. Mayorov, S. Morozov, A. Zhukov, P. Blake, L. Ponomarenko, I. Grigorieva, K. Novoselov, F. Guinea, et al. *Dirac cones reshaped by interaction effects in suspended graphene*. Nat. Phys. **7** (9), 701–704 (2011). 20

[Engel12] M. Engel, M. Steiner, A. Lombardo, A. C. Ferrari, H. v. Löhneysen, P. Avouris, and R. Krupke. *Light–matter interaction in a microcavity-controlled graphene transistor*. Nat. Commun. **3**, 906 (2012). 30

[Fang12] Z. Fang, Y. Wang, Z. Liu, A. Schlather, P. M. Ajayan, F. H. Koppens, P. Nordlander, and N. J. Halas. *Plasmon-induced doping of graphene*. ACS Nano **6** (11), 10222–10228 (2012). 49, 50

[Fang14] H. Fang, C. Battaglia, C. Carraro, S. Nemsak, B. Ozdol, J. S. Kang, H. A. Bechtel, S. B. Desai, F. Kronast, A. A. Unal, G. Conti, C. Conlon, G. K. Palsson, M. C. Martin, A. M. Minor, C. S. Fadley, E. Yablonovitch, R. Maboudian, and A. Javey. *Strong interlayer coupling in van der Waals heterostructures built from single-layer chalcogenides*. Proc. Natl. Acad. Sci. U. S. A. **111** (17), 6198–6202 (2014). 46, 182

[Faugeras15] C. Faugeras, S. Berciaud, P. Leszczynski, Y. Henni, K. Nogajewski, M. Orlita, T. Taniguchi, K. Watanabe, C. Forsythe, P. Kim, R. Jalil, A. K. Geim, D. M. Basko, and M. Potemski. *Landau Level Spectroscopy of Electron-Electron Interactions in Graphene*. Phys. Rev. Lett. **114**, 126804 (2015). 20

[Federspiel15a] F. Federspiel. *Etude optique du transfert d'énergie entre une nanostructure semiconductrice unique et un feuillet de graphène*. PhD thesis, Université de Strasbourg, (2015). 13, 48

[Federspiel15b] F. Federspiel, G. Froehlicher, M. Nasilowski, S. Pedetti, A. Mahmood, B. Doudin, S. Park, J.-O. Lee, D. Halley, B. Dubertret, et al. *Distance dependence of the energy transfer rate from a single semiconductor nanostructure to graphene*. Nano Lett. **15** (2), 1252–1258 (2015). 46, 47, 209, 233

[Feng15] Y. Feng, W. Zhou, Y. Wang, J. Zhou, E. Liu, Y. Fu, Z. Ni, X. Wu, H. Yuan, F. Miao, B. Wang, X. Wan, and D. Xing. *Raman vibrational spectra of bulk to monolayer* ReS_2 *with lower symmetry*. Phys. Rev. B **92**, 054110 (2015). 210

[Ferrari00] A. C. Ferrari and J. Robertson. *Interpretation of Raman spectra of disordered and amorphous carbon*. Phys. Rev. B **61** (20), 14095–14107 (2000). 123

[Ferrari06] A. C. Ferrari, J. C. Meyer, V. Scardaci, C. Casiraghi, M. Lazzeri, F. Mauri, S. Piscanec, D. Jiang, K. S. Novoselov, S. Roth, and A. K. Geim. *Raman Spectrum of Graphene and Graphene Layers*. Phys. Rev. Lett. **97**, 187401 (2006). 24, 102

[Ferrari13] A. C. Ferrari and D. M. Basko. *Raman spectroscopy as a versatile tool for studying the properties of graphene*. Nat. Nanotechnol. **8** (4), 235–246 (2013). 13, 25, 26, 61, 71, 96, 99, 101, 103, 104, 215, 217

[Ferrari15] A. C. Ferrari, F. Bonaccorso, V. Fal'Ko, K. S. Novoselov, S. Roche, P. Bøggild, S. Borini, F. H. Koppens, V. Palermo, N. Pugno, et al. *Science and technology roadmap for graphene, related two-dimensional crystals, and hybrid systems*. Nanoscale **7** (11), 4598–4810 (2015). 13, 214

[Feynman60] R. P. Feynman. *There's plenty of room at the bottom*. Engineering and science **23** (5), 22–36 (1960). 11, 213

[Fogler14] M. M. Fogler, L. V. Butov, and K. S. Novoselov. *High-temperature superfluidity with indirect excitons in van der Waals heterostructures*. Nat. Commun. **5** (2014). 13

[Förster48] T. Förster. *Zwischenmolekulare energiewanderung und fluoreszenz*. Ann. Phys. **437** (1-2), 55–75 (1948). 47

[Forster13] F. Forster, A. Molina-Sanchez, S. Engels, A. Epping, K. Watanabe, T. Taniguchi, L. Wirtz, and C. Stampfer. *Dielectric screening of the Kohn anomaly of graphene on hexagonal boron nitride*. Phys. Rev. B **88**, 085419 (2013). 186, 189

[Fox10] M. Fox. *Optical properties of solids*, volume 3. Oxford university press, 2010. 69, 163, 166

[Frank11] O. Frank, M. Mohr, J. Maultzsch, C. Thomsen, I. Riaz, R. Jalil, K. S. Novoselov, G. Tsoukleri, J. Parthenios, K. Papagelis, et al. *Raman 2D-band splitting in graphene: theory and experiment*. ACS Nano **5** (3), 2231–2239 (2011). 102

[Freitag10] M. Freitag, H.-Y. Chiu, M. Steiner, V. Perebeinos, and P. Avouris. *Thermal infrared emission from biased graphene*. Nat. Nanotechnol. **5** (7), 497-501 (2010). 22, 30

[Frindt63] R. Frindt and A. Yoffe. *Physical properties of layer structures: optical properties and photoconductivity of thin crystals of molybdenum disulphide*. In *Proceedings of the Royal Society of London A: Mathematical, Physical and Engineering Sciences*, volume 273, pages 69–83. The Royal Society, (1963). 12

[Frindt66] R. F. Frindt. *Single crystals of MoS2 several molecular layers thick*. J. Appl. Phys. **37** (4), 1928–1929 (1966). 11, 79, 213

[Froehlicher15] G. Froehlicher and S. Berciaud. *Raman spectroscopy of electrochemically gated graphene transistors: Geometrical capacitance, electron-phonon, electron-electron, and electron-defect scattering*. Phys. Rev. B **91**, 205413 (2015). 123

[Fromm13] F. Fromm, P. Wehrfritz, M. Hundhausen, and T. Seyller. *Looking behind the scenes: Raman spectroscopy of top-gated epitaxial graphene through the substrate*. New J. Phys. **15** (11), 113006 (2013). 120

[Fuchs08] J.-N. Fuchs and M. O. Goerbig. *Introduction to the physical properties of graphene*. Lecture Notes (2008). 19

[Furchi14a] M. M. Furchi, D. K. Polyushkin, A. Pospischil, and T. Mueller. *Mechanisms of photoconductivity in atomically thin MoS2*. Nano Lett. **14** (11), 6165–6170 (2014). 40

[Furchi14b] M. M. Furchi, A. Pospischil, F. Libisch, J. Burgdörfer, and T. Mueller. *Photovoltaic Effect in an Electrically Tunable van der Waals Heterojunction*. Nano Lett. **14** (8), 4785–4791 (2014). 51, 52, 182

[Gabor11] N. M. Gabor, J. C. Song, Q. Ma, N. L. Nair, T. Taychatanapat, K. Watanabe, T. Taniguchi, L. S. Levitov, and P. Jarillo-Herrero. *Hot carrier–assisted intrinsic photoresponse in graphene*. Science **334** (6056), 648–652 (2011). 30, 31

[Gan13] X. Gan, R.-J. Shiue, Y. Gao, I. Meric, T. F. Heinz, K. Shepard, J. Hone, S. Assefa, and D. Englund. *Chip-integrated ultrafast graphene photodetector with high responsivity*. Nat. Photonics **7** (11), 883–887 (2013). 30

[Gao16] J. Gao, B. Li, J. Tan, P. Chow, T.-M. Lu, and N. Koratkar. *Aging of transition metal dichalcogenide monolayers*. ACS Nano **10** (2), 2628–2635 (2016). 35, 82, 196

[Gaudreau13] L. Gaudreau, K. Tielrooij, G. Prawiroatmodjo, J. Osmond, F. G. de Abajo, and F. Koppens. *Universal distance-scaling of nonradiative energy transfer to graphene*. Nano Lett. **13** (5), 2030–2035 (2013). 47, 233

[Geim07] A. K. Geim and K. S. Novoselov. *The Rise of Graphene*. Nat. Mater. **6**, 183-191 (2007). 28

[Geim13] A. K. Geim and I. V. Grigorieva. *Van der Waals heterostructures*. Nature **499** (7459), 419–425 (2013). 12, 42, 214

[George08] P. A. George, J. Strait, J. Dawlaty, S. Shivaraman, M. Chandrashekhar, F. Rana, and M. G. Spencer. *Ultrafast optical-pump terahertz-probe spectroscopy of the carrier relaxation and recombination dynamics in epitaxial graphene*. Nano Lett. **8** (12), 4248–4251 (2008). 22

[Ghosh83] P. N. Ghosh and C. R. Maiti. *Interlayer force and Davydov splitting in* $2H-MoS_2$. Phys. Rev. B **28**, 2237–2239 (1983). 142

[Ghosh10] S. Ghosh, W. Bao, D. L. Nika, S. Subrina, E. P. Pokatilov, C. N. Lau, and A. A. Balandin. *Dimensional crossover of thermal transport in few-layer graphene*. Nat. Mater. **9** (7), 555–558 (2010). 12, 214

[Giannozzi09] P. Giannozzi, S. Baroni, N. Bonini, M. Calandra, R. Car, C. Cavazzoni, D. Ceresoli, G. L. Chiarotti, M. Cococcioni, I. Dabo, A. D. Corso, S. de Gironcoli, S. Fabris, G. Fratesi, R. Gebauer, U. Gerstmann, C. Gougoussis, A. Kokalj, M. Lazzeri, L. Martin-Samos, N. Marzari, F. Mauri, R. Mazzarello, S. Paolini, A. Pasquarello, L. Paulatto, C. Sbraccia, S. Scandolo, G. Sclauzero, A. P. Seitsonen, A. Smogunov, P. Umari, and R. M. Wentzcovitch. *QUANTUM ESPRESSO: a modular and open-source software project for quantum simulations of materials*. J. Phys.: Condens. Matter **21** (39), 395502 (2009). 139

[Giovannetti08] G. Giovannetti, P. A. Khomyakov, G. Brocks, V. M. Karpan, J. van den Brink, and P. J. Kelly. *Doping Graphene with Metal Contacts*. Phys. Rev. Lett. **101**, 026803 (2008). 29

[Glazov15] M. Glazov, E. Ivchenko, G. Wang, T. Amand, X. Marie, B. Urbaszek, and B. Liu. *Spin and valley dynamics of excitons in transition metal dichalcogenide monolayers*. physica status solidi (b) **252** (11), 2349–2362 (2015). 37, 38, 226

[Goldstein16] T. Goldstein, S.-Y. Chen, D. Xiao, A. Ramasubramaniam, and J. Yan. *Raman scattering and anomalous Stokes anti-Stokes ratio in MoTe2 atomic layers*. arXiv preprint arXiv:1603.03740 (2016). 73

[Gorbachev11] R. V. Gorbachev, I. Riaz, R. R. Nair, R. Jalil, L. Britnell, B. D. Belle, E. W. Hill, K. S. Novoselov, K. Watanabe, T. Taniguchi, et al. *Hunting for monolayer boron nitride: optical and Raman signatures*. Small **7** (4), 465–468 (2011). 92

[Graf07] D. Graf, F. Molitor, K. Ensslin, C. Stampfer, A. Jungen, C. Hierold, and L. Wirtz. *Spatially resolved Raman spectroscopy of single-and few-layer graphene*. Nano Lett. **7** (2), 238–242 (2007). 26, 102

[Grüneis09] A. Grüneis, J. Serrano, A. Bosak, M. Lazzeri, S. L. Molodtsov, L. Wirtz, C. Attaccalite, M. Krisch, A. Rubio, F. Mauri, and T. Pichler. *Phonon surface mapping of graphite: Disentangling quasi-degenerate phonon dispersions*. Phys. Rev. B **80**, 085423 (2009). 23, 24

[Grzeszczyk16] M. Grzeszczyk, K. Gołasa, M. Zinkiewicz, K. Nogajewski, M. R. Molas, M. Potemski, A. Wysmołek, and A. Babiński. *Raman scattering of few-layers $MoTe_2$*. 2D Mater. **3** (2), 025010 (2016). 151, 154, 161, 206

[Guo15a] H. Guo, T. Yang, M. Yamamoto, L. Zhou, R. Ishikawa, K. Ueno, K. Tsukagoshi, Z. Zhang, M. S. Dresselhaus, and R. Saito. *Double resonance Raman modes in monolayer and few-layer* $MoTe_2$. Phys. Rev. B **91**, 205415 (2015). 129, 223

[Guo15b] Y. Guo, D. Sun, B. Ouyang, A. Raja, J. Song, T. F. Heinz, and L. E. Brus. *Probing the dynamics of the metallic-to-semiconducting structural phase transformation in MoS2 crystals*. Nano Lett. **15** (8), 5081–5088 (2015). 32

[Gutiérrez12] H. R. Gutiérrez, N. Perea-López, A. L. Elías, A. Berkdemir, B. Wang, R. Lv, F. López-Urías, V. H. Crespi, H. Terrones, and M. Terrones. *Extraordinary room-temperature photoluminescence in triangular WS2 monolayers*. Nano Lett. **13** (8), 3447–3454 (2012). 34

[Haigh12] S. Haigh, A. Gholinia, R. Jalil, S. Romani, L. Britnell, D. Elias, K. Novoselov, L. Ponomarenko, A. Geim, and R. Gorbachev. *Cross-sectional imaging of individual layers and buried interfaces of graphene-based heterostructures and superlattices*. Nat. Mater. **11** (9), 764–767 (2012). 44

[Hasegawa06] Y. Hasegawa, R. Konno, H. Nakano, and M. Kohmoto. *Zero modes of tight-binding electrons on the honeycomb lattice*. Phys. Rev. B **74**, 033413 (2006). 19

[Haug92] A. Haug. *Auger recombination in quantum well semiconductors: calculation with realistic energy bands*. Semicond. Sci. Technol. **7** (11), 1337 (1992). 177

[He14a] J. He, N. Kumar, M. Z. Bellus, H.-Y. Chiu, D. He, Y. Wang, and H. Zhao. *Electron transfer and coupling in graphene–tungsten disulfide van der Waals heterostructures*. Nat. Commun. **5** (2014). 46, 182, 187, 195, 201

[He14b] K. He, N. Kumar, L. Zhao, Z. Wang, K. F. Mak, H. Zhao, and J. Shan. *Tightly Bound Excitons in Monolayer* WSe_2. Phys. Rev. Lett. **113** (2), 026803 (2014). 35, 36

[Hecht01] E. Hecht. *Optics (4^{th} Edition)*. Addison-Wesley, 2001. 252, 254

[Herziger12] F. Herziger, P. May, and J. Maultzsch. *Layer-number determination in graphene by out-of-plane phonons*. Phys. Rev. B **85**, 235447 (2012). 27

[Hilton92] M. R. Hilton and P. D. Fleischauer. *Applications of solid lubricant films in spacecraft*. Surf. Coat. Technol. **54**, 435–441 (1992). 11

[Ho97] C. H. Ho, P. C. Liao, Y. S. Huang, T. R. Yang, and K. K. Tiong. *Optical absorption of ReS2 and ReSe2 single crystals*. J. Appl. Phys. **81** (9), 6380-6383 (1997). 32, 147, 210

[Ho98] C. H. Ho, Y. S. Huang, K. K. Tiong, and P. C. Liao. *Absorption-edge anisotropy in* ReS_2 *and* $ReSe_2$ *layered semiconductors*. Phys. Rev. B **58**, 16130–16135 (1998). 32, 147, 210

[Ho04] C. H. Ho, H. W. Lee, and C. C. Wu. *Polarization sensitive behaviour of the band-edge transitions in ReS 2 and ReSe 2 layered semiconductors*. J. Phys.: Condens. Matter **16** (32), 5937 (2004). 32, 147, 210

[Hofmann14] J. Hofmann, E. Barnes, and S. Das Sarma. *Why Does Graphene Behave as a Weakly Interacting System?* Phys. Rev. Lett. **113**, 105502 (2014). 20

[Hofstadter76] D. R. Hofstadter. *Energy levels and wave functions of Bloch electrons in rational and irrational magnetic fields*. Phys. Rev. B **14**, 2239–2249 (1976). 12, 214

[Hong14] X. Hong, J. Kim, S.-F. Shi, Y. Zhang, C. Jin, Y. Sun, S. Tongay, J. Wu, Y. Zhang, and F. Wang. *Ultrafast charge transfer in atomically thin* MoS_2/WS_2 *heterostructures*. Nat. Nanotechnol. **9** (9), 682–686 (2014). 46, 47, 182

[Houdy06] P. Houdy, C. Dupas, and M. Lahmani. *Les nanosciences. 1-Nanotechnologies et nanophysique*, volume 737. La Collection Echelle, Edition Bellin, 2006. 42

[Huang09] M. Huang, H. Yan, C. Chen, D. Song, T. F. Heinz, and J. Hone. *Phonon softening and crystallographic orientation of strained graphene studied by Raman spectroscopy*. Proceedings of the National Academy of Sciences **106** (18), 7304–7308 (2009). 26, 96

[Huang10] M. Huang, H. Yan, T. F. Heinz, and J. Hone. *Probing strain-induced electronic structure change in graphene by Raman spectroscopy*. Nano Lett. **10** (10), 4074–4079 (2010). 102

[Hunt13] B. Hunt, J. Sanchez-Yamagishi, A. Young, M. Yankowitz, B. J. LeRoy, K. Watanabe, T. Taniguchi, P. Moon, M. Koshino, P. Jarillo-Herrero, et al. *Massive Dirac fermions and Hofstadter butterfly in a van der Waals heterostructure*. Science **340** (6139), 1427–1430 (2013). 12, 214

[Jackson99] J. D. Jackson. *Classical electrodynamics*. Wiley, 1999. 67, 70

[Jares-Erijman03] E. A. Jares-Erijman and T. M. Jovin. *FRET imaging*. Nat. Biotechnol. **21** (11), 1387–1395 (2003). 47

[Joensen86] P. Joensen, R. Frindt, and S. R. Morrison. *Single-layer MoS2*. Mater. Res. Bull. **21** (4), 457–461 (1986). 11, 213

[Jones13] A. M. Jones, H. Yu, N. J. Ghimire, S. Wu, G. Aivazian, J. S. Ross, B. Zhao, J. Yan, D. G. Mandrus, D. Xiao, et al. *Optical generation of excitonic valley coherence in monolayer WSe2*. Nat. Nanotechnol. **8** (9), 634–638 (2013). 37

[Jones16] A. M. Jones, H. Yu, J. R. Schaibley, J. Yan, D. G. Mandrus, T. Taniguchi, K. Watanabe, H. Dery, W. Yao, and X. Xu. *Excitonic luminescence upconversion in a two-dimensional semiconductor*. Nat. Phys. **12** (4), 323–327 (2016). 205

[Ju14] L. Ju, J. Velasco Jr, E. Huang, S. Kahn, C. Nosiglia, H.-Z. Tsai, W. Yang, T. Taniguchi, K. Watanabe, Y. Zhang, et al. *Photoinduced doping in heterostructures of graphene and boron nitride*. Nat. Nanotechnol. **9** (5), 348–352 (2014). 209

[Jung09] N. Jung, N. Kim, S. Jockusch, N. J. Turro, P. Kim, and L. Brus. *Charge Transfer Chemical Doping of Few Layer Graphenes: Charge Distribution and Band Gap Formation*. Nano Lett. **9** (12), 4133–4137 (2009). 27

[Kaasbjerg12] K. Kaasbjerg, K. S. Thygesen, and K. W. Jacobsen. *Phonon-limited mobility in n-type single-layer MoS_2 from first principles*. Phys. Rev. B **85**, 115317 (2012). 39

[Kalbac10] M. Kalbac, A. Reina-Cecco, H. Farhat, J. Kong, L. Kavan, and M. S. Dresselhaus. *The Influence of Strong Electron and Hole Doping on the Raman Intensity of Chemical Vapor-Deposition Graphene*. ACS Nano **4** (10), 6055–6063 (2010). 96, 97, 105, 109, 111, 116, 122

[Kampfrath05] T. Kampfrath, L. Perfetti, F. Schapper, C. Frischkorn, and M. Wolf. *Strongly Coupled Optical Phonons in the Ultrafast Dynamics of the Electronic Energy and Current Relaxation in Graphite*. Phys. Rev. Lett. **95**, 187403 (2005). 22

[Karssemeijer11] L. Karssemeijer and A. Fasolino. *Phonons of graphene and graphitic materials derived from the empirical potential LCBOPII*. Surf. Sci. **605** (17), 1611–1615 (2011). 151

[Katzke04] H. Katzke, P. Tolédano, and W. Depmeier. *Phase transitions between polytypes and intralayer superstructures in transition metal dichalcogenides*. Phys. Rev. B **69**, 134111 (2004). 32

[Khelladi75] F. Z. Khelladi. *Davydov splitting in raman spectra of anthracene C14 H10 and C14 D10 single crystals*. Chem. Phys. Lett. **34** (3), 490–496 (1975). 128

[Kheng93] K. Kheng, R. T. Cox, M. Y. d' Aubigné, F. Bassani, K. Saminadayar, and S. Tatarenko. *Observation of negatively charged excitons X^- in semiconductor quantum wells*. Phys. Rev. Lett. **71**, 1752–1755 (1993). 37

[Kim15a] K. Kim, S. Larentis, B. Fallahazad, K. Lee, J. Xue, D. C. Dillen, C. M. Corbet, and E. Tutuc. *Band alignment in WSe2–graphene heterostructures*. ACS Nano **9** (4), 4527–4532 (2015). 44, 200, 208

[Kim15b] Y. D. Kim, H. Kim, Y. Cho, J. H. Ryoo, C.-H. Park, P. Kim, Y. S. Kim, S. Lee, Y. Li, S.-N. Park, et al. *Bright visible light emission from graphene*. Nat. Nanotechnol. (2015). 22, 30, 31

[Kim16] K. Kim, J.-U. Lee, D. Nam, and H. Cheong. *Davydov splitting and excitonic resonance effects in Raman spectra of few-Layer MoSe2*. ACS Nano **10** (8), 8113–8120 (2016). 144, 145, 151, 155, 158, 161, 206

[Knox08] K. R. Knox, S. Wang, A. Morgante, D. Cvetko, A. Locatelli, T. O. Mentes, M. A. Niño, P. Kim, and R. M. Osgood. *Spectromicroscopy of single and multilayer graphene supported by a weakly interacting substrate*. Phys. Rev. B **78**, 201408 (2008). 219

[Kohn59] W. Kohn. *Image of the Fermi Surface in the Vibration Spectrum of a Metal*. Phys. Rev. Lett. **2**, 393–394 (1959). 23, 111

[Kośmider13] K. Kośmider and J. Fernández-Rossier. *Electronic properties of the MoS_2-WS_2 heterojunction*. Phys. Rev. B **87**, 075451 (2013). 44

[Kolobov16] A. V. Kolobov and J. Tominaga. *Two-Dimensional Transition-Metal Dichalcogenides*, volume 239. Springer, 2016. 13, 215

[Komsa13] H.-P. Komsa and A. V. Krasheninnikov. *Electronic structures and optical properties of realistic transition metal dichalcogenide heterostructures from first principles*. Phys. Rev. B **88**, 085318 (2013). 186

[Konstantatos12] G. Konstantatos, M. Badioli, L. Gaudreau, J. Osmond, M. Bernechea, F. P. G. de Arquer, F. Gatti, and F. H. Koppens. *Hybrid graphene-quantum dot phototransistors with ultrahigh gain*. Nat. Nanotechnol. **7** (6), 363–368 (2012). 49, 50

[Koppens14] F. Koppens, T. Mueller, P. Avouris, A. Ferrari, M. Vitiello, and M. Polini. *Photodetectors based on graphene, other two-dimensional materials and hybrid systems*. Nat. Nanotechnol. **9** (10), 780–793 (2014). 13, 30, 31, 52, 215

[Korn11] T. Korn, S. Heydrich, M. Hirmer, J. Schmutzler, and C. Schüller. *Low-temperature photocarrier dynamics in monolayer MoS2*. Appl. Phys. Lett. **99** (10), 102109 (2011). 37, 176, 182

[Kozawa16] D. Kozawa, A. Carvalho, I. Verzhbitskiy, F. Giustiniano, Y. Miyauchi, S. Mouri, A. Castro Neto, K. Matsuda, and G. Eda. *Evidence for fast interlayer energy transfer in MoSe2/WS2 heterostructures*. Nano Lett. (2016). 46, 48, 233

[Kretinin14] A. Kretinin, Y. Cao, J. Tu, G. Yu, R. Jalil, K. Novoselov, S. Haigh, A. Gholinia, A. Mishchenko, M. Lozada, et al. *Electronic properties of graphene encapsulated with different two-dimensional atomic crystals*. Nano Lett. **14** (6), 3270–3276 (2014). 43, 44, 228

[Kufer15] D. Kufer, I. Nikitskiy, T. Lasanta, G. Navickaite, F. H. Koppens, and G. Konstantatos. *Hybrid 2D–0D MoS2–PbS quantum dot photodetectors*. Adv. Mater. **27** (1), 176–180 (2015). 49

[Kumar13] N. Kumar, S. Najmaei, Q. Cui, F. Ceballos, P. M. Ajayan, J. Lou, and H. Zhao. *Second harmonic microscopy of monolayer MoS_2*. Phys. Rev. B **87**, 161403 (2013). 33

[Kumar14] N. Kumar, Q. Cui, F. Ceballos, D. He, Y. Wang, and H. Zhao. *Exciton-exciton annihilation in $MoSe_2$ monolayers*. Phys. Rev. B **89**, 125427 (2014). 174, 176, 226

[Kürti02] J. Kürti, V. Zólyomi, A. Grüneis, and H. Kuzmany. *Double resonant Raman phenomena enhanced by van Hove singularities in single-wall carbon nanotubes*. Phys. Rev. B **65**, 165433 (2002). 102

[Lagarde14] D. Lagarde, L. Bouet, X. Marie, C. R. Zhu, B. L. Liu, T. Amand, P. H. Tan, and B. Urbaszek. *Carrier and Polarization Dynamics in Monolayer* MoS_2. Phys. Rev. Lett. **112**, 047401 (2014). 37

[Landau80] L. D. Landau and E. Lifshitz. *Statistical physics, part I*, (1980). 11

[Larentis12] S. Larentis, B. Fallahazad, and E. Tutuc. *Field-effect transistors and intrinsic mobility in ultra-thin MoSe2 layers*. Appl. Phys. Lett. **101** (22), 223104 (2012). 194

[Late14] D. J. Late, S. N. Shirodkar, U. V. Waghmare, V. P. Dravid, and C. Rao. *Thermal Expansion, Anharmonicity and Temperature-Dependent Raman Spectra of Single- and Few-Layer MoSe2 and WSe2*. ChemPhysChem **15** (8), 1592–1598 (2014). 194

[Lazzeri06] M. Lazzeri and F. Mauri. *Nonadiabatic Kohn Anomaly in a Doped Graphene Monolayer*. Phys. Rev. Lett. **97** (26), 266407 (2006). 109, 110, 111, 113, 220

[Lazzeri08] M. Lazzeri, C. Attaccalite, L. Wirtz, and F. Mauri. *Impact of the electron-electron correlation on phonon dispersion: Failure of LDA and GGA DFT functionals in graphene and graphite*. Phys. Rev. B **78**, 081406 (2008). 23, 24

[Lee08] C. Lee, X. Wei, J. W. Kysar, and J. Hone. *Measurement of the elastic properties and intrinsic strength of monolayer graphene*. Science **321** (5887), 385–388 (2008). 12, 214

[Lee10] C. Lee, H. Yan, L. E. Brus, T. F. Heinz, J. Hone, and S. Ryu. *Anomalous Lattice Vibrations of Single- and Few-Layer* MoS_2. ACS Nano **4** (5), 2695–2700 (2010). 39, 128, 132, 133, 147, 155

[Lee12a] H. S. Lee, S.-W. Min, Y.-G. Chang, M. K. Park, T. Nam, H. Kim, J. H. Kim, S. Ryu, and S. Im. *MoS2 nanosheet phototransistors with thickness-modulated optical energy gap*. Nano Lett. **12** (7), 3695–3700 (2012). 40

[Lee12b] J.-U. Lee, D. Yoon, and H. Cheong. *Estimation of Young's modulus of graphene by Raman spectroscopy*. Nano Lett. **12** (9), 4444–4448 (2012). 121

[Lee12c] J. E. Lee, G. Ahn, J. Shim, Y. S. Lee, and S. Ryu. *Optical separation of mechanical strain from charge doping in graphene*. Nat. Commun. **3**, 1024 (2012). 115, 120, 121, 221, 222, 259

[Lee14a] C.-H. Lee, G.-H. Lee, A. M. van der Zande, W. Chen, Y. Li, M. Han, X. Cui, G. Arefe, C. Nuckolls, T. F. Heinz, J. Guo, J. Hone, and P. Kim. *Atomically thin p–n junctions with van der Waals heterointerfaces*. Nat. Nanotechnol. **9** (9), 676–681 (2014). 46, 47, 51, 52, 182

[Lee14b] J. Lee, W. Bao, L. Ju, P. J. Schuck, F. Wang, and A. Weber-Bargioni. *Switching Individual Quantum Dot Emission through Electrically Controlling Resonant Energy Transfer to Graphene*. Nano Lett. **14**, 7115 (2014). 48, 209

[Lee15a] G.-H. Lee, X. Cui, Y. D. Kim, G. Arefe, X. Zhang, C.-H. Lee, F. Ye, K. Watanabe, T. Taniguchi, P. Kim, et al. *Highly stable, dual-gated MoS2 transistors encapsulated by hexagonal Boron Nitride with gate-controllable contact, resistance, and threshold voltage*. ACS Nano **9** (7), 7019–7026 (2015). 35, 82

[Lee15b] J.-U. Lee, J. Park, Y.-W. Son, and H. Cheong. *Anomalous excitonic resonance Raman effects in few-layered* MoS_2. Nanoscale **7** (7), 3229–3236 (2015). 155, 206

[Lezama14] I. G. Lezama, A. Ubaldini, M. Longobardi, E. Giannini, C. Renner, A. B. Kuzmenko, and A. F. Morpurgo. *Surface transport and band gap structure of exfoliated 2H-*$MoTe_2$ *crystals*. 2D Mater. **1** (2), 021002 (2014). 169, 173

[Lezama15] I. G. Lezama, A. Arora, A. Ubaldini, C. Barreteau, E. Giannini, M. Potemski, and A. F. Morpurgo. *Indirect-to-Direct Band Gap Crossover in Few-Layer* $MoTe_2$. Nano Lett. **15** (4), 2336–2342 (2015). 147, 169, 171, 172

[Li08] Z. Q. Li, E. A. Henriksen, Z. Jiang, Z. Hao, M. C. Martin, P. Kim, H. L. Stormer, and D. N. Basov. *Dirac charge dynamics in graphene by infrared spectroscopy*. Nat. Phys. **4** (7), 532–535 (2008). 28, 29

[Li11] Q. Li, E. H. Hwang, and S. Das Sarma. *Disorder-induced temperature-dependent transport in graphene: Puddles, impurities, activation, and diffusion*. Phys. Rev. B **84** (11), 115442 (2011). 28, 112, 220

[Li12a] H. Li, Q. Zhang, C. C. R. Yap, B. K. Tay, T. H. T. Edwin, A. Olivier, and D. Baillargeat. *From Bulk to Monolayer* MoS_2*: Evolution of Raman Scattering*. Adv. Funct. Mater. **22** (7), 1385–1390 (2012). 128, 132, 155

[Li12b] S.-L. Li, H. Miyazaki, H. Song, H. Kuramochi, S. Nakaharai, and K. Tsukagoshi. *Quantitative Raman spectrum and reliable thickness identification for atomic layers on insulating substrates*. ACS Nano **6** (8), 7381–7388 (2012). 92, 251, 257

[Li13] Y. Li, Y. Rao, K. F. Mak, Y. You, S. Wang, C. R. Dean, and T. F. Heinz. *Probing symmetry properties of few-layer MoS2 and h-BN by optical second-harmonic generation*. Nano Lett. **13** (7), 3329–3333 (2013). 33

[Li14] Y. Li, A. Chernikov, X. Zhang, A. Rigosi, H. M. Hill, A. M. van der Zande, D. A. Chenet, E.-M. Shih, J. Hone, and T. F. Heinz. *Measurement of the optical dielectric function of monolayer transition-metal dichalcogenides:* MoS_2, $MoSe_2$, WS_2, *and* WSe_2. Phys. Rev. B **90**, 205422 (2014). 195, 208

[Liang13] Y. Liang, S. Huang, R. Soklaski, and L. Yang. *Quasiparticle band-edge energy and band offsets of monolayer of molybdenum and tungsten chalcogenides*. Appl. Phys. Lett. **103** (4), 042106 (2013). 44, 45, 200

[Lin15] Y.-C. Lin, H.-P. Komsa, C.-H. Yeh, T. Björkman, Z.-Y. Liang, C.-H. Ho, Y.-S. Huang, P.-W. Chiu, A. V. Krasheninnikov, and K. Suenaga. *Single-Layer ReS2: Two-Dimensional Semiconductor with Tunable In-Plane Anisotropy*. ACS Nano **9** (11), 11249-11257 (2015). 211

[Liu13] J. Liu, Q. Li, Y. Zou, Q. Qian, Y. Jin, G. Li, K. Jiang, and S. Fan. *The Dependence of Graphene Raman D-band on Carrier Density*. Nano Lett. **13** (12), 6170-6175 (2013). 87, 217

[Liu15a] E. Liu, Y. Fu, Y. Wang, Y. Feng, H. Liu, X. Wan, W. Zhou, B. Wang, L. Shao, C.-H. Ho, Y.-S. Huang, Z. Cao, L. Wang, A. Li, J. Zeng, F. Song, X. Wang, Y. Shi, H. Yuan, H. Y. Hwang, Y. Cui, F. Miao, and D. Xing. *Integrated digital inverters based on two-dimensional anisotropic ReS2 field-effect transistors*. Nat. Commun. **6**, 6991 (2015). 210, 211

[Liu15b] X. Liu, T. Galfsky, Z. Sun, F. Xia, E.-c. Lin, Y.-H. Lee, S. Kéna-Cohen, and V. M. Menon. *Strong light–matter coupling in two-dimensional atomic crystals*. Nat. Photonics **9** (1), 30–34 (2015). 49

[Liu16] W. Liu, B. Lee, C. H. Naylor, H.-S. Ee, J. Park, A. C. Johnson, and R. Agarwal. *Strong Exciton–Plasmon Coupling in MoS2 Coupled with Plasmonic Lattice*. Nano Lett. **16** (2), 1262–1269 (2016). 49

[Lopez-Sanchez13] O. Lopez-Sanchez, D. Lembke, M. Kayci, A. Radenovic, and A. Kis. *Ultrasensitive photodetectors based on monolayer MoS2*. Nat. Nanotechnol. **8** (7), 497–501 (2013). 40, 41

[Lorchat16] E. Lorchat, G. Froehlicher, and S. Berciaud. *Splitting of Interlayer Shear Modes and Photon Energy Dependent Anisotropic Raman Response in N-Layer $ReSe_2$ and ReS_2*. ACS Nano **10** (2), 2752–2760 (2016). 10.1021/acsnano.5b07844. 147, 210, 211, 234

[Loudon64] R. Loudon. *The Raman effect in crystals*. Adv. Phys. **13**, 423 (1964). 75, 76, 96, 129

[Lu04] C. Lu, Q. Fu, S. Huang, and J. Liu. *Polymer Electrolyte-Gated Carbon Nanotube Field-Effect Transistor*. Nano Lett. **4** (4), 623-627 (2004). 87, 217

[Lui10] C. H. Lui, K. F. Mak, J. Shan, and T. F. Heinz. *Ultrafast Photoluminescence from Graphene*. Phys. Rev. Lett. **105**, 127404 (2010). 22

[Lui13] C. H. Lui and T. F. Heinz. *Measurement of layer breathing mode vibrations in few-layer graphene*. Phys. Rev. B **87** (12), 121404 (2013). 27

[Lui14] C. H. Lui, Z. Ye, C. Keiser, X. Xiao, and R. He. *Temperature-Activated Layer-Breathing Vibrations in Few-Layer Graphene*. Nano Lett. **14** (8), 4615–4621 (2014). 27, 131, 151

[Lui15] C. H. Lui, Z. Ye, C. Ji, K.-C. Chiu, C.-T. Chou, T. I. Andersen, C. Means-Shively, H. Anderson, J.-M. Wu, T. Kidd, Y.-H. Lee, and R. He. *Observation of interlayer phonon modes in van der Waals heterostructures*. Phys. Rev. B **91**, 165403 (2015). 181

[Luo12] Z. Luo, C. Cong, J. Zhang, Q. Xiong, and T. Yu. *Direct observation of inner and outer G' band double-resonance Raman scattering in free standing graphene*. Appl. Phys. Lett. **100** (24) (2012). 103, 185

[Luo13a] X. Luo, Y. Zhao, J. Zhang, M. Toh, C. Kloc, Q. Xiong, and S. Y. Quek. *Effects of lower symmetry and dimensionality on Raman spectra in two-dimensional WSe_2*. Phys. Rev. B **88**, 195313 (2013). 128, 132, 133, 206

[Luo13b] X. Luo, Y. Zhao, J. Zhang, Q. Xiong, and S. Y. Quek. *Anomalous frequency trends in MoS_2 thin films attributed to surface effects*. Phys. Rev. B **88**, 075320 (2013). 128, 132, 133, 136, 139, 142, 155, 225

[Luryi88] S. Luryi. *Quantum capacitance devices*. Appl. Phys. Lett. **52** (6), 501–503 (1988). 28

[Lyo00] S. K. Lyo. *Energy transfer of excitons between quantum wells separated by a wide barrier*. Phys. Rev. B **62**, 13641–13656 (2000). 48, 210

[Mafra11] D. Mafra, E. Moujaes, S. Doorn, H. Htoon, R. Nunes, and M. Pimenta. *A study of inner process double-resonance Raman scattering in bilayer graphene*. Carbon **49** (5), 1511–1515 (2011). 102

[Mak08] K. F. Mak, M. Y. Sfeir, Y. Wu, C. H. Lui, J. A. Misewich, and T. F. Heinz. *Measurement of the Optical Conductivity of Graphene*. Phys. Rev. Lett. **101**, 196405 (2008). 12, 22, 214

[Mak10] K. F. Mak, C. Lee, J. Hone, J. Shan, and T. F. Heinz. *Atomically Thin MoS_2: A New Direct-Gap Semiconductor*. Phys. Rev. Lett. **105** (13), 136805 (2010). 33, 34, 35, 169, 170, 225

[Mak12a] K. F. Mak, K. He, J. Shan, and T. F. Heinz. *Control of valley polarization in monolayer MoS2 by optical helicity*. Nat. Nanotechnol. **7** (8), 494–498 (2012). 37

[Mak12b] K. F. Mak, L. Ju, F. Wang, and T. F. Heinz. *Optical spectroscopy of graphene: from the far infrared to the ultraviolet*. Solid State Commun. **152** (15), 1341–1349 (2012). 12, 21, 22, 214

[Mak13] K. F. Mak, K. He, C. Lee, G. H. Lee, J. Hone, T. F. Heinz, and J. Shan. *Tightly bound trions in monolayer MoS2*. Nat. Mater. **12** (3), 207–211 (2013). 37

[Mak14] K. F. Mak, K. L. McGill, J. Park, and P. L. McEuen. *The valley Hall effect in MoS_2 transistors*. Science **344** (6191), 1489–1492 (2014). 38

[Mak16] K. F. Mak and J. Shan. *Photonics and optoelectronics of 2D semiconductor transition metal dichalcogenides*. Nat. Photonics **10** (4), 216–226 (2016). 12, 13, 35, 37, 39, 41, 52, 174, 214, 215, 226

[Malard07] L. M. Malard, J. Nilsson, D. C. Elias, J. C. Brant, F. Plentz, E. S. Alves, A. H. Castro Neto, and M. A. Pimenta. *Probing the electronic structure of bilayer graphene by Raman scattering*. Phys. Rev. B **76**, 201401 (2007). 26

[Malard09a] L. M. Malard, M. H. D. Guimarães, D. L. Mafra, M. S. C. Mazzoni, and A. Jorio. *Group-theory analysis of electrons and phonons in N-layer graphene systems*. Phys. Rev. B **79**, 125426 (2009). 57

[Malard09b] L. M. Malard, M. A. Pimenta, G. Dresselhaus, and M. S. Dresselhaus. *Raman spectroscopy in graphene*. Phys. Rep. **473** (5–6), 51 – 87 (2009). 26, 96, 101, 217

[Malard13] L. M. Malard, T. V. Alencar, A. P. M. Barboza, K. F. Mak, and A. M. de Paula. *Observation of intense second harmonic generation from MoS_2 atomic crystals*. Phys. Rev. B **87**, 201401 (2013). 33

[Martin08] J. Martin, N. Akerman, G. Ulbricht, T. Lohmann, J. H. Smet, K. von Klitzing, and A. Yacoby. *Observation of electron–hole puddles in graphene using a scanning single-electron transistor*. Nat. Phys. **4** (2), 144–148 (2008). 112, 113, 118, 220

[Massicotte16a] M. Massicotte, P. Schmidt, F. Vialla, K. Schädler, A. Reserbat-Plantey, K. Watanabe, T. Taniguchi, K. Tielrooij, and F. Koppens. *Picosecond photoresponse in van der Waals heterostructures*. Nat. Nanotechnol. **11** (1), 42–46 (2016). 50, 51, 179, 182

[Massicotte16b] M. Massicotte, P. Schmidt, F. Vialla, K. Watanabe, T. Taniguchi, K. J. Tielrooij, and F. H. L. Koppens. *Photo-thermionic effect in vertical graphene heterostructures*. Nat. Commun. **7**, 12174 (2016). 50

[Maultzsch04a] J. Maultzsch, S. Reich, and C. Thomsen. *Double-resonant Raman scattering in graphite: Interference effects, selection rules, and phonon dispersion*. Phys. Rev. B **70** (15), 155403 (2004). 100, 101

[Maultzsch04b] J. Maultzsch, S. Reich, C. Thomsen, H. Requardt, and P. Ordejón. *Phonon Dispersion in Graphite*. Phys. Rev. Lett. **92**, 075501 (2004). 23, 24

[Maultzsch05] J. Maultzsch, R. Pomraenke, S. Reich, E. Chang, D. Prezzi, A. Ruini, E. Molinari, M. S. Strano, C. Thomsen, and C. Lienau. *Exciton binding energies in carbon nanotubes from two-photon photoluminescence*. Phys. Rev. B **72**, 241402 (2005). 35

[McCreary14] K. M. McCreary, A. T. Hanbicki, J. T. Robinson, E. Cobas, J. C. Culbertson, A. L. Friedman, G. G. Jernigan, and B. T. Jonker. *Large-Area Synthesis of Continuous and Uniform MoS_2 Monolayer Films on Graphene*. Adv. Funct. Mater. **24** (41), 6449–6454 (2014). 186

[McIntyre71] J. McIntyre and D. Aspnes. *Differential reflection spectroscopy of very thin surface films*. Surf. Sci. **24** (2), 417–434 (1971). 35, 160

[McNaught97] A. D. McNaught, A. Wilkinson, et al. *Compendium of chemical terminology. IUPAC recommendations*. Oxford (United Kingdom) Blackwell, 1997. 128

[Meitl06] M. A. Meitl, Z.-T. Zhu, V. Kumar, K. J. Lee, X. Feng, Y. Y. Huang, I. Adesida, R. G. Nuzzo, and J. A. Rogers. *Transfer printing by kinetic control of adhesion to an elastomeric stamp*. Nat. Mater. **5** (1), 33–38 (2006). 81, 82

[Meric08] I. Meric, M. Y. Han, A. F. Young, B. Ozyilmaz, P. Kim, and K. L. Shepard. *Current saturation in zero-bandgap, top-gated graphene field-effect transistors*. Nat. Nanotechnol. **3** (11), 654–659 (2008). 108

[Metten13] D. Metten, F. Federspiel, M. Romeo, and S. Berciaud. *Probing built-in strain in freestanding graphene monolayers by Raman spectroscopy*. physica status solidi (b) **250** (12), 2681–2686 (2013). 121

[Metten14] D. Metten, F. Federspiel, M. Romeo, and S. Berciaud. *All-Optical Blister Test of Suspended Graphene Using Micro-Raman Spectroscopy*. Phys. Rev. Appl **2**, 054008 (2014). 120, 121, 122, 186, 190

[Metten15] D. Metten, G. Froehlicher, and S. Berciaud. *Doping-and interference-free measurement of I2D/IG in suspended monolayer graphene blisters*. physica status solidi (b) **252** (11), 2390–2394 (2015). 118

[Metten16] D. Metten. *Probing the opto-electronic and mechanical properties of suspended graphene membranes by Raman spectroscopy*. PhD thesis, University of Strasbourg, (2016). 13, 26, 221, 222

[Michel12] K. H. Michel and B. Verberck. *Theory of rigid-plane phonon modes in layered crystals*. Phys. Rev. B **85** (9), 094303 (2012). 135, 141, 149, 151

[Miller15] B. Miller, E. Parzinger, A. Vernickel, A. W. Holleitner, and U. Wurstbauer. *Photogating of mono-and few-layer MoS2*. Appl. Phys. Lett. **106** (12), 122103 (2015). 194

[Mitoma13] N. Mitoma, R. Nouchi, and K. Tanigaki. *Photo-oxidation of graphene in the presence of water*. The Journal of Physical Chemistry C **117** (3), 1453–1456 (2013). 198

[Mohiuddin09] T. M. G. Mohiuddin, A. Lombardo, R. R. Nair, A. Bonetti, G. Savini, R. Jalil, N. Bonini, D. M. Basko, C. Galiotis, N. Marzari, K. S. Novoselov, A. K. Geim, and A. C. Ferrari. *Uniaxial strain in graphene by Raman spectroscopy: G peak splitting, Grüneisen parameters, and sample orientation*. Phys. Rev. B **79**, 205433 (2009). 26, 96

[Mohr07] M. Mohr, J. Maultzsch, E. Dobardžić, S. Reich, I. Milošević, M. Damnjanović, A. Bosak, M. Krisch, and C. Thomsen. *Phonon dispersion of graphite by inelastic x-ray scattering*. Phys. Rev. B **76**, 035439 (2007). 23, 24

[Mohr09] M. Mohr, K. Papagelis, J. Maultzsch, and C. Thomsen. *Two-dimensional electronic and vibrational band structure of uniaxially strained graphene from ab initio calculations*. Phys. Rev. B **80**, 205410 (2009). 26, 96

[Mohr10] M. Mohr, J. Maultzsch, and C. Thomsen. *Splitting of the Raman 2D band of graphene subjected to strain*. Phys. Rev. B **82**, 201409 (2010). 102

[Moleca] *Molecular examples for point groups*. https://www.staff.ncl.ac.uk/j.p.goss/symmetry/Molecules_pov.html. Accessed: 2016-08-25. 243, 247

[Molecb] *Point Group Symmetry Character Tables*. http://www.webqc.org/symmetry.php. Accessed: 2016-08-25. 243, 247

[Molina-Sánchez11] A. Molina-Sánchez and L. Wirtz. *Phonons in single-layer and few-layer* MoS_2 *and* WS_2. Phys. Rev. B **84** (15), 155413 (2011). 40, 128, 132, 142

[Molina-Sánchez13] A. Molina-Sánchez, D. Sangalli, K. Hummer, A. Marini, and L. Wirtz. *Effect of spin-orbit interaction on the optical spectra of single-layer, double-layer, and bulk* MoS_2. Phys. Rev. B **88** (4), 045412 (2013). 35

[Moody16] G. Moody, J. Schaibley, and X. Xu. *Exciton dynamics in monolayer transition metal dichalcogenides*. JOSA B **33** (7), C39–C49 (2016). 39, 174, 176, 226

[Mounet05] N. Mounet and N. Marzari. *First-principles determination of the structural, vibrational and thermodynamic properties of diamond, graphite, and derivatives*. Phys. Rev. B **71**, 205214 (2005). 23

[Mouri14] S. Mouri, Y. Miyauchi, M. Toh, W. Zhao, G. Eda, and K. Matsuda. *Nonlinear photoluminescence in atomically thin layered* WSe_2 *arising from diffusion-assisted exciton-exciton annihilation*. Phys. Rev. B **90**, 155449 (2014). 174, 176, 226

[Mueller10] T. Mueller, F. Xia, and P. Avouris. *Graphene photodetectors for high-speed optical communications*. Nat. Photonics **4** (5), 297–301 (2010). 30

[Mueller16] T. Mueller. *TMD-Based Photodetectors, Light Emitters and Photovoltaics*. 2D Materials for Nanoelectronics **17**, 241 (2016). 13, 52, 215

[Mulliken55] R. S. Mulliken. *Report on notation for the spectra of polyatomic molecules*. J. Chem. Phys. **23** (11), 1997 (1955). 56, 244

[Mulliken56] R. S. Mulliken. *Erratum: report on notation for the spectra of polyatomic molecules*. J. Chem. Phys. **24** (5), 1118–1118 (1956). 56, 244

[Nagler15] P. Nagler, G. Plechinger, C. Schüller, and T. Korn. *Observation of anisotropic interlayer Raman modes in few-layer ReS2*. Phys. Status Solidi RRL (2015). 210

[Nair08] R. R. Nair, P. Blake, A. N. Grigorenko, K. S. Novoselov, T. J. Booth, T. Stauber, N. M. Peres, and A. K. Geim. *Fine structure constant defines visual transparency of graphene*. Science **320** (5881), 1308–1308 (2008). 12, 22, 214

[Nan14] H. Nan, Z. Wang, W. Wang, Z. Liang, Y. Lu, Q. Chen, D. He, P. Tan, F. Miao, X. Wang, et al. *Strong photoluminescence enhancement of MoS2 through defect engineering and oxygen bonding*. ACS Nano **8** (6), 5738–5745 (2014). 35, 82

[Nemanich77] R. Nemanich, G. Lucovsky, and S. Solin. *Infrared active optical vibrations of graphite*. Solid State Commun. **23** (2), 117–120 (1977). 61

[Nemes-Incze08] P. Nemes-Incze, Z. Osváth, K. Kamarás, and L. Biró. *Anomalies in thickness measurements of graphene and few layer graphite crystals by tapping mode atomic force microscopy*. Carbon **46** (11), 1435–1442 (2008). 147

[Neumann15] C. Neumann, S. Reichardt, P. Venezuela, M. Drögeler, L. Banszerus, M. Schmitz, K. Watanabe, T. Taniguchi, F. Mauri, B. Beschoten, et al. *Raman spectroscopy as probe of nanometre-scale strain variations in graphene*. Nat. Commun. **6** (2015). 186, 189

[Nicklow72] R. Nicklow, N. Wakabayashi, and H. G. Smith. *Lattice Dynamics of Pyrolytic Graphite*. Phys. Rev. B **5**, 4951–4962 (1972). 23

[Norris08] D. J. Norris, A. L. Efros, and S. C. Erwin. *Doped nanocrystals*. Science **319** (5871), 1776–1779 (2008). 44, 45

[Novoselov04] K. S. Novoselov, A. K. Geim, S. V. Morozov, D. Jiang, Y. Zhang, S. V. Dubonos, I. V. Grigorieva, and A. A. Firsov. *Electric field effect in atomically thin carbon films*. Science **306** (5696), 666–669 (2004). 11, 12, 27, 29, 79, 213

[Novoselov05a] K. S. Novoselov, A. K. Geim, S. V. Morozov, D. Jiang, M. I. Katsnelson, I. V. Grigorieva, S. V. Dubonos, and A. A. Firsov. *Two-dimensional gas of massless Dirac fermions in graphene*. Nature **438** (7065), 197 - 200 (2005). 12, 21, 29, 213

[Novoselov05b] K. Novoselov, D. Jiang, F. Schedin, T. Booth, V. Khotkevich, S. Morozov, and A. Geim. *Two-dimensional atomic crystals*. Proc. Natl. Acad. Sci. U.S.A. **102** (30), 10451–10453 (2005). 11, 79, 213

[Novoselov16] K. Novoselov, A. Mishchenko, A. Carvalho, and A. C. Neto. *2D materials and van der Waals heterostructures*. Science **353** (6298), aac9439 (2016). 42, 43, 52

[Oshima88] C. Oshima, T. Aizawa, R. Souda, Y. Ishizawa, and Y. Sumiyoshi. *Surface phonon dispersion curves of graphite (0001) over the entire energy region*. Solid State Commun. **65** (12), 1601–1604 (1988). 23

[Palummo15] M. Palummo, M. Bernardi, and J. C. Grossman. *Exciton radiative lifetimes in two-dimensional transition metal dichalcogenides*. Nano Lett. **15** (5), 2794–2800 (2015). 37

[Paradisi15] A. Paradisi, J. Biscaras, and A. Shukla. *Space charge induced electrostatic doping of two-dimensional materials: graphene as a case study*. Appl. Phys. Lett. **107** (14), 143103 (2015). 208, 209

[Partoens06] B. Partoens and F. M. Peeters. *From graphene to graphite: Electronic structure around the K point*. Phys. Rev. B **74**, 075404 (2006). 26

[Partoens07] B. Partoens and F. M. Peeters. *Normal and Dirac fermions in graphene multilayers: Tight-binding description of the electronic structure*. Phys. Rev. B **75**, 193402 (2007). 26

[Peres06] N. M. R. Peres, A. H. Castro Neto, and F. Guinea. *Conductance quantization in mesoscopic graphene*. Phys. Rev. B **73**, 195411 (2006). 29

[Pierucci16a] D. Pierucci, H. Henck, J. Avila, A. Balan, C. H. Naylor, G. Patriarche, Y. J. Dappe, M. G. Silly, F. Sirotti, A. C. Johnson, et al. *Band alignment and minigaps in monolayer MoS2-graphene van der Waals heterostructures*. Nano Lett. (2016). 44, 186

[Pierucci16b] D. Pierucci, H. Henck, C. H. Naylor, H. Sediri, E. Lhuillier, A. Balan, J. E. Rault, Y. J. Dappe, F. Bertran, P. Le Fèvre, et al. *Large area molybdenum disulphide-epitaxial graphene vertical Van der Waals heterostructures*. Sci. Rep. **6**, 26656 (2016). 182, 187

[Pisana07] S. Pisana, M. Lazzeri, C. Casiraghi, K. S. Novoselov, A. K. Geim, A. C. Ferrari, and F. Mauri. *Breakdown of the adiabatic Born-Oppenheimer approximation in graphene*. Nat. Mater. **6** (3), 198–201 (2007). 26, 106, 109, 110, 111, 113, 220

[Piscanec04] S. Piscanec, M. Lazzeri, F. Mauri, A. C. Ferrari, and J. Robertson. *Kohn Anomalies and Electron-Phonon Interactions in Graphite*. Phys. Rev. Lett. **93**, 185503 (2004). 23, 104, 109, 220

[Piscanec07] S. Piscanec, M. Lazzeri, J. Robertson, A. C. Ferrari, and F. Mauri. *Optical phonons in carbon nanotubes: Kohn anomalies, Peierls distortions, and dynamic effects*. Phys. Rev. B **75**, 035427 (2007). 109

[Pizzocchero16] F. Pizzocchero, L. Gammelgaard, B. S. Jessen, J. M. Caridad, L. Wang, J. Hone, P. Bøggild, and T. J. Booth. *The hot pick-up technique for batch assembly of van der Waals heterostructures*. Nat. Commun. **7**, 11894 (2016). 43, 85

[Plechinger12] G. Plechinger, S. Heydrich, J. Eroms, D. Weiss, C. Schüller, and T. Korn. *Raman spectroscopy of the interlayer shear mode in few-layer* MoS_2 *flakes*. Appl. Phys. Lett. **101** (10), 101906 (2012). 128, 131, 225

[Plechinger15] G. Plechinger, P. Nagler, J. Kraus, N. Paradiso, C. Strunk, C. Schüller, and T. Korn. *Identification of excitons, trions and biexcitons in single-layer WS2*. physica status solidi (RRL)-Rapid Research Letters **9** (8), 457–461 (2015). 37

[Polyzos15] I. Polyzos, M. Bianchi, L. Rizzi, E. N. Koukaras, J. Parthenios, K. Papagelis, R. Sordan, and C. Galiotis. *Suspended monolayer graphene under true uniaxial deformation*. Nanoscale **7** (30), 13033–13042 (2015). 96

[Ponomarenko13] L. Ponomarenko, R. Gorbachev, G. Yu, D. Elias, R. Jalil, A. Patel, A. Mishchenko, A. Mayorov, C. Woods, J. Wallbank, et al. *Cloning of Dirac fermions in graphene superlattices*. Nature **497** (7451), 594–597 (2013). 12, 214

[Pospischil13] A. Pospischil, M. Humer, M. M. Furchi, D. Bachmann, R. Guider, T. Fromherz, and T. Mueller. *CMOS-compatible graphene photodetector covering all optical communication bands*. Nat. Photonics **7** (11), 892–896 (2013). 30

[Pospischil14] A. Pospischil, M. M. Furchi, and T. Mueller. *Solar-energy conversion and light emission in an atomic monolayer p-n diode*. Nat. Nanotechnol. **advance online publication** (2014). 40, 41

[Prasai15] D. Prasai, A. R. Klots, A. Newaz, J. S. Niezgoda, N. J. Orfield, C. A. Escobar, A. Wynn, A. Efimov, G. K. Jennings, S. J. Rosenthal, et al. *Electrical Control of near-Field Energy Transfer between Quantum Dots and Two-Dimensional Semiconductors*. Nano Lett. **15** (7), 4374–4380 (2015). 48

[Prins14] F. Prins, A. J. Goodman, and W. A. Tisdale. *Reduced dielectric screening and enhanced energy transfer in single-and few-layer MoS2*. Nano Lett. **14** (11), 6087–6091 (2014). 48

[Qiu12] H. Qiu, L. Pan, Z. Yao, J. Li, Y. Shi, and X. Wang. *Electrical characterization of back-gated bi-layer MoS2 field-effect transistors and the effect of ambient on their performances*. Appl. Phys. Lett. **100** (12), 123104 (2012). 35, 82

[Qiu13] D. Y. Qiu, F. H. da Jornada, and S. G. Louie. *Optical Spectrum of* MoS_2*: Many-Body Effects and Diversity of Exciton States*. Phys. Rev. Lett. **111**, 216805 (2013). 35

[Raja16] A. Raja, A. Montoya-Castillo, J. Zultak, X.-X. Zhang, Z. Ye, C. Roquelet, D. A. Chenet, A. M. van der Zande, P. Huang, S. Jockusch, et al. *Energy transfer from quantum dots to graphene and MoS2: The role of absorption and screening in two-dimensional materials*. Nano Lett. **16** (4), 2328–2333 (2016). 48

[Ramasubramaniam12] A. Ramasubramaniam. *Large excitonic effects in monolayers of molybdenum and tungsten dichalcogenides*. Phys. Rev. B **86**, 115409 (2012). 35

[Reich02] S. Reich, J. Maultzsch, C. Thomsen, and P. Ordejón. *Tight-binding description of graphene*. Phys. Rev. B **66**, 035412 (2002). 19

[Reich04] S. Reich and C. Thomsen. *Raman spectroscopy of graphite*. Philosophical Transactions of the Royal Society of London A: Mathematical, Physical and Engineering Sciences **362** (1824), 2271–2288 (2004). 24

[Reich08] S. Reich, C. Thomsen, and J. Maultzsch. *Carbon nanotubes: basic concepts and physical properties*. John Wiley & Sons, 2008. 73

[Ribeiro-Soares14] J. Ribeiro-Soares, R. M. Almeida, E. B. Barros, P. T. Araujo, M. S. Dresselhaus, L. G. Cançado, and A. Jorio. *Group theory analysis of phonons in two-dimensional transition metal dichalcogenides*. Phys. Rev. B **90** (11), 115438 (2014). 32, 33, 63, 64, 65

[Rivera15] P. Rivera, J. R. Schaibley, A. M. Jones, J. S. Ross, S. Wu, G. Aivazian, P. Klement, K. Seyler, G. Clark, N. J. Ghimire, et al. *Observation of long-lived interlayer excitons in monolayer MoSe2–WSe2 heterostructures*. Nat. Commun. **6** (2015). 46, 47, 52, 182

[Rivera16] P. Rivera, K. L. Seyler, H. Yu, J. R. Schaibley, J. Yan, D. G. Mandrus, W. Yao, and X. Xu. *Valley-polarized exciton dynamics in a 2D semiconductor heterostructure*. Science **351** (6274), 688–691 (2016). 46, 47

[Robert16a] C. Robert, D. Lagarde, F. Cadiz, G. Wang, B. Lassagne, T. Amand, A. Balocchi, P. Renucci, S. Tongay, B. Urbaszek, and X. Marie. *Exciton radiative lifetime in transition metal dichalcogenide monolayers*. Phys. Rev. B **93**, 205423 (2016). 37, 39, 176

[Robert16b] C. Robert, R. Picard, D. Lagarde, G. Wang, J. P. Echeverry, F. Cadiz, P. Renucci, A. Högele, T. Amand, X. Marie, I. C. Gerber, and B. Urbaszek. *Excitonic properties of semiconducting monolayer and bilayer* $MoTe_2$. Phys. Rev. B **94**, 155425 (2016). 171, 172

[Robin16] A. Robin, E. Lhuillier, X. Xu, S. Ithurria, H. Aubin, A. Ouerghi, and B. Dubertret. *Engineering the Charge Transfer in all 2D Graphene-Nanoplatelets Heterostructure Photodetectors*. Sci. Rep. **6** (2016). 49, 50

[Roddaro07] S. Roddaro, P. Pingue, V. Piazza, V. Pellegrini, and F. Beltram. *The optical visibility of graphene: interference colors of ultrathin graphite on SiO2*. Nano Lett. **7** (9), 2707–2710 (2007). 81, 92

[Roquelet10] C. Roquelet, D. Garrot, J.-S. Lauret, C. Voisin, V. Alain-Rizzo, P. Roussignol, J. Delaire, and E. Deleporte. *Quantum efficiency of energy transfer in noncovalent carbon nanotube/porphyrin compounds*. Appl. Phys. Lett. **97** (14), 141918 (2010). 200, 233

[Rosencher02] E. Rosencher and B. Vinter. *Optoelectronics*. Cambridge University Press, 2002. 44, 52

[Ross13] J. S. Ross, S. Wu, H. Yu, N. J. Ghimire, A. M. Jones, G. Aivazian, J. Yan, D. G. Mandrus, D. Xiao, W. Yao, et al. *Electrical control of neutral and charged excitons in a monolayer semiconductor*. Nat. Commun. **4**, 1474 (2013). 36, 37, 182, 195, 210

[Ross14] J. S. Ross, P. Klement, A. M. Jones, N. J. Ghimire, J. Yan, D. G. Mandrus, T. Taniguchi, K. Watanabe, K. Kitamura, W. Yao, D. H. Cobden, and X. Xu. *Electrically tunable excitonic light-emitting diodes based on monolayer* WSe_2 *p-n junctions*. Nat. Nanotechnol. **advance online publication** (2014). 40

[Ruppert14] C. Ruppert, O. B. Aslan, and T. F. Heinz. *Optical Properties and Band Gap of Single- and Few-Layer* $MoTe_2$ *Crystals*. Nano Lett. **14** (11), 6231–6236 (2014). 34, 39, 132, 147, 169, 170, 171, 172, 173, 225

[Ryu10] S. Ryu, L. Liu, S. Berciaud, Y.-J. Yu, H. Liu, P. Kim, G. W. Flynn, and L. E. Brus. *Atmospheric Oxygen Binding and Hole Doping in Deformed Graphene on a* SiO_2 *Substrate*. Nano Lett. **10** (12), 4944-4951 (2010). 191

[Sallen12] G. Sallen, L. Bouet, X. Marie, G. Wang, C. R. Zhu, W. P. Han, Y. Lu, P. H. Tan, T. Amand, B. L. Liu, and B. Urbaszek. *Robust optical emission polarization in* MoS_2 *monolayers through selective valley excitation*. Phys. Rev. B **86**, 081301 (2012). 37

[Scheuschner15] N. Scheuschner, R. Gillen, M. Staiger, and J. Maultzsch. *Interlayer resonant Raman modes in few-layer* MoS_2. Phys. Rev. B **91**, 235409 (2015). 206

[Schoenflies91] A. Schoenflies. *Krystallsysteme und Krystallstructur*. Druck und Verlag von BG Teubner, 1891. 56, 237, 238

[Shi13] H. Shi, R. Yan, S. Bertolazzi, J. Brivio, B. Gao, A. Kis, D. Jena, H. G. Xing, and L. Huang. *Exciton dynamics in suspended monolayer and few-layer MoS2 2D crystals*. ACS Nano **7** (2), 1072–1080 (2013). 37

[Shim14] G. W. Shim, K. Yoo, S.-B. Seo, J. Shin, D. Y. Jung, I.-S. Kang, C. W. Ahn, B. J. Cho, and S.-Y. Choi. *Large-area single-layer* $MoSe_2$ *and its van der Waals heterostructures*. ACS Nano **8** (7), 6655–6662 (2014). 182, 187

[Shimotani06] H. Shimotani, H. Asanuma, J. Takeya, and Y. Iwasa. *Electrolyte-gated charge accumulation in organic single crystals*. Appl. Phys. Lett. **89** (20), 203501 (2006). 109, 219

[Siebentritt97] S. Siebentritt, R. Pues, K.-H. Rieder, and A. M. Shikin. *Surface phonon dispersion in graphite and in a lanthanum graphite intercalation compound*. Phys. Rev. B **55**, 7927–7934 (1997). 23

[Song16] Q. J. Song, Q. H. Tan, X. Zhang, J. B. Wu, B. W. Sheng, Y. Wan, X. Q. Wang, L. Dai, and P. H. Tan. *Physical origin of Davydov splitting and resonant Raman spectroscopy of Davydov components in multilayer* $MoTe_2$. Phys. Rev. B **93**, 115409 (2016). 151, 154, 159, 160, 161, 206

[Soubelet16] P. Soubelet, A. E. Bruchhausen, A. Fainstein, K. Nogajewski, and C. Faugeras. *Resonance effects in the Raman scattering of monolayer and few-layer* $MoSe_2$. Phys. Rev. B **93**, 155407 (2016). 144, 158, 206

[Splendiani10] A. Splendiani, L. Sun, Y. Zhang, T. Li, J. Kim, C.-Y. Chim, G. Galli, and F. Wang. *Emerging Photoluminescence in Monolayer* MoS_2. Nano Lett. **10** (4), 1271–1275 (2010). 33, 34, 169, 225

[Staiger15] M. Staiger, R. Gillen, N. Scheuschner, O. Ochedowski, F. Kampmann, M. Schleberger, C. Thomsen, and J. Maultzsch. *Splitting of monolayer out-of-plane* $A_1^{'}$ *Raman mode in few-layer* WS_2. Phys. Rev. B **91**, 195419 (2015). 128, 155, 225

[Sun14] D. Sun, Y. Rao, G. A. Reider, G. Chen, Y. You, L. Brézin, A. R. Harutyunyan, and T. F. Heinz. *Observation of Rapid Exciton–Exciton Annihilation in Monolayer Molybdenum Disulfide*. Nano Lett. **14** (10), 5625-5629 (2014). 174, 176, 177, 226

[Sundaram13] R. Sundaram, M. Engel, A. Lombardo, R. Krupke, A. Ferrari, P. Avouris, and M. Steiner. *Electroluminescence in single layer MoS2*. Nano Lett. **13** (4), 1416–1421 (2013). 40

[Symmo] *Symétrie moléculaire. Eléments de théorie des groupes.* http://www.lct.jussieu.fr/pagesperso/chaquin/5.GroupesSymetrie.pdf. Accessed: 2016-08-27. 237

[Tan07] Y.-W. Tan, Y. Zhang, K. Bolotin, Y. Zhao, S. Adam, E. H. Hwang, S. Das Sarma, H. L. Stormer, and P. Kim. *Measurement of Scattering Rate and Minimum Conductivity in Graphene*. Phys. Rev. Lett. **99**, 246803 (2007). 29

[Tan12] P. H. Tan, W. P. Han, W. J. Zhao, Z. H. Wu, K. Chang, H. Wang, Y. F. Wang, N. Bonini, N. Marzari, and N. Pugno. *The shear mode of multilayer graphene*. Nat. Mater. **11** (4), 294–300 (2012). 27, 131, 149, 151

[Taylor96] R. Taylor, R. Adams, J. Ryan, and R. Park. *Exciton recombination dynamics in ZnCdSe/ZnSe quantum wells*. J. Cryst. Growth **159** (1–4), 822 - 825 (1996). 177

[Taylor02] P. L. Taylor and O. Heinonen. *A quantum approach to condensed matter physics*. Cambridge University Press, 2002. 109

[Thomsen00] C. Thomsen and S. Reich. *Double Resonant Raman Scattering in Graphite*. Phys. Rev. Lett. **85** (24), 5214–5217 (2000). 99, 101, 104

[Tiberj13] A. Tiberj, M. Rubio-Roy, M. Paillet, J.-R. Huntzinger, P. Landois, M. Mikolasek, S. Contreras, J.-L. Sauvajol, E. Dujardin, and A.-A. Zahab. *Reversible optical doping of graphene*. Sci. Rep. **3** (2013). 120

[Tielrooij13] K. Tielrooij, J. Song, S. A. Jensen, A. Centeno, A. Pesquera, A. Z. Elorza, M. Bonn, L. Levitov, and F. Koppens. *Photoexcitation cascade and multiple hot-carrier generation in graphene*. Nat. Phys. **9** (4), 248–252 (2013). 22, 30

[Tielrooij15] K. Tielrooij, L. Orona, A. Ferrier, M. Badioli, G. Navickaite, S. Coop, S. Nanot, B. Kalinic, T. Cesca, L. Gaudreau, et al. *Electrical control of optical emitter relaxation pathways enabled by graphene*. Nat. Phys. **11** (3), 281–287 (2015). 48, 209

[Tiong99] K. Tiong, C. Ho, and Y. Huang. *The electrical transport properties of ReS2 and ReSe2 layered crystals*. Solid State Commun. **111** (11), 635 - 640 (1999). 32, 147, 210, 211

[Tisler13] J. Tisler, T. Oeckinghaus, R. J. Stöhr, R. Kolesov, R. Reuter, F. Reinhard, and J. Wrachtrup. *Single defect center scanning near-field optical microscopy on graphene*. Nano Lett. **13** (7), 3152–3156 (2013). 47, 233

[Tongay12] S. Tongay, J. Zhou, C. Ataca, K. Lo, T. S. Matthews, J. Li, J. C. Grossman, and J. Wu. *Thermally Driven Crossover from Indirect toward Direct Bandgap in 2D Semiconductors:* $MoSe_2$ *versus* MoS_2. Nano Lett. **12** (11), 5576–5580 (2012). 171

[Tongay13] S. Tongay, J. Zhou, C. Ataca, J. Liu, J. S. Kang, T. S. Matthews, L. You, J. Li, J. C. Grossman, and J. Wu. *Broad-range modulation of light emission in two-dimensional semiconductors by molecular physisorption gating*. Nano Lett. **13** (6), 2831–2836 (2013). 35, 82

[Tongay14] S. Tongay, H. Sahin, C. Ko, A. Luce, W. Fan, K. Liu, J. Zhou, Y.-S. Huang, C.-H. Ho, J. Yan, D. F. Ogletree, S. Aloni, J. Ji, S. Li, J. Li, F. M. Peeters, and J. Wu. *Monolayer behaviour in bulk* ReS_2 *due to electronic and vibrational decoupling*. Nat. Commun. **5**, 3252 (2014). 211

[Tonndorf13] P. Tonndorf, R. Schmidt, P. Böttger, X. Zhang, J. Börner, A. Liebig, M. Albrecht, C. Kloc, O. Gordan, D. R. T. Zahn, S. Michaelis de Vasconcellos, and R. Bratschitsch. *Photoluminescence emission and Raman response of monolayer* MoS_2, $MoSe_2$, *and* WSe_2. Opt. Express **21** (4), 4908 (2013). 34, 35, 128, 132, 144, 155, 169, 170, 174, 182, 225, 232

[Tuinstra70] F. Tuinstra and J. L. Koenig. *Raman Spectrum of Graphite*. The Journal of Chemical Physics **53** (3), 1126-1130 (1970). 24, 99

[Ugeda14] M. M. Ugeda, A. J. Bradley, S.-F. Shi, F. H. da Jornada, Y. Zhang, D. Y. Qiu, W. Ruan, S.-K. Mo, Z. Hussain, Z.-X. Shen, F. Wang, S. G. Louie, and M. F. Crommie. *Giant bandgap renormalization and excitonic effects in a monolayer transition metal dichalcogenide semiconductor*. Nat. Mater. **5**, 1091 (2014). 35, 44, 45, 195

[Umari01] P. Umari, A. Pasquarello, and A. Dal Corso. *Raman scattering intensities in α-quartz: A first-principles investigation*. Phys. Rev. B **63**, 094305 (2001). 142

[Venezuela11] P. Venezuela, M. Lazzeri, and F. Mauri. *Theory of double-resonant Raman spectra in graphene: Intensity and line shape of defect-induced and two-phonon bands*. Phys. Rev. B **84** (3), 035433 (2011). 23, 24, 100, 101, 102, 104, 117

[Vicarelli12] L. Vicarelli, M. Vitiello, D. Coquillat, A. Lombardo, A. Ferrari, W. Knap, M. Polini, V. Pellegrini, and A. Tredicucci. *Graphene field-effect transistors as room-temperature terahertz detectors*. Nat. Mater. **11** (10), 865–871 (2012). 30

[Wallace47] P. R. Wallace. *The band theory of graphite*. Phys. Rev. **71** (9), 622 (1947). 19

[Wang05] F. Wang, G. Dukovic, L. E. Brus, and T. F. Heinz. *The optical resonances in carbon nanotubes arise from excitons*. Science **308** (5723), 838–841 (2005). 35

[Wang08] F. Wang, Y. Zhang, C. Tian, C. Girit, A. Zettl, M. Crommie, and Y. Shen. *Gate-variable optical transitions in graphene*. Science **320** (5873), 206-209 (2008). 29

[Wang12] Q. H. Wang, K. Kalantar-Zadeh, A. Kis, J. N. Coleman, and M. S. Strano. *Electronics and optoelectronics of two-dimensional transition metal dichalcogenides*. Nat. Nanotechnol. **7** (11), 699–712 (2012). 12, 214

[Wang13] L. Wang, I. Meric, P. Huang, Q. Gao, Y. Gao, H. Tran, T. Taniguchi, K. Watanabe, L. Campos, D. Muller, et al. *One-dimensional electrical contact to a two-dimensional material*. Science **342** (6158), 614–617 (2013). 43

[Wang14] G. Wang, L. Bouet, D. Lagarde, M. Vidal, A. Balocchi, T. Amand, X. Marie, and B. Urbaszek. *Valley dynamics probed through charged and neutral exciton emission in monolayer* WSe_2. Phys. Rev. B **90**, 075413 (2014). 37

[Wang15a] G. Wang, I. Gerber, L. Bouet, D. Lagarde, A. Balocchi, M. Vidal, T. Amand, X. Marie, and B. Urbaszek. *Exciton states in monolayer* $MoSe_2$*: impact on interband transitions*. 2D Mater. **2** (4), 045005 (2015). 182, 195

[Wang15b] G. Wang, X. Marie, I. Gerber, T. Amand, D. Lagarde, L. Bouet, M. Vidal, A. Balocchi, and B. Urbaszek. *Giant Enhancement of the Optical Second-Harmonic Emission of* WSe_2 *Monolayers by Laser Excitation at Exciton Resonances*. Phys. Rev. Lett. **114**, 097403 (2015). 35, 36

[Wang15c] G. Wang, E. Palleau, T. Amand, S. Tongay, X. Marie, and B. Urbaszek. *Polarization and time-resolved photoluminescence spectroscopy of excitons in* $MoSe_2$ *monolayers*. Appl. Phys. Lett. **106** (11) (2015). 182, 195

[Wang16a] K. Wang, B. Huang, M. Tian, F. Ceballos, M.-W. Lin, M. Mahjouri-Samani, A. Boulesbaa, A. A. Puretzky, C. M. Rouleau, M. Yoon, et al. *Interlayer Coupling*

in Twisted WSe2/WS2 Bilayer Heterostructures Revealed by Optical Spectroscopy. ACS Nano **10** (7), 6612–6622 (2016). 46, 47

[Wang16b] S. Wang, S.-L. Li, T. Chervy, A. Shalabney, S. Azzini, E. Orgiu, J. A. Hutchison, C. Genet, P. Samorì, and T. W. Ebbesen. *Coherent Coupling of WS2 Monolayers with Metallic Photonic Nanostructures at Room Temperature*. Nano Lett. (2016). 49

[Wang16c] Z. Wang, Z. Dong, Y. Gu, Y.-H. Chang, L. Zhang, L.-J. Li, W. Zhao, G. Eda, W. Zhang, G. Grinblat, et al. *Giant photoluminescence enhancement in tungsten-diselenide–gold plasmonic hybrid structures*. Nat. Commun. **7** (2016). 49

[Wieting80] T. Wieting, A. Grisel, and F. Levy. *Interlayer bonding and localized charge in $MoSe_2$ and α-$MoTe_2$*. Physica B+ C **99** (1), 337–342 (1980). 128, 129, 137, 142, 223

[Wilson69] J. Wilson and A. Yoffe. *The transition metal dichalcogenides discussion and interpretation of the observed optical, electrical and structural properties*. Adv. Phys. **18** (73), 193–335 (1969). 12, 32, 35, 63, 210

[Wirtz04] L. Wirtz and A. Rubio. *The phonon dispersion of graphite revisited*. Solid State Commun. **131** (3), 141–152 (2004). 23

[Wirtz05] L. Wirtz, M. Lazzeri, F. Mauri, and A. Rubio. *Raman spectra of BN nanotubes: Ab initio and bond-polarizability model calculations*. Phys. Rev. B **71**, 241402 (2005). 142

[Withers15] F. Withers, O. Del Pozo-Zamudio, A. Mishchenko, A. P. Rooney, A. Gholinia, K. Watanabe, T. Taniguchi, S. J. Haigh, A. K. Geim, A. I. Tartakovskii, and K. S. Novoselov. *Light-emitting diodes by band-structure engineering in van der Waals heterostructures*. Nat. Mater. **14** (3), 301 (2015). 50, 51

[Wolverson14] D. Wolverson, S. Crampin, A. S. Kazemi, A. Ilie, and S. J. Bending. *Raman Spectra of Monolayer, Few-Layer, and Bulk $ReSe_2$: An Anisotropic Layered Semiconductor*. ACS Nano **8** (11), 11154 (2014). 210

[Xia09] F. Xia, T. Mueller, Y.-m. Lin, A. Valdes-Garcia, and P. Avouris. *Ultrafast graphene photodetector*. Nat. Nanotechnol. **4** (12), 839–843 (2009). 30

[Xia14] F. Xia, H. Wang, D. Xiao, M. Dubey, and A. Ramasubramaniam. *Two-dimensional material nanophotonics*. Nat. Photonics **8** (12), 899–907 (2014). 12, 13, 214, 215

[Xu09] X. Xu, N. M. Gabor, J. S. Alden, A. M. van der Zande, and P. L. McEuen. *Photothermoelectric effect at a graphene interface junction*. Nano Lett. **10** (2), 562–566 (2009). 30

[Xu11a] H. Xu, Z. Zhang, and L.-M. Peng. *Measurements and microscopic model of quantum capacitance in graphene*. Appl. Phys. Lett. **98** (13), 133122 (2011). 112, 220

[Xu11b] H. Xu, Z. Zhang, Z. Wang, S. Wang, X. Liang, and L.-M. Peng. *Quantum Capacitance Limited Vertical Scaling of Graphene Field-Effect Transistor*. ACS Nano **5** (3), 2340–2347 (2011). 108, 109, 219

[Xu13] M. Xu, T. Liang, M. Shi, and H. Chen. *Graphene-Like Two-Dimensional Materials*. Chem. Rev. **113** (5), 3766-3798 (2013). 12, 32

[Xu14] X. Xu, W. Yao, D. Xiao, and T. F. Heinz. *Spin and pseudospins in layered transition metal dichalcogenides*. Nat. Phys. **10** (5), 343–350 (2014). 12, 37, 38, 214

[Xue11] J. Xue, J. Sanchez-Yamagishi, D. Bulmash, P. Jacquod, A. Deshpande, K. Watanabe, T. Taniguchi, P. Jarillo-Herrero, and B. J. LeRoy. *Scanning tunnelling microscopy and spectroscopy of ultra-flat graphene on hexagonal boron nitride*. Nat. Mater. **10** (4), 282–285 (2011). 113, 118, 220

[Yamamoto14] M. Yamamoto, S. T. Wang, M. Ni, Y.-F. Lin, S.-L. Li, S. Aikawa, W.-B. Jian, K. Ueno, K. Wakabayashi, and K. Tsukagoshi. *Strong Enhancement of Raman Scattering from a Bulk-Inactive Vibrational Mode in Few-Layer* $MoTe_2$. ACS Nano **8** (4), 3895–3903 (2014). 128, 129, 132, 133, 147, 223

[Yan07] J. Yan, Y. Zhang, P. Kim, and A. Pinczuk. *Electric Field Effect Tuning of Electron-Phonon Coupling in Graphene*. Phys. Rev. Lett. **98** (16), 166802 (2007). 26, 106, 109, 111, 113

[Yan08a] J.-A. Yan, W. Y. Ruan, and M. Y. Chou. *Phonon dispersions and vibrational properties of monolayer, bilayer, and trilayer graphene: Density-functional perturbation theory*. Phys. Rev. B **77**, 125401 (2008). 23

[Yan08b] J. Yan, E. Henriksen, P. Kim, and A. Pinczuk. *Observation of Anomalous Phonon Softening in Bilayer Graphene*. Phys. Rev. Lett. **101**, 136804 (2008). 109, 111, 113

[Yanagisawa05] H. Yanagisawa, T. Tanaka, Y. Ishida, M. Matsue, E. Rokuta, S. Otani, and C. Oshima. *Analysis of phonons in graphene sheets by means of HREELS measurement and ab initio calculation*. Surf. Interface Anal. **37** (2), 133–136 (2005). 23

[Yang15] J. Yang, T. Lü, Y. W. Myint, J. Pei, D. Macdonald, J.-C. Zheng, and Y. Lu. *Robust Excitons and Trions in Monolayer* $MoTe_2$. ACS Nano **9** (6), 6603–6609 (2015). 37, 39, 169, 172

[Ye14] Z. Ye, T. Cao, K. O'Brien, H. Zhu, X. Yin, Y. Wang, S. G. Louie, and X. Zhang. *Probing excitonic dark states in single-layer tungsten disulphide*. Nature **513** (7517), 214–218 (2014). 35

[Yin11] Z. Yin, H. Li, H. Li, L. Jiang, Y. Shi, Y. Sun, G. Lu, Q. Zhang, X. Chen, and H. Zhang. *Single-layer MoS2 phototransistors*. ACS Nano **6** (1), 74–80 (2011). 40

[Yoon09] D. Yoon, H. Moon, Y.-W. Son, J. S. Choi, B. H. Park, Y. H. Cha, Y. D. Kim, and H. Cheong. *Interference effect on Raman spectrum of graphene on SiO_2/Si*. Phys. Rev. B **80** (12), 125422 (2009). 92, 251, 257

[Yoon11] D. Yoon, Y.-W. Son, and H. Cheong. *Strain-Dependent Splitting of the Double-Resonance Raman Scattering Band in Graphene*. Phys. Rev. Lett. **106**, 155502 (2011). 102

[You15] Y. You, X.-X. Zhang, T. C. Berkelbach, M. S. Hybertsen, D. R. Reichman, and T. F. Heinz. *Observation of biexcitons in monolayer WSe_2*. Nat. Phys. **11** (6), 477–481 (2015). 37, 174

[Yu09] Y.-J. Yu, Y. Zhao, S. Ryu, L. E. Brus, K. S. Kim, and P. Kim. *Tuning the graphene work function by electric field effect*. Nano Lett. **9** (10), 3430–3434 (2009). 44, 45, 200

[Yu10] P. Yu and M. Cardona. *Fundamentals of semiconductors: physics and materials properties*. Springer Science & Business Media, 2010. 55, 67, 70, 72, 73, 75, 237

[Yu13] W. J. Yu, Y. Liu, H. Zhou, A. Yin, Z. Li, Y. Huang, and X. Duan. *Highly efficient gate-tunable photocurrent generation in vertical heterostructures of layered materials*. Nat. Nanotechnol. **8** (12), 952–958 (2013). 49

[Yu14] Y. Yu, S. Hu, L. Su, L. Huang, Y. Liu, Z. Jin, A. A. Purezky, D. B. Geohegan, K. W. Kim, Y. Zhang, et al. *Equally efficient interlayer exciton relaxation and improved absorption in epitaxial and nonepitaxial MoS2/WS2 heterostructures*. Nano Lett. **15** (1), 486–491 (2014). 46, 182

[Yu15] H. Yu, Y. Wang, Q. Tong, X. Xu, and W. Yao. *Anomalous Light Cones and Valley Optical Selection Rules of Interlayer Excitons in Twisted Heterobilayers*. Phys. Rev. Lett. **115**, 187002 (2015). 47

[Yu16] Y. Yu, Y. Yu, C. Xu, A. Barrette, K. Gundogdu, and L. Cao. *Fundamental limits of exciton-exciton annihilation for light emission in transition metal dichalcogenide monolayers*. Phys. Rev. B **93**, 201111 (2016). 174, 175, 176, 226

[Yuan15] L. Yuan and L. Huang. *Exciton dynamics and annihilation in WS_2 2D semiconductors*. Nanoscale **7**, 7402-7408 (2015). 174, 176, 226

[Zabel11] J. Zabel, R. R. Nair, A. Ott, T. Georgiou, A. K. Geim, K. S. Novoselov, and C. Casiraghi. *Raman Spectroscopy of Graphene and Bilayer under Biaxial Strain: Bubbles and Balloons*. Nano Lett. **12** (2), 617–621 (2011). 121

[Zeng12] H. Zeng, B. Zhu, K. Liu, J. Fan, X. Cui, and Q. M. Zhang. *Low-frequency Raman modes and electronic excitations in atomically thin* MoS_2 *films*. Phys. Rev. B **86** (24), 241301 (2012). 128, 131, 225

[Zeng13] H. Zeng, G.-B. Liu, J. Dai, Y. Yan, B. Zhu, R. He, L. Xie, S. Xu, X. Chen, W. Yao, et al. *Optical signature of symmetry variations and spin-valley coupling in atomically thin tungsten dichalcogenides*. Sci. Rep. **3** (2013). 33, 170

[Zhang05] Y. Zhang, Y.-W. Tan, H. L. Stormer, and P. Kim. *Experimental observation of the quantum Hall effect and Berry's phase in graphene*. Nature **438** (7065), 201-204 (2005). 12, 27, 29, 213

[Zhang13] X. Zhang, W. P. Han, J. B. Wu, S. Milana, Y. Lu, Q. Q. Li, A. C. Ferrari, and P. H. Tan. *Raman spectroscopy of shear and layer breathing modes in multilayer* MoS_2. Phys. Rev. B **87**, 115413 (2013). 128, 131, 149, 151, 225

[Zhang14] W. Zhang, C.-P. Chuu, J.-K. Huang, C.-H. Chen, M.-L. Tsai, Y.-H. Chang, C.-T. Liang, Y.-Z. Chen, Y.-L. Chueh, J.-H. He, M.-Y. Chou, and L.-J. Li. *Ultrahigh-Gain Photodetectors Based on Atomically Thin Graphene-*MoS_2 *Heterostructures*. Sci. Rep. **4** (2014). 45, 46, 49, 179, 187, 199, 203

[Zhang15a] X.-X. Zhang, Y. You, S. Y. F. Zhao, and T. F. Heinz. *Experimental Evidence for Dark Excitons in Monolayer* WSe_2. Phys. Rev. Lett. **115**, 257403 (2015). 39, 176, 182

[Zhang15b] X. Zhang, X.-F. Qiao, W. Shi, J.-B. Wu, D.-S. Jiang, and P.-H. Tan. *Phonon and Raman scattering of two-dimensional transition metal dichalcogenides from monolayer, multilayer to bulk material*. Chem. Soc. Rev. **44**, 2757 (2015). 13, 39, 155, 215

[Zhang16] K. Zhang, T. Zhang, G. Cheng, T. Li, S. Wang, W. Wei, X. Zhou, W. Yu, Y. Sun, P. Wang, et al. *Interlayer Transition and Infrared Photodetection in Atomically Thin Type-II MoTe2/MoS2 van der Waals Heterostructures*. ACS Nano **10** (3), 3852–3858 (2016). 46

[Zhao10] W. Zhao, P. Tan, J. Zhang, and J. Liu. *Charge transfer and optical phonon mixing in few-layer graphene chemically doped with sulfuric acid*. Phys. Rev. B **82**, 245423 (2010). 27

[Zhao12] W. Zhao, Z. Ghorannevis, L. Chu, M. Toh, C. Kloc, P.-H. Tan, and G. Eda. *Evolution of electronic structure in atomically thin sheets of* WS_2 *and* WSe_2. ACS Nano **7** (1), 791- (2012). 169, 170

[Zhao13] Y. Zhao, X. Luo, H. Li, J. Zhang, P. T. Araujo, C. K. Gan, J. Wu, H. Zhang, S. Y. Quek, M. S. Dresselhaus, and Q. Xiong. *Interlayer Breathing and Shear Modes in Few-Trilayer* MoS_2 *and* WSe_2. Nano Lett. **13** (3), 1007–1015 (2013). 128, 131, 132, 133, 141, 149, 151, 225

[Zhao15] H. Zhao, J. Wu, H. Zhong, Q. Guo, X. Wang, F. Xia, L. Yang, P. Tan, and H. Wang. *Interlayer interactions in anisotropic atomically thin rhenium diselenide*. Nano Res. **8** (11), 3651-3661 (2015). 210, 211

[Zhao16] W. Zhao, S. Wang, B. Liu, I. Verzhbitskiy, S. Li, F. Giustiniano, D. Kozawa, K. P. Loh, K. Matsuda, K. Okamoto, et al. *Exciton–Plasmon Coupling and Electromagnetically Induced Transparency in Monolayer Semiconductors Hybridized with Ag Nanoparticles*. Adv. Mater. (2016). 49

[Zhu15] B. Zhu, X. Chen, and X. Cui. *Exciton Binding Energy of Monolayer* WS_2. Sci. Rep. **5**, 9218 (2015). 35, 36, 174, 226

UNIVERSITÉ DE STRASBOURG

Guillaume FROEHLICHER

ECOLE DOCTORALE pcp

Optical spectroscopy of two-dimensional materials: graphene, transition metal dichalcogenides and van der Waals heterostructures

Résumé

Au cours de ce projet, nous avons utilisé la microspectroscopie Raman et de photoluminescence pour étudier des matériaux bidimensionnels (graphène et dichalcogénures de métaux de transition) et des hétérostructures de van der Waals. Tout d'abord, à l'aide de transistors de graphène munis d'une grille électrochimique, nous montrons que la spectroscopie Raman est un outil extrêmement performant pour caractériser précisément des échantillons de graphène. Puis, nous explorons l'évolution des propriétés physiques de N couches de dichalcogénures de métaux de transition semi-conducteurs, en particulier de ditellurure de molybdène ($MoTe_2$) et de diséléniure de molybdène ($MoSe_2$). Dans ces structures lamellaires, nous observons la séparation de Davydov des phonons optiques au point Γ, que nous décrivons à l'aide d'un modèle de chaîne linéaire. Enfin, nous présentons une étude toute optique du transfert de charge et d'énergie dans des hétérostructures de van der Waals constituées de monocouches de graphène et de $MoSe_2$. Ce travail de thèse met en évidence la riche photophysique de ces matériaux atomiquement fins et leur potentiel en vue de la réalisation de nouveaux dispositifs optoélectroniques.

Mots-clés : spectroscopie Raman, spectroscopie de photoluminescence, matériaux bidimensionnels, graphène, dichalcogénures de métaux de transition, hétérostructures de van der Waals, couplage électron-phonon, séparation de Davydov, excitons, annihilation exciton-exciton, transfert de charge, transfert d'énergie.

Abstract

In this project, we have used micro-Raman and micro-photoluminescence spectroscopy to study two-dimensional materials (graphene and transition metal dichalcogenides) and van der Waals heterostructures. First, using electrochemically-gated graphene transistors, we show that Raman spectroscopy is an extremely sensitive tool for advanced characterizations of graphene samples. Then, we investigate the evolution of the physical properties of N-layer semiconducting transition metal dichalcogenides, in particular molybdenum ditelluride ($MoTe_2$) and molybdenum diselenide ($MoSe_2$). In these layered structures, the Davydov splitting of zone-center optical phonons is observed and remarkably well described by a 'textbook' force constant model. We then describe an all-optical study of interlayer charge and energy transfer in van der Waals heterostructures made of graphene and $MoSe_2$ monolayers. This work sheds light on the very rich photophysics of these atomically thin two-dimensional materials and on their potential in view of optoelectronic applications.

Keywords: Raman spectroscopy, photoluminescence spectroscopy, two-dimensional materials, graphene, transition metal dichalcogenides, van der Waals heterostrucutures, electron-phonon coupling, Davydov splitting, excitons, exciton-exciton annihilation, charge transfer, energy transfer.